INFORMATION TO USERS

.

University of Alberta

Hydraulics of Simple Habitat Structures in Open Channels

by

Hamid Shamloo ⓒ

A thesis submitted to the

Faculty of Graduate Studies and Research

in partial fulfillment of the requirements for the degree of

Doctor of Philosophy

in

Water Resources Engineering

Department of Civil and Environmental Engineering

Edmonton, Alberta

Spring 1997

Canada

<div align="center">

University of Alberta

Library Release Form

</div>

Name of Author : **Hamid Shamloo**

Title of Thesis: **Hydraulics of Simple Habitat Structures in Open Channels**

Degree: **Doctor of Philosophy**

Year this Degree Granted: **1997**

Permission is hereby granted to the university of Alberta Library to reproduce single copies of this thesis and to lend or sell such copies for private, scholarly, or scientific research purposes only.

The author reserves all other publication and other rights in association with the copyright in the thesis, and except as herein before provided, neither the thesis nor any substantial portion thereof may be printed or otherwise reproduced in any material form whatever without the author's prior written permission.

...Hamid Shamloo

Hamid Shamloo

30 masjed alley, Emamat St.

Tehrannow,Tehran,Iran,17416

Date: ...NOV. 6, 1996

University of Alberta

Faculty of Graduate Studies and Research
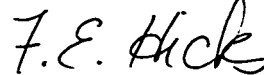
The undersigned certify that they have read, and recommend to the Faculty of Graduate Studies and Research for acceptance, a thesis entitled **Hydraulics of Simple Habitat Structures in Open Channels** submitted by **Hamid Shamloo** in partial fulfillment of the requirements for the degree of **Doctor of Philosophy** in Water Resources Engineering.
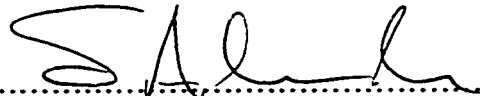
....
Supervisor, Dr. N. Rajaratnam
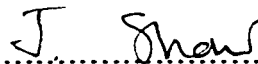
....
Dr. P.M. Steffler
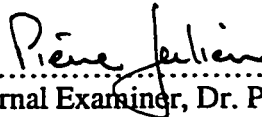
....
Dr. F.E. Hicks

....
Dr. S.D.B. Alexander

....
Dr. J. Shaw

....
External Examiner, Dr. P.Y. Julien

Date: ...4 Nov 96...

بِسْمِ ا للهِ الرَّحْمَنِ الرَّحِيمِ

أَوَلَمْ يَرَ الَّذِينَ كَفَرُوا أَنَّ السَّماوَاتِ
وَالأَرْضَ كَانَتَا رَتْقًا فَفَتَقْنَاهُمَا وَجَعَلْنَا مِنَ الْمَاءِ
كُلَّ شَيْءٍ حَيٍّ أَفَلا يُؤْمِنُونَ .

(سورة الأنبياء ــ آية ٣٠)

In the Name of Allah the Most Gracious, the Most Merciful

"Do not those who disbelieve see that the
heavens and the earth were joined together,
then We (God Almighty) tore them asunder?
And We made of water every living thing.
Will they not then believe?"

The Quran, 21:30

ABSTRACT

Study of the hydraulics of fish habitat structures in rivers, such as the wakes of big rocks in shallow open channel flow, can lead to a better design for these structures. The wakes of simplified obstacles like hemispheres have been studied, including the structure of the flow and the scour around such obstacles. Based on the behaviour of the free surface, four regimes of flow for different relative depths, ratio of flow depth d to body height h, have been recognized and the systems of vortices active in each regime were defined and studied.

Velocity field in the longitudinal and transverse directions was measured on smooth and rough (mobile and rigid) beds. Flow regimes with the relative depth d/h < 1.3 had wider wakes and different scour patterns. The extent of the horse-shoe vortex and downwash of the flow from the top of the body could be found by velocity measurements. Bed shear stress measurements in smooth and rough beds indicated a significant increase in former one. The scour profiles measured at consecutive times prior to the equlibrium state at the sides and in front of the obstacle were found to be similar at different times time and from experiment to experiment and could be related to the depth of scour. Other body shapes such as cubes and natural rocks were also examined. The shape of the scour pattern and its geometry downstream of the body were found to be a function of the flow regime and the shape of the body.

The analysis of velocity profiles behind the body at the plane of symmetry and the transverse direction was satisfactory for a limited distance. Several pier scour prediction methods were examined to determine if they can be used for predicting the scour depth for simple habitat structures. It was found that these methods overestimate the depth of scour for these structures for the relative depths studied and these would would have to be revised to predict the scour for habitat structures. It is recommended that further investigations be performed to study the effects of different parameters on the scour of single rocks as well as rock clusters.

ACKNOWLEDGMENTS

TABLE OF CONTENTS

CHAPTER 8. CONCLUSIONS AND RECOMMENDATIONS

LIST OF TABLES

LIST OF FIGURES

LIST OF SYMBOLS

Note: Symbols which have been used only once or twice are not included in the following list. They have been defined at the appropriate places.

A	wave amplitude (L)
B, B_s, B'_s	constants in velocity profile equations
b	half-width of the wake (L)
$\bar{b}$	distance from the center of the wake where defect velocity is close to zero
C	constant in the law of the wall
C_1, C_2	coefficients in wake equations
C_0	strength of horse-shoe vortex as used in Qadar's equation
c_f	local skin friction coefficient
C_p	pressure coefficient
C_D	drag coefficient
D	obstacle diameter (L)
D_{50}	mean sand diameter (L)
$D_5,...,D_{95}$	sand characteristics (L)
d	depth of flow (L), diameter of the Preston tube (L)
d_s	scour depth measured below the ambient channel bed level (L)
f_{max}	maximun response frequency
F	Froude number
F_D	drag force
g	acceleration due to the gravity (L/T^2)
G	body force in Holmholt's theorem
h	height of the obstacle (L)
h_1,h_2,h_3	pressure heads sensed by different tubes of yaw or pitch probe (L)
h_0	static piezometric pressure (M/T^2/L)

k	characteristic length scale of roughness element (L)
k_s	Nikuradse's equivalent sand roughness (L)
K_s	coefficient of sediment size
K_{max}	maximum wave-number
l	heigth of the cylinder (L)
L	micro scale of turbulence (L)
L_x	macro scale of turbulence (L)
m	arithmatic mean of observed values
n	frequency of the vortex shedding
p	pressure $(M/T^2/L)$
p_s	turbulent fluctuation of pressure $(M/T^2/L)$
P_t	total pressure $(M/T^2/L)$
P_s	static pressure $(M/T^2/L)$
$K_1,...,K_5$	calibration coefficients
$K_{10},...,K_{50}$	calibration coefficients
Q	volumetric water discharge rate (L^3/T)
r	radius of the vortex tube (L) or distance from the center line of the wake
R	Reynolds number, result in uncertainty analysis
S	Strouhal number
S_c	specific gravity
t	time (T)
u, v, w	mean velocity components (L/T)
u', v', w'	fluctuating components of the velocity (L/T)
u_{1m}	maximum velocity defect at the center of the wake (L/T)
u*	shear velocity (L/T)
u*c	critical shear velocity (L/T)
U	average velocity of the flow (L/T)

U_∞	free stream velocity (L/T)
U_y	ambient velocity at a distance y above channel bed (L/T)
U_{2D}	ambient velocity at z=2D (L/T)
V	velocity vector (L/T)
W	flume width (L), uncertainty intervals
x_s	location of the boundary layer separation upstream of the cylinder (L)
x_v	location of the primary vortex upstream of the cylinder (L)
$\overline{x,y,z,}$	dimensionless coordinates for scour hole
y_s	clear water scour (L)
$Y_B,$	characteristic lengths of scour hole (L)
α_r	angle of repose
δ^*	boundary layer displacement thickness (L)
Δ	$(\rho_s - \rho)/\rho$
ϕ	angle of pitch, fluctuation potential
ϕ'	standard deviation of angle of pitch
κ	Karman constant, a measure of vortex sheet strength
θ	angle of yaw
θ'	standard deviation of angle of yaw
ρ	density of water (M/L^3)
ρ_s	density of sediment (M/L^3)
ν	kinematic viscosity (L^2/T)
σ	standard deviation of the grain-size distribution
σ_g	geometric standard deviation of the sand
σ_u	standard deviation of velocity
τ	bed shear stress (M/T^2/L)
τ_c	critical bed shear stress (M/T^2/L)
τ_0	mean bed shear stress (M/T^2/L)

λ	wave length (L) or the ratio of y/b
Γ	circulation in Helmholt's theorem

CHAPTER 1

INTRODUCTION

1.1 Flow Pattern and Scour Around Fish Habitat Structures

Fish habitat structures in rivers are usually built when the lives of migrating or resident fish are endangered by man-made changes, such as river training or construction of dams and other hydraulic structures. A reduction in the discharge downstream of these dams or uniformly rapid flow of trained rivers changes the natural habitat of the fish, e.g., where they can rest, seek refuge and feed. Natural channels are usually divided into fast and slow sections. Fish can rest in slow flow regions and save their energy to move upstream in fast flow regions. The areas of deep flow in rivers, with their lower velocity, provide fish with refuge and a safer place to rest. Fish habitat structures built in streams and rivers provide these feeding and resting areas for fish.

A variety of different habitat structures such as groins, V-weirs, pools, single rocks or clusters of rocks are built in rivers to compensate for the adverse effects of the man-made changes and to produce a better environment for fish. The rocks provide slower and deeper flow inside their scour holes, and provide necessary shadow as a proper refuge for fish. A number of these rocks have been installed singly or in clusters in several streams and rivers in western Canada. At present, there are only rough guidelines for the design of these structures (Lowe, 1992). It would be useful to understand the hydraulics of these structures so they can be reliably designed and built.

The resting and feeding areas provided by these habitat structures are essentially their wakes. In these wakes, the water depths would be increased due to the scour produced and the velocities would be pool-like. Even though wakes have been studied extensively in Fluid Mechanics literature (see for example, Schlichting (1979) and Chang (1970)), most of these studies deal with deeply submerged wakes, which are Reynolds number controlled. In contrast, the wakes produced by the habitat structures are

in shallow water, with the depth of flow "d" approaching the height "h" of the structure. As a result, the flow is modified greatly by the structure, with significant changes to the water surface. These wakes may be affected significantly by the Froude number of the approaching flow, and by the Reynolds number. The erosion around these structures is also an important part of the problem.

The complicated nature of this problem is simplified by studying a single rock instead of a cluster of rocks which are more often used in rivers. To further simplify the problem, a hemisphere is used to simulate the natural rock on the smooth bed. To simulate roughness on the bed, a uniform sand bed is used to produce erosion around the body.

1.2   Objectives of This Thesis

In this study the focus is on flow patterns and the vortex systems around mounted obstacles on the bed and their scour patterns. Objectives of this study are:

(a)   A detailed visualization of the flow patterns, vortex systems, wake of the body and scour patterns under the effects of relative depth of the flow in comparison with other classes of flows and obstacles studied in Hydraulics and Fluid Mechanics and studies carried out on habitat structures.

(b)   Investigation of the similarities in velocity profiles in the plane of symmetry and lateral direction downstream of the obstacle.

(c)   Investigation of the effects of roughness and shape of the body on the scour depth and scour patterns by measuring bed shear stress around the mounted body in smooth, rigid rough and mobile bed in the presence and absence of the scour hole.

(d)   Investigation of the similarities for the scour profiles measured at consecutive times before the equilibrium state around the body.

2

1.3   Organization of Thesis

Chapter 1 presents a general introduction on the applications and objectives of this study. Chapter 2 summarizes the available literature on the wake of free bodies, cylinders, mounted bodies and habitat structures. This chapter briefly considers vorticity and its effects on the problem under consideration. The wake structure and its characteristics are discussed in this chapter as well.

Chapter 3 describes the experimental arrangement, instrumentation and techniques employed to study this problem. Experiments are classified and the specifications of each set and its general undisturbed flow characteristics are presented. A brief review of experimental errors and uncertainties is also presented.

Chapter 4 presents the results of the flow visualization, both on rigid and mobile beds. Different regimes of flow are defined as functions of the Froude number and the relative depth. The difference among the vortex systems is also discussed.

Chapter 5 presents the experimental results on the smooth bed. The measurements of the velocity and bed shear stress fields are presented here, along with a brief description . Chapter 6 describes the results of the measurements on the rough bed consisting of both the rigid and mobile beds. the results of measurements of velocity, bed shear stress fields and scour characteristics are also presented in this chapter.

Chapter 7 presents a general analysis of the problem and the application of similarity concepts to the velocity and scour fields. Chapter 8 summarizes the conclusions of the entire study and provides recommendations for future studies in this field.

CHAPTER 2

THEORETICAL ASPECTS AND REVIEW
OF PREVIOUS INVESTIGATIONS

2.1 Introduction

Owing to the multi-functional nature of bluff bodies, such as rocks in rivers, flow around such bodies should be studied from different perspectives. The presence of large obstacles in the flow changes the flow characteristics and creates a system of vortices around the body which affects the flow pattern. Therefore, the study of the vortex system is an essential part of this investigation. Separation of the flow from the body, and the existence of the recirculation region and the wake, are phenomena which also change the velocity field and other flow characteristics. These are also studied in detail. Mobile bed, which itself is the subject of many investigations, adds complexity to the problem . All these different aspects should be considered in the study of flow around the body.

Furthermore, the study of free-ended obstacles in a shallow open-channel flow is an area of research that has only recently come under study and very few investigations have been carried out. Therefore, examining other areas of research related to this problem was necessary. For example, the wakes of two-dimensional bluff bodies have been investigated extensively by researchers, but the three-dimensional behavior of flow around bluff bodies has not been studied in detail. Most of the studies on the wakes of obstacles have been conducted in wind tunnels, for structures such as towers and chimney stacks. The number of studies related to three-dimensional behavior of flow past an obstacle in a flow with a free surface is even more limited. Related literature will be presented and discussed in the following sections.

2.2 Vorticity in the Flow

Flow around an obstacle mounted on a river bed or a laboratory flume produces a series of vortices in its wake as well as on the front side. Investigation of these vortices and the circulating mass of flow in the near wake requires an understanding of vorticity and the governing equations. Vorticity (the "sinews and muscles of fluid motions"_Kuchemann, 1965) is defined as "twice the average angular velocity around an infinitesimal circle" (Saffman, 1993), or simply as curl of the velocity. Vorticity is responsible for the existence of major flow structures around the body and scour. An understanding of vorticity is essential to this study; hence the following section will provide a brief introduction to the origin of vorticity and its significant properties.

Vorticity can be described by Helmholtz's theorems of vortex motion and Kelvin's circulation theorem. Kelvin (1869) expressed that "the circulation around any material circuit in an ideal fluid is invariant" (Saffman, 1993) and Helmholtz (1858) proposed that for an incompressible fluid "a vortex tube moves with the fluid and its strength remains constant" (Saffman 1993 and Batchelor 1967). Based on an extension of these theorems, the rate of change in circulation (Γ) associated with a closed curve in a viscous fluid is governed by the torques produced by all the forces acting in the fluid:

$$\frac{D\Gamma}{Dt} = -\oint \frac{dp}{\rho} + \oint G.dr + \oint v\nabla^2 U.dr \qquad (2.1)$$

where ρ is density, p is the pressure, G is the body force, v is the kinematic viscosity, U is the velocity and r is the radius of the vortex tube. The first term on the right hand side (RHS) shows the pressure torque which is zero for barotropic fluids, for which a single valued pressure-density relation exists. The second term denotes a body-force torque and would be zero if the body force, G, is irrotational or conservative (Fan and Tsuchiya, 1990). Therefore, forces which are centrally directed, such as gravity, would have no

effect on circulation, whereas Coriolis force would affect it. The last term on the RHS represents the torque produced by viscous forces acting on the fluid elements.

The Eq. (2.1) can be developed into the vorticity (transport) equation for conservative external forces (Saffman, 1993) as:

$$\frac{\partial \overline{\omega}}{\partial t} + \overline{U}.\nabla\overline{\omega} = (\overline{\omega}.\nabla)\overline{U} + \nu\nabla^2\overline{\omega} + \frac{1}{\rho^2}\nabla\rho \wedge \nabla p - \overline{\omega}(\nabla.\overline{U}) \qquad (2.2)$$

In Eq. 2.2 the first and second terms on the left hand side (LHS) show the rate of change of vorticity $\overline{\omega}$ of an infinitesimal element (particle), or simply the flux of vorticity. The first term on the RHS, represents the tilting and stretching effects in two-dimensional and axisymmetric flows, which would be zero due to the fact that vorticity is normal to the plane of flow and orthogonal to ∇U everywhere. But for a three dimensional asymmetric case, it would be present. The second term on the RHS shows viscous diffusion. The third term represents the baroclinic torque or density gradient source term (buoyancy force). For incompressible fluid with no change in density, this term becomes zero because the surfaces of constant density (isopycnics) are parallel to the surfaces of constant pressure (isobars). Therefore, the third and forth terms can not be used together.

Based on these equations, vorticity can only be generated if there is a gradient of velocity or pressure at the boundary. In a no-slip condition, vorticity is generated instantaneously at the first moment of the initiation of motion and is concentrated at the boundary. By separation of this boundary layer from the bluff body, vorticity spreads in to the irrotational field by viscous diffusion. In an incompressible flow, based on equation 2.2, vorticity flux across a material surface element varies only as a consequence of the local diffusion of the vorticity through viscous action. The vorticity flux is confined to its vicinity and (only) by convection vorticity distribution stretches downstream and the circulation region develops (Rimon and Cheng, 1969).

6

2.3 Vortex System and Flow patterns Around the Body

2.3.1 Flow around free bodies

When a body is far away from walls and boundaries, its wake can be called a free wake. There are some similarities between free wake and wake behind cylinders and mounted obstacles on the bed. The structure of the wake behind a free body shall be presented first. A discussion of the separation of the flow from the body is required as a first step. When the relative speed between the body and the surrounding fluid is very small, so that the Reynolds number $R=UL/v$ is small, the flow will follow the body surface where U is the relative speed and L is a characteristic length. In this case the surface body contour forms a streamline which is called the dividing streamline. Above a critical R, the flow separates from the body. The R at which separation occurs is not a constant but is a function of the shape, surface texture of the body and the turbulence intensity in the flow. As R increases, a closed region behind the body forms by the attachment of the separated streamlines. This closed type of region can be called a wake in a narrow sense while in a more general and broader sense the definition of wake would cover the entire region of non-zero vorticity downstream of the body.

The flow behind the body can be divided into three different regions, namely:

1- Recirculation region or closed wake: Due to the significant difference between the velocity in the free stream and the wake, a recirculating region occurs in which reverse flow or negative velocity is present. The vorticity present in the separated shear layer is dominant compared with the viscous effects and turbulent diffusion. Vortex formation, growth and shedding also occur here. The velocity at the separation lines on the body is higher than average velocity. The vorticity is intensified around the bed and can cause severe scour due to the stretching of the vortex tube by convection.

2- Near-wake region: In this region, the shear layer and wall effects (for wall mounted obstacles) are important and the velocity profiles and shear stress distributions are not

7

generally similar. This region also can be called the flow development region. Sometimes both the recirculation region and the flow development region are called the near wake.

3. Far wake region: The far wake structure does not depend strongly on the type of body, so similarity in velocity profiles can be achieved in this region, which includes the rest of the wake. Further, the velocity defect becomes small compared to the freestream velocity.

In this study, because of the geometry of the flow and the mounted body on the bed, the focus is on flow visualization in the recirculation region and measurements are limited to the near wake of the obstacle. Fan and Tsuchiya (1990) described the near wake of a deeply submerged free body in a very detailed manner and their description is used here extensively. At high R, due to the presence of high convection and low diffusion, flow at the upstream and sides of a body is approximately irrotational. Separation of the flow from the bluff body produces free shear layers. These free shear layers bound the wake behind the cylinder in which the velocity outside the wake is equal to the free stream velocity and in which inside velocity is much less, and hence the free layers tend to roll up into discrete, swirling vortices. Due to the lower velocity and pressure in the inner side (wake side) of the free shear layer, the outer side flow curls inside and creates a circulation region inside the wake behind the body. After separation, the shear layer shed from the body becomes thicker and forms a closed wake behind the body. The thickness of shear layer increases with higher R due to the occurrence of transition to turbulence closer to the body, resulting in a smaller recirculation region (Goldstein, 1938).

If a steady state exists around the body, the rates of vorticity transported into and out of the circulation region will balance. Therefore, a uniform (in plane flow) or radially linear vorticity distribution will exist around the center of each vortical flow, or standing vortex core. For a free body, this standing vortex core can be named as a vortex ring or an arch-vortex for a free ended body mounted on the bed, such as rocks (Figure 2.1). This

8

means that the flow in the vortex core can be treated simply as an inviscid flow, though still rotational, since the effects of viscosity have essentially vanished in this state. Free shear layer covering the "closed wake" or "recirculation region" of a free body can be divided in two sections: interior layer and exterior layer. Fluid elements in the interior layer around the rear stagnation point of the recirculation region go to the internal wake and re-enter the free shear layer along the rear "base" of the body. The fluid elements at the exterior part of the free shear layer move to the downstream and leave the recirculation region for the far wake (Figure 2.1). Therefore, flow around a free body would consist of: (1) irrotational flow or potential flow outside the body and its wake, (2) inviscid rotational flow inside the closed wake (a doublet of vortex cores in a plane flow; a vortex-core ring in axisymmetric flow), (3) thin boundary layer around the surface enclosing the body and its closed wake, and (4) "external and internal wakes" along the axis of symmetry resulting from the division of the shear layer into two layers.

The general wake structure can be explained by the dual-wake-structure concept as two regions of primary wake and secondary wake. The primary wake is usually an enclosed region immediately behind the body with circulatory flow patterns and in close association with the body (Fan and Tsuchiya, 1990). The secondary wake has an open structure with a less defined region, including free layers and shedding vortices from the primary wake in the form of Karman vortex street, which extends far downstream. The three dimensional wake can not be described easily due to varying degrees of flow instability occurring over a wide range of R. Under this condition, the wake structure is commonly represented according to five categories depending on the R. These categories are: (1) a steady wake with a negligible circulation region; (2) a steady wake with a well-developed circulation region followed by a laminar stream-wise tail; (3) an unsteady wake with large-scale vortical structures; (4) an unsteady wake with a high degree of turbulence; and (5) a highly turbulent wake. Category (3) consists of a regular succession of vortex filaments. Among possible configurations of discharged vortex filaments

proposed in the literature, such as toroidal vortex rings, a helical vortex, bispiral vortices and horse-shoe vortex loops, the most plausible configuration is a non-axisymmetric vortex ring as the primary wake followed by a series of the horse-shoe vortex loops. Category (4) is characterized by a progressive wave motion with a rotating flow separation region. Category (5) may consist of a pair of stream wise line vortices trailing from a vortex ring fragment attached to the body.

Tsuchiya (1987) found that by connecting each series of data points which represent the descent velocity of each vortex center at the wake, the vortex velocity in primary wake was constant. However, once the vortex leaves the primary wake it accelerates and approaches the free stream velocity. Therefore, it could be said that the vortex within the primary wake is "protected" from external disturbances; however, once leaving the primary wake it interacts with the external flow and is carried downstream by the fast stream.

Cantwell and Coles (1983) found a sharp relaxation of the mean velocity defect along the wake centerline behind a circular cylinder. They attributed this rapid acceleration to very intense mixing occurring in the near wake. It was also concluded that the point along the wake centerline where a rapid acceleration takes place may correspond to the end point of the circulation region (in an average sense) bounded by the primary wake. They also found that this high level of mixing is the cause of high turbulence, specially close to the saddle points between vortices. Based on their measurements, they concluded that a substantial part of the turbulence production was concentrated near the saddles. They proposed that the primary mechanism of turbulence production in the wake was vortex stretching near the saddles. The rapid decay of defect velocity shows a sharp demarcation between primary and secondary wakes. Cantwell and Coles (1983) found the end of the formation region to be located at roughly x/D=1.0 - 1.5.

2.3.2 Flow around cylinders

A significant number of investigations have been carried out on the scour around bridge piers, which is often considered as almost a two-dimensional flow. These investigations can be used as the first step in studying the fully three-dimensional behavior of the flow around open ended objects in the flow. For a cylinder mounted on the bed, the number of standing vortex cores increases to two: cast-off vortices and horse-shoe vortices. The cast-off vortices are generated behind the separation line from the body (Figure 2.2). In the case of the flow around a cylinder placed vertically on a wall, such as a bridge pier, the cast-off vortices are restricted to the sides of cylinder, while the top portion of the body is out of the flow. But for an open-ended body, these vortices can be shed from the sides and from the top of the body. The second type of standing vortices are horse-shoe vortices, HS vortices, which are generated between the frontal face of the object and the ground plate.

The wake behind an obstacle, especially in the case of a long cylinder, is affected by the Reynolds number. For a very low R, a symmetric pair of stationary vortices are present in the recirculation region. When the Reynolds number increases, the separated shear layer becomes unstable and complicates the flow behavior. The separated boundary layer from the body which covers the recirculation region can be explained by R variations. For R < 1 the viscous effects are dominant and inertial effects can be neglected where flow attaches to the body with no separation. At higher R, a laminar boundary layer (laminar BL) forms over the whole surface. Then the BL separates on either side near the rear of the cylinder and a narrow turbulent wake develops. With further increase of the R (10-60), the laminar separation points on either side of the rear of the stream wise diameter move rapidly outwards and forward to points near the opposite ends of a transverse diameter. This results in a corresponding increase in wake width. For R of 60-160, a pair of symmetrical vortices will begin to develop on either side of the center line behind the laminar separation points; these will grow with time (at

particular R), continuously stretching downstream until a stage is reached when they become unsymmetrical and the system breaks down, one vortex becoming detached and moving away downstream.

The subsequent wake motion which is typical of that within the range $140 < R < 5 \times 10^4$, is oscillatory in character. This motion was investigated by von Karman (1929). He showed that a stable system of vortices will be shed alternately from the laminar separation points on either side of the cylinder. Thus, an attached standing vortex will be generated in the region behind the separation point on one side, while a corresponding vortex on the other side will break away from the cylinder and move downstream in the wake. When the attached vortex reaches a particular strength, it will in turn break away and a new vortex will begin to develop again on the second side, and so on. The wake thus consists of a procession of vortices of equal strength, equally spaced but opposite in sign (Karman vortex street). After creation of vortices behind the body, the flow around the body bends the axes of the vortices. Close to the bed there is an interaction between the horse-shoe vortex and these vortices which causes the trailing parts to oscillate laterally and vertically at the frequency of the vortex shedding, n, or Strouhal number S of 0.2. These cast-off vortices have vertical low pressure centers which cause lifting of sediments similar to a small tornado (Breusers and Raudkivi, 1991).

Horse shoe vortices are dominant features in front of the body. By studying these vortices more can be learned about the flow behaviour around the obstacle. A HS vortex will produce high wall shear stress beneath it, which causes erosion and produces a scour hole around the base of an obstacle on an erodible bed, such as a bridge pier or a telegraph pole surrounded by a snow drift. The presence of the cylinder produces a pressure gradient in its vicinity. In front of the cylinder, there is an adverse pressure gradient which causes the boundary layer to separate three-dimensionally some distance upstream of the cylinder. After the three-dimensional separation of the boundary layer, its lower regions roll up and generate a vortex system upstream of the obstacle. Then the two

sides of this vortex system are swept around the base of cylinder by the flow and create a vortex with a characteristic shape referred to as horse-shoe vortex.

Schwind (1962) was one of the early researchers who studied the HS vortex. He carried out a series of experiments in a wind tunnel to investigate the different vortex systems upstream of a 60 degree wedge for different wind velocities. He observed that for a low velocity there was a steady separation in which observation of the vortices was difficult, and that perhaps was possible only in plane of symmetry. At a higher velocity, there was a single steady clockwise rotating vortex and a small triangular-shaped counter-rotating vortex. By increasing the velocity, in addition to the main rotating vortex and counter-rotating one, a second rotating vortex was observed further upstream of the counter-rotating vortex, along with a second and smaller counter-rotating vortex. Further increase of the velocity caused an oscillation in the two rotating vortices, while the oscillation amplitude increased with the velocity.

Then the main vortex gained a regular oscillatory motion, moving towards the wedge and back again, and sometimes combining with the second rotating vortex or passing beneath the second vortex, and probably combining with an invisible rotating vortex. All these variations were possible even at one velocity and there was no distinctly defined velocity determining the presence of these vortices. The exact number of vortices was seen to depend upon the flow speed and wedge size, and more vortices appeared as the speed increased. In the oscillation period, the two largest clock-wise rotating vortices move towards one another and apart again. At higher speed, the larger clock-wise vortex isolated from the rest of system and as velocity increased, the flow became turbulent.

Baker (1979) investigated the HS vortex system around the base of a cylinder for a LBL separation. He found that the laminar HS vortices are similar to the turbulent ones in many aspects. He showed that the pressure distribution in the plane of symmetry upstream of the cylinder can be classified into two categories. When Reynolds number, R, was less than 5000, the curves had minima which were proved by flow visualization to

be at the center of the primary vortex in a steady state. The vortex position could be determined from such pressure distributions. At higher R, the curves had no minima and flow visualization showed that there was an unsteady vortex system. He showed also that by increasing R, x_v/D increases and as D/δ^* increases, x_v/D decreases, where x_v is the position of primary vortex from the center of the cylinder, D is the cylinder diameter, and δ^* is the boundary layer displacement thickness.

To investigate the source of the vortex system oscillation and its behavior, Baker (1979) carried out some experiments with a hot-wire probe and analyzed the frequency spectra. He found that at any speed, there are four different wave forms :

a) a steady trace with no oscillation ;

b) a low frequency oscillation $(S = nD/U = 0.26)$;

c) a high frequency oscillation $(S = 0.4$ to $0.6)$; and

d) an irregular turbulent trace;

where S is the Strouhal number, n is the frequency of waves, D is the diameter of the cylinder and U is the average velocity of the flow. All these different frequencies existed in all the flow states and the flow switched from one state to another randomly. At the lowest speed, state (a) was observed more than the others. By increasing the velocity, states b, c and d become the most often observed states.

To clarify the source of the oscillation of the vortex system in front of the cylinder, Baker (1979) tried to eliminate the probable causes. For example, to check the vortex shedding of the cylinder, he used a cylinder with splitter plate with a streamlined model, but the results were almost identical to the case of a simple cylinder. He concluded that the vortex shedding could not be a possible cause of the oscillation. He even showed that the disturbances present in the boundary layer upstream of the model did not affect the HS vortex oscillation. He was not able to identify the source of oscillation but suggested that at a certain value of R and D/δ^*, the HS vortex itself becomes unstable for some unidentified reason and begins to oscillate in one of two

natural modes. The higher frequency mode became more dominant as the R increased. He found that the skin friction coefficient beneath the primary vortex was five times its value at the upstream of the cylinder.

Baker (1980) investigated the HS vortex formed around the base of the cylinder for a turbulent boundary layer. He distinguished four different vortices upstream of the cylinder. There was a small anti-clockwise vortex just upstream of the surface of the cylinder which was caused by the separation of the boundary layer on the upstream face of the cylinder. Upstream of this small vortex, there was the primary vortex whose separation from the bed caused a small anti-clockwise vortex close to the bed. Baker could also observe another clockwise vortex upstream the primary vortex.

By oil-flow visualization, Baker (1980) was able to show the saddle point of primary and secondary separation lines which were composed of the ordinary separation points. By long exposure (1/15 s to 1/60 s) photographs of smoke-flow visualization, he observed the time, mean position of the HS vortices on the plane of symmetry upstream of the cylinder and also the position of the primary vortex. By short exposure (1/500 s to 1/1000 s) photographs, he was able to see the large-scale turbulence upstream of the boundary layer which distorted as convected in to the vortex system.

Head and Bandyopadhyay (1978) tried to explain these distortions. They considered the turbulent boundary layers as collections of hair pin vortices with their "ends" emerging from the laminar sub-layer. These hair-pin vortices usually had an angle of 40 degrees to the floor. This angle is the resultant of two opposite forces of upward self-induced force and downward mean shear stress. The latter case decreases approaching the separation point and causes the angle of inclination to be raised by self-induced forces up to 90 degrees (distortion).

By measuring the pressure at the plane of symmetry it was observed that the pressure is leveling out beneath the HS vortex system. Flow visualization indicated that this dip in the pressure distribution corresponds to the center of the primary HS vortex

(Baker, 1980). The variation of pressure distribution for different Reynolds numbers was very small and it was concluded that the position of the primary HS vortex is almost invariant. Baker also found that as D/δ^* increased, the pressure coefficient (C_p) increased too, where δ^* is the boundary layer displacement. He showed that such a behavior is consistent with the observed fact that the vertical dimensions of the vortex system do not change with the flow parameters. As D/δ^* increased, the HS vortex moved closer to the cylinder. By studying the variation of x_s/D and x_{s1}/D with l/D, he found that the length of the separated region scales on the cylinder diameter, when the cylinder is tall, and on the cylinder height when the cylinder is short, where l is the height of cylinder and x_s is the distance from the cylinder to the boundary layer separation position on the plane of symmetry, and x_{s1} is the distance from the cylinder center to the secondary saddle point of separation. Oil-flow visualization showed that for $4000 < R < 90000$, only 4 vortex systems existed.

Qadar (1981) conducted a series of laboratory and field experiments and found that the scour depth in front of the bridge pier is related to the strength of the HS vortex, which is believed to be the basic mechanism of the scour. In his laboratory experiments, he used three sizes of wooden blocks of 0.025m, 0.05m and 0.075m ; and three sizes of sediments: 0.17 mm, 0.7 mm, and 1.5 mm. The HS vortex develops a scour hole in the bed and gradually sinks into the hole while expanding its size. He found that the radius of the HS vortex is almost 0.1 times the width of the pier. By measuring the velocity of the vortex at its perimeter, he also showed that the vortex velocity decreases by the width of the pier. Considering several sets of data, he proposed that the maximum depth of scour is a function of the strength of the HS vortex :

$$d_s = K_s (C_o)^n \qquad (2.3)$$

16

where d_s is the maximum scour depth below the original bed level, C_o is the initial strength of the vortex calculated as product of vortex velocity and its radius, and n is an exponent found experimentally to be equal to 1.28, and K_s is the coefficient of sediment size, with a value of 538 for sediment of diameter less than 0.5 mm. The coefficient and exponent were different for coarser sediment. Based on his results, he proposed that the sediment size is only important at the initial stages of scouring process and the final scour depth depends only on the sediment transport capacity of the vortex for sediment particles less than 0.5 mm in diameter.

2.3.3 Flow around free-ended bluff bodies

Schlichting (1936) studied the flow past a bluff three-dimensional obstacle to evaluate the surface roughness effects. Kelmin et al. (1939) studied the drag of a sphere placed on ground plate and Hunt (1971) carried out some experiments on flow past a building. Peterka and Cermak (1977) measured the mean velocity defect and turbulence in the wake behind a building.

S. Okamoto (1979) studied the turbulent shear flow behind a sphere placed on the plane boundary in a wind tunnel. He measured the distribution of pressure, surface-pressure on the sphere, velocity, drag and lift coefficients. He found two types of vortices: HS vortices and arch vortices. Arch vortices are actually those cast-off vortices in cylinders, or ring vortices in free bodies. Okamoto proposed that the arch vortices are attached on low pressure areas behind the sphere and rotate about them to fall down. The position of high pressure was the point of reattachment of the outer streamline of the recirculation region behind the sphere. He found, by observing the flow with the tuft grid method, that the horse-shoe vortex becomes flat at $x/D = 4$ and disappears about $x/D = 5$, where x is the distance downstream of the center of the sphere in the stream wise direction, D is the diameter of the sphere and y is the distance from the center of the sphere in lateral direction. The negative static-pressure coefficient in a region behind the

sphere, 0.3 < y/D < 1.5 for 2 < x/D < 5, was assumed to be due to the HS vortex. The sign of this coefficient changed to positive at x/D=5 where the HS vortex disappeared. He showed that the decrease of the shear layer thickness downstream of the sphere is proportional to $(x/D)^{-0.4}$, and he also found that the peak velocity defect moves away from the centerline in proportion to $(x/D)^{0.69}$. This fact indicated that the wall-wake behind a sphere becomes low and spreads transversely with increasing downstream distance. Due to the presence of a strong downwash behind the sphere, the recirculation region was shortened and limited to 2.5 D. By studying the iso-pressure lines and using flow visualization, it was observed that the separation line on the sphere is shifted backward when it is approaching the ground plate.

T. Okamoto and M. Yagita (1973) carried out some experiments on flow past a circular cylinder mounted on the floor of a wind tunnel with a free end which was immersed in a uniform stream. They investigated the ffect of the downwash from the free end of the cylinder on the turbulent wake behind the finite cylinder. They measured the spanwise velocity profiles at a fixed point downstream of the cylinder (x/D = 6) in the center plane, for different values of l/D where l is the length of the cylinder. They found that for l/D < 9, the free end effect reaches the root of the cylinder, but the wake behind the portion of the free end is similar for l/D > 12. It was shown that there were two peaks in the defect velocity distribution in transverse direction downstream of the body which indicates there is a velocity excess due to the downwash, an important feature of the wake of the finite cylinder. In the constant velocity profiles of a horizontal plane close to the free end, there was a velocity excess due to the presence of the downwash close to the POS at x/D > 45.

T. Okamoto et al. (1977) measured the constant pressure profiles for the flow past a cone placed on the flat plate and observed that there is a peak of positive pressure on the X-axis behind the cone for vertex angles of 60°, 90°, and 120°. They found that this peak increases with the vertex angle. They suggested that the peak is caused by the downwash

18

of the free stream across the cone and its position indicates the scale of the vortex region behind the cone. A positive pressure gradient occurs in front of the cone due to the reduction in velocity, which causes the boundary layer to separate from the flat plate in front of the cone and forms the HS vortices, or as they named them, the neck-lace-vortices. These HS vortices had axes of rotation parallel to the flow and they moved downstream. There were two HS vortices for the cone of vertex angle 60. These two vortices had axes which rotated in the same direction. Therefore, the two vortices began to coil around each other in the vicinity of the sides of the cone. They decayed gradually and increased the velocity in the wake of the cone. The profiles of the defect velocity inside the wake had two peaks. They explained it as the effect of the downwash of the free stream from the top of the cone and the existence of a secondary flow due to the HS vortices. This increase of the velocity at the center is referred to as a "negative wake effect".

S. Okamoto (1979) conducted a series of experiments to investigate the turbulent shear flow behind a hemisphere-cylinder placed on the ground floor. He used a hemisphere on top of a circular cylinder with an aspect ratio of one. He observed that the arch vortices were shed downstream and were gradually inclined by a strong downwash behind the obstacle until they almost touched the ground plate. He showed, from the pressure distribution on the ground plane, that there were two areas in which the pressure was the lowest. It was within these two areas that the roots of the arch vortices were attached to the ground plane. He suggested that the arch vortices rotate about these attachment points and then gradually lean forward.

Using a hot-wire anemometer, he found that the S of the arch vortex shedding for a hemisphere-cylinder is less than that of circular cylinders and spheres. He deduced that it is caused due to the strong downwash behind a hemisphere-cylinder. The recirculation region was considerably reduced compared with that in a two-dimensional wake. The reattachment of the outer streamline enclosing the recirculation region could be found at

19

the position of the highest pressure on the ground plane. As well, the peak velocity defect, at horizontal center section, Z/D = 0.5, was shifted laterally and increased moving downstream. He proposed that the velocity defect in the center section (z = 0) for x/D > 3.0 is :

$$\frac{(U_\infty - U)}{U_\infty} = 0.95\left(\frac{X}{D}\right)^{-1.62} \tag{2.4}$$

where U_- is free-stream velocity and U the time-mean velocity in the stream wise direction. This was close to Hunt's result for the wake behind buildings :

$$\frac{(U_\infty - U)}{U_\infty} \propto X^{-1.5} \tag{2.5}$$

Moving downstream, the thickness of the shear layer decreased and the peak velocity defect moved away from the center line (y = 0). Okamoto (1979) concluded that the wall-wake behind a three-dimensional obstacle becomes thin and spreads transversely further downstream. It was found that the velocity defect in the center section of a hemisphere-cylinder was nearly equal to that of a circular cylinder and a sphere.

2.3.4 Vortex stability

Karman (1911,1912) studied the two-dimensional wake structure and its stability behind a cylindrical body. He established a theoretical base for the stability of asymmetric double rows of vortices shedding from the body, which is named as Karman vortex street. Vortex streets can be seen for R of 40 to 10^5. The vortex street behavior is better understood in the near wake region, but it is not well understood in the vortex generation zone.

For the near wake region, Fopple (1913) proved theoretically that the vortex pair is stable for symmetric disturbances but unstable for asymmetric ones. Therefore, when in a real flow, most of the disturbances are not symmetric, above a critical value of R, and

20

the vortices in the generation zone become asymmetric, creating Karman vortex street. The region between the rear surface of the body and the first appearance of the Karman vortex street is called the vortex formation region or primary wake. At a low R, the wake consists of a standing vortex ring in a steady flow. By increasing the R and the oscillation of the vortex ring, the flow becomes unsteady and vortices start to shed.

Helmholtz or Rayleigh instability is the basic form of instability and occurs in the shear layer (or a sheet of velocity discontinuity) of an ideal fluid. A simple sinusoidal wave forms at the interface along the shear layer and grows to an unstable condition (Fan and Tsuchiya, 1990):

$$y = \eta(x,t) \qquad (2.6)$$

$$\eta(x,t) = A.\exp\left[\frac{2\pi i}{\lambda}(x - \kappa t)\right] \qquad (2.7)$$

$$\kappa = \frac{u_{out} + u_{in}}{2} \pm i\frac{u_{out} - u_{in}}{2} \qquad (2.8)$$

where A is the amplitude, λ is the wave length, x is the distance along the flow direction, t is the time, and κ is a measure of the sheet strength.

Stretching or shrinking of a vortex in an unsteady flow increases or decreases the strength of vortex based on Kelvin's conservation of circulation theorem. This change, in turn, causes an increase or decrease in the wave length of a disturbance, which means the more compressed the sheet, the shorter the wave and the more the instability. The external disturbances due to turbulence in the flow promotes further instability. The above process of stretching and shrinking, plus dissipation and diffusion of vorticity by viscosity, breaks up the deformed sheet to blobs of vorticity which then are shed from the edges.

The large vortex structures that keep their identity in flow are called coherent structures. The stability of vortices can be studied in this context too. For example, while ring vortices are stable, hair pin vortices are unstable in nature. In theory, upward infinite velocity at its tip results in pinching off the tip from the legs. This kind of instability might be the cause of the cascade of vortices separating from the arch vortices in the formation region downstream of the body.

The study of the formation region can lead to a better understanding of this process. The formation region downstream of cylinder is laterally bounded by two shear layers separated from the body (two dimensional flow). The wave type of instability of the shear layers generates small scale vortices which in turn cause mixing of the external flow and the wake. The growth of the shear layers is controlled by these small scale vortices. The interaction of the small scale vortices with larger scale Karman vortices becomes stronger at higher R (> 10^4) causing the merging of small ones to the Karman vortices, where the formation region is reduced to a small region behind the body. Therefore, the mechanism of transition to turbulence in the near wake is mainly governed by the interaction between these two type of vortices in the formation region and the mixing or free shear layer (Kourta et al., 1987). In three dimensional disturbances, Karman vortices are usually unstable due to the short wave lengths along the axis of the vortex street, which destroys the general pattern (Rosenhead, 1953).

Significant growth of shear layer after separation from the body can be attributed to the pairing of vortices (Brown and Roshko, 1974, Winant and Browand, 1974). Contrary to the Kolmogrov cascade theory, in which the energy goes from the large scale to the smaller scale, here the smaller scale vortices pair and create larger scale vortices. This pairing is known as the cause of large scale mixing between the internal wake region and the external flow.

2.3.5 Vortex shedding

There are different interpretations for vortex shedding. Perhaps one of the best descriptions is that of Tsuchiya and Fan (1986). In two dimensional systems, periodic shedding can take place either asymmetrically or symmetrically. The asymmetric vortex formation-shedding mechanism consists of the roll-up of a vortex sheet, the growth of a circular vortex and the cut-off of the vorticity supply to the growing vortex. The vortex sheet instability occurring independently on each side of a body is responsible for the symmetric shedding.

During the steady shedding period, the large scale vortices are generated by the separation of the external flow from the body edges. The vorticity created in this respect is conveyed along the free shear layer. This free shear layer, or vortex sheet, tends to roll up into a spiral form due to the differences in the characteristic velocities between the outer and inner boundaries of the shear layer, and due to the pressure defect in the near wake. This rolled-up vortex sheet then forms a circular-cross-sectioned vortex, which is attached to the body base via the shear layer, and grows as vorticity is continuously supplied through the shear layer.

The asymmetric shedding often predominates the symmetrical shedding due to the non-linear interaction between the two vorticity layers of opposite sense emanating from the body edges, and partly from biased/asymmetric disturbances often induced by the external flow. In the asymmetric case, the grown up vortex draws the shear layer and the external flow inside the wake and they laterally travel the width of the wake. Then part of this flow is attracted towards the base of the body, i.e., as a reverse flow, due to the incompletion of the defect pressure recovery behind the body (Figure 2.3). The laterally outward flow along the body base promotes the tendency for the external flow to separate from the edges. Therefore, the entrainment of the shear layer and external irrotational flow cuts the further supply of the vorticity from the separation point to the growing vortex, resulting in shedding of this vortex.

In the case of the parallel shedding, the vortex continues to grow until it becomes strong enough to draw the external flow and opposite shear layer across the wake. When this happens, oppositely signed vorticity of sufficient concentration cuts off further supply of vorticity to the vortex and the vortex ceases to grow in strength and starts detaching from the body. At this moment, the vortex is said to be shed. Gerrard (1966) described the shedding in a similar way. The cut-off stream divides the primary wake, or the formation region, from the shed viscous-decaying vortex. The roll-up of the vortex sheet through the cut-off of the vorticity supply on one side of the body constitute half a cycle of the vortex formation-shedding process. If the above process happens simultaneously, symmetric shedding may take place.

The vortex shedding mechanism in a three dimensional wake is more complicated and probably consists of a chain of vortex loops. The instability of the wake flow causes the unsteadiness of the flow and makes the structure of the wake complex while it is interactive with the external flow. The wake instability depends on R when it exceeds a certain critical value. The dynamics of vortical motion play a key role in wake formation and shedding. In three dimensional systems, the formation-shedding mechanism consists of a cycle of building up and release of vorticity (Fan and Tsuchiya, 1990).

Magarrey and Bishop (1961 a) suggested that a simple cycle of build-up and release of vorticity could explain the periodic discharge of vortex elements. The vorticity is initially concentrated in an imperfect vortex ring located within the vortex sheet downstream of the body. Where the vortex strength is greatest, a portion of the ring is ejected. After the vortex element has been shed, the ring immediately begins to reform, initiating the discharge of a comparable vortex element from the diametrically opposite portion of the ring. The shedding process repeats at a near constant frequency. Emergence of an imperfect ring (daughter vortex filament) out of a mother ring and reformation / mending of the mother ring requires a series of topological transformations of the vortex ring, such as pinching-off, disconnection and reconnection of vortex filaments. These

transformations, according to Helmholtz's theorem, are not possible in inviscid fluids where the strands of finite vortex systems must be completely closed at all times in the interior of uniform fluid but in real viscous fluid, they are allowed.

2.3.6 Shedding Frequency

There is a unique relationship between the Reynolds number and a dimensionless parameter involving the shedding frequency n, known as the Strouhal number, defined by the expression:

$$S = \frac{nD}{U} \qquad (2.9)$$

where D is the diameter of cylinder (for a case of shedding from a cylinder), and U is the free stream velocity. By measuring the frequency of the vortex shedding it has been found that there is a definite relationship between S and R, for each geometry and over a specified R range (Fan and Tsuchiya, 1990). For a two dimensional body with the maximum transverse dimension chosen as characteristic length, the S is almost insensitive to R in the range of 10^3 to 10^5. The S for vortex shedding from fixed solid spheres (Moller, 1938 ; Goldburg and Florsheim, 1966; Achenbach, 1974) increases monotonically from 0.1 to 2 as R increases from 400 to 6000, reaching a maximum value equal to 6000, and decreasing if beyond this value.

For vortex shedding from a cylinder, the separation points move very slowly forward as R is increased. For values of R > 700, S remains constant at about 0.21. The oscillation frequency increases linearly with speed until, at a R of about 5×10^4, the frequency begins to rise very rapidly and a change of flow pattern develops, and the shedding frequency becomes random (Houghton and Carruthers, 1976). At a critical R range of 4×10^5 to 5×10^5 boundary layer changes to turbulent and the width of the wake and the drag decreases. The behavior of a smooth sphere is almost the same under

similarly varying conditions with different R but the vortex street doesn't develop behind a sphere.

Reported S in the intermediate range of $10^3 < R < 10^4$ are scattered, but most of the researchers indicated a similar Strouhal number, S, for a comparably small R ($R < 10^3$) or large one ($R > 10^4$). Sakamoto and Haniu (1990) measured the frequency of vortex shedding from a sphere placed in the wind tunnel by power spectrum analysis of fluctuating velocity detected by a hot-wire probe. They also determined the vortex shedding frequency of the sphere mounted in the water channel by measuring the time necessary for a sequence of fifty vortices to be shed. They found two different S for R< 1.5×10^4, which are the high-mode and low-mode S. By reaching the R of 300, the hair-pin-vortices begin to shed from the sphere periodically and form laminar vortices up to R $= 800$. By further increase of R, the wake flow becomes turbulent by alternate fluctuation of vortices up to R $=3.7 \times 10^5$, which is called upper critical R.

For $800 < R < 10^4$, there was a low-mode S. So Sakamoto and Haniu (1990) concluded that the low-mode S is caused by the progressive wave motion of the wake with alternate fluctuations. In the same range of R ($R > 800$), cylindrical vortices defined as vortex tubes, begin to periodically shed with a high-mode S. Based on this fact, they proposed that the high-mode S is caused by shedding of the vortex tube, which is generated by the pulsation of the vortex sheet. They suggested that this is the small scale instability of the separating shear layer which forms the vortex tube. Therefore, the high-mode and low-mode of S exist together for this range of R.

2.3.7 Wake analysis

Wake characteristics such as velocity distribution and its rate of growth are affected by the flow boundaries, shape of the body and flow characteristics. Research began with the work of (Schlichting,1930) on plane wakes and gradually expanded to

more complicated topics, such as wall-wake and three dimensional wakes. In the following section some of available solutions for simpler geometries are presented.

For an obstacle mounted on the wall or bed, a wall-wake occurs, such as that behind a rock in an open-channel. The size of the body is the main parameter that affects the wake. Only obstacles with sizes capable of protruding out of the boundary layer could bring significant changes in the velocity profiles downstream of the body. The bed characteristics could also have an influence on the wall-wake. While the wake of an obstacle far away from the wall can oscillate freely about the plane of symmetry, the oscillation of its counterpart on a wall is prevented (Roshko 1954, 1955). The presence of the wall also reduces the form drag of the body up to 40% (Arie and Rouse 1956).

Rai (1974), in a study of plane turbulent wall-wake in a wind tunnel, assumed that the wall-wake consisted of an outer region and an inner wall region. At the outer region of the wake and away from the wall, the flow behaves as a plane turbulent wake. Where inertial forces are dominant over the viscous forces, the effect of the wall on the flow characteristics is negligible. Therefore, the velocity and shear stress distribution of a plane turbulent wake can be used in this region of the flow. But close to the bed, in the inner region of the wall-wake, the effects of the bed can not be neglected and the flow behaves similar to the inner region of a turbulent boundary layer. An overlap zone between these two regions of wall-wake is present, and at the wall - contrary to the plane turbulent free wake - the velocity reaches zero (Figure 2.4).

The characteristics of the wake in the outer region of the plane wall-wake are similar to that of the plane free turbulent wake. Reynolds equations for the two-dimensional free wake in the Cartesian coordinate system can be written as :

$$u\frac{\partial u}{\partial x}+v\frac{\partial u}{\partial y}=-\frac{1}{\rho}\frac{\partial p}{\partial x}+v\left(\frac{\partial^2 u}{\partial x^2}+\frac{\partial^2 u}{\partial y^2}\right)-\left(\frac{\partial \overline{u'^2}}{\partial x}+\frac{\partial \overline{u'v'}}{\partial y}\right) \qquad (2.10)$$

27

$$u\frac{\partial v}{\partial x} + v\frac{\partial v}{\partial y} = -\frac{1}{\rho}\frac{\partial p}{\partial y} + v\left(\frac{\partial^2 v}{\partial x^2} + \frac{\partial^2 v}{\partial y^2}\right) - \left(\frac{\partial \overline{u'v'}}{\partial x} + \frac{\partial \overline{v'^2}}{\partial y}\right) \qquad (2.11)$$

and the equation of continuity as :

$$\frac{\partial u}{\partial x} + \frac{\partial v}{\partial y} = 0 \qquad (2.12)$$

where u and v are the mean velocity components, u' and v' are the fluctuating components of the velocity, p is the mean pressure, ρ is the mass density, and v is the kinematic viscosity of the fluid. Using the boundary layer simplifications, one can reduce the above equations to a simple set of equations for a plane wall-wake with zero pressure gradient as :

$$u\frac{\partial u}{\partial x} + v\frac{\partial u}{\partial y} = \frac{1}{\rho}\frac{\partial \tau}{\partial y} \qquad (2.13)$$

$$\frac{\partial u}{\partial x} + \frac{\partial v}{\partial y} = 0 \qquad (2.14)$$

By integrating the above equations and applying the boundary conditions, the momentum integral equation can be obtained as :

$$\frac{d}{dx}\int_0^\infty \rho \cdot u \cdot (U_0 - u)dy = 0 \qquad (2.15)$$

Integrating both sides of the above equation with respect to x, we get:

$$\int_0^\infty \rho \cdot u \cdot (U_0 - u)dy = constant = F_D \qquad (2.16)$$

28

where the constant F_D is the drag. The scales which have been used to non-dimensionalize velocity and length are the maximum velocity defect at the center, u_{1m}, and the half-width of the wake, b, which is the ordinate at which the velocity defect is $u_{1m}/2$ (Figure 2.4). Based on similarity principles for flows independent of the Reynolds number, these two parameters would be functions of x only and can be shown as :

$$\frac{U - u}{u_{1m}} = f(y / b) \qquad (2.17)$$

$$\frac{\tau}{\rho u_{1m}^2} = g(y / b) \qquad (2.18)$$

Substituting these scales in equation (2.16) we can get :

$$\frac{u_{1m}}{U_0} b \int_0^\infty f d\lambda - \left(\frac{u_{1m}}{U_0}\right)^2 b \int_0^\infty f^2 d\lambda = \frac{F_D}{\rho U_0^2} \qquad (2.19)$$

where $\lambda = y/b$. In Eq. 2.19 for far wake region, $U_{1m} << U_0$, the term $\left(\dfrac{u_{1m}}{U_0}\right)^2$ can be neglected and we get:

$$\frac{u_{1m}}{U_0} b \int_0^\infty f d\lambda \cong \frac{F_D}{\rho U_0^2} \qquad (2.20)$$

Then by considering the drag force as $F_D = C_{D0} \dfrac{\rho U_0^2}{2} . h$ and assuming $u_{1m} \propto x^p$ and $b \propto x^q$ we can get :

$$\frac{u_{1m}}{U_0} = C_1 (x / h C_{D0})^{-1/2} \qquad (2.21)$$

$$\frac{b}{hC_{D0}} = C_2(x / hC_{D0})^{1/2} \qquad (2.22)$$

where the coefficients C_1 and C_2 were determined experimentally by Schlichting (1930) as 1 and 0.25 respectively. The velocity profile and shear stress distribution can be derived similar to the Schlichting's (1930) derivation. He derived the following equations for the far wake region of a plane turbulent wake based on Prandtl's mixing length hypothesis :

$$\frac{U_0 - u}{u_{1m}} = \left(1 - 0.293.\lambda^{3/2}\right)^2 \qquad (2.23)$$

$$\frac{\tau}{\rho u_{1m}^2} = 0.128\lambda\left(1 - 0.293\lambda^{3/2}\right)^2 \qquad (2.24)$$

Rai (1974) found that the set of Eqs. 2.21 to 2.24 can define the flow characteristics in the outer region of the far wake of a turbulent wall-wake. But for the near-wake region, where u_{1m} is approximately of the same order as U_0, the term $\left(\dfrac{u_{1m}}{U_0}\right)^2$ can not be neglected in equation (2.19). Based on an energy integral equation, Rai (1974) derived the following equations for near-wake, $\dfrac{x}{hC_{D0}} > 40$, of a plane turbulent wake :

$$\frac{u_{1m}}{U_0} = 1.35(x / hC_{D0})^{-1/2} \qquad (2.25)$$

$$\frac{b}{hC_{D0}} = 0.44(x / hC_{D0})^{1/2} \qquad (2.26)$$

For the inner region of the wake-wall, the law of the wall proved to be satisfactorily in agreement with the experimental results.

The wake characteristics downstream of a cylinder can be derived in a similar way for the far-wake as :

$$\frac{u_1}{u_{1m}} = \left(1 - \lambda^{3/2}\right)^2 \qquad (2.27)$$

$$\frac{u_{1m}}{U_0} = \frac{1}{\sqrt{(x/dC_D)}} \qquad (2.28)$$

$$b = \frac{1}{4}\sqrt{xdC_D} \qquad (2.29)$$

The characteristics of the axisymmetric turbulent wakes in the far-wake region. $x/d > 50$, can be derived based on slender flow approximations and performing an order of magnitude analysis as:

$$\frac{u_{1m}}{U_0} = \frac{C_1}{\left[\frac{x}{\sqrt{C_D}}d\right]^{2/3}} \qquad (2.30)$$

$$\frac{u_1}{u_{1m}} = \left[1 - (r/\bar{b})^{3/2}\right]^2 \qquad (2.31)$$

$$\frac{b}{\sqrt{C_D}d} = C_2\left[\frac{x}{\sqrt{C_D}d}\right]^{1/3} \qquad (2.32)$$

where r is the distance from the center line and $\bar{b}$ is the value of r where u_1 is close to zero. The experimental results of Hall and Hislop (1938) agrees with Eq. 2.31. The wake of a disk was studied by Carmody (1964) who found that the velocity profiles were similar at $x/d > 15$ and $C_1 = 0.36$ and $C_2 = 0.60$. Chevray (1968) studied the wake behind

a spheroid of an aspect ratio of six and found that $C_1=1.84$ and $C_2=0.24$. For the wake behind a rectangular plate of aspect ratio of 1, C_1 was 1.0 and $C_2 = 0.28$, and for an aspect ratio of 10, C_1 was 0.5 and $C_2=0.6$ (Cooper and Lutzky, 19 55).

2.4　Flow Pattern and Scour Around the Bodies in Open-Channels

Detrimental effects of hydraulic structures on rivers can be reduced by using various forms of fish habitat structures, such as placement of big rocks or rock clusters. As a means of enhancing the rearing habitat for fish, large boulders, which were called fish rocks by Fisher and Klingeman (1984), have been used in rivers. To understand the performance of these habitat structures, the hydraulic characteristics and scouring pattern around them should be studied. These large elements have dimensions of the same order as the depth of flow, and change the flow field, local water velocity and direction, as well creating scoured area near the substrate. Also, the HS vortices are known as the main scouring agent in these fish rocks.

Fisher and Klingeman (1984) carried out a series of experiments in a rectangular flat-bed flume 4.9 m long, 1.1 m wide and 0.5 m deep and studied local scour around fish rocks. Coarse sand ($D_{50} = 1.5$ mm) was used as the bed material. They found typical HS vortices similar to those occurring at piers. It was observed that as the scour depth increased with time at the upstream face of a rock, the rock settled and shifted slightly upstream, partly into the scour hole. The depth of scour upstream of the rock increased with depth of water to a maximum value and then decreased as depth of water continued to increase. Maximum ratio of the scour volume to the rock volume occurs at the ratio of water depth to height of rock of 0.4 to 0.6.

Cullen (1991) conducted a series of experiments in a flume 11 m long, 1.2 m wide, and 1.2 m deep with a moveable section that was 2.4 m long, 1.2 m wide, and 0.2 m deep. The substrate thickness was 4.6 mm with a standard deviation of 0.6 mm. He

32

found three different vortices around the fish rocks, namely: Karman vortex, trailing vortex and HS vortex. He classified the shedding vortices from the sides as Karman vortices and vortices separating from the back surface of the body as trailing vortices.

Dwivedi et al. (1992) carried out some preliminary observations on the wake structure behind a hemispherical object as a model for a boulder or fish-rock. They conducted their experiments in two flumes. One flume was 7 m long, 0.46 m wide, 0.45 m deep and the other was 18 m long, 1.22 m wide, 0.65 m deep. Three sizes of hemispherical blocks of diameters 13 cm, 10.4 cm, and 7 cm were used. Different ratios of depth of approaching flow to the height of body (submergence ratio or relative depth) varying from 0.1 to 3.0 were used. They showed that the submergence ratio and the Froude number, F, of the approaching flow were the most effective factors. For a very subcritical flow and a high relative depth, the flow behavior seemed to be like that of a wake for submerged body, with a small depression close to the hemisphere. But by decreasing the ratio and in turn increasing F, the water surface level changed considerably in the vicinity of the body. The recirculation region behind the body moved to the water surface when Froude number increased at the same relative depth. At relative depth of one, the recirculation region occupied the total depth. With the same ratio and larger F, this region moved to the water surface.

Dwivedi et al. (1992) found that the recirculation region behind the hemisphere was reduced due to the strong downwash over the hemisphere. By increasing the depth of water, the recirculation region at the water surface decreased, and, at a submergence ratio of more than 1.5 in the 7 m long flume and 2.0 in the 18 m long flume, this recirculation region disappeared totally. But in both cases, the wake exists at the bed. It was observed that the flume dimensions affected the width of wake at the water surface but did not affect the wake width at the bed. The drop of water level behind the hemisphere was insignificant beyond a submergence ratio of 4 and generally did not affect the flow characteristics significantly. As the submergence ratio increases, the frequency of eddy

33

shedding decreases, which might be due to the increase in downwash. The velocity of wake behind the body was increased, as a negative wake effect, by arch vortices which cause secondary flow, and also by the downwash of the free stream. The wake length at the bottom of the flume increases by decreasing the submergence ratio. At a high submergence ratio, only the HS vortices were observed. The normalized length of recirculation region in terms of the flow was found to increase with the submergence ratio.

Zgheib (1993) investigated the effect of large bed elements on the flow to explain the behaviour of high gradient mountain streams. Using a laboratory flume, he studied the transition from localized supercritical to subcritical flow around large bed elements to determine the energy loss. He proposed that this flow is similar to a truncated jet distorted by stream channel boundary. He used smooth and angular rocks of different sizes and shape in a 10 m long flume of 1 m width. In his research, he focused mainly on the flow deflection phenomenon upstream of the large bed elements and classified them as: backward breaking jet, stationary non-breaking jet, and forward shooting jet. He defined the large bed elements as those which are not transportable by the flow. Mohanty and Peterson (1959) defined tumbling flow as dominant scattered regions of alternate acceleration and deceleration through critical flow over large bed elements. The large bed elements may occupy a significant portion of the depth of flow, or may even protrude through the flow surface.

Jarrett (1984) observed in his data that in high-gradient, natural mountain streams, the Froude number is generally less than unity. Even with increase in slope, the Froude number does not tend to increase. The cross-section of variations, bank roughness and spill resistance control the flow and keep it subcritical, though only for very localized areas. These very limited supercritical flows are highly unstable and energy of flow tends to modify the stream channel to keep it subcritical.

Tamai et al. (1987) studied the flow structure outside the recirculating zone and the frontal region of a hemisphere mounted on the bed of a laboratory re-circulating flume at relative depths of 15 and 8.57 (very deep submergence). By means of flow visualization they could differentiate two ranges of vortex structure around the body. First, for R of 900 (based on the radius of the hemisphere), arched vortex tubes formed successively along the separation line and then sloped gradually downwards, due to the presence of a strong downwash in the recirculation zone. Then, after almost touching the bed, each vortex tube was individually shed downstream, leaving the recirculating zone in a single row. As a result of the higher velocity in upper layers of the flow, vortex tubes were stretched after shedding. Each vortex tube became entangled with its successor. They found that the Strouhal number of the formation of vortex tubes was the same as that of the shedding vortex tubes from the recirculation zone. Higher S and R resulted in the smaller distance between successive vortex tubes.

They showed that for R number more than 2000, the evolution of these vortex tubes changed dramatically. In this range of R, due to the larger S number, the intervals of vortex shedding was decreased. The reduced distance between arched vortices in the recirculation zone caused a coalescence between successive vortices. Then these coalescent vortices shed from the edge of the recirculating zone as before, but in two parallel rows. As a result of this coalescence the frequency of shedding vortices from the body was different from the frequency of the shedding vortices from the recirculation zone. Their proposal was confirmed, by spectrum analysis of the data, i.e., higher frequency of vortex shedding from the body than that of the recirculation zone. For the Reynolds number higher than 2000 the Strouhal number for formation zone continues to increase, whereas the Strouhal number for shedding region decreases with R.

Tamai et al. (1987) also showed that the number and the characteristics of HS vortices in front of the body depend on the R number. As a scale of HS vortex, the height of its center h, in the range of 0.1 to 0.25 h/r where r is the radius of the body, decreased

by increasing R. The number of HS vortices increased by increasing the Reynolds number up to a critical value, after which the number of vortices decreased. They proposed that the number of the HS vortices decreases because in higher R the vortices start to fluctuate horizontally and then coalesce. The non-dimensional width of the front recirculation zone was constant for single HS vortex and increased with the number of the vortices up to a critical R, and kept its value in the supercritical regime.

Martinuzzi and Tropea (1993) studied the flow field around the surface-mounted, prismatic obstacles to differentiate between a two-dimensional obstacle along the width of the channel and a three-dimensional body. They used different flow visualization techniques such as crystal violet, oil-film and laser-sheet. They observed up to four HS vortices upstream of the obstacle. It was found that the reattachment length for a three dimensional body is much shorter than that of a two-dimensional one. Logan and Lin (1982) and Fackrell and Pearce (1981) arrived at the same conclusions. It was proposed that in the case of a three-dimensional body, part of the flow goes around the body whereas in a two-dimensional body (a rib spanning the entire width of channel) most of the deflected fluid flows above the top of the body, enlarging the recirculation zone.

Using flow visualization, Martinuzzi and Tropea (1993) observed that the distance between the outer limits of the wake of a cube on the bed decreased up to an approximate reattachment point and then increased again. They postulated that the recirculation region entrains the surrounding fluid towards the axis of symmetry. This may be due to the fact that after separation of the flow from the body, flow from the sides tends to bend inside, owing to the difference between the outside velocity and the wake velocity. As well, the direction of the rotation of the HS vortex is inward and helps the general inward flow. After the reattachment point, the initial rapid expansion of the wake is due to the increase of the mass flux in the wake close to the channel floor (as the shear layer reattaches and is subsequently entrained by the HS vortex). Further downstream, the wake grows more slowly as fluid is gradually entrained from the surrounding flow.

36

Martinuzzi and Tropea (1993) observed that in large aspect ratio, width to height, the legs of the HS vortex did not affect the middle of the wake because they were away from the wake center. Therefore, the wake is almost plane and the lateral component of velocity ,w, is negligible. As well, the longer the width of the body, the less the curvature of the separation line around the body. According to the above observation, the flow acceleration over the top of the body would be less and the deflected flow goes aside rather than over the top. Therefore, the less the relative depth, the less would be the maximum pressure at the front and the minimum pressure at the back. In fact, more fluid is channeled along the sides and less from the top when the relative depth decreases.

Based on this observation, they proposed that there were two states for separation region upstream of the body. In the first mode, high-inertia fluid was deflected on the front face of the obstacle and returned upstream in a jet adjacent to the wall which moved against the pressure gradient (Martinuzzi and Tropea, 1993). As the fluid lost its energy, it rolled up to form a system of up to four vortices, which characterizes the second mode. Therefore, Baker (1980, 1991) indicated only the second mode and Eckeler and Awad (1991), the first mode.

Larousse et al. (1991) found that the two legs of the HS vortex behind a cube downstream of the reattachment point were still present and they remained adjacent to one another, with no further stream wise vortices occurring in between. The location of the legs further downstream became closer to the axis of symmetry. It was proposed that the influence of the recirculation vortex entrained the inner portions of the HS vortex and drew the legs towards the axis of symmetry.

Hunt et al. (1978) showed that fluid is exchanged between the different separation regions around a three-dimensional obstacle. Therefore, the separation "bubble" formed around the body cannot be closed. Instead, the separated regions have fluid passing through them and are the origins of line vortices that are shed into the downstream flow. Schofield and Logan (1990) investigated the flow around three-dimensional obstacles and

37

confirmed the above finding as well. They found that the bed shear stress behind a three-dimensional obstacle recovers faster due to the additional mixing induced by the stream wise vortices. As the aspect ratio of a prism increased, the stream wise vortices moved away from the centerline, decreasing the mixing along it, which resulted in a slower recovery rate. The mean velocity profiles also indicated the same trend to return to the equilibrium faster than that of a two-dimensional one, due to the presence of stream wise vortices.

2.5   Local Scour

Scouring as a natural process is not limited to the effect of man-made structures. Its might can also be seen by observing natural morphologic changes in the rivers. Scouring can happen when flow conditions change, such as when the presence of an obstacle capable of increasing the sediment transport capacity in its vicinity causes severe scour or deposition of sediment particles.

Scouring in a river or stream can occur due to various natural processes, irrespective of the presence of structures or obstacles in that environment. This type of scour is called *General scour* . It occurs due to the increased capacity of a river to carry sediment during flood, or because of man-made alterations, such as cut-off meanders or mining of sand and gravel in rivers and on flood plains. *Constriction scour* occurs when a structure causes the narrowing of a water way such as bridges or the re-channeling of flood plain flow. This kind of scour happens when the cross section of a river at a crossing is reduced by encroachment of the embankments on the flood plain or even on the river channel. The flow concentration and higher velocity of flow at the constriction are the cause of scour here. *Local scour* occurs directly due to the impact of the structure on the flow. The magnitude of this type of scour depends on the characteristics of the structure and has to be added to the *general scour* and *constriction scour* to get the *total scour*.

38

Scour can occur for a wide range of flow and bed materials. *Clear-water scour* occurs when the bed shear stress in the normal flow far upstream of the obstacle is less than the critical bed shear stress necessary to initiate the motion of sediment particles at the bed. Therefore, the bed material in natural flow condition away from the scour area would be undisturbed. When the bed shear stress is more than the critical shear stress in the absence of the structure, *Live-bed* scour would occur. In this case, the bed material is transported by the flow and as a result there would be a general movement of sediment at the bed. This causes a constant flow of sediment to enter the scour hole from the upstream side and when it equals the amount of material removed from the scour hole, the equilibrium scour depth occurs. In the *clear-water* scour the equilibrium scour depth depends only on the time and there is no supply of sediment from upstream side to the scour hole.

In bridge pier studies, four main flow patterns have been distinguished: 1-down flow, 2- HS vortex, 3- Cast-off vortices and wake, 4- Bow wave (Breusers & Raudkivi, 1991). The bow wave could not be observed in the present study for the relative depths of more than 1. For relative depths of less than one, due to the round shape of the body, the bow wave could not be generated. Downflow has been known as a major parameter in scour around the bridge piers. Therefore, numerous investigations been carried out to study its effects and magnitude. Breusers and Raudkivi (1991) have presented a coherent discussion of this problem. In the vertical plane of symmetry, when the flow hits the body of the pier, the velocity reduces to zero. But due to a decrease of the velocity from the surface downwards in general flow, the stagnation pressures ($\rho u^2/2$) decrease with the same trend from the surface towards the bed. Therefore, there is a downward piezometric pressure gradient in front of the pier. This downflow gains its maximum strength below the bed level in the presence of a scour hole and 0.05 to 0.02 pier diameter upstream of the pier and at about one pier diameter below the bed level. Its maximum magnitude

reaches 0.8 times the mean approach flow velocity (Breusers and Raudkivi 1991).

Raudkivi (1991)proposed that the HS vortex is a consequence of scour - not the cause of it - that HS vorteex transports the material away from the scour hole and pushes the downflow to the body, making it closer to the body. But it was clear in this study that even in a rigid bed, the HS vortices are present and the scour only intensifies their strength. He found that the legs of the HS vortex only a few pier diameters downstream of the body lose their identity and become part of the general turbulence present in the wake of the body.

The scour develops at the sides of the hemisphere and then propagates upstream and creates a scour hole in most of the perimeter of the body except the wake area. This scour hole is concentric with the hemisphere. The deposited bar at the back makes it hard for sediments to be removed from the scour hole at the front by the flow and HS vortex. so anything that decreases the height of these deposit bars, increases the scour depth. The "vacuum cleaner" effect of the cast-off vortices at the wake might lower the bed and help the scour at the front.

The strength of the downflow in the case of a hemisphere type of obstacle is not significant due to the round shape of the body, and it only becomes important after development of scour hole. Downflow for a cube type of body might be as important as piers. If the part of the obstacle covered by the bed material is deep enough, the effect of the downflow increases. The detailed flow pattern of the downflow has been described by Breusers and Raudkivi (1991). The downflow as vertical jet erodes the bed material around the body. The eroded material is then carried downstream by the aid of both the accelerated flow at the sides and the spiral motion of the HS vortex. At the very front of the pier, the downflow hits the bed and makes a steep slope type of groove, then turns its direction to an upward flow when it gets diverted to the upstream side by the aid of the HS vortex. This action of strong down flow creates a very sharp face for the inner scour

hole and then creates a shallow hole in the outer circle around the body with a slope equal to the angle of repose of sediment.

At the equilibrium stage the difference between these two parts is very small. Strong upward flow helps to maintain a slope steeper than the natural angle of repose of sediment, which occasionally collapses at its rim like small avalanches. Therefore, the deeper part is created by the down flow and the shallower part is the result of the deflection of the down flow to the upstream by the HS vortex. The bed materials, after being transported by the flow, get deposited on the bar at the downstream side of the body. The equilibrium stage would be reached when the effects of the temporal mean shear stress, the weight of the particle and the turbulent agitation are balanced or in equilibrium. For the live-bed scour, an excess shear stress is needed to carry the particles from the scour hole.

2.6   Effect of Specific Parameters

Characteristics of the sediment, the flow, the geometry of the body and the channel affect the maximum local scour depth.

2.6.1 Effect of sediment grading

Due to the possible similarity between the flow patterns around the bridge pier and free ended obstacle, it is useful to consider some of the results from studies on erosion near piers. Raudkivi and Ettema (1977 a, b) studied the effect of grain size distribution on the local depth of scour. Their results show that normalized maximum clear-water scour relative to the pier diameter, y_s/D, is a function of σ/D_{50} in which σ is the standard deviation of the grain-size distribution, y_s is the clear-water scour, and D_{50} is the median particle size. They found that for a coarse grained, non-ripple forming sediment (d > 0.7 mm) of a single grain size (σ close to zero), y_s/D =2.1 - 2.3 with no

dependence on grain size. When there is a grain size distribution, the smaller sand grains are removed and larger ones remain and create an armor layer and prevent a large y_s/D.

In fine grain sands, $d < 0.7$ mm, ripples develop when the bed shear stress is close to the critical value. Then sediment is transported to the scour hole from the upstream side and fills it, reducing the ratio of y_s/D to 1.4-1.5. Therefore, probable scour depth can be estimated only if the value of σ/D_{50} of the bed material is known (Raudkivi and Ettema, 1977 a-b). It was also found that the grading affects the maximum value of y_s/D but not the amount of time required to reach the equilibrium.

2.6.2 Effect of body and sediment size

Ettema (1980) showed, based on his laboratory data for six pier sizes and range of sediment sizes from $D_{50} = 0.24$ mm to 7.80 mm, that the maximum value of clear-water scour $(y_s/D)_{max}$ does not depend on the particle size if the value of D/D_{50} is larger than about 25. The initial phase of scour is the same for different values of D/D_{50}, but erosion phase and equilibrium stages are different. For coarse sediments, $D/D_{50} < 30$, the stones are large relative to the width of the groove excavated by the down flow, and the bed is fairly porous. A significant fraction of the down flow energy is dissipated by flow penetration into the porous sands. The peak, $y_s/D=2.2$, occurs at $D/D_{50} = 50$.

The pier size affects the time it takes to reach the equilibrium stage but not the value of y_s/D, neglecting the effects of relative depth y/D, and relative grain size D/D_{50}. The larger the piers the larger the scour volume and the more the time it takes for scour to develop at a given stress ratio. For clear-water scour, it was reported that it took 3 to 4 days to reach its equilibrium stage for $u_*/u_{*c} = 0.9$ to 0.95.

Threshold or initiation of movement of a particle due to the action of fluid flow can be defined when the destabilizing forces of fluid drag and lift exceed the stabilizing force of gravity. Shields curve describes the initiation of motion for uniform sediment in

unidirectional flow with a negligible bed slope and an average level of turbulence. It defines the threshold in terms of a dimensionless shear stress entrainment function :

$$Q_c = \frac{\tau_c}{\rho g \Delta d} = \frac{u_{*c}^2}{g \Delta d} \qquad (2.33)$$

where $\Delta = (\rho_s - \rho) / \rho$ and grain Reynolds number : $R_e* = \frac{u*d}{v}$ where $u* = \sqrt{\frac{\tau_o}{\rho}}$ is the shear velocity and τ is the bed shear stress. To overcome the difficulty of having the shear velocity in both axes of Shields diagram the data on the threshold can be described by a dimensionless particle size :

$$D_* = 2.15 R_* ; R_* < 1 \qquad (2.34)$$

$$D_* = 2.5 R_*^{4/5} ; 1 < R_* < 10 \qquad (2.35)$$

$$D_* = 3.8 R_*^{5/8} ; R_* > 10 \qquad (2.36)$$

where $\qquad D* = \left(\frac{\Delta g d^3}{v^2} \right)^{\frac{1}{3}}$

If the size of sediments is less than 0.7 mm there would be a no-ripple-forming condition in which $u*$ can be as large as 0.95 $u*_c$. with no disturbance at the upstream side on the bed. For smaller size ($d < 0.7$ mm), ripples develop on the bed which cause a small amount of sediment transport (Breusers & Raudkivi , 1991). These ripples can develop at $u* < 0.6 \, u*_c$.

2.6.3 Effect of flow depth

Observations in bridge piers show that for shallow flows, the scour depth increases with depth of flow but, for larger water depths, the scour depth is almost independent of depth. Depth affects the u_*/u_{*c} and y/D. If u_*/u_{*c} is constant, the effect of the flow depth for y/D larger than 2 to 3 can be neglected (Breusers et al. 1977). By decreasing the flow depth, surface roller which acts like bow wave in boat motion, interacts with HS vortex in piers. Having opposite direction of rotation, the surface roller decreases the effect of down flow, hence the scour depth. In shallow flow, the equilibrium scour depth decreases with particle size for the same values of u_*/u_{*c} and y/D. The finer the sediment relative to pier size, the smaller is the range of influence of flow depth. For fine sediments, y_S is almost independent of y when $y/D=2$, whereas for coarse sediments, this ratio may be closer to six.
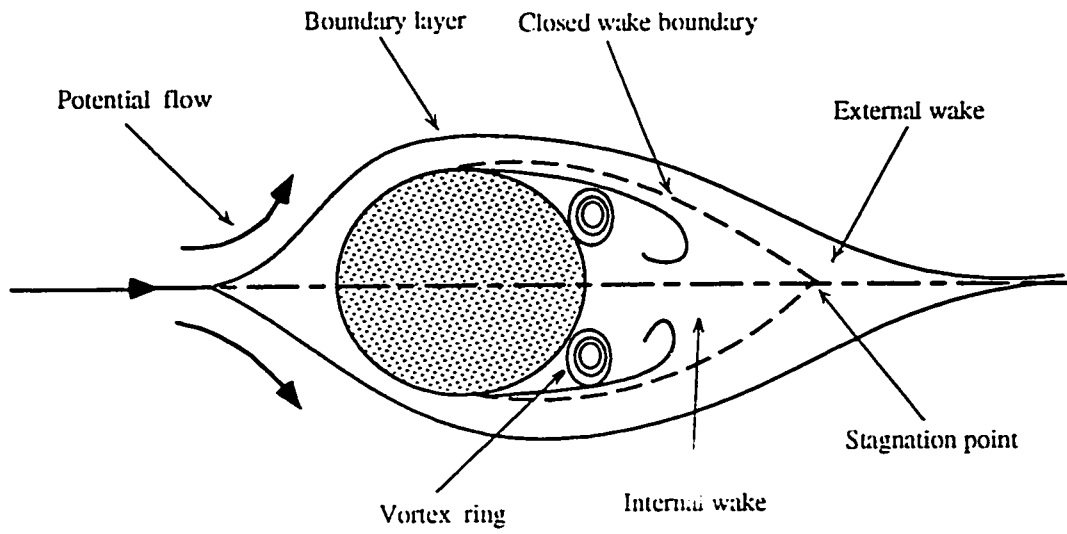
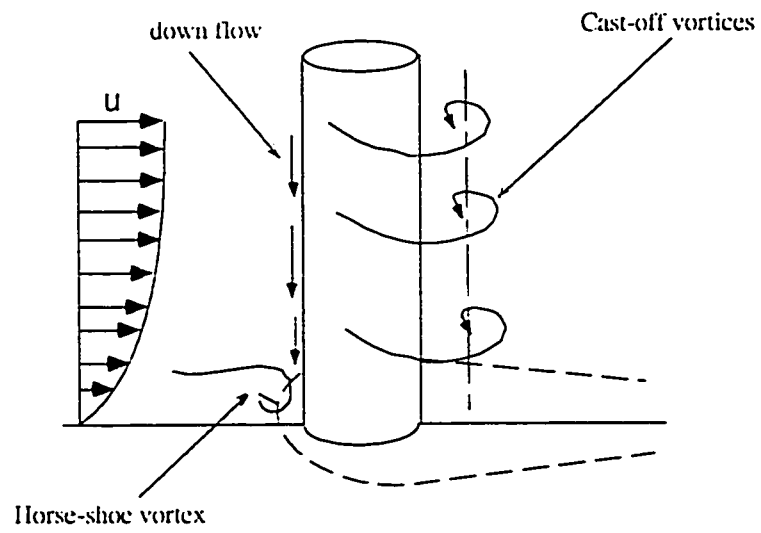Figure 2.1: Vortex System Around a Free Body
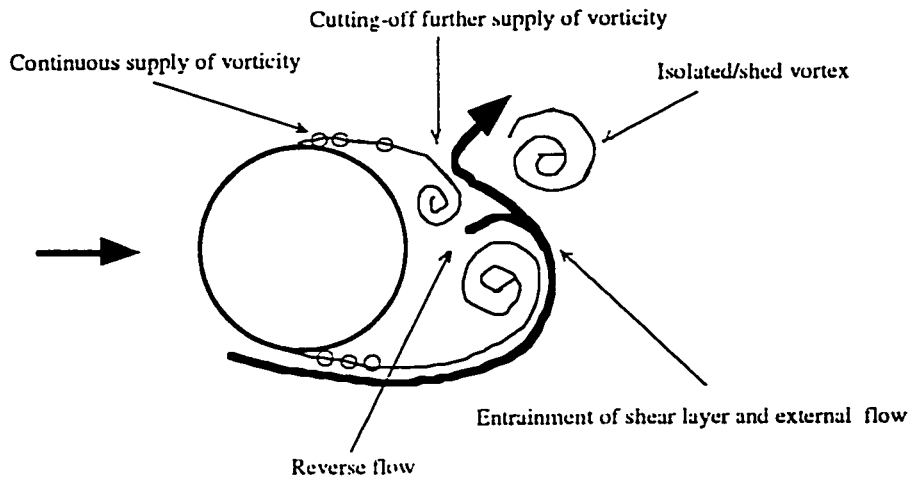

Figure 2.2 : Vortex System Around a Cylinder

45

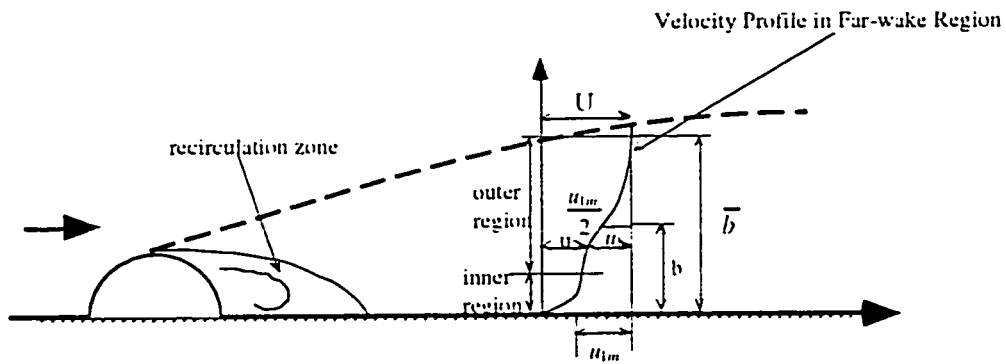Figure 2.3: Asymmetric Vortex Shedding in Two Dimensions

Figure 2.4 : Two-dimensional Wall-Wake

CHAPTER 3

EXPERIMENTAL ARRANGEMENT AND
INSTRUMENTATION TECHNIQUES

3.1   Introduction

This chapter describes the laboratory equipment and experimental procedure used in this study. The characteristics of model and natural rocks, and bed materials are presented, along with the results of preliminary tests for defining the state of flow in the laboratory flume.

3.2.   Experimental Facilities

3.2.1 Laboratory flumes

The experiments were carried out in two different flumes. Flume #2 was 1.08 m wide and 0.2 m high. It was used for a limited number of flow visualizations on the mobile bed. This flume was originally used for an extensive investigation on curved channel flow. Only the straight part of the flume at its upstream end was used to observe the flow. The bed and walls were made of plexiglass and a sediment layer of 50 mm of fine sand, D_{50}=0.25 mm, was used and a sphere was glued to the center of the flume.

The rest of the flow visualization, velocity field and bed shear stress measurements were carried out in flume #1. This flume was 18 m long, 1.22 m wide and 0.65 m high. The bed was non-erodible, made of smooth aluminum, with Plexiglas side walls. The flume had an adjustable bed slope and a tailgate to control the downstream flow depth. The slope of the flume could be adjusted by an electric motor which controlled three pairs of synchronized screws located under the bed. Measurements of the water surface profiles, scour depth, velocity and shear stress were accomplished by using a traverse installed on the flume. It was capable of holding different types of probes and point gauges and could be moved along the channel, laterally or vertically.

An underground sump network and a Fairbanks-Morse 20 hp propeller pump supplied water to the inlet-tank of the flume. A 200 mm diameter Faxboro Magnetic Flow Meter was used to measure the discharge. A Fluke 8000A digital multi-meter measured the flow rate with an accuracy of 0.1 L/s. The maximum flow rate was about 75 L/s with one-half liter fluctuation in long period runs.

The inlet-tank was 2.44 m long and 1.8 m wide with a smooth semicircular contraction from the walls and floor into the flume (Figure 3.2). A series of 100 mm diameter pipes with a length of about 1 m were used in layers inside the inlet tank to straighten the flow. To intercept and control the highly turbulent flow, a weir made of masonry bricks was installed before the flow straighteners. Synthetic material in a honeycomb pattern was used on both sides of the flow straighteners to dissipate the turbulence further. Then a sloping board at a 45 degree angle to the head tank bed was installed to intersect the curved surface of the inlet tangentially, to prevent the occurrence of longitudinal vortex due to the contraction configuration. Furthermore, to depress surface waves, a wooden board at the water surface was used. The straightness of the flume's bed was checked as well.

For the simulation of the mobile bed, an arrangement shown in Figure 3.1 was used. In the mobile bed runs, a sediment recess of sufficient depth was provided for the development of scour around the body. A false floor, 110 mm high and 10.5 m long was provided on the original aluminum floor. The thickness of the sediment layer was 20 mm on the raised floor, except for the sediment recess. In this flume, two different sizes of coarser sands were used, with D_{50} of 1.11 mm and 2.1mm. The dimensions of sediment recess was designed based on the previous experiments in Flume #2. Dimensions of 0.61 m by 1.22 m around the body and a depth of 130 mm were found to be enough in most of the experiments. A rough steel mesh, 1.22 m long, was used at the upstream end of the false floor to provide a smooth transition from the deep inlet flow to the shallow flow on the wooden frame. The length of the mobile bed here allowed the presence of a uniform

and fully developed flow. For simulation of an obstacle in a rough bed, a hemisphere made of Styrofoam mounted on a cylinder was installed in the center of the sediment recess on the original bed. This location was used as the center of the coordinates (Figure 3.1). A natural rock was later placed on the sand surface at the center of the sediment recess, to watch the scour patterns.

To measure bed shear stress at the threshold of movement of sediment around the body, a rigid bed was used. A wooden board was placed on the sediment recess while the same size sediment was glued on it. The location of the hemisphere, as before, was at the center of the board. In this way by providing the same roughness at the bed, sediment particles were prevented from moving. Therefore, the scour could not be developed and bed shear stress measurements at the vicinity of the body indicated the condition in which the sands started to move i.e., the threshold of sediment movement. The rigid bed setup is shown in Figure 3.2 a. A smooth bed was used for the velocity field measurements and flow visualization, with a simple Styrofoam hemisphere glued on the aluminum bed. The smooth bed setup in the absence of the false floor is shown in Figure 3.2 b.

3.2.2 Sand types

In alluvial or non-cohesive sediment the grain size and density are the characteristics which affect the sediment transport most. These characteristics of the sediment should be studied prior to the actual measurements. As a simple guide, the median size is used to classify the size of sands. Based on British standard BS1377 : (1975) sands are classified as: fine sand 125-500 μm, coarse sand 0.5-1.0 mm, very coarse sand 1-2 mm. The other characteristics of sands can be derived from the particle size distribution or sieve analysis. If the value of D_{95}/D_5 in the cumulative distribution curve is less than 4-5 or if the geometric standard deviation of the sand, $\sigma_g = D_{84.1}/D_{50} = D_{50}/D_{15.9}$, is less than 1.35, the sand can be considered uniform (Breusers & Raudkivi, 1991). For hydraulic calculations, an effective grain size of D_{50} is

adequate when there is a relatively narrow grain size distribution but for a graded bed materia, D_{75} or D_{80} is more appropriate.

Flow over non-uniform sediment causes a more complex erosion, so in this study only uniform sediment were used. In non-uniform sediment the coarser grains tend to armor the surface that reduces the effective roughness, which in turn causes the bed forms to be lower and flatter compared with uniform grains (Breusers & Raudkivi, 1991). The sediment transport can also vary with time in a constant flow rate, and even approaches zero. Bed features such as ripples, dunes, and anti-dunes can occur whenever the bed shear stress, caused by the high velocity, exceeds the threshold values. Ripples usually develop at $U_0/U_c > 0.6$.

In the study of the mobile and rigid beds, three different types of natural quartz sand were used. The finer sand with D_{50} of 0.25 mm was used for preliminary flow visualization of mobile bed in Flume #2. The two coarser ones were used in Flume #1. The sand with D_{50} of 1.11 mm consisted of very similar material while the other one with D_{50} of 2.12 mm had angular edges and materials of different colors. The grain size distributions of these sands are shown in Figure 3.3. The sediment with D_{50} of 1.11 mm and 2.1 mm which were used in the measurements of bed shear stress and scour, fell in the uniform class category (Table 3.1). The fine sand of type one was only used in two preliminary observations in Flume #2.

3.2.3 Pressure transducers

Transducers were used to measure the pressure and velocity by conversion of the differential pressure to voltage. Validyane DP45-16 differential pressure variable reluctance transducers were used. The pressure range for DP45-16 based on the manufacturer's catalogue, was ±35 mm of water (±1.4 inches) or ±0.35 K Pascal and ±0.25% accuracy on the full scale. Therefore a maximum velocity of 0.83 m/s with an accuracy of ±0.1778 m/s could be expected. Validyane CD379 Battery operated portable

digital transducer indicators were used to display the output of the pressure transducers in digital form, which then could be transferred to a data acquisition system for analysis. Their zero adjust range was ±10 mV/V and they were capable of ±1999 counts for full scale output from the transducer.

Table 3.1 Sediment characteristics

	sand # 1	sand # 2	sand # 3
Mean diameter. D_{50} (mm)	0.25	1.11	2.12
$D_{84.1}$ (mm)	0.351	1.32	2.54
$D_{15.9}$ (mm)	0.169	0.9	1.54
geometric standard deviation, σ_g	1.44	1.20	1.29
Specific gravity. S_c	2.65	2.65	2.65
Angle of repose. α_r (degree)	26	28	30
Critical shear stress, τ_c (Pascal)	0.185	0.64	1.46

In order to calibrate the transducers, they were connected to a known head of ±1 inch of water. By connecting the indicator to the transducers, the outputs for heads of zero and ±1 inch of water were adjusted using both zero and span screws on the indicator so they could show zero and ±1 volt respectively. In the case of Prandtl tube in one dimensional velocity measurements, the range of zero to 1 inch of water was needed because the differential pressure would always be positive. For two dimensional velocimetry, the range of ±1 inch of water was examined due to presence of both positive and negative directions.

After fixing the limits of zero and ±1 volt for zero and ±1 inch of head, using 0.1 inch of water increments, the range ±1 inch was calibrated. It was found that in most cases, starting from +1 inch head towards -1 inch head, the corresponding voltage went

beyond -1 volt even before reaching -1 inch head or did not reach -1 inch at -1 volt. So the fitted curve did not have its limit at -1 volt and was calibrated to the maximum value less than -1 inch. By curve fitting, several equations of Polynomial or Power type were used to represent the conversion of head to the voltage, which all were close to linear function. The calibration was checked during the process of measurements and it was found to be almost invariant. An example of the calibration can be seen in Figure 3.4.

3.2.4 Data acquisition system

Several different types of probes were used in this study to measure the velocity and shear stress fields. To accommodate all these measurements, a data acquisition system consisting of a fx II Macintosh computer, equipped with data acquisition board was employed. This system was located in the T. Blench Hydraulics Lab. The Lab View program, which is a graphic language was used for measurement of bed shear stress and the velocity field by Prandtl tube, Pitch probe and Yaw probe. The program used the calibration equations of the transducers and different probes and then could compute different variables. The standard deviation of the measured data , σ_d, was part of the program output. Different parameters could also be set, such as the number of the samples, sampling frequency and characteristics of probes and roughness.

Based on the magnitude of turbulence present in the flow, the period of each measurement was set. The usual sample number was 6000 for Prandtl tube (for one dimensional velocimetry), with 40 micro seconds interval. This provided a duration of 240 seconds with a frequency of 25 Hz. The frequency for two dimensional velocimetry was 12.5, with a duration of 200 seconds. In more turbulent flow, the sample number and the duration of the measurements had to be increased to obtain a better average.

3.3 Velocity Measurements

Several types and sizes of probes were used to measure the velocity. Pitot-static tubes or Prandtl tubes were used for measuring one dimensional velocity. Pitch or yaw probes were used in two dimensional velocity measurements. The types and sizes of these probes and their calibrations are presented in this section.

3.3.1 Pitot-static tube

The pitot-static tube was used to measure the velocity of the undisturbed flow at the plane of symmetry when there was no obstacle on the bed. It was also used for bed shear stress measurements at the plane of symmetry (POS) of the disturbed flow where it was assumed that bed shear stress is uni-directional due to symmetry. Two different commercial tubes were used with external diameters of 3 mm and 1.6 mm.

Initially, the intent was to use the standard deviation of the velocity measurements σ_d as a measure of velocity fluctuations, which reflects the turbulence in the flow. But considering the very high frequency requirement and some doubts about the validity of the output signals as the true indicators of turbulence, such as decay of turbulent flow inside the plastic tubes, the standard deviations were used just as indicators and not actual turbulence characteristics. The details are discussed in Chapter (3.3.3).

3.3.2 Yaw and pitch probes

Where the velocity has only two components, yaw and pitch probes were used. In this case, knowing the approximate plane of this velocity, its two components could be measured. If there was a third component, it had to be checked as to whether its magnitude and direction were important. When the third component had an angle of less than 5 to 10 degrees, yaw and pitch probes were used. Very close to the body, where all three components of the velocity were important, they could not be used.

This study used a series of yaw and pitch probes made and calibrated in T. Blench Hydraulics laboratory by Rajaratnam and Muralidhar (1967). The details of the development and calibration of these probes can be found in their reports. The pitch and yaw probes were made of three stainless steel tubes. To make a probe, these three smaller tubes are rigidly soldered together, while the nose of the probe was machined. The central tube is perfectly flat and the side tubes are chamferred at an angle of 45°. The large yaw probe was 2.8 mm thick and the smaller one was 1.1 mm thick. The vertical thickness of the pitch probe was 9.9 mm.

Rajaratnam and Muralidhar (1967) discussed the working principles of these probes based on simple pressure head equations. To detect the velocity in a horizontal plane of the tube, the yaw probe, referring to the angle of yaw or θ between the tube and the velocity vector, can be oriented parallel to the flume's wall. In the vertical plane, pitch angle or ϕ defines the angle between the velocity vector and the probe, which then is referred to as pitch probe. Therefore, the piezometric heads at the nose of the three tubes making the probe can be written as :

$$h_1 = h_0 + K_1 \frac{V^2}{2g} \qquad (3.1)$$

$$h_2 = h_0 + K_2 \frac{V^2}{2g} \qquad (3.2)$$

$$h_3 = h_0 + K_3 \frac{V^2}{2g} \qquad (3.3)$$

where h_0 is the static piezometric pressure head at the point and V is the velocity vector. K_1, K_2, and K_3 are the calibration coefficients and are functions of only the yaw or pitch

angle for a given probe, neglecting viscous effects and other minor correction factors. Combining the three previous equations, one can obtain the following equations:

$$\frac{h_2 - h_3}{h_2 - h_1} = \frac{K_2 - K_3}{K_2 - K_1} = K_4 \qquad (3.4)$$

and

$$V = \frac{\sqrt{2g(h_2 - h_1)}}{\sqrt{K_2 - K_1}} = K_5 \sqrt{2g(h_2 - h_1)} \qquad (3.5)$$

defining two new coefficients of K_4 and K_5. The probes were calibrated (in the potential core of a plane turbulent wall jet produced by a deeply submerged sluice gate) for known angles in the range of zero to 60 degrees resulting in calibration curves for K_1 to K_5 as only a function of θ. The results were symmetrical for the other side (zero to -60°). The results of calibration of the yaw and pitch probes were very close, so only one calibration curve was used for both of them (Figure 3.5 a).

The calibration equations were fed into the computer program of the data acquisition system. Then by entering the output of the pressure transducers to the system, the direction of the velocity vector and its magnitude and σ_d of velocity could be obtained. In the calibration of the yaw and the pitch probes according to Rajaratnam and Muralidhar (1967), the side on which the velocity attacks the probe can be either of the two side tubes. Therefore, the differential pressure between the middle tube and the tube on the side the velocity is attacking should always be less than the differential pressure between the middle tube and the tube on the other side. These were considered in the data acquisition system and the setup of the equipment so that the sign of the output velocity was always adjusted to the defined coordinate system. The steps which lead to the calculation of these functions are:

1. differential pressures of h_2-h_3 and h_2-h_1 are measured ;

2. K_4 could be obtained from Eq. (3.4);

55

3. having K_4, θ can be found from Figure 3.5;

4. then K_5 could be calculated as a function of θ from Figure 3.5;

5. magnitude of the velocity, V, could be obtained from Eq. (3.5).

3.3.3 Use of total head tubes in turbulence measurement

Existence of data acquisition systems with a high rate of data collection and analysis might provide a proper means to use pressure-based tubes to measure turbulence characteristics. Generally in flows free of turbulence and any other unsteadiness, pressures and velocities at a given point in space are constant in value and differentials in the steady pressure at two points in the flow reflect differences in velocity:

$$P_t = P_s + \frac{1}{2}\rho U^2 \qquad (3.6)$$

$$U = \sqrt{\frac{2(P_t - P_s)}{\rho}} \qquad (3.7)$$

where P_t is the total pressure and P_s is the static pressure and U is the flow velocity. This equation is accurate if the probe does not disturb the flow and the probe is carefully aligned parallel to the stream. But there are some effects on the total-pressure measurements in practice, such as a shift of the effective center of the probe towards the high-velocity region; creation of an asymmetric flow around the tube by the wall; and more importantly, the time mean total pressure does not correspond to the time mean velocity due to turbulence. R. J. Goldenstein (1983) indicates this inequality properly, and his findings are used here extensively. In a general form of Eq. (1) the fluctuation of the pressure and velocity are included. For a simple two-dimensional flow, Euler's equation reads:

56

$$\frac{\partial(U+u)}{\partial t} + (U+u)\frac{\partial(U+u)}{\partial s} = -\frac{1}{\rho}\frac{\partial(P_s+p_s)}{\partial s} \qquad (3.8)$$

where u and p_s are the turbulent fluctuations of velocity and static pressure respectively ,while P_S and U are the mean values. For inviscid, irrotational flow, i.e., zero vorticity. after integration we get :

$$\frac{P_s+p_s}{\rho} + \frac{(U+u)^2}{2} + \phi = \text{const.} \qquad (3.9)$$

After time averaging it becomes:

$$\frac{P_s}{\rho} + \frac{(U^2+\overline{u^2})}{2} = \text{const.} \qquad (3.10)$$

and the difference between these last two equations is :

$$\frac{P_s}{\rho} + uU + \phi = 0 \qquad (3.11)$$

where ϕ is the fluctuating potential and in a locally irrotational region of the flow would be the same at the stagnation point in the flow and on a nearby point away from the stagnation point. Therefore, in the vicinity of the probe, the total pressure could be calculated by the Bernoulli equation:

$$(P+p)_t = \frac{1}{2}\rho(U+u)^2 + P_s + p_s \qquad (3.12)$$

which after expansion and by taking the average, the fluctuating pressure and the time-averaging becomes:

$$p_t = p_s + \frac{1}{2}\rho\left(u^2 - \overline{u^2}\right) \qquad (3.13)$$

$$P_t = P_s + \frac{1}{2}\rho\left(U^2 + \overline{u^2}\right) \qquad (3.14)$$

in which $\frac{\rho}{2}\overline{u^2}$ is an extra term compared with the ideal flow (Eq. 3.6), which represents

an error in measurement of total pressure by this kind of probe. Also, it can be shown

that :

$$\frac{U}{[2(P_t - p_s)/\rho]^{\frac{1}{2}}} = \left(1 + \frac{\overline{u^2}}{U^2}\right)^{-\frac{1}{2}} = 1 - \frac{1}{2}\frac{\overline{u^2}}{U^2} + \text{h.o.terms} \qquad (3.15)$$

where $\frac{1}{2}\frac{\overline{u^2}}{U^2}$ appears as an extra term. But in most flows the relative intensity of

turbulence , $\frac{\sqrt{\left(\overline{u^2}\right)}}{U}$, is less than 0.2. Therefore, in these cases it can be seen that the

contribution of this extra term is small in the average differential pressure when we

compare the average velocity in both non-turbulent (U) and turbulent flow ($\overline{U}$):

$$\overline{U} \cong U\left(1 + \frac{\overline{u^2}}{U^2}\right)^{\frac{1}{2}} \cong U\left(1 + \frac{1}{2}\frac{\overline{u^2}}{U^2}\right) \cong U(1 + 0.02) \qquad (3.16)$$

Measuring the static pressure and the total presuure separately can yield both the mean

and the fluctuating components of the velocity and pressure.

Ippen and Raichlen (1957) were probably the first to use a total head probe to

measure turbulence by connecting it to a pressure transducer. Arndt and Ippen (1970) also

deduced the turbulence intensities from total pressure fluctuations and showed reasonable

agreement with hot-wire anemometer results. Nezu and Nakagawa (1993) indicated that it

would not be appropriate to use a total pressure tube to measure turbulence characteristics

due to the fact that the output includes the effect of pressure fluctuations and cannot be

used for direct measurement of velocity fluctuations. Further more the wave pressure is transfered through the tubes, which, considering the length and rigidity of these plastic tubes used for connecting the probe and transducer, causes the decay of turbulence. The effect of this kind of tube setup on the measurement of the turbulence has not been investigated properly. Using the probes also causes the disturbance of the flow which is not suitable for precise measurements compared with Laser Doppler Anemometery.

Further, the frequency of sampling should be enough to get the fine structure of the turbulence. Nezu and Nakagawa (1993) suggested that the best scales are the microscale L and the maximum wave-number K_{max} where frequency more than that could be interpreted as noise. In spectral distribution analysis, the dimensionless wave-number $L_x k_{max}$, where L_x is the macro scale of turbulence, should be at least 100 to catch the eddies in viscous subrange. L_x can be scaled with the flow depth in the outer region of flow. So maximum response frequency f_{max} and the microscale L of turbulence would be calculated as :

$$f_{max} = K_{max} \cdot \frac{U}{2\pi} \geq \frac{100U}{2\pi L_x} \cong \left(\frac{50}{\pi} \frac{U}{h} \right) \qquad (3.17)$$

$$L = \frac{1}{K_{max}} \leq L_x / 100 \cong \frac{h}{100} \qquad (3.18)$$

Then the sampling frequency of data processing should satisfy the Nyquisit frequency to allow the elimination of data aliasing. Therefore, for some of the experimental runs in this study, the frequency requirement would be as : 98 Hz for run AS1; 190 Hz for run BS1; and 142 Hz for run CS1.

Turbulence intensity can be used as a measure of the turbulent fluctuations. that is, the magnitude of departure of instantaneous velocity u from mean velocity U or standard deviation of the random velocity from the average velocity (STD of u). The

59

measured STD of the velocity across the channel at depth of y/h=0.5 shows that inside the wake the velocity changes more and decreases laterally toward the outside region. The defect velocity profiles indicated that the STD of the velocity did not show the presence of the legs of the horse-shoe vortex and changes in the velocity. This may possibly be due to the fine changes in velocity, which is not sensed by the STD profile.

The STD profile of velocity at the Plane of symmetry downstream of the obstacle, Run AS1, shows an increase of the STD of velocity at mid-depth of the flow, following a decrease toward the wall and again close to the wall an increase. In similar wind tunnel experiments by Okamoto (1979), the turbulence intensity increases all the way towards the wall and there was no decline. But far away from the hemisphere the STD profile shows a constant increase similar to the wind tunnel measurements. This may be due to the fact that the fine scales of turbulence are not measured, or simply because of the difference between the two experiments.

The STD of the velocity almost matches the STD of the pitch angle and shows that at about y/h = 0.8, although turbulence is not high but velocity changes a lot. So there would be a regular change of the velocity and hence shedding of vortices.

3.4 Effect of Roughness on the Velocity Profile

The velocity distribution for a uniform flow over a uniformly rough bed can be described by the following equation :

$$\frac{u}{u_*} = 5.75 \log \frac{y}{k} + B \qquad (3.19)$$

where u is the time-averaged velocity at a normal distance y from the datum; k is the characteristic length scale of the roughness elements of the rough bed, usually taken as median size of sand or D_{50} ; B is a function of the roughness Reynolds number $(u_* k/\nu)$

and u_* is the the shear velocity. In Eq. 3.19, von Karman constant κ was assumed to be equal to 0.4.

In practice, the roughness is expressed in terms of Nikuradse's (1933) equivalent sand roughness, k_s. The revised form of Eq. 3.6 then can be shown to be:

$$\frac{u}{u_*} = \frac{1}{\kappa}\ln\left(\frac{y}{k_s}\right) + B_s \qquad (3.20)$$

where B_s is a function of $u_* k_s/v$. In measurements of the bed shear stress and shear velocity, such as Preston method, it is necessary to determine k_s. The evaluation of the k_s also helps to classify the flow over the rough boundary as smooth, transitional and fully rough flow. The following equation can be derived from Eq. 3.19 and 3.20:

$$\frac{k_s}{k} = \exp\left[\kappa(B_s - B)\right] \qquad (3.21)$$

Defining the datum at 0.2 times the sand diameter lower than the sand surface (Einstein and El-Samni, 1949 and Hollingshead, 1972), y could be measured. Knowing the k, y and u_*, from Chapter 3.7.1, B can be computed in Eq. (3.6). Knowing the relation between the B_s and k_s (Nikuradse, 1933 ; Figure 3.6) the value of k_s would be determined by trial and error from Eq. 3.8. The lengthy procedure of the trial and error can be avoided by rearranging the Eq. 3.6 and Eq. 3.7 in a different way as :

$$B - \frac{1}{\kappa}\ln\left(\frac{ku_*}{v}\right) = B_s - \frac{1}{\kappa}\ln\left(\frac{k_s u_*}{v}\right) = B_s' \qquad (3.22)$$

where the variation of the newly defined variable B_s' can be plotted based on the known values of B_s (Figure 3.6). Then by knowing the values of the variables on the left hand

side of the Eq. (3.9), which are B, k and u∗, B'ₛ can be calculated, which in turn determines the value of u_*k_s/v, and then k_s and B_s from the Figure 3.6.

The effects of roughness on the flow is not similar for all different values of k_s. Nikuradse classified the effect of roughness based on u_*k_s/v. In a hydraulically smooth flow, $u_*k_s/v \leq 3.5$, the roughness elements are smaller than the thickness of the viscous sub layer and are completely submerged by this layer where B_s can be determined as :

$$B_s = \frac{1}{\kappa}\ln\left(\frac{u_*k_s}{v}\right) + 5.5 \qquad (3.23)$$

which by substitution in the Eq. (3.7) shows the velocity profile on the smooth bed:

$$\frac{u_*}{u} = \frac{1}{\kappa}\ln\left(\frac{yu_*}{v}\right) + 5.5 \qquad (3.24)$$

By increasing the size of the roughness, $3.5 \leq u_*k_s/v \leq 70$, some of them protrude out of the viscous sub layer and cause partial mixture of this layer with the turbulent flow. In this transition zone the value of B_s has been approximated by Nikuradse in three levels as :

$$\text{for} \quad 3.5 \leq u_*k_s/v \leq 7.1 \quad B_s = 6.59 + 3.5\log\left(\frac{u_*k_s}{v}\right) \qquad (3.25\ a)$$

$$\text{for} \quad 7.1 \leq u_*k_s/v \leq 14.1 \quad B_s = 9.58 \qquad (3.25\ b)$$

$$\text{for} \quad 14.1 \leq u_*k_s/v \leq 70 \quad B_s = 11.5 - 1.62\log\left(\frac{u_*k_s}{v}\right) \qquad (3.25\ c)$$

For $u_*k_s/v \geq 70$, the taller roughness elements are able to destroy the viscous sublayer completely by protrusion out of this layer. Under this condition the flow is

called rough turbulent flow, where the B_s assumes a constant value of 8.5 and the velocity profile equation changes to :

$$\frac{u_*}{u} = \frac{1}{\kappa}\ln\left(\frac{y}{k_s}\right) + 8.5 \qquad (3.26)$$

The variation of Bs and Bs' with the roughness Reynolds number is shown in Figure 3.6.

3.5   Bed Shear Stress Measurement

The bed shear stress measurements were used to determine the state of sediment transport close to the bed. They show whether the flow is capable of moving the sand or not, and therefore also shed some light on the study of the scour around the obstacle. There are several methods of measuring the bed shear stress or friction velocity, such as (Nezu and Nakagawa, 1993):

1. u_* can be calculated in uniform flow as $u_* = \sqrt{gRS}$ where R is the hydraulic radius and S is the channel slope (sectional average bed shear stress);

2. u_* can be determined by measuring velocity profile and considering log law;

3. u_* can be determined based on the Reynolds stress distribution, $-\overline{uv}(y)$, as: $\dfrac{\tau}{\rho} \equiv -\overline{uv} + \upsilon\dfrac{\partial U}{\partial y} = u_*^2\left(1 - \dfrac{y}{h}\right)$;

4. In the case of the existence of a viscous sub layer, it can be determined from : $u/u_* = yu_*/v$;

5. It can be measured directly by aid of Preston tube or a shear plate and friction laws.

The accuracy of the first method depends directly on small deflections of the bed and that of the water surface. It also would be an overall value and not a local one which may not be useful in open channel flow. Viscous sub-layer measurements are very difficult to make and so the fourth method was not used here. The third method is very good for turbulent measurements, which need appropriate equipment such as LDA. Therefore, the description of the methods 2 and 5 -which were feasible in this study- are

63

presented here. The velocity profile method was used for u* measurements in undisturbed flow and the Preston tube method was used in local bed shear measurements in disturbed flows.

3.5.1 Velocity profile method

The velocity profile can be employed to measure the friction velocity, which in turn is used to compute the bed shear stress. The velocity profile is defined by theKarman-Prandtl law of wall over smooth surface as :

$$\frac{u}{u_*} = 5.75 \log \frac{yu_*}{v} + C \qquad (3.27)$$

where C is a constant and v is the kinematic viscosity. Plotting the measured velocity profile on a semi-log paper results in a straight line in the log-law region. Then, by curve fitting, a best straight line can be derived for this velocity profile. The slope of this fitted line would be proportional to the friction velocity, which can be calculated based on only two points of the line of Eq. 3.27 as :

$$\sqrt{\frac{\tau_0}{\rho}} \equiv u_* = \frac{u_2 - u_1}{5.75 \log\left(\frac{y_2}{y_1}\right)} \qquad (3.28)$$

This method is also applicable for rough beds (Eq. 3.7). In such cases, finding the proper datum in vertical direction is important. Einstein and El-Samni (1949) and Hollingshead (1972) found that the 0.2 times sand diameter below the tops of the sand grains provides the best datum. In this study the datum in the rough bed was selected based on this guideline.

64

Obtaining the bed shear stress based on point measurements, such as in the Preston method, would not be accurate enough, especially if the measured value is going to be used as the basis of many other measurements or further studies. Some error might occur if placing the nose of the probe on the bed, causing protrusion of the probe in the sands resulting in disturbing of the datum. Therefore, the velocity profile method using the measured points on the profile was chosen as a more reliable method. This method was used to measure the bed shear stress at the POS of the undisturbed flow and the results were used to establish a basis for all the disturbed flow measurements.

3.5.2 Preston tube method

In turbulent flows, measurement of bed shear stress has always been a difficult task. To overcome this problem, Preston (1954) assumed that the law of the wall or the universal inner law is valid. Then he related the differential pressure of a total head tube (the so-called Preston tube) resting on the wall and the undisturbed static pressure to the wall shear stress in a non-dimensional form as :

$$\frac{\tau_0 d^2}{4\rho \upsilon^2} = F\left(\frac{\Delta p d^2}{4\rho \upsilon^2}\right) \qquad (3.29)$$

where Δp is the differential or dynamic pressure, d is the external diameter of the Preston tube, τ_0 is the bed shear stress and ρ and υ are the fluid density and the kinematic viscosity of the fluid respectively, and F denotes functional dependence. The function F can be then be derived from the measurements in fully developed pipe flow. Patel (1965) suggested a definitive form of function F, which has been used in this study for smooth bed. Some of his equations of calibrations were not explicit, which required a trial and error procedure. Therefore, explicit expressions have been derived from the original

65

equations (Table 3.1). In this way, the trial and error procedure is eliminated and the shear stress can be calculated easily.

When the Preston tube is placed over a rough boundary, the corresponding relation becomes:

$$\frac{\Delta p}{\tau_0} = F_r\left(\frac{\Delta p d^2}{4\rho v^2}, \frac{d}{k_s}\right) \qquad (3.30)$$

Hollingshead and Rajaratnam (1980) proposed an analytical form for the above relation where the law of the wall is assumed to be valid for rough surfaces. With their calibration chart, Preston tubes can be used to calculate the bed shear stress on smooth and approximately uniform rough boundaries. They measured bed shear stress on a sand-paper roughness and two hemispherical roughness with 4 different Preston tubes for d/k_s ratio varying from 1 to 25. Comparison between the analytical calibration curves and the experimental results was satisfactory for the hemispherical roughness and fair for the sand-paper roughness.

Based on their calibration curve in fully rough flow, measured differential pressure is only a function of d/k_s and so the F_r has a constant value. In this way, the calculations in the fully rough flow were much easier than the rest of the calibration curves when acquiring the shear stress manually. Fortunately, these different analytical calibration curves have been incorporated into this study's data acquisition system. Therefore, the bed shear stress could be measured directly by entering the k_s value and the diameter of probe, and the level of the datum.

3.5.3 Bed shear stress measurements

When the direction of τ_0 is known in deflected flow, the Preston tube is able to measure the shear stress directly. But when its direction is not known, this technique is not applicable. For such cases, Rajaratnam and Muralidhar (1968) used the yaw probe as a Preston tube. The size of the three tubes that made the yaw probe was similar to that of the Preston tube. Assuming an angle of θ between the yaw probe and the direction of the shear stress on the bed, the total pressures for the different tubes may be written as :

$$p_1 = p_0 + K_{10}\Delta p \qquad (3.31)$$

$$p_2 = p_0 + K_{20}\Delta p \qquad (3.32)$$

$$p_3 = p_0 + K_{30}\Delta p \qquad (3.33)$$

where p_0 is the static pressure; K_{10}, K_{20} and K_{30} are the respective calibration factors, which were assumed to be only a function of the θ at the bed, similar to their free stream counterparts. By combining the Eqs. 3.31 to 3.33 it was determined:

$$K_0 = \frac{p_3 - p_2}{p_1 - p_2} = \frac{K_{30} - K_{20}}{K_{10} - K_{20}} \qquad (3.34)$$

and

$$\Delta p = \frac{p_1 - p_2}{K_{10} - K_{20}} = \frac{p_1 - p_2}{K_{50}} \qquad (3.35)$$

Here again K_0 and K_{50} are assumed to be a function of only θ. Comparison of these calibration factors with the free stream curves showed that the K_{10} value was in good agreement with the free stream curve for θ to 40 degrees, beyond which there was some scatter. For the other two factors, K_{20} and K_{30}, the results were somewhat lower than the

67

corresponding free stream curves. In general the K_0 value was very close to that of the free stream. The variation of these coefficients is shown in Figure 3.5 b.

The procedure for computing the magnitude and the direction of the bed shear stress by the computer program is as follows:

1. measurement of the differential pressures (p_3-p_2) and (p_1-p_2) by transducers ;

2. calculation of K_0 from Eq. 3.34;

3. finding θ as a function of K_0 from Figure 3.5 b;

4. Finding K_{50} from Figure 3.5 b;

5. finding Δp from Eq. 3.35; and finally

6. computing shear stress from Eq. 3.29 and Eq. 3.30 for smooth and rough beds respectively.

3.6   Series of Experiments

In this study, a number of experiments were conducted for different flow conditions, with several different obstacles and bed roughnesses. A list of these experiments and the related parameters is shown in Table 3.3. The experiments are classified as different series. The series which were run only for flow visualization are denoted in the list by two characters such as series V1, W5 and X1. A series of flow visualizations in flume #1, denoted as series V, were carried out to investigate the general vortex system around the body with a very low R. In series W, the existence of different regimes was visualized. The only experiments in flume #2 are denoted by series X, which were carried out as a primary visualization of the scour patterns on the mobile bed.

The series of experiments conducted for measurement purposes are denoted with a label of multiple-characters. The first character in a label is denoted as the relative depth of the flow, such as A, B, C, D. These four series are representatives of: very deep flow with a high relative depth: series D ($d/h > 4$); moderate relative depth: series A ($4 < d/h <$ 1.3); relative depths close to the height of the obstacle: series B ($1.3 < d/h <1$); and finally

68

a low relative depth less than 1, i.e. the depth of flow is less than the height of the body: series C. The second character indicates the nature of the bed such as S for smooth bed, R for rigid bed and M for mobile bed. In mobile bed, a thick layer of sand allowed the scour to develop, whereas in the rigid bed sand was glued to the bed and was not allowed to move. Therefore, the rigid bed could simulate threshold of movement of the sediment particles just before development of the scour hole. The aluminum bed of the flume provided a smooth bed for series S.

The third character indicates the type of the obstacle used in the flume. The undisturbed flow with no obstacle is denoted by 0. Two sizes of hemisphere, with diameters of 13 and 74 mm, are indicated with 1 and 2. A cube of 74 mm side length is denoted as number 3. A natural rock is number 4. The fourth character denotes the size of the sands used as sediment on the bed. Two median sizes of 1.1 and 2.1 mm were used. and are denoted as #1 and #2.

All measurements had to be carried out in a region of fully developed flow. This condition was checked by comparison of velocity profiles upstream and downstream of the body prior to its installation in the undisturbed flow. The ratio of width to depth of flow was varied from 9.4 to 16.5, which ensured the existence of a one dimensional flow. at least in the central part of the flume. The ratio of the opposing dimension of the body to the flow , for example, diameter of the hemisphere, to the median size of the sand, D_{50}. ranged from 35 to 117. To keep the problem as simple as possible only uniform sands were used . The geometric standard deviation of the sands was always less than 1.35. The shear ratio, τ_0/τ_c, was kept lower than unity, thereby avoiding any general sand movement and development of bed forms in the upstream reaches.

3.7   Experimental Procedure

The experiments can be categorized according to smooth, rigid and mobile bed runs. In any of these three series, to assess the flow development prior to the installation

of the obstacle on the bed, the undisturbed uniform flow was established. Knowing the range of the relative depth, the desired flow condition could be achieved by adjusting the tailgate and the slope of the flume. Then the uniformity of the flow was checked by measuring the depth of the flow in a reach 2 m in length at the upstream and downstream of the obstacle. Adjustments were made until the variation of the depth was less than 2 mm. Velocity profiles were taken at the plane of symmetry 1m upstream and 1m downstream of the obstacle. The collapse of the velocity profiles on one curve (Figure 3.7) indicates the existence of the uniform flow. Then the bed shear stress was measured in the absence of the obstacle to be used as the reference for the disturbed flow.

In the case of the smooth bed runs, after the undisturbed flow measurement was made, the obstacle was glued to the dried bed by silicon. This was done on the rigid bed as well, where sands were glued to the bed to prevent scour. For the mobile bed, after filling the sediment recess, a layer of 20 mm sand covered the false floor. Then the tailgate was raised to the required level and the flume was filled slowly to the level of the surface sediment. At this stage, the pump was started with a very small discharge to prevent any large velocity on the sediment. In this way, the disturbing effect of the existing flow on the levelled bed was minimized. Then, after the water level reached the approximate desired water level, the valve was opened to the desired discharge.

The tailgate used in flume # 1 had a thickness above the flume bed and this created significant backwater effects even when the tailgate was fully down. Increase of the slope did not improve the outlet condition because it caused a hydraulic jump at the entry, with a very low Froude number subcritical flow downstream. It was not possible to obtain higher Froude numbers for the series BS and CS in the presence of the tailgate, so it was removed. Because of steep curvature at the flume entrance, another problem occurred in the form of an undular jump.

An undular jump is known to have very small energy dissipating capacity, so it can propagate downstream for a long distance without being dissipated. Therefore, at the

location of the obstacle, significant turbulence and surface waviness was present. This type of rough surface may not have any effect on the average velocity, but surface water and its patterns and the vortex system around the body might be distorted by these unwanted waves. Therefore a wave depressor (in the form of a floating wooden board with the same width as the channel) was used to eliminate the undular jump at the very beginning of the flume. By decreasing the slope, the flowing water beneath the wave depressor was smooth and subcritical.

In series V, W and X, only flow visualization was carried out. In series AS, BS, CS and DS, in addition to the flow visualization, velocity profiles were taken in the POS and along the width of the channel downstream of the body for different levels and stations. The bed shear stress measurement was made in the POS and in several lateral lines around the body both for smooth and rigid beds. In the mobile bed runs, the scour profile was measured before and after equilibrium stage along the POS upstream and downstream of the body and also at its side. Some velocity measurements were accomplished in the scour hole as well. It took a long time to reach the equilibrium stage in clear water scour. This has also been reported by other researchers (Raudkivi and Breusers 1990). In this study, it was achieved after 2 to 3 days.

3.8   Undisturbed Flow Measurements

All experiments should be conducted in fully developed uniform flow regions for both smooth and mobile beds. In mobile bed, the state of the roughness of the flow was also investigated. The location of the body on the bed was chosen so that the flow become fully developed and uniform. To check the existence of uniform flow, velocity profiles were taken at the center of the body, 1 m upstream and 1 m downstream of it before installation. The focus of this study was to study the effect of the free water surface on the flow characteristics around the body when the depth of flow is of the same order of magnitude as the height of the obstacle with a Froude number similar to the real

71

field situation. Therefore, the flow conditions were chosen to meet these aims. The relative depths of 4 to 0.65 and Froude numbers as low as 0.074 for flow visualization and up to 0.5 for velocity and bed shear stress measurements have been used.

The velocity profiles at these three locations collapsed to one profile (Figure 3.7 a, b). They showed that the flow is not only a fully developed one but is also invariant in longitudinal direction, at least in the vicinity of the section at which the flow measurements were conducted. The turbulent mixing of the flow is higher in mobile bed runs due to the presence of the rough bed and higher shear stress. This fact can be observed in the velocity profiles, where the velocity gradients are steeper in mobile beds. A dip in the velocity profile close to the free surface, in case of Expt. DS0 with a width to depth ratio of about 3, can be attributed to the effect of secondary flow in narrow channels. Small differences in velocity between profiles can be observed in some of the Figures and this might be due to the effect of the free overfall and backwater effect at the end of the flume. Other characteristics of the undisturbed flows are shown in Table 3.4.

The value of σ_u as described in Chapter 3.3.3 was not considered as real value of turbulent fluctuations, but it could indicate the trend of these fluctuations. The profiles of σ_u for the smooth bed show a stronger turbulent fluctuation close to the bed with higher values in faster flows, Expt. AS0, BS0 (Figure 3.8 a). The scatter of the fluctuations is more for deeper flows of Expts. AS0 and DS0 compared with Expts. CS0 and BS0. In the mobile bed runs, the maximum fluctuations occurred at a higher level, around 20-30 mm above the bed (Figure 3.8 b). The turbulent fluctuations were higher compared with the smooth bed for the same average velocity, Expts. BS0 and BM02. There was more general scatter in the mobile bed.

The velocity profiles have been used to calculate the bed shear stress as explained in Section 3.5.1. The plots of fitted line for these profiles are shown in Figure 3.9 (a,b) both for smooth bed and rough bed. The calculated shear velocity is used to plot the

velocity profiles along with the log law in Figures 3.10 and 3.11. The dip in the velocity profile of the Expt. DS0 can also be detected in Figure 3.10 d.

In the law of the wall, the wall region can be defined by the characteristic scales of length and velocity of v/u^* and u^*. Two formulas can be used in the inner region of the boundary layer as the law of the wall. For viscous-sub-layer the equation $u^+=y^+$ can be used where $u^+=v/u*$ and $y^+=yu*/v$ for a range of $y^+< B$. The value of B, Van Driest's (1956) damping function, would be 26 after Van Driest for the boundary layer and Nezu and Rodi (1986) for open channel flow. The log-law formula can be used for the range of $B<y^+<0.2 R*$ where $R*=h/u^+=u*h/v$:

$$u*=1/\kappa \ln(y^+)+A \qquad (3.36)$$

The Karman constant κ and integration constant A are to be experimentally determined in the wall region of the flow where $y/h < 0.2$. Keulegan (1938) recommended the corresponded values of A and κ in pipe flow be used in open channel flow for practical cases. In most cases, the smooth-pipe flow values of Nikuradse are used, $\kappa=0.4$ and $A=5.5$. But based on recent investigations the log law is only valid in the wall region and instead of simply adjusting these two values in standard log law, a wake function should be added, usually Coles' (1956) wake function. For open channel flow, Nezu and Rodi (1986) recommended that the Karman constant κ and the integral constant A have the universal values of 0.41 and 5.29 respectively, regardless of the Reynolds and Froude numbers. The log law based on these two values are shown with a dotted line in Figure 3.10. As seen in this figure, the suggested values do not make any better fit for log law and in fact the original values shown with solid lines perform better than them.

Another way of checking the status of the flow development is calculation of the boundary layer growth in the entrance region. Classical smooth flat plate boundary layer theory (Schelichting, 1968 pp. 598-599) can be used as a simple way to determine BL

growth theoretically. The equation for BL under the zero pressure gradient. no acceleration or deceleration, would be :

$$\delta_x = 0.37x\left(\frac{Ux}{\upsilon}\right)^{-\frac{1}{5}} \qquad (3.37)$$

where δ_x is the thickness of the BL and U is the outer potential velocity and x the length from the entry. This equation is valid in range of $5x10^5 < \frac{Ux}{\upsilon} < 6x10^6$. The more general form of this equation for higher range of $\frac{Ux}{\upsilon}$ would be as following (Schelichting, 1968 p. 602):

$$c_f \equiv \frac{\tau_0}{\frac{1}{2}\rho U^2} = \left[2\log\left(\frac{Ux}{\upsilon}\right) - 0.65\right]^{-2.3} \qquad (3.38)$$

where cC_f is the skin friction. When the BL reaches the surface, the whole depth of the flow would be considered as the boundary layer, and from this point on the flow would be uniform. Therefore, equating δ_x with the depth of flow provides us with the boundary layer development length.

In rough flow, the development length depends on k_s value as well. So the general form of equation for rough surfaces would be (Schlichting, 1968 pp. 610-613):

$$c_f \equiv \frac{\tau_0}{\frac{1}{2}\rho U^2} = f\left\langle\frac{Ux}{\upsilon}, \frac{x}{k_s}\right\rangle \qquad (3.39)$$

or

$$c_f \equiv \frac{\tau_0}{\frac{1}{2}\rho U^2} = f\left\langle \frac{Ux}{\upsilon}, \frac{k_s U}{\upsilon} \right\rangle \qquad (3.40)$$

The specific form of the above equation can be used in fully rough flow as:

$$c_f \equiv \frac{\tau_0}{\frac{1}{2}\rho U^2} = \left[2.87 + 1.58\log\left(\frac{x}{k_s}\right) \right]^{-2.5} \qquad (3.41)$$

whereas for transitionally rough flow it can be determined graphically (Figure 21.7 of Schelichting, 1968 p. 611).

Yalin (1972) modified the above equation in terms of flow depth to calculate the development length, L, by equating the fully developed surface velocity (from the logarithmic velocity distribution) to the free stream velocity for the BL. The presence of a piezometric pressure gradient was not considered in this equation :

$$\frac{L}{d} = 0.0152 \frac{k_s}{d} e^m \qquad (3.42)$$

where m can be calculated from following equation :

$$m = 2.3\left[\ln 30.1\frac{d}{k_s} \right]^{\frac{4}{5}} \qquad (3.43)$$

The development lengths are calculated based on these equations and are presented in table 3.4 .

3.9 Experimental Errors and Uncertainties

In any experimental study, the reliability of the measured data as the basis for proposed theories is of primary importance to the researchers. It is the researcher's responsibility to measure the reliability of their results. In regards to reliability estimates, experiments fall into two overlapping categories: single-sample and multiple-sample experiments. Multiple-sample experiments are those in which uncertainties are evaluated by a sufficiently large number of measurements, using different methods, instruments and observers so that statistical evaluation of the results can be made. Single-sample experiments are those in which uncertainties are not found by repetition.

There are many publications dealing with estimation of reliability in multiple-sample experiments, but most engineering experiments, including this study, fall under the single-sample category. Many experiments that are assumed to be multiple-sample are actually in part single-sample, due to the presence of several factors reducing the effect of repetition. The observation of scales by a single observer, in general, does not provide consistent results and even different observers might not have independent observations. Different observers using the same equipment might present different results, and instruments of different designs, in general, will not give the same results.

In one of the first attempts to deal with this problem, Kline and McClintock (1953) presented a useful method to describe uncertainties for single-sample engineering experiments. They also proposed a method to calculate the propagation of these uncertainties into the results. Before describing this method defining some terms is necessary. An *error* is defined as the difference between the true and measured values of a variable and the *uncertainty* a possible value the error might have. While the error is a fixed value, its corresponding uncertainty may vary significantly. A variable is a basic quantity observed directly and the *result* may be obtained by making corrections to or calculations with the recorded values of the variables. *Propagation of uncertainty* means the way in which uncertainties in the variables affect the uncertainty in the results.

76

Errors may be classified into three categories: Accidental errors, fixed errors, and mistakes. *Accidental errors* or personal errors are those varying errors which cause differences between repeated readings, with no apparent reason. *Fixed errors* are those which cause repeated readings to be in error by the same amount with no apparent reason. Then, if the reason is known, it might be corrected, such as a dent on a probe. *Mistakes* are completely erroneous readings of scales, watches, and so on. These kind of errors are usually detectable and can be discarded as "way-out". Usually it is assumed that all the fixed errors and mistakes have been detected and eliminated. Therefore, only random errors would be considered in error analysis.

The frequency distribution of accidental errors can be assumed to be a normal, "Gaussian", one. But due to the small number of observations, the distribution function can't be established. Yet it is possible to describe it by an operational statement based on the statistical concept of a confidence limit. Consequently, the experimenter must rely on his/her past experience and judgment. The statement then may include his/her best estimate of what would happen if the experiment was repeated an indefinitely large number of times. Kline and McClintock (1953) proposed that a good concise way to describe the uncertainty in each variable is to specify the mean of the readings and an uncertainty interval with a specified confidence level. If the arithmetic mean of observed values is represented by m and the uncertainty interval by W, the uncertainty can be described by:

$$m \pm W, \text{(confidence level)} \qquad (3.44)$$

for example for a pressure tube reading:

$$\text{Pressure} = 52.1 \pm 0.5 \text{ Pascal } (95\%)$$

77

Based on this statement, the experimenter believes that the true value of the pressure is 52.1 Pascal and if a large number of repetition was made, 95% of the observations would fall within ± 0.5 Pascal of it. The uncertainty interval, w, is not a variable but a fixed value selected so that the experimenter could estimate that with assumed confidence level (here 95%) the error is less than W.

Kline and McClintock (1953) then computed the propagation of uncertainty, Eq. 3.44, into a result, R. The result was assumed to be a linear function of "n" independent variables V_1, V_2, ...V_n. , each of which is normally distributed, with respective uncertainty intervals of W_1, W_2,....,W_n, all with similar confidence levels. Let the result be defined as :

$$R = R(V_1, V_2, ..., V_n)$$
(3.45)

Then the relation between the interval for the variables, w_i, and the interval for the result, w_R, is:

$$W_R = \left[\left(\frac{\partial R}{\partial V_1} W_1 \right)^2 + \left(\frac{\partial R}{\partial V_2} W_2 \right)^2 + ... + \left(\frac{\partial R}{\partial V_n} W_n \right)^2 \right]^{1/2}$$
(3.46)

Eq. 3.46 have been used successfully for uncertainty analysis in fluid mechanics. Sometimes Eq. 3.45 can be written in the following form :

$$R = RV_1^{m_1} V_2^{m_2} .... V_n^{m_n}$$
(3.47)

Then by substitution of Eq. 3.47 into Eq. 3.46 the more useful form can be obtained as:

$$\frac{W_R}{R} = \left[\left(m_1 \frac{W_1}{V_1} \right)^2 + \left(m_2 \frac{W_2}{V_2} \right)^2 + ... + \left(m_n \frac{W_n}{V_n} \right)^2 \right]^{1/2}$$
(3.48)

78

From this equation, the share of uncertainty for each variable in the total uncertainty of the result can be detected. If improvement in accuracy is necessary, the most effective instruments or measurements can be chosen. Uncertainty measurements can provide necessary information to accuratly find which instrument has to be improved.

3.9.1 Estimate of uncertainty

In this section possible sources of errors for measured variables are described and the uncertainties of the results are calculated based on Eq. 3.48. The confidence level for all estimates is chosen to be 95%(or 19 to 1 odds or 1 in 20 chances).

The geometries of the flume and the obstacles were measured with instruments that provide an uncertainty of ± 0.5 mm. The depth of the flow was measured based on the knowledge of the water surface level and the bed level. The uncertainty of measurement in the latter was ± 0.5 mm and ± 1 mm for the former , due to the existence of waves and rough surfaces. The resultant uncertainty in the depth of flow was then computed to be ± 1.12 mm by Eq. 3.46.

In calculating the average velocity, three variables are involved; discharge Q, flume width W and flow depth y_0 ($U_0 = Q/Wy_0$). The estimate for the uncertainty in measuring the discharge was ± 0.5 L/s. As an example, the uncertainty in measuring the average velocity of the Expt. AS0 can be calculated as following:

$$Q = 54 \pm 0.5 \text{ L/s,}$$

$$W = 1220 \pm 0.5 \text{ mm,}$$

$$y_0 = 120 \pm 1.12 \text{ mm.}$$

Thus the measured velocity would be $U_0 = 0.054/(1.22 \times 0.12) = 0.369$ m/s. Then the uncertainty can be calculated from Eq. 3.47 and 3.48 :

79

$$R = V_1^{m_1} V_2^{m_2} V_3^{m_3} = Q^1 W^{-1} y_0^{-1}$$

$$\frac{W_{U_0}}{U_0} = \left[\left(1 \times \frac{0.5}{54}\right)^2 + \left(-1 \times \frac{0.5}{1220}\right)^2 + \left(-1 \times \frac{0.5}{120}\right)^2\right]^{1/2}$$

$$\frac{W_{U_0}}{U_0} = \left[8.6 \times 10^{-5} + 1.68 \times 10^{-7} + 8.71 \times 10^{-5}\right]^{1/2} = 1.73\%$$

The uncertainty in velocity measurement is therefore 0.0064 m/s. This shows that the accuracy in the measurement of the discharge and the depth of the flow are the main factors, and the necessary improvement should be focused on these two terms only.

The accuracy of the pressure transducer DP45-16, based on the manufacturer's catalogue, was ±0.25% of the full scale, including the effects of linearity, hysteresis and repeatability. The range of this transducer was ±35 mm of water (±1.4 inches) or 0.35 K Pascal. The calibration of the transducers in the lab showed higher accuracy but still 0.25% of the full scale was used. The full scale of the calibration for the unidirectional flow was 25.4 mm, with the positive side between zero to 1 inch of water head. For two-dimensional flow full scale of the calibration was 50.8 mm, with a range of -1 inch to +1 inch of water. The uncertainty in the differential pressure measurement for the latter was around ±0.254 mm of water and for the former ±0.127.

The velocity was measured by pitot-static tube in uni-directional flow and by yaw and pitch probes in two-dimensional flows. The accuracy of the velocity measurements in 1D-flow depends mainly on the alignment, turbulence and wall effects. The pitot-static tubes are insensitive to error in alignment of less than 5°. The accuracy in alignment of the probe was ±2° which caused no error. The Prandtl type of probes are insensitive to the effect of isotropic turbulence, which in this study was the case for unidirectional flows of undisturbed flows. There was no correction to compensate the wall-effect. Therefore, an uncertainty estimate was based only on the pressure transducer. The resulting equation, based on Eq. 3.48, was $W_{U_0} / U_0 = W / 2h$. The uncertainty

80

calculated, based on this equation for minimum measured velocity of 0.1 m/s ,was 12%, which then dropped to 3% for velocity of 0.2 m/s, 1.4% for $U_0=0.3$ m/s and 0.8% for $U_0=0.4$ m/s. The lower velocities were measured usually close to the bed. The overall uncertainty was less than the calculated one due to the averaging of a large number of samples taken at one point.

In disturbed flow, the velocity was measured by pitch and yaw probes. Different types of errors in these measurements made the estimate of uncertainty difficult. Errors included: the presence of a velocity or pressure gradient across the three holes of the probe, thickness error, probe misalignment, mis-fit of the calibration curves and existence of the third component of velocity. Therefore, velocity measured at POS by pitch probe had less error. There were more errors where there was a strong gradient of velocity, such as divergent flow at the sides or in front of the body. To reduce the effect of the third component of the velocity, most of the measurements were taken where the angle of this component was less than 5-10°. Calculating the combined effects of all these parameters on the resultant accuracy of the measurements would be very cumbersome. Therefore, only rough estimates can be made to show the direction and crude size of these errors based on flow visualization and inspection of velocity profiles. Some of these parameters are negligible in measuring the velocity magnitude for small yaw and pitch probes ($<$ 15°), which provides an accuracy as good as the pitot-static probe. The misalignment uncertainty above the bed ($<$ 15 mm) for low angles ($<$ 30°) could be estimated as ± 2". This uncertainty increased to around ± 2-8° closer to the bed and ± 2 to 5° at the sides of the body.

In the measurement of the bed shear stress, the presence of the vertical component of the velocity might be a source of error. But it was found that the angle of pitch was usually less than 5° so its effect was negligible. Due to the nature of the bed in rigid and mobile bed, there was an error in placing the nose of the probe at the bed level. The loose nature of sediment in mobile bed usually caused intrusion of the probe inside the bed

resulting in an underestimation of the shear stress. In the case of the rigid bed, there was an overestimation of the bed shear stress. The uncertainty in angle of yaw was estimated to be 5 and 8° for smooth and rigid bed respectively.
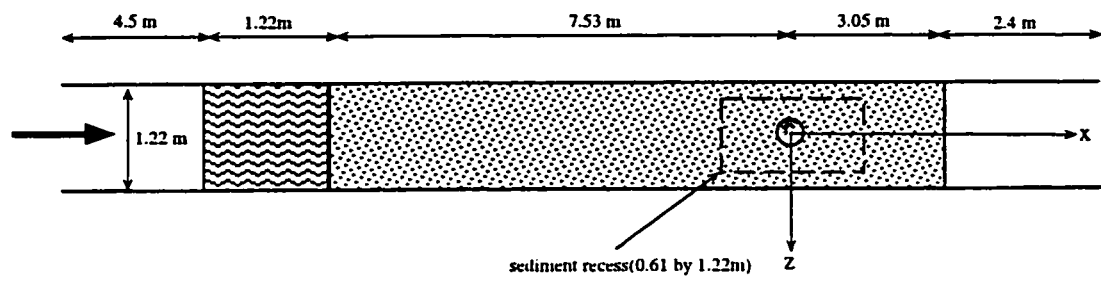
(a) Plan view
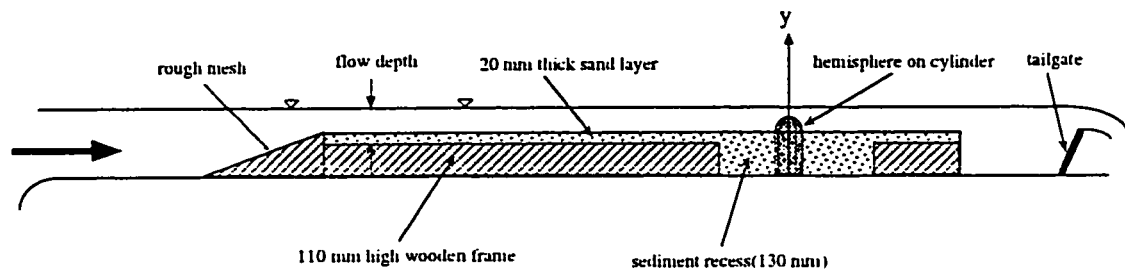
(b) Side view

Figure 3.1 Laboratory flume Arrangement for Mobile bed Experiments

83
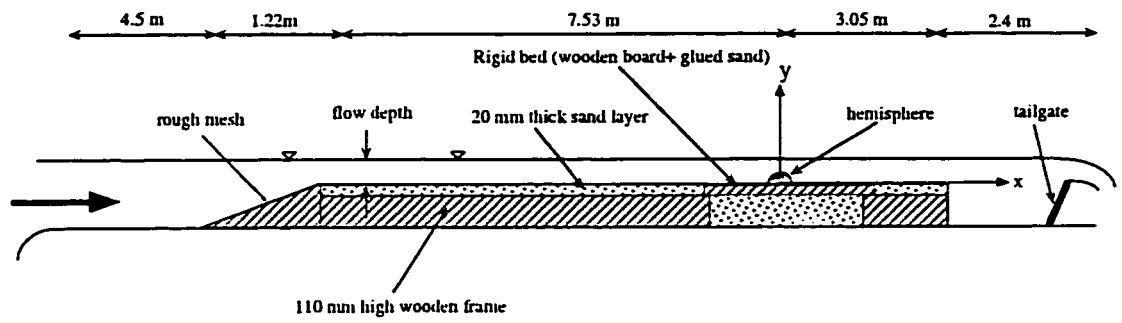
(a) Rigid bed
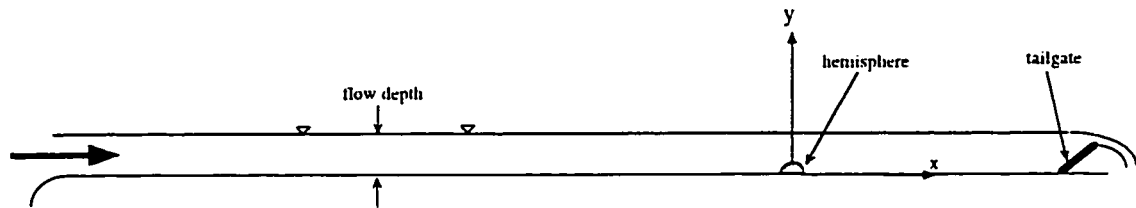
(b) Smooth bed

Figure 3.2 Laboratory flume Arrangement for rigid and smooth bed Experiments
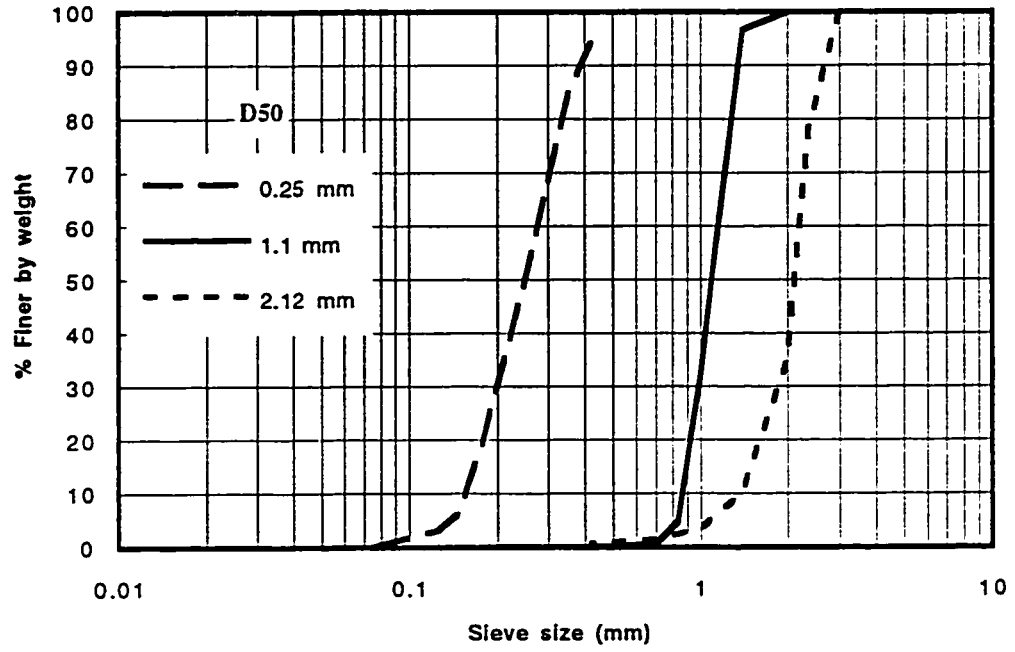
Figure 3.3 Grain Size Distribution of Sands
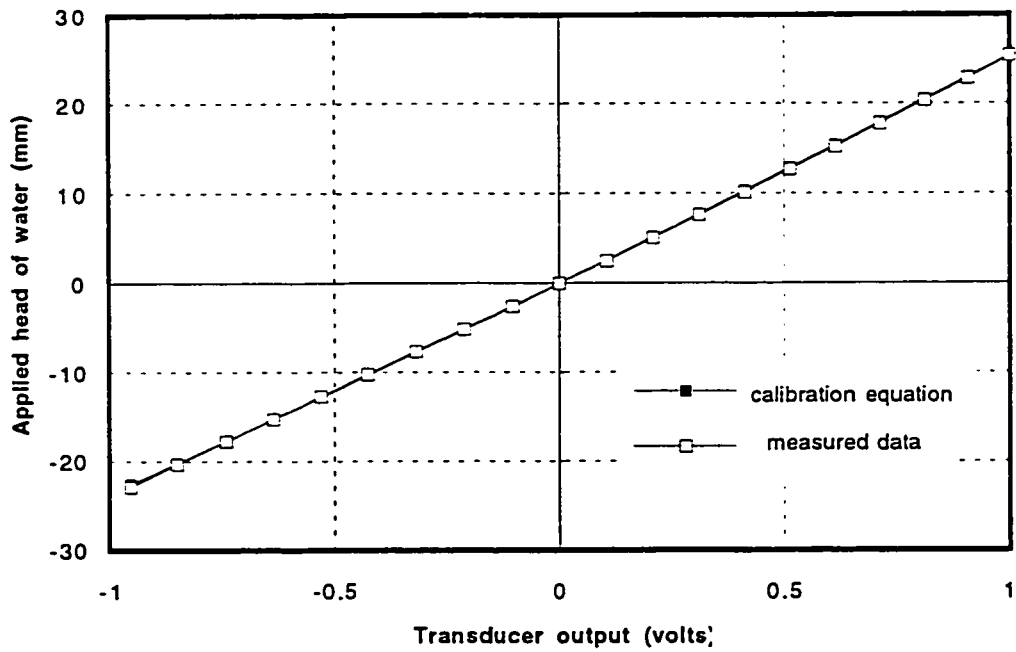
Figure 3.4 Typical Calibration chart of a pressure transducer

(a)

Angle of Yaw (Degrees)
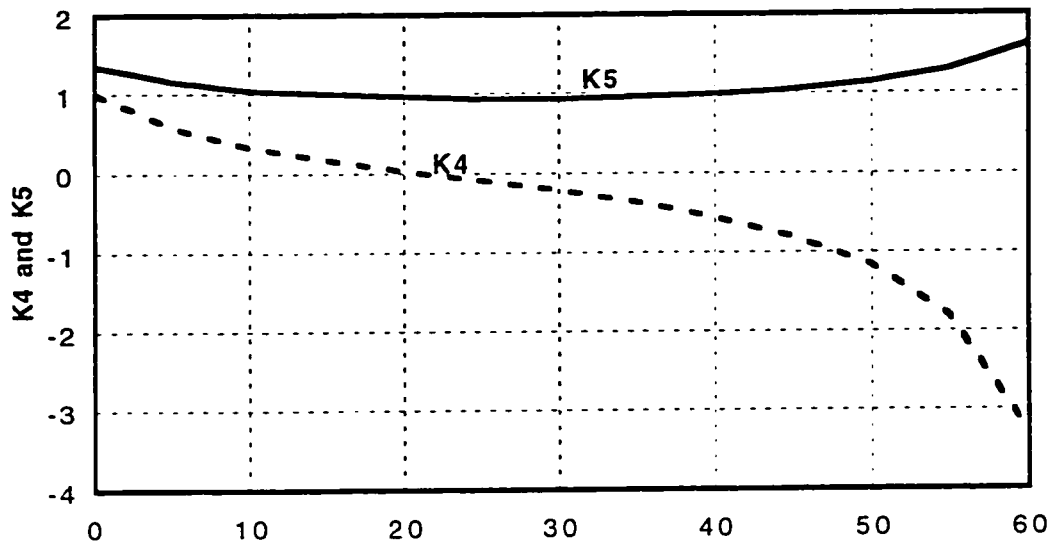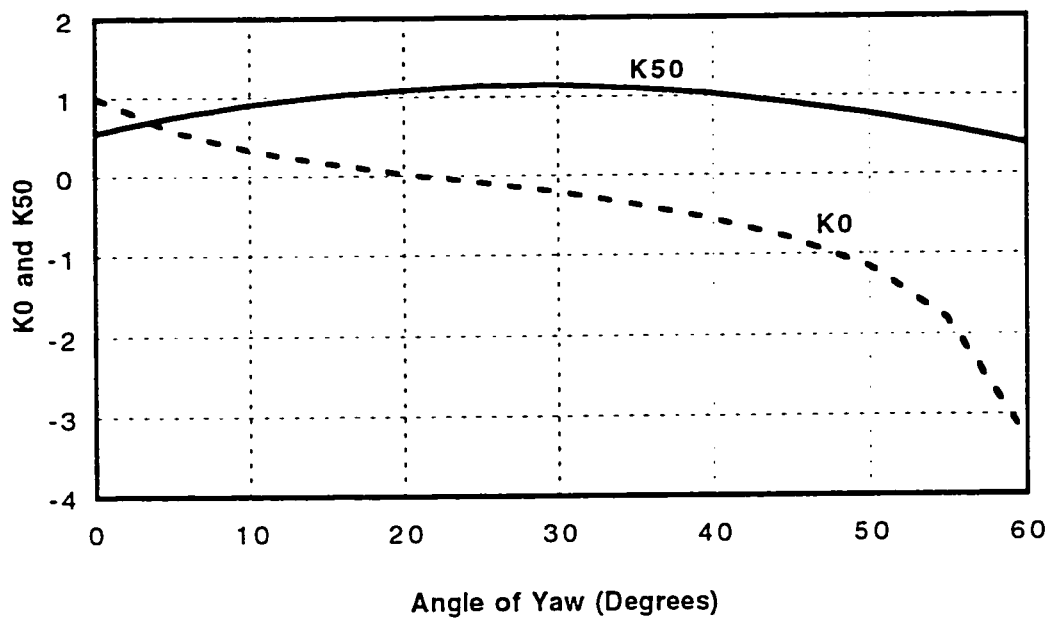
(b)

Figure 3.5 Calibration curves for the yaw Probes;
(a) Velocity and (b) bed shear stress
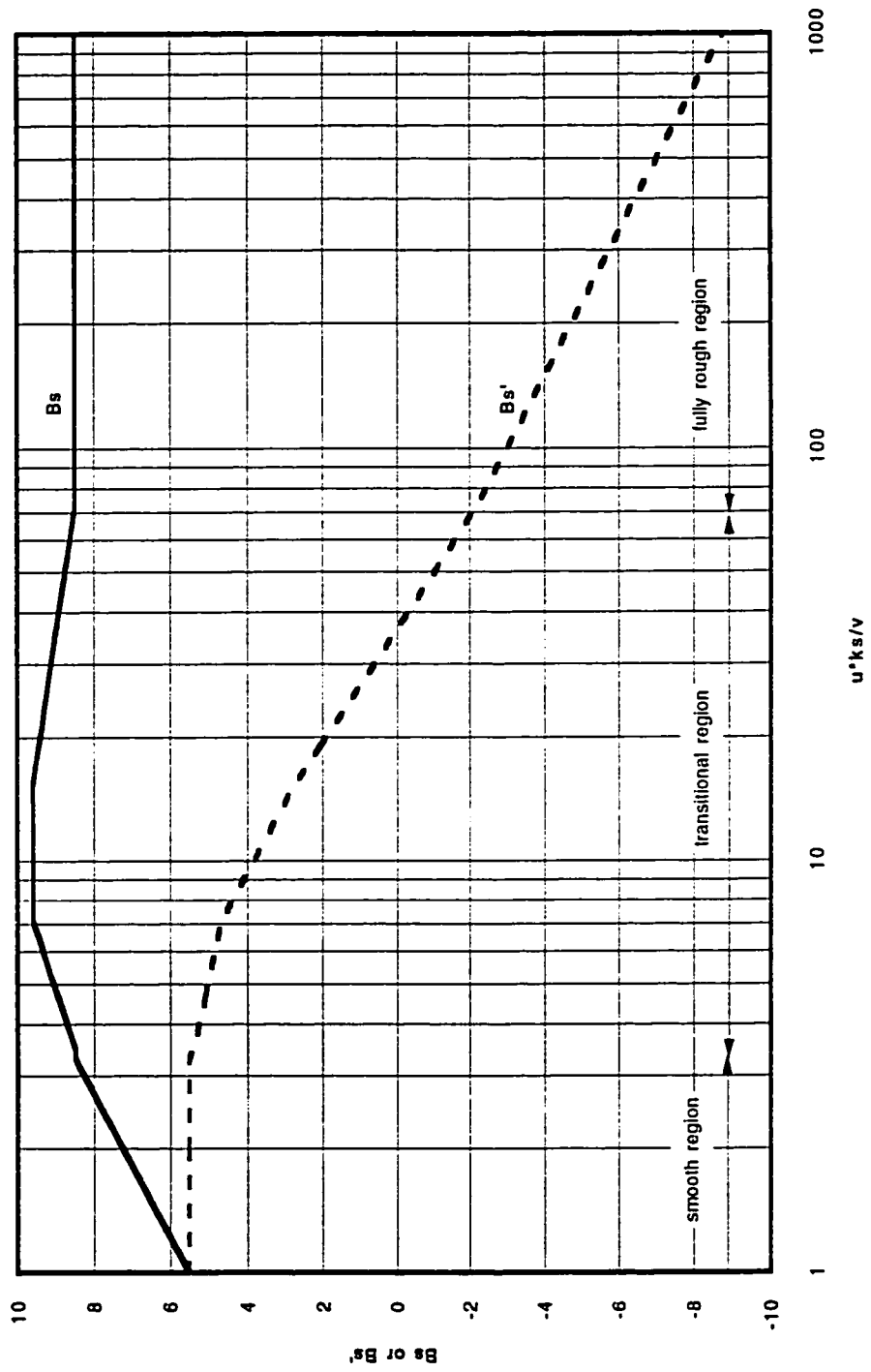
Figure 3. 6 Variation of Bs and Bs' with Rrpughness Reynolds Number

87
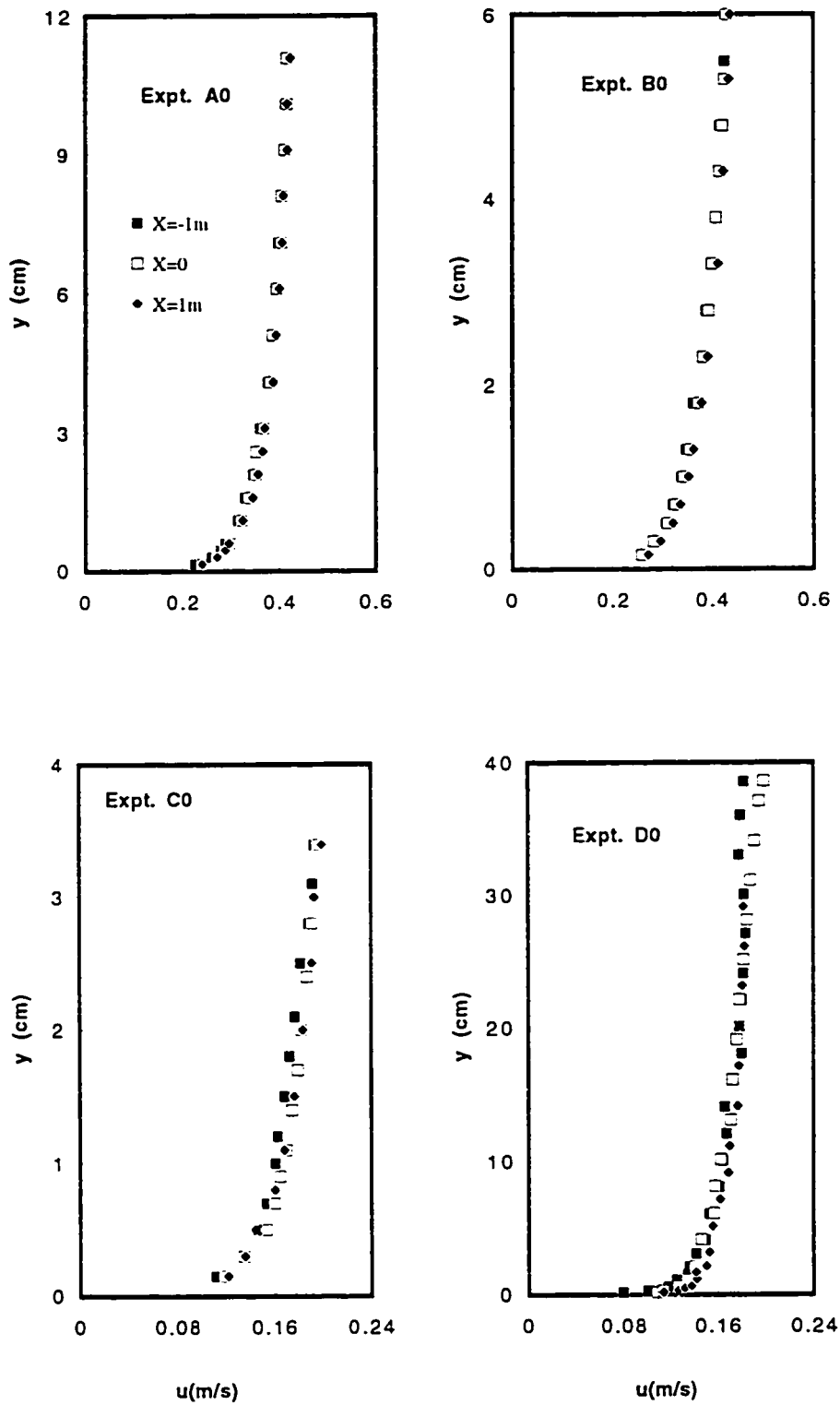
Figure 3.7 (a) Velocity Profiles of Undisturbed Flows on Smooth Bed
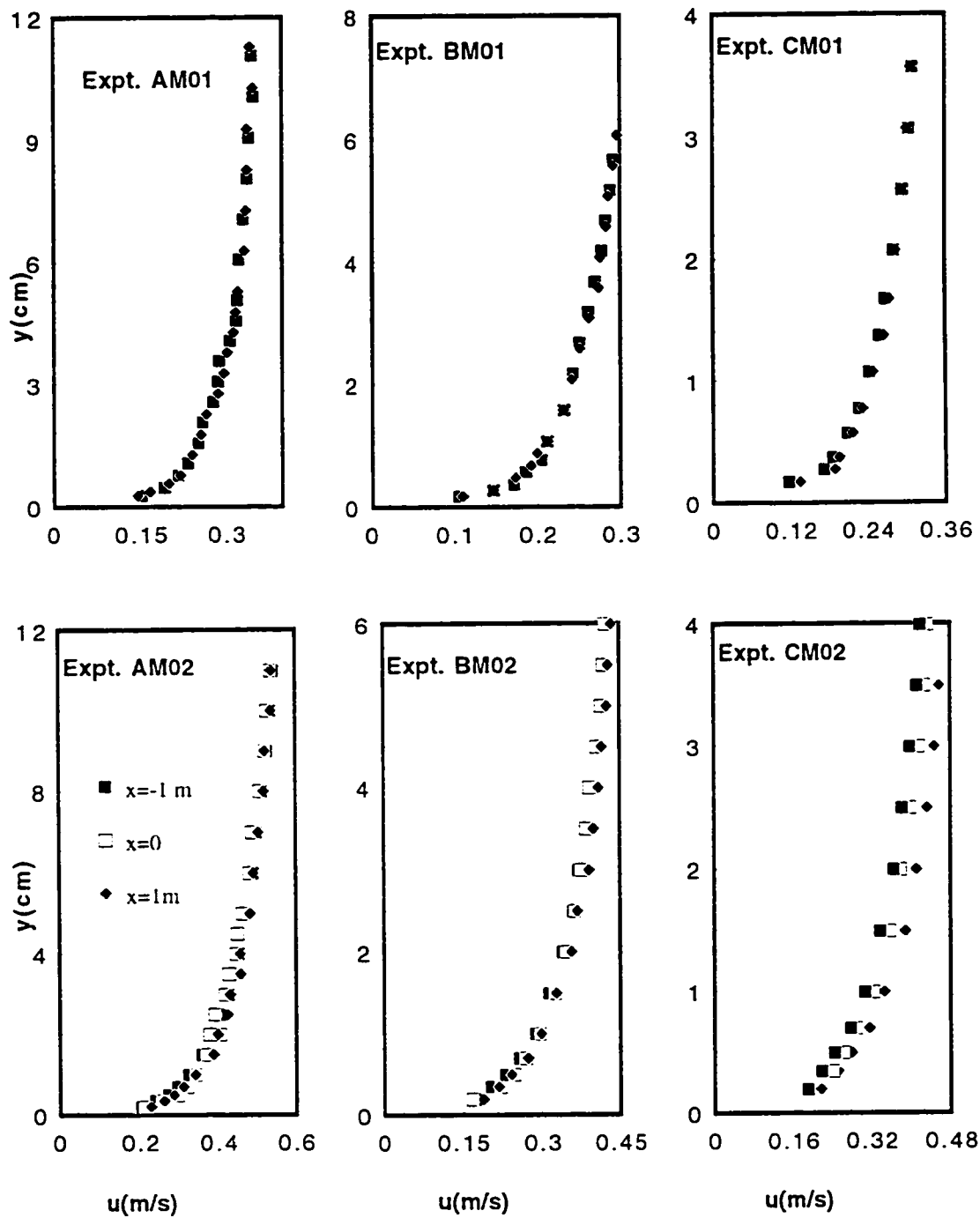
Figure 3.7 (b) Velocity Pprofiles of Undisturbed Flows on Rough Bed
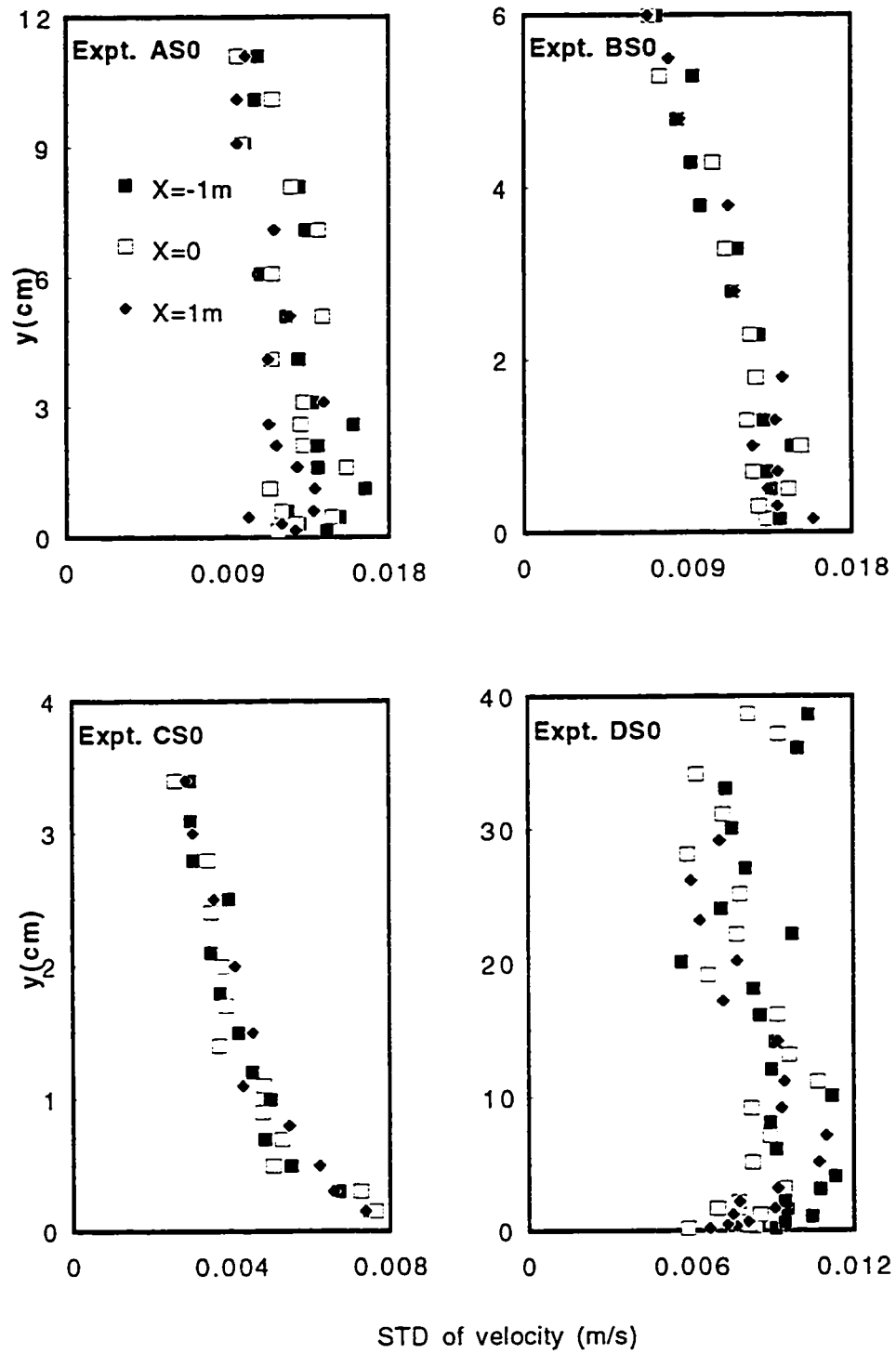
Figure 3.8 (a) STD of Velocity in Undisturbed Flow for Smooth bed
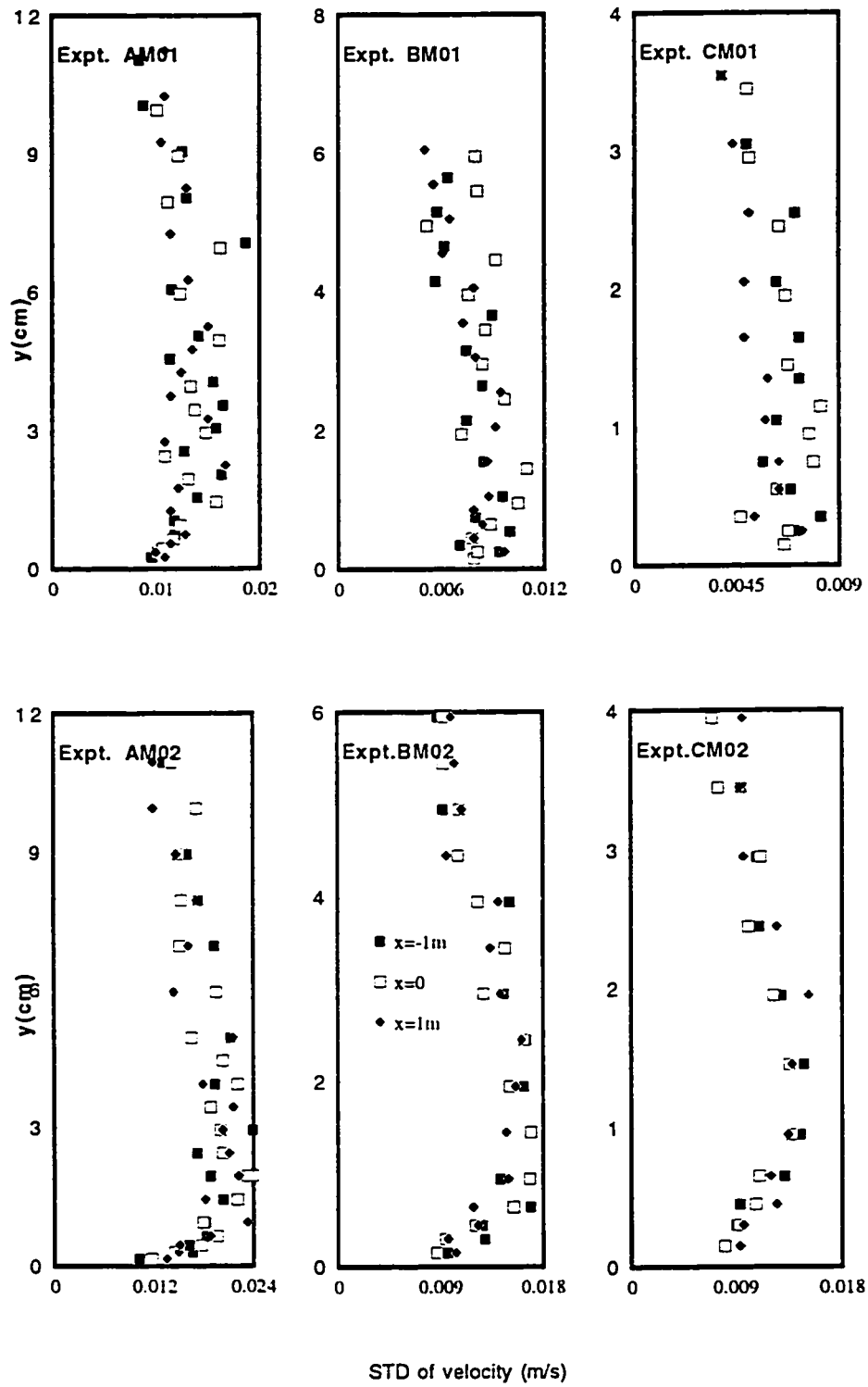
Figure 3.8 (b) STD of Velocity in Undisturbed Flow for Rough Bed
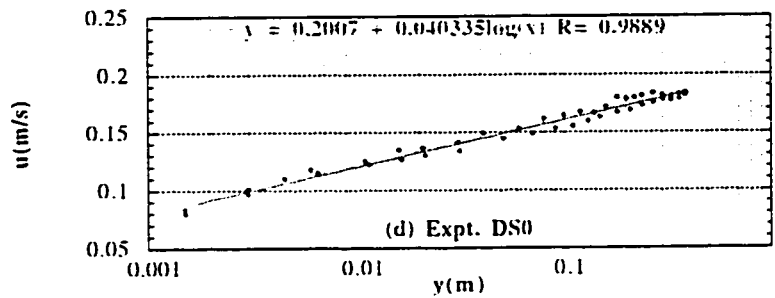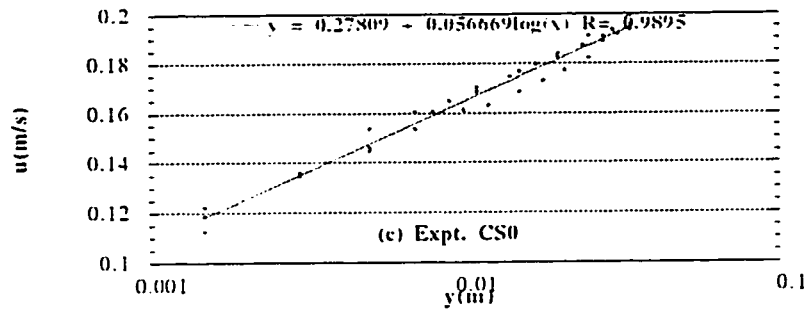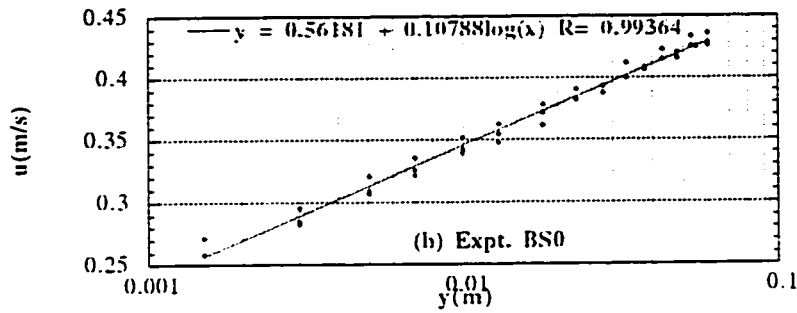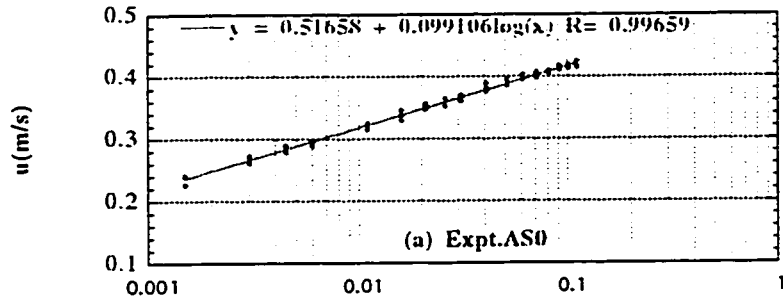
Figure 3.9 (a-d): Fitted line for Velocity Profiles (Smooth bed)
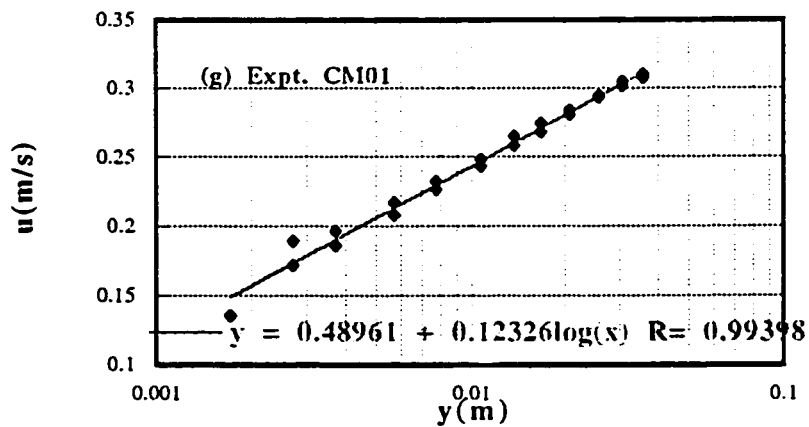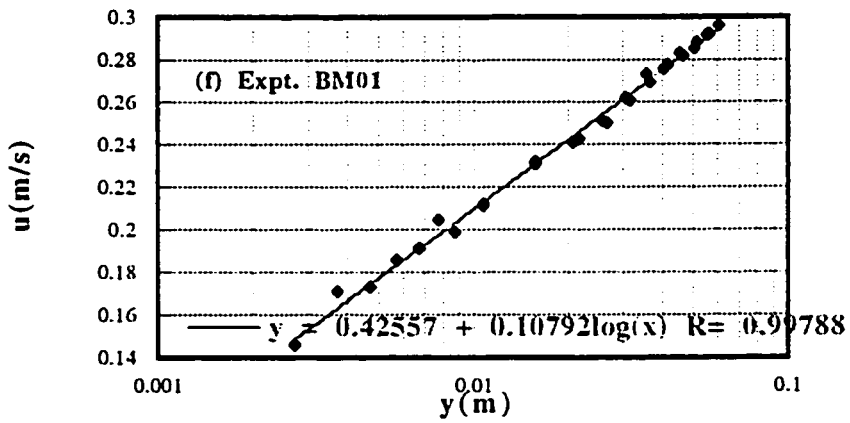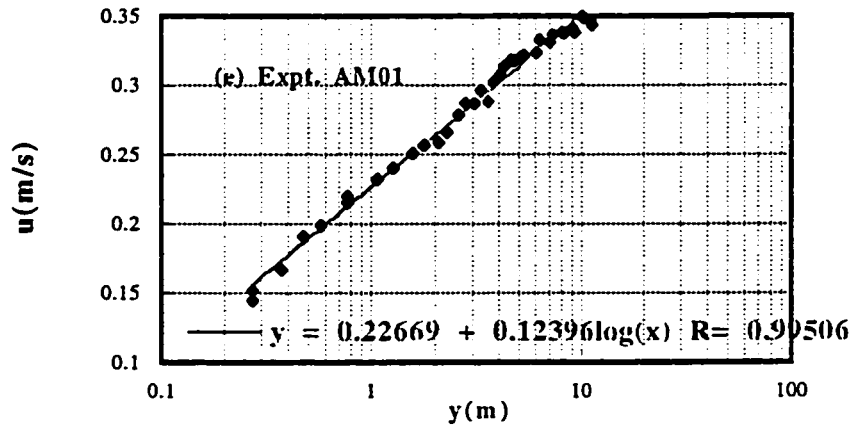
Figure 3.9 (e-g): Fitted line for Velocity Profiles (Rough bed)
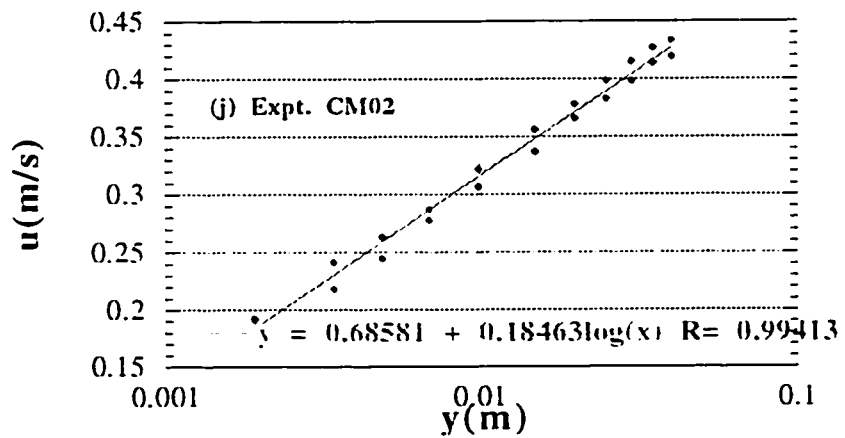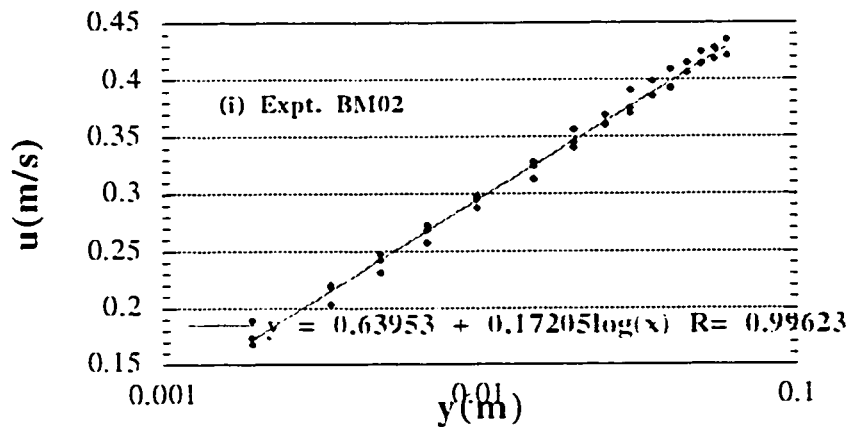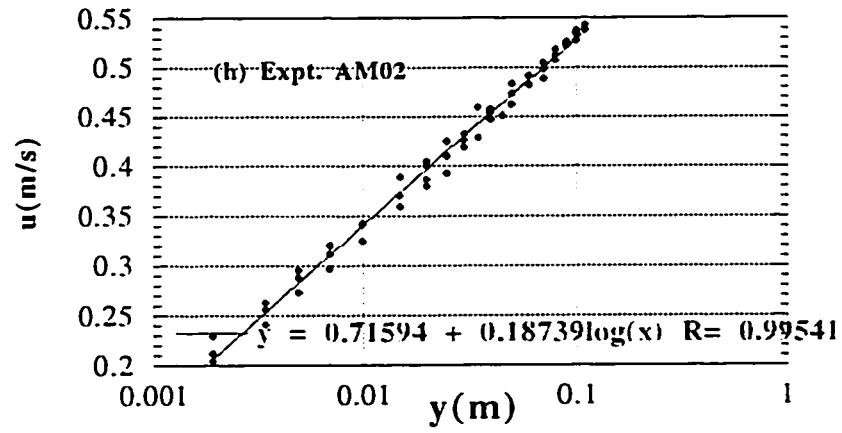
Figure 3.9 (i-j): Fitted line for Velocity Profiles (Rough bed)

94
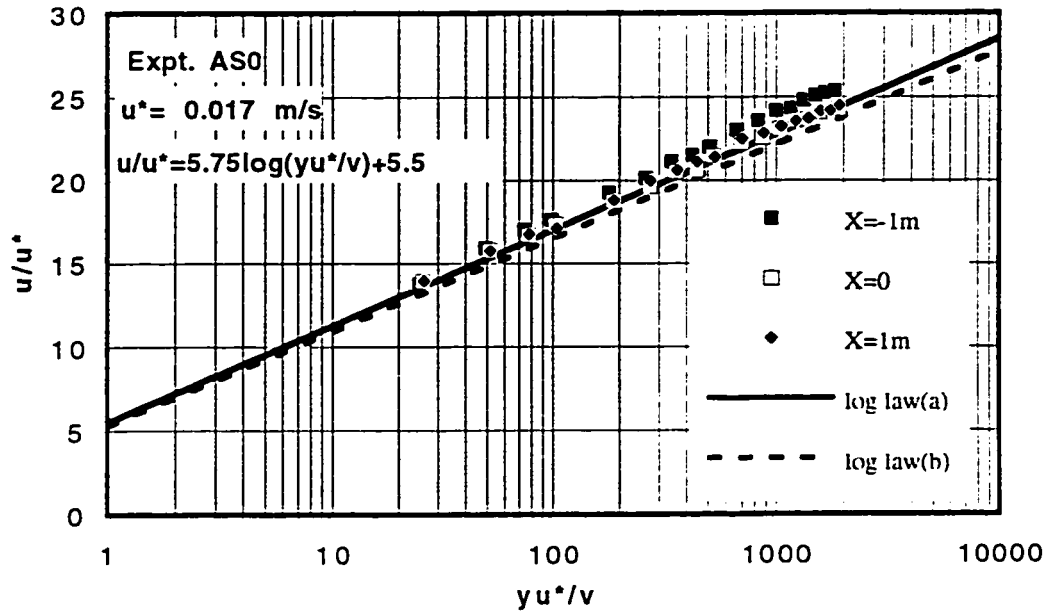
(a)
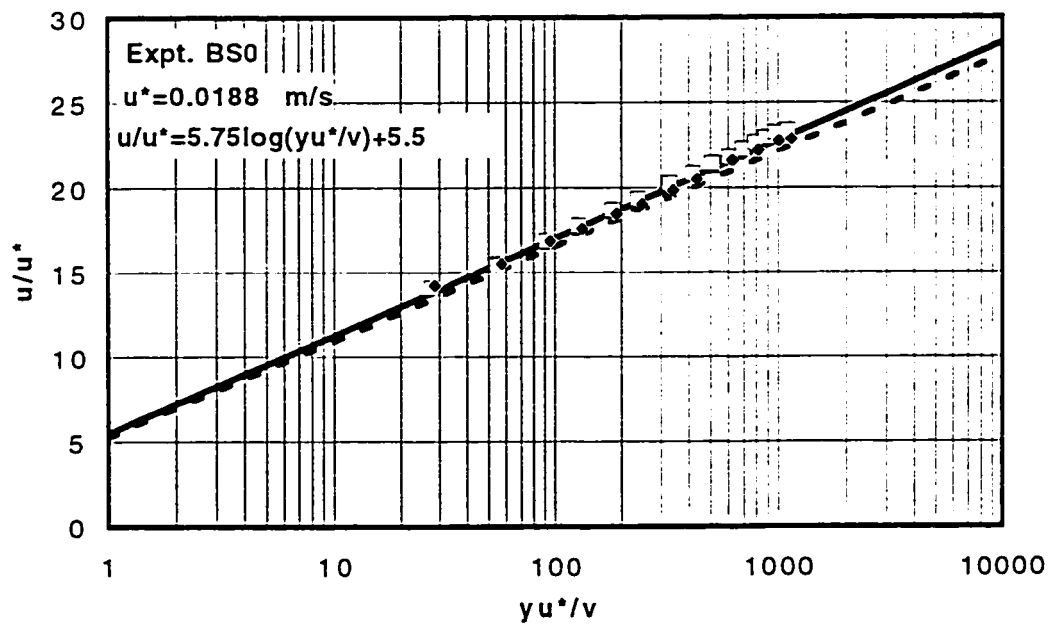
(b)

Figure 3.10(a,b) Comparison of velocity profiles with log law for smooth bed
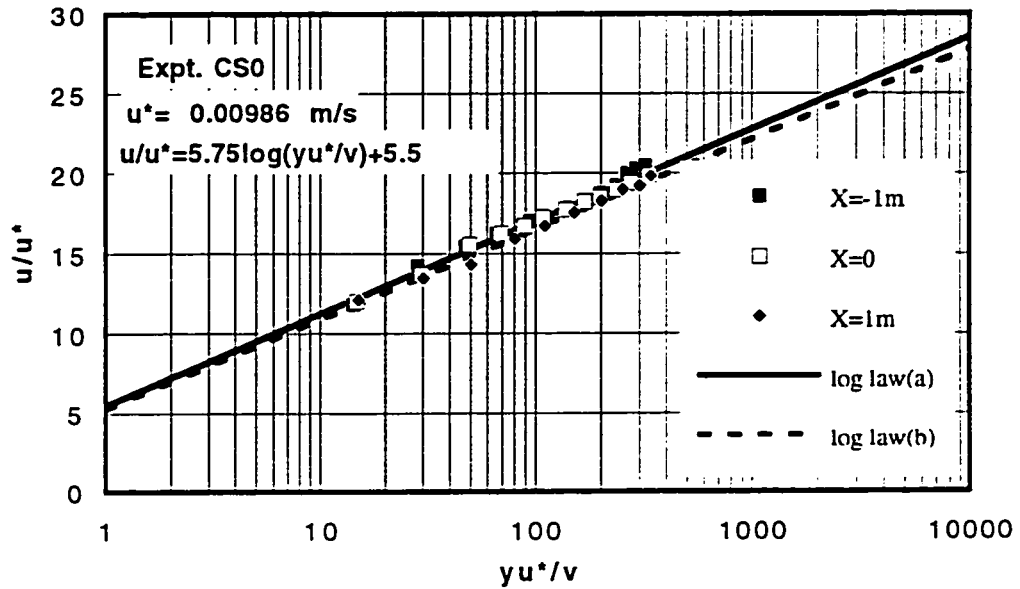
(c)
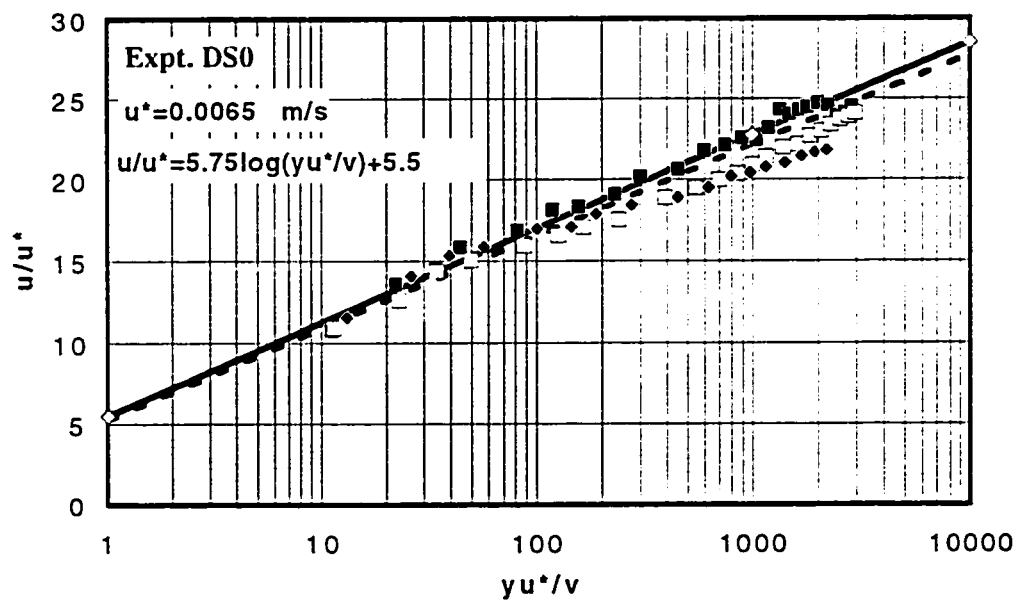
(d)

Figure 3.10 (c.d) Comparison of velocity profiles with log law for smooth bed
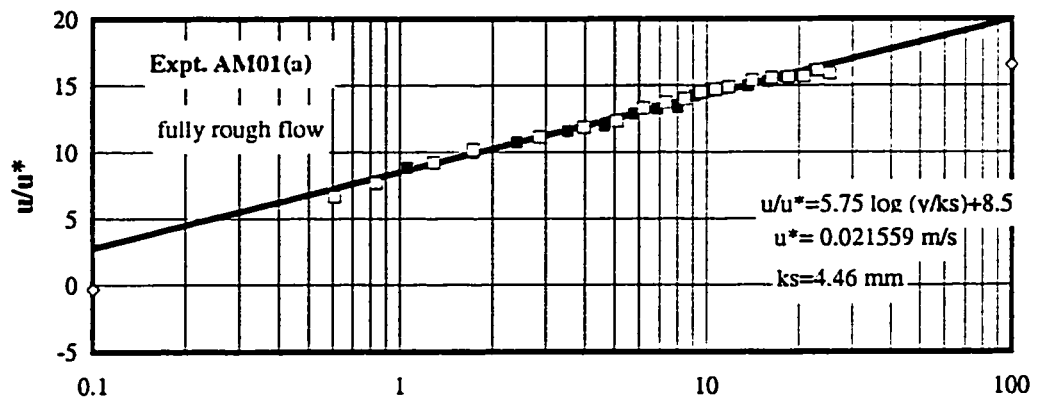
(a)
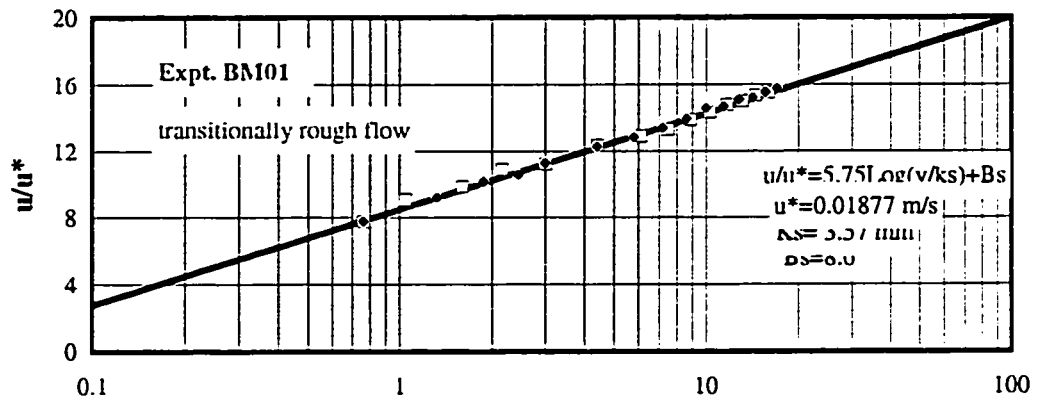
(b)
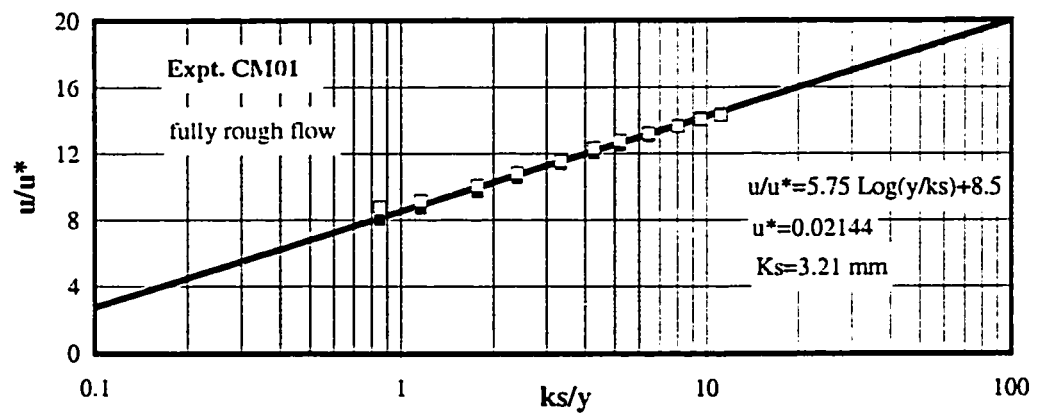
(c)

Figure 3.11 (a-c) Comparison of Velocity Profiles with Log Law for Rough Bed at x=-1m,zero and 1m

(d)

Expt. AM02

Fully rough flow

$u/u^* = 5.75 \ Log(y/ks) + 8.5$

$u^* = 0.03259$ m/s

Ks=4.55 mm

y-axis: u/u*
x-axis: 0.1, 1, 10, 100
y-axis values: 0, 4, 8, 12, 16, 20

(e)

Expt. BM02

Fully rough flow

$u/u^* = 5.75 \ Log(y/ks) + 8.5$

$u^* = 0.0299$ m/s

Ks=5.74 mm

y-axis: u/u*
x-axis: 0.1, 1, 10, 100
y-axis values: 0, 4, 8, 12, 16, 20

(f)

Expt. CM02

Fully rough flow

$u/u^* = 5.75 \ Log(y/ks) + 8.5$

$u^* = 0.0321$ m/s

Ks= 5.79 mm

y-axis: u/u*
x-axis: 0.1, 1, ks/y, 10, 100
y-axis values: 0, 4, 8, 12, 16, 20
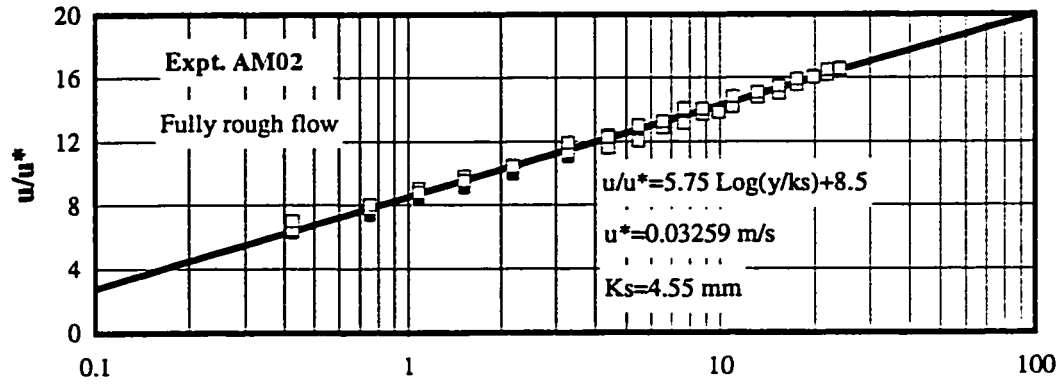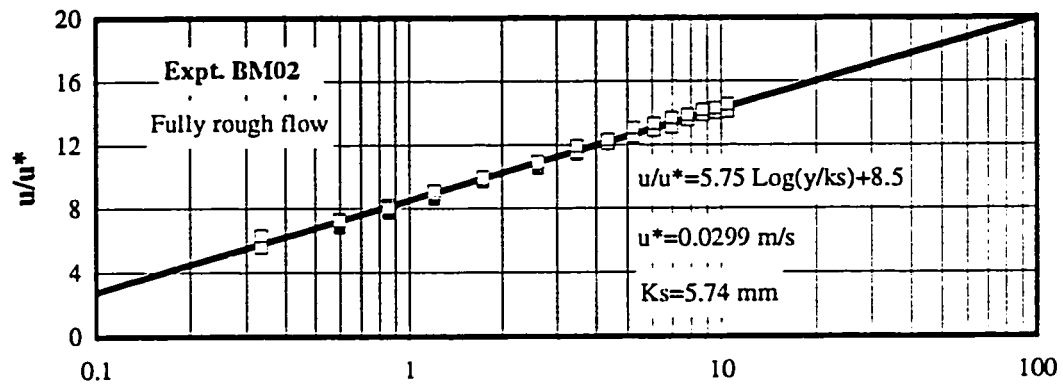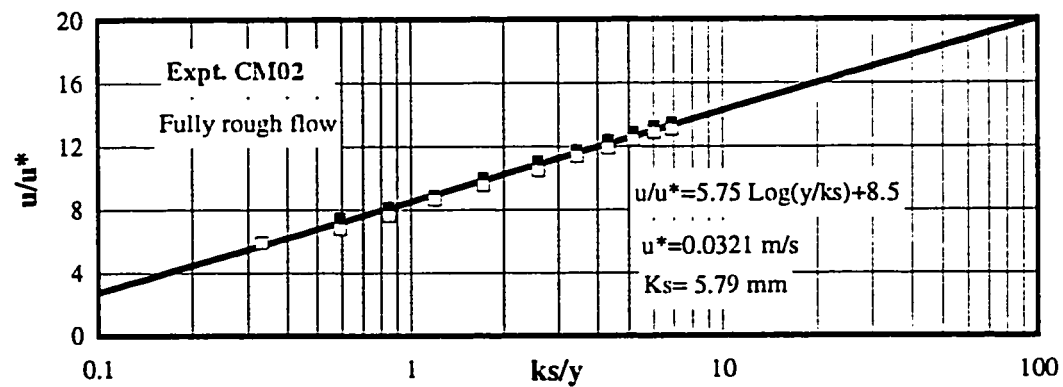
Figure 3.11 (d-f) Comparison of Velocity Profiles with Log Law
in Rough Bed at x=-1m,zero and 1m

Table 3.2 Explicit Equations for Patel's Preston Tube Calibration Curves

	Region 1	Region2	Region 3
Original equations (Patel)	$y_* = 0.5\,x_* + 0.037$	$y_* = 0.8287-0.1381\,x_* + 0.1437\,x_*^2 - 0.006x_*^3$	$x_* = y_* + 2\log(1.59\,y_* +4.1)$
Range of validity (Patel)	$y_* < 1.5$	$1.5<y_* <3.5$	$3.5<y_* <5.3$
Range in terms of τ_{0*}	$\tau_{0*}<32$	$32<\tau_{0*}<3,162$	$3162<\tau_{0*}<199,526$
y_* in terms of x_*	$y_* = 0.5\,x_* + 0.037$	$y_* = 0.8287-0.1381\,x_* + 0.1437\,x_*^2 - 0.006x_*^3$	$y_* = -0.96562+0.71911\,x_* + 0.017594\,x_*^2 - 0.00053x_*^3$
x_* in terms of y_*	$x_* = -0.074+2\,y_*$	$x_* = -0.61306+3.0882y_* - 0.57057y_*^2 +0.055727y_*^3$	$x_* = 1.3272+1.2866y_* - 0.024433y_*^2 +0.00106y_*^3$
Range in terms of x_*	$x_* <2.926$	$2.926<x_* <5.59$	$5.59<x_* <7.619$
Range interms of Δp_*	$\Delta p_* < 843$	$843 <\Delta p_* < 389,045$	$389,045 <\Delta p_* < 41,591,061$
$\Delta p / \tau_0$ in terms of x_*	$\Delta p / \tau_0 = -21.848+35.705x_* - 17.775x_*^2+3.8403x_*^3$	$\Delta p / \tau_0 = 55.869- 58.619x_* +20.378x_*^2-1.2946x_*^3$	$\Delta p / \tau_0 = 10.699+2.751x_* +12.8804x_*^2+0.021509x_*^3$

Note: $x_* = \log\left(\dfrac{\Delta p d^2}{4\rho\upsilon^2}\right) = \log(\Delta p_*)$ and $y_* = \log\left(\dfrac{\tau_0 d^2}{4\rho\upsilon^2}\right) = \log(\tau_{0*})$ by definition

Table 3.3 List of Experiments

Series	No.	D(mm)	h(mm)	Q(L/s)	d(mm)	Uo(m/s)	F	R	d/h	Slope x0.001	Remarks
A	AS0	–	–	54	120	0.037	0.011	44,262	–	1.47	tailgate
	AS1	130	65	54	120	0.037	0.011	44,262	1.85	1.47	tailgate
	AS2	74	37	34	70	0.040	0.015	27,869	1.89	1.47	No tailgate
	AR11	130	65	40	120	0.027	0.008	32,787	1.85	1.47	tailgate
	AM01	–	–	40	120	0.027	0.008	32,787	–	1.47	tailgate
	AM11	130	65	40	120	0.027	0.008	32,787	1.85	1.47	tailgate
	AM21	74	37	20	70	0.023	0.009	16,393	1.89	1.47	tailgate
	AM31	74	37	20	70	0.023	0.009	16,393	1.89	1.47	///+cube
	AM41	140	95	40	120	0.027	0.008	32,787	1.26	1.47	natural rock
	AM02	130	–	65	120	0.044	0.013	53,279	–	2.35	tailgate
	AM12	130	65	65	120	0.044	0.013	53,279	1.85	2.35	tailgate
B	BS0	–	–	30	72	0.034	0.013	24,590	–	1.18	No tailgate
	BS1	130	65	30	72	0.034	0.013	24,590	1.11	1.18	///////
	BR11	130	65	20	70	0.023	0.009	16,393	1.08	1.47	tailgate
	BM01	–	–	20	70	0.023	0.009	16,393	–	1.47	tailgate
	BM11	130	65	20	70	0.023	0.009	16,393	1.08	1.47	tailgate
	BM21	74	37	13	40	0.027	0.013	10,656	1.08	1.47	tailgate
	BM31	74	37	13	40	0.027	0.013	10,656	1.08	1.47	///+cube
	BM02	130	65	30	70	0.035	0.013	24,590	1.08	2.35	tailgate
	BM12	130	65	30	70	0.035	0.013	24,590	1.08	2.35	tailgate
C	CS0	–	–	8	42	0.016	0.008	6,557	–	1.18	No tailgate
	CS1	130	65	8	42	0.016	0.008	6,557	0.65	1.18	No tailgate
	CR11	130	65	13	40	0.027	0.013	10,656	0.62	1.18	tailgate
	CM01	–	–	13	40	0.027	0.013	10,656	–	1.18	tailgate
	CM11	130	65	13	40	0.027	0.013	10,656	0.62	1.18	tailgate
	CM02	–	–	20	45	0.036	0.017	16,393	–	2.35	tailgate
	CM12	130	65	20	45	0.036	0.017	16,393	0.69	2.35	tailgate
D	DS0	–	–	70	393	0.015	0.002	57,377	–	1.47	tailgate
	DS1	130	65	68	268	0.021	0.004	55,738	4.12	1.47	tailgate
	DS2	74	37	65	157.5	0.034	0.009	53,279	4.26	1.47	tailgate
V	V1	130	65	4	426	0.001	0.000	3,279	6.55	1.47	tailgate
	V2	130	65	12	205	0.005	0.001	9,836	3.15	1.47	tailgate
	V3	130	65	12	120	0.008	0.002	9,836	1.85	1.47	tailgate
	V4	130	65	12	60	0.016	0.007	9,836	0.92	1.47	tailgate
W	W1	74	37	25	61	0.034	0.014	20,492	1.65	1.47	No tailgate
	W2	74	37	20	55	0.030	0.013	16,393	1.49	1.47	///////
	W3	74	37	18	53	0.028	0.012	14,754	1.43	1.47	///////
	W4	74	37	15	49	0.025	0.011	12,295	1.32	1.47	///////
	W5	74	37	10	43	0.019	0.009	8,197	1.16	1.47	///////
	W6	74	37	10	41	0.020	0.010	8,197	1.11	1.76	///////
	W7	74	37	10	39	0.021	0.011	8,197	1.05	2.06	///////
	W8	74	37	10	36	0.023	0.012	8,197	0.97	2.65	///////
	W9	74	37	15	44	0.028	0.013	12,295	1.19	2.65	///////
	W10	74	37	18	48	0.031	0.014	14,754	1.30	2.65	///////
	W11	74	37	20	49	0.033	0.015	16,393	1.32	2.65	///////
	W12	74	37	25	54	0.038	0.016	20,492	1.46	2.65	///////
	W13	74	37	30	58	0.042	0.018	24,590		2.65	///////
	W14	74	37	34	65	0.043	0.017	27,869	1.76	2.65	///////
	W15	74	37	10	32	0.026	0.014	8,197	0.86	3.23	///////
	W16	74	37	12	35.5	0.028	0.015	9,836	0.96	3.23	///////
	W17	74	37	15	39.5	0.031	0.016	12,295	1.07	3.23	///////
	W18	74	37	15	38.5	0.032	0.016	12,295	1.04	3.53	///////
	W19	74	37	15	35	0.035	0.019	12,295	0.95	4.11	///////
X	X1	130	65	30	105	0.027	0.008	28,037	1.62		round flume
	X2	130	55	15	65	0.022	0.009	14,019	1.18		round flume

Table 3.4 Undisturbed Flow Characteristics

Expt. Series	ASO	BSO	CSO	DSO	AM01	BM01	CM01	AM02	BM02	CM02
Channel width, W (m)	1.22	1.22	1.22	1.22	1.22	1.22	1.22	1.22	1.22	1.22
Discharge, Q (l/s)	54	30	8	65	40	20	13	65	30	20
Depth of water, y_0(mm)	120	72	42	390	120	70	40	120	70	45
Average velocity, U_o m/s	0.369	0.342	0.156	0.137	0.273	0.234	0.266	0.444	0.351	0.364
Surface velocity, U_m m/s	0.420	0.426	0.195	0.182	0.346	0.296	0.310	0.543	0.420	0.430
Froude number	0.340	0.406	0.243	0.070	0.252	0.283	0.425	0.409	0.424	0.548
Nature of bed	Smooth	Smooth	Smooth	Smooth	sand bed	sand bed	sand bed	sand bed	sand bed	sand bed
sand size, D_{50} (mm)	-	-	-	-	1.11	1.11	1.11	2.12	2.12	2.12
Geometric STD of sand	-	-	-	-	1.2	1.2	1.2	1.29	1.29	1.29
Critical shear stress of sand, τ_c	-	-	-	-	0.64	0.64	0.64	1.46	1.46	1.46
Bed shear stress, τ_o(Pa)	0.297	0.352	0.097	0.0492	0.4648	0.352	0.4595	1.062	0.894	1.03
ratio shear stress τ_o/τ_c	-	-	-	-	0.73	0.55	0.72	0.73	0.61	0.71
shear velocity, $u*$ (m/s)	0.01723	0.01876	0.00986	0.00700	0.02156	0.01877	0.02144	0.03259	0.02990	0.03210
Nature of turbulent flow	Smooth	Smooth	Smooth	Smooth	fullyrough	transition	fullyrough	fullyrough	fullyrough	fullyrough
Particle Reynolds #, D_{50} u*/v	-	-	-	-	23.9	20.8	23.8	69.1	63.4	68.1
Roughness Reynolds #, ksu*/v	-	-	-	-	96.2	67.0	68.8	148.3	171.6	185.9
sand equivalantRoughness,ks(mm)	-	-	-	-	4.46	3.57	3.21	4.55	5.74	5.79
ks/D_{50}	-	-	-	-	4.02	3.22	2.89	2.15	2.71	2.73
Estimated B.L.T. (m)Eq. 3.37	6.2307	3.30191	1.38458	22.0595						
Estimated B.L.T. (m)Eq. 3.38	4.43231	1.92785	0.98069	22.5285						
Estimated B.L.T. (m)Eq. 3.41					1.784523	1.242208	0.569267	2.480932	0.820094	0.588952
Estimated B.L.T. (m)Eq. 3.42	-				2.456474	1.319738	0.665591	2.444019	1.157632	0.651253

CHAPTER 4

GENERAL NATURE OF THE FLOW

4.1   Introduction

Flow around an obstacle is three dimensional and complex and thus needs to be observed and understood prior to making detailed measurements. A reasonable way of advancing our knowledge of complex flows is to carry out flow visualization studies. To become familiar with any flow containing a major vortex system, flow visualization is an essential first step. Even making a model of different vortices and evolution of the vortex system might help in understanding flow characteristics. In this chapter the results of flow visualization for mounted obstacles on the smooth and mobile bed of two laboratory flumes will be presented. The effect of the relative depth and Froude number on the flow characteristics and existing vortex system will also be described.

4.2   Smooth Bed

There are several methods of flow visualization, such as hydrogen bubble technique, oil-flow visualization, and dye plumes, that are useful in studying different flow characteristics. In this study, dye plumes were used in flow visualization to study the effects of different parameters on flow around the body. Based on Helmholtz theorem, if the vortex tube can keep its own identity it is possible to trace the vorticity by dye. The rate of diffusion of the vorticity is much faster than the dye but in a convection dominated flow, diffusion is negligible, hence dye can trace the vorticity. But it should be noted that the dye is a scalar quantity, whereas vorticity is a vector. So dye can only show the location and will not provide any other information.

Observations were made in Flume 1 with flow depths of 60 to 425 mm with corresponding Froude number, F, of 0.214 to 0.004 and Reynolds number, R, (based on the depth of flow) as low as 3300 (Table 3.3). To observe the separation of the vortices

from the top and sides of the obstacle, very low R was used while using the 130 mm diameter hemispherical obstacle. To create a higher F in Flume 1 for different relative depths, a smaller diameter, D=74 mm, was used. The height of the body as before was the radius of the sphere, h=37 mm. The hemispheres were mounted on the aluminum bed which was considered smooth. Relative depth of 0.86 to 4.26 with F of 0.272 to 0.56 were examined (Table 3.3).

4.2.1 Vortex system and general flow patterns

In the first part of the flow visualization, the general flow patterns around the body were studied, such as the vortex system, wake phenomena and the separation points on the bed in front of the obstacle and on the body itself. The dye plume was used first with a deeply submerged obstacle and very sub-critical flow (F=0.004). This low Froude number flow helped in studying the main features of the flow while it provided enough time to visualize them. Later on, the use of higher Froude number showed that these features were still there for deep flows, and some of them, like the HS vortex, were even stronger in shallow flows.

To show the origin of the high shear stress region around the obstacle, dye plumes were introduced close to the bed and the region upstream of the obstacle was covered. Due to the presence of the adverse pressure gradient in front of the hemisphere, the approach velocity decreased and reduced to zero at the stagnation point on the bed, upstream of the body where the flow separated from the bed. The reduction of the flow velocity close to the bed caused the decrease of the bed shear stress. Therefore, the weak bed shear stress was not able to erode the dye from the bed, leaving the dye just where bed shear stress was reduced, which left a colored band like a horse-shoe (Figure 4.1). The weak bed shear stress region was located between two areas of high bed shear stress. The outer clear zone belonged to the general high bed shear stress of approach flow and the inner one belonged to the HS vortex.

At the stagnation point or more precisely the stagnation line, the separation of the boundary layer occurred. A part of this separated boundary layer formed a horse-shoe vortex (HS vortex) of large circulation in front of the body which produced a high shear stress on the bed. The high shear stress was able to remove all the dye sticking to the bed and produced a dye-free zone. The HS vortex at the front of the obstacle rotates almost completely in a vertical plane but its two legs are moved downstream by convection and so rotates in a helical manner. The effect and presence of the HS vortex could be observed not more than 2-3 times the diameter of the body at its downstream and then it combined with the general wake behind the obstacle (Figures 4.1-5).

Due to the oscillation of the HS vortex, the dye-free region was much wider than the actual width of the HS vortex itself. To find the actual height of the HS vortex and its spinning direction, dye was introduced, as before to the flow at the upstream of the body. But due to the rapid mixing process above the bed, the whole front side of the body was clouded by the dye, making it difficult to observe the HS vortex separately. Therefore, to capture the movement and spinning of the HS vortex, the dye was injected right at its core to prevent the mixing. By predicting the back and forth motion of the HS vortex and with injection of dye right at its center, its approximate size could be observed (Figure 4.2).

The number of active HS vortices in front of the body was not limited to one. The general explanation above refers only to the primary vortex, which is also the strongest one. As a result of the rotation of the primary HS vortex, a series of smaller less significant vortices was generated (Figure 4.8). The rotation of the primary HS vortex was clockwise, but as part of its reaction included some counter clockwise vortices. The chain of HS vortices gets weaker in strength away from the obstacle and closer to the separation point at the upstream side. Stronger vortices were located at a higher level, away from the bed and rotated clockwise. After each clockwise rotating vortex there was a weak counter clockwise rotating vortex at the lower level close to the bed. There was a

very tiny vortex between the primary vortex and the front of the body which was hard to visualize most of the time. By flow visualization, it was possible to observe up to four of these vortices. Therefore the clear region around the body shows the approximate location of the cascade of these HS vortices, considering their oscillation. Baker (1979, 1980) and Martinuzzi and Tropea (1993) could distinguish up to four HS vortices. Schwind (1962) found for a wedge that the exact number of vortices depends upon the flow speed and wedge size; more vortices appeared as the speed increased. In the oscillation period of his experiments, the two largest clock-wise rotating vortices move towards each other and apart again. At higher speed, the larger clock-wise vortex isolated from the rest of system and as velocity increased the flow became turbulent. T. Okamoto et al. (1977) found two HS vortices for the cone of vertex angle 60. These two vortices had axes which rotate in the same direction. Therefore, the two vortices began to coil around each other in the vicinity of the cone sides. The number of HS vortices in the experiments of Tamai et al. (1987) increased by increasing the R number up to a critical R, after which the number of vortices decreased. They proposed that the number of the HS vortices decreases because in higher R number the vortices start to fluctuate horizontally and then coalesce.

The separated flow from the sides of the body and the two legs of the HS vortex combined with each other in the wake of the hemisphere. When the relative depth, d/h, was more than one, the separation of flow from the top and the sides of the obstacle produced an arch-vortex. The arch-vortex behaves like a half-vortex-ring and could be observed by dye injection at the sides and top of the obstacle. Significant growth of the shear layer after separation from the body can be attributed to the pairing of vortices (Brown and Roshko, 1974, Winant and Browand,1974). Shedding of the arch-vortex from the body can be clearly seen in Figure 4.3. The roots of the arch-vortex could be observed by dye injection immediately downstream of the body on the bed (Figure 4.4). The legs of the arch-vortex were perpendicular to the bed while the legs of the HS vortex

were parallel to it (Figures 4.1-7). Injection of dye immediately downstream of the obstacle showed the separation line from the body and vertical and horizontal extent of the wake (Figures 4.5-6). Observations from the sides of the obstacle showed the approximate height of the HS vortex (Figure 4.2).

Downstream of the body in high relative flow depth, there was a recirculation zone which was generated by the separated flow from the body (Expts. D1, D2, A1). The extent of the recirculation region behind the body was determined by continuous injection of dye. The dye needle was moved from downstream towards the body at several depths including the depth of one-half the hemisphere height. In a region about 1.5-2 diameters downstream of the body, the movement of dye changed to a turbulent state with no dominant direction. By moving the needle closer to the body the backward motion of the flow could be seen clearly. The transition zone shows the reattachment of separated stream lines from the top of the body to the bed (Figure 4.9). The free shear layer which separates the potential flow from the recirculation zone in the wake, is indicated by the dotted area in the figures. The dye at the bed shows that the flow immediately downstream from the body moves towards the centre and then moves away from it. Martinuzzi and Tropea (1993) postulated that the recirculation region entrains the surrounding fluid towards the axis of symmetry due to the difference between the outside velocity and the wake velocity. Also, the direction of the rotation of the HS vortex is inward and helps the general inward flow. After the reattachment point, the initial rapid expansion of the wake is due to the increase of the mass flux in the wake close to the channel floor as the shear layer reattaches and is subsequently entrained by the HS vortex. Further downstream, the wake grows more slowly as fluid is gradually entrained from the surrounding flow. Larousse et al. (1991) also proposed that this is the influence of the recirculation vortex which entrained the inner portions of the HS vortex and drew the legs towards the axis of symmetry.

4.2.2 Effects of free surface

After the observation of general flow patterns around the body, a series of flow visualization experiments were conducted to investigate the effect of free surface on the flow for different relative depth and Froude number. For each relative depth a range of F was studied to check the effect of these two parameters separately. Based on the result of this flow visualization, the effect of these two parameters on the flow around the mounted body can be explained by four different regimes, which are discussed in the following sections.

For relative depths greater than one, it was observed that the flow passing from the top of the body can be divided into the upper and lower layer. The lower layer under the effect of the free shear layer could get mixed with the wake region, while the top layer which depends upon the relative depth of the flow, might not mix with the recirculation zone. Flows with the relative depth of more than 4 can be classified in regime 1 (Expts. D1, D2). In regime 1 the effect of the body is not felt at the surface and there is no mixing of the top layer with the wake region (Figure 4.9).

If the layer of the flow passing over the top of the body does have a medium thickness, $1.3 < d/h < 4$, its upper layer would not mix with the wake region due to the weak effect of the free shear layer, but the free surface gets distorted in the form of standing waves (Figure 4.13). These characteristics can be referred to as regime 2. Expts. A1, A2, W14, W2, W12, W4, Figures. 4.10 (a-f). In regime 2 the direction of the top flow is forward everywhere. But if the relative depth of flow is low enough, the free shear layer causes the mixing of the whole depth of the flow and some backward flow could be observed at the water surface. This would be the case for the regime 3 of the flow, Expts. W9, W10, W11, W5, Figures. 4.12 (a-g). Regime 4 occurs when the relative depth is less than one and the top of the obstacle is above the water surface and Karman vortex street is strongly present with a strong backward flow behind the body, Expts. W8, W19, C1, Figures 4.14-9 (a,b).

The water surface near the body is affected by the relative depth d/h as well as the F of the approaching flow. By decreasing the relative depth, the effect of the body on the water surface profile became more significant. A number of small surface waves occurred. Higher F was found to be important in increasing the wave heights and it also affected the number of waves.

4.2.2.1 Wake of the body in regime 1

In regime 1, flows of relative depths of 4.12 and 4.26 and F of 0.128 and 0.272 respectively (Expt. D1 and D2) were observed. For a deep submerged body and a sub-critical flow, there was a very thick flow passing above the top of the body. The passing flow from the top of the body was divided into two layers. The top layer is adjacent to the free surface. It moves in the forward direction and acts as a potential flow. There was no change in the free surface water profile and it was smooth, with no effect of the obstacle at all. Whereas in the lower layer, the flow adjacent to the body separated from the obstacle in the form of arch-vortices and created a free shear layer. The vortex system around the obstacle in a fully submerged flow is shown in Figure 4.7 where the arch vortices shed from the body cover the whole recirculation region. Inside the recirculation zone, the flow is backwards due to the clockwise rotation of the arch-vortices and the large difference between the outer velocity and inner velocity of the wake. The turbulence in the free shear layer appeared to be significant. This high degree of turbulence caused a very strong mixing zone in which the lower layer of passing flow mixed with the flow in the recirculation region and a great exchange of momentum occurred between the low momentum recirculation region and the high momentum forward flow.

4.2.2.2 Wake of the body in regime 2

In regime 2, a number of flows were studied ranging from a relative depth of 1.89 to 1.46 and a Froude number of 0.34 to 0.562. For a relative depth of 1.85 and F of 0.34 (Expt. A1), there was a rise in the water surface level upstream of the body and then a drop downstream with a series of 3 surface waves across the width of the flume. The sides of these waves became distorted by the oncoming flow as they were carried downstream and their extent was less than 3D. With a higher F of 0.48 and a relative depth of 1.89 (Expt. A2), the number of surface waves increased to 7 distinct ones with higher heights than before (Figures 4.10a-13). These waves were visible even at 10D which is about 3 times the length of the former case (lower F in Expt. A1). The length of the wake, the recirculation zone, was less than 1D and it was attached to the bed with a strong backward flow adjacent to the bed (Figure 4.10 b). Other investigations have suggested a similar trend. Cantwell and Coles (1983) found the length of the wake to be roughly x/D=1.0 - 1.5. S. Okamoto (1979) also found that, due to the presence of a strong downwash behind the sphere, the recirculation region was shortened and limited to 2.5 D. S. Okamoto (1979) for a hemisphere-cylinder and Martinuzzi and Tropea (1993) for a prismatic obstacle, showed that the recirculation region was considerably reduced compared with that in a two-dimensional wake. Logan and Lin (1982) and Fackrell and Pearce (1981) also indicated the same conclusions in comparison between a three dimensional body and a long obstacle, such as a rib spanning the entire width of channel. They proposed that in the case of a three dimensional body, part of the flow goes around the body, whereas in a two dimensional body, most of the deflected fluid flows above the top of the body, enlarging the recirculation zone.

The oscillation downstream of the wake was significant. This oscillation indicates the presence of the vortex shedding from the body, which was suppressed by the thick layer of water flowing on top of the body. This layer and its downwash effect would be

diminished for relative depths of about 1, and the pronounced oscillation could be observed in form of Karman vortex street in certain R .

For a higher F of 0.537 and a relative depth of 1.76 (Expt. W14), the dip in the water level at the body location was very significant and the number of the waves was limited to two (Figure 4.10 c). The length of the wake due to this high F was reduced to a small distance away from the hemisphere, 0.2-0.3 D, and for the rest of the flow, a strong forward flow was present. Traces of dye showed a weak rotation beneath these strong waves.

With a F of 0.434 and a decreased relative depth, d/h=1.65 (Expt. W1), the oscillation downstream of the wake increased by almost the same wake length as in Expt. A1. By further decreasing the relative depth, this trend continued and the heights of the surface waves increased, with lesser wave length at distances closer to the body. In this way the disturbance due to the presence of the surface waves could be transferred easier to the bottom layer, i.e., the recirculation zone.

With a relative depth of 1.49 and a F of 0.405 (Expt. W2) the number of waves was 3 to 4 with a strong forward velocity at the central region of the flow downstream of the body (Figure 4.10 d). This fast flow at the plane of symmetry might be the continuation of the accelerated flow above the body. The flow at the surface moved forward, whereas at a small distance below the water surface it dived down and mixed with the recirculation zone due to the closer location of the free shear layer. For a higher F of 0.52, and a similar relative depth of 1.46 (Expt. W12), the number of surface waves was restricted to 2 strong waves (Figure 4.10 e). A higher Froude number generated high momentum surface waves and a stronger free shear layer, which caused the trapped flow inside the high standing wave to dive down and mix with the recirculation region. For a relative depth of 1.57 and a F of 0.562 (Expt. W13), the only present surface wave had a higher height where the sign of breaking waves could be observed at its upstream side (Figure 4.10 f). Here a high F caused a very significant standing wave but the moderate

thickness of the top layer prevented mixing of this layer with the recirculation zone. The backward flow was limited to a small region (0.2 D) close to the body.

4.2.2.3 Wake of the body in regime 3

In regime 3, the relative depths of the observed flows were in the range of 1.11 to 1.32 and the Froude number ranges from 0.294 to 0.481. In this regime, the strength of the vortex ring is not similar for the whole perimeter of the body due to the small thickness of the flow above the body which causes a weak separation (Figure 4.11). For a relative depth of 1.32 and a F of 0.362 (Expt. W4), there were 2 strong waves immediately downstream of the body (Figure4.12 a-b). While for the higher relative depths, the transition from one wave to another was very smooth and the wave length was large. These waves were very close to each other because they had very short wave lengths. The presence of a very fast current at the central portion of the surface waves was more significant and the water surface became very rough at this central region. Under this condition, the surface waves started to interact with the highly turbulent recirculation zone due to the decrease of the top layer thickness. The dye injected to the surface waves could be traced moving and mixing with the recirculation zone, whereas in the higher relative depth it proceeded straight forward with no mixing.

By increasing the F to 0.447 and a similar relative depth of 1.3 (Expt. W10), two surface waves were present. A small portion of the backward flow could be observed downstream of these surface waves at the surface (Figure 4.12 c). But on the bed, except for a small portion of the backward flow in the recirculation zone attaching to the body, all the injected dye behind the body was moved forward by fast flow coming from the sides of the body. The height of the backward flow in the wake behind the body can be divided into two layers, a top layer of backward flow and a lower level. The top layer of the backward flow after hitting the body in a clockwise rotation moved upwards to the surface and joined the separated flow from the top and the surface waves again. The

lower layer of the backward flow in the recirculation zone dived down after hitting the body in a counter clockwise movement and was swept by the forward flow from the sides. It then created a forward flow downstream of the body on the bed. Further increase of F to 0.481 with a similar relative depth of 1.32 (Expt. W11), reduced the number of surface waves to one and it caused a significant mixing with the smaller recirculation region behind the body (Figure 4.12 d).

In the above range of relative depth there was a strong flow separation from the top of the obstacle and by joining with the separated flow from the sides, a strong arch vortex was created. A strong forward flow (in the layer on the top of the wake) caused a strong recirculation zone in which the backward flow at the bed was easily observable. Due to the existence of a strong backward flow in the wake, an upward flow on the downstream side of the body wall could be seen which was climbing up to the separation point on the top of the body just around the plane of symmetry.

By decreasing the relative depth to 1.16 with a F of 0.294 (Expt. W5), while the backward flow existed at the surface, just downstream of the small wake, there was a strong forward flow at the bed (Figure 4.12 f). The flow climbed up from the upstream side of the body and transformed into a thin layer of fast moving flow over the top of the body. It moved forward for a small distance downstream before being stopped by a strong backward flow at the surface, which caused it to dive down and mix with the recirculation region. It seemed that the contribution of the (weak) separated flow from the top of the body was limited to a small region of the wake behind the obstacle. It means that the zone of influence of the separated flow from the top was much smaller than that from the side flows.

The surface backward flow behind the body, after being deflected by the forward flow, dived down to the bed and in a counter clockwise rotation generated a forward flow at the bed (Figure 4.12 g). The forward flow of the separated shear layer from the top of body, after being deflected by the backward flow, dived down and in a clockwise rotation

112

created a small recirculation region and a backward flow in the vicinity of the body. With a higher F of 0.425 and a similar relative depth of 1.19, Expt. W9, a thin layer of flow passed over the top of the body and created two short length waves and a backward flow at the surface which was extended well beyond them (Figure 4.12 e). At the bed there was a very small backward flow attached to the body, 0.1D in length, and then further downstream the forward flow was dominant everywhere.

Going to the relative depth of 1.11 and a F of 0.315 (Expt. W6), the flow behaved like Expt. W5, but the surface backward flow in the wake became stronger and longer, 2D in length, than the bottom back flow, which was 1D in length. Therefore, the wake is stronger in the top flow and shorter and weaker in the lower flow level. The arch vortex could not be formed with relative depths of about 1 in its complete form as it was in the higher relative depths. The top portion of the vortex ring was very weak compared with separated flows from the sides or could not be formed at all. Therefore, it might be concluded that the separated flow from the sides causes a strong and fast forward flow in the absence of the top flow, which in turn reduces the size of the wake and strength of the backward flow at the bed level (Figure 4.12 g).

4.2.2.4 Wake of the body in regime 4

In regime 4, when the relative depth is less than about one, the downwash over the body disappears and the wake becomes two-dimensional with the appearance of the Karman vortex street and the disappearance of the arch vortices (Figures 4.15-16). Therefore, there is no arch vortex in regime 4. Karman vortex street can be observed easily in this type of flow (Figures 4.14-16 b). Once the boundary layer has separated in form of a vortex from one side, for example, the right side, it grew and moved towards the left, then after a while, another one is shed from the left and grew towards the right and surrounded the right one (Figure 4.16 b). All the system moved downstream while these processes were in progress.

113

Experiments W8 and W19 with relative depths of 0.97 and 0.95 and F of 0.384 and 0.6 respectively somehow show a two dimensional wake phenomena. The top of the obstacle protruded from the flow and a strong shedding of the vortices was observed downstream of the body. The length of the backward flow at the surface was almost 2D for Expt. W8 and around 1D for Expt. W19 (Figure 4.16 a). This backward flow proceeded towards the body without any resistance from the downwash flow and after being stopped by the body in a counterclockwise rotation, joined the forward flow at the bed. A significant portion of the flow downstream of the body, i.e., almost the lower half of the depth, was in forward direction. The large difference between the velocity of the forward flow and the backward flow caused a highly turbulent shear layer in which any particle of the flow away from the bed and the surface could turn and join the opposite direction of the other layer. The movement of the forward flow was not straight but inclined towards the center as can be seen in Figures 4.12 g and 4.16 b. The extent of the backward flow at the surface shows the vortex generation zone and the forward flow downstream of it belongs to the vortex street area. Based on the above observation, the size of the vortex generation zone would be reduced by increasing of F value.

4.2.3 General results of the smooth bed experiments

As a general result of the flow visualization, it can be proposed that the forward flow consisting of the surface waves induced by the separated flow from the top of the body is resisted by the general backward flow induced by the separated flow from the sides. This means that while the general rotation of the arch-vortex or simply a vortex ring separated from the body is the same, the general forward direction of the downwash would be obstructed by the backward flow induced by the side flows. At the same time there is no resistance to the separated top flow by the arch-vortex because the source of the rotation of the top part of the arch-vortex is indeed the downwash itself. If the surface flow is powerful enough, it can create a strong forward flow which is able to move

114

downstream in spite of the effect of the side flows. This occurs if there is a thick flow over the body, i.e. a high relative depth and a high Froude number. That is why, in regimes 3 and 4, the backward flow at the top layer was weaker than the lower forward flow.

By comparing Expts. W9, W10 and W11 it can be seen that for similar relative depths, the higher Froude number could cause shorter backward flow at the surface due to its higher momentum. Reduction of this momentum, for example, decreases the relative depth, and causes the backward flow to be dominant, which results in the obstruction of the forward flow and restricts it to the vicinity of the body. The extent of the progress of the forward flow induced by the top separated flow depends on the Froude number and the relative depth. In the case of regime 4 where there is no top flow, the difference between the level of water at the front of the body and its downstream side caused a strong gravity flow. This allowed no possible room for backwater flow in the wake behind the body on the bed, so the backwater flow was totally absent there.

In general, the specification of these four regimes can be summarized as follows :
1. In regime 1, due to the deep submergence, the top layer of flow passing above the obstacle was not affected by the presence of the body, whereas the lower layer mixed with the recirculation zone. In the top layer, the direction of the velocity was forward everywhere and the presence of the backwater flow was limited to the region inside the recirculation zone attached to the body and the bed, away from the surface. The vortex system around the body consisted of a HS vortex and an arch-vortex with the latter one covering the recirculation region behind the body. Within the range of these experiments, there was no evidence of Froude number affecting the flow in this regime.
2. In regime 2, with a medium relative depth of flow, the top layer still did not mix with the recirculation zone, but the effect of the body on the free surface began in form of surface waves. The number and the strength of the surface waves depended on the relative depth and the Froude number of the flow. For higher relative depths in Expts A1

115

and A2, an increase in the Froude number caused an increase in the number of surface waves from 3 to 7, whereas in the lower relative depths in Expts. of W2, W12 and W13 an increase in F caused a decrease in the number of surface waves from 4 to 1.

For a higher Froude number, the waves were higher and usually with smaller wave length. Higher F also reduced the length of the recirculation zone from 1D to 0.2 D and caused more water surface drop on the body. The wake was oscillating due to the shedding of the vortices from the body. This oscillation was found to be a function of the relative depth and it increases with increasing relative depth. For the lower range of relative depth, a high velocity with a rough surface was observed at the plane of symmetry, which may be caused by the accelerated flow from the top of the body. In the lower range of relative depth, the thickness of the forward flow at the top layer was reduced, i.e., getting closer to the free shear layer. The HS vortex and the arch-vortex were still present in this regime.

3. In regime 3, due to the small thickness of the layer of flow passing above the body, not only were the surface waves present but also, both the top layer and the lower layer combined with each other and mixed with the recirculation region. In this case some backward flow was present at the surface of the flow due to the dominant effect of the separated flows from the sides. This backward flow became stronger and longer by decreasing the relative depth. Therefore, the wake geometry changed to a new one, having a longer recirculation at the surface than at the bed. While the HS vortex was active, the arch-vortex was present in the upper range of relative depths. In the lower relative depths its effect, if there was any, was restricted to a small region immediately downstream of the body.

By increasing the Froude number from 0.362 to 0.481 in Expts. W4, W10 and W11, the number of surface waves decreased from 2 to 1, with a higher height and a smaller wave length similar to the Regime 2. The presence of the fast current at the central region of the surface flow was more significant with a rougher surface, perhaps

due to the reduction in the thickness of the flow above the body and an increase in the flow acceleration there. The backward flow at the bed decreased to a small portion in the vicinity of the body. The upper layer of the backward flow in the wake (in a clockwise rotation) joined the forward flow of the separated flow from the body and the surface waves. The lower layer (in a counter-clockwise rotation) joined the forward flow from the sides of the body at the bottom.

4. Regime 4 occurs when the relative depth is less than one resulting in the protrusion of the body out of the water. There was a strong backwater flow at the top layer of the flow in the vicinity of the body, that is, the vortex generation zone. The oscillation of the wake in its complete form can be seen in form of Karman vortex street downstream of the vortex generation zone in the absence of the top flow and its downwash effect. By increasing the Froude number, the length of the vortex generation zone decreased as well. The arch-vortex was absent in this regime due to the missing part of the separated flow from the top of the body.

4.3   Mobile Bed

The flow visualization in a flume with the smooth bed helps to understand the general behavior of the flow and the vortex system around the obstacle. But in a mobile bed where the bed is no longer smooth, the geometry of the bed was changed by the flow severity, depending upon the flow characteristics, the size and gradation of the sediment. Then the flow was changed due to the effects of new changes in its boundary, i.e., the bed. The process of interaction between the bed and the flow continues and takes 2-3 days to reach a stable condition.

To investigate the effects of the mobile bed, and especially the scour around the body mounted on the bed a series of flow visualizations was conducted in flumes #1 and 2. As a preliminary part of this study, the first observation was made in flume #2, with a fine sand of $D_{50} = 0.25$ mm and a sphere made of Styrofoam. The fine size of the sand

117

allowed observation of the fine flow patterns, simply by watching the sand migration. But for coarser sands, due to the lack of sufficient shear stress at the bed, only the grains of sand closer to the body (where there was higher shear stress) could be moved. Therefore, the geometry of the scour and the deposition on the bed did not describe the fine flow patterns properly at the vicinity of the body.

In the next stage, for more detailed measurements, experiments were carried out in flume #1. The details of this set up are described in chapter 4. In this flume, two larger sizes of sand were used.The median sizes D_{50} were 1.11 and 2.1 mm for sediments #1 and #2 respectively. For each type of sand, different regimes of flow were examined to simulate different flow conditions in rivers. Based on the past experiments in flume # 2, it was found that the depth of scour in front of the body can be greater than the designated height of the hemisphere. Therefore, to accomodate a possible deeper scour, the hemisphere was mounted on top of a cylinder of the same diameter with the cylinder buried in the sand, leaving only the hemisphere out of the bed. In this way there was enough room for scour to develop.

The shape of the body has a great effect on the flow patterns around its surroundings. To investigate this aspect of the problem, a cube was used instead of the hemisphere on the cylinder. For the same reason as before, instead of a cylinder with a circular base, a square base was used with the same dimension as the cube. Then to check the difference between the flow patterns of artificial obstacles (such as a hemisphere and a cube with the natural one) a natural rock was used as the obstacle.

4.3.1 General scour patterns in fine sand

At the first stage of flow visualization, a Styrofoam sphere with a diameter of 130 mm was mounted to the bed of flume # 2 and a piece (of height 20 mm) was cut from the main body to facilitate its positioning on the bed. Then upstream and downstream of the mounted body was covered with fine sand to a thickness of 45 mm, which left a

hemisphere of height 65 mm out of the sand, i.e., the radius of the sphere. By adjusting the tailgate, the whole flume was filled slowly with water and the effect of the existing flow on the bed was minimized. After the water level reached the approximate desired level, the valve was opened until the desired discharge was obtained. For a relative depth of 1.62 and Froude number of 0.263, Expt. X1, the flow was run for more than a day to reach a state close to the table condition.

The scour first occurred at the sides of the body, at a small distance upstream of the lateral symmetry line of the body (where the flow accelerated most), and then propagated upstream (Figures 4.17-23 a). By gradual increase of the scour at these points, signs of scour in front of the body with a smaller depth were observed. Then, by combining the two scour holes at the sides, a horse-shoe-type scour hole at the front half of the obstacle formed. This scour was a direct result of the existence of a HS vortex. Due to the fast spinning of the HS vortex at the upstream side of the body, a low pressure region at the core of the vortex was present, which along with a high bed shear stress caused the sand particles to be lifted from the bed. Exiting from the high velocity region, the flow lost its momentum and then the grains of sediment from the scour hole were deposited immediately downstream of the scour hole. By piling up the sediment downstream of the symmetry line, a small hill of sand was visible. Then, due to the separation of the flow from the top of this small deposited sand, a highly turbulent flow caused a low pressure region downstream of the side of the hill with a large difference in velocity, which then created a new scour hole (Figure 4.23 b).

The growth of the scour hole around the body (which indicated the position of the primary HS vortex) caused a stronger down flow at the upstream side of the body wall and, in turn, helped the HS vortex spin faster, resulting in a deeper scour. Due to the effect of this down flow, the scour hole divided into two distinct regions. First was a deeper scour hole adjacent to the body with a steeper slope of the sediment wall at its

upstream side. Second was a wider and shallower region with a flatter slope at the upstream side of the first scour hole (Figures 4.19-23 c).

It was clearly visible that a separate HS vortex was spinning inside this deeper and inner scour hole. Due to the restricted geometry of the hole it could not oscillate freely, contrary to that in the smooth bed. The spinning vortex inside this scour hole caused a high bed shear stress which in turn could deepen the hole. The high bed shear stress at its upstream wall keep the sands in a slope steeper than their natural angle of repose. By deepening the scour hole, due to the restricted strength of the HS vortices in the vicinity of the body, a second and flatter slope occurred with a slope closer to the natural angle of repose. These two stages of slopes generated a wider scour hole.

The divided geometry of the upstream scour hole and its vortices had some effects on the downstream scour. Due to the difference in the strength of the outgoing HS vortices from this horse-shoe scour hole, the resulting deposition hills were formed differently. The stronger vortex was closer to the body and it left the body walls with a tighter angle than that of the outer vortex. The latter one on its way out of the HS-scour hole, caused a wider angle and flowed over the external wall of the deposited sand hill (causing a steep slope on its side) and separated from the general pathway of the inner vortex. Whereas, the inner vortex flowing with a higher strength created more deposition in a wider region and closer to the longitudinal axis of the flume (Figure 4.23 d).

Therefore, there were two different scour holes due to the action of these two HS vortices. One large scour hole was after the main deposited sand hill of the inner vortex, closer to the longitudinal axis. The other one was at the sides of the body due to the outer vortex separation from the sand hill. In this way there were two scour holes after the first deposited sand hill in each side of the body. One was smaller but deeper at the outer side, and the other was larger and shallower at the middle.

As the the HS-scour hole grew further, more sediment deposited on the sand hill and gradually two sand hills at the sides of the body merged towards the downstream end

of the body. The edges of these two sand deposits met each other at the downstream side of the body at the plane of symmetry, while the two middle scour holes merged towards each other as well. A deposited sand wall of small height separated the two middle scour holes and created a heart-shape deposit (Figure 4.23 d). Each of the four scour holes generated their own deposit and scour area, and over time, it resulted in a cascade of scour holes and deposited sand hills along the channel. The depth and the significance of scours and hills at the end of the cascade decreased further downstream of the body. As well, outer scour holes, which were formed due to the flow coming from the flatter slope, had less strength. They could proceed slower and in a less significant manner than the inner ones and stopped sooner than the middle one, hence a shorter length. At the end of this procedure and in stable conditions, a series of dune like identities was visible due to the connection of the edges of the deposited and scour regions.

For a relative depth of 1.18 and Froude number of 0.27, Expt. X2, the middle scour hole downstream of the body had its own cascade of smaller scours and depositions while the side scours propagated almost with the same rate downstream. The ability of all scours to propagate downstream caused them to join each other further downstream. The depth of the scours was more than that of Expt. X1, probably due to the higher strength of the HS vortex in the absence of the downwash effect. The height of the deposition immediately downstream of the body in Expt. X2 was higher than the previous experiment, Expt. X1, whereas the scour depth in the main scour hole was smaller.

The scour pattern in Expt. X2 was similar to a V-fan starting from the center of the body, and then expanding towards the flume walls. The scour pattern downstream of the body was wider than that of Expt. X1, with a larger relative depth (Figures 4.20-24). The scour pattern downstream of Expt. X1 after the side patterns were stopped was restricted to the middle pattern, which had a constant width. In Expt. X1, the flow divided into two parts and could move from the top of the body and its sides, so only the stronger inner HS vortex plus the downwash from the top of the body caused a progressive middle

scour pattern. The weaker divided flow from the sides affected the bed less. But in Expt. X2, the downwash from the top was missed and almost the whole flow had to proceed from the sides of the body, causing a strong flow at the sides (which were able to propagate further downstream). The propagation of the middle scour could be due to the very fine sand, which needs only a weak bed shear stress to be lifted in the absence of a strong downwash. Then, after some time, the rest of the deposited sand hills joined each other and established several lines of dunes downstream. The thin layer of the top flow had no considerable effect on the scour pattern downstream of the body.

4.3.2 Scour patterns in coarse sand

Experiments in flume #1 were conducted mainly for scour measurements. Those results are presented in chapter 6. The observation on the flow patterns and scour around the body are presented here. The start and the propagation of the scour pattern for Expt. AM11, with a relative depth of 1.85 and a Froude number of 0.252, was similar to Expt. X1, but some finer scour patterns were missed due to the presence of coarser sands. The scour patterns were confined to the center with almost a constant width (Figures 4.19 and 4.23 c). It was observed that the band of the scour pattern downstream of the body was not symmetrical. This was observed in all other experiments with high relative depth where the cascade of the scour pattern was attracted to one side. In the case of a lower relative depth such as in Expt. BM11 and CM11, the patterns were symmetrical (Figure 4.24).

In Expt. BM11 with a relative depth of 1.08 and F of 0.283, the cascade of scour patterns at the POS stopped after a small distance downstream. But at the sides of the body the scour patterns expanded toward the walls away from the POS as two wings of the scour fan (Figures 4.20-24). The flow visualization showed that the cascade of scours and depositions in the wings was located between two outgoing streams from the front scour holes. The inner HS vortex came out of the front scour hole while the wing was at

its outer side. The flow from the outer ring of front scour hole came out from the side of the body, while the scour wing was at its inner side. There was a strong gravity flow at the sides due to the significant difference between the water level at the back and the front of the body. The profile of the bed behind the body at the POS showed a short scour and then a deposition. This deposition was lowered further downstream and finally became flat much sooner than the two side wings, resulting in a much shorter scour pattern in the middle. The stronger scour patterns at the wings indicated that the strength of the HS vortex at the sides was greater than the flow behind the body.

The presence of the deposition behind the hemisphere was probably due to the effect of the backward flow. Looking from the top of the body, the rotation of the shedding vortices from the body was towards the POS, an inward direction, which then changed to a backward direction towards the body on the POS. The lifted sediments from the front of the scour hole, after loosing their momentum, fell downwards on their way towards the center in this inward flow, creating a deposition at the center. The backward flow prevented the migration of these settled sediments while its velocity decreased closer to the stagnation point on the body, creating more deposition. The absence of the downwash flow from the top of the hemisphere prevented any resistance to this backward flow. The end of the deposition at the center indicated the end of backward flow or vortex generation zone. Then the backward flow gradually changed to a forward flow further downstream with a velocity similar to the original approach flow. So, after the deposition and obtaining the original forward flow, the excess bed shear stress diminished with distance and the bed became flat again. Whereas, at the sides, the stronger flow continued to create scour patterns.

In Expt. CM11, with a relative depth of 0.62 and F of 0.425, the scour patterns were very similar to that of Expt. BM11. The width of the scour pattern at the side wings was more than that of Expt. BM11, which had a deeper scour. Due to the deeper scour, the thin layer of sand was removed totally in some parts of the bed downstream of the

main deposition and the original smooth bed could be seen. As well, the expansion of the scour fan was greater than that in Expt. BM11 and its wings reached the walls of the flume further downstream.

In the center line of the deposition area behind the body, there was a longitudinal band of shallow scour which was not present in Expt. BM11. It may be due to the presence of a very strong backward flow at the center, which could move the already settled sediment or prevent the settlement of those sediments lifted and moved by inward flow of shed vortices. In Expt. BM11, the backward flow was not that strong due to the presence of a small layer of downwash. The stepped shape of the main deposition area was present here too. This stepped shape might be due to the separation of the flow from the top of the deposition.

The presence of a small scour immediately downstream of the body in Expts. AM11, BM11 and CM11, was probably due to the very turbulent flow at that region. The flow going out from the front scour hole created a very steep slope at the sides of the body. This steep upward slope led the outgoing stream to the water surface, colliding with the other side's leg where the water surface rose locally in the form of boiling water.

A smaller hemisphere of 74 mm in diameter was used in Expt. AM21. The relative depth was 1.89 and the Froude number was 0.283. As expected, the general scour pattern was similar to that in Expt. AM11, but with a shorter extension of the cascade of scour patterns, perhaps due to the presence of a smaller diameter. The ratio of the diameter to the size of sediment was less, so the bed was relatively rougher than in Expt. AM11, causing the loss of finer scour patterns and confining the number of scour holes to two major ones at the center. In Expt. BM21, the same smaller hemisphere as in Expt. AM21 was used. The relative depth was 1.08 and the Froude number was 0.425. The scour patterns were located mainly at the center with a constant width, contrary to that in Expt. BM11. The length of the scour pattern was larger than that in Expt. AM21.

4.3.3 Scour Patterns produced by Other Shapes

A cube of 74 mm side length was used in Expt. AM31. The relative depth was 1.89 and the Froude number was 0.283. It was found that the two stages of scour in front of the body were more pronounced than that for the hemisphere (Figures 4.21-25). There was a short flat portion separating these two slopes. The separated flows from the sides of the body moved forward in a parallel manner, different from that for the hemisphere. It was the flat side at the back of the body which prevented these two side flows from meeting each other. The deposits at the sides of the body could not join each other, therefore a flat space was left in between (Figure 4.21). Martinuzzi and Tropea (1993) observed that in large aspect ratio, width to height, the legs of the HS vortex didn't affect the middle of the wake because they were away from the wake center. The scour pattern was very symmetrical downstream of the body and the flat part at the center line was present along the whole length. The width of the scour pattern was wider than those in the Expts. AM11 and AM21 and may be due to the shape of the body.

For a smaller relative depth of 1.08 and F of 0.425 in Expt. BM31, the scour pattern was observed for the cube obstacle. The results were similar to those in Expt. BM11, with expanding wings of scour patterns at its sides (Figure 4.22). There was a flat bed with no scour patterns between these two wings. The width of the wings was larger than that in Expt. BM11.

To observe the differences in the characteristics of the flow patterns and the scour around the artificial bodies and a natural obstacle, a natural rock weighting 2.987 kg was used in Expt. AM41 (Figures 4.18-26). The relative depth was 1.26 and the Froude number was 0.252. The rock was similar to an ellipsoid and its larger diameter, 16 cm, was oriented along the flow direction. Its width was 14 cm and its height was 9.5 cm.

The scour propagation started at two points very close to the nose of the rock where the flow was ascending the steep curvature at the front and also at the back where the flow separated from the bluff body. These two separation points were very close for

125

the hemisphere. There were two vast scour holes downstream of the rock with a strong backward flow separating them. At the interface of the side scour holes and the backward flow there were two small hills of deposited sand which later joined each other at the back of the body making a large deposition (Figures 4.18-26). The deposited hill acted as a border between the scour hole and the wake, separating the forward flow from the backward flow. The length of the main scour hole was equal to the size of the recirculation zone before propagating downstream and then it increased to around 3D. The general scour pattern was similar to that in Expt. AM31. After the progress of the scour hole at the front of the body, it gradually depleted the underside of the rock. Then the nose of the rock collapsed into the scour hole, while the back side of the rock remained in a higher position, supported by the deposition at the back.

Due to the decrease of the width of the rock at its bottom, the HS vortex formed when the approach flow separated from the bed at the front of the body was much smaller and weaker than that for the largest sized rock. Therefore, the scour is smaller than that for the hemisphere. As well, due to the absence of the cylinder, there was no strong downflow in front of the body. Hence the scour hole was shallower compared to that in Expt. AM11. Therefore, scour is a function of the shape of the rock and it is greatly influenced by its bottom width and its curvature at the front and the back .

4.3.4 General results of the mobile bed experiments

In general, based on these flow visualizations some major differences could be observed among the different flow regimes of the hemisphere on top of the cylinder which are presented as follows:

1. The scour pattern in the higher relative depths of regimes 1 and 2, Expts. X1, AM11, at the middle propagated downstream but the side scours did not. In the lower relative depths of regimes 3 and 4, Expts. BM11, CM11, in the absence of the downwash, the side scours could propagate while the middle scour could not, creating a scour fan with two

126

wings . In Expt. X2, due to the presence of very fine sands on the bed, even the middle scour could proceed, creating a scour fan which featured scour holes and depositions everywhere.

2. The width of the scour pattern in the high relative depths of regimes 1 and 2 was almost constant while it expanded to the sides further downstream in the lower regimes of 3 and 4.

3. The height of the deposition behind the body in Expt. X2 was more than that in Expt. X1 and the depth of the main scour hole was less.

4. The scour patterns of regimes 1 and 2 were not symmetrical longitudinally and were inclined towards one side of the flume, whereas in regimes 3 and 4, it was very symmetrical. The reason might be the effect of stronger side flows in lower relative depths, which might have been caused by small disturbances of the bed.

5. The scour wings were wider with deeper scour in regime 4, Expt. CM11, than that of regime 3, Expt. BM11, which might have been caused by the total absence of the downwash in the regime and its higher Froude number. The regime 4 scour wings were also expanded more than those of tregime 3 where they touched the flume walls.

6. The profile of the main deposition downstream of the body was stepped and cut after a short distance downstream of the body for regimes of 3 and 4, with the exception of that in Expt. X2, where due to the presence of finer sands, the scour pattern was extended further downstream. But in the lower relative depths of regime 4, there was a longitudinal band of shallow scour at the axis of the deposition, probably due to the stronger backward flow there.

Other general important observations and the differences among the different types of obstacles are presented here, as follows:

1- On the profile of the bed downstream of the body there was a small scour before the general deposition in all regimes where at the surface in the same place there was a portion of boiling water (Figure 4.27). This was due to the presence of very

127

turbulent flow which prevented sediment from settling. Due to the very steep slope of the bed at the sides of the body, two outgoing flows touched the free surface and met each other immediately behind the body, which caused a very turbulent flow and even raised the water level locally.

2- The smaller obstacle used in Expt. AM21 caused a shorter scour pattern than that in Expt. AM11. This was due to the relatively coarser sediment compared with the size of the body, or due to weaker effect of the smaller body on the flow.

3- Using the cubic obstacle caused the difference of the two slopes of scour hole in front of the body to be pronounced, with a flat portion in between. The deposition of sediment at the sides could not join each other and left a flat space in between. This may have been caused by the shape of the body, which caused the two separated flows from the sides to move parallel and prevented them from leaning toward the center. The scour pattern was wider than those in Expts. AM11 and AM21 for the same reason. The width of the wing in Expt. BM31 was more than that in Expt. BM11.

4- The scour patterns were found to be strongly influenced by the shape and the characteristics of the body, including the streamlining and the location of the separation of the flow. In the scour patterns of a natural rock of ellipsoid shape, the strengths of the HS vortex and the separated flow were less, causing a smaller scour hole. This was due to the smaller width of the rock at its bottom and weaker down flow. There were two starting scours at the beginning, around the two separation points of flow at the front and the back. The development of the scour hole at the front of the body caused the nose of the rock to sink into the hole, whereas the back side of the rock kept its level.

5- The hemisphere on the cylinder acted similar to a rock which is deeply rooted in the bed with a height more than its width. Therefore, the scour at the front was similar to that for a bridge pier due to their similarity in the down flow effects. But at the

downstream of the body, the scour pattern was different from that for the bridge pier due to the downwash effect.

Figure 4.1: Trace of horse-shoe vortex and separation line on the bed
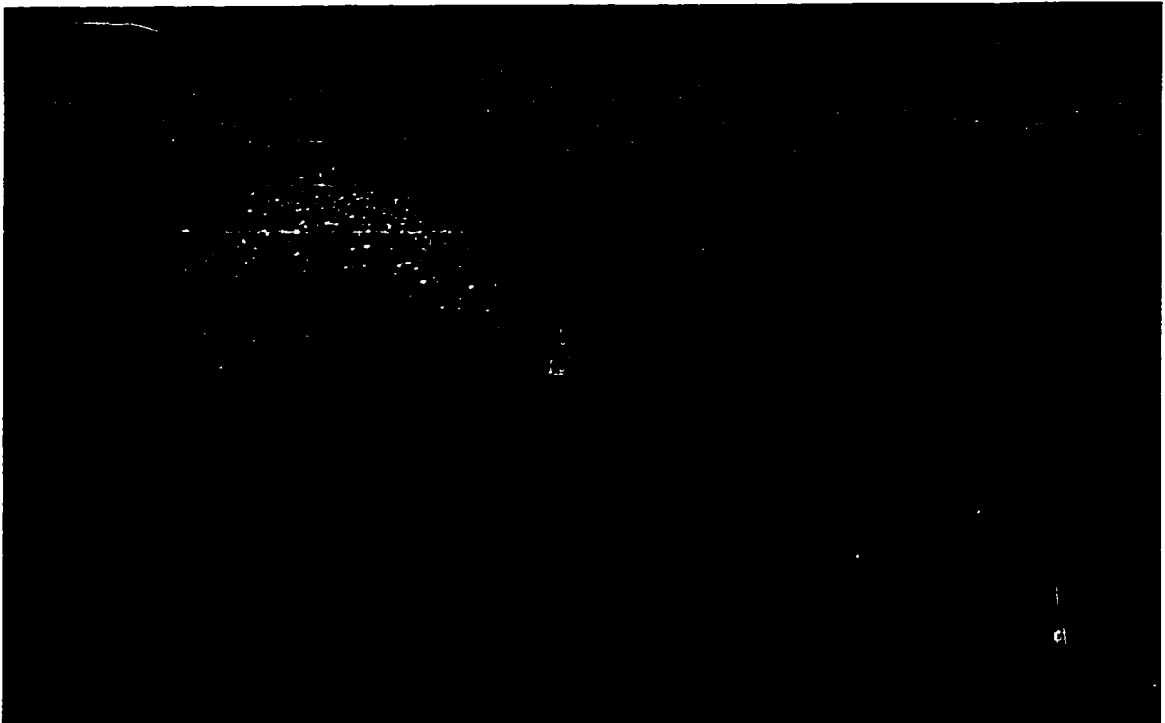
Figure 4.2: Sectional view of the spinning horse-shoe vortex in front of the body
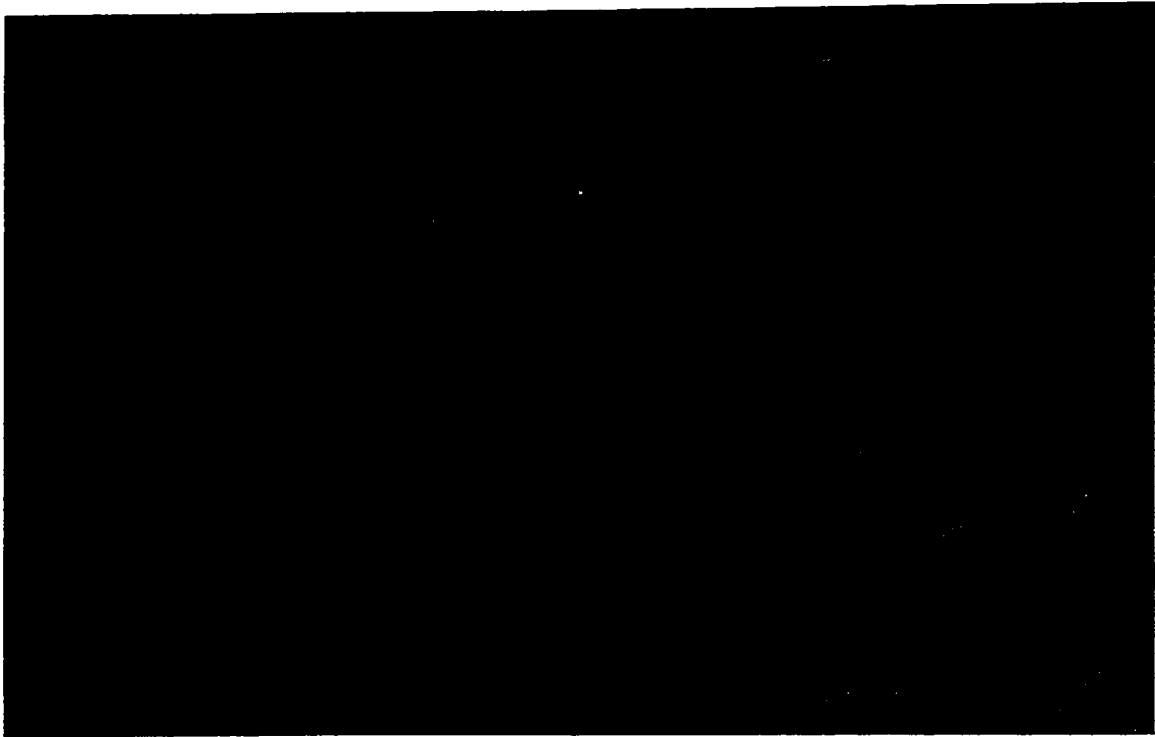
Figure 4.3: Picture of vortex shedding from the top of the body (arch-vortex)
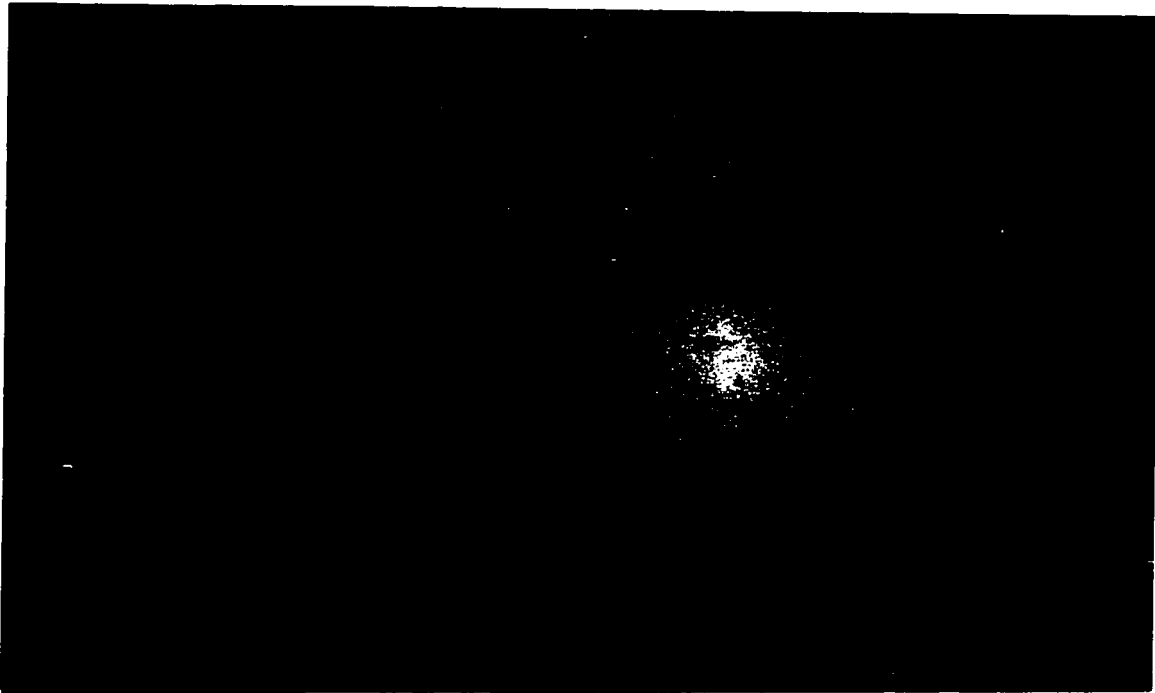
Figure 4.4: Picture of roots of arch-vortex behind the body

131
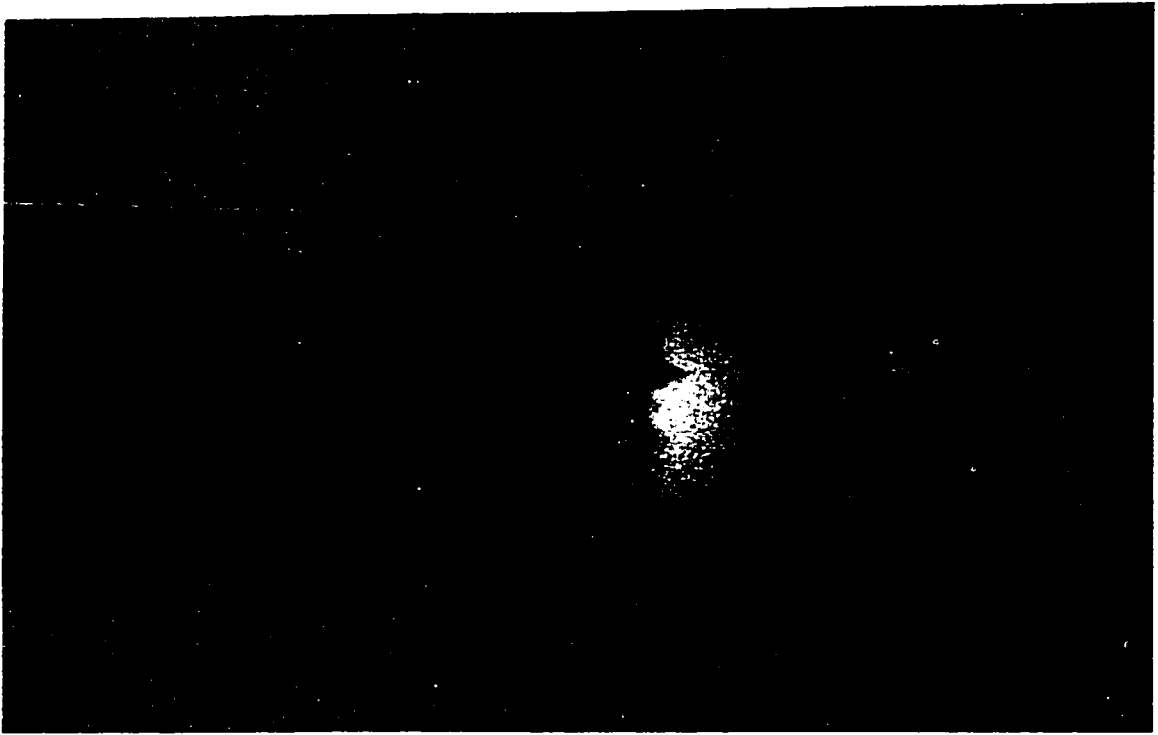
Figure 4.5: Plan view of the separation line on the body and its wake
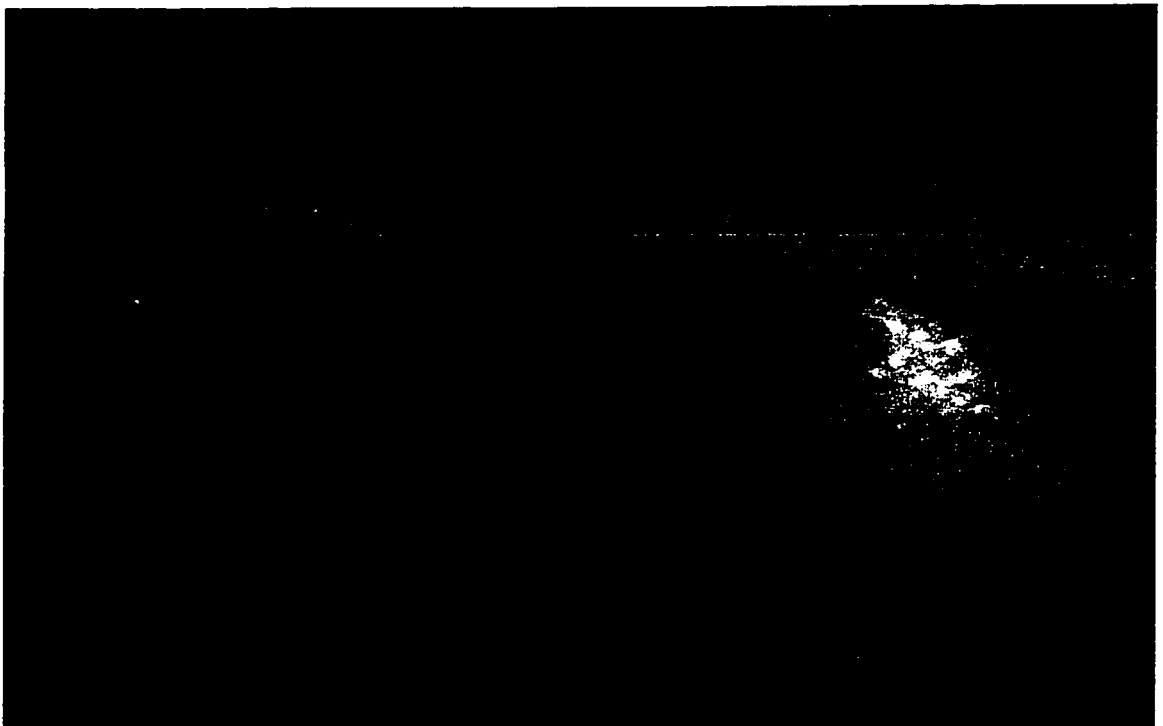
Figure 4.6: Sectional view of the separation line on the body and its wake
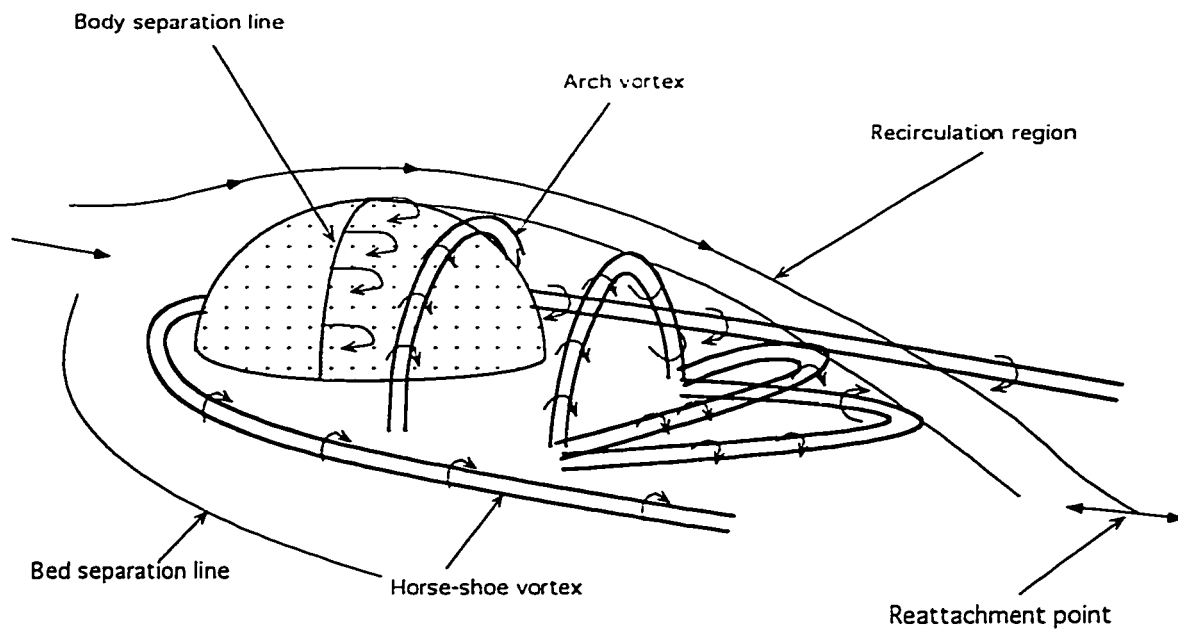
Figure 4.7. Vortex system around the obstacle for deeply submerged flow (Regimes 1&2)
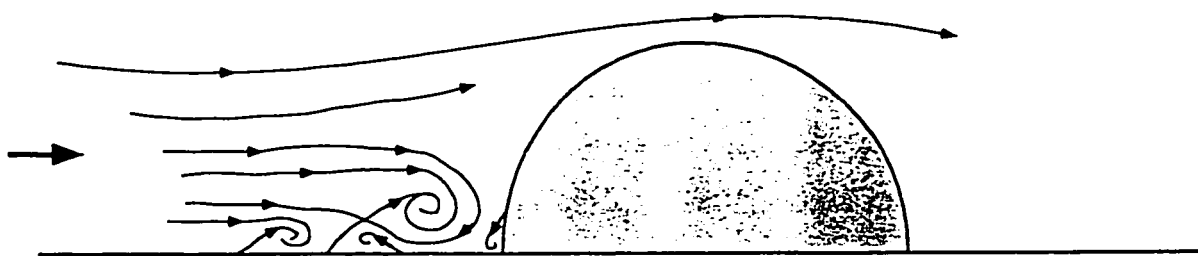
Figure 4.8 : Horse-shoe Vortices Around the Mounted Body

133

Water Surface
▽
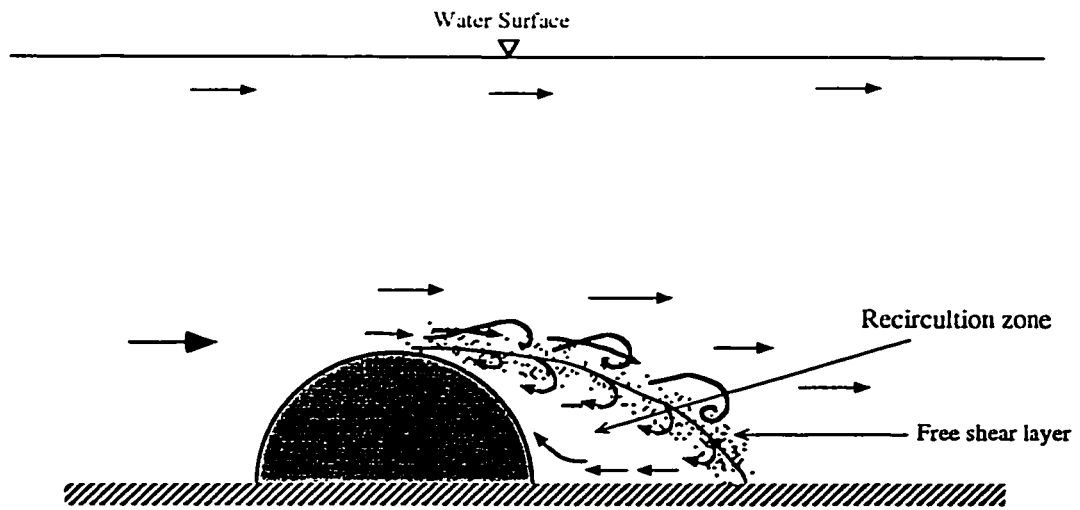
Figure 4.9 Sketch of the sectional view of the wake in regime 1 (Expt. DS1, DS2)

Recircultion zone

Free shear layer

surface waves

Recircultion zone

Free shear layer
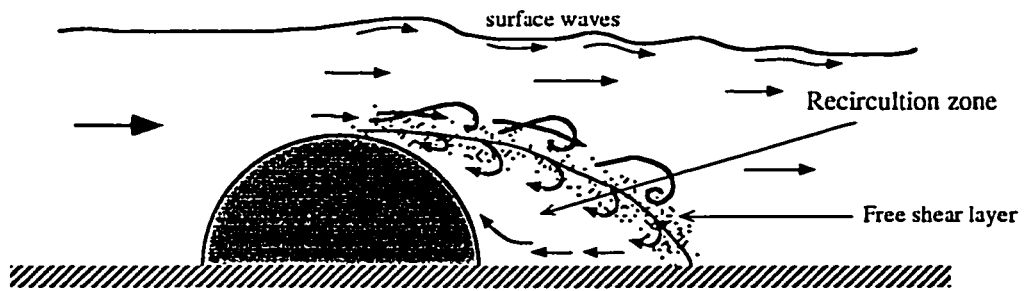
(a): Sectional view of Expt. A2 (F= 0.48, d/h=1.89)
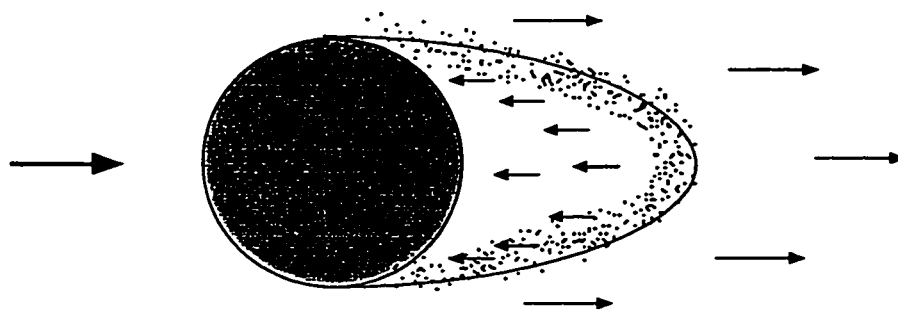
(b): Expt. A2 (Plan at the bed)

Figure 4.10 : Sketches of Expt. in regime 2 (a) POS of AS2, (b) AS2 Bed plan

134
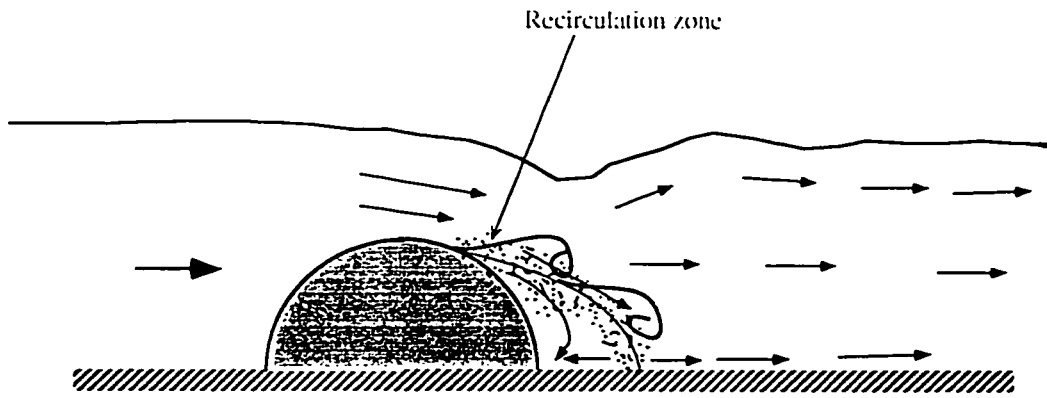
(c): Expt. W14 (F=0.537, d/h=1.76)
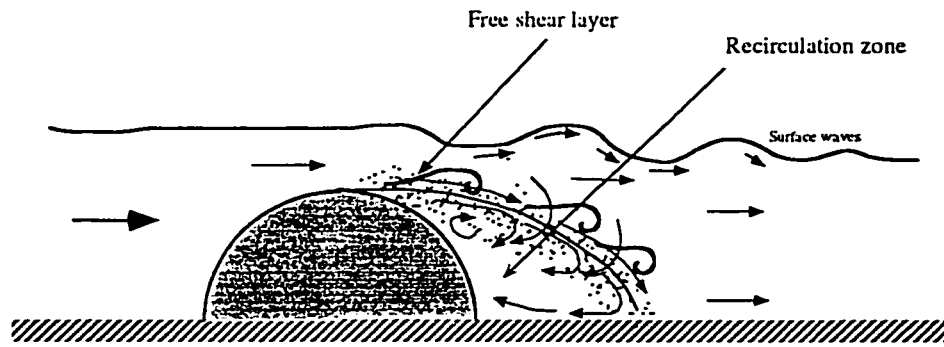
(d): Expt. W2 (F=0.405, d/h=1.49)
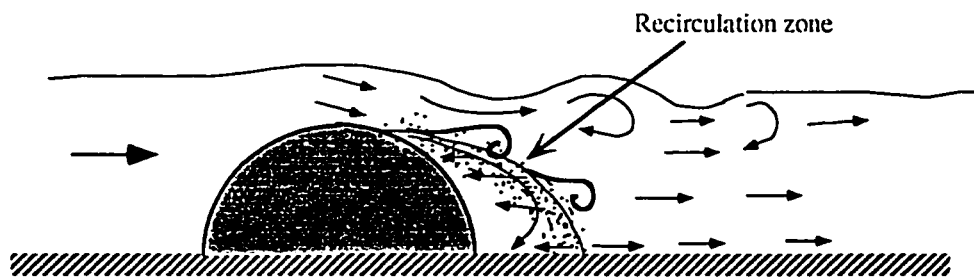
(e): Expt. W12 (F=0.52, d/h=1.46)

Figure 4.10 (c-e) : POS sketches of Expt. in Regime 2 (c):W14, (d): W2, (e):W12
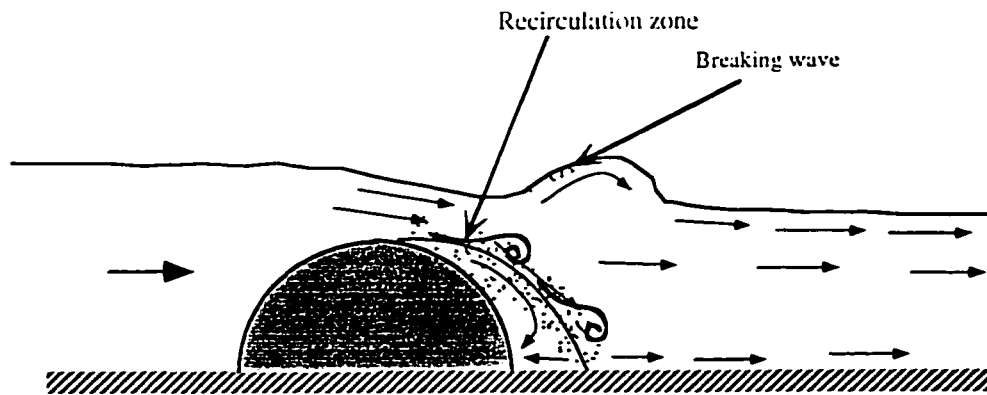
(f): Expt. W13 (F=0.562, d/h=1.57)

Figure 4.10 (f) : Sketches of Expt. W13 in Regime 2
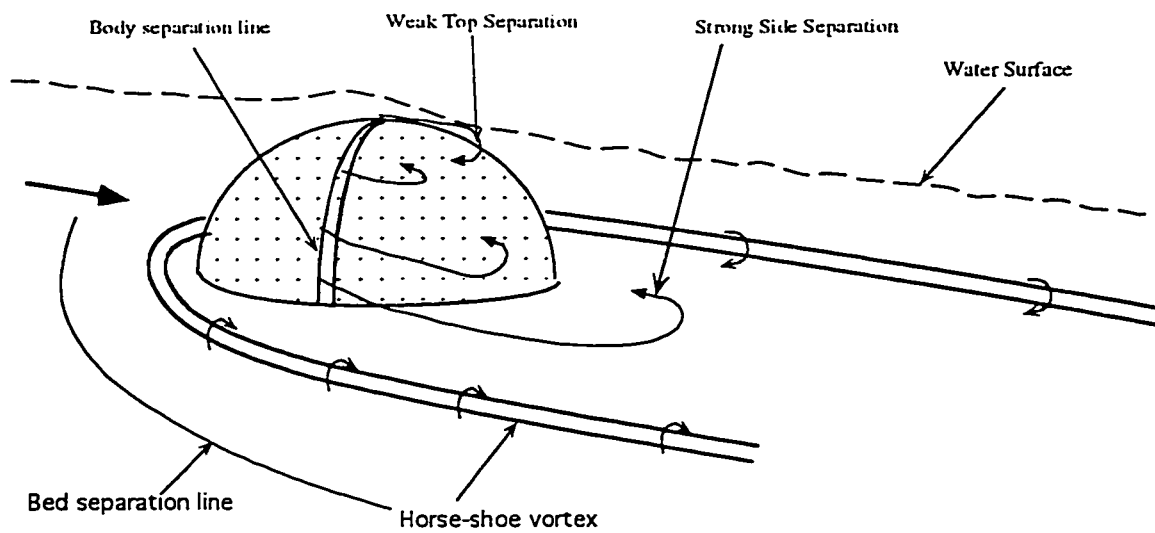
Figure 4.11 : Vortex system around the obstacle in Regime 3
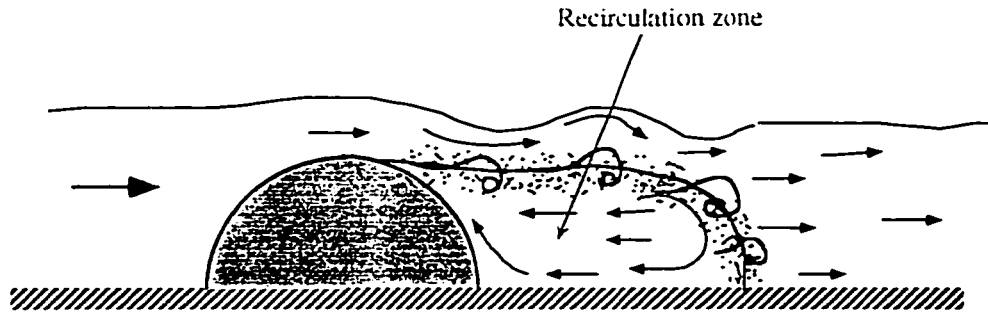
(a): Sectional view of Expt. W4 (F=0.362, d/h=1.32)
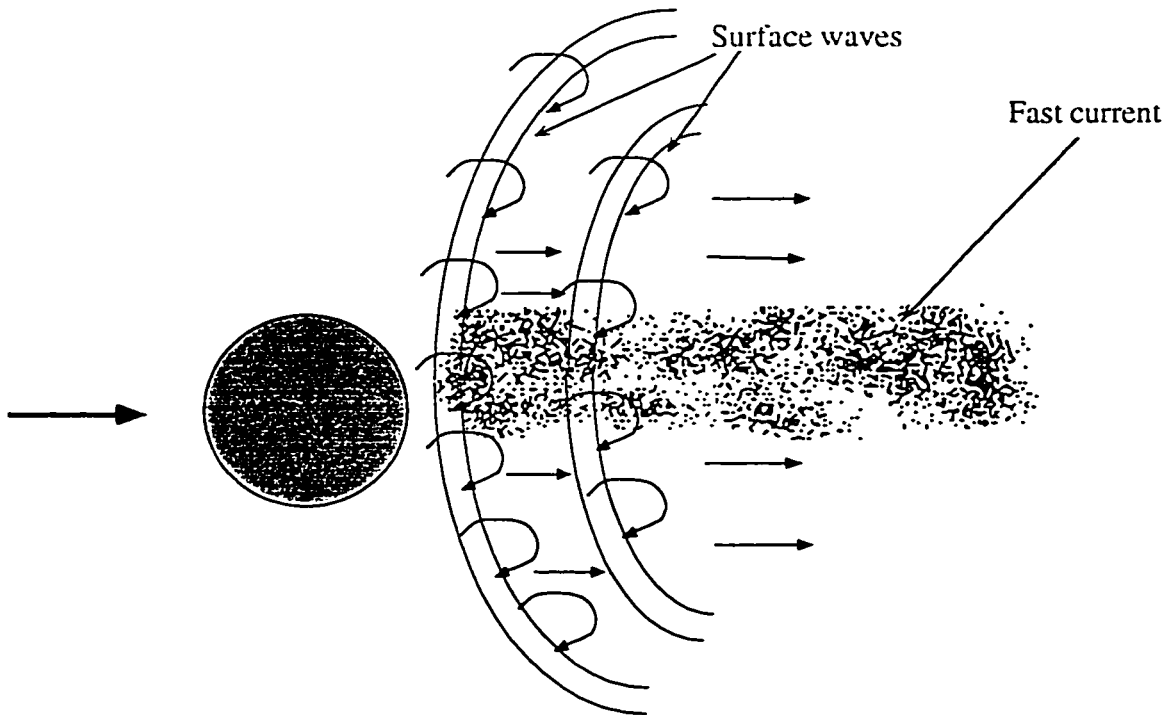
(b): Expt. W4 (surface plan)

Figure 4.12 (a,b) : Sketches of Expt. in Regime 3, (a): POS of W4, (b): Plan view of W4
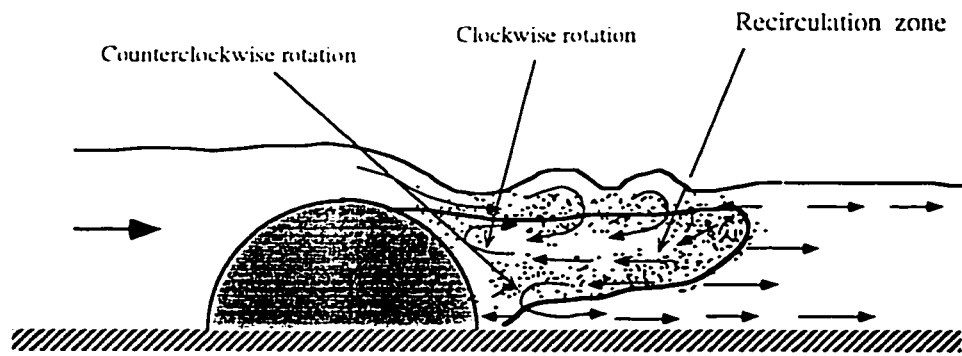
(c): Expt. W10 (F=0.447, d/h=1.3)
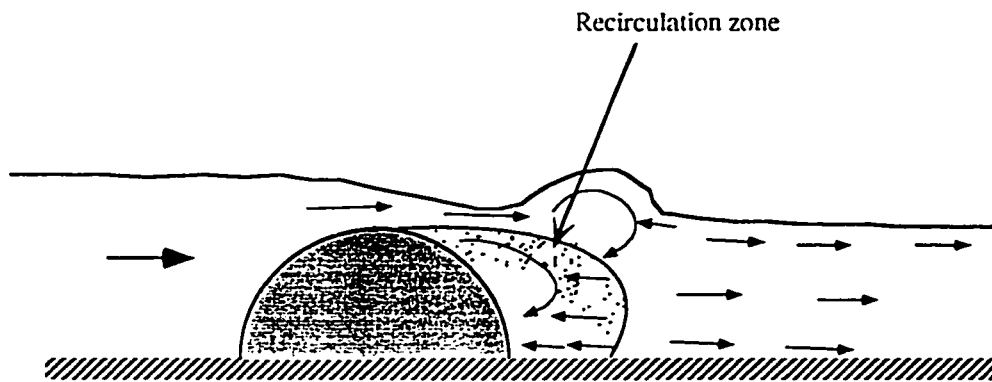
(d): Expt. W11 (F=0.481, d/h=1.32)
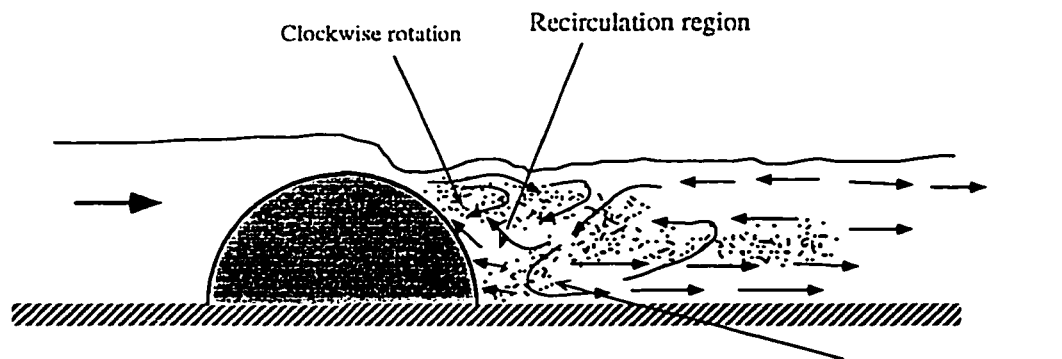
(e): Expt. W9 (F=0.425, d/h=1.19)

Figure 4.12 (c-e): Sketches of Expt. in Regime 3 (c) W10, (d) W11, (e) W9)

Recirculation zone

Free shear layer
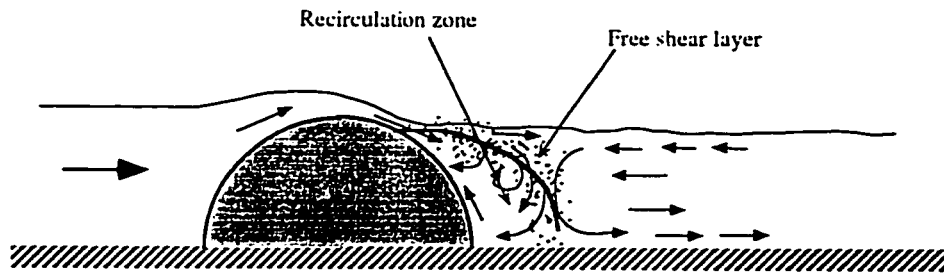
(f): Expt. W5 (F=0.292, d/h=1.16)
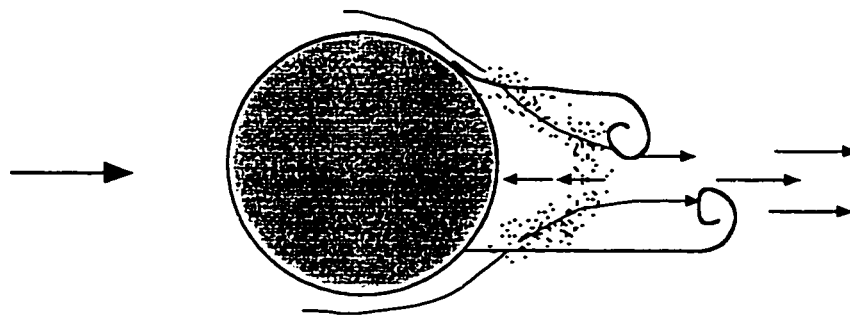
(g): Expt. W5 (bed plan)

Figure 4.12 (f, g): Sketches of Expt. in Regime 3, (f) POS W5, (g) W5 Bed plan
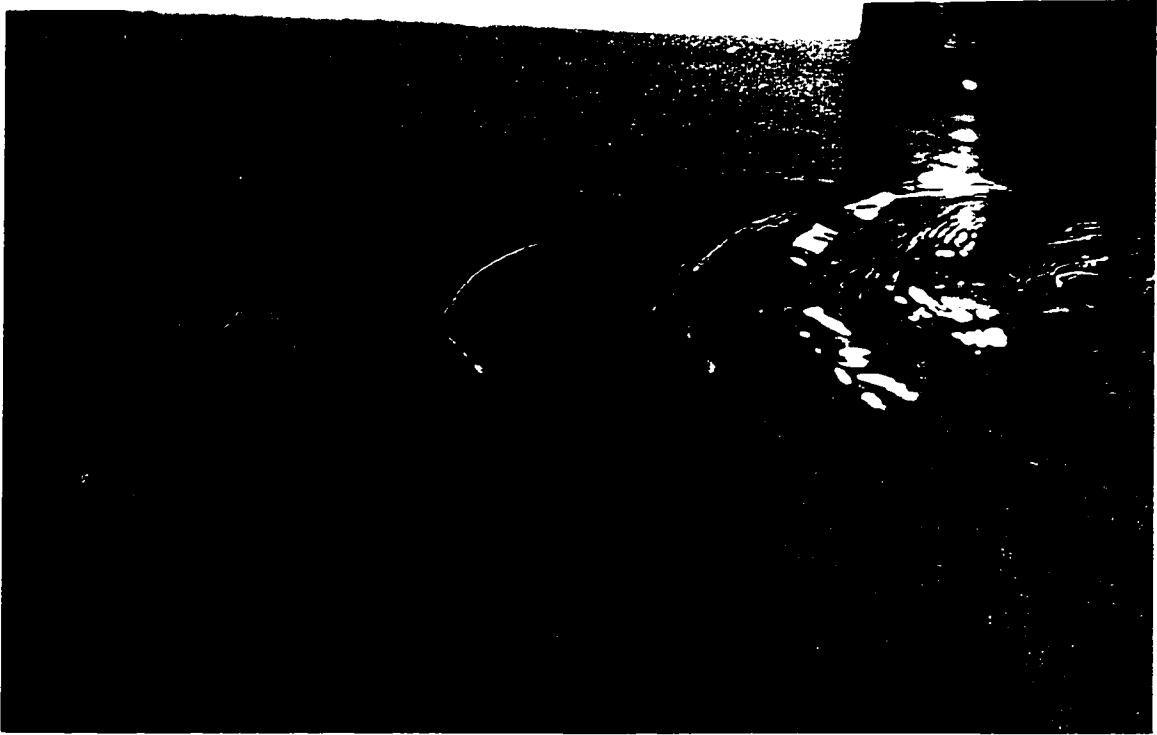
Figure 4.13: Picture of surface water waves downstream of the body in regime 2
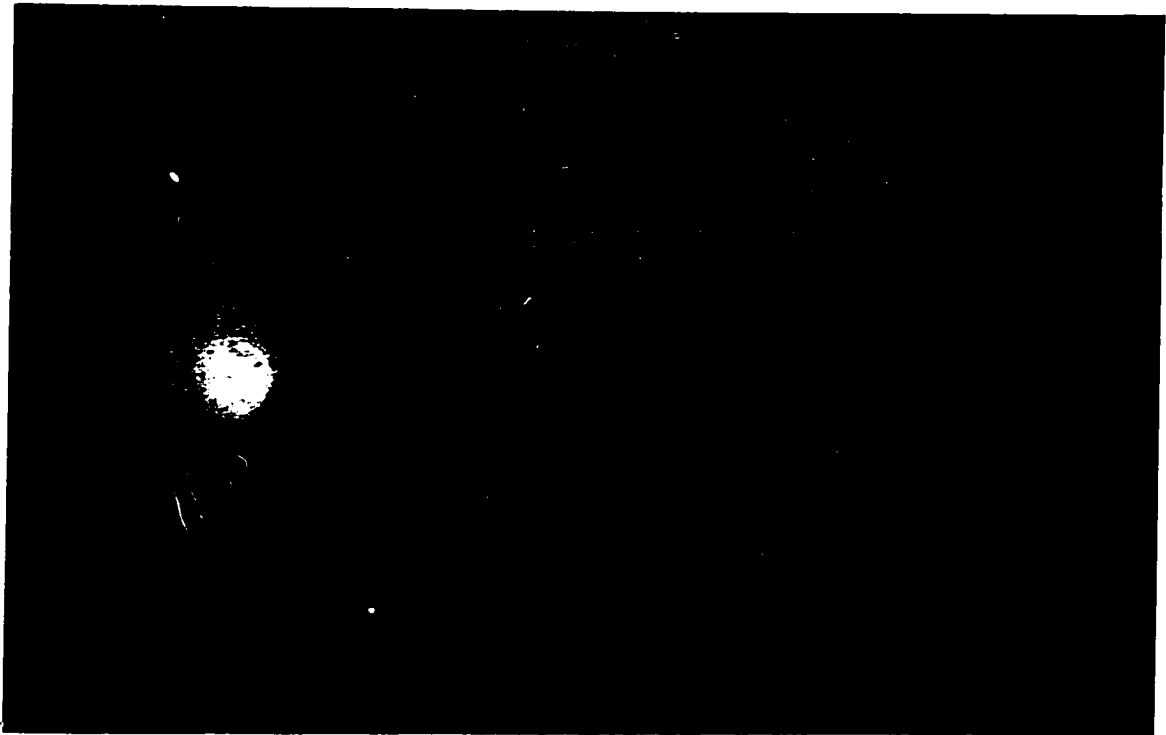
Figure 4.14: Picture of Karman vortices downstream of the body in regime 4
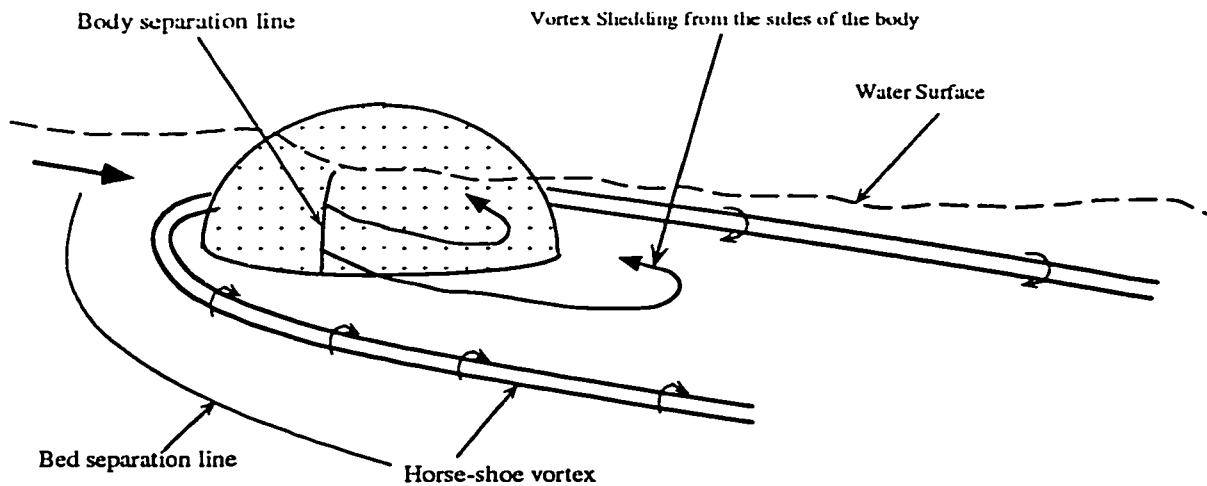
Figure 4.15 : Vortex system around the obstacle in Regime 4
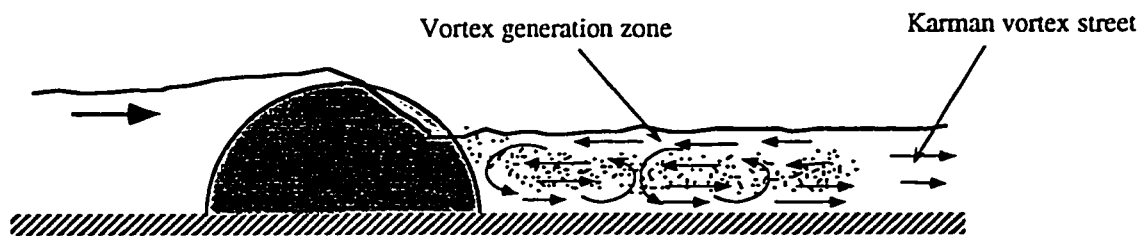
(a): POS of Expt. W8 (F=0.384, d/h=0.97)
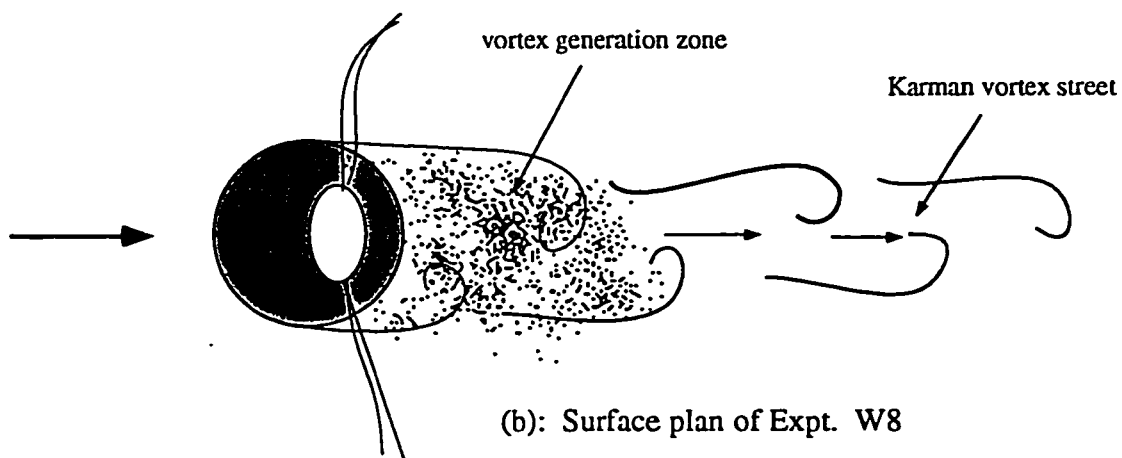
(b): Surface plan of Expt. W8

Figure 4.16 (a,b): Sketches of Expt.W8 in Regime 4: (a) POS , (b) surface plan
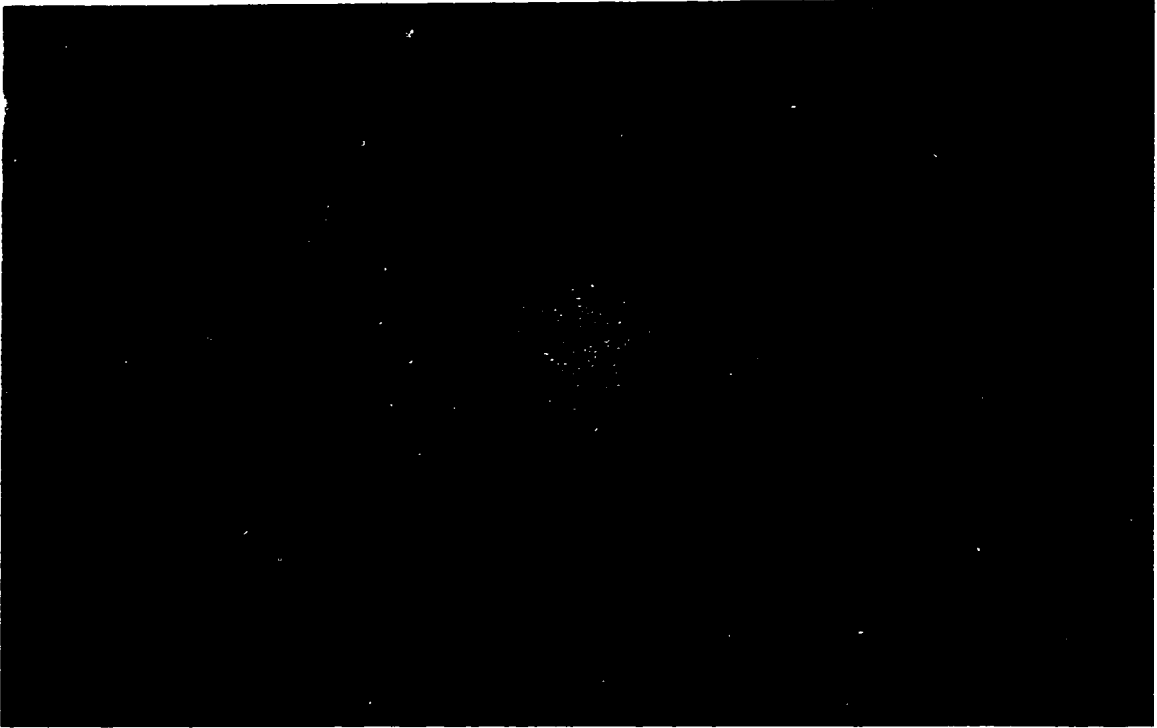
Figure 4.17: Initial stage of the scour around the body
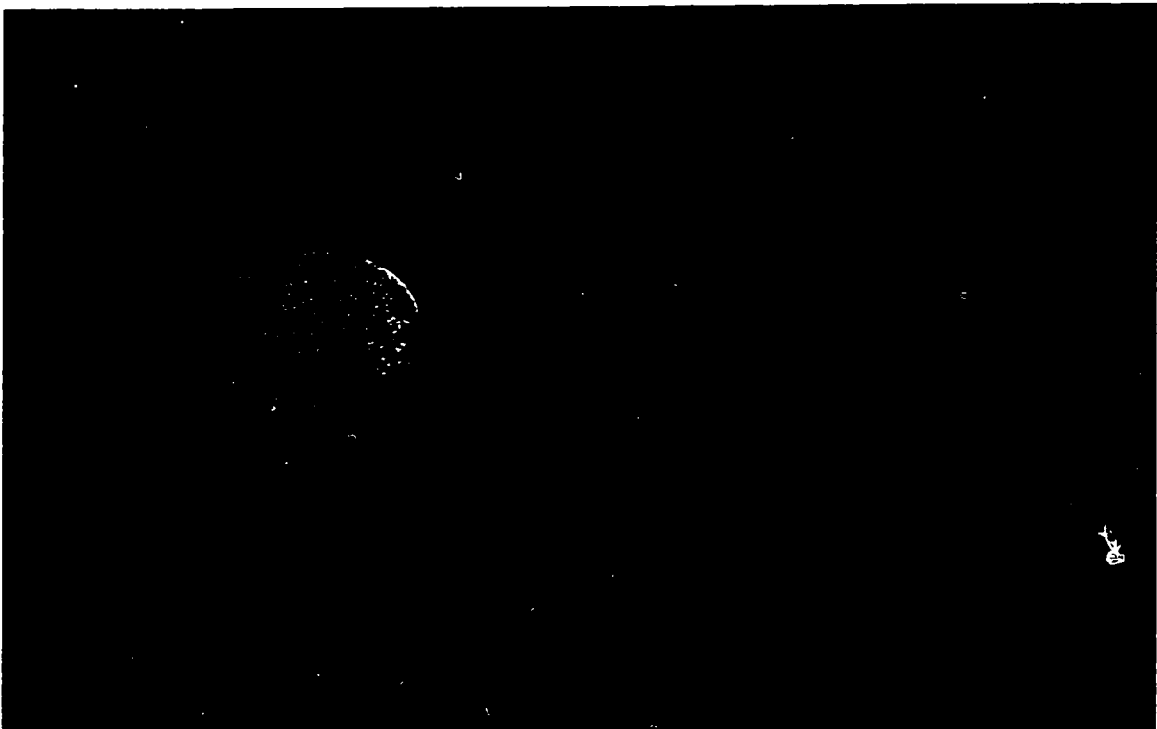
Figure 4.18: Scour pattern of a natural rock in regime 2
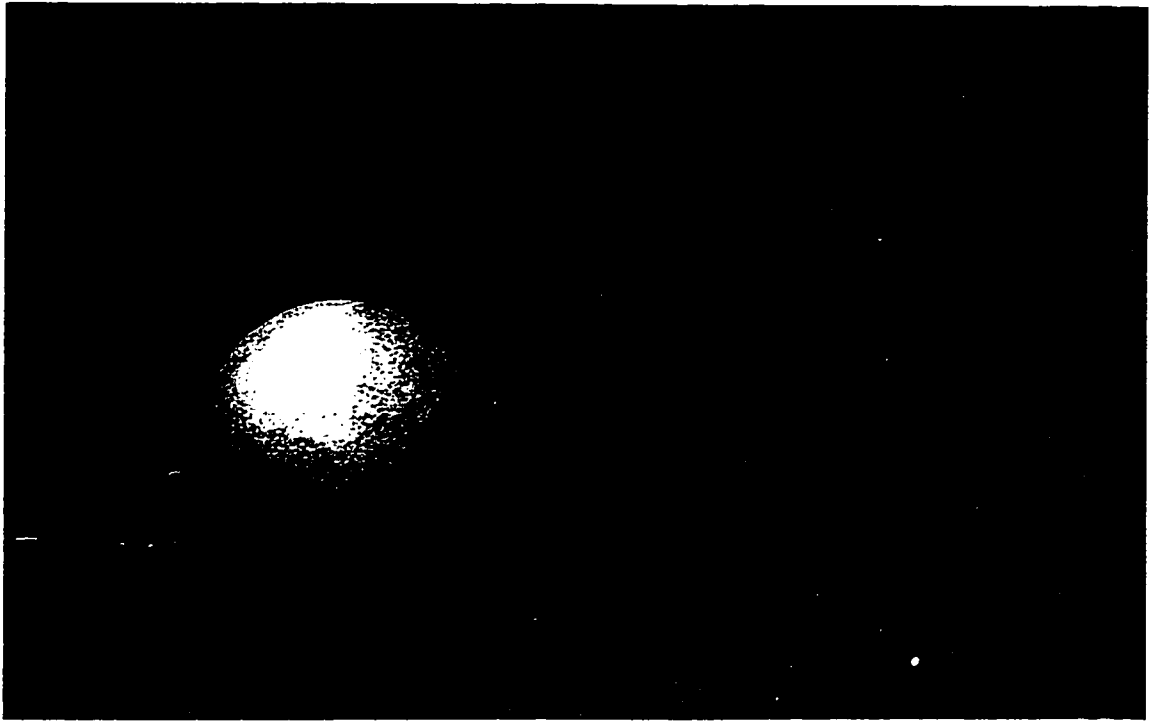
Figure 4.19: Scour pattern around the hemisphere in regime 2
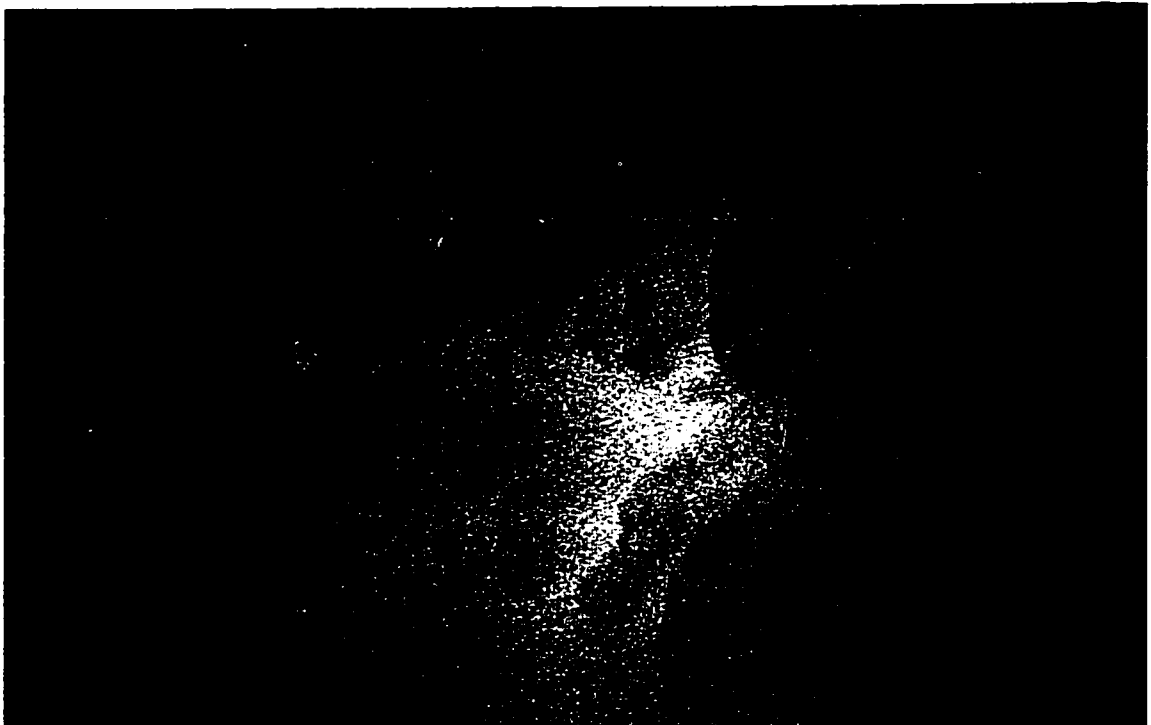
Figure 4.20: Scour pattern around the hemisphere in regime 3

143
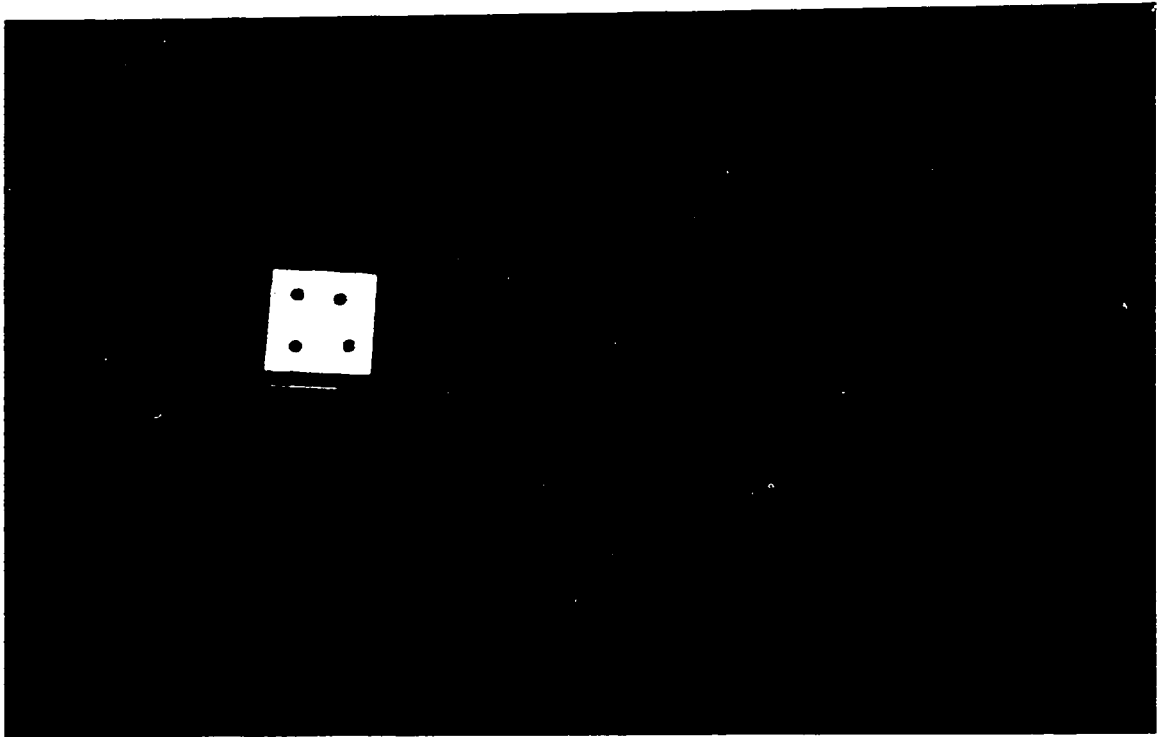
Figure 4.21: Scour pattern around the cube in regime 2
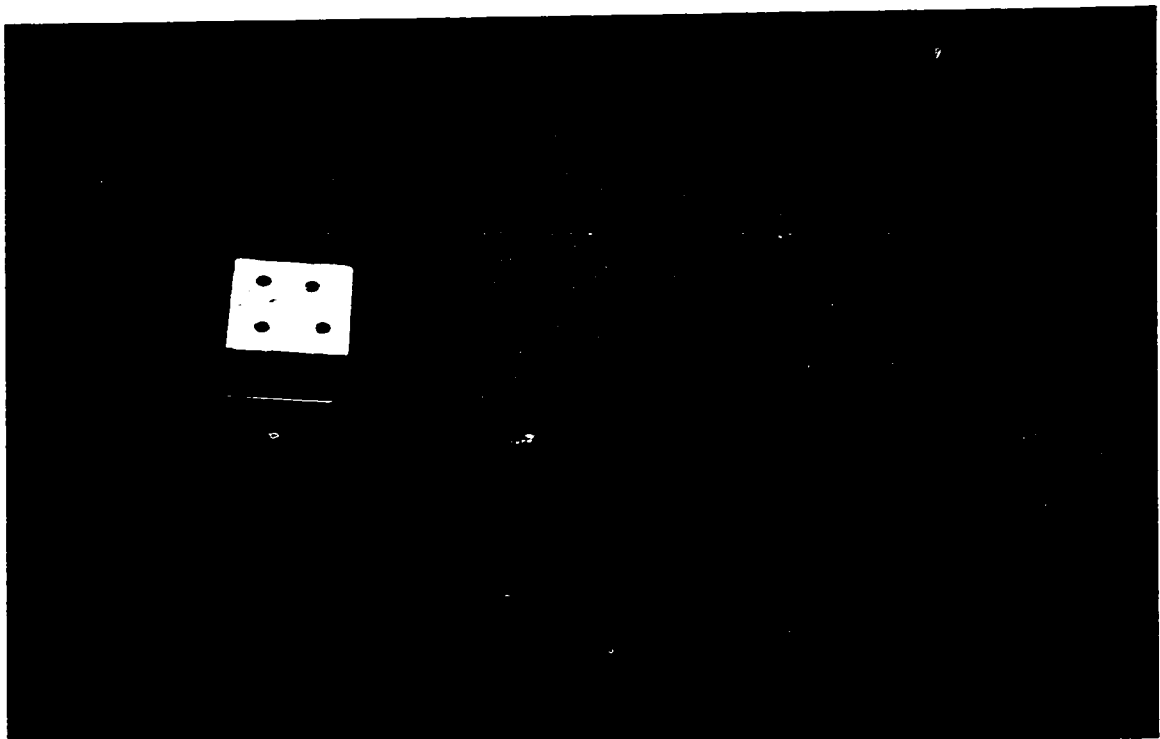
Figure 4.22: Scour pattern around the cube in regime 3

(a) Plan view

x-x Section

(b) Plan view

x-x Section

inner HS-vortex

outer HS-vortex

(c) Plan view

x-x Section

The inner HS-vortex

The outer scour hole

The outer HS-vortex

The inner scour hole

(d) Plan view

scour

deposition

bed material
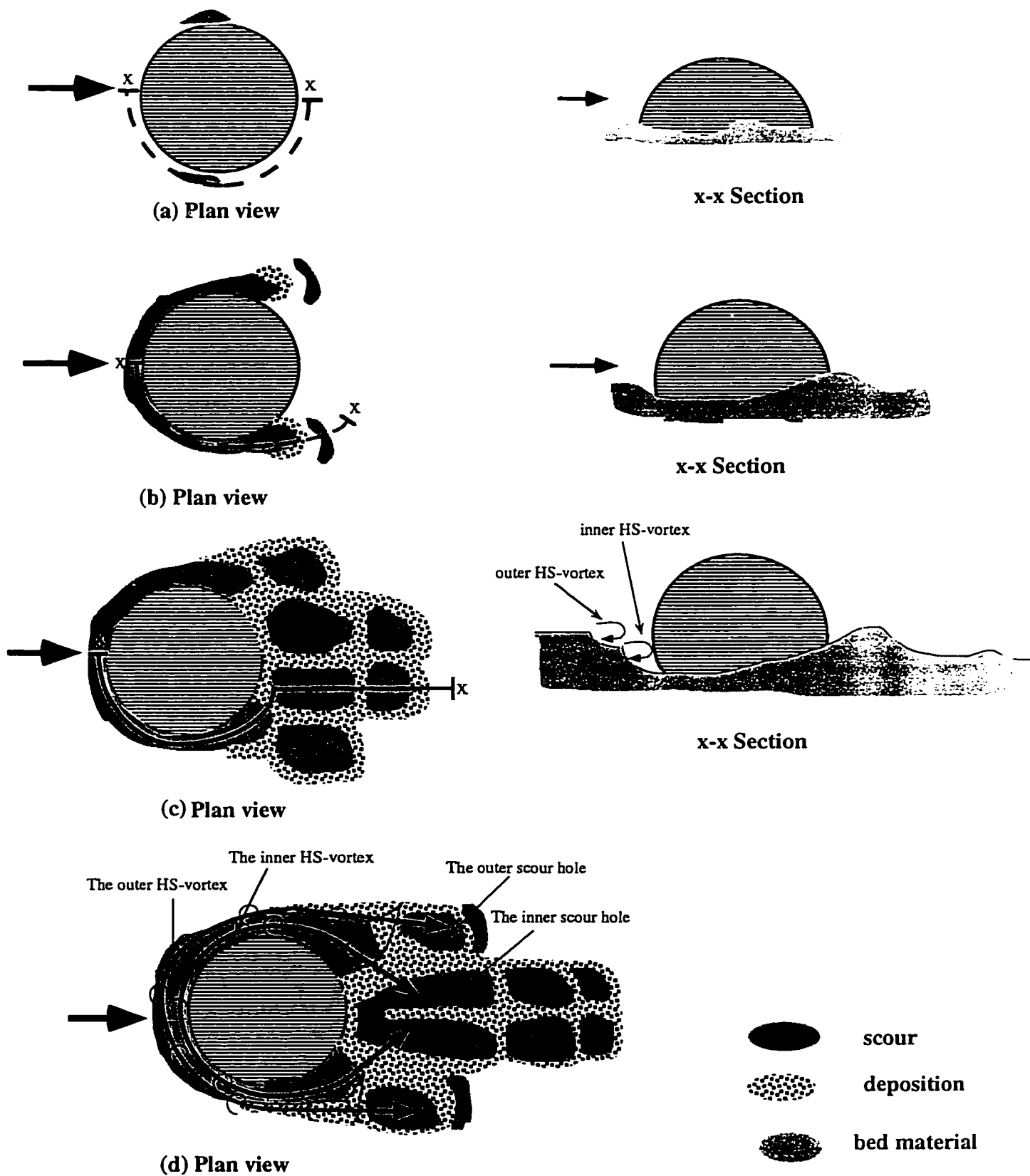
Figure 4.23 : Sketch of the process of scour and deposition in Regime 2 (Expt. X1)

145
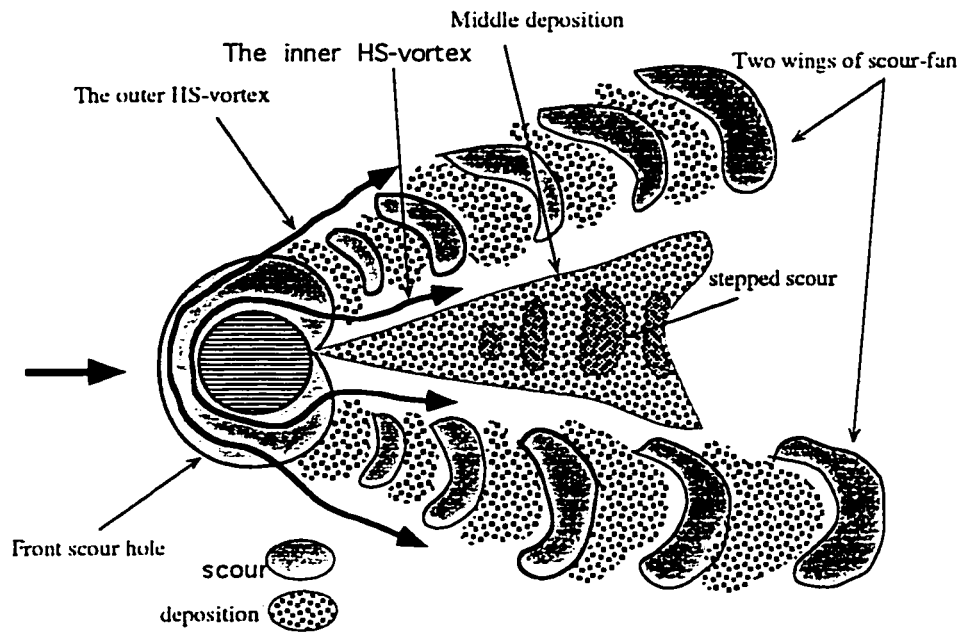
Figure 4.24: Sketch of the scour pattern in Regime 3 (Expt. BM11)
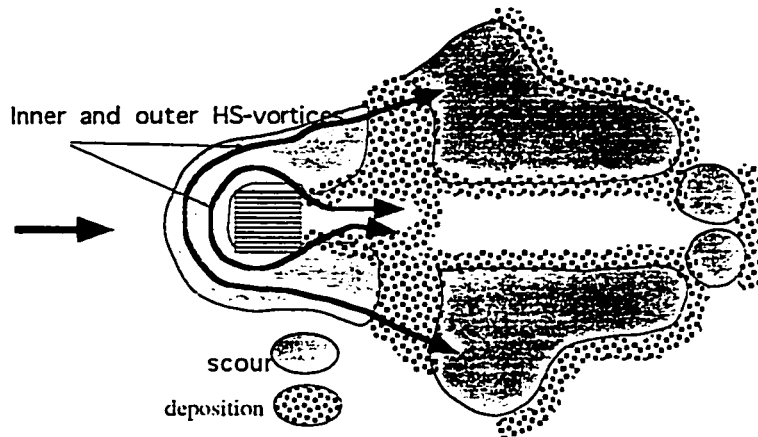
Figure 4.25: Sketch of the scour pattern of a cube in Regime 2 (Expt. AM31)
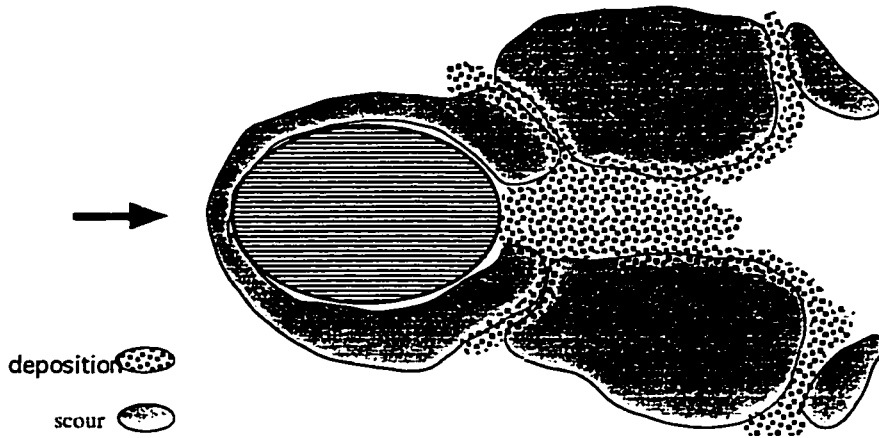
Figure 4.26 : Sketch of the scour pattern of a rock in Regime 2 (Expt. AM41)
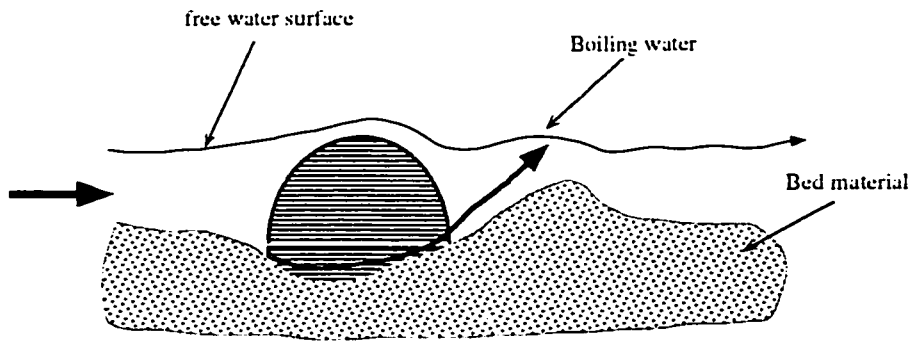
Figure 4.27: Sketch of a boiling portion at the water surface (Expt. BM11)

CHAPTER 5

EXPERIMENTAL RESULTS FOR SMOOTH BED

5.1 Introduction

Flow visualization revealed the most important features of the flow around the body qualitatively. Based on these guidelines, some measurements were carried out to investigate the effects of the bed mounted obstacle on the flow field. The natural obstacles on the mobile bed develop scour and deposition patterns. Due to the lack of published data, even for simplified form of natural rocks, a series of experiments was conducted on smooth beds to investigate the characteristics of the flow in the absence of sediments on the bed. Velocity field and bed shear stress were measured extensively for several flow conditions and the results are presented in this chapter. The result of the experiments on the mobile bed are presented in chapter 6.

In agreement with the coordinate system presented in chapter 3, Figures 3.1 and 3.2, a rectangular Cartesian coordinate system is used in chapter 5 and 6. Velocity components in the (x, y, z) directions are denoted by (u, v, w) respectively and are shown in Figure 5.1 (a). The angles of pitch ϕ and yaw θ for the velocity vector are shown in Figure 5.1 (b) and (c) respectively.

5.2. Water Surface Profiles

The effects of the relative depth and Froude number on the water surface were investigated in different regimes. The water surface was measured by point gauge from -3D upstream of body to +5 D downstream on plane of symmetry where D is the diameter of the hemisphere mounted on the bed. Water surface profiles are sketched for regimes 1 to 4 (DS, AS, BS and CS) and their measured values are presented in the Figures 5.2 and 5.3 respectively. The depth of the flow and the horizontal distance from

the body are non-dimensionalized by the height of the body and the diameter of the hemisphere respectively. The surface profiles for the small hemisphere are shown in Figure 5.3 for regimes 1 and 2.

The surface profiles of two deeply submerged bodies in experiments DS1 and DS2 with relative depths of 4.12 and 4.26, do not indicate any effect of the body. The rest of the experiments had a wavy surface due to the presence of the obstacle. In general, there was a rise in the water surface level upstream of the body and then a drop of surface level close to the center of the obstacle. There was a series of water surface fluctuations across the width of the flume downstream of the body similar to standing waves which at their sides became distorted downward as they were carried further downstream. The rise of the water surface profile downstream of the obstacle in Figure 5.3 represents the crest of these standing waves. The number, height and the wave length of these waves appeared to depend on the relative depth of the flow and its Froude number and this aspect was discussed in chapter 4. For example, the effect of the F can be seen for two experiments of AS1 and AS2 with similar relative depths but different values of F. The height of the waves is more in AS2 (with F of 0.48) than that of the Expt. AS1 (with F of 0.34).

5.3   Velocity Measurements

5.3.1 Velocity profiles on the plane of symmetry

Velocity Profiles in the plane of symmetry were measured by pitch probe to investigate the variation of the magnitude of the velocity, and its direction upstream of the obstacle and in its wake. Several velocity profiles were measured at different stations upstream and downstream of the hemisphere. The time averaged longitudinal component of the velocity vectors u can be observed in Figure 5.4 a-f, pitch angle profiles ϕ in Figures 5.6 (a-f), vertical velocity profiles v in Figures 5.7 (a-f), and standard deviation of the pitch angles ϕ' and velocity in Figures 5.8 (a-f) and 5.9 (a-f) respectively.

149

The effect of the obstacle on the velocity profiles is clearly presented in Figures 5.4 (a-f), where, on the upstream side of the body, the velocity profiles are retarded approaching towards the body. The slowing down of the velocity is not present in the upper level of the profiles of regime 1, Expts. DS1 and DS2, where y/h> 1.5. For values of y/h< 1.5, the effect of the body is visible (x/D= -1). The negligible change of the velocity profiles further upstream is mostly due to the small effect of the body on total flow field in deeply submerged flow, and less importantly, due to the low velocity of the flow in Expt. DS1(Uo=0.208 m/s). The higher velocity of Uo=0.338 m/s in Expt. DS2 does not change the slowing down process of upstream profiles significantly, but it creates a fully developed type of flow. The upper part of the velocity profile in Expt. DS1 acts similar to the potential flow, i.e., the boundary layer is not developed enough to reach the water surface. A small dip can be seen in the profile of Expt. DS1.

The pronounced slowing down of the velocity can be seen for the relative distances of x/D=-3 to -0.77 in Figure 5.4 (c). Here the upper part of the profiles are deflected too, indicating gradual decrease of the velocity. But the possible free movement of the flow above the hemisphere causes this portion to move faster and with less deflection compared with the lower portion. The retardation of velocity becomes more significant in regimes 3 and 4 with smaller relative depth, Expts. BS1 and CS1. In these two experiments, the absence of the top layer of the flow causes more divergence of the approaching flow. The difference between far upstream profiles at x/D=-7.69 and closer ones at x/D=-3 is in the order of 0.03 m/s, but the difference for x/D= -1 is on the average 0.2 m/s. In general, the presence of the body is sensed by the flow, even in far upstream profiles. It only becomes considerable just close to the body where x/D is of the order of -1.

In most of the upstream profiles the magnitude of the velocity is decreased in all points of the profile, showing an overall velocity reduction. It indicates that discharge passing on the plane of symmetry decreases approaching towards the body. The deflected

flow on the POS has to go to the sides to compensate this velocity reduction at POS resulting in an increase of discharge in those sections. This fact can be observed more clearly by calculation of the longitudinal profile of the flux of discharge in POS (Figure 5.5). This was accomplished by assuming zero velocity at the bed level and also assuming that the surface velocity is equal to its immediate lower measurable point in the profile. The velocity between two measured points was assumed to vary linearly. As it can be seen from this figure, the flux of the discharge decreases continuously approaching the body and then increases downstream, but it doesn't reach to its upstream level even at x/D=10 (Expt. AS1), indicating the presence of a lower velocity inside the wake region. This Figure clearly shows the diversion of the discharge approaching the obstacle and its incomplete convergence in the near wake region.

Downstream of the body, profiles of the velocity show more deviation from the original undisturbed flow. In Figure 5.4 (a), Expt. DS1, the layer of flow passing over the top of the body shows a jet-like decay, which is more significant in Expt. AS1 (profiles of x/D= 0 to 1.69 in Figure 5.4 c). By missing the top layer in Expts. BS1 and CS1 this process can not be seen in Figures (e) and (f). Due to the presence of a high level of turbulence in free shear layer covering the recirculation zone in series D, A and B, the pitch probe (which was calibrated for a range of ±60 degree) could not even measure the velocity well before entering the actual recirculation zone. As a result, the profiles could not show the turning point of zero velocity or back flow velocity. Inside the recirculation region, a limited number of samples and backward velocity could be measured, but some out of range readings made calculation of an acceptable velocity average difficult. Further, the flow is strongly 3-D and any measurements with a pitch probe would be questionable.

Moving further downstream and away from the recirculation zone, the velocity profiles start to develop. The downstream profiles (Expts. DS1 and DS2 in Figure 5.4 a and b) show a developing flow where the velocity increases consistently in longitudinal

direction. At x/D=2, immediately downstream of the recirculation region, the velocity profile has two curvatures: the first one shows decrease of velocity moving from the surface towards the bed and at about 0.6 h it reaches its minimum and then starts to increase which diminishes again at the bed, i.e., as the second one. This trend in change of the velocity profile is very similar to that of the wall wake profile. The evolution of the velocity profiles in the wall-wake can be seen clearly in profiles of x/D=2 to 5, Expts. AS1 and AS2, Figure 5.4 (c) and (d). Further downstream, profiles of x/D=10, 15, 20 and away from the effect of wall wake, start to develop and get their original form far upstream. The developing process of Expt. BS1 and CS1 can be seen in Figures (e) and (f) for profiles of x/D=4 to 10 and x/D= 2 to 8 where the wall wake is absent. The profile of x/D=1 in Expt. CS1 shows almost constant velocity through the whole depth, indicating a high level of turbulence capable of mixing the flow thoroughly.

The variation of pitch angles are presented in Figure 5.6 (a-f). The far upstream profiles of the pitch angles, Expts. DS1 and DS2 in Figure (a-b), show a very flat velocity vector with an angle of pitch close to zero (x/D=-10 to -2). The zero angle at the bed and a minimum negative angle around 0.15h is a typical profile close to the bed where there is a clockwise vorticity in the boundary layer. Approaching towards the body in the profile of x/D=-1, Expt. DS1 in Figure (a), the lower part of the profile shows a dive down of the velocity vectors, with no positive or upward flow. In the same profile in the higher velocity, Figure (b) Expt. DS2, there is a dive down in less than half of the height of the body and then up to the height of y/h=3 there is an upward flow with its maximum at around y/h=1.

The same phenomenon can be seen in regime 2, profile of x/D=-0.77 Expt. AS1 Figure (c). This profile in AS2 was not measured. In Expt. AS1, the pitch angle changes its gradient at two points. The first one occurs around 0.6 to 0.7h and the second one occurs very close to the bed (like far upstream ones). The negative angles indicate downward velocity toward the bed in the lower region of more retarded profiles of x/D=-

1 and -0.77. The negative angle of the velocity vector decreases moving from the bed towards the surface up to y/h=0.6 and then changes to positive. This indicates the change in direction of the flow towards the surface from the middle depth (trying to find its way above the body). Therefore, flow in the vicinity of the body in regime 2 is divided in two parts, the lower part dives down and moves to the sides of the flow and partly creates the HS vortex and the second part flows over the top of the body, i.e., positive angle. In regimes 3 and 4, Expts. BS1 and BS2 in Figures 5.6 (e, f), there is no change of the velocity direction up to the x/D=-1. Then at this stage, the dive down of the flow increases dramatically, almost twice as much as before, due to the effect of the body with no sign of upward flow which is reasonable.

A jet-like flow passing over the top of the body is observable in Expt. DS1 Figure 5.6 (a), with a positive pitch angle. In the same profile in regime 2, Expt. AS1 Figure 5.6 (c), the top flow divides in two parts, the upper layer dives down and the lower layer flows upward with positive sign due to the curvature of the hemisphere. Further downstream and above the recirculation zone, significant dive down of the velocity flow can be seen in x/D=0.5 of Figure (a) and in x/D=1 and 1.5 of Figure 5.6 (c).

This significant deflection of the velocity vectors toward the bed immediately downstream of the hemisphere and their decrease in profiles further downstream suggests that there is a reattachment point inbetween. It shows that the flow, after passing the top of the body, dives down while covering the recirculation zone and then is deflected by the bed. The maximum vertical velocity occurs at about y/h=1 where flow enters the free shear layer. Downward angles of up to 30 degrees can be seen in this part of the flow, profile of x/D=0.5 Figure (a). The deflected flow by the bed can be traced in Figure (b) and (c) for profile of x/D=2. Further downstream and away from the recirculation zone, comparing the profiles of x/D=2 to 20 in Figure (a) to (f), the downward flow starts to return to its original neutral horizontal direction.

The profiles of vertical velocity, v, are presented in Figures 5.7 (a-f). The shape and trend of these profiles are similar with that of the pitch angle profiles in Figures 5.6 (a-f). The value of the vertical velocity is normalized with average sectional velocity of the flow, Uo, which shows values as high as -0.3 at x/D=0.5 and 1 where the flow is diving down from the top of the body and there are lower values of -0.1 to -0.15 after the reattachment point, regime 1 and 2 (Figures 5.6, a-d). The value of v/Uo is almost constant downstream of the recirculation region demonstrating existence of a considerable mixing process. The maximum v/Uo reaches to -0.08 for regime 3 and -0.14 for regime 4 in Figures (e) and (f) respectively.

The standard deviations of pitch angle ϕ' are presented in Figure 5.8 (a-f). These profiles show that the fluctuation of the pitch angle in the flow is negligible upstream of the body. But downstream of the body ϕ' is high, about 18 degrees in Figure (c) for measurable points, entering the free shear layer. Further downstream, moving from the surface towards the bed, ϕ' increases up to a certain depth, y/h=0.5, and then it decreases approaching the bed, Figures (a-d). Then the profile of ϕ' becomes flatter far away from the obstacle. In regimes 3 and 4 the profiles of ϕ' can be divided in two parts. In the first part, ϕ' gradually increases in the upstream profiles, Figures (e, f) for x/D of -7.69 to -1. In the second part downstream of the body, ϕ' decreases moving further downstream, profiles of x/D=1 to 10.

The profiles of standard deviation of the velocity vectors, u', are presented in Figures 5.9 (a-f). The value of u' is normalized with the average sectional velocity Uo. There is a general trend in profiles of u' in regimes 1 and 2, Figures a-d. They increase moving towards the bed, reaching their maximum on the bed for in upstream sections, which is in agreement with usual open-channel turbulence density profile. In downstream profiles before reaching the bed, there is a region of high u' after the recirculation zone at y/h=0.5 to 1, about u'/Uo=0.13 for Figure (a) and (c), and then u' decreases toward zero. This fact indicates that turbulence in the wake is higher than that of usual profile in open-

channel, where the maximum occurs at the bed. There is considerable scatter in Figures (c) and (d) while keeping the same trend. In regimes 3 and 4, Figures (e) and (f), the upstream profiles are acting similar to that of regimes 1 and 2. But in the downstream profiles of the Expt. BS1 the maximum u' occurs close to the surface and decreases downward. In Expt. CS1 the values of u' downstream of the body is almost constant, with some scatter. In both cases the values of u' gets smaller further downstream, getting away from effect of the body with a weaker wake. Due to the thickness of the pitch probe used in this experiment, measurements in depths closer than 0.4 cm to the bed were not possible.

The horizontal component of the velocity vectors are plotted against the universal law of the wall to investigate the effect of the body on the flow (Figures 5.10 a-f). The deviation of the velocity profiles from log law can be seen in regime 1, Figures (a) and (b), where a dip in velocity close to the water surface is clear in Expts. DS1 and DS2. The maximum deviation occurs immediately upstream and downstream of the body. Then the flow returns to its original form and collapses on to the log law, as shown by profiles of x/D=2 to 20 in Figure (b). This trend is more pronounced in regimes 2, 3 and 4 where far upstream profiles are closer to the log law indicating small effect of the body. Approaching towards the body, they deviate from the log law. In the immediate downstream profiles, the deviation is significant but moving further away from the body, the profiles become closer to the log law again indicating the flow development process. There is a significant deviation for the profiles immediately upstream of the body. This may be due to the use of small shear velocity at the decelerating zone in normalizing of the large velocity of the top layer of the flow in regime 2.

5.3.2 Spanwise velocity measurement in different depths

In the last section, the measurements of velocity by pitch probe showed the variation of velocity at the central section of the flow, which defines the behavior of the

wake of the body in a vertical plane. To investigate the variation of velocity in a transverse direction for different levels above the bed, some measurements were made by the yaw probe at a station immediately downstream of the recirculation zone or at the closest measurable station to the body. The profiles of the spanwise characteristics of the velocity in different depths downstream of the obstacle can be seen in Figures 5.11 to 5.16. The closest measurable profile downstream of the body was located at x/D=2 for regimes 1 and 2, series D and A, while for regimes 3 and 4 it was only possible to measure them at x/D=4 and 5 respectively. In these regimes, the high degree of turbulence and significant vorticity behind the body prevented any measurements, despite the existence of a general forward flow even well before values of x/D=4 or 5. The accuracy of the velocity measurements with yaw probe was tested by measuring the velocity for whole width of the wake (Figure 5.17 a). The Figure shows a good symmetry of measurements. Therefore, a half width of the wake can also represent the other half.

The transverse profiles of normalized horizontal velocity are presented in Figure 5.11 (a-f). The sectional average velocity Uo was found to be an unsuitable scale for normalizing the velocity in total depth of a transverse section . The changes of velocity at each level can be studied most appropriately by average undisturbed velocity of that level itself, U_y. There is a large transverse gradient of the velocity in the inner part of the wake which becomes small in the outer region. The width of this inner wake in regimes 1 and 2, Figures (a-e), is roughly equal to the diameter of the body while its counterpart in regime 3 and 4, Figures (e-f), is almost twice the diameter of the body, which indicates a significant increase in width of the wake in the lower relative depths.

The minimum u/U_y at the z/D=0 increases from 0.1 to 0.3 indicating decrease of the strength of wake moving from the very bottom to the surface. A sharper decrease in the velocity was found at the center of the wake for flows with higher Froude number, comparing the profiles of Expts. DS1 and DS2, Figures (a) and (b). The same trend can be seen in regime 2, Expts. AS1 and AS2, where the higher F in Expt. AS2 causes a

faster velocity recovery, moving from y/h=0.1 to 0.4. Using the U_y as scale causes all the profiles to get close to their undisturbed value of u/Uy=1 where the effect of the body is negligible.

In Figure (a), Expt. DS1, the maximum velocity occurs at y/h=0.5 and then it decreases significantly in a lateral direction reaching to u/Uy=1, i.e. free external velocity. This phenomenon can not be seen in the other regimes and it might be referred to as the effect of secondary flow in this deeply submerged flow. Besides this general reduction of the velocity in regime 1, a hump can be noticed around z/D=0.5 to 0.6 for a very short distance of about 0.1 to 0.2 z/D in all profiles. This decrease is noticeable close to the bed and negligible in further distance above the bed. It can be traced in Expt. DS2 at about 0.8 z/D, and in regime 2 it is more noticeable where it occurs at z/D=0.7 for the ratios of y/h up to 0.5. In regimes 3 and 4, by widening the size of the wake, it occurs at z/D=1 to 1.5. In these two regimes the hump is somewhat weaker than that of regimes 1 and 2, which might be attributed to the fact that measurements was only possible much further away from the body, comparing x/D=2 in regime 2 with 5 in regime 4. The scatter in measurements of regimes 3 and 4 was less than that of regimes 1 and 2, which shows they are more uniform, probably due to the lack of downwash flow.

The profiles of defect velocity are presented in Figures 5.12 (a-f). The defect velocity is often used in wake study and has a long history in wake literature. Therefore, these profiles are presented along with the usual spanwise velocity profiles. In general, defect profiles can be interpreted similar to the velocity profiles. Moving from center line to the walls, the defect velocity decreases dramatically and then it increases smoothly. The transition of a low velocity to the high outer velocity indicates existence of a turbulent region at the center which mixes smoothly with the outer region. Transition from high turbulence to a smooth mixing region is disrupted by a raise in the defect velocity curve in profiles closer to the bed. But the slope of this hump is different from the general slope of velocity transition and seems to be unrelated.

157

By looking at the flow and dye flow visualization the location of the HS vortex was found to be the same as these humps. So the origin of these humps in velocity and defect profiles is the secondary flow caused by HS vortices, and not the general secondary flow caused by the wake itself. The legs of the HS vortex are extended downstream and cause a secondary flow in the transverse direction. They also decrease the mixing process of the rapid velocity of the free stream and the low velocity inside the wake. The raise in the profile indicates the disruption of the mixing process by induced low velocity of the HS vortex. The effect of the secondary flow caused by the vortices changes the slope of the profile significantly and makes the wake region wider (or, in other words, causes sharper change between the wake and the free stream).

In the profiles of the 0.1 D, 0.15 D and 0.2 D, Figure 5.12 (c), there is a drop in the middle of the hump. This seems to follow a trend which repeats itself in these three profiles. This drop might be attributed to the presence of two vortex legs in one side of the body. It has been discussed in the literature and visualized in this study that several HS vortices are created in front of the obstacle (Baker, 1979-1980). The legs of these vortices curled around each other when they passed the sides of the obstacle. Therefore, there is a good possibility that this double hump is an indication of the existence of two legs of HS vortices, one originated from primary vortex and the other one from secondary vortex, but with less effect. If there are more legs, they could not be detected due to limited sensitivity of the probes and the small effects the legs. Further detailed measurements would be essential to support this.

Spanwise profiles of yaw angles are presented in Figures 5.13 (a-f). The symmetry of the yaw angle measurements by yaw probe was assessed in advance to avoid the measurements of whole width of the wake. This result is presented in Figure 5.16 (b). The existence of symmetry in this figure indicates that the measurements can be limited to one half of the wake. Due to the presence of the steep gradient of the yaw angle close to the point of symmetry, center of the wake, even a small error in allocation of this point

causes a considerable deviation from the zero value. Despite the careful measurements of yaw angle, a minor deviation from zero angle is present in some figures due to the difficulty in locating the point of symmetry, z= 0, and in defining zero angle for the probe itself (considering the accuracy of the yaw angle measurements).

There is a sharp decrease of yaw angle moving away from the center line with a minimum at about 0.2 z/D and then a rapid increase up to 0.8 to 1.2 z/D. A gradual increase of the yaw angle occurs afterward, towards the wall reaching neutral direction, i.e., zero angle. Therefore, at around 0.8 to 1.2 z/D the velocity direction towards the center line increases reaching its maximum at 0.2 z/D. Then, due to the existence of symmetry, it has to go to zero very fast. This fact agrees well with flow visualization where the separated flow from the sides, in form of a vortex ring, curls inward creating a transverse component of velocity, -w. The significant variation of yaw angle in a small distance causes a considerable turbulence in the flow. The magnitude of the yaw angle is greater in lower layers and closer to the bed, indicating a stronger wake at the bed. The amount of error in the measurements at the center line increases closer to the bed as well. The minimum value of yaw angle reaches to -18 degrees.

Increase of Froude number in series D and B, Expts. DS1-DS2 and AS1-AS2, with similar relative depths mitigates the minimum yaw angle from -18 to -7 and from -15 to -9.5 respectively. This change in minimum yaw angle can be attributed to the fact that by increasing the F, the separated flow in the form of vortices are convected downstream with a stronger forward flow, which in turn weakens their induced secondary flow. A small deflection of the velocity further away from the body, z/D=1.4 to 2, in Figure (a) shows the effect of secondary flow in deeply submerged flow.

The profiles of normalized lateral velocity are presented in Figures 5.14 (a-f). Following the same trend of yaw angle profiles, the maximum inward w/Uo reaches up to 0.16. Larger lateral velocity at lower layers of the flow suggests that there is a stronger lateral velocity close to the bed, which then decreases at the surface under the effect of

the forward flow. The lateral velocity was larger closer to the bed in regimes 1 to 3, whereas in regime 4 it was larger close to the surface. This fact could be attributed to the presence of the forward flow on top of the wake in the former regimes, causing a weaker wake at the surface. Comparing the high and low F for series A and D, it is found that the value of lateral velocity decreases with increase of F, keeping the relative depth constant. Comparing the regime 4, Figure 5.14 (f), to other regimes with higher relative depths, it can be concluded that the changes of the lateral velocity along the depth of the flow is less than the others. This fact indicates the presence of a more uniform flow when there is no downwash, i.e., y/h<1.

The standard deviation of the yaw angles, θ', are presented in Figures 5.15 (a-f). These values can be interpreted as an indicator of fluctuation of yaw angle. High values of up to 18 degrees indicate a high turbulence, especially closer to the bed. The profiles of θ' show that the width of the wake is larger in regimes 3 and 4, Figure (e) and (f), than in regimes 1 and 2 . The STD of the velocity, u', are presented in Figures 5.16 (a-f). The value of u' is normalized by average sectional velocity, Uo. The existing scatter is higher in these profiles but they generally indicate a higher fluctuation of the velocity at the central region of the flow, i.e., the wake, and in lower layers of the flow, at the bed. The maximum value of u'/Uo reaches to 0.06.

5.3.3 Spanwise velocity measurements in different stations

To investigate the wake decay downstream of the obstacle, spanwise profiles of velocity at the y/h=0.5 for regimes 1, 2, 3 and y/h=0.2 in regime 4 were measured by yaw probe at several stations. These results are presented in Figures 5.18 to 5.24. The profiles at y/h=0.5, y/h=0.2 for series C, are selected as representatives of the wake at each station. Measurements were carried out at the first measurable station downstream of the body, usually after the recirculation zone in series D, A, and after the vortex generation zone in series B and C. Due to the restriction in longitudinal direction of the

160

flume downstream of the body, the furthest measuring station for obstacle #1 was 10D, and for hemisphere # 2 was 20 D before flow was affected by the tailgate.

The profiles of normalized velocity for different stations are presented in Figures 5.18 (a-f). The sectional average velocity, Uo, is used as the scale to normalize the velocity because there is no variation in y/h in profiles for each series. A significant recovery of the velocity, 0.4 to 0.7 u/Uo, occurs at the central region in a short distance of less than 10-20 D. The magnitude of the velocity increases very fast from z/D= 0 to z/D=0.5, i.e., obstacle sides, in regimes 1 and 2, Figures (a-d), and with milder slope to z/D=1.2 in regimes 3 and 4, Figures (e-f), indicating a larger wake in the latter regimes. A noticeable decrease of the velocity is present in Figure (a) where the aspect ratio of the flume is small, B/d=4.5, while it is absent for similar relative depth in figure (b) but with larger aspect ratio of B/d=7.7. Therefore, this large hump in velocity profile of Expt. DS1 can be attributed to the secondary flow.

There is a small hump in the velocity profiles at around z/D=0.6, which is more visible in figure (c). This hump shows that after increase of the velocity at the center of wake towards the outer region, there is a reduction of velocity which can be attributed to the presence of the HS vortex. The legs of HS vortex caused a local secondary flow which disrupted the mixing process of the wake and the free stream. This shows that the secondary flow gets weaker as it propagates further downstream. In addition the legs of HS vortex are moving apart when the hump in the profile moves away from the center, progressing downstream, Figure (c). The hump can not be traced in profiles further than x/D=3-4. It indicates that up to this distance the legs of HS vortex keep their identity, but afterwards by mixing with inner flow, they loose their identity and become part of the wake. This fact might be responsible for preventing the presence of these humps in Figures (e-f), where in both cases the measurements are made at stations further than x/D=4. S. Okamoto (1979), by observing the flow motion with the tuft grid method, also found that the horse-shoe vortex becomes flat at x/D = 4 and disappears about x/D = 5.

161

The negative static-pressure coefficient in a region behind the sphere, $0.3 < z/D < 1.5$ for $2 < x/D < 5$, was assumed to be a result of the HS vortex in his experiments. The sign of this coefficient changed to positive at $x/D=5$ where the HS vortex disappeared. He also found that the peak velocity defect moves away from the centerline.

Comparing the profiles of different regimes, a significant difference is noticeable. In regimes 3 and 4, Figures (e-f), velocity recovery continues even as far as $x/D=20$ where still there is a considerable difference between the velocity at the central region and free stream velocity at sides. But in regimes 1 and 2, Figures (a-d), the flow in the central region of the wake starts to move faster than the free stream velocity after $x/D=4$-6. The flow from the top of the body creates a downwash which convects flow of the inner wake region and its effects overcome the velocity deficit further downstream of the body and its recirculation zone. Even in this case the effect of the wake of the flow can be traced in these profiles at about $z/D=0.5$ to 1 where a decrease of the velocity is present, Figure (c) at $x/D=10$. But there is no downwash in regimes 3 and 4, so the velocity requires a much longer distance to recover and the wake is still strong in range of these measurements. T. Okamoto and M. Yagita (1973) also found that there were two peaks in the defect velocity distribution in transverse direction downstream of the body. This was a feature of the wake of the finite cylinder, indicating an access velocity due to the downwash. T. Okamoto et al. (1977) indicated the same feature and explained it as the effect of the downwash of the free stream from the top of the cone and the existence of a secondary flow due to the HS vortices. This increase of the velocity at the center is known as a "negative wake effect".

The spanwise profiles of defect velocity are presented in Figures 5.19 (a-f). The lower values of defect velocity at the central region in Figures (a-d) show the downwash effect. A comparison between the profile at $x/D=2$ and 6 in Figure (b) clearly shows the difference between the state of the flow before and after the effect of the downwash. The presence of the legs of HS vortices are clear in Figure (c). Closely spaced profiles in

Figures (e-f) indicate the existence of a more uniform flow in regimes 3 and 4. Some of the characteristics of the wake can be described better by defect velocity profiles which consider existing literature on wake studies.

The profiles of the yaw angles θ are presented in Figures 5.20 (a-f) and the profiles of the normalized lateral velocity w/Uo in Figures 5.21 (a-f). Similar to the profiles in section 5.3.2, there is a minimum θ and w close to the POS which reaches to zero both at the POS and away from it. These values are stronger for profiles closer to the body, i.e., smaller x/D. Increasing x/D the lateral velocity decreases and after x/D=4 the trend of profiles of w/Uo and θ changes. Before x/D=4 there are two minimums in yaw angle profiles, Figures 5.20 (a-d), or two minimum w/Uo in the vicinity of the centerline for whole width of the wake, Figures 5.21 (a-d), with a maximum value at the center line. After this point, there is a transition in which the two minimum w/Uo gradually become two maximum, with a minimum at the center line. This process is not present in Figures 5.20 and 5.21 (e-f) which represent regimes 3 and 4. In these regimes the variation of the yaw angle and w covers a wider part of the flow compared with regimes 1 and 2. It can be concluded again that the layer of flow on top of the body affects the central region of the wake. At a small distance downstream of the body, the two larger lateral velocity peak become a less significant minimum lateral velocity at the centerline. Therefore, while according to the Figures 5.18 (a-d) the value of u/Uo is maximum at the central region, the lateral velocity is diminishing in this region.

The profiles of standard deviation of yaw angles θ' are presented in Figures 5.22 (a-f). Due to the presence of high fluctuation of the velocity in middle section of the flow at the downstream of the hemisphere, the values of θ' are high, 10 degrees in Figure (a). They decrease moving away from the POS and propagating further downstream. The change of the value of θ' in Figures (a-d) extends less in width of the flow, 0.5 z/D, than 1.2 to 2 z/D in Figures (e-f), which indicates existence of a wider wake in the latter case.

163

The width of these changes in Figure (f) is more than that in Figure (e). The value of θ' decreases moving downstream of the body.

The profiles of standard deviation of velocity, u', are presented in Figures 5.23 (a-f). The inner section of the wakes has higher values of the fluctuation. These values are normalized by U_o and are in the range of 0.05.

5.4 Bed Shear Stress Measurements

Bed shear stress, τ_0, is the main factor causing sediment transport and scour around the body. Measured τ_0 shows the areas of high bed shear stress in the simple and idealized case of hemisphere on the smooth bed. It also indicates the possible regions where the scour might start. Like velocity measurements, τ_0 is measured both on the POS and transverse direction. In the POS measurements, a simple Prandtl tube was used and in the transverse direction, τ_0 was measured by yaw probe based on Preston technique.

The measured data on the POS are presented in Figure 5.24 (a-f). The undisturbed bed shear stress at the bed has been used to normalize the bed shear stress. These results are presented in Figure 5.25 (a-f). The general trend in these figures indicates that the τ_0 decreases as x/D decreases due to the slowing down of the flow velocity. Its value far upstream of the body matches its undisturbed counterpart, showing a ratio of one and then decreasing toward zero at the vicinity of the separation point. The negative values between the separation point and the body are measured by turning the probe against the body to sense the reverse flow caused by HS vortices. The negative values at downstream of the body are measured in a similar manner and indicate the presence of the backward flow in the recirculation region or vortex generation zone. Further downstream, forward velocity develops causing higher shear value (up to 20% more) compared with its upstream value. This increase of τ_0 may be caused by the presence of high turbulence in the wake.

Measurements in regimes 1 and 2, Figures 5.25 (a-d), do not show any negative values more than $\tau/\tau_0 = -1$, which indicates that the shear stress caused by HS vortex in front of the body is actually less than its upstream values. But in regimes 3 and 4, Figures 5.25 (e, f), the measured τ_0 close to the body are up to 40% more than their upstream values. In regime 4, Figure 5.25 (f), measurements could not be taken before $x/D=2$ due to the high fluctuations in the flow. The process of flow development downstream of the body in regime 3 is different, Figure (e), when it shows a large value very close to the body and then decreases around $x/D=1$. Based on the flow visualization, the large value of τ_0 might be attributed to the presence of a high momentum flow coming from the sides of the body, causing the region of backward flow at the bed to be very small, Figure 5.24. Therefore, the peak of the τ_0 immediately downstream of the body indicates the effect of the side flows on the POS. Further downstream, part of the energy of the flow is dissipated when two side flows face each other, showing a decrease of the τ_0. Then the flow starts to develop again.

Several transverse profiles were measured along the width of the channel and the results are presented in figures 5.26 (a-d). The maximum τ/τ_0 in Figure (a) is 1.6 at the $x/D=0$ due to the acceleration of the flow at the sides of the body. It reaches to 2.5 in Figure (b) for the same relative depth but with higher velocity and Froude number. The same trend can be observed in regime 2, Figures (c-d), where this ratio is 1.9 for Expt. AS1 and 3.4 for Expt. AS2. This shows the clear effect of the larger velocity on the increase of the τ_0. Therefore, the bed shear stress reaches its maximum only at the sides of the body. Baker (1979), (for a circular cylinder in a wind tunnel) found that the skin friction coefficient beneath the primary vortex was five times its value at the upstream of the cylinder, which is much higher than this study's measured values, probably due to the weakness of the downflow here.

The measurements show that very close to the body τ_0 is small, Profile $x/D=0$ at Figure (a), due to the effect of the boundary, and then it increases significantly away from

the body in a very short distance. The high shear stress is also present in other downstream profiles, but its maximum remains at the vicinity of the x/D=0. These profiles have their maximum at about z/D=0.5, then τ_0 decreases moving towards the POS, z/D < 0.5. The profiles of x/D=-0.5 confirm the results of the POS measurements when they show a decrease in the bed shear stress immediately upstream of the body despite the presence of the HS vortex.

The transverse profiles of the yaw angle of the bed shear stress are presented in Figures 5.27 (a-d). Upstream profiles indicate the deflection of the bed shear stress approaching the body. Upstream of the body the flow diverges away from it and then converges further downstream. The positive angle of the yaw at profiles of x/D= -1 and -0.5 shows the magnitude of this diversion clearly when its maximum reaches 55° in Figure (d). The downstream profiles indicate the convergence of the flow by their inward negative values. The higher yaw angles in Figures (b-d) shows the effect of the higher velocity and F in regimes 1 and 2 compared to Figures (a-c).

(a) Velocity components

(b) Sectional View, Angle of Pitch

(c) Plan View , Yaw Angle
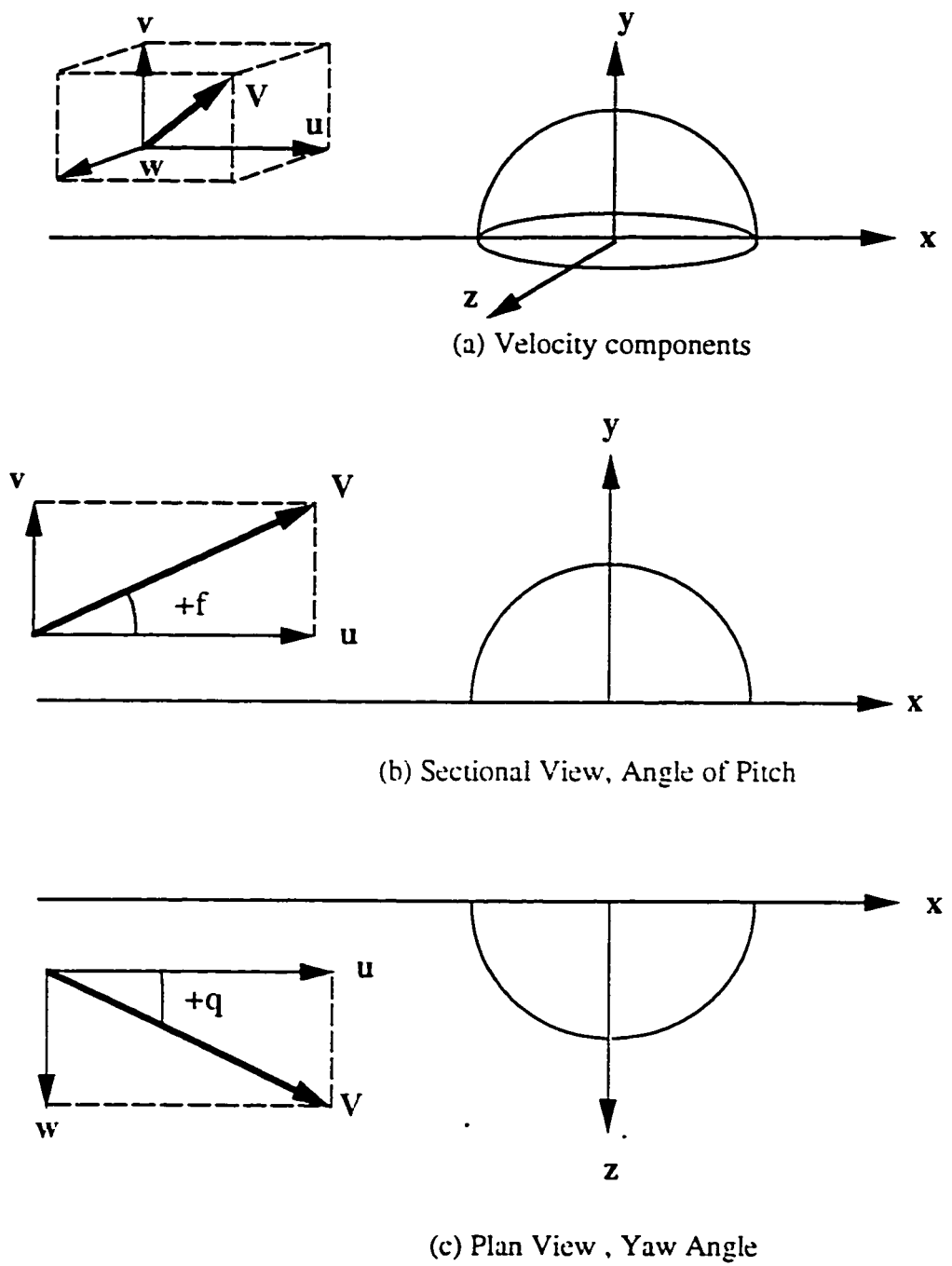
Figure 5.1. Sketch of (a) Velocity components, (b) pitch angle, (c) yaw angle
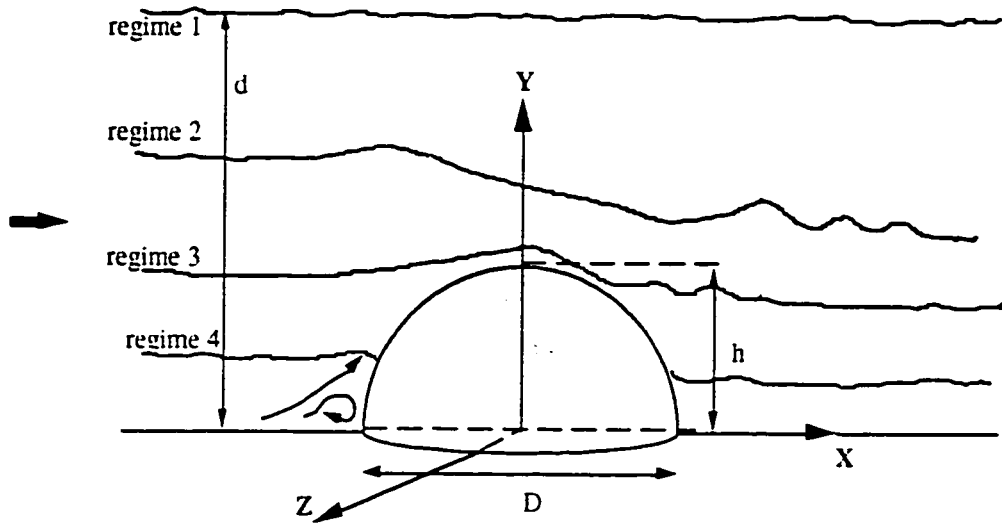
Figure 5.2. Sketch of Different Regimes of Water Surface Profiles
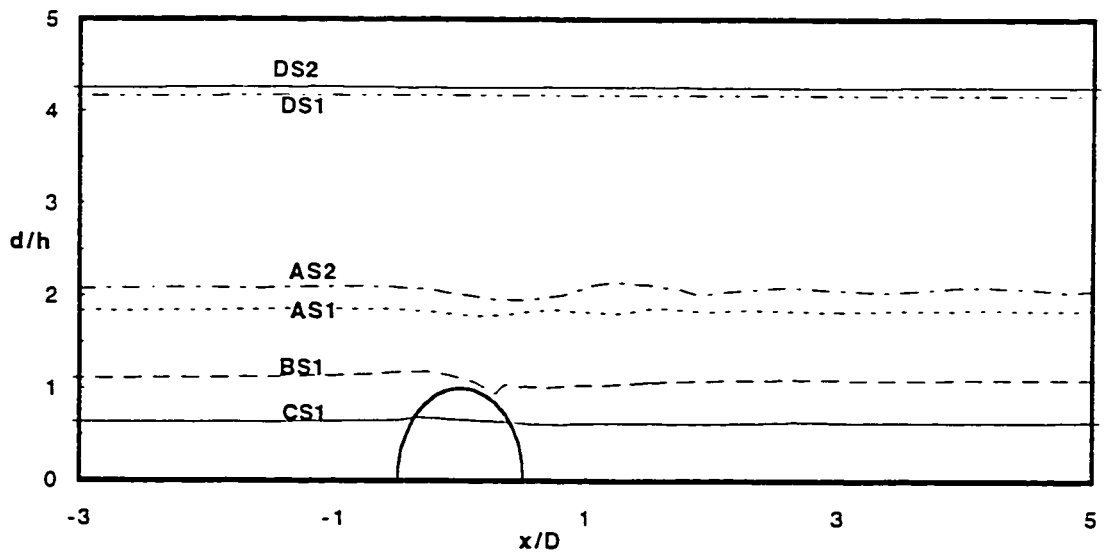
Figure 5.3 Measured water surface profiles for Smooth Bed

168
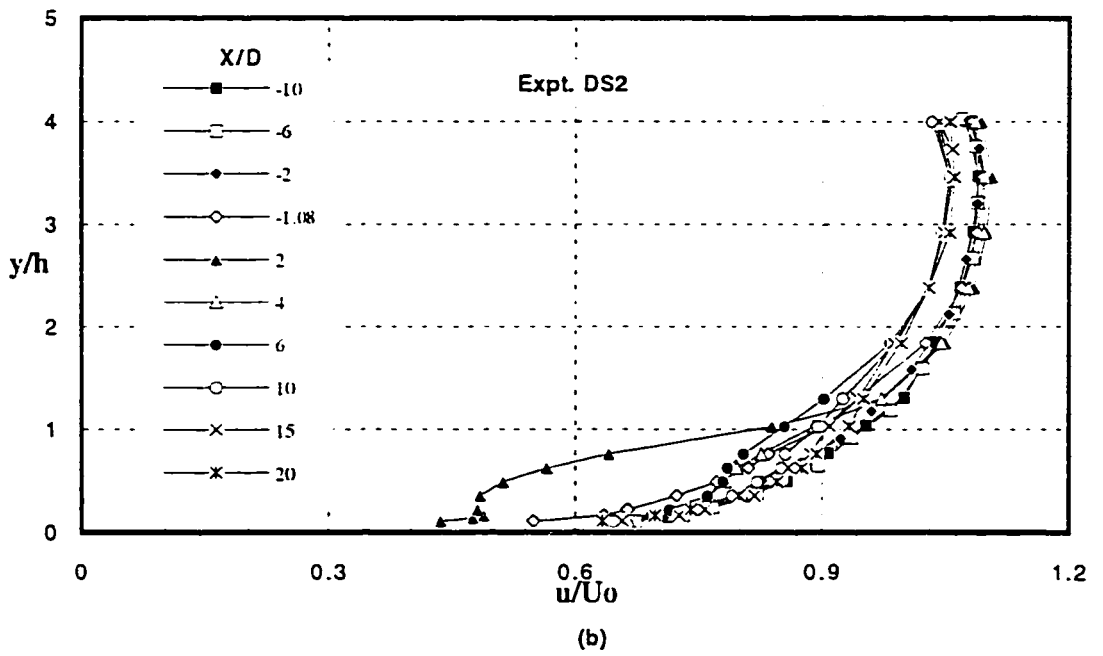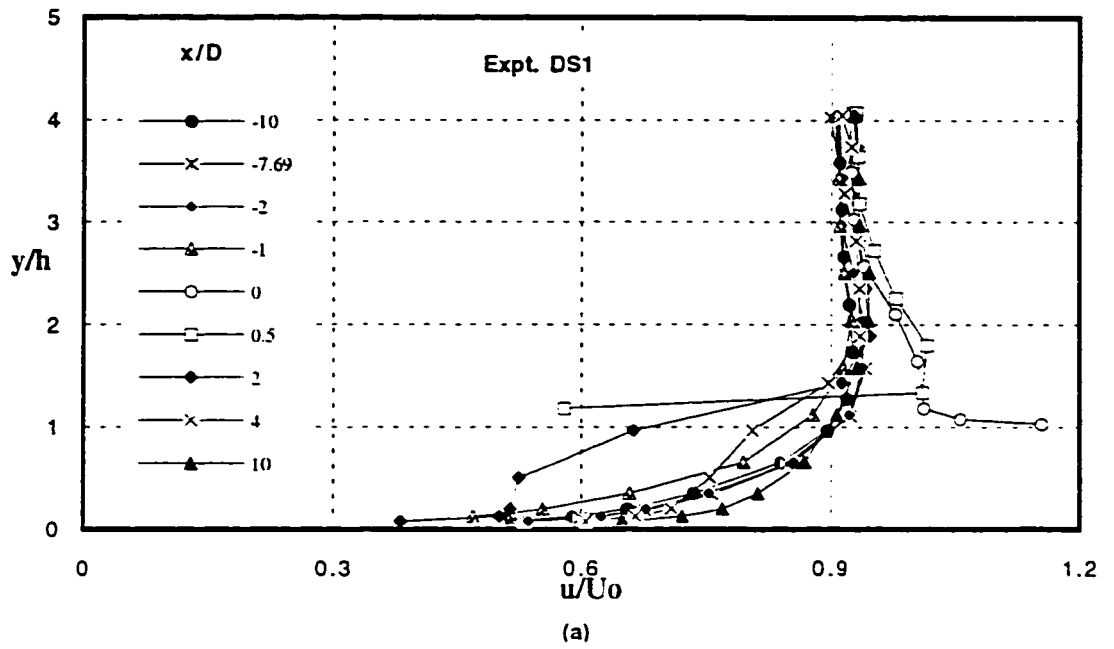
Figure 5.4 (a-b) Profiles of Normalized Horizontal Velocity on the POS

169
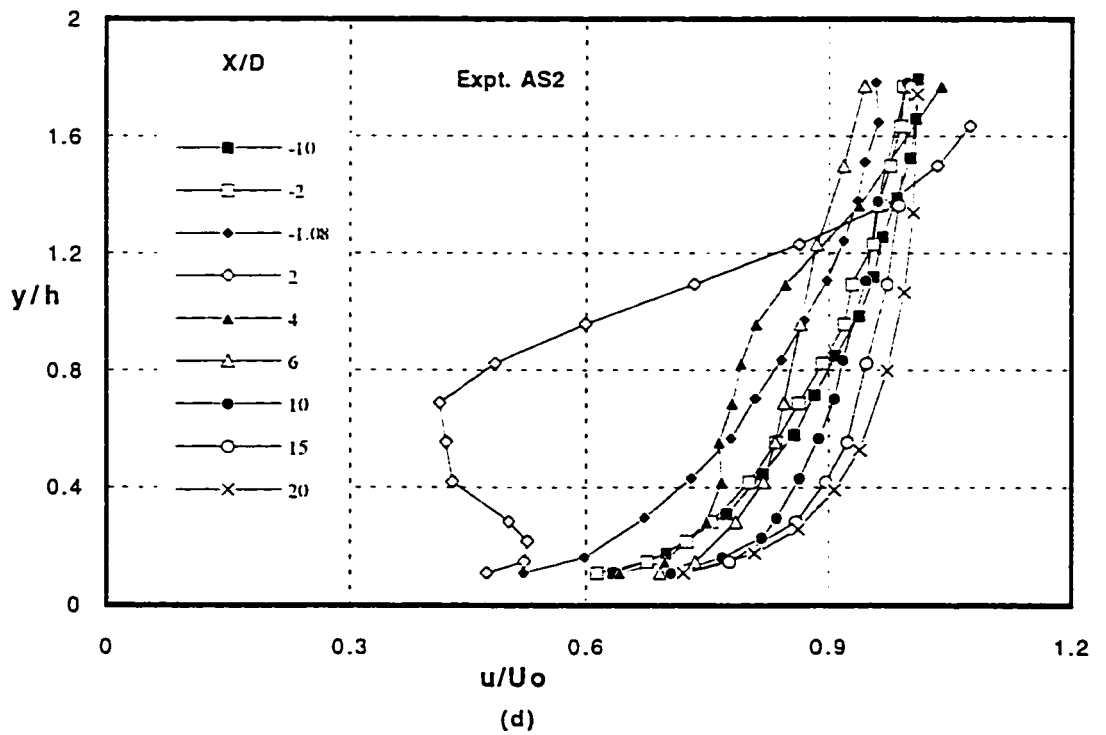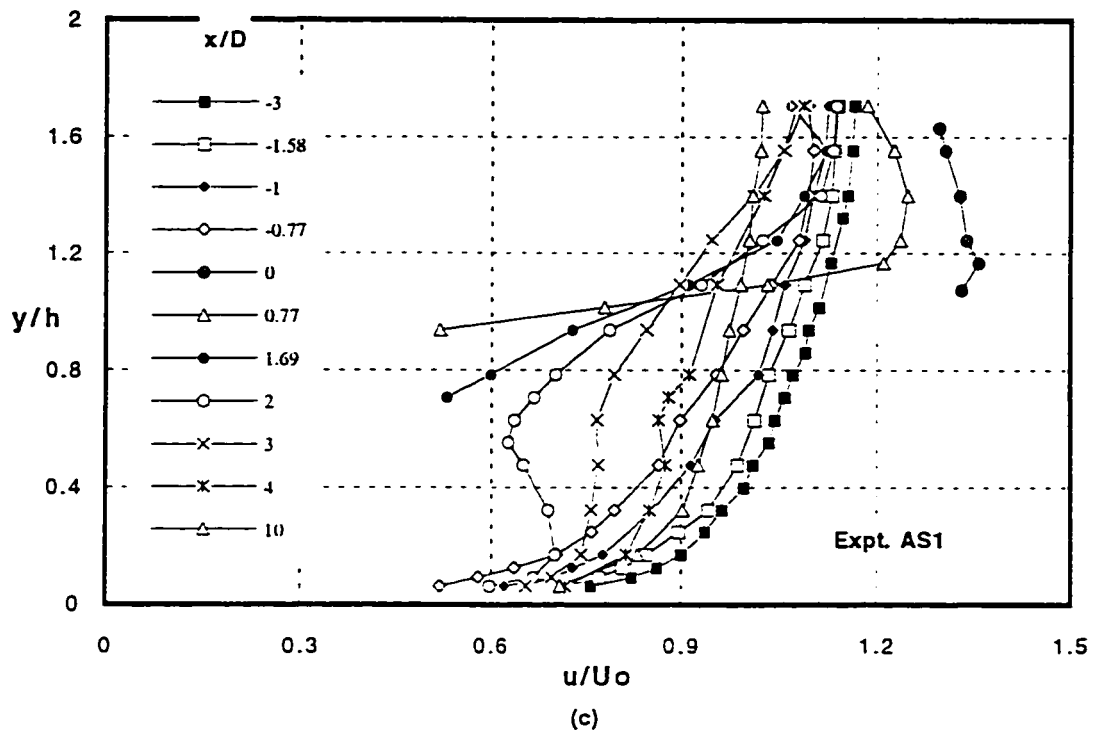
Figure 5.4 (c-d) Profiles of Normalized Horizontal Velocity on the POS

(e)

(f)
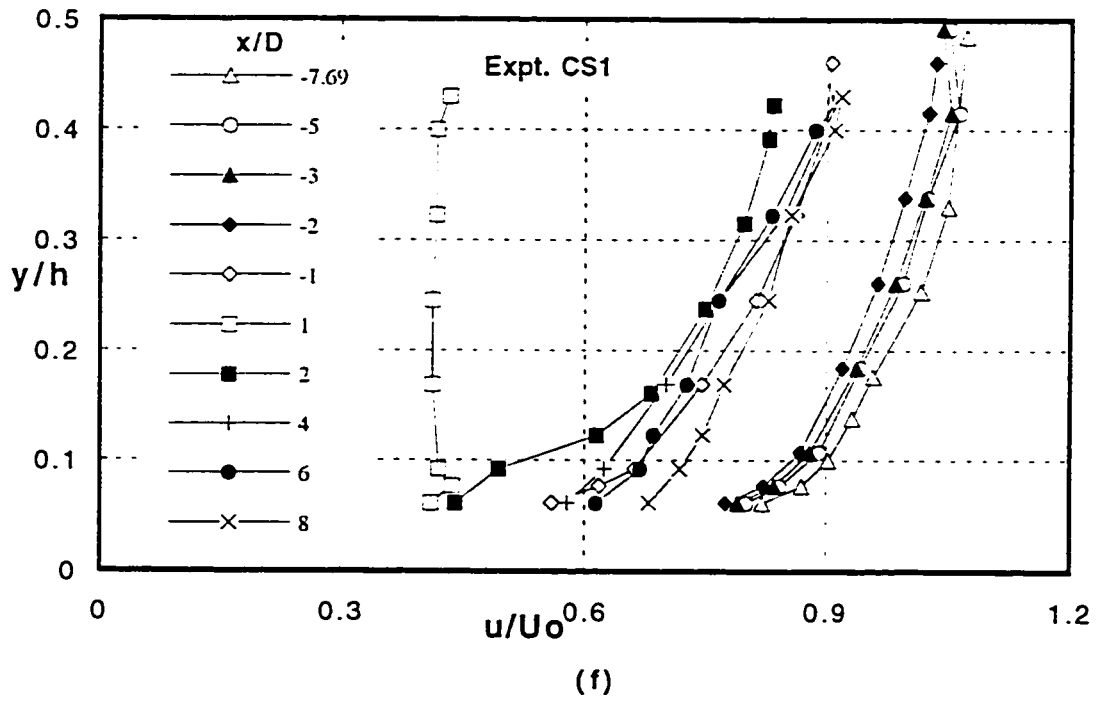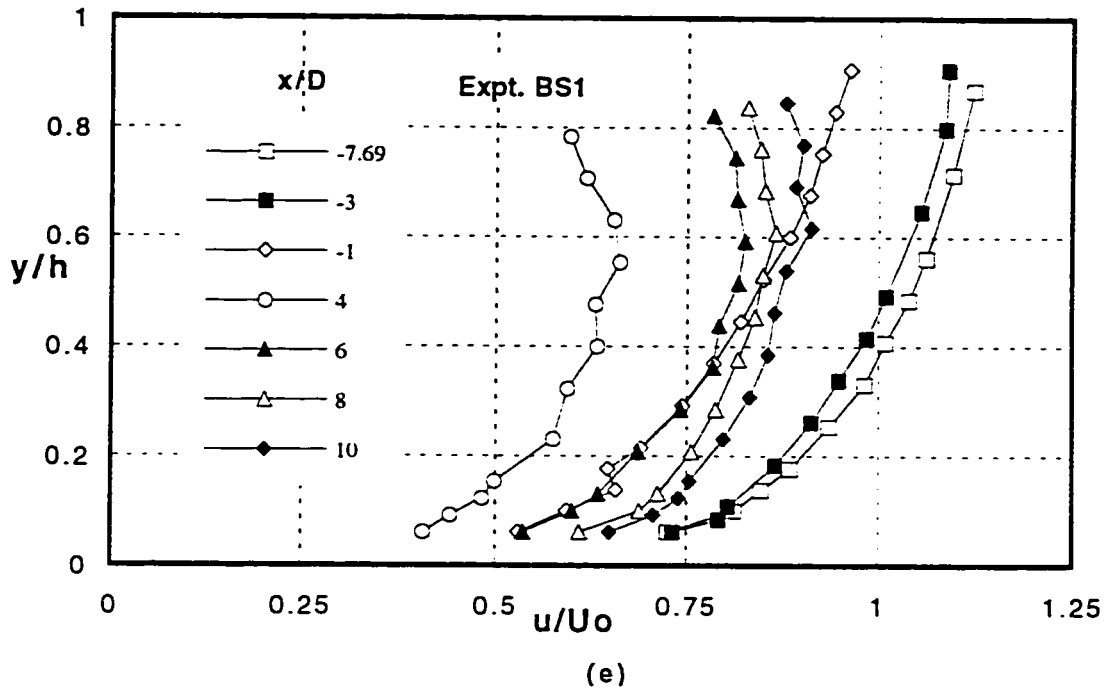
Figure 5.4 (e-f) Profiles of Normalized Horizontal velocity on the POS

171
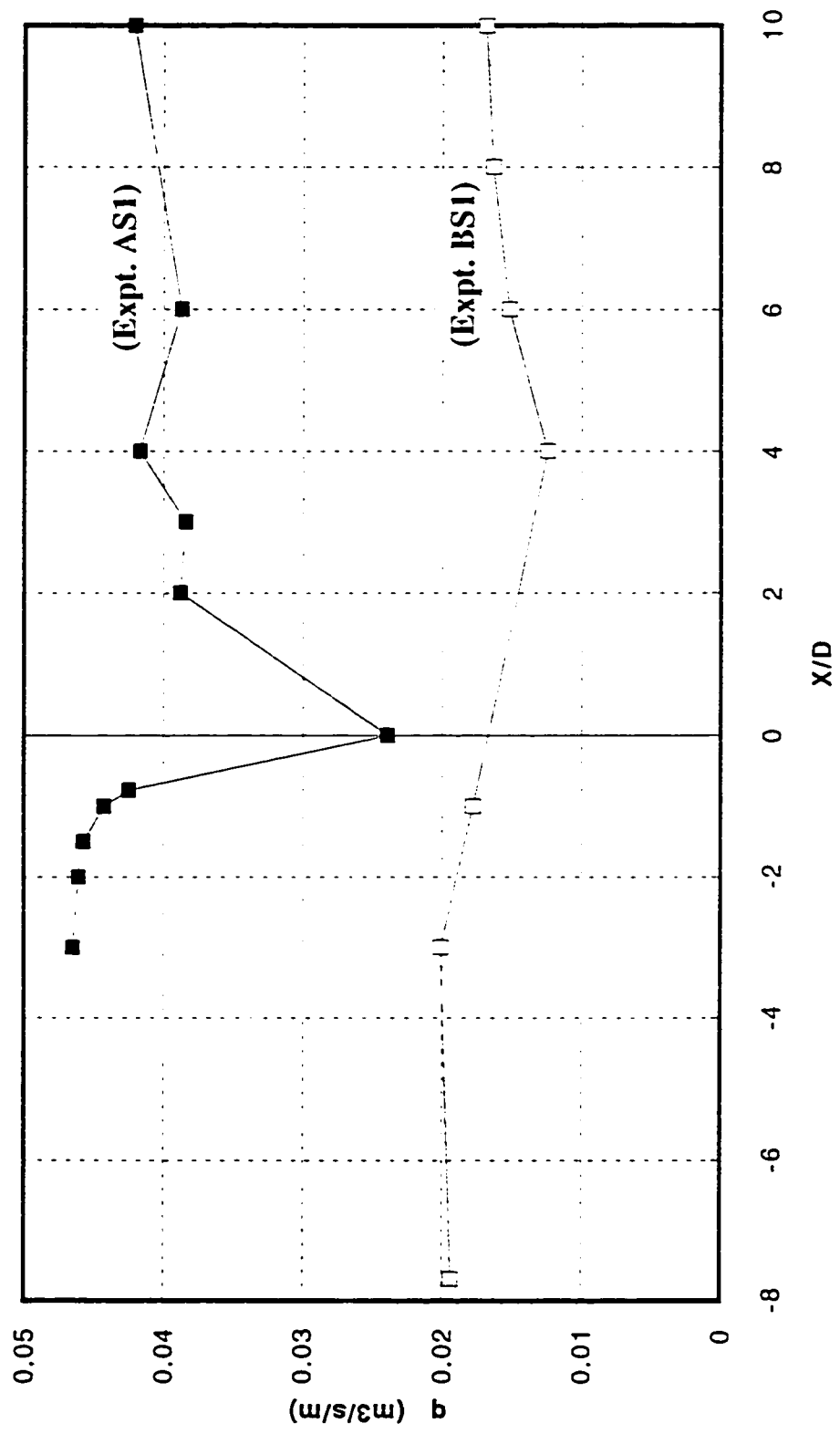
Figure 5.5 Longitudinal Profile of Volumetric Flux on the Plane of Symmetry
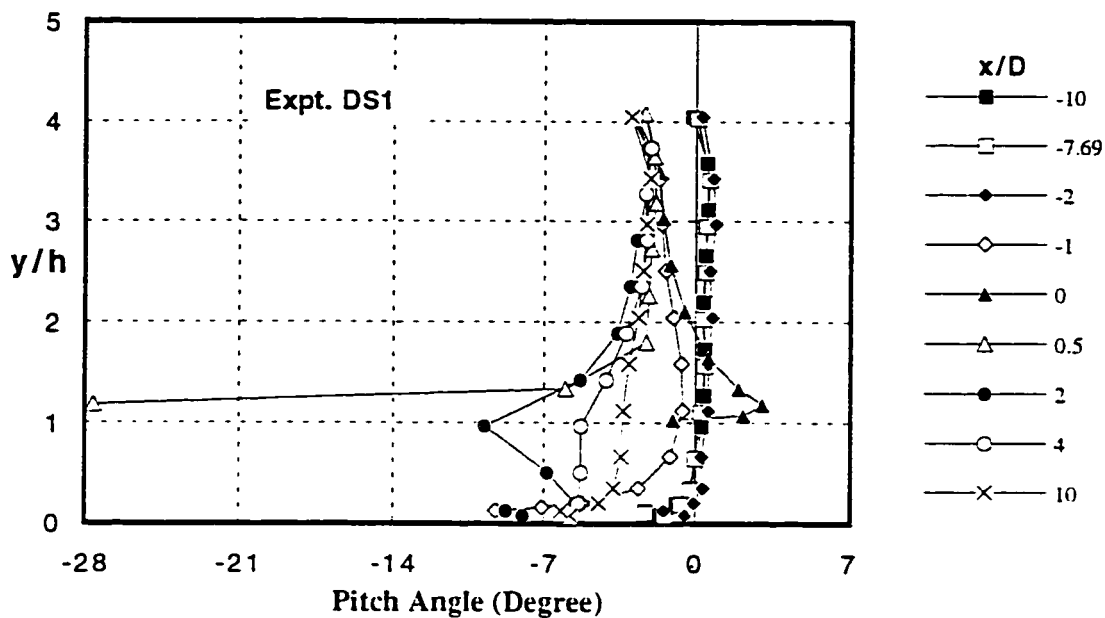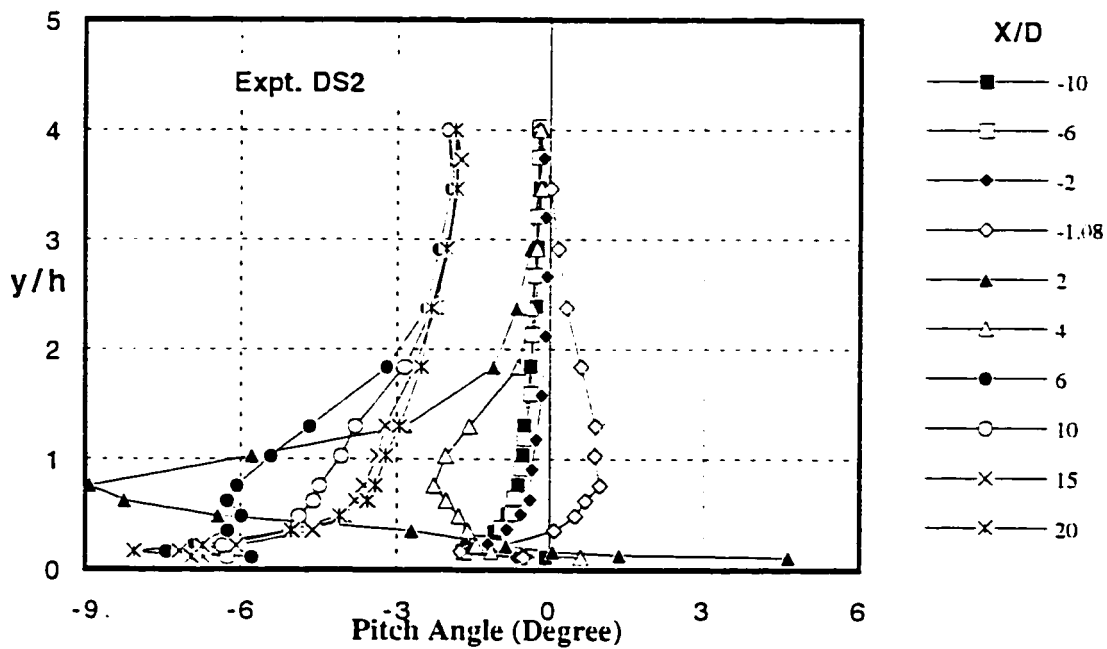
Figure 5.6 (a-b) Profiles of Pitch Angles on the POS
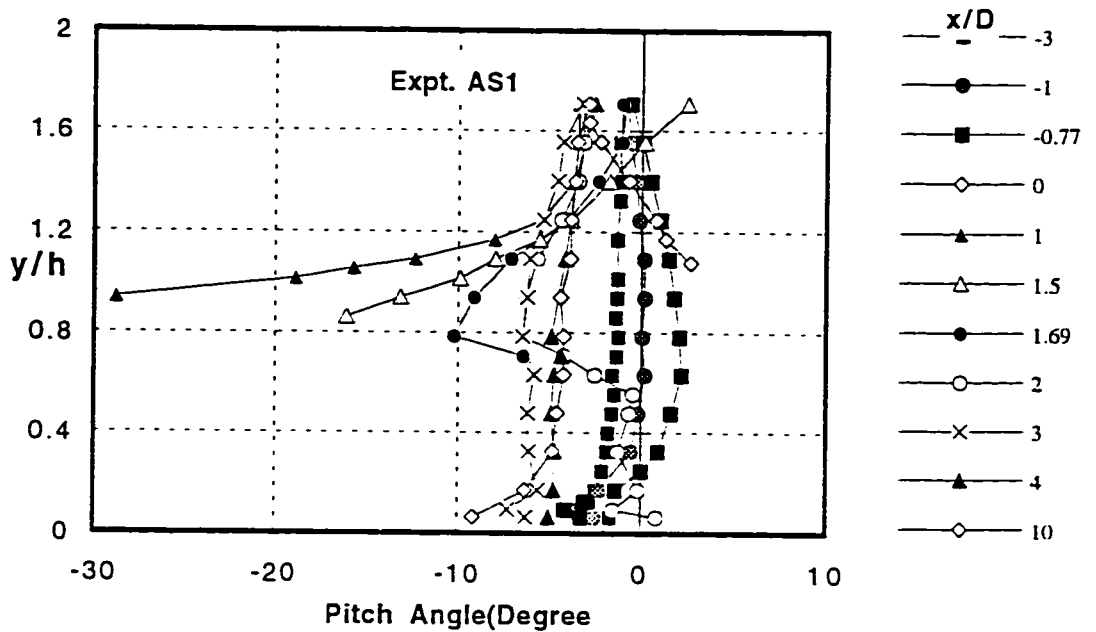
(c)
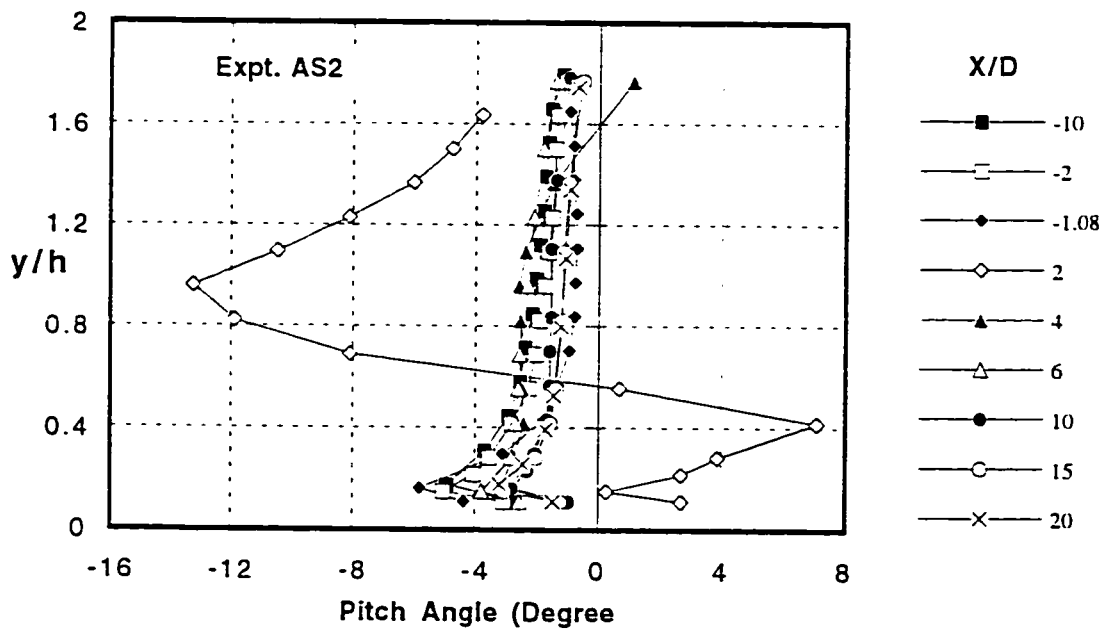
(d)

Figure 5.6 (c-d) Profiles of Pitch Angles on the POS

174
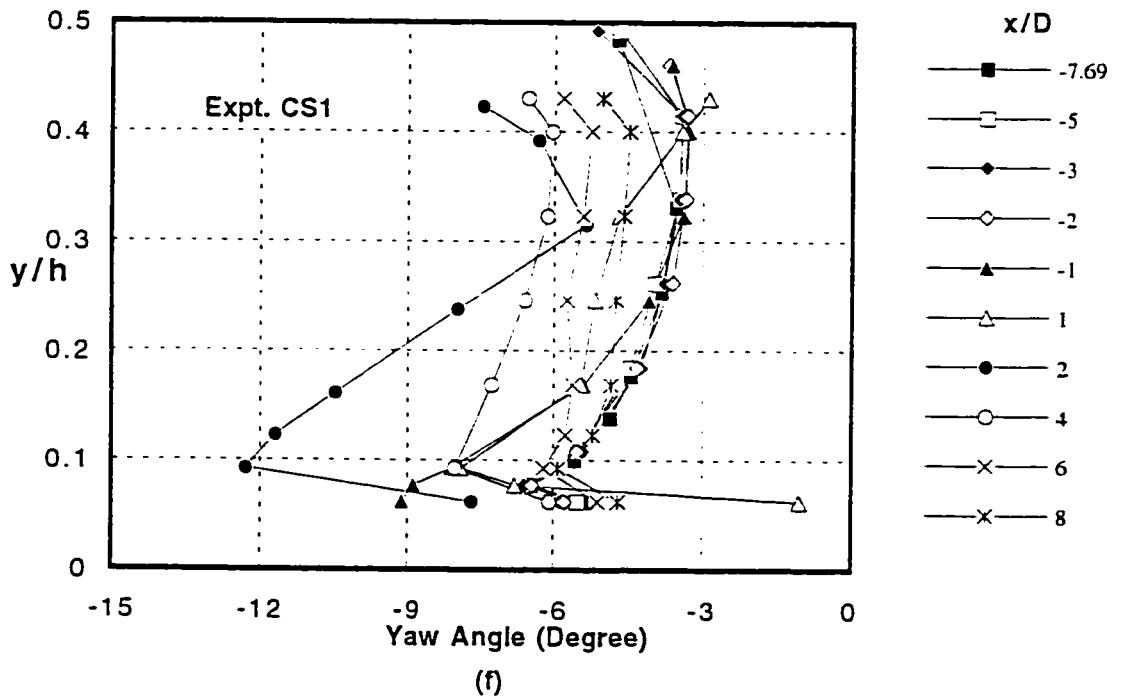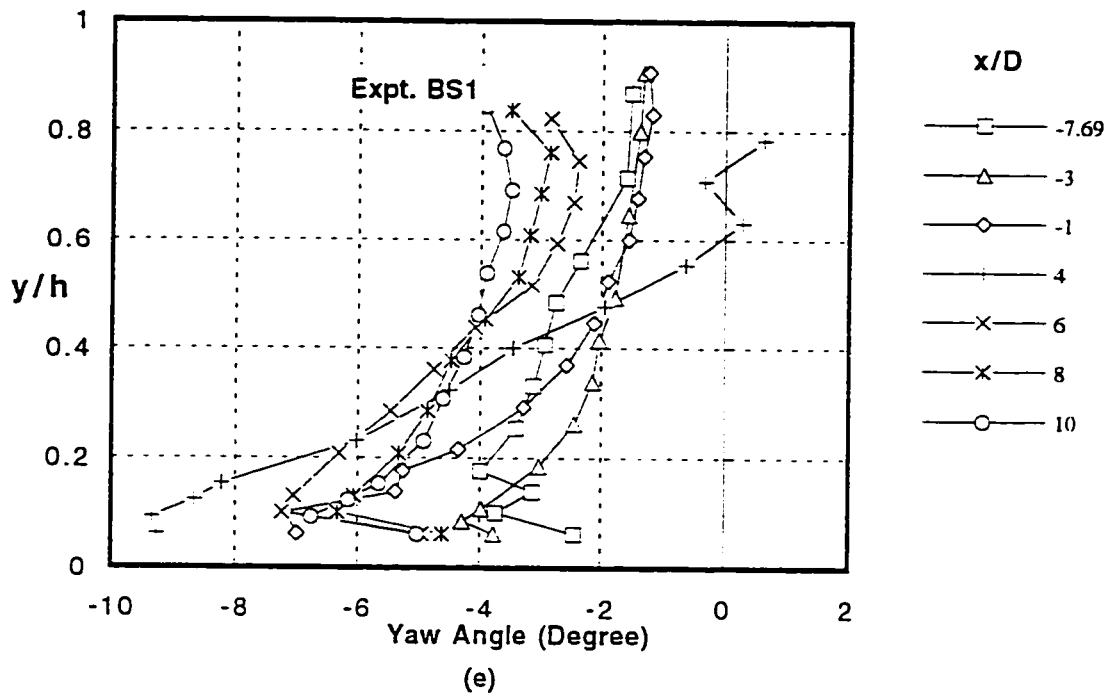
Figure 5.6 (e-f) Profiles of Pitch Angles on the POS
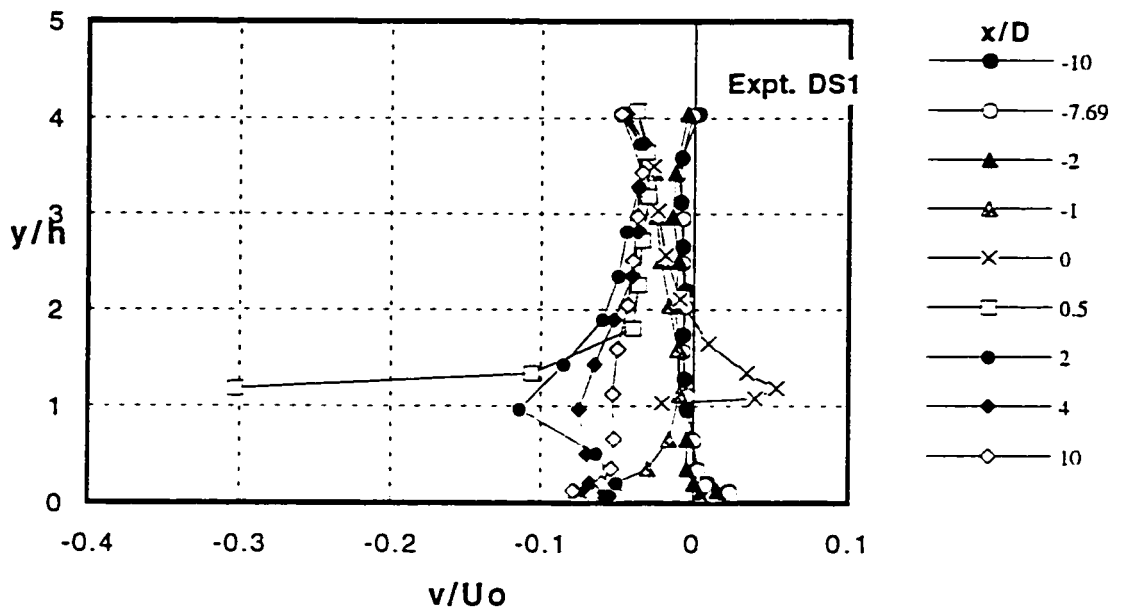
(a)
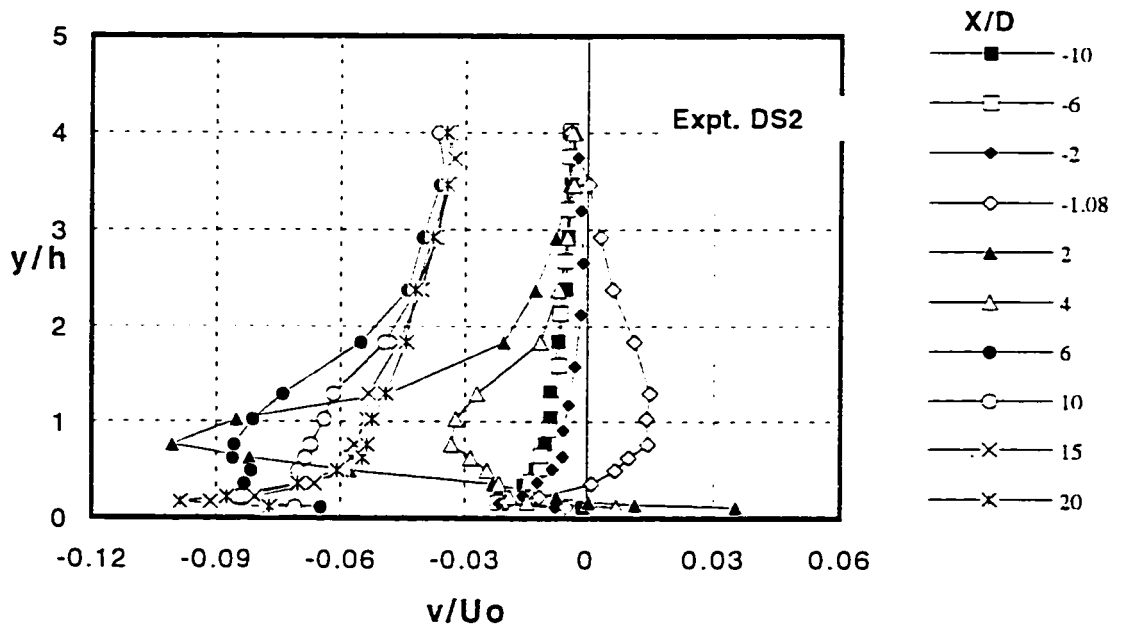
(b)

Figure 5.7 (a-b) Profiles of Normalized Vertical Velocity on the POS
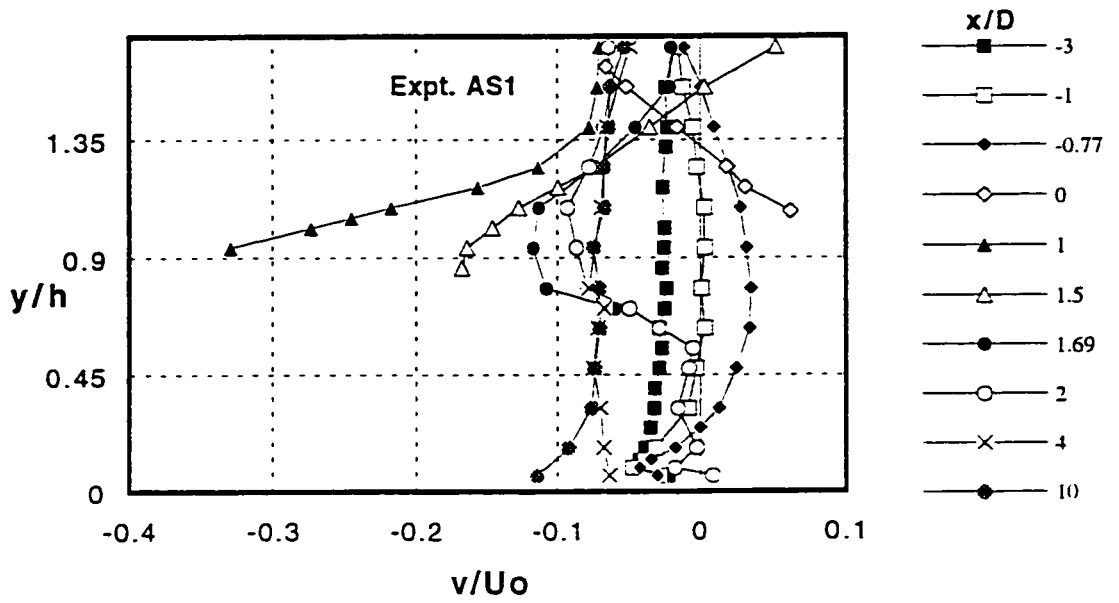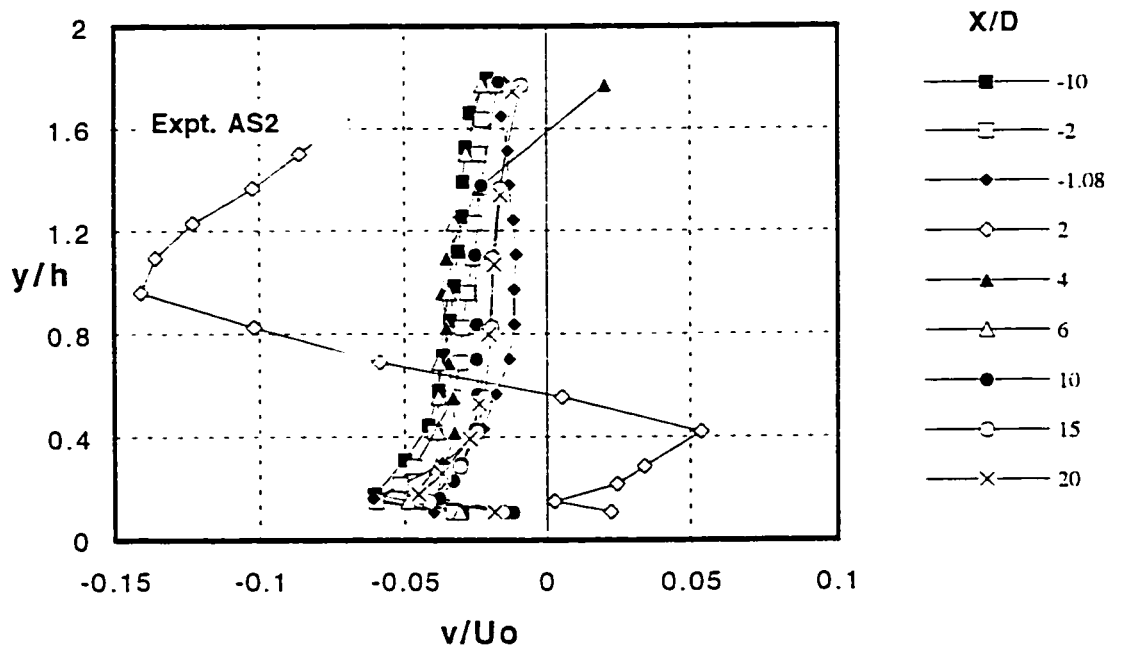
Figure 5.7 (c-d) profiles of Normalized Vertical Velocity on the POS

177
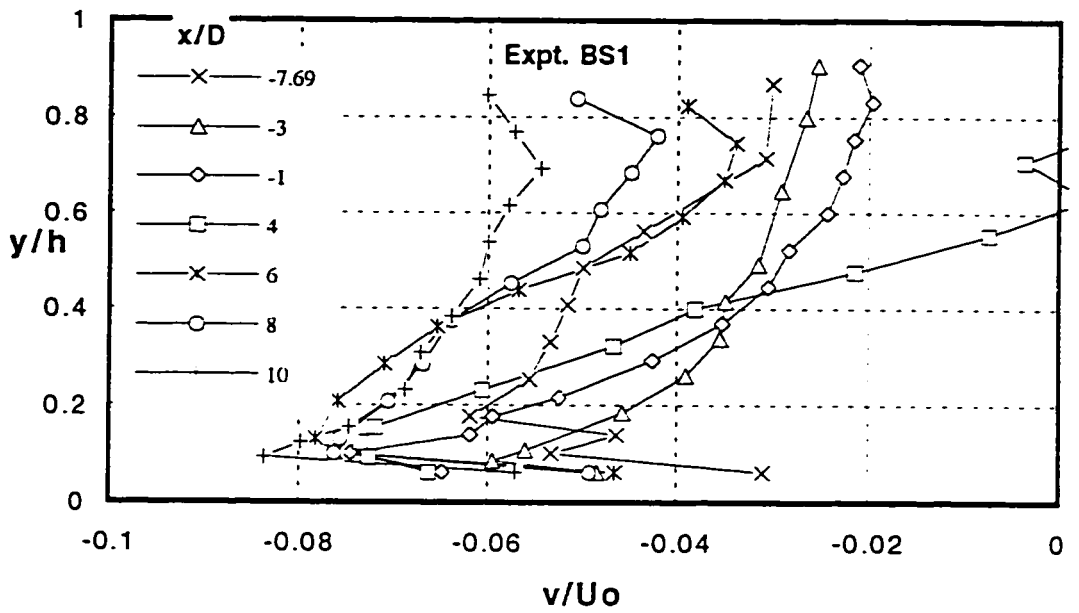
(e)
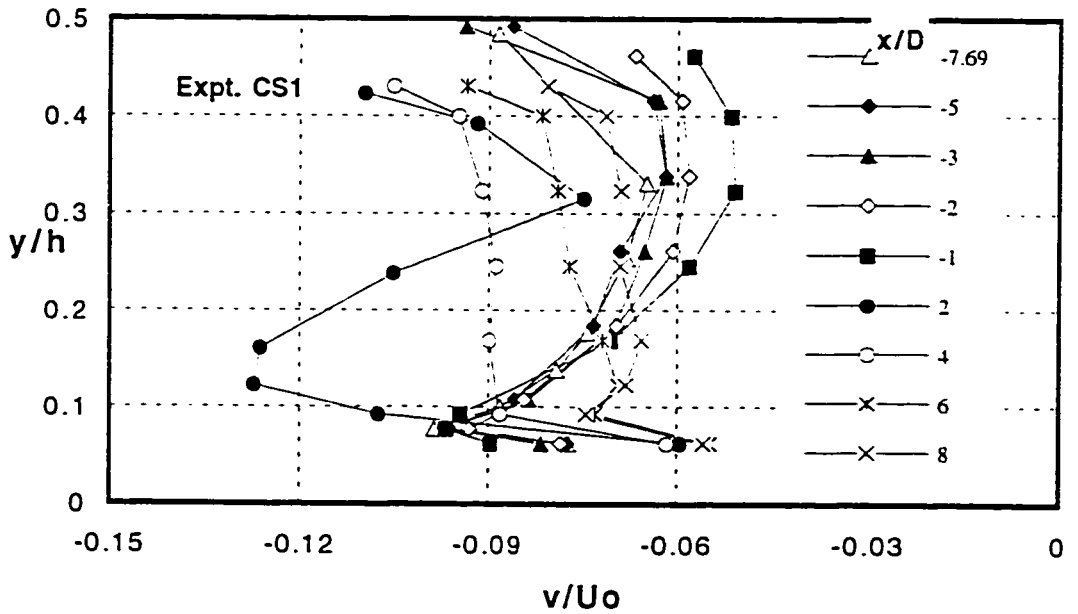
(f)

Figure 5.7 (e-f) Profiles of Normalized Vertical velocity on the POS
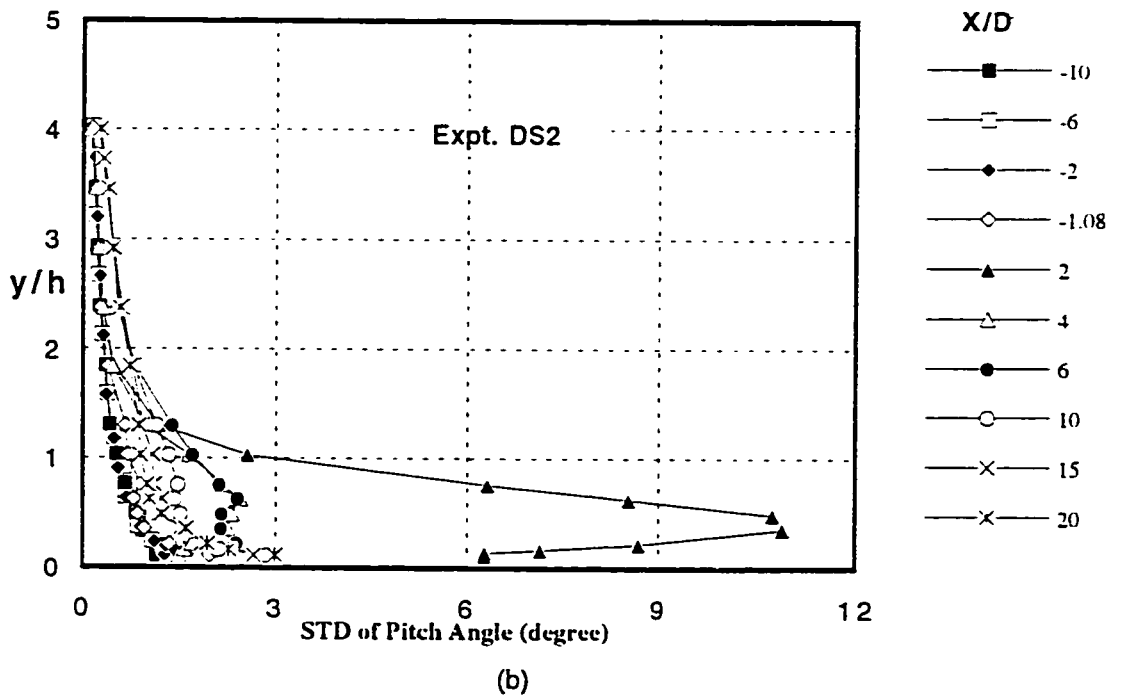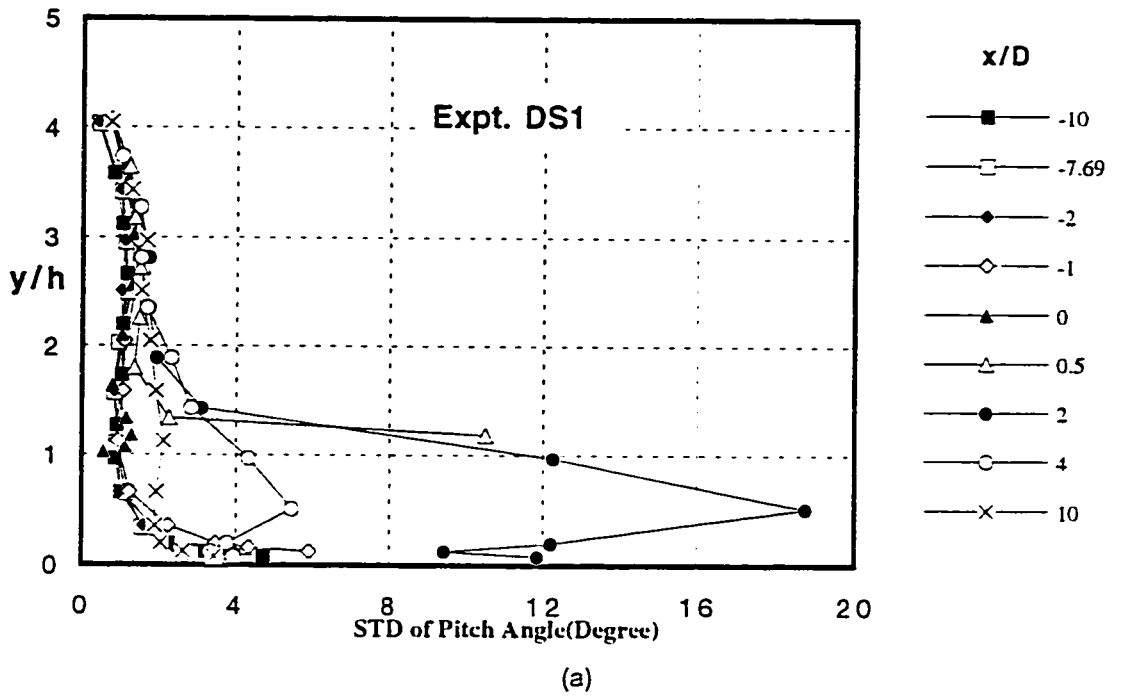
Figure 5.8 (a-b) Profiles of STD of Pitch Angles on the POS
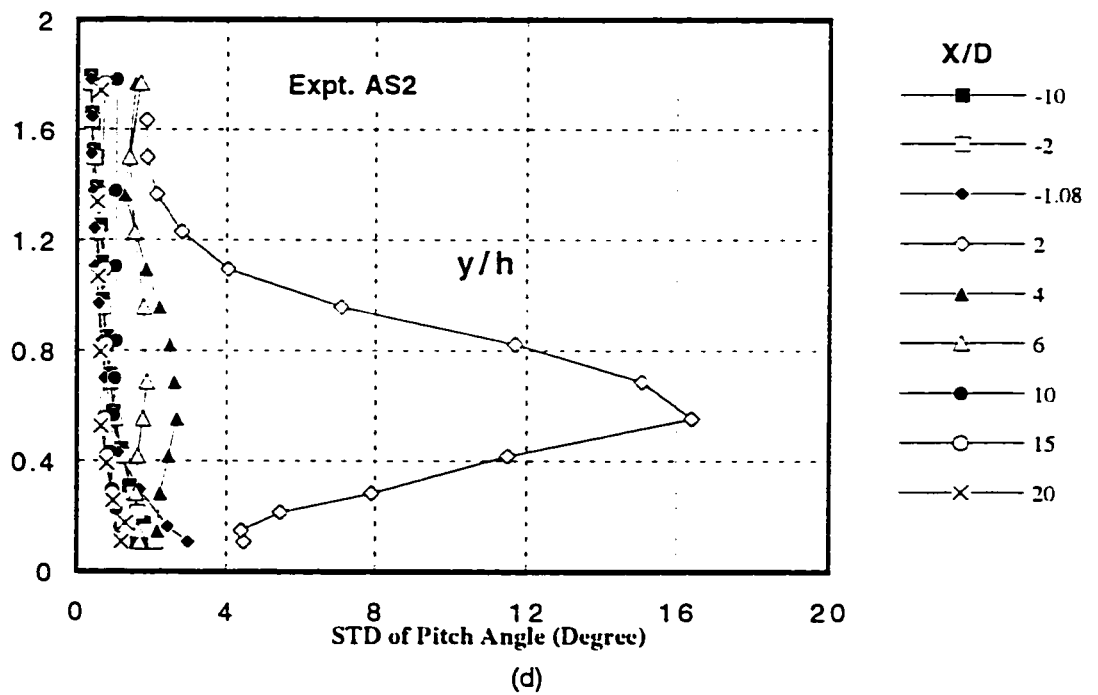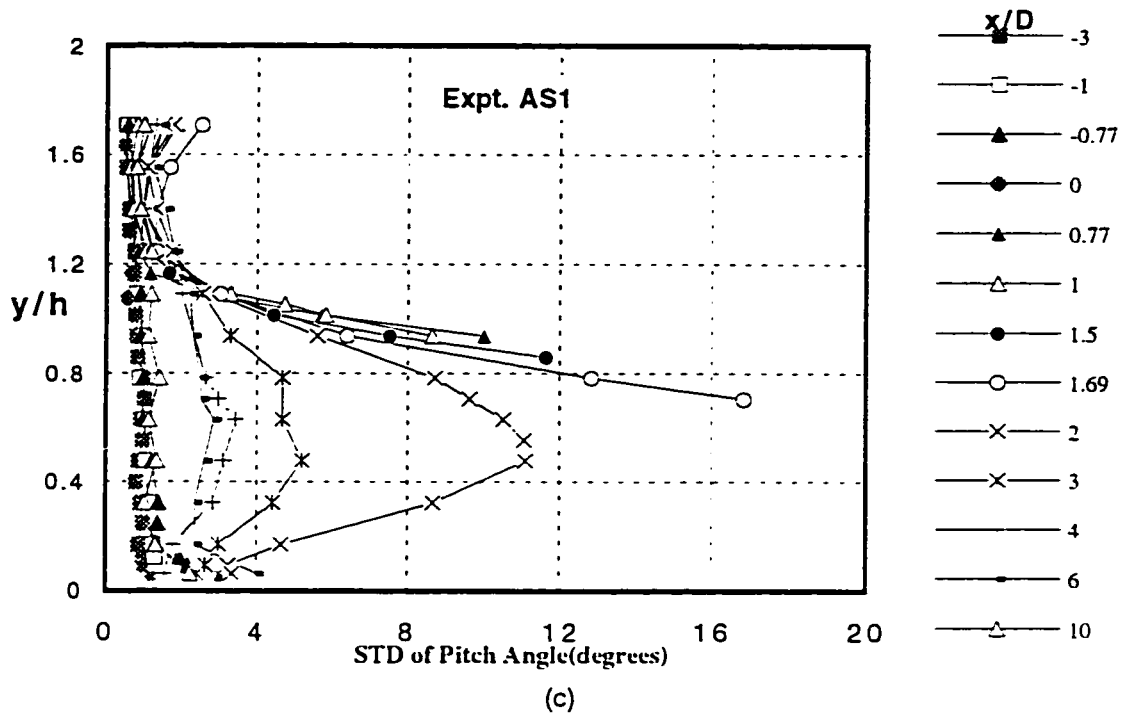
Figure 5.8 (c-d) Profiles of STD of Pitch Angles on the POS
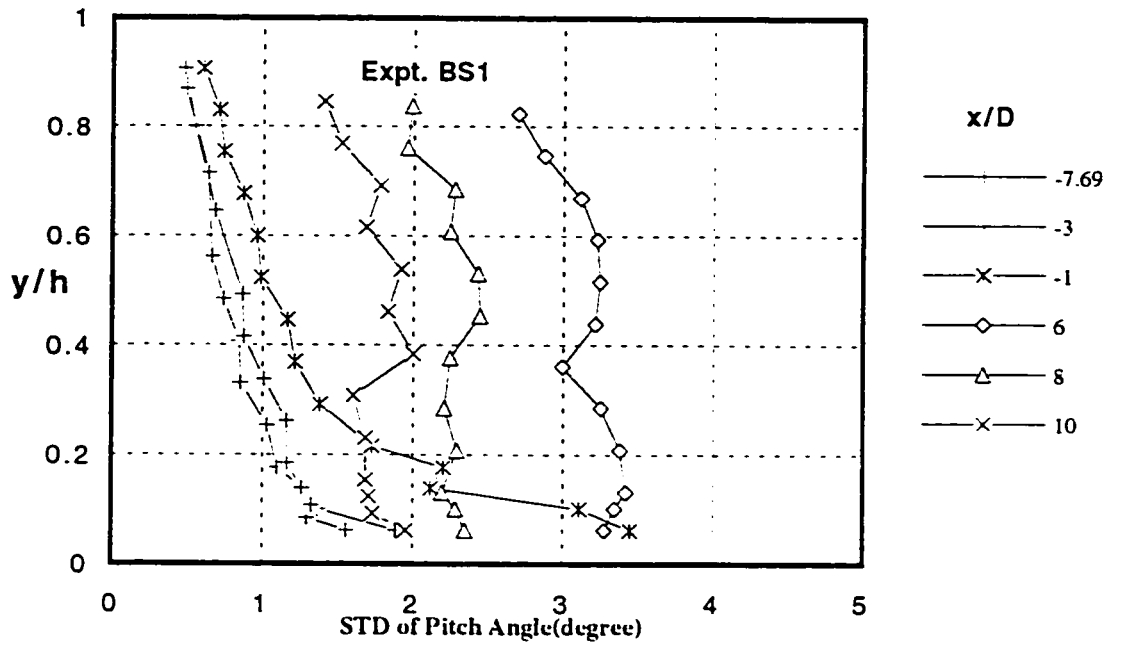
(e)
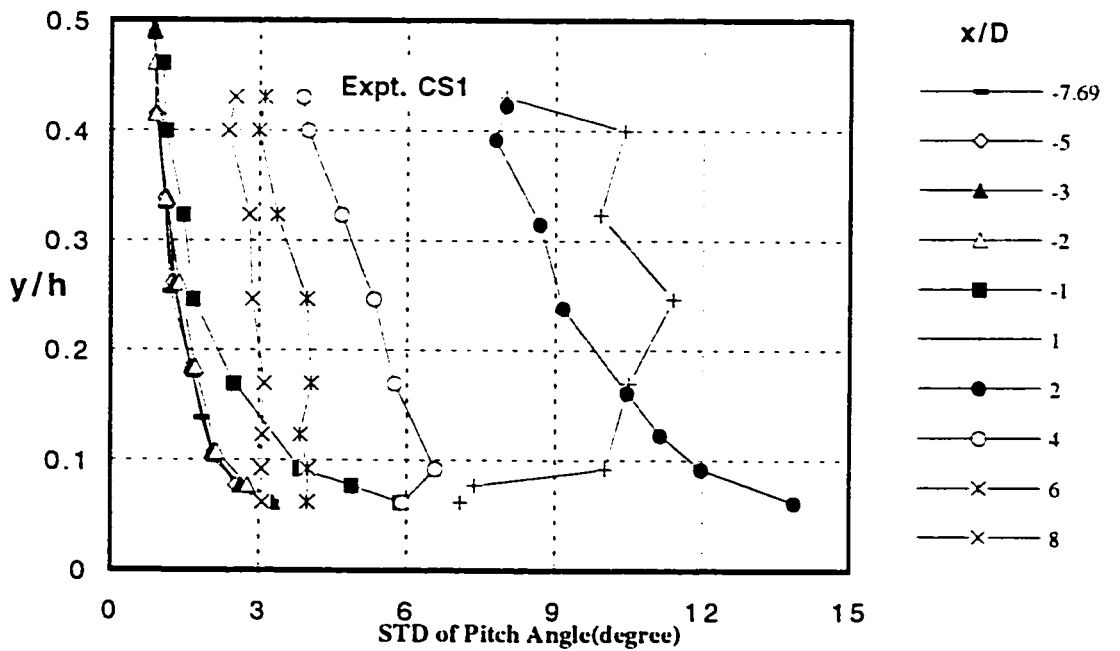
(f)

Figure 5.8 (e-f) Profiles of STD of Pitch Angles on the POS
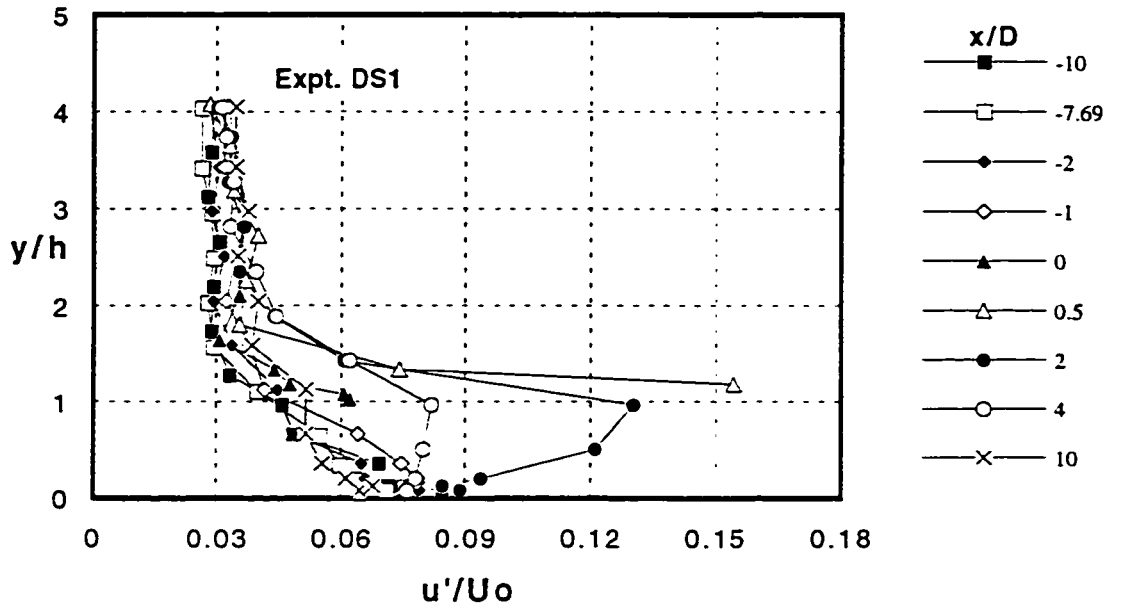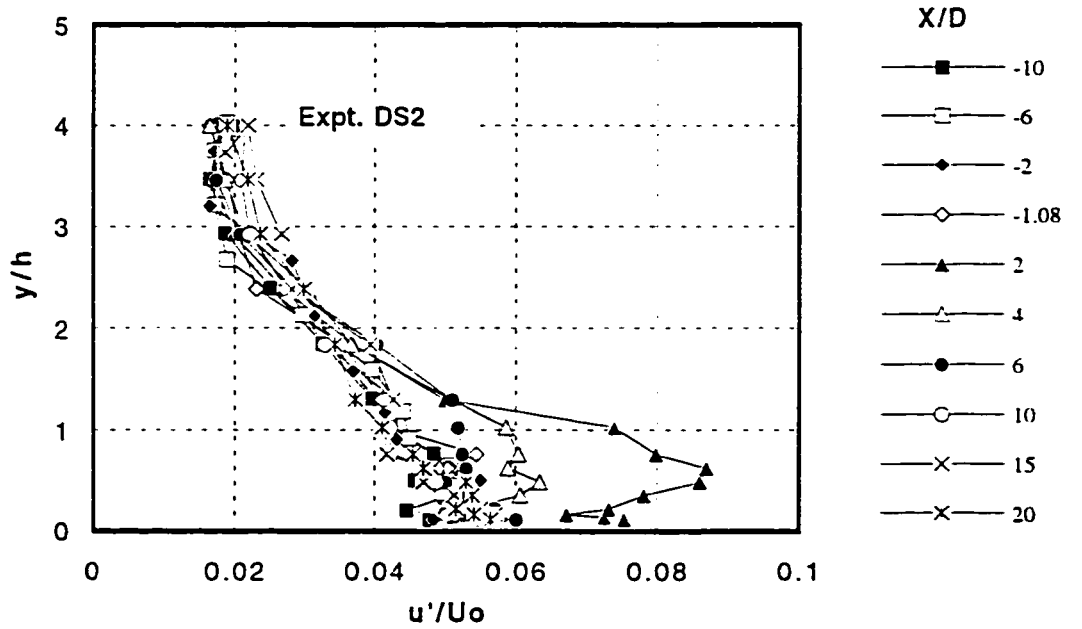
Figure 5.9 (a-b) Profiles of Normalized STD of Velocity on the POS
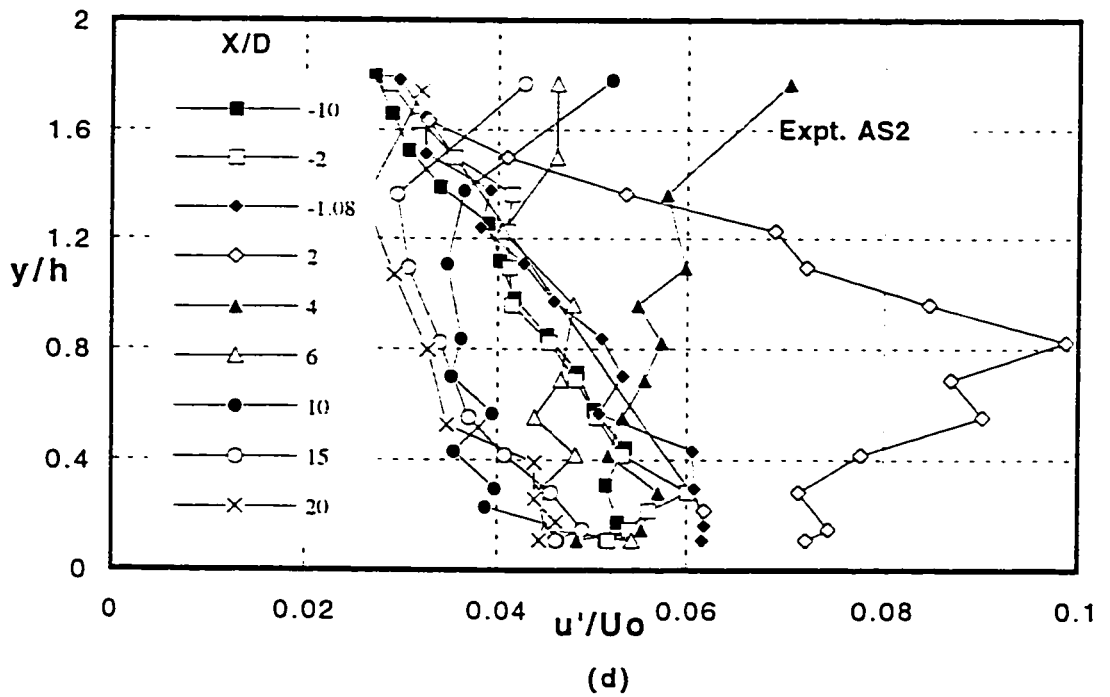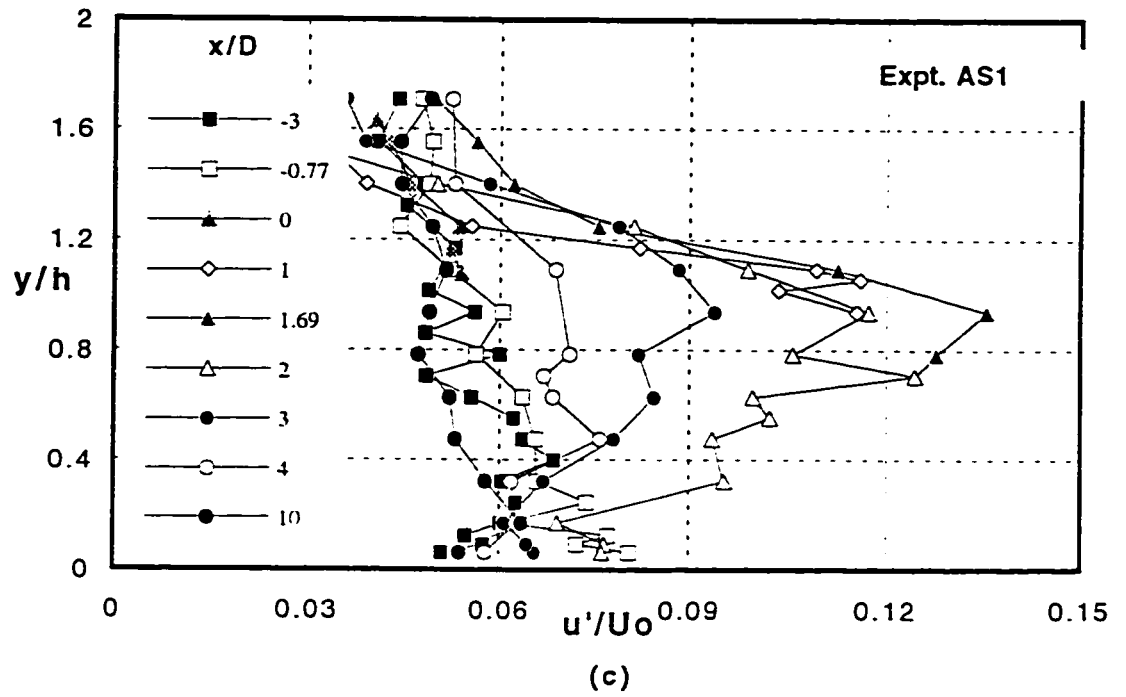
Figure 5.9 (c-d) Profiles of Normalized STD of Velocity on the POS

183
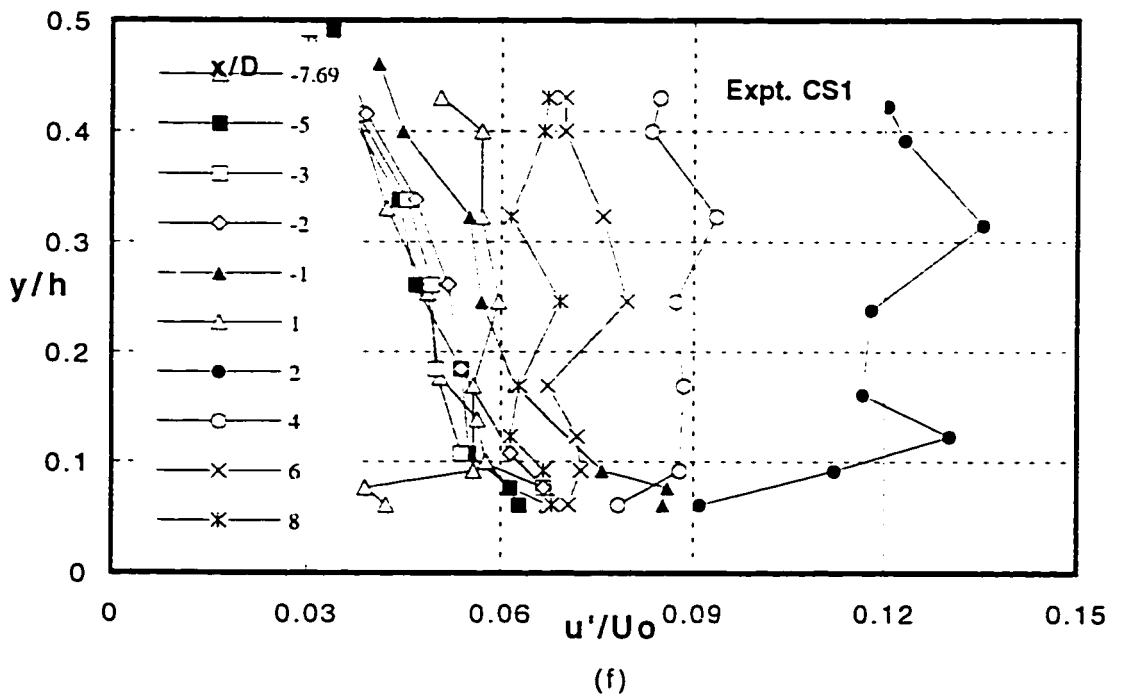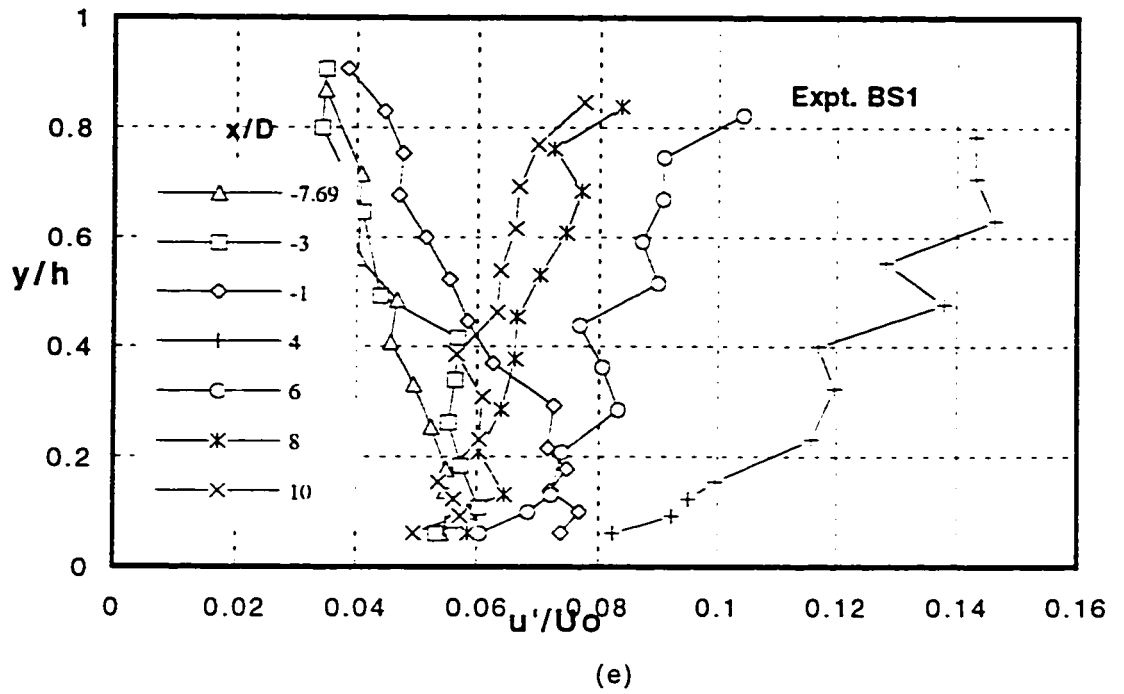
Figure 5.9 (e-f) Profiles of NormalizednSTD of Velocity on the POS

184
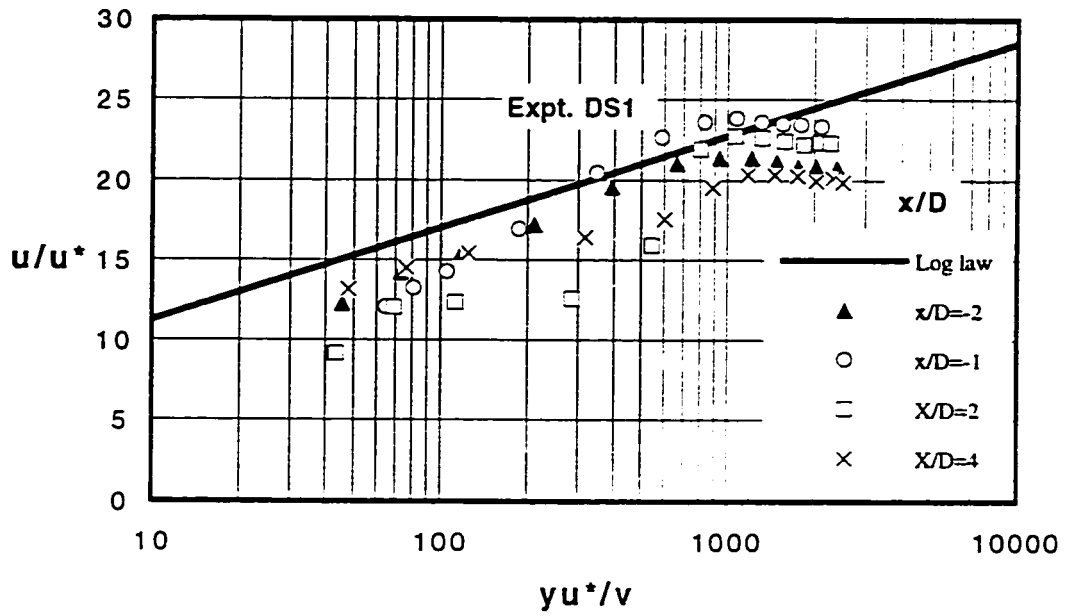
(a)
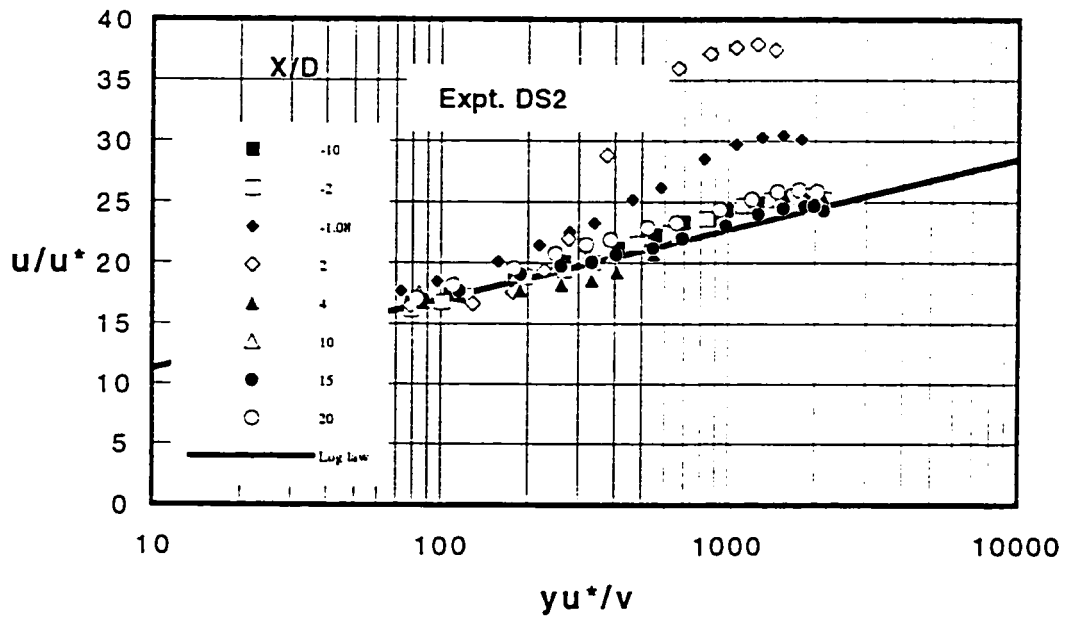
(b)

Figure 5.10 (a-b) Comparison of Velocity Profiles with Law of the Wall

185
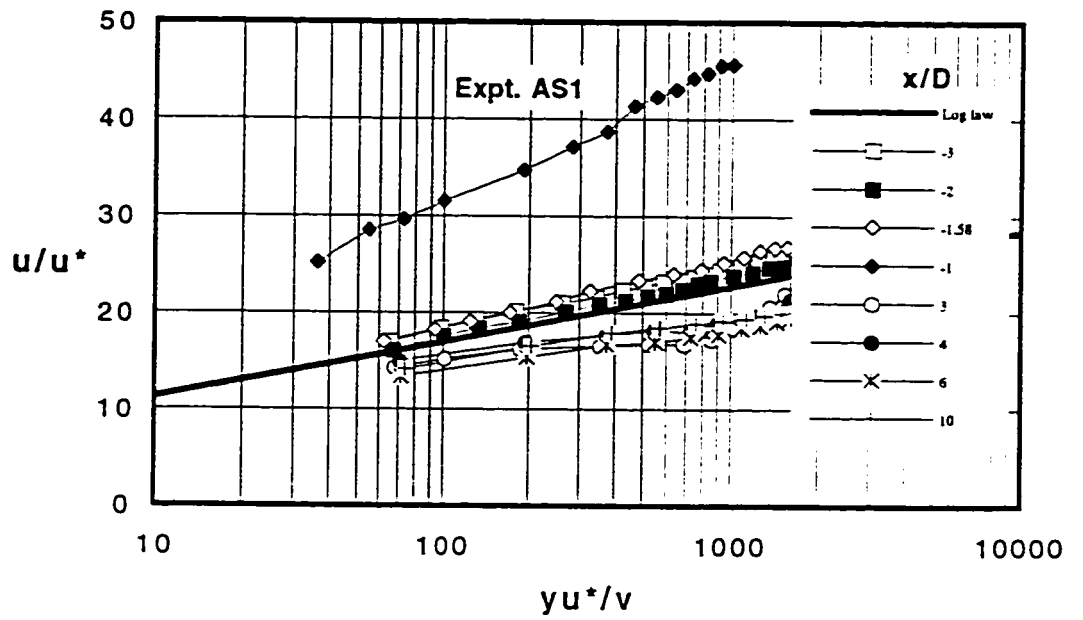
(c)
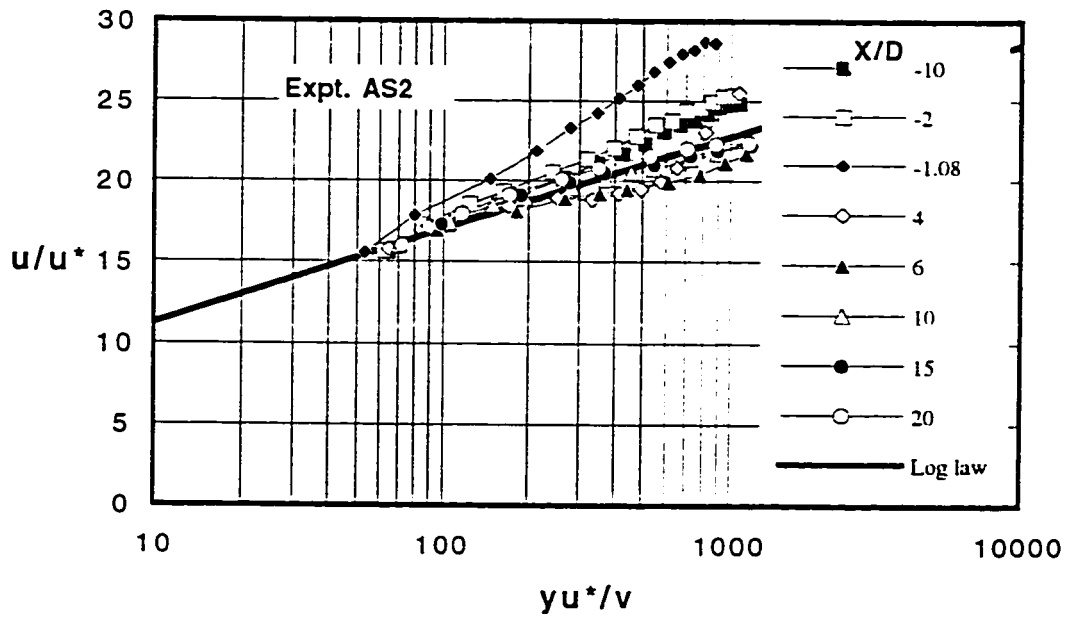
(d)

Figure 5.10 (c-d) Comparison of Velocity Profiles with the Law of the wall
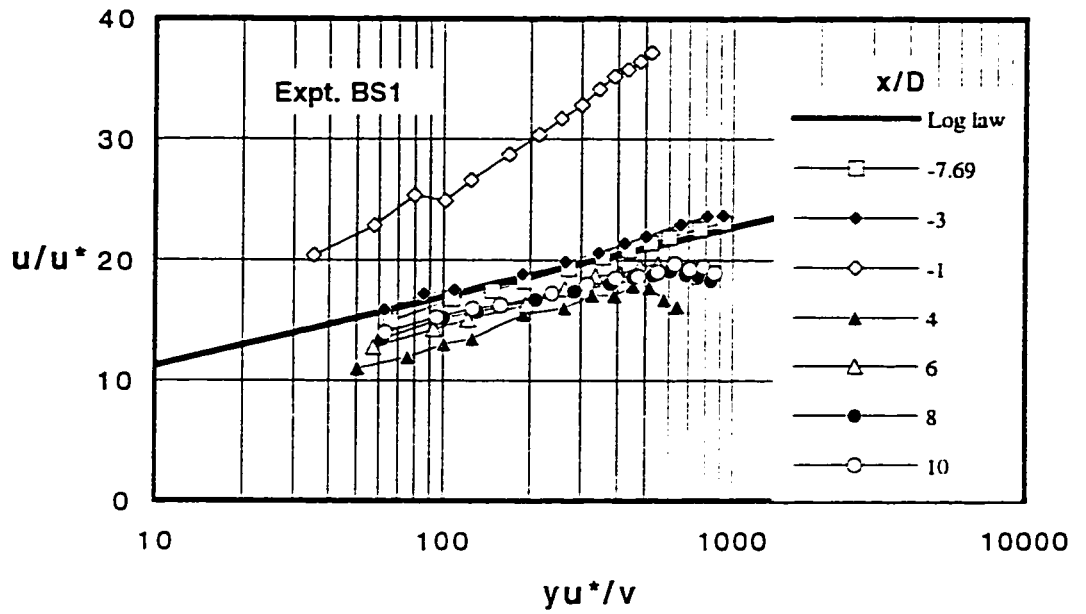
(e)
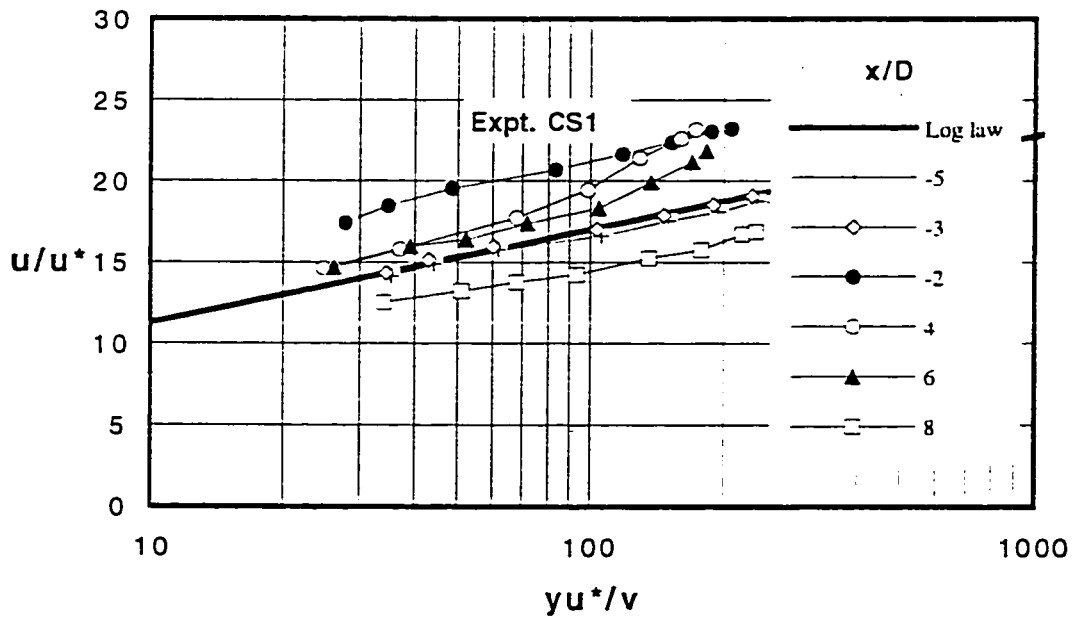
(f)

Figure 5.10 (e-f) Comparison of Velocity Profiles with the Law of the Wall
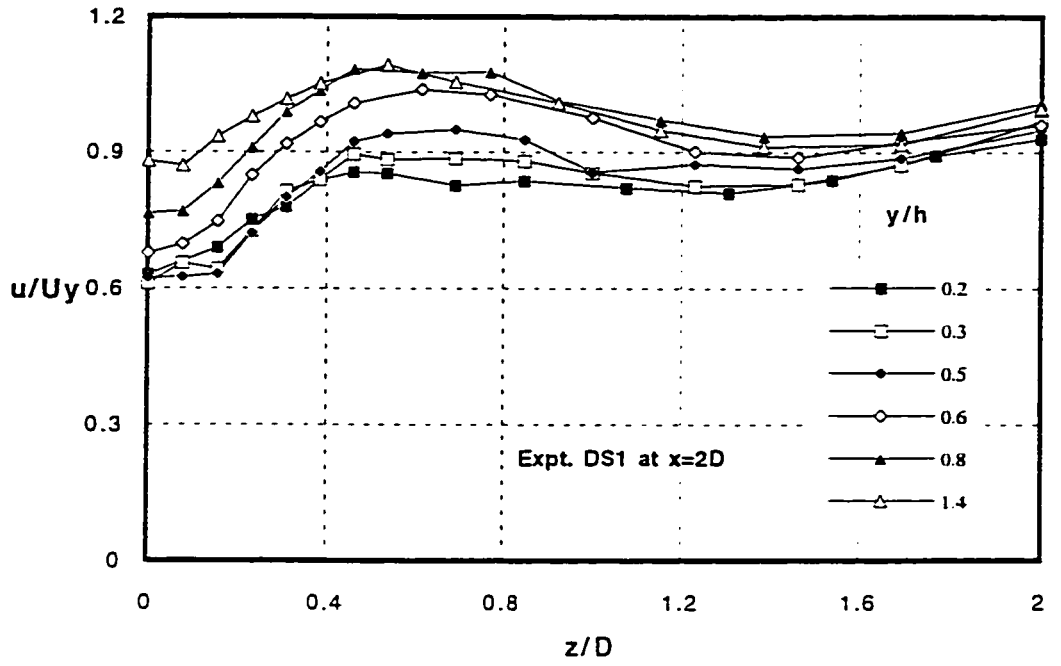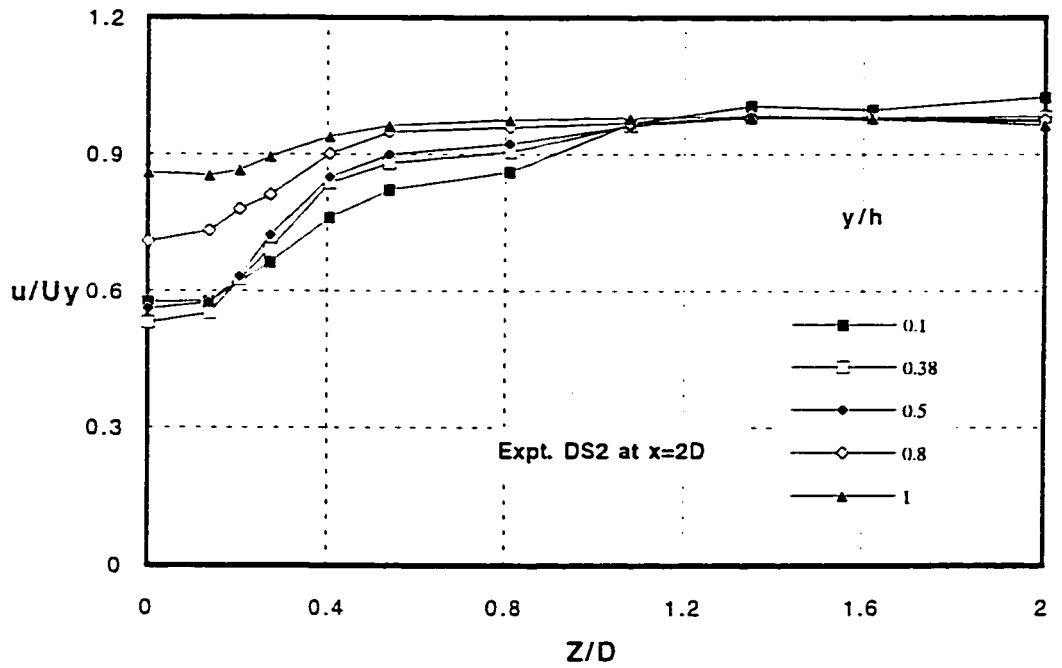
Figure 5.11 (a-b) Spanwise Profiles of Normalized Velocity at Different Depths

188
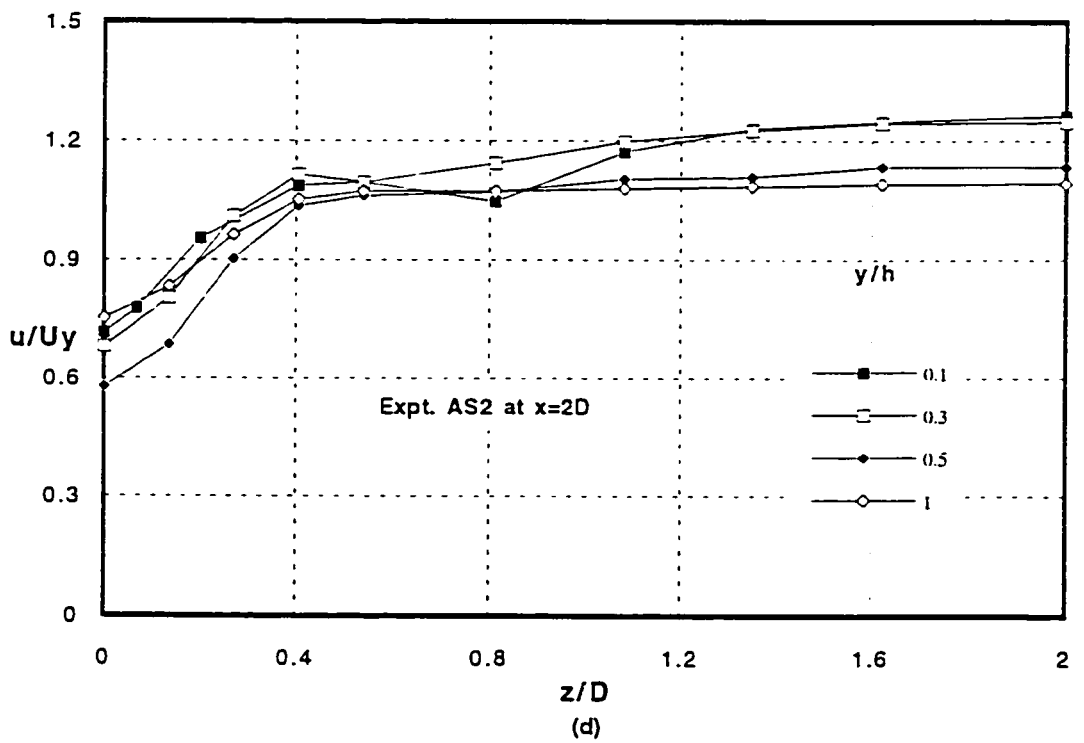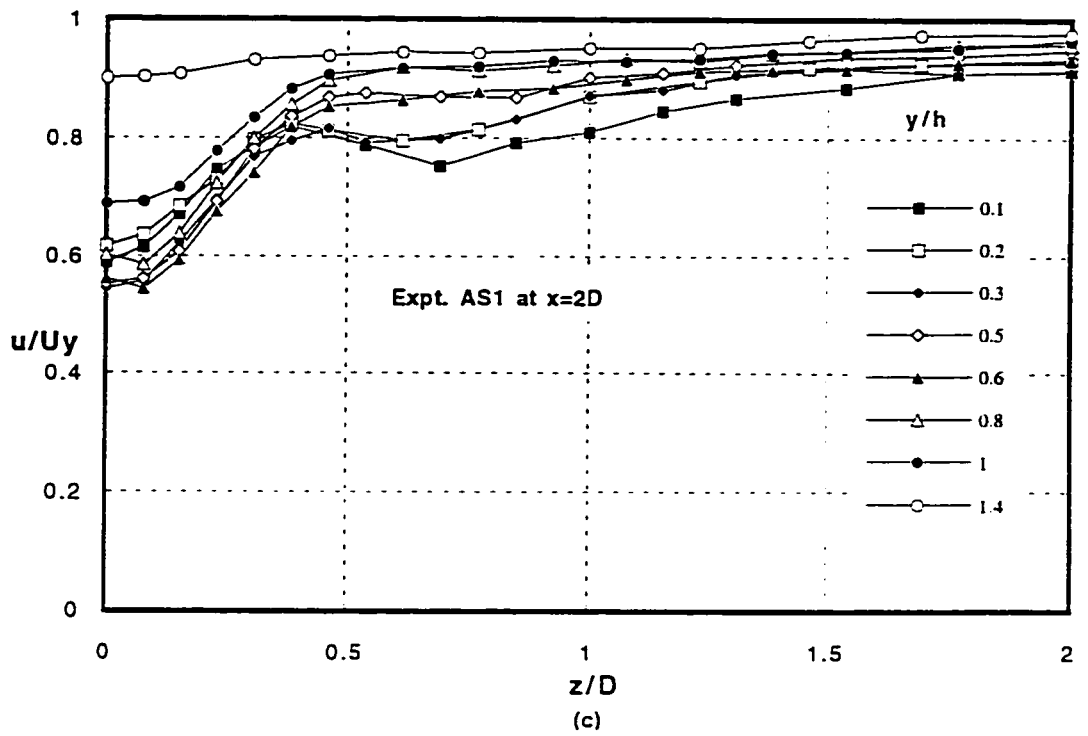
Figure 5.11 (c-d) Spanwise Profiles of Normalized Velocity at Different depths
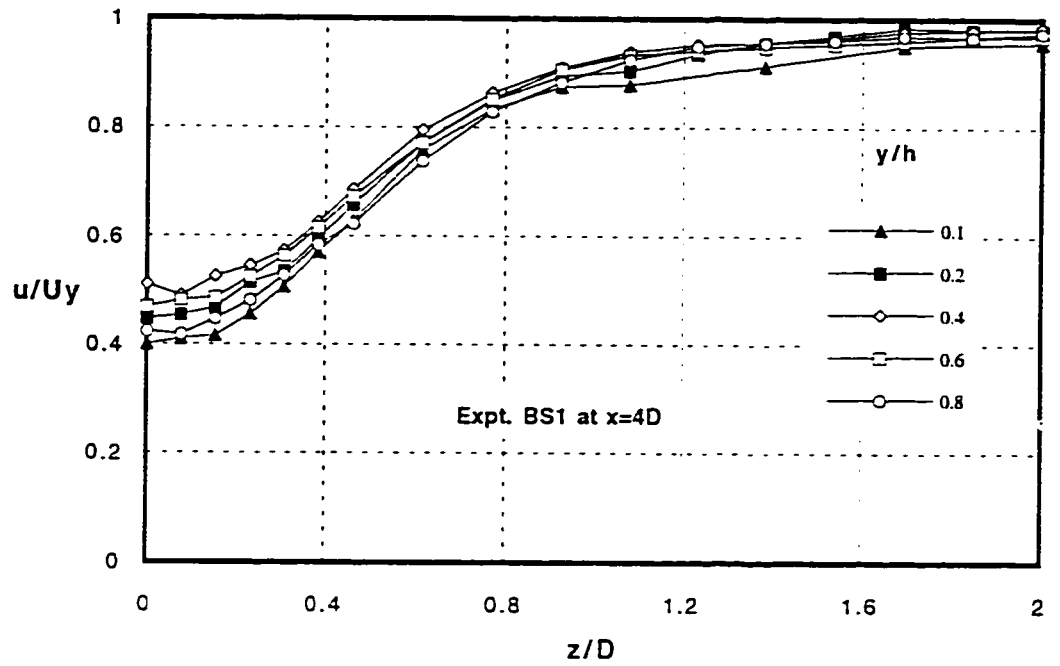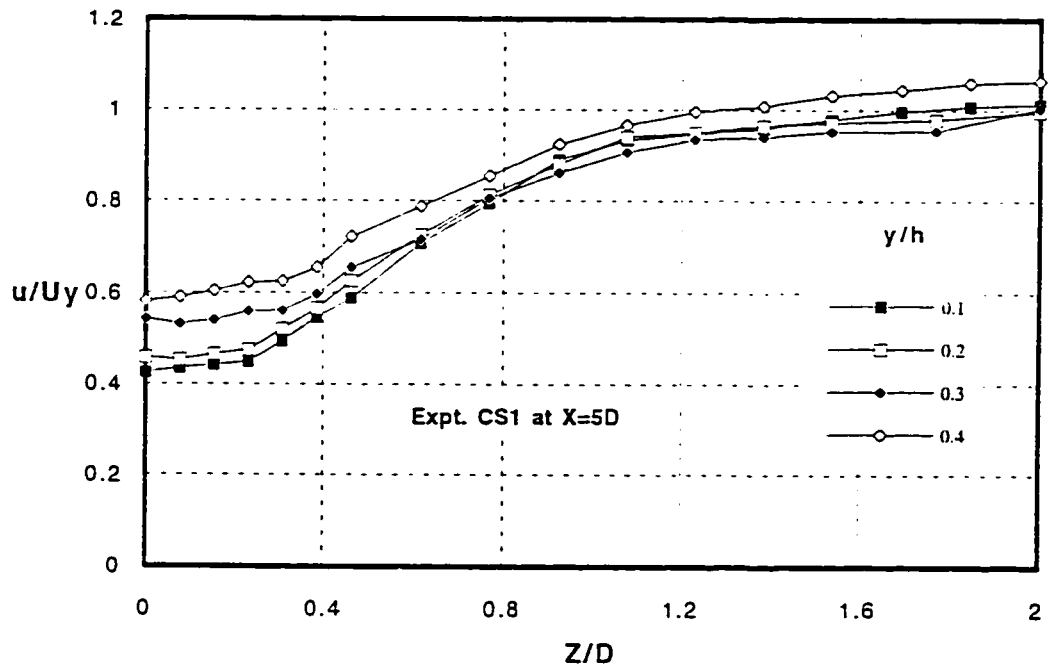
Figure 5.11 (e-f) Spanwise Profiles of Normalized Velocity at Different Depths
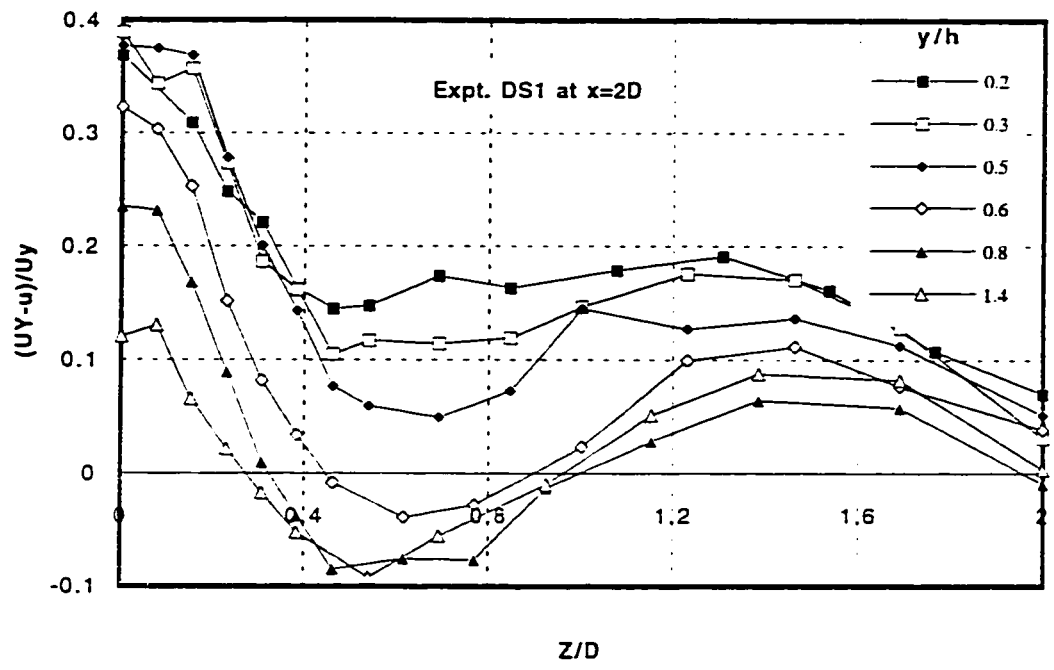
(c)
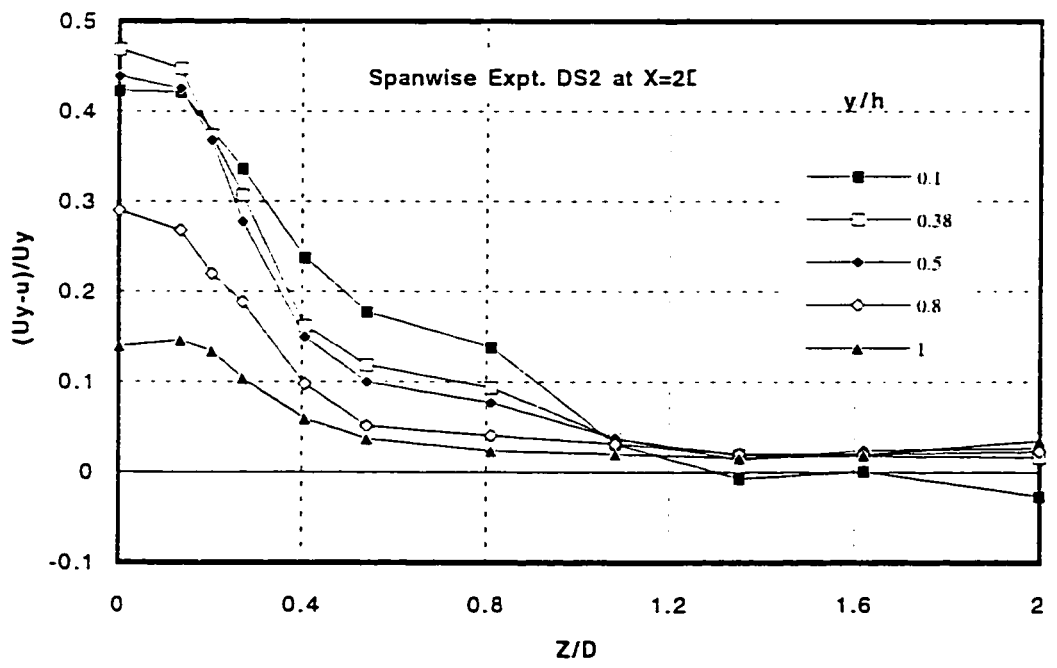
(d)

Figure 5.12 (a-b) Spanwise Profiles of Defect Velocity at Different Depths
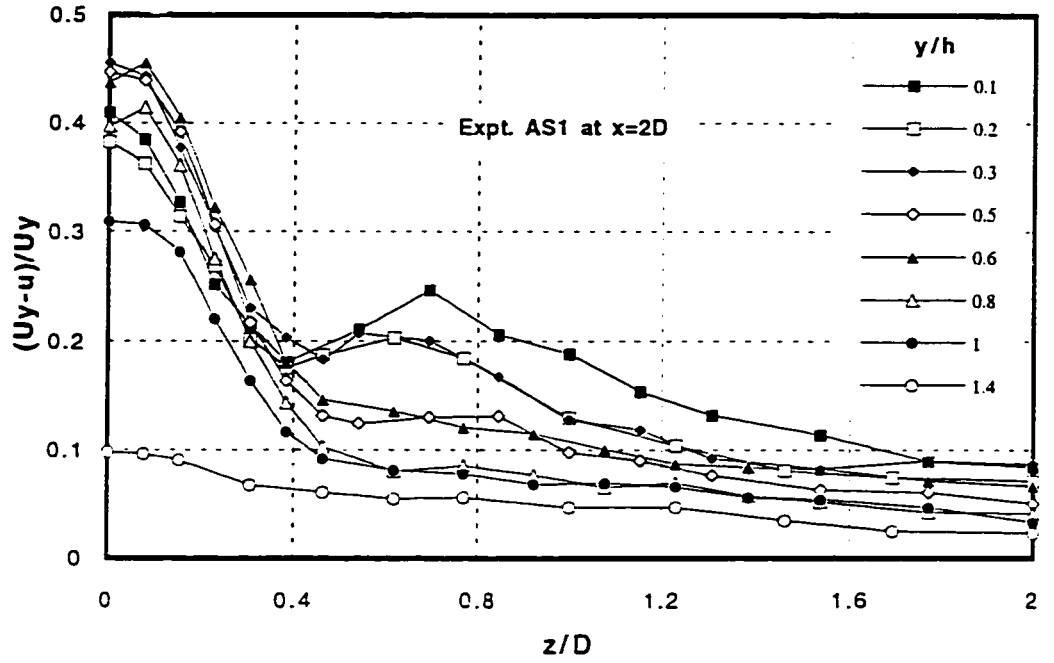
(c)
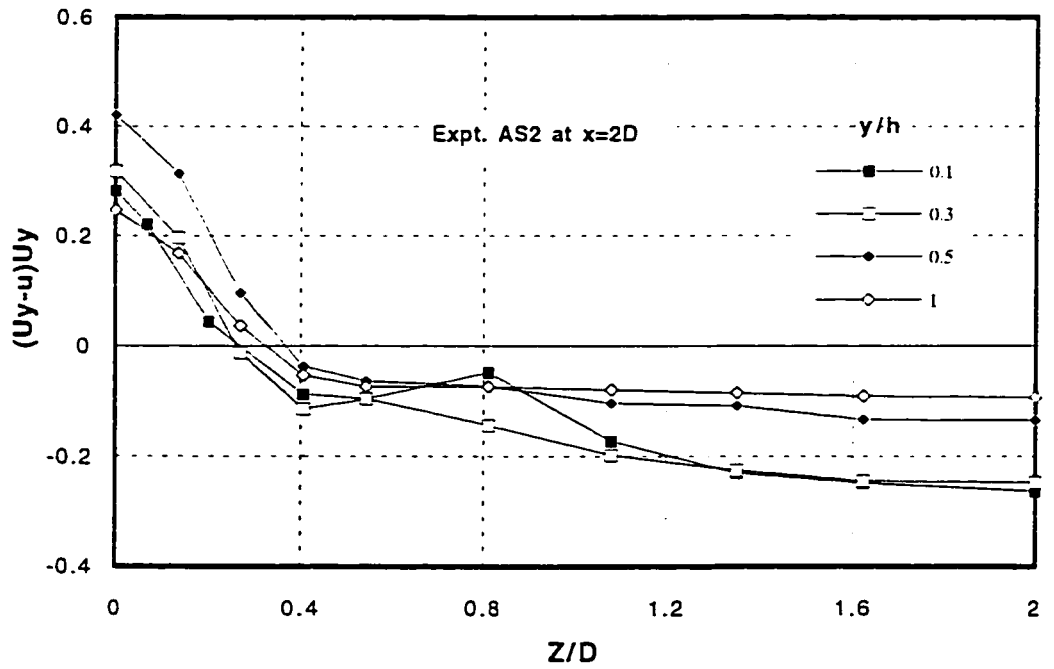
(d)

Figure 5.12 (c-d) Spanwise Profiles of Defect Velocity at Different Depths
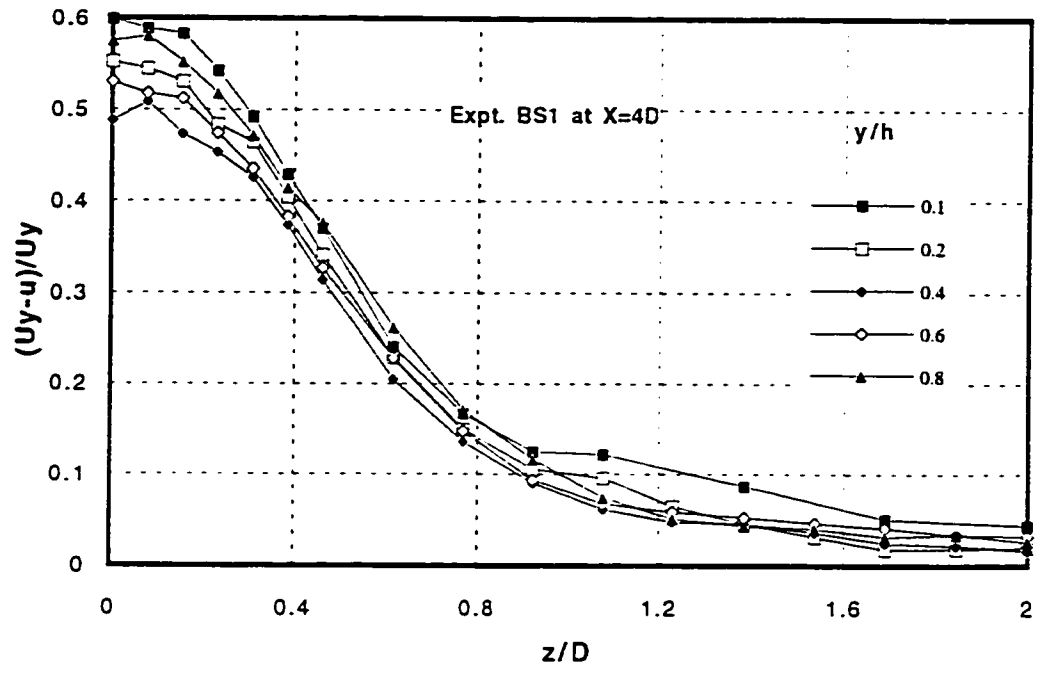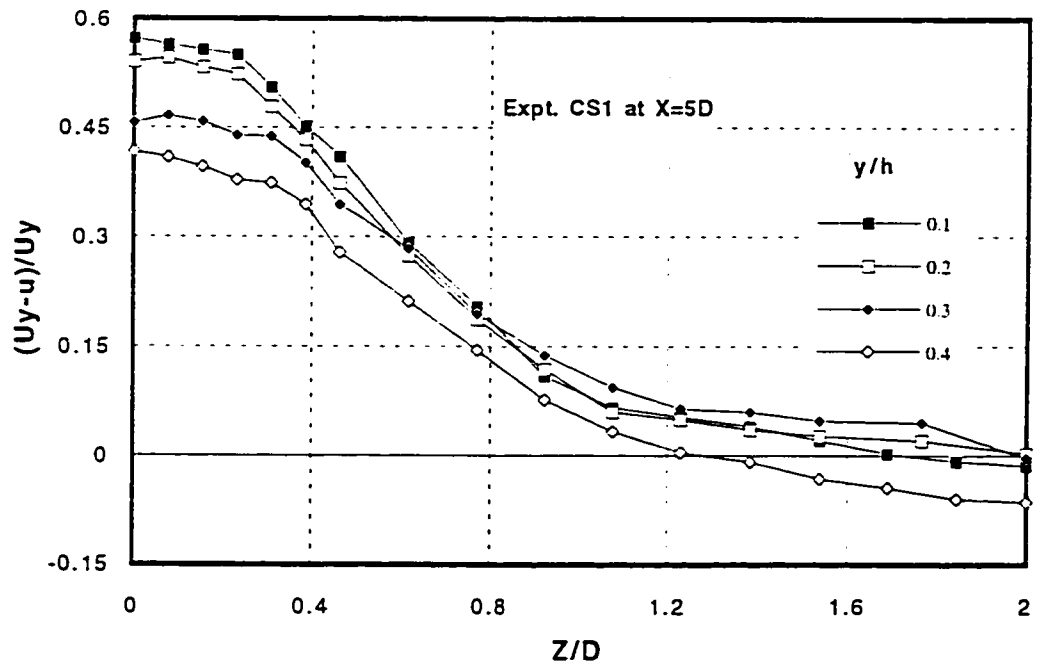
Figure 5.12 (e-f) Spanwise Profiles of Defect Velocity at Different Depths
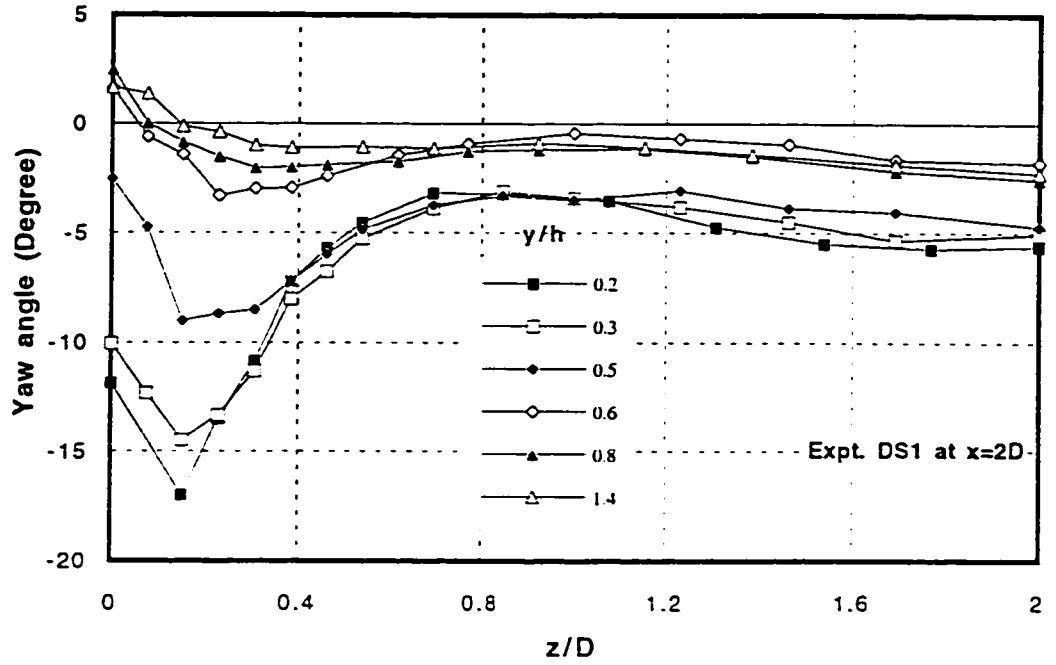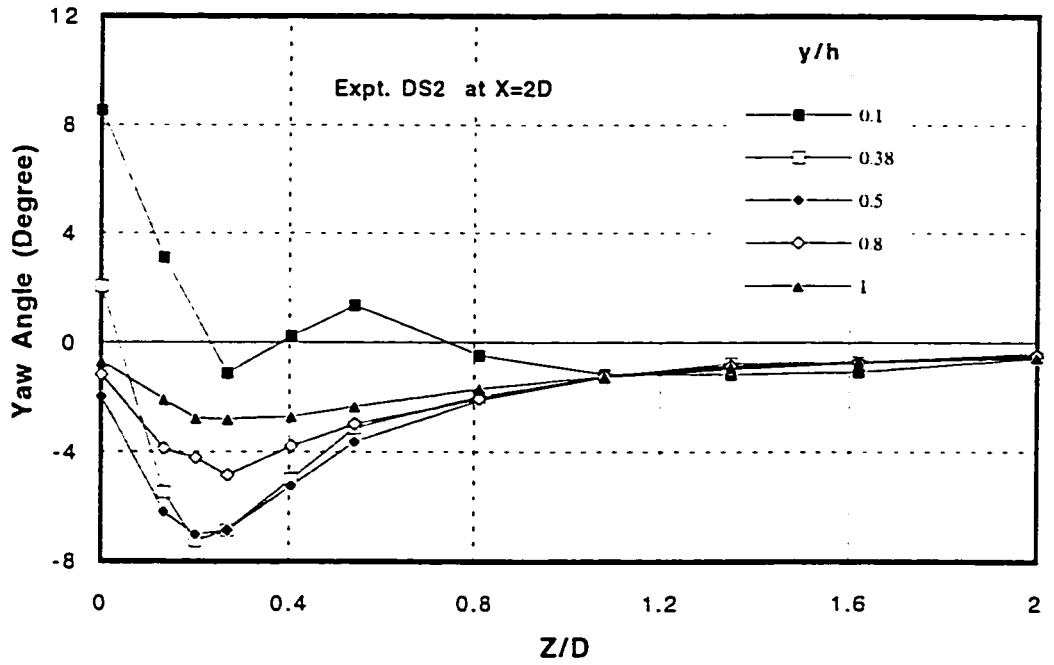
Figure 5.13 (a-b) Spanwise Profiles of yaw Angles at Different Depths
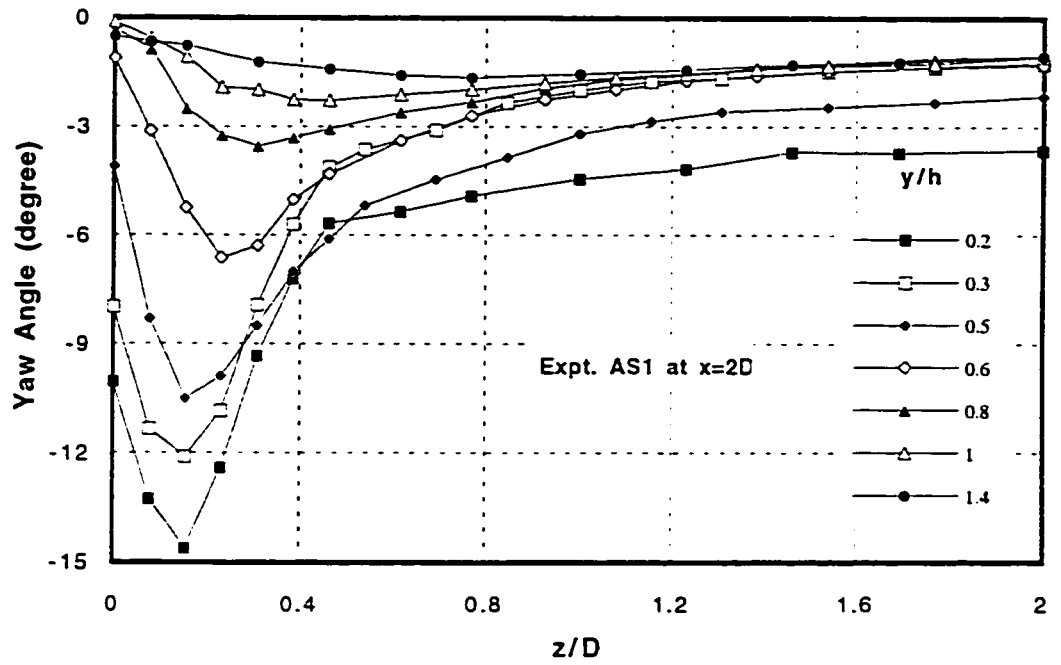
(c)
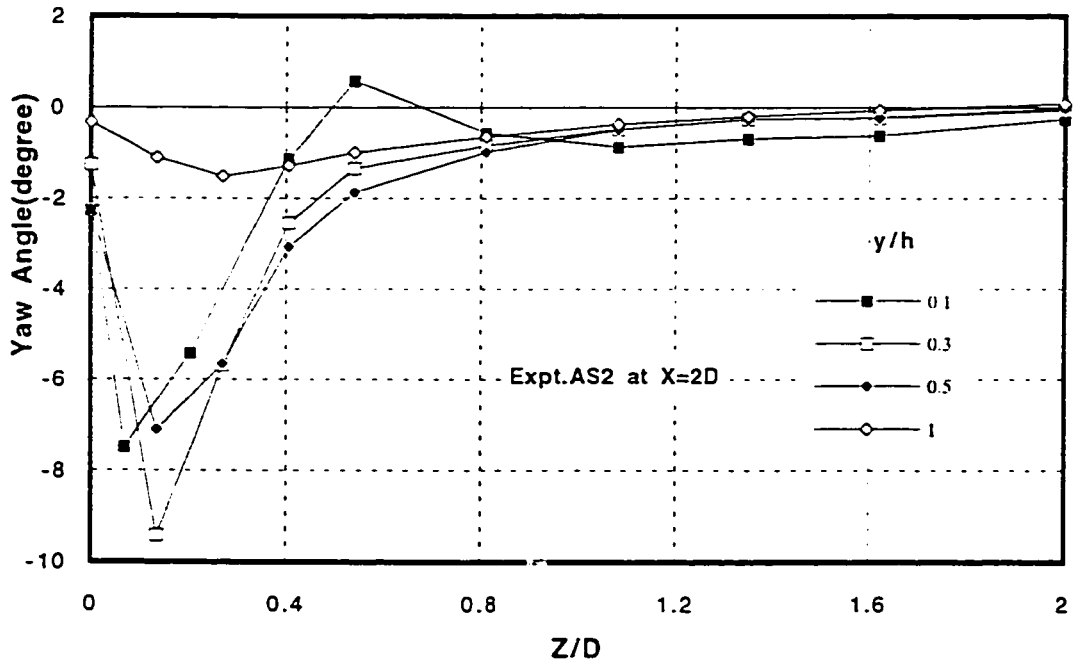
(d)

Figure 5.13 (c-d) Spanwise Profiles of yaw Angles at Different Depths

195
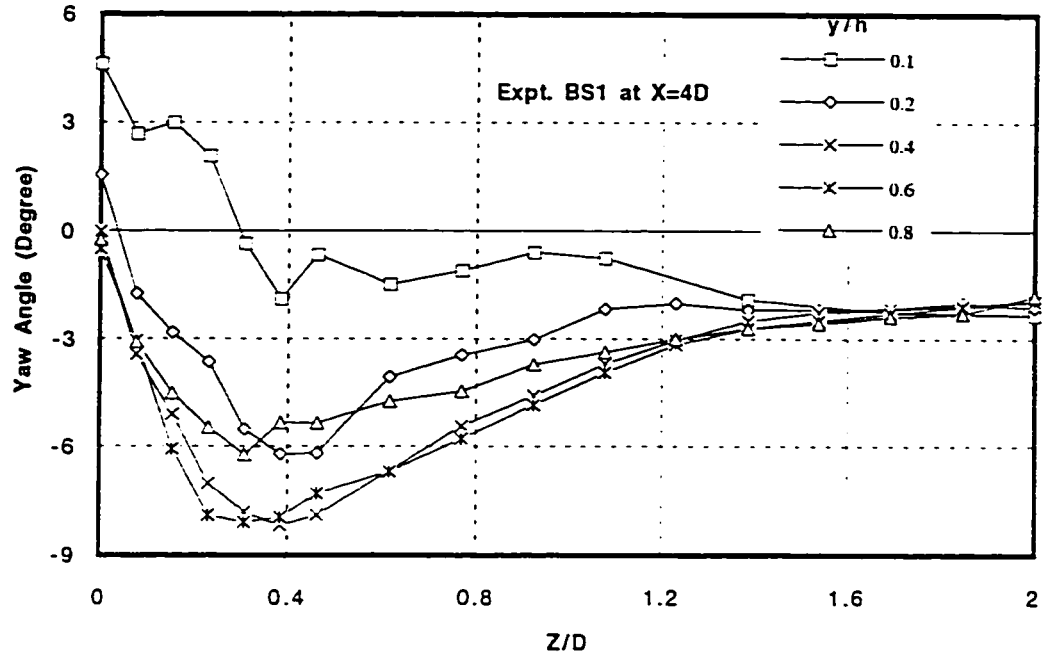
(e)
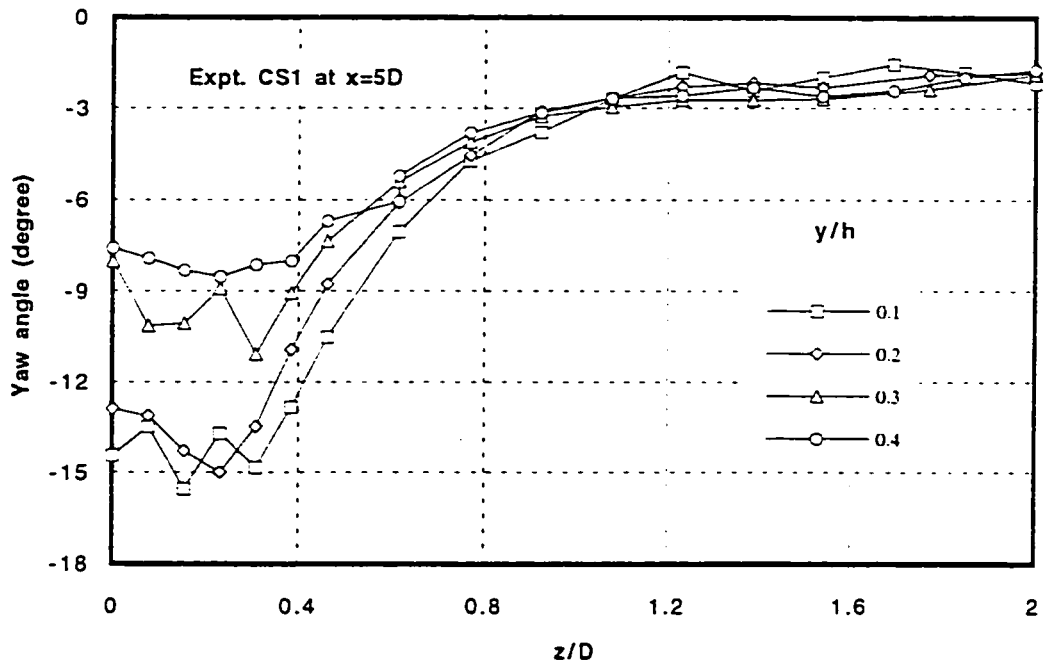
(f)

Figure 5.13 (e-f) Spanwise Profiles of Yaw Angles at Different Depths

196
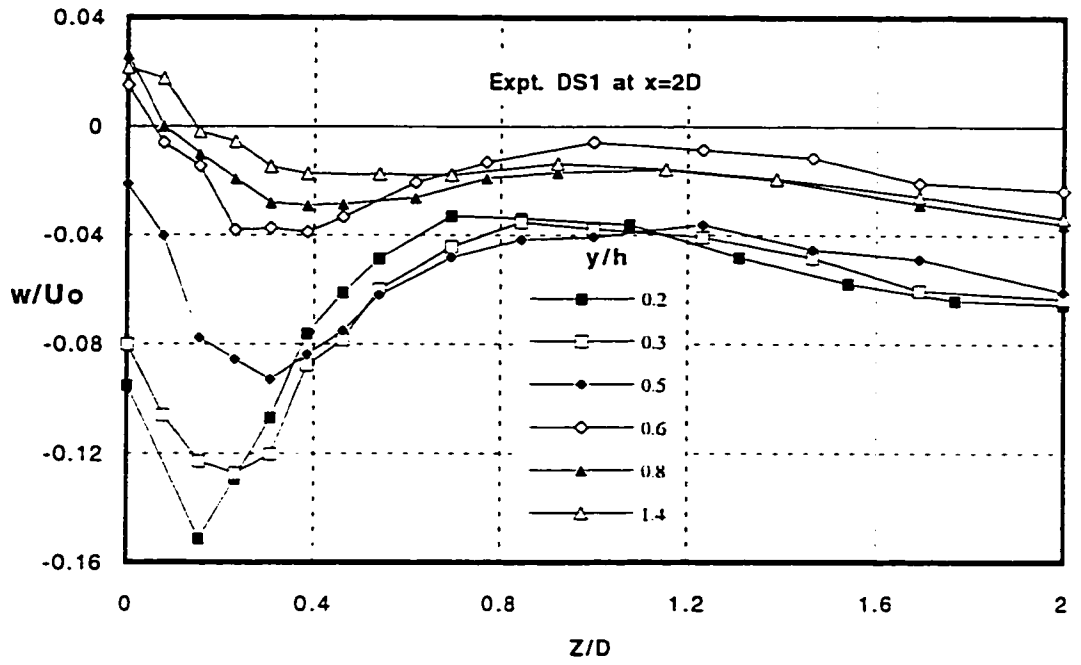
(a)
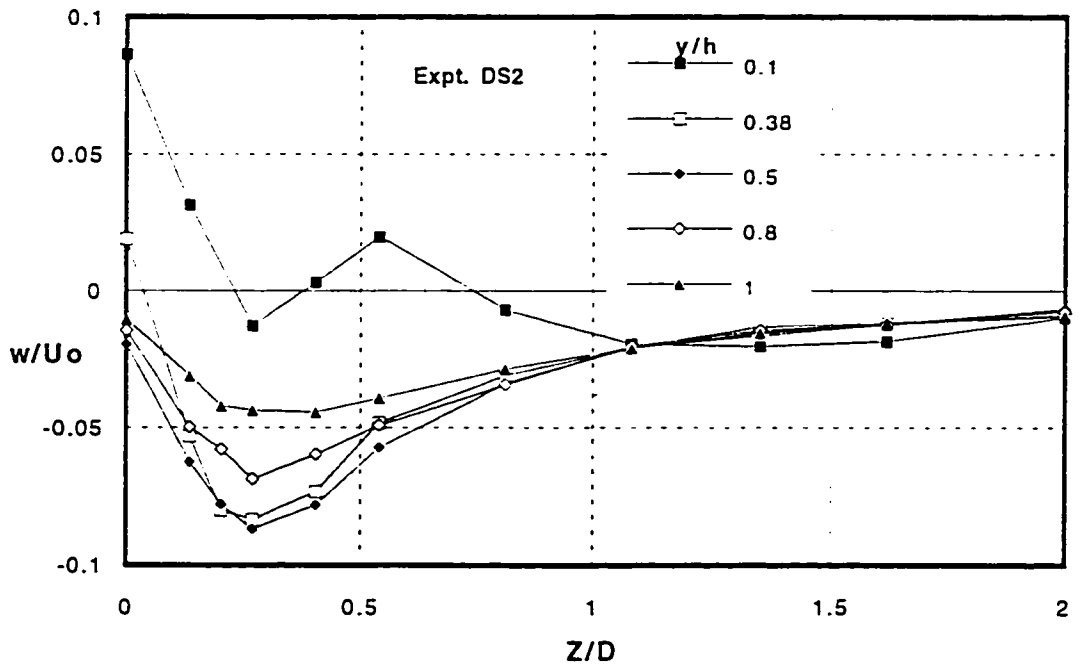
(b)

Figure 5.14 (a-b) Spanwise Profiles of Normalized lateral Velocity at Different Depths
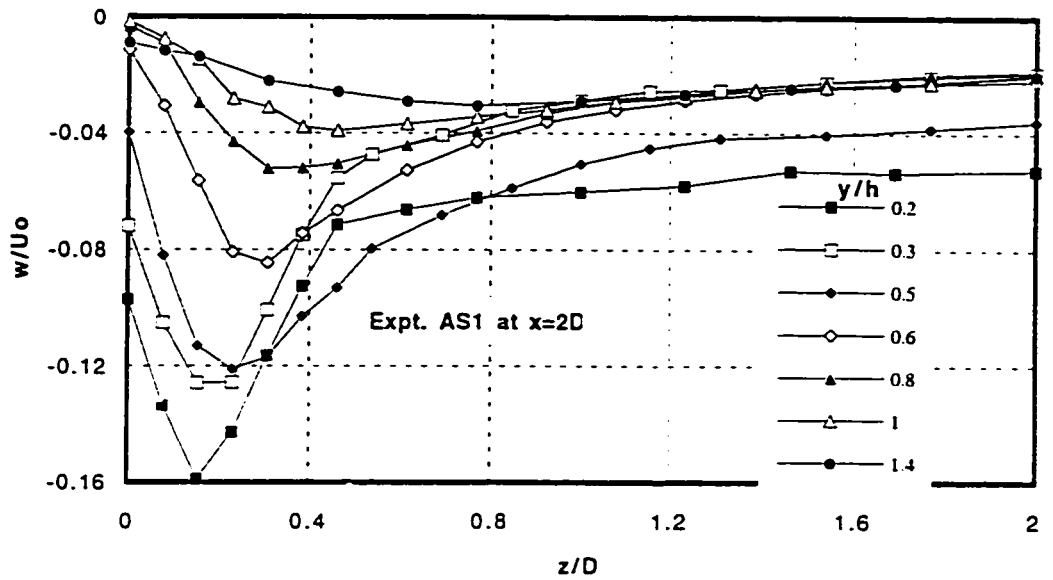
(c)
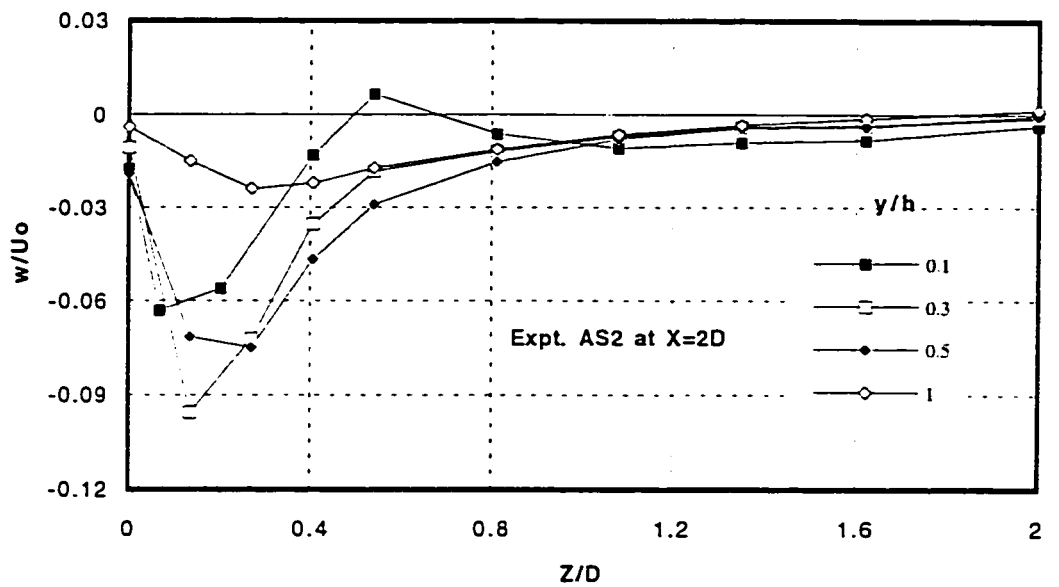
(d)

Figure 5.14 (c-d) Spanwise Profiles of Normalized lateral Velocity
at Different Depths
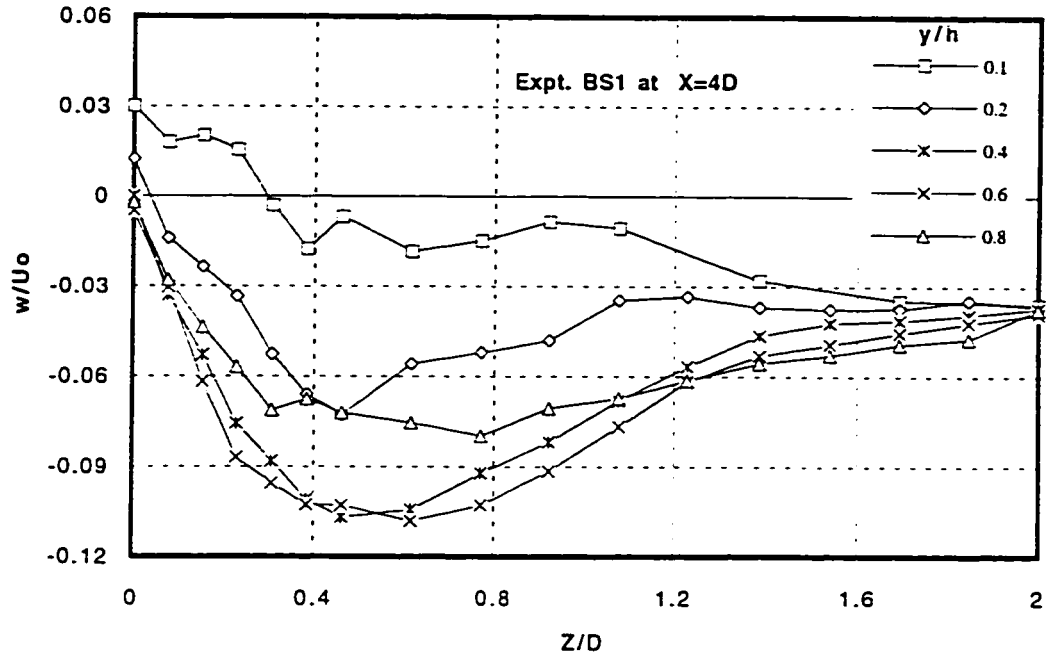
(e)
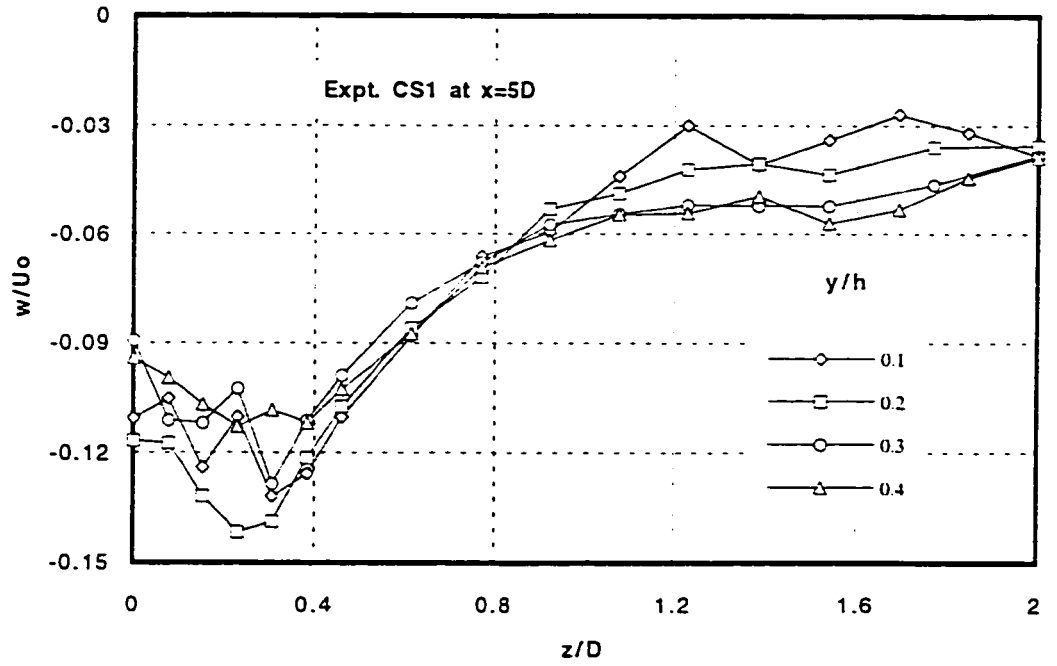
(f)

Figure 5.14 (e-f) Spanwise Profiles of Normalized lateral Velocity at Different Depths

199
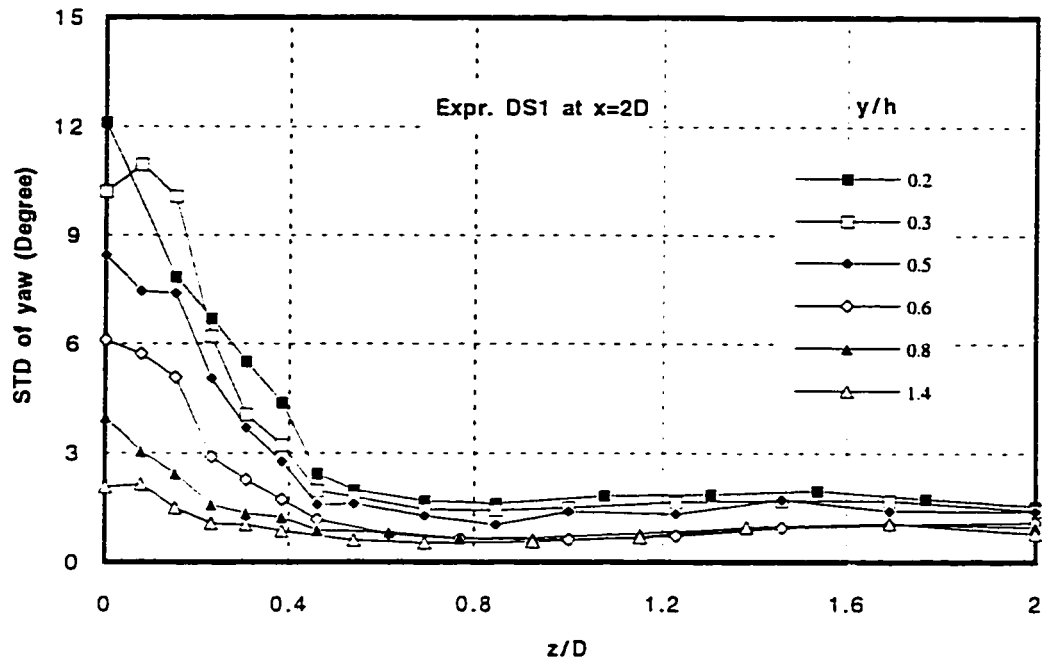
(a)
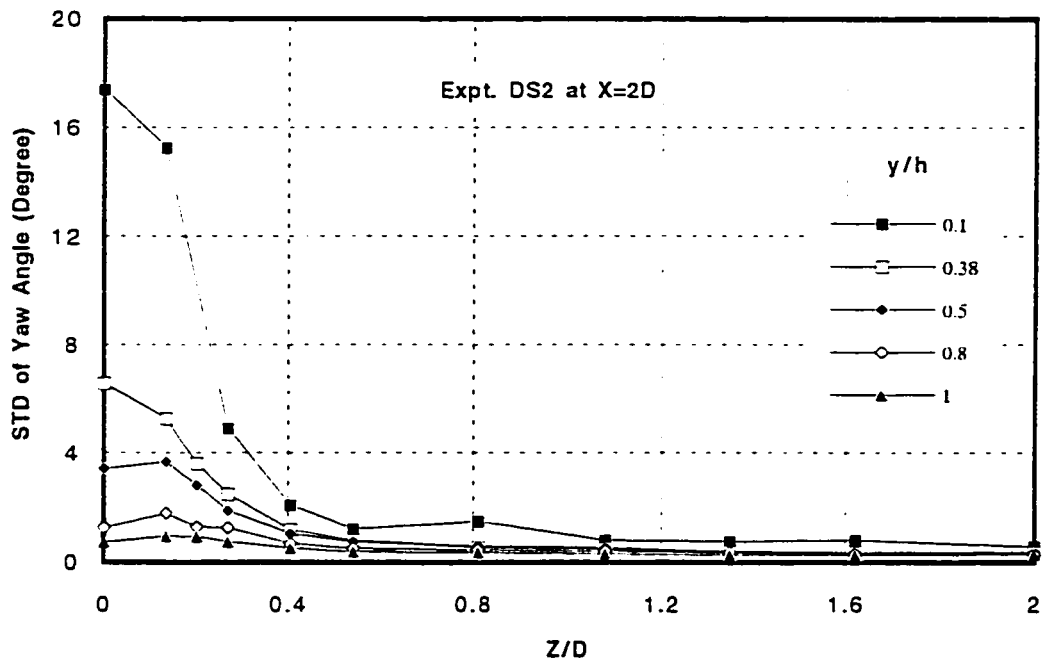
(b)

Figure 5.15 (a-b) Spanwise Profiles of STD of Yaw Angle at Different Depths

200
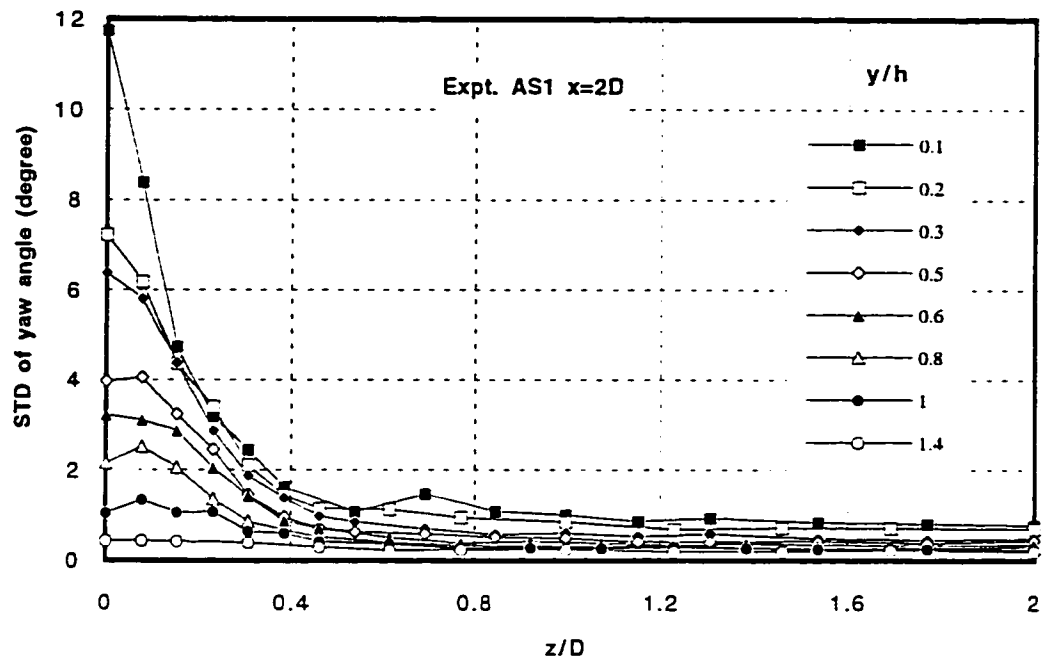
(c)
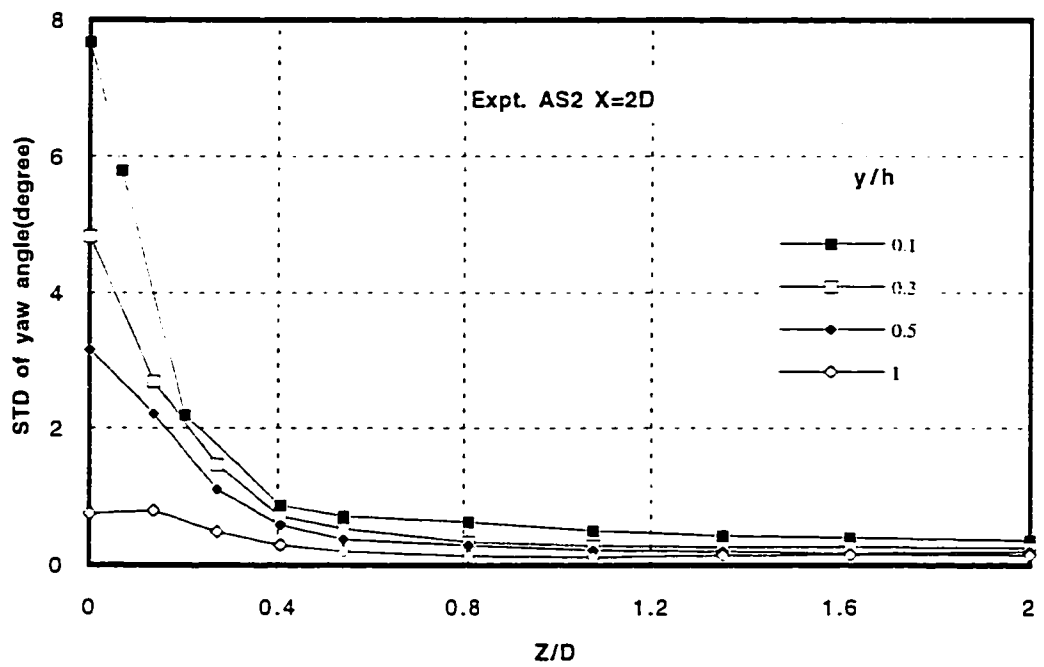
(d)

Figure 5.15 (c-d) Spanwise Profiles of STD of Yaw Angle at Different Depths
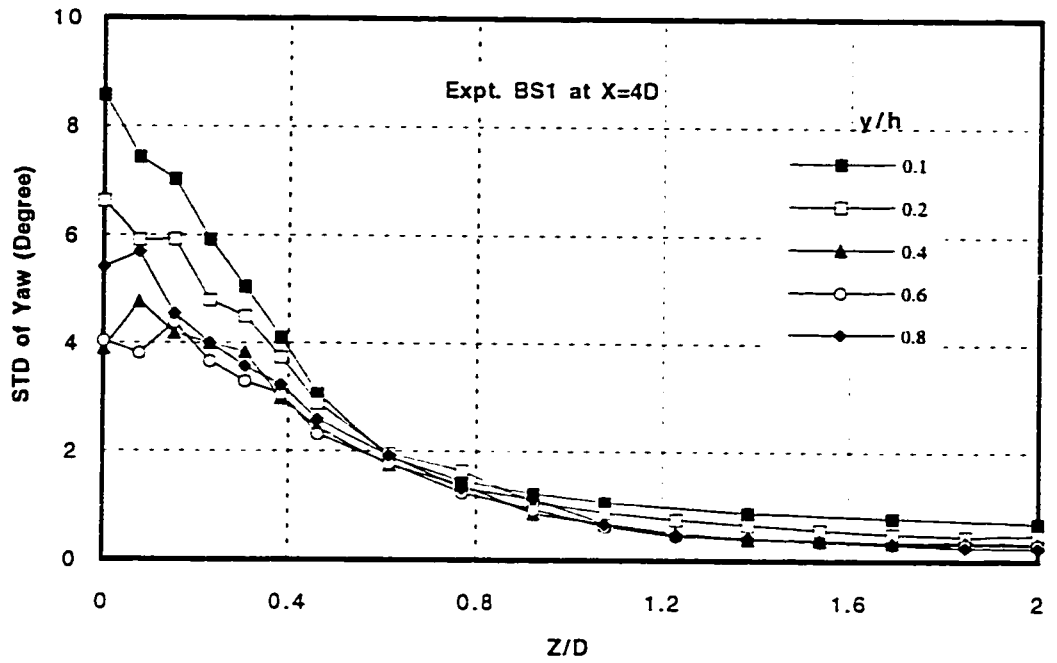
(e)
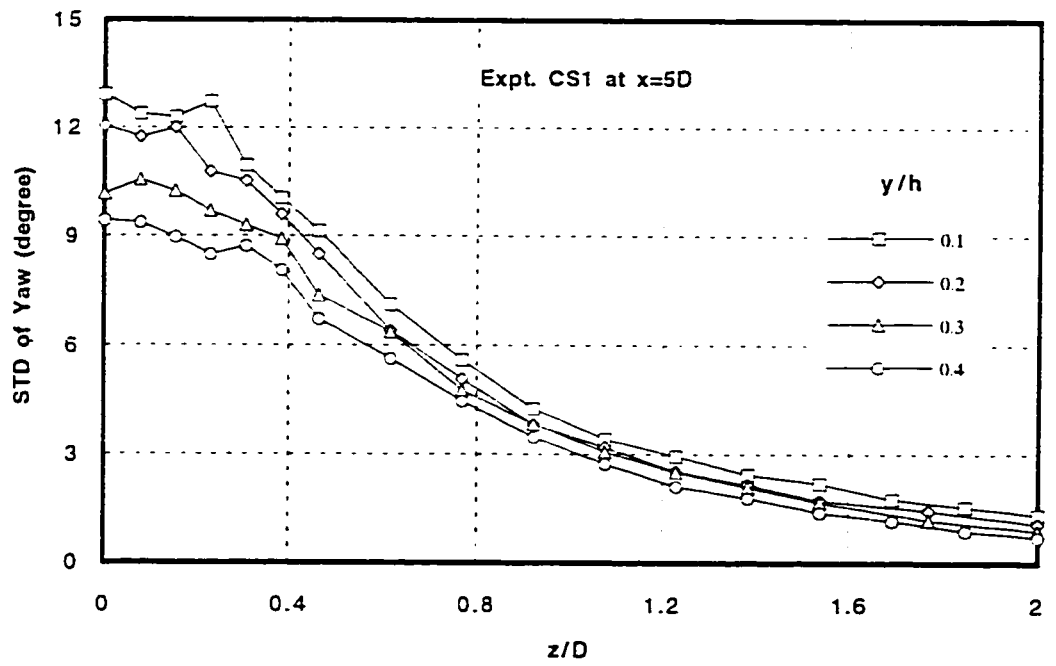
(f)

Figure 5.15 (e-f) Spanwise Profiles of STD of Yaw Angle at Different Depths
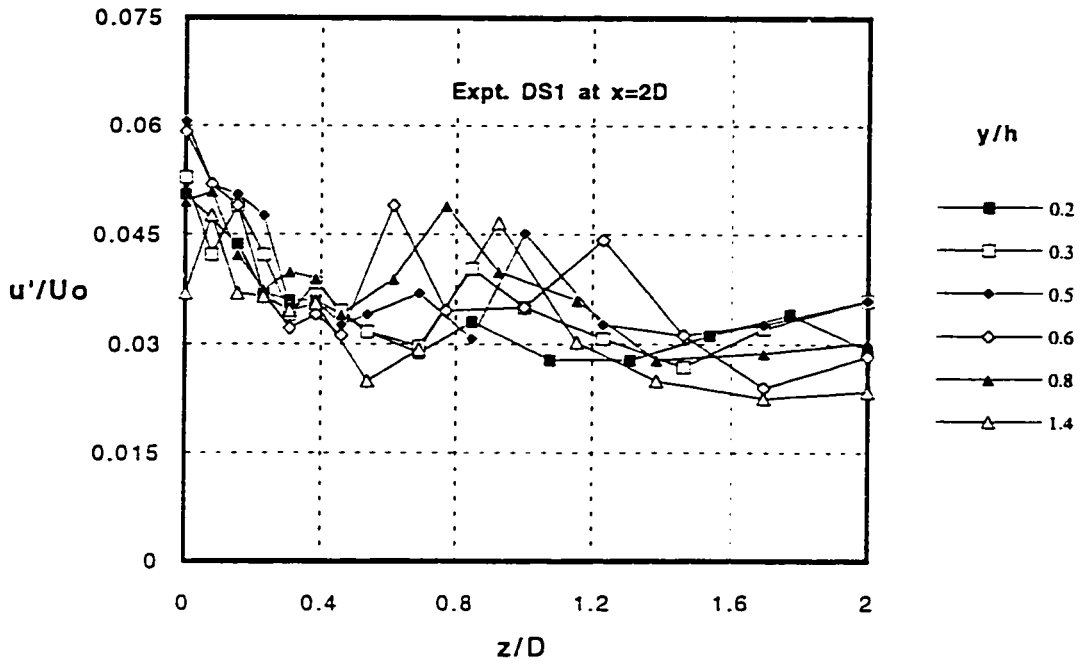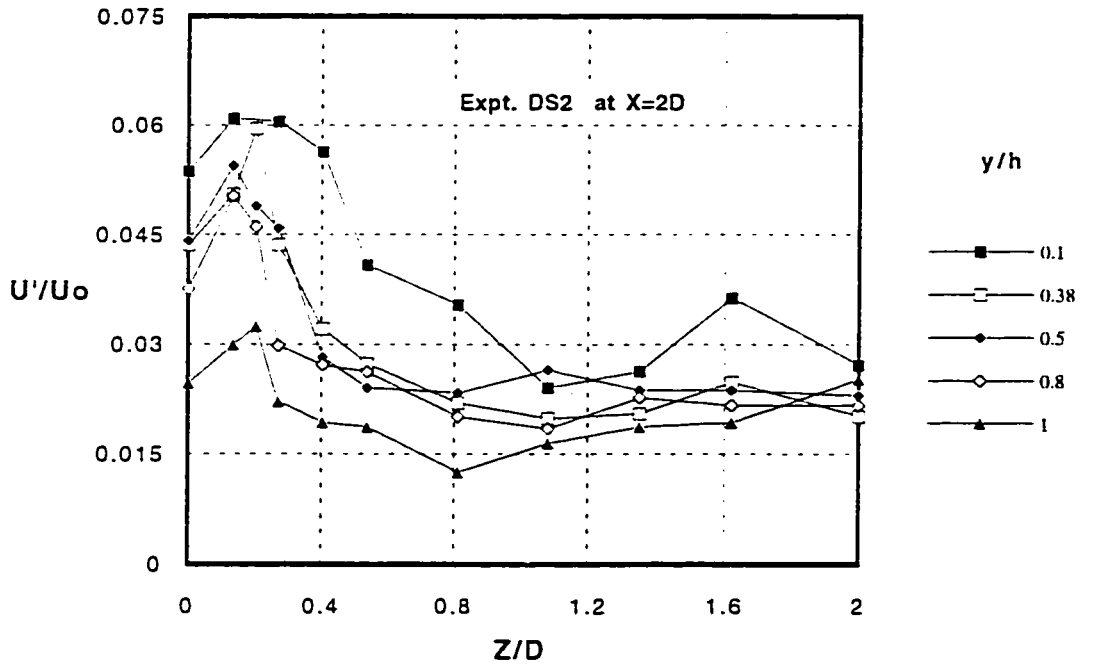
Figure 5.16 (a-b) Spanwise Profiles of u' at Different Depths
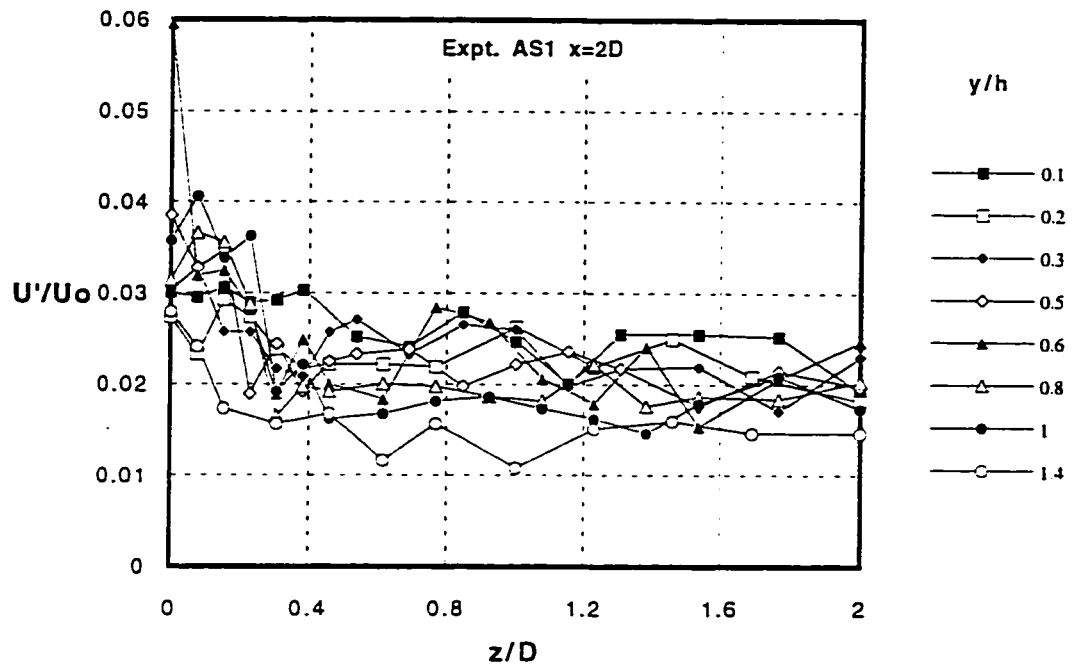
(c)
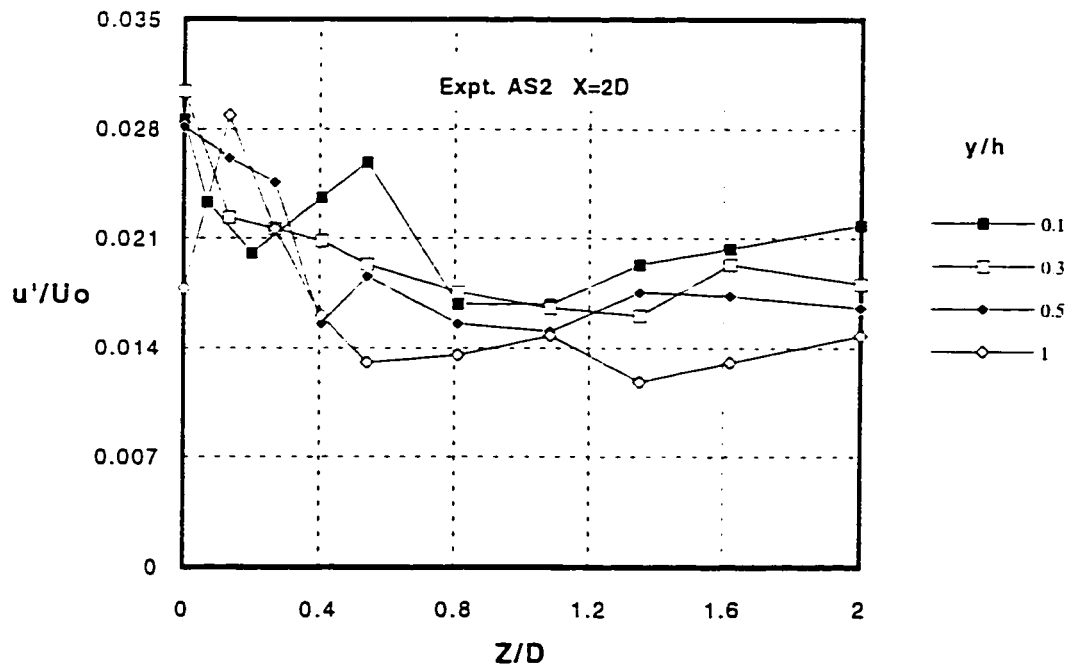
(d)

Figure 5.16 (c-d) Spanwise Profiles of u' at Different Depths
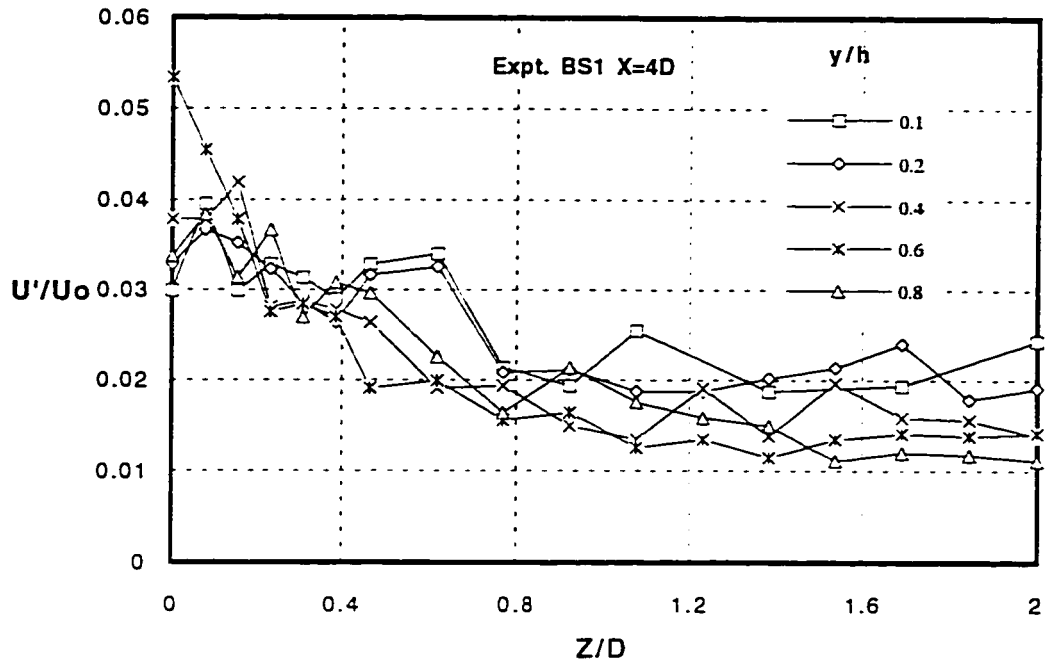
(e)
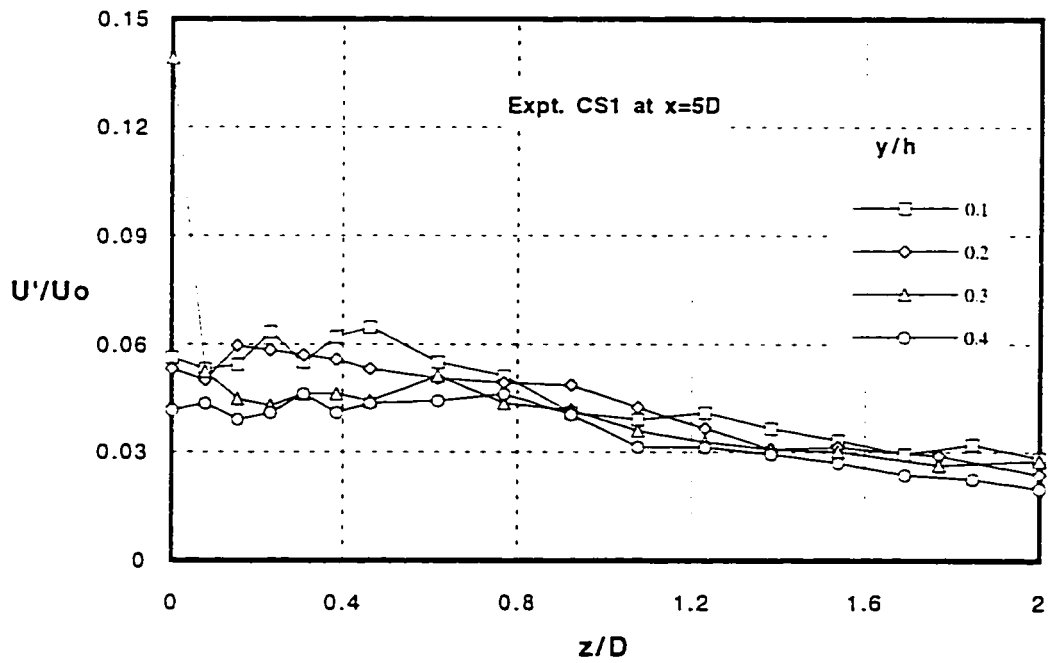
(f)

Figure 5.16 (e-f) Spanwise Profiles of u' at Different Depths
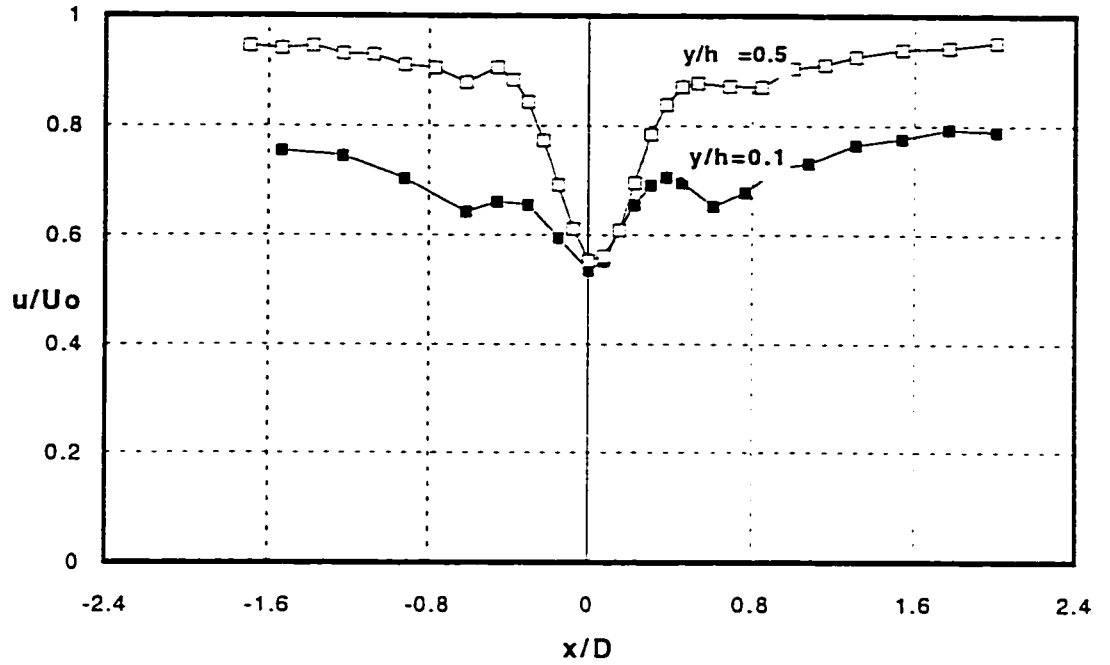
(a)
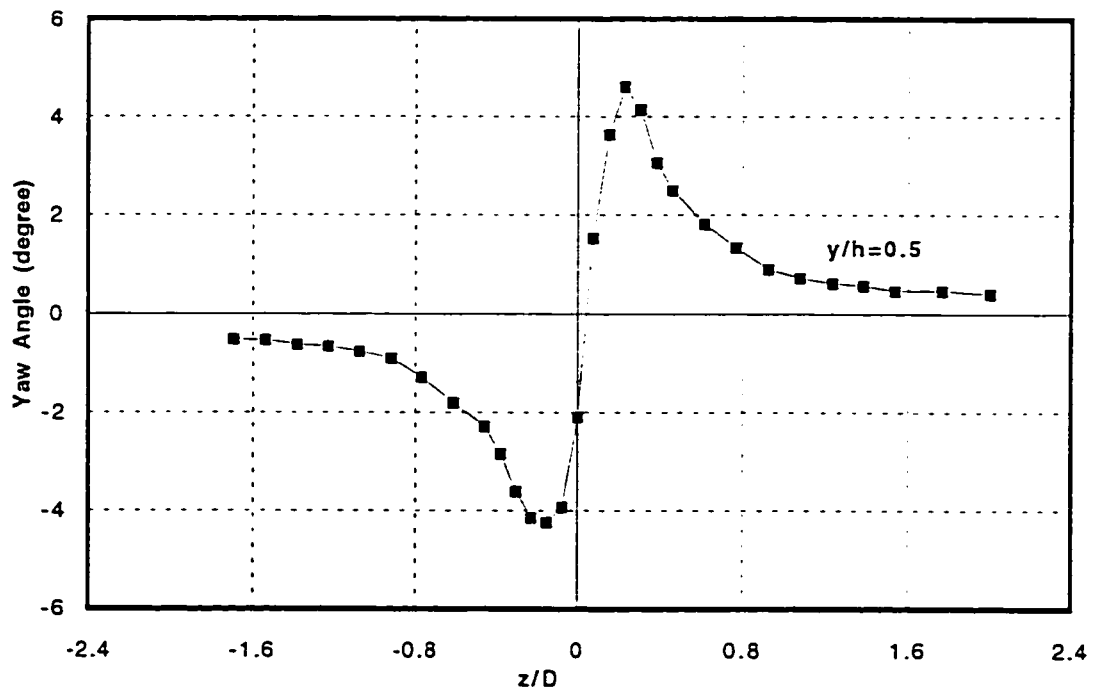
(b)

Figure 5.17 Symmetry Check in Expt. AS1 at x=2D for (a) Velocity; (b) Yaw Angle
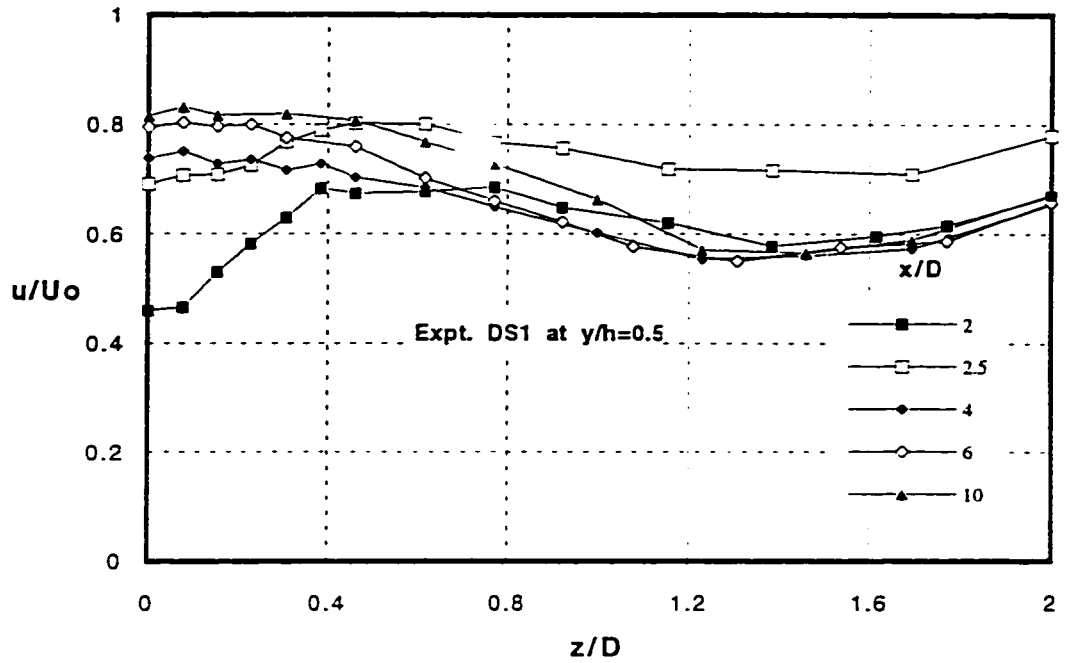
(a)
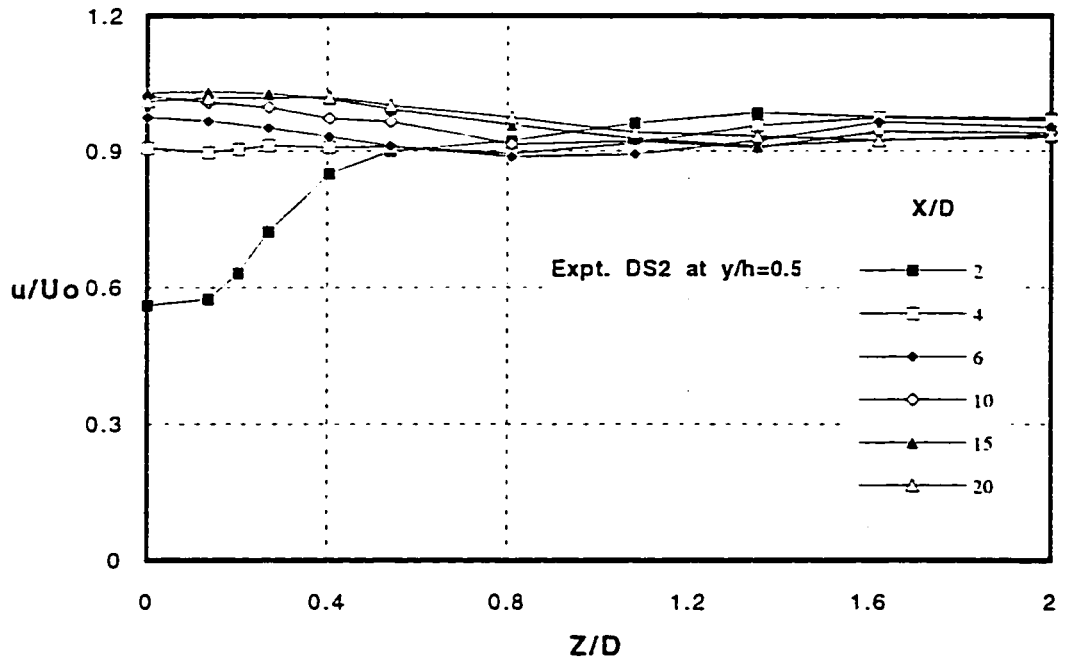
(b)

Figure 5.18 (a-b) Profiles of Spanwise Normalized Velocity for Different Stations

207
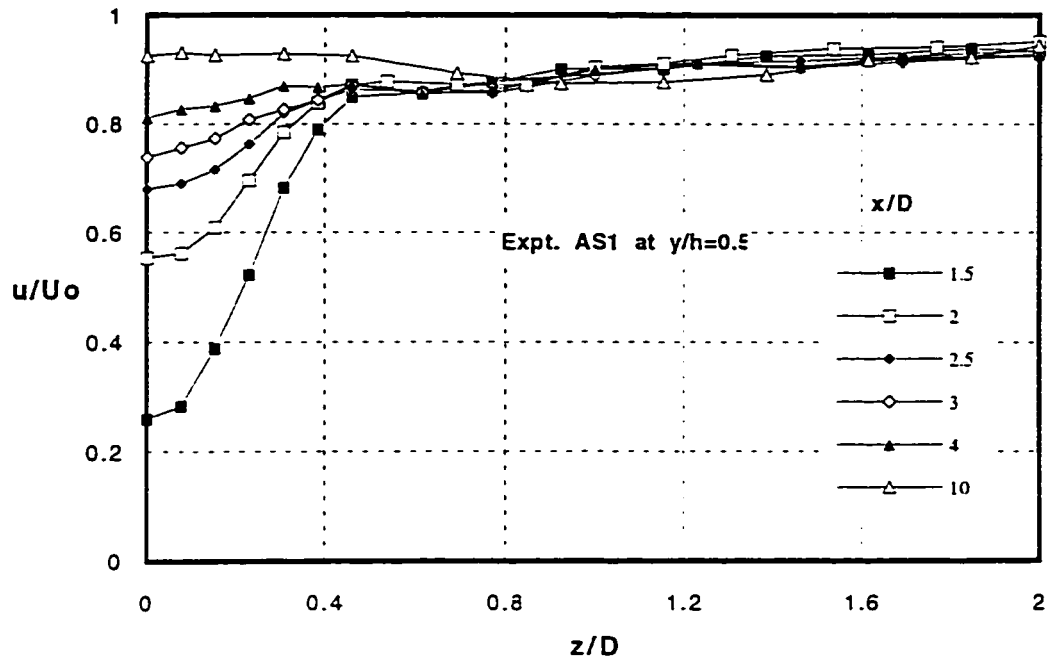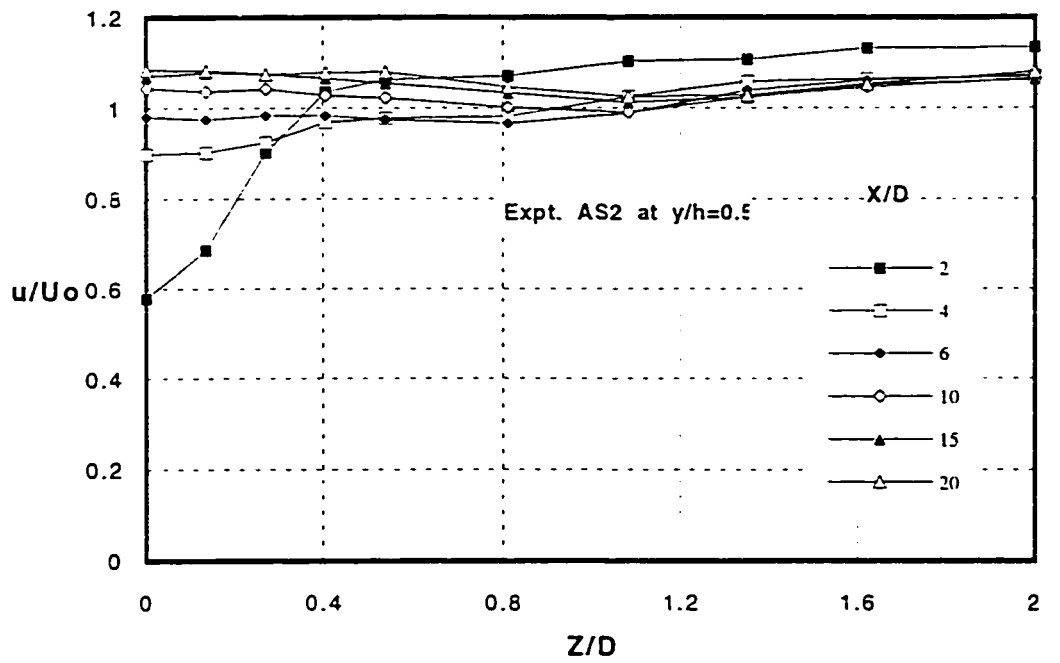
Figure 5.18 (c-d) Profiles of Spanwise Normalized Velocity
for Different Stations
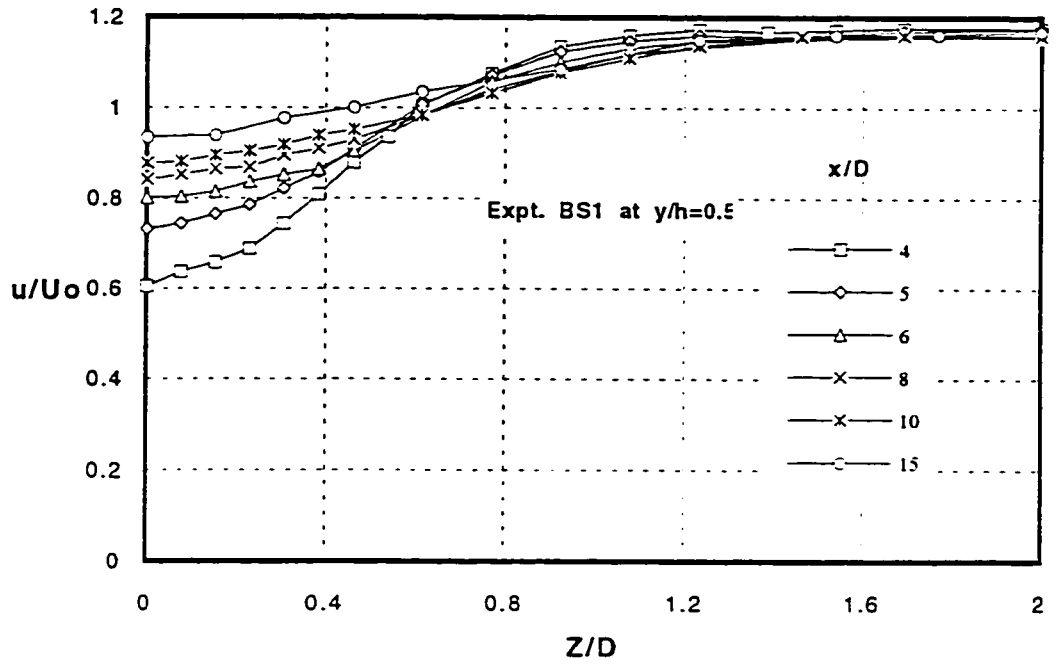
(e)
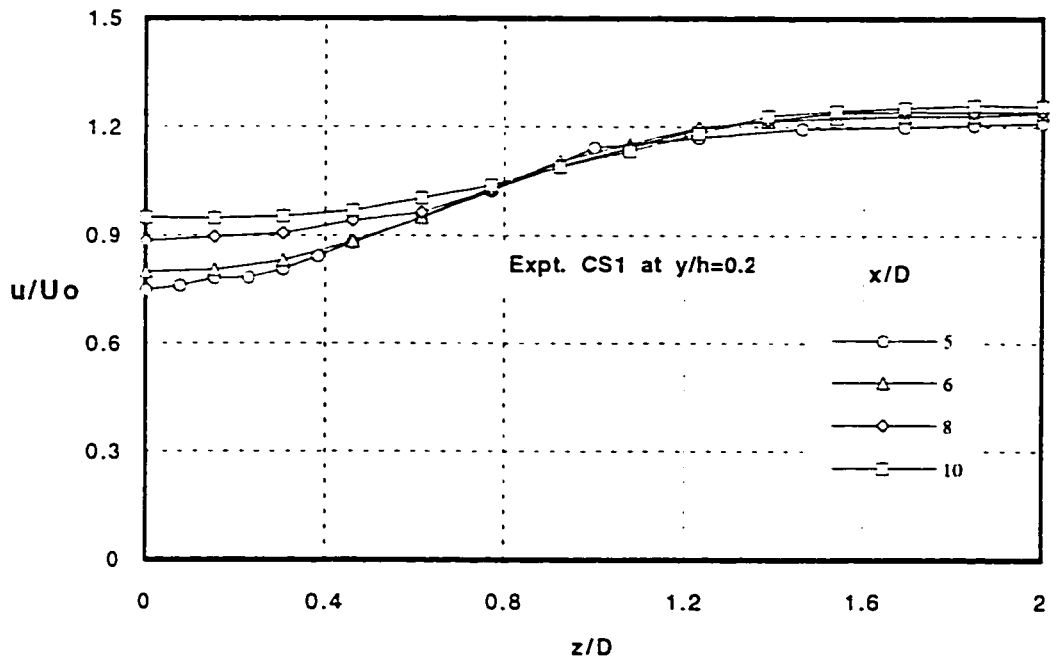
(f)

Figure 5.18 (e-f) Spanwise Normalized Velocity for Different Stations

209
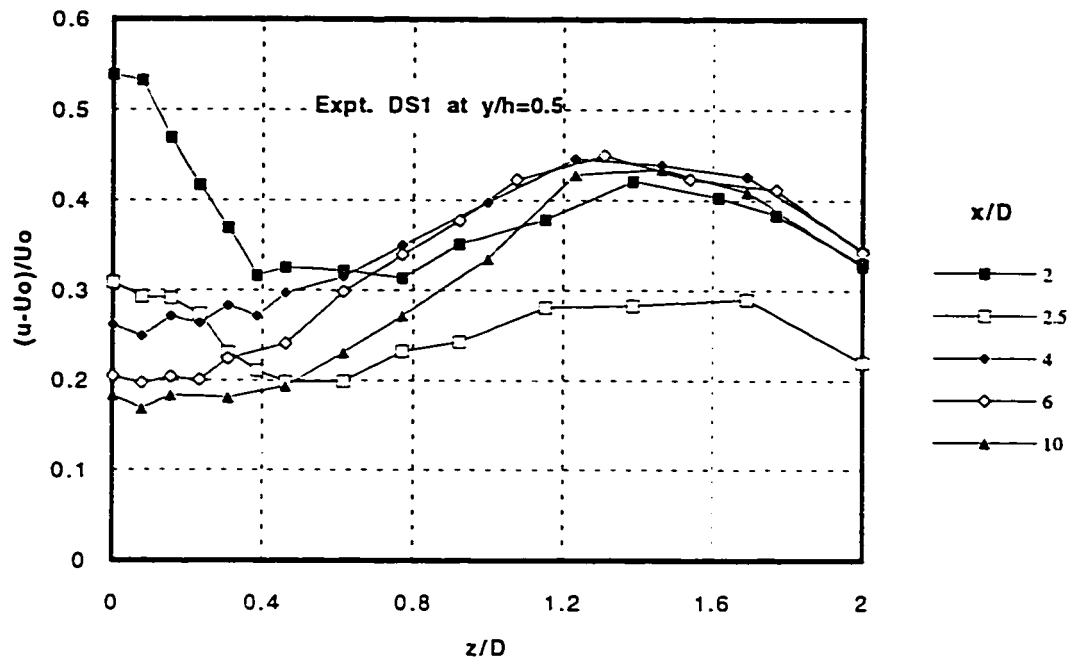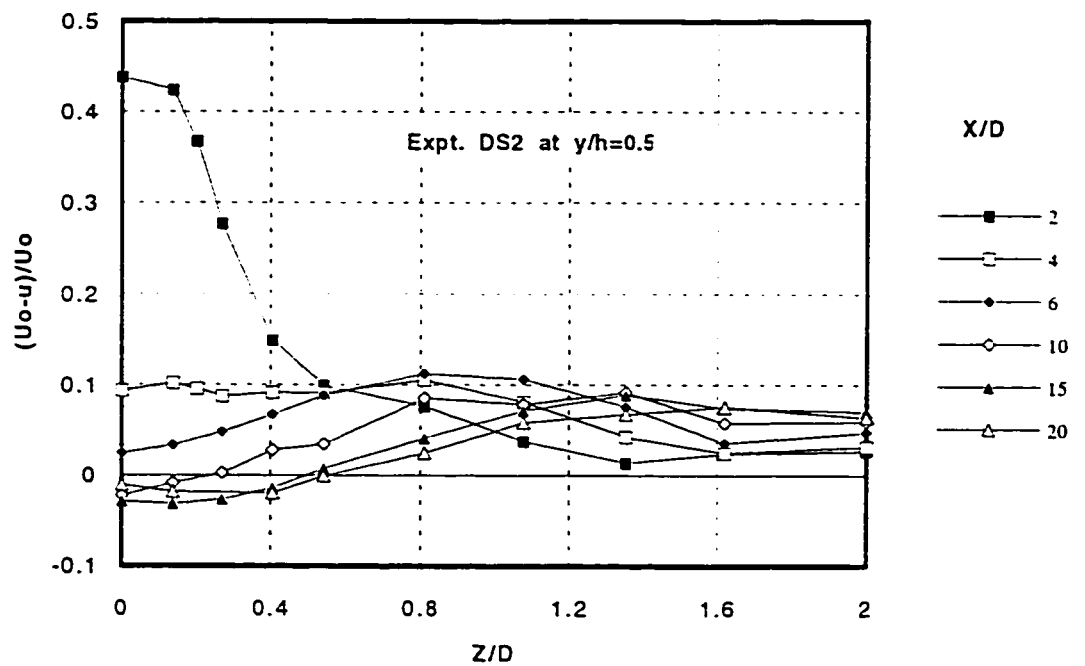
Figure 5.19 (a-b) Profiles of Spanwise Defect Velocity in Different Stations
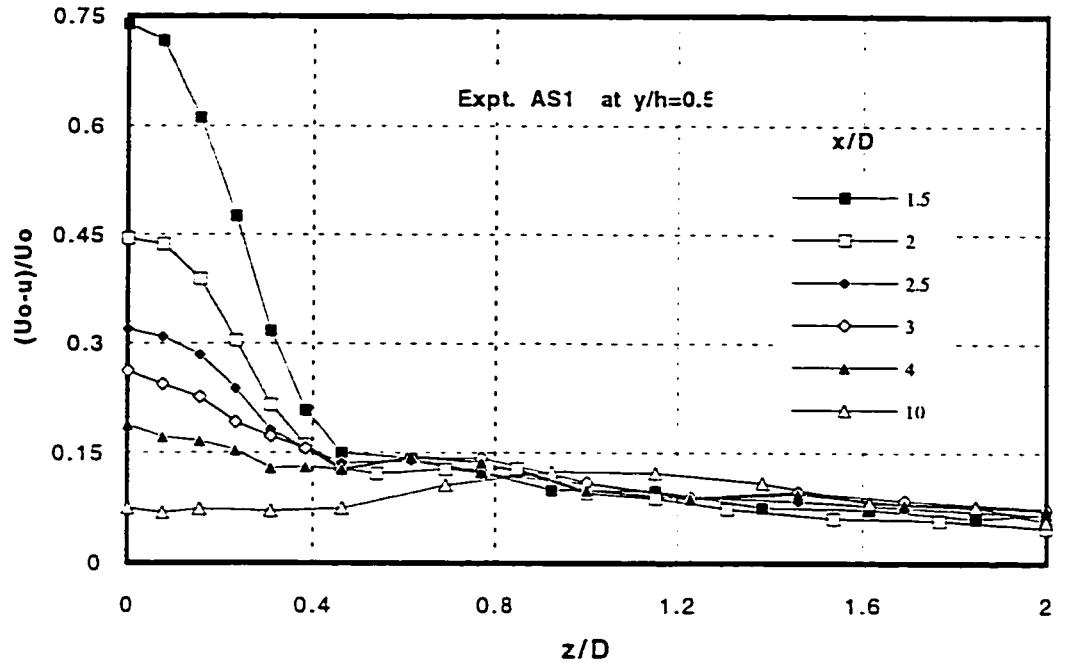
(c)
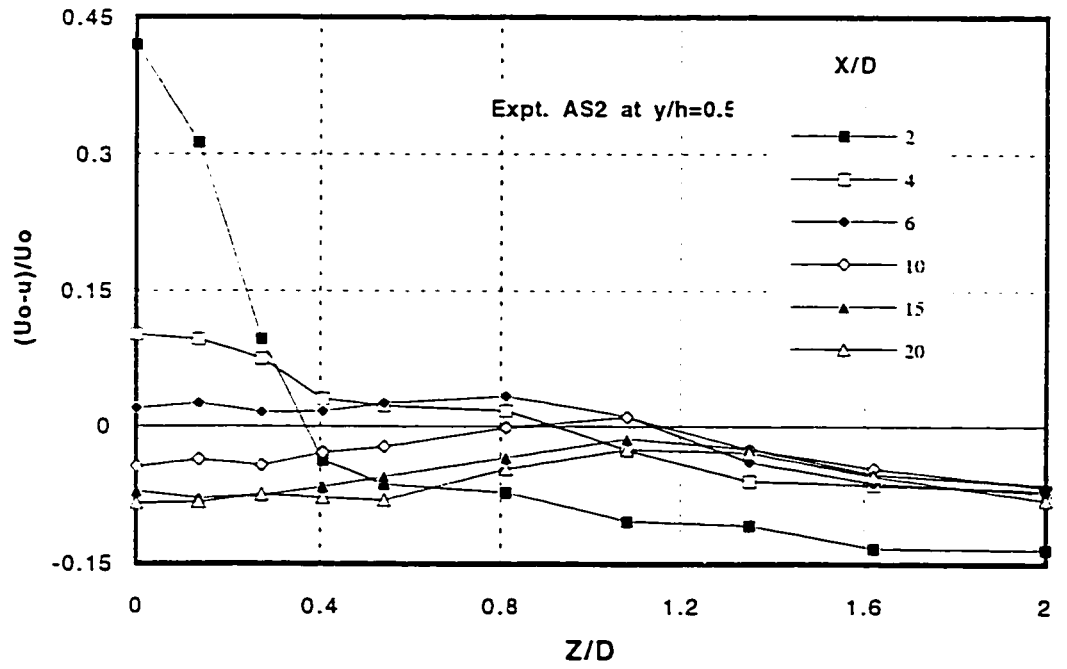
(d)

Figure 5.19 (c-d) Profiles of Spanwise Defect Velocity in Different Stations

211
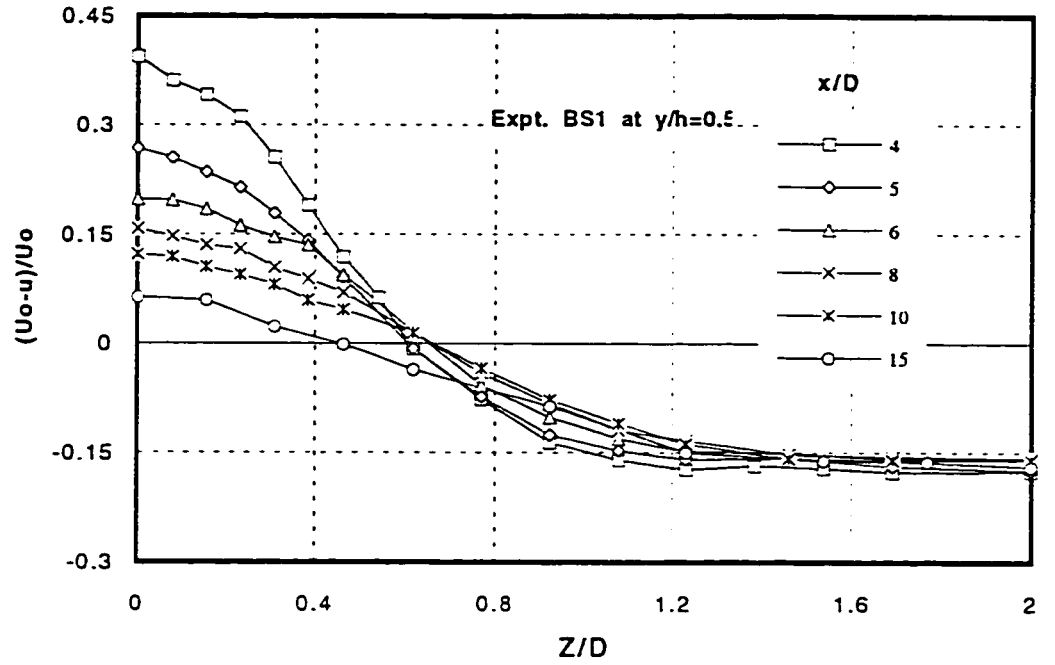
(e)
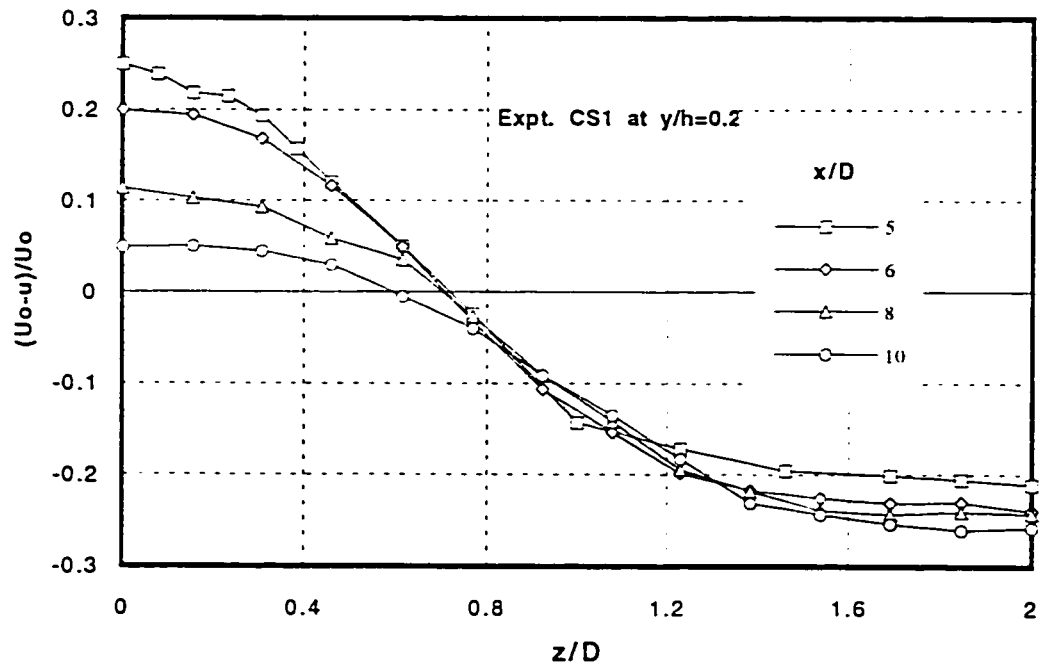
(f)

Figure 5.19 (e-f) Profiles of Spanwise Defect Velocity in Different Stations
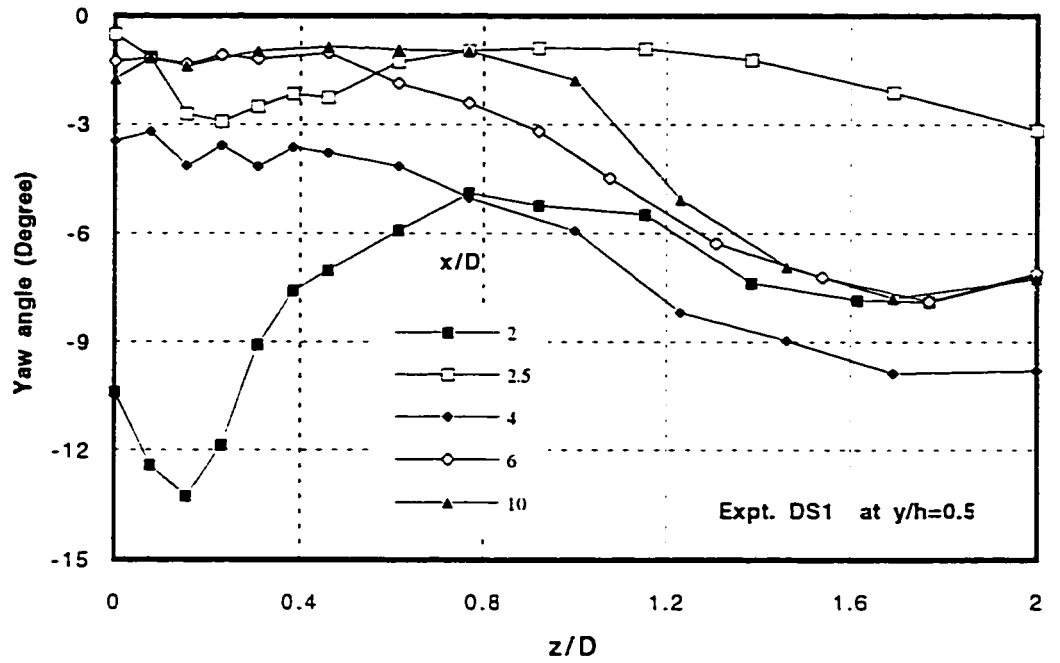
(a)
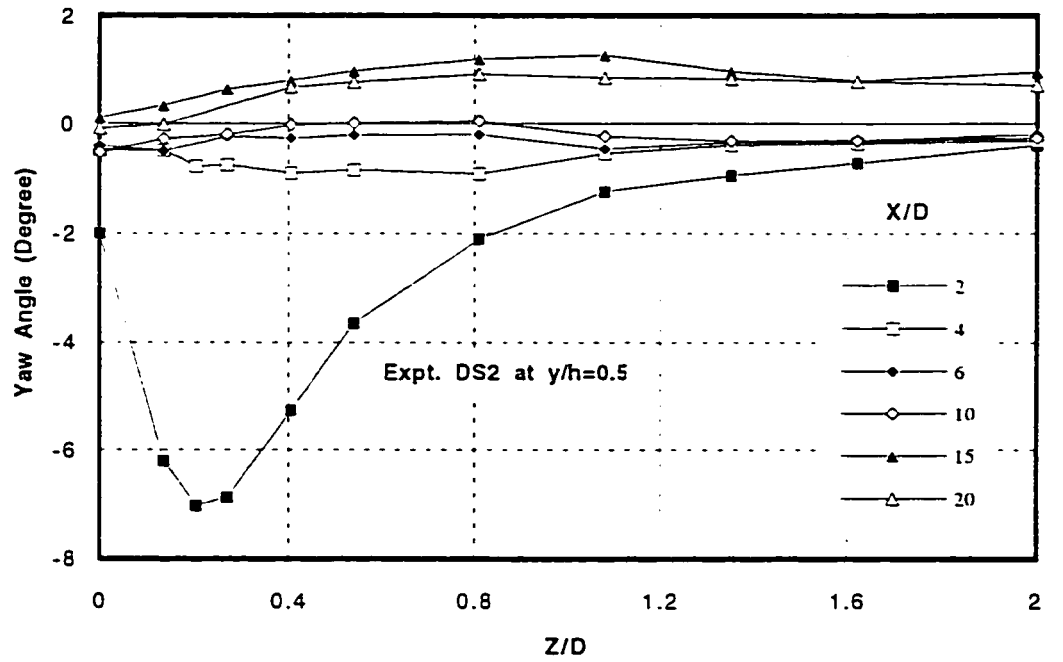
(b)

Figure 5.20 (a-b) Spanwise Profiles of Yaw Angles in Different Stations
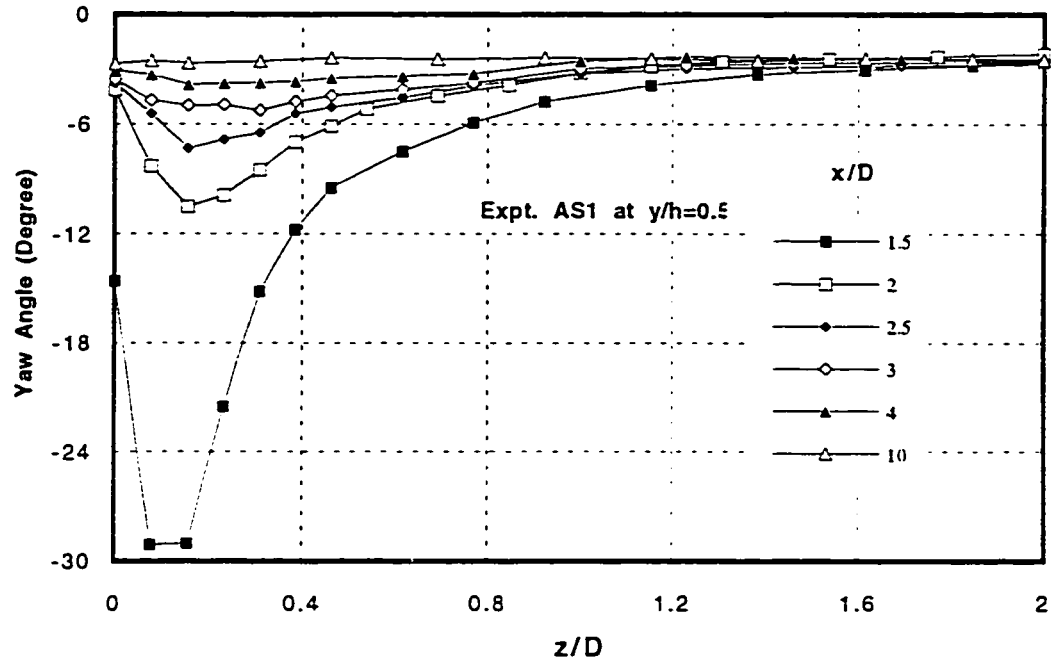
(c)
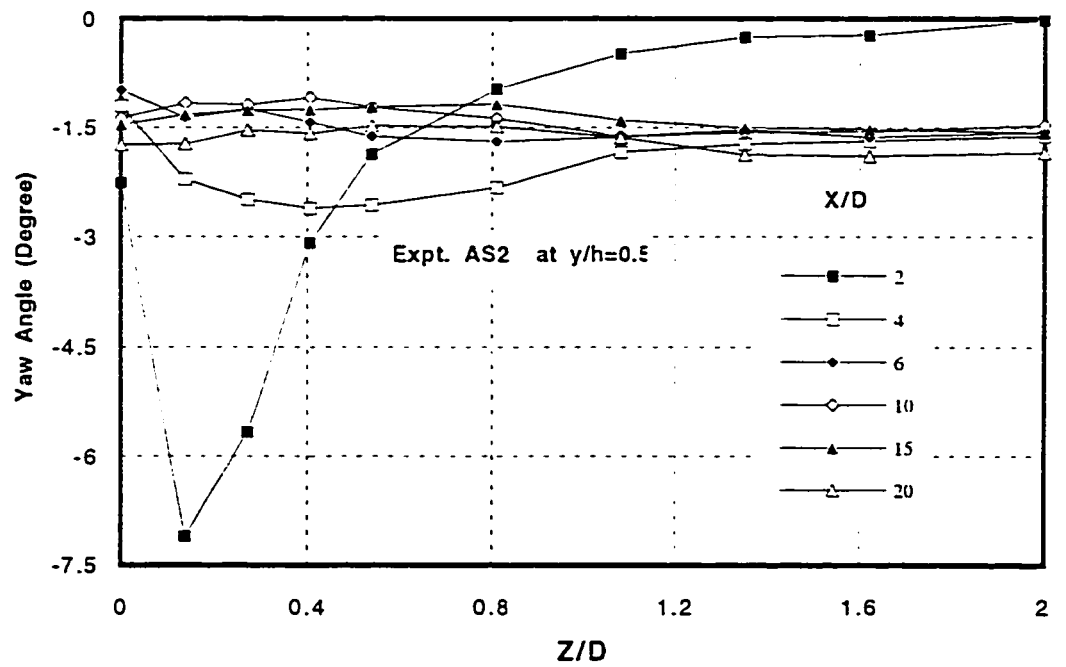
(d)

Figure 5.20 (c-d) Spanwise Profiles of Yaw Angles in Different Stations
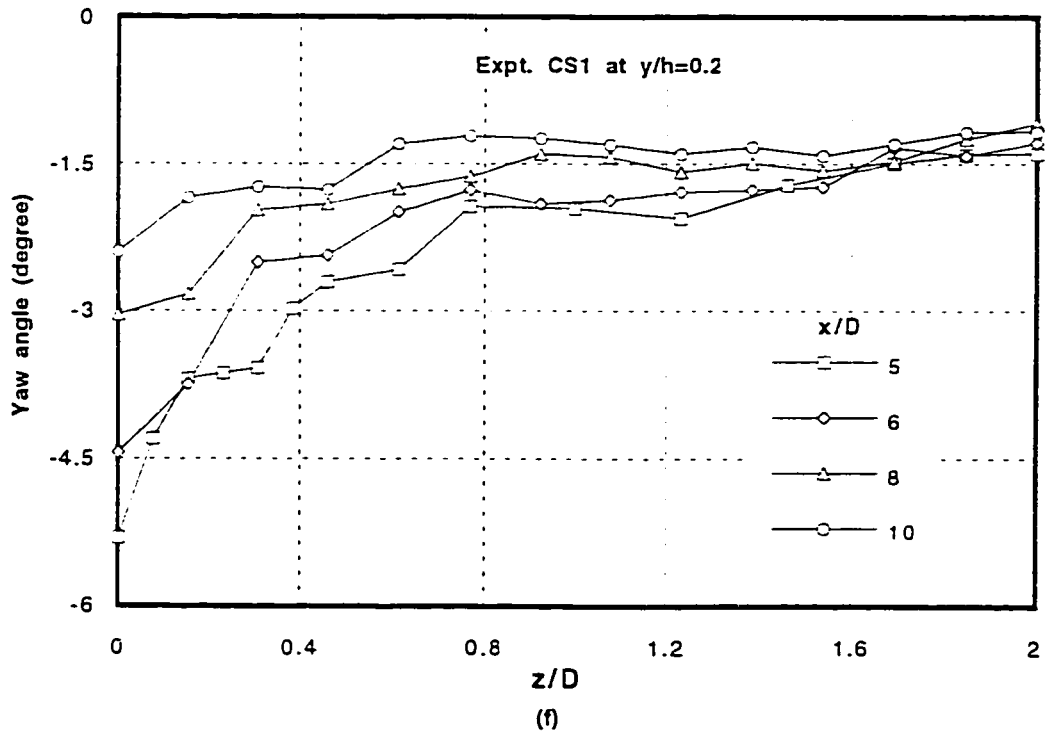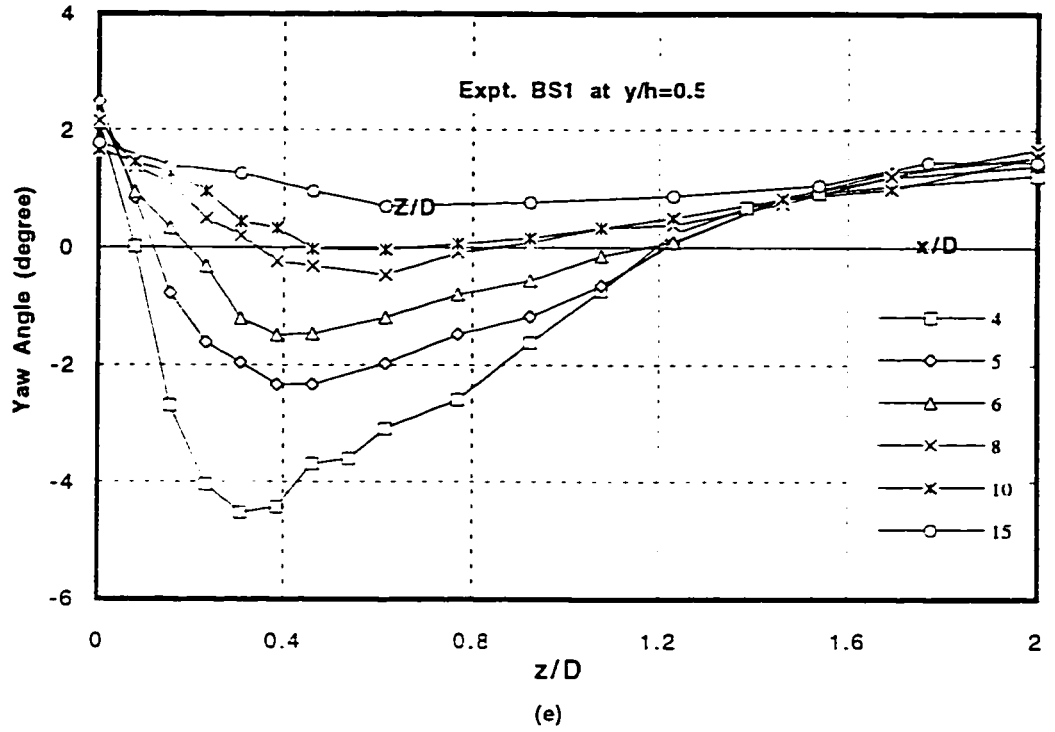
Figure 5.20 (e-f) Spanwise Profiles of Yaw Angles in Different Stations

215
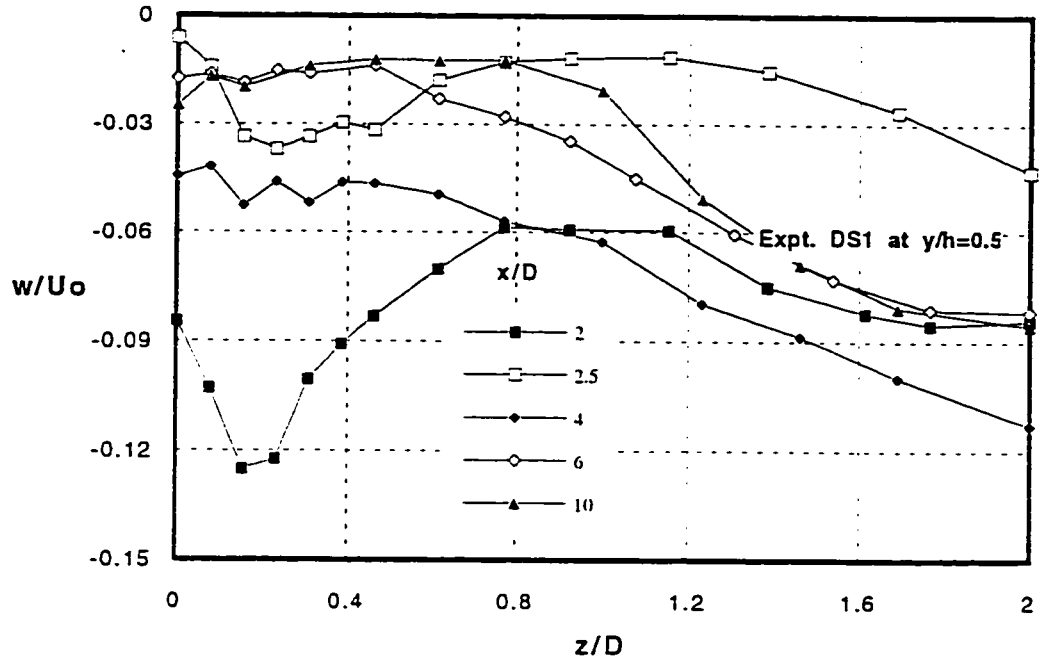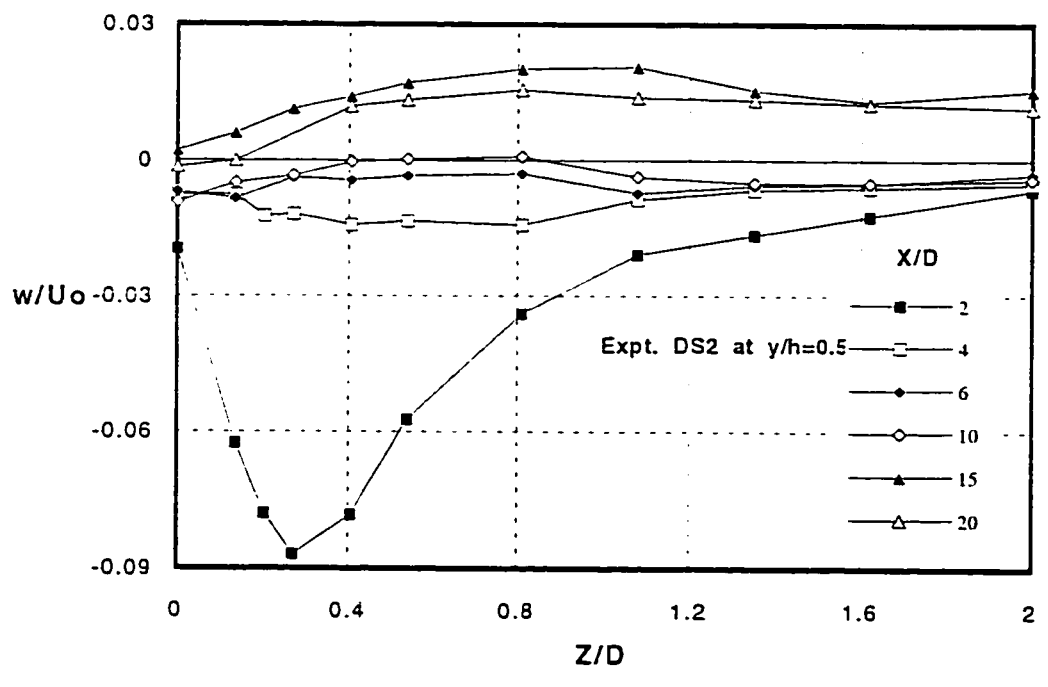
Figure 5.21 (a-b) Spanwise Profiles of Lateral Velocity in Different Stations

216
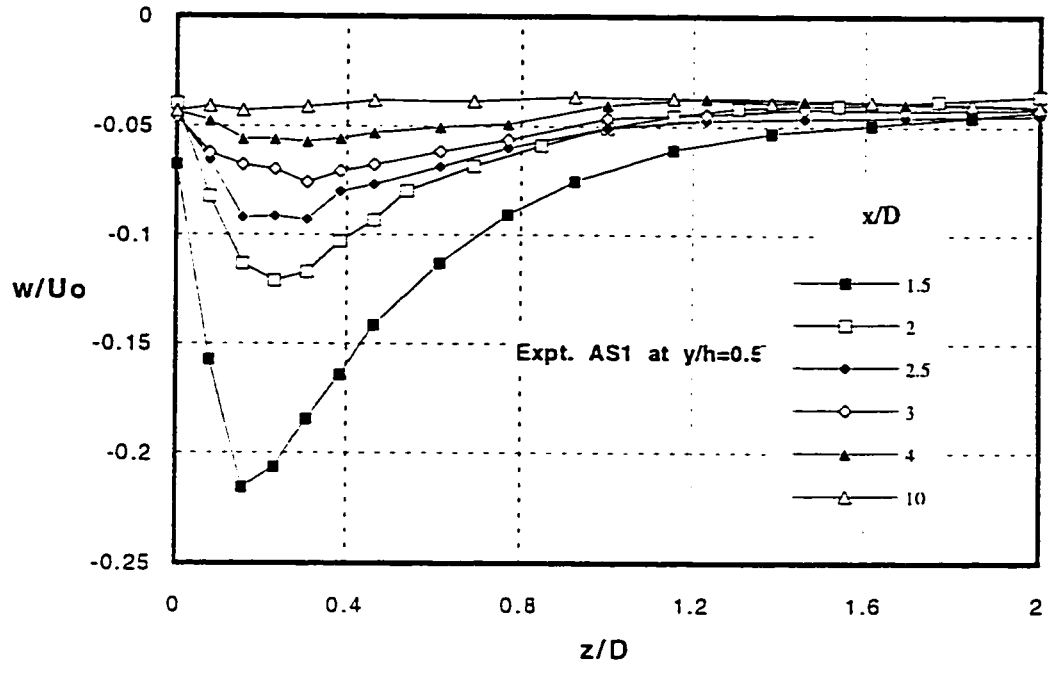
(c)
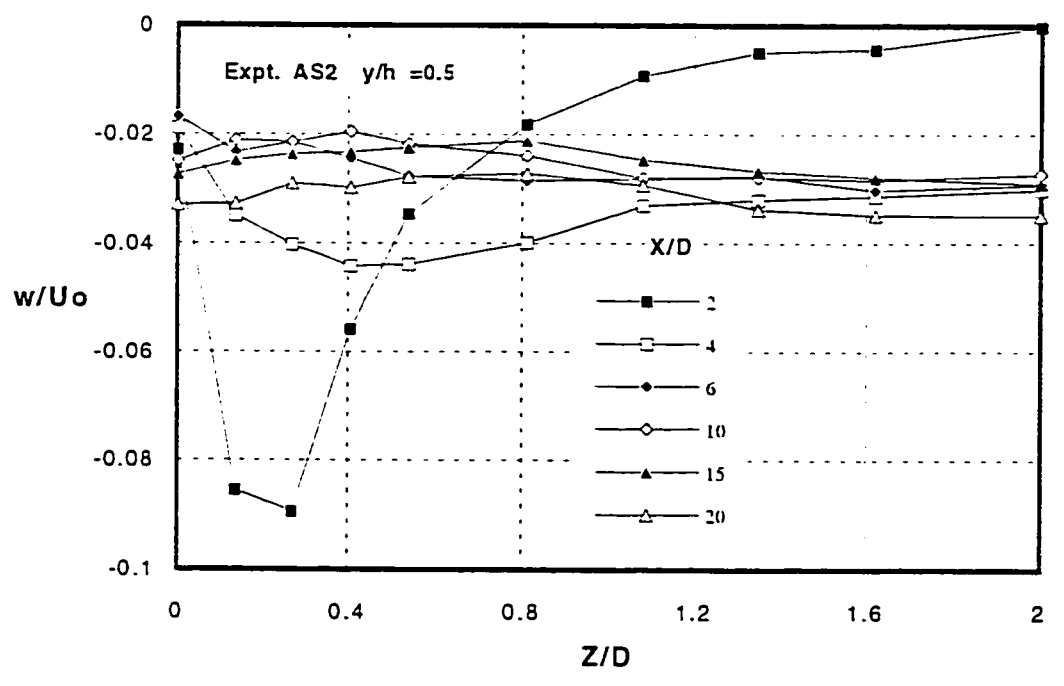
(d)

Figure 5.21 (c-d) Spanwise Profiles of Lateral Velocity in Different Stations
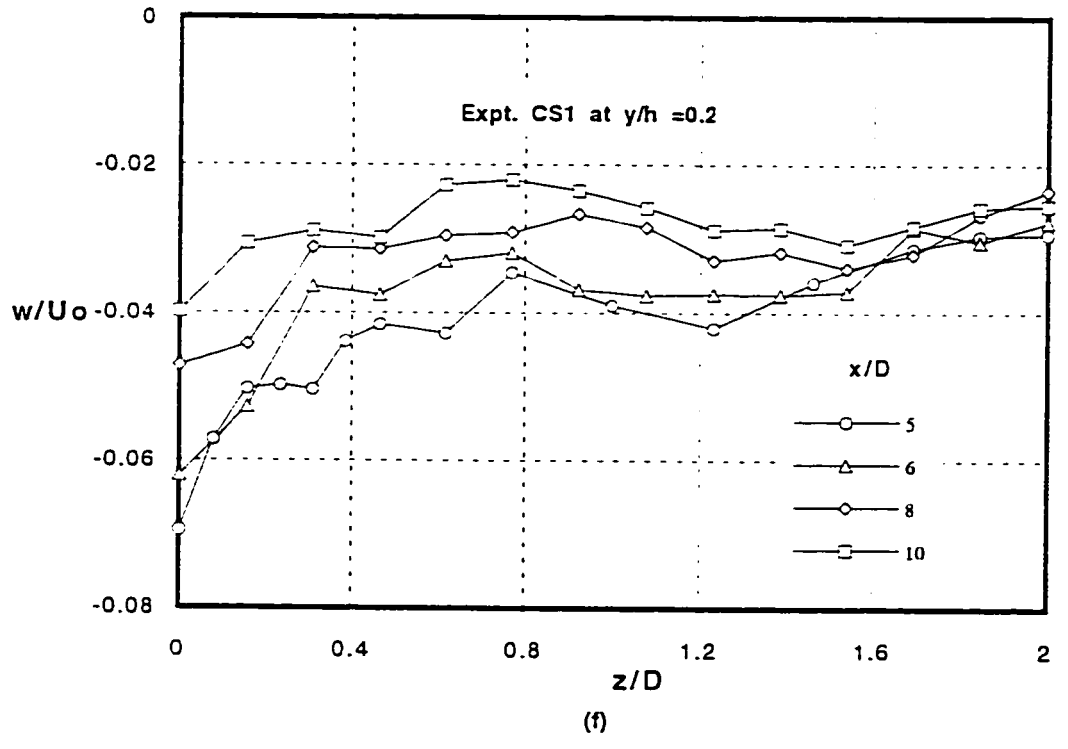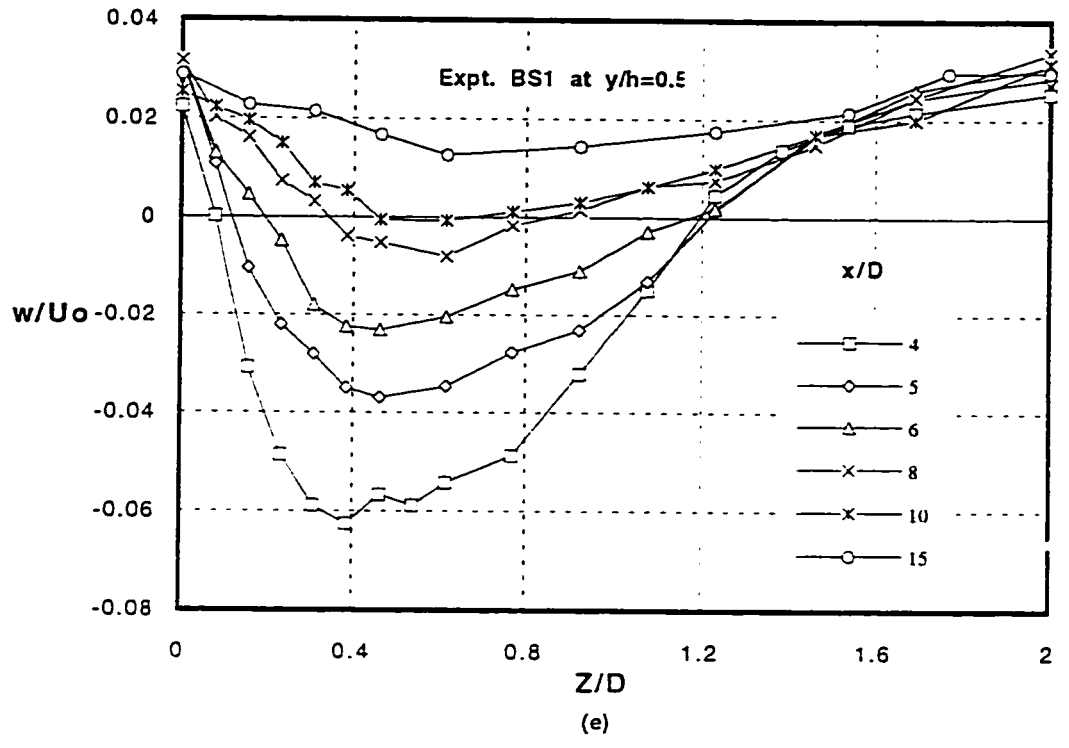
Figure 5.21 (e-f) Spanwise Profiles of Lateral Velocity in Different Stations
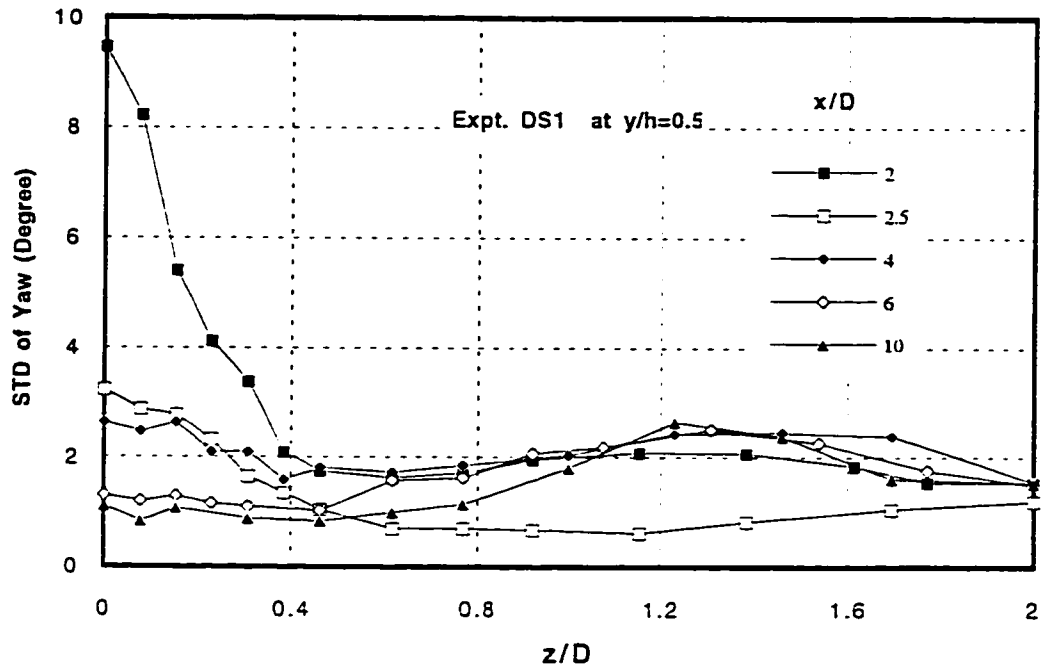
(a)
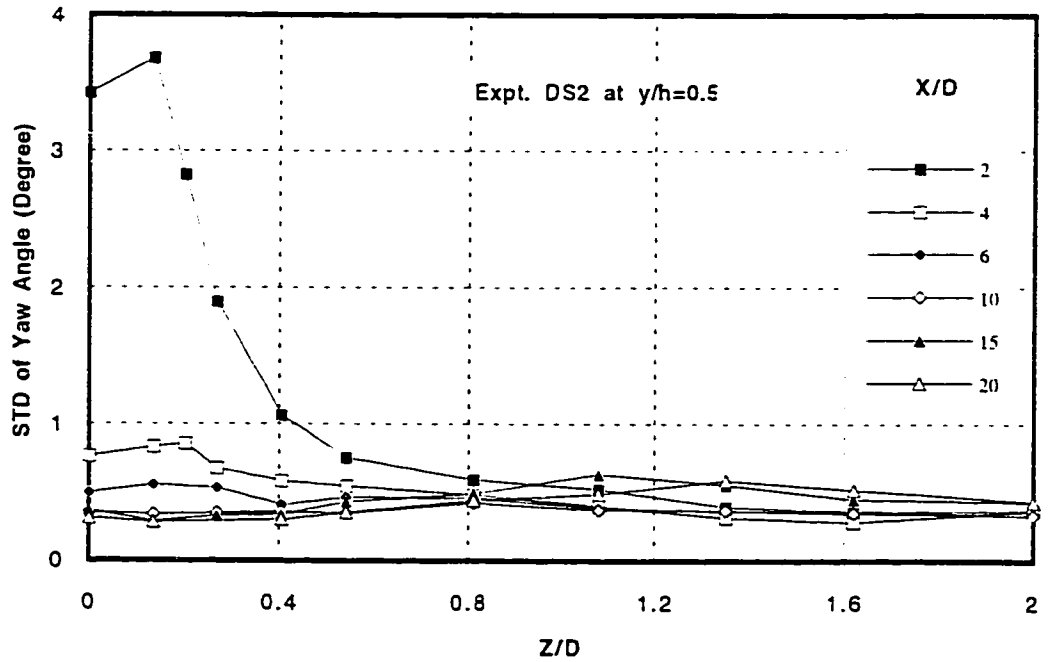
(b)

Figure 5.22 (a-b) Spanwise Profiles of STD of Yaw Angle in Different Stations
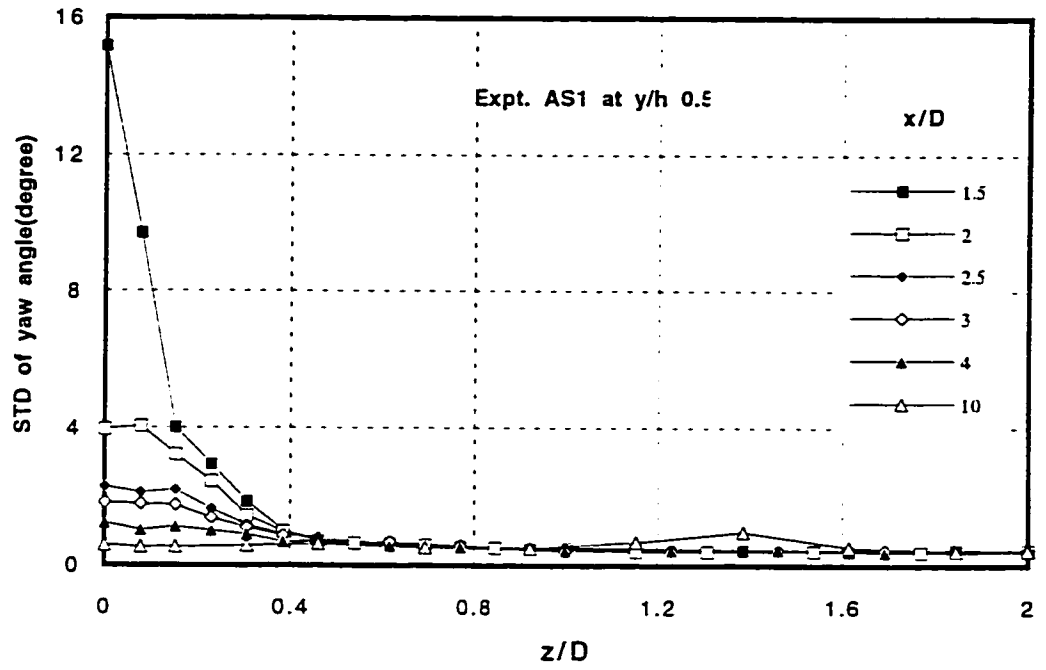
(c)
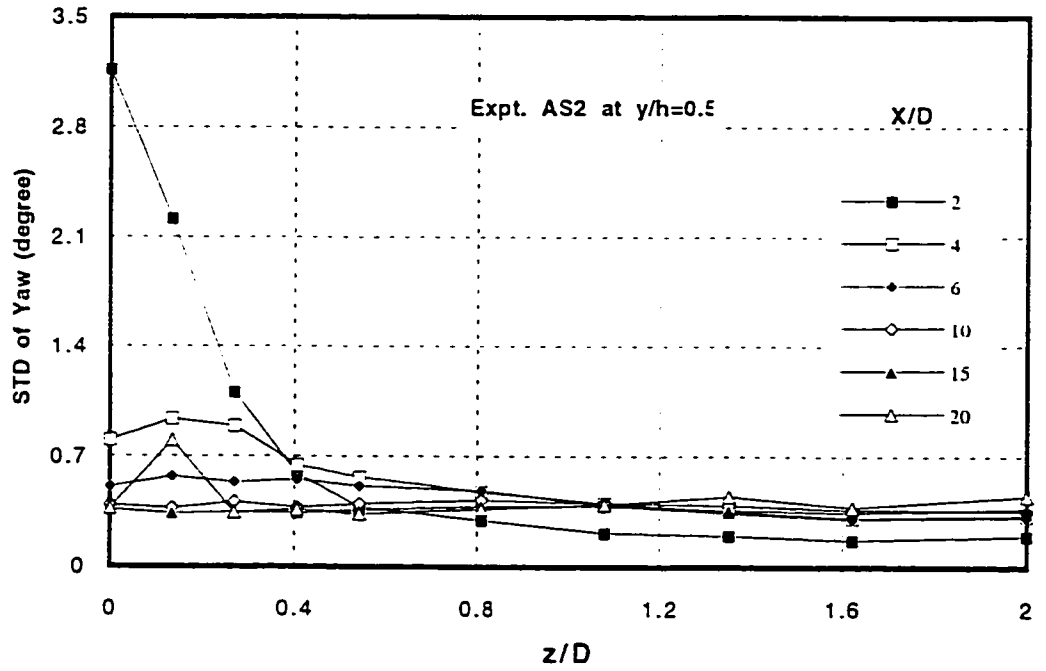
(d)

Figure 5.22 (c-d) Spanwise Profiles of STD of Yaw Angle in Different Stations
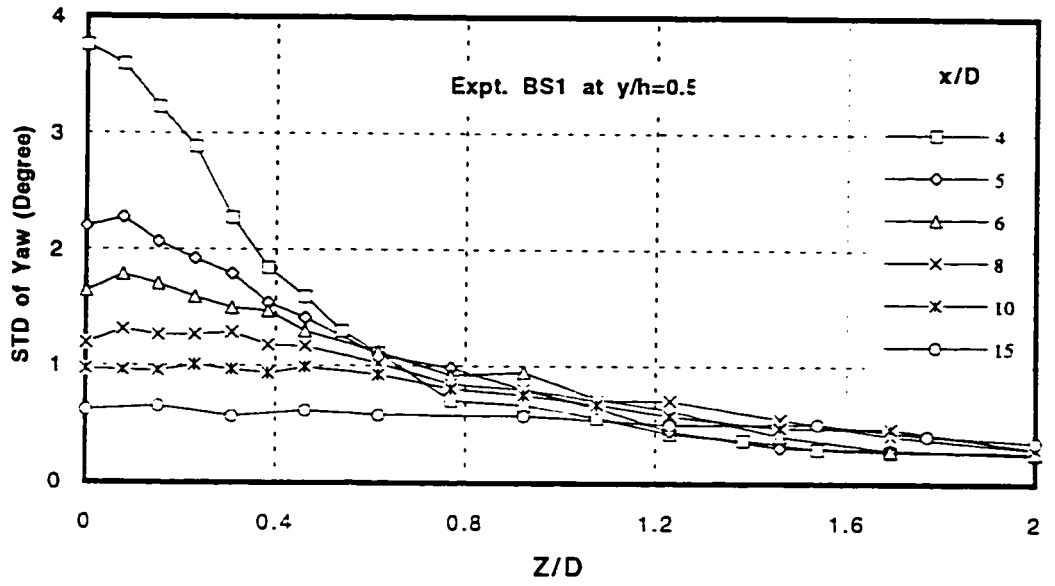
(e)
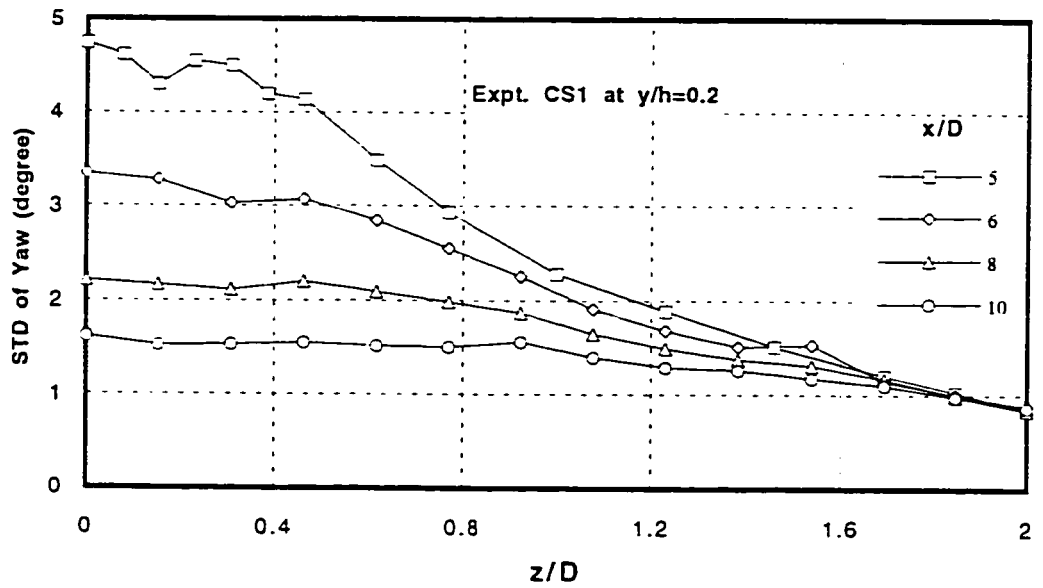
(f)

Figure 5.22 (e-f) Spanwise Profiles of STD of Yaw Angle
in Different Stations

221
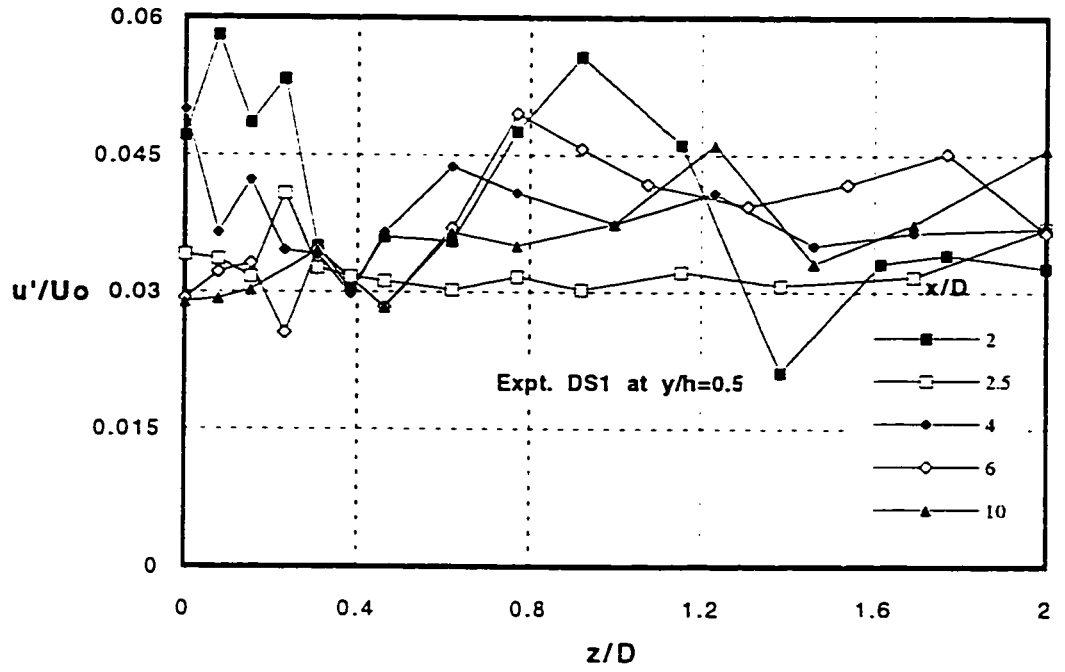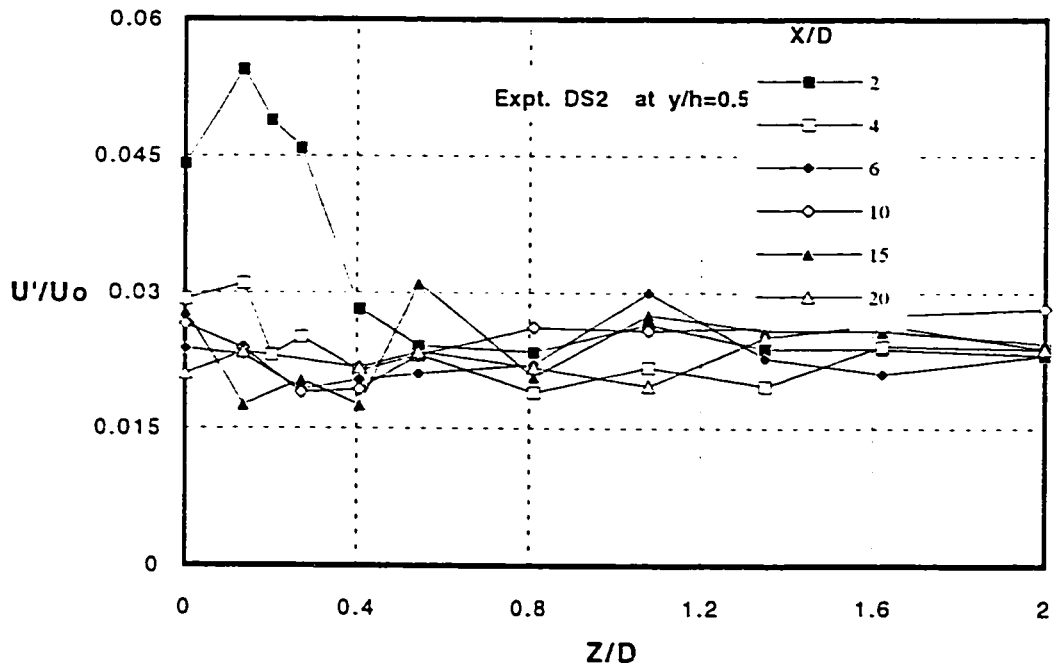
Figure 5.23 (a-b) Spanwise Profiles of u'/Uo in Different Stations

(c)

(d)
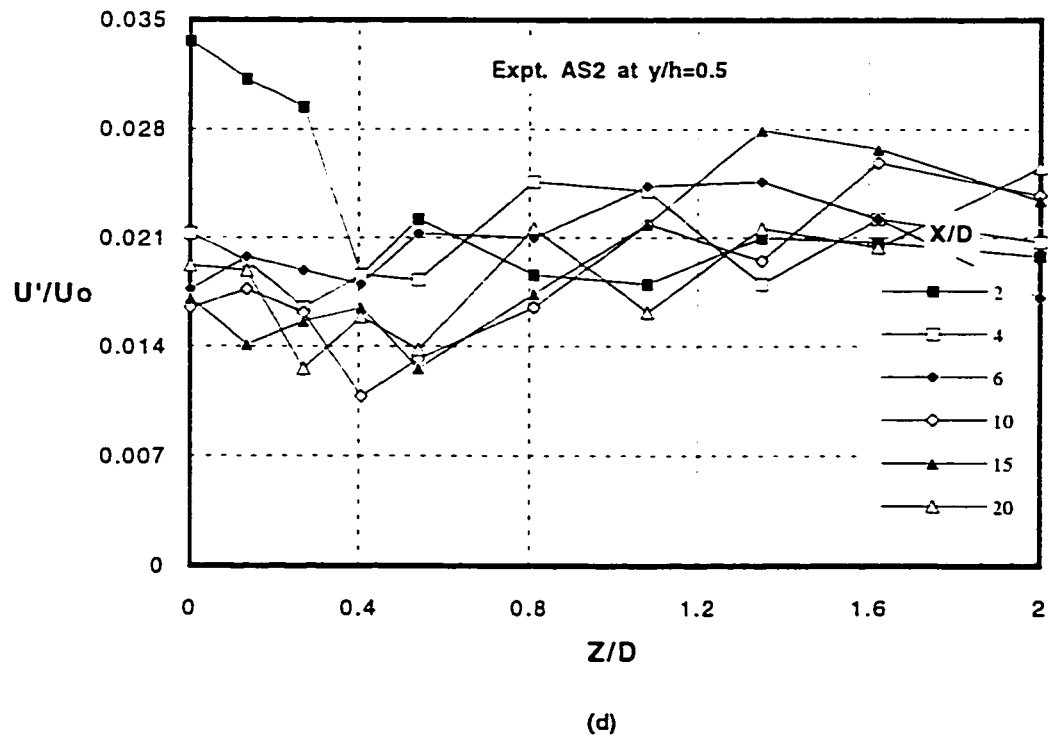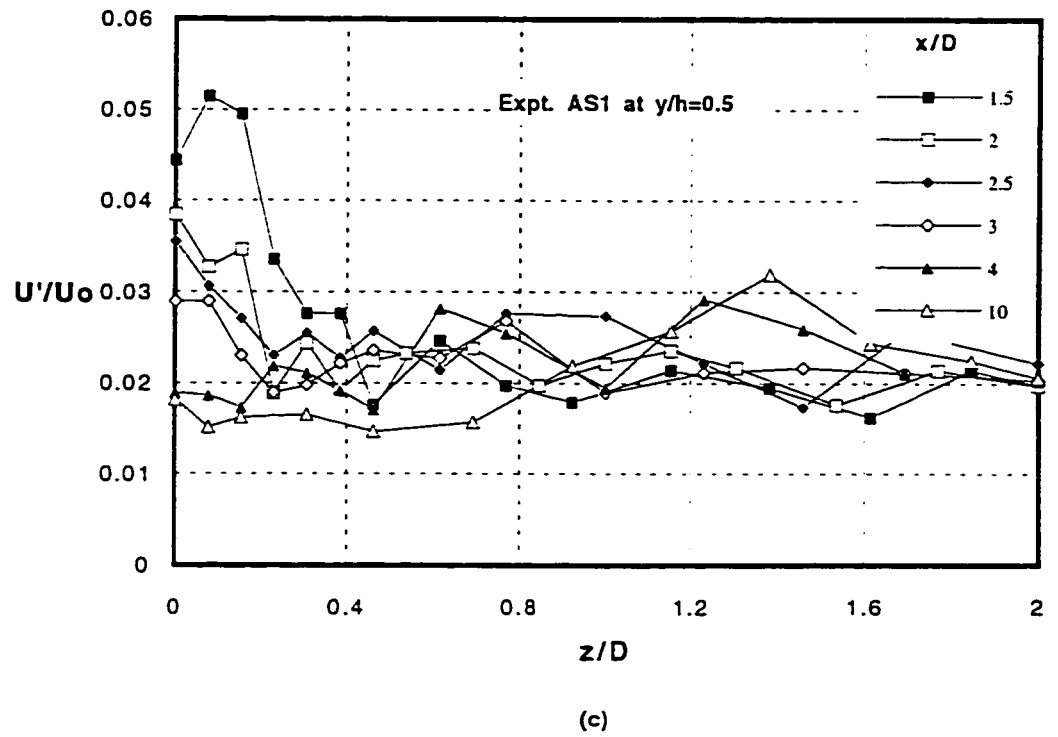
Figure 5.23 (c-d) Spanwise Profiles of u'/Uo in Different Stations

Please Note

Page(s) missing in number only; text follows.
Filmed as received.

224

UMI
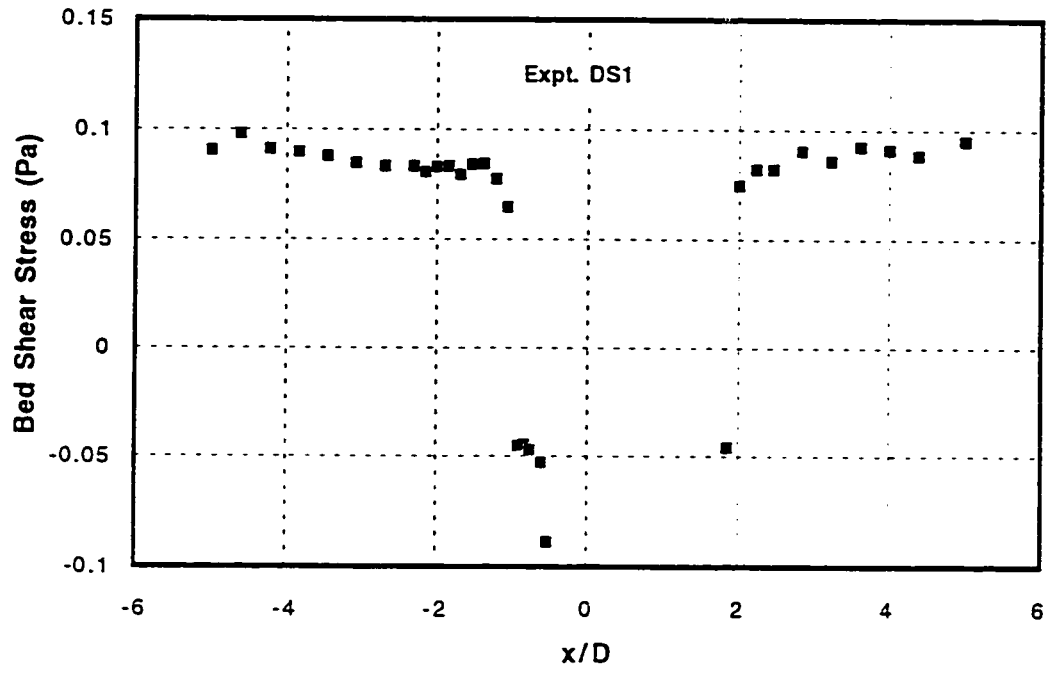
(a)
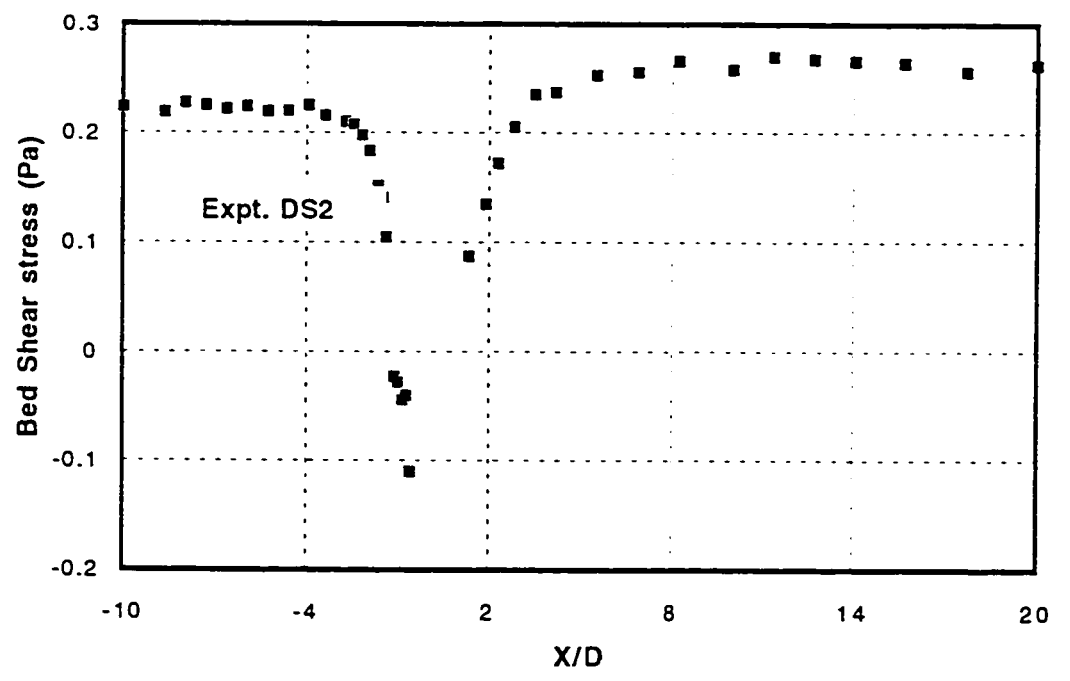
(b)

Figure 5.24 (a-b) Shear Stress Profile on the POS
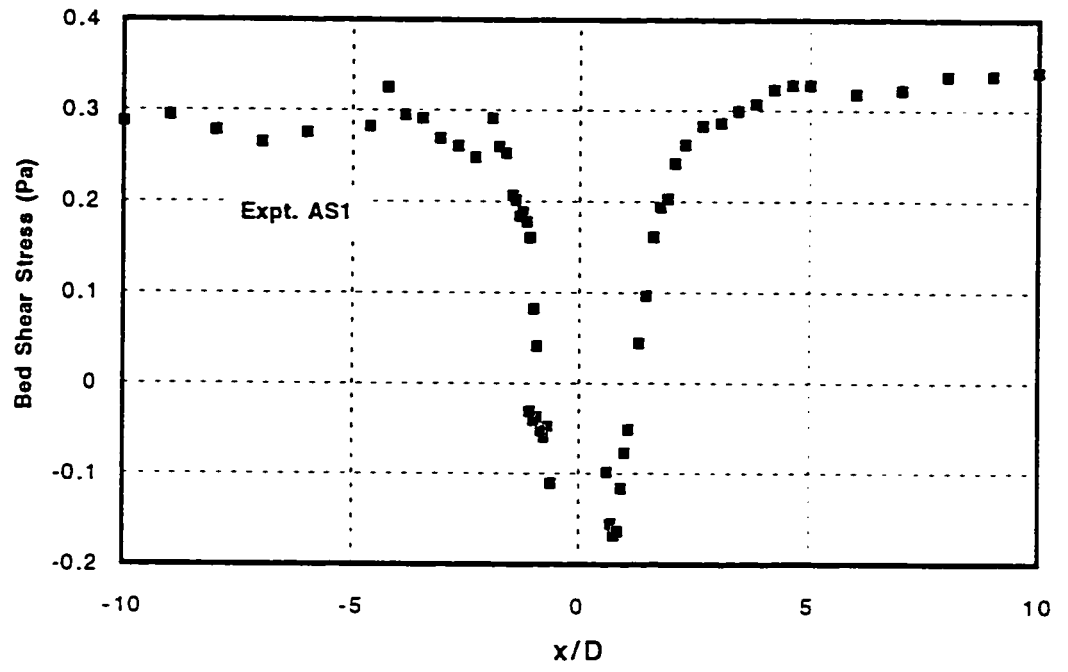
(c)
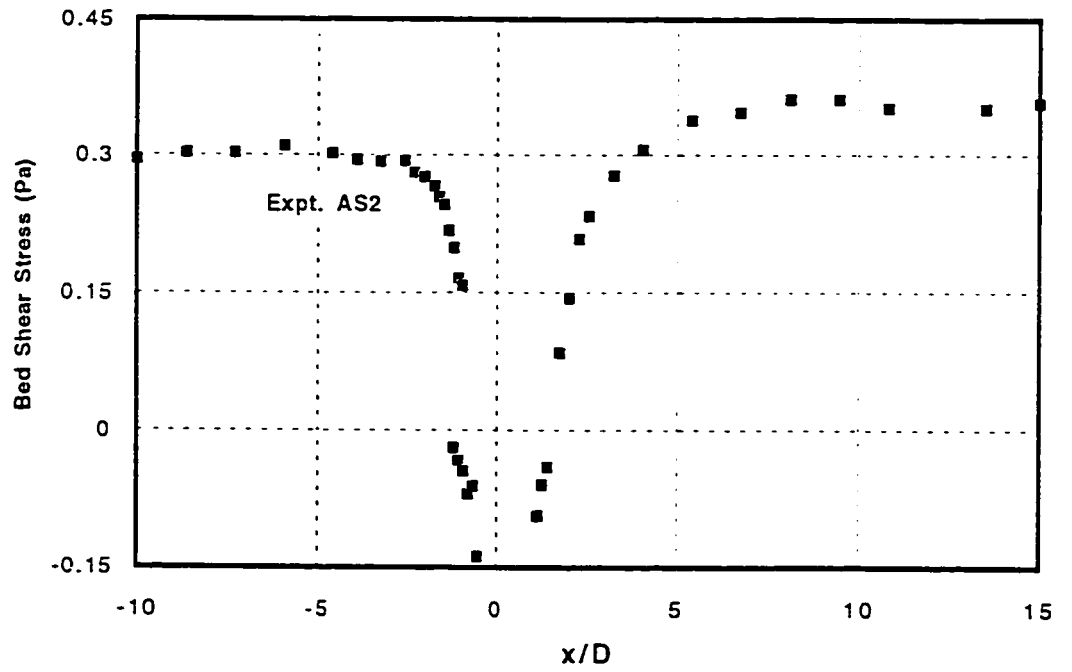
(d)

Figure 5.24 (c-d) Shear Stress Profile on the POS

226
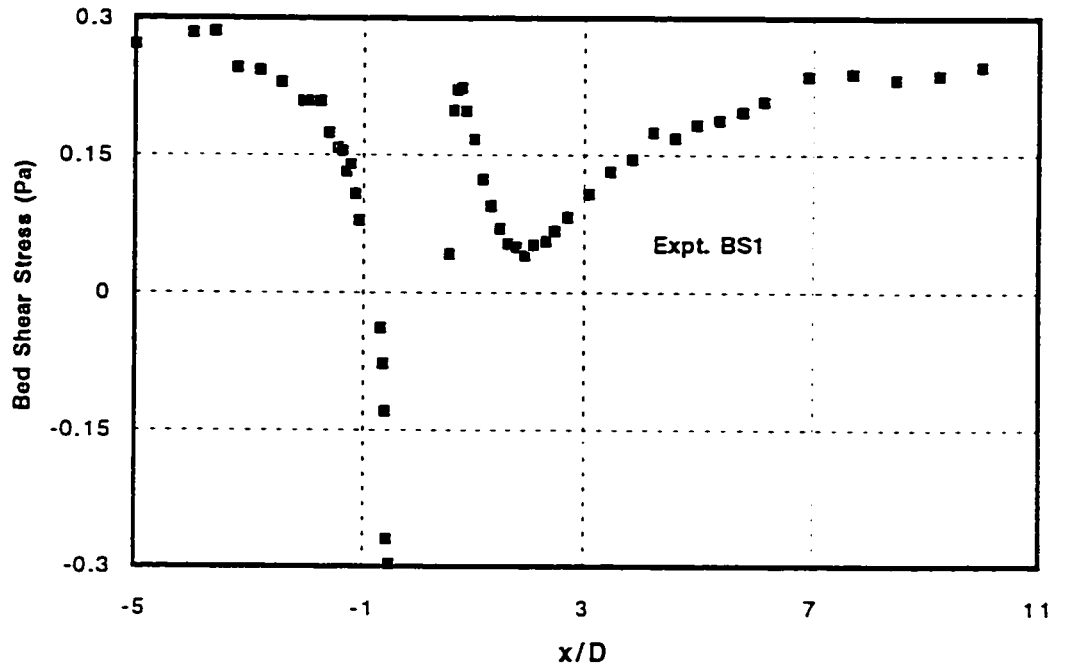
(e)
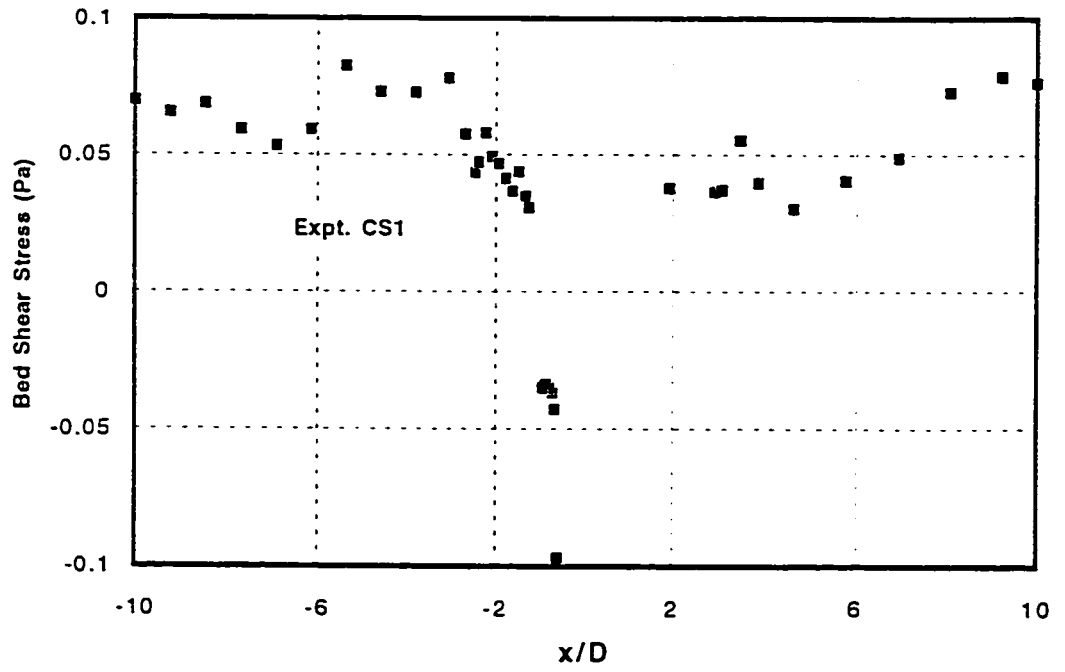
(f)

Figure 5.24 (e-f) Shear Stress Profile on the POS
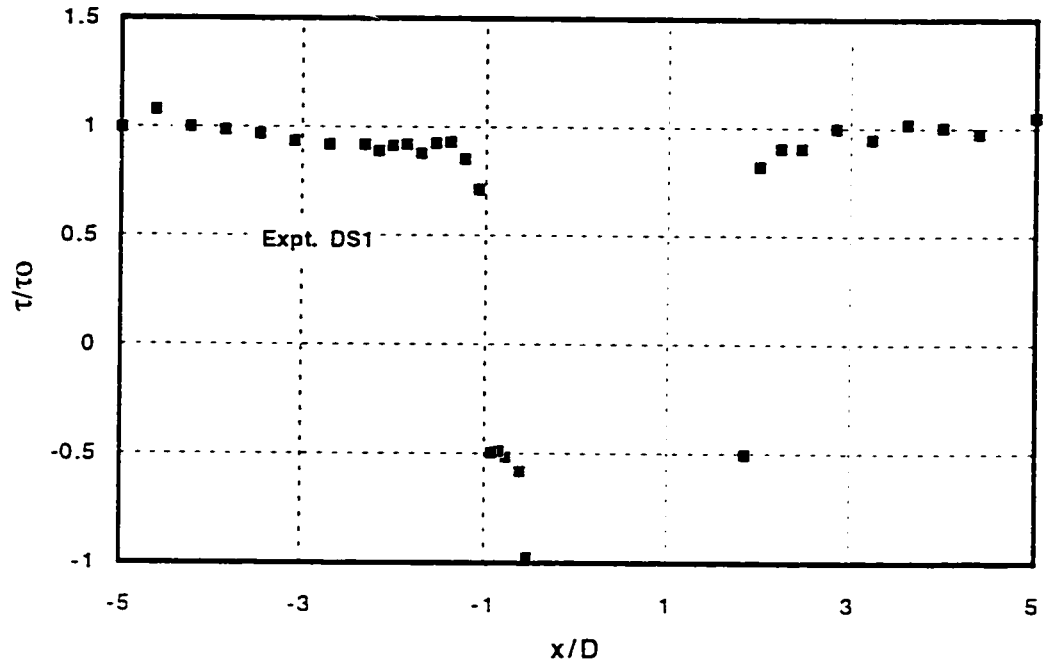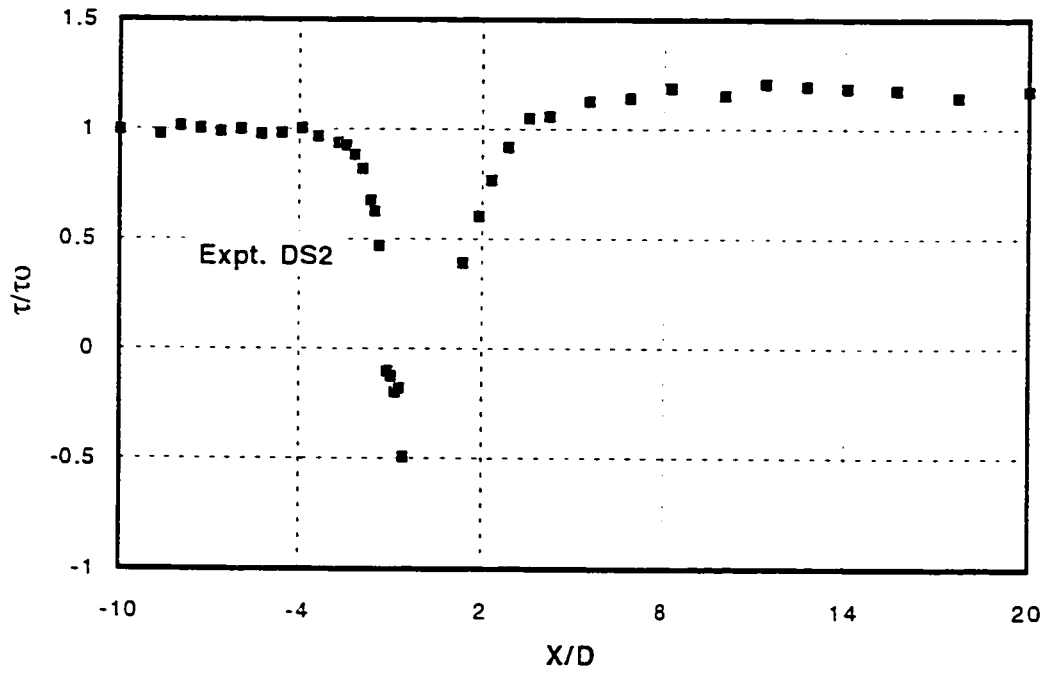
Figure 5.25 (a-b) Normalized Shear Stress Profile on the POS

Expt. AS1

(c)

Expt. AS2
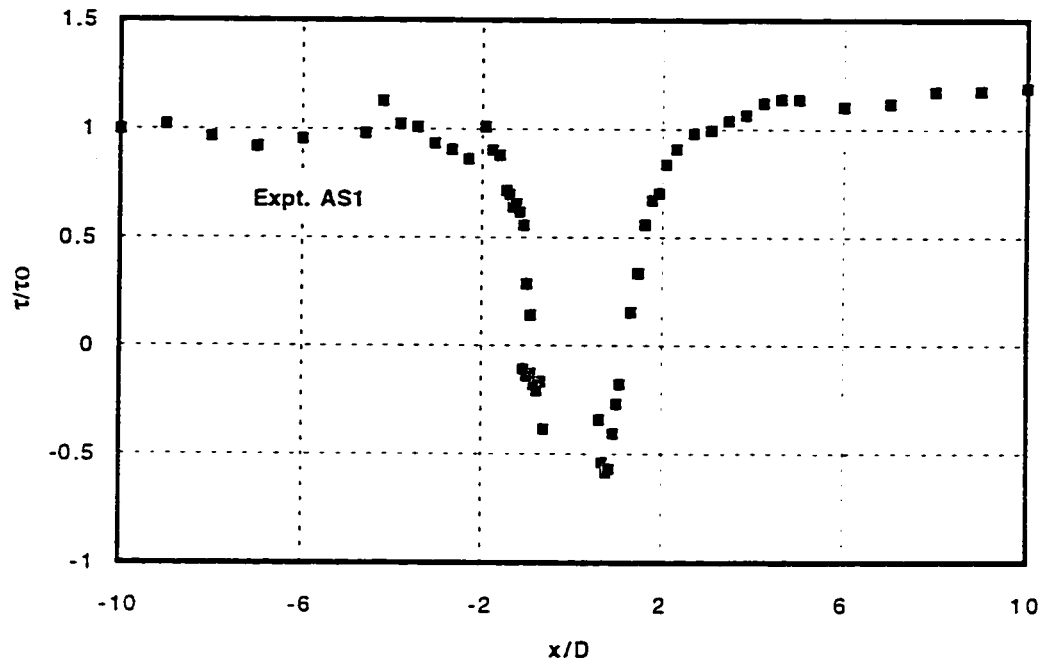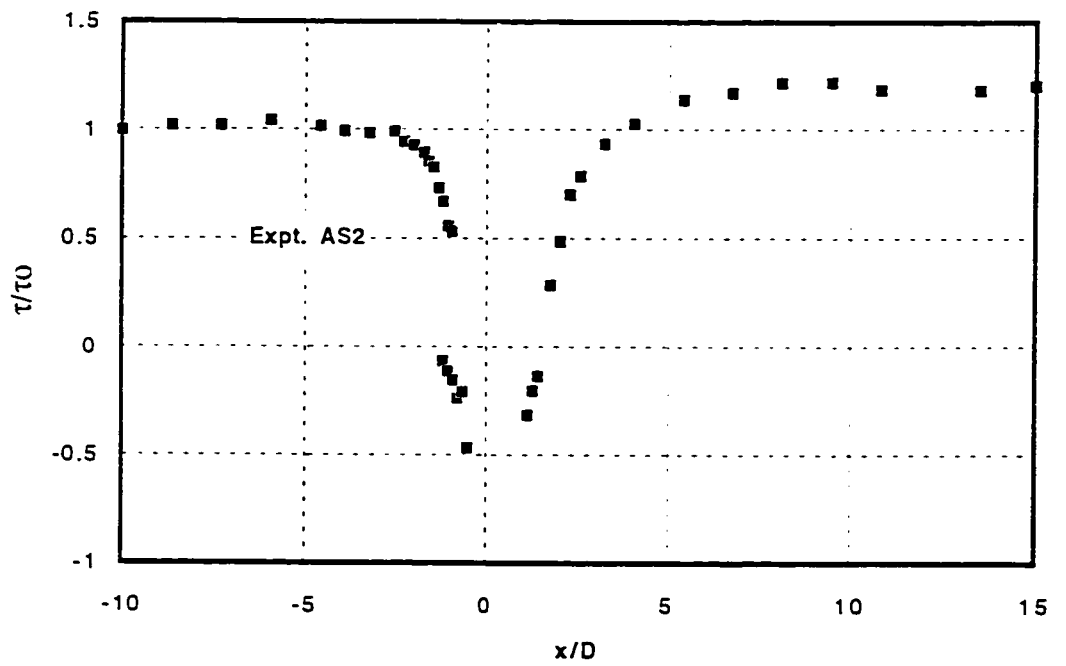
(c)

Figure 5.25 (c-d) Normalized Shear Stress Profile on the POS

(e)

(f)
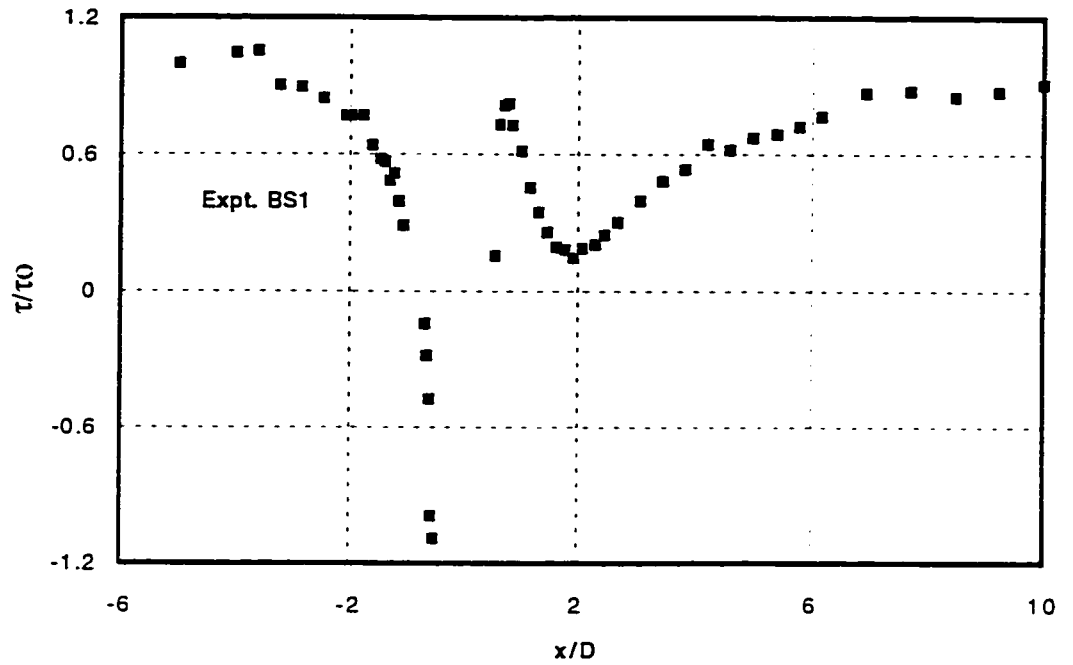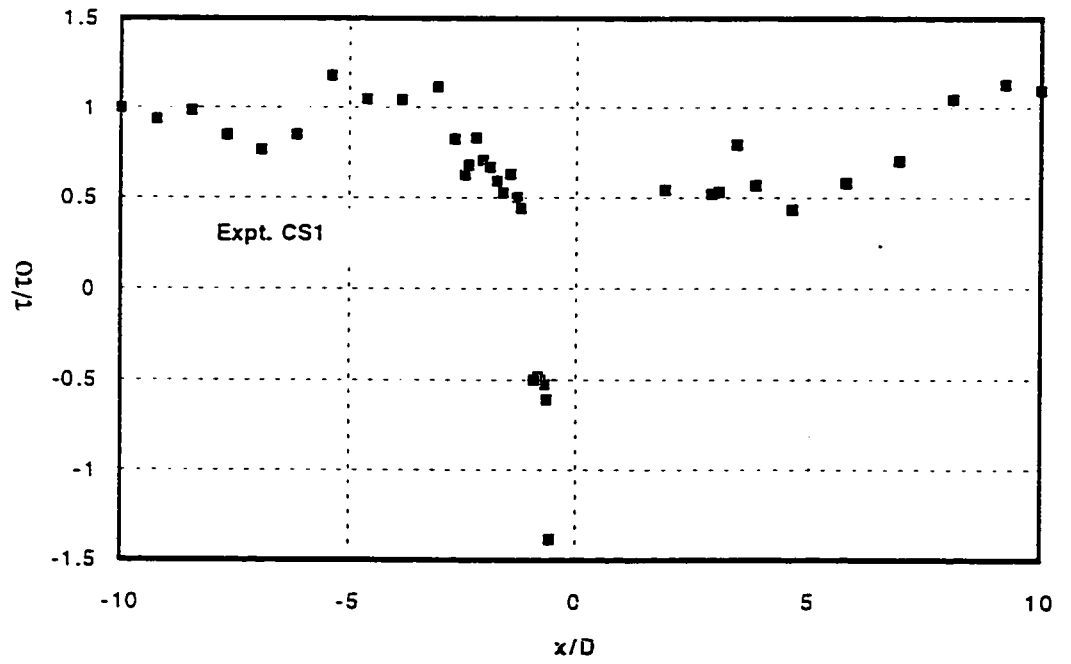
Figure 5.25 (e-f) Normalized Shear Stress Profile at POS

(e)

(f)
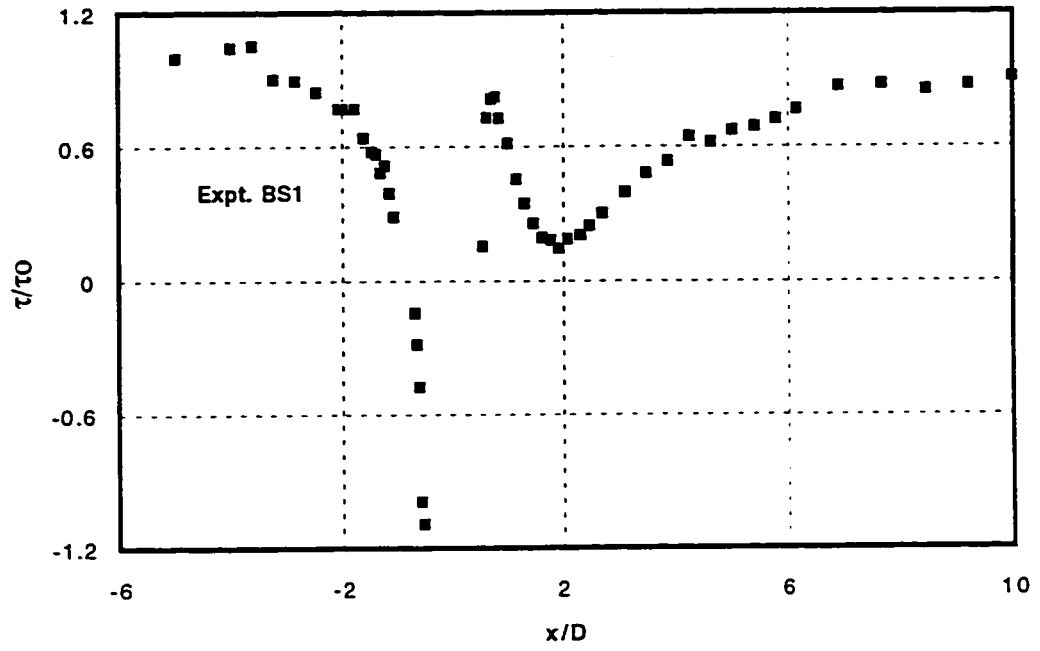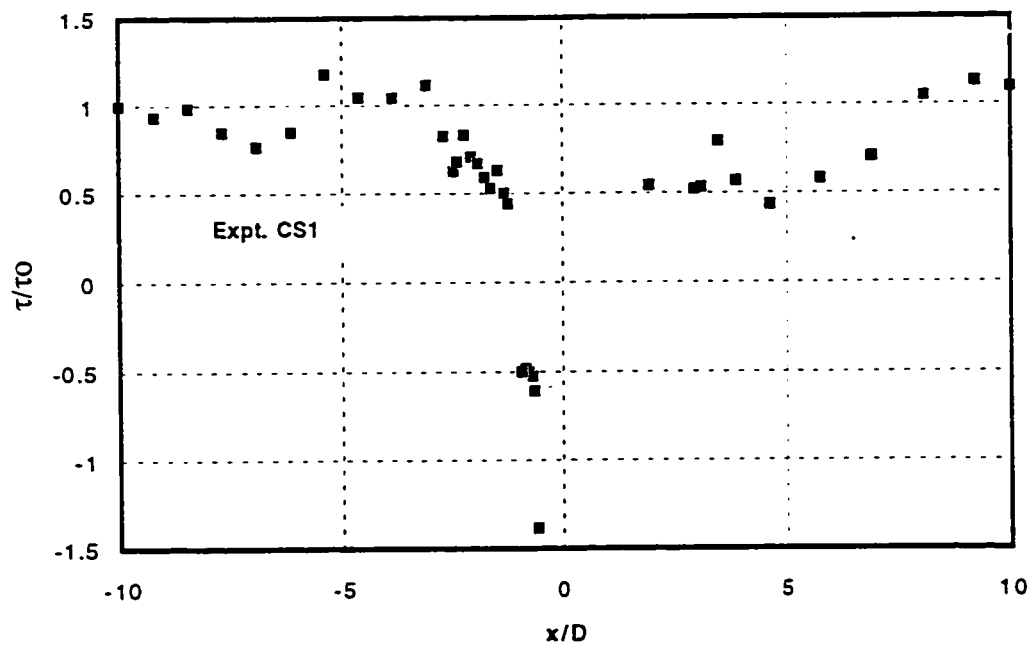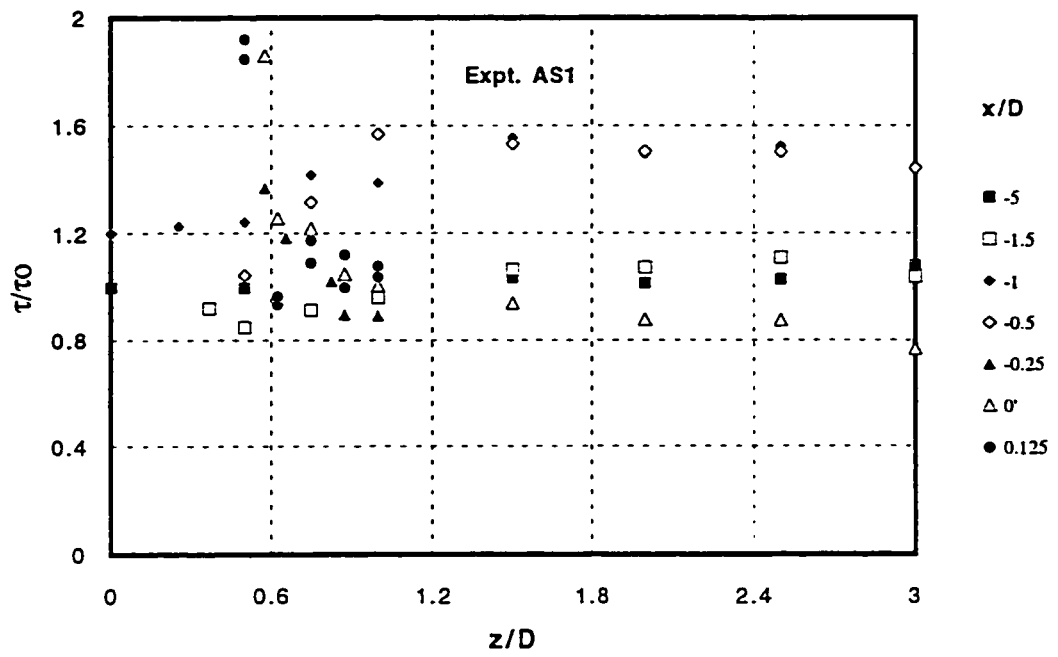
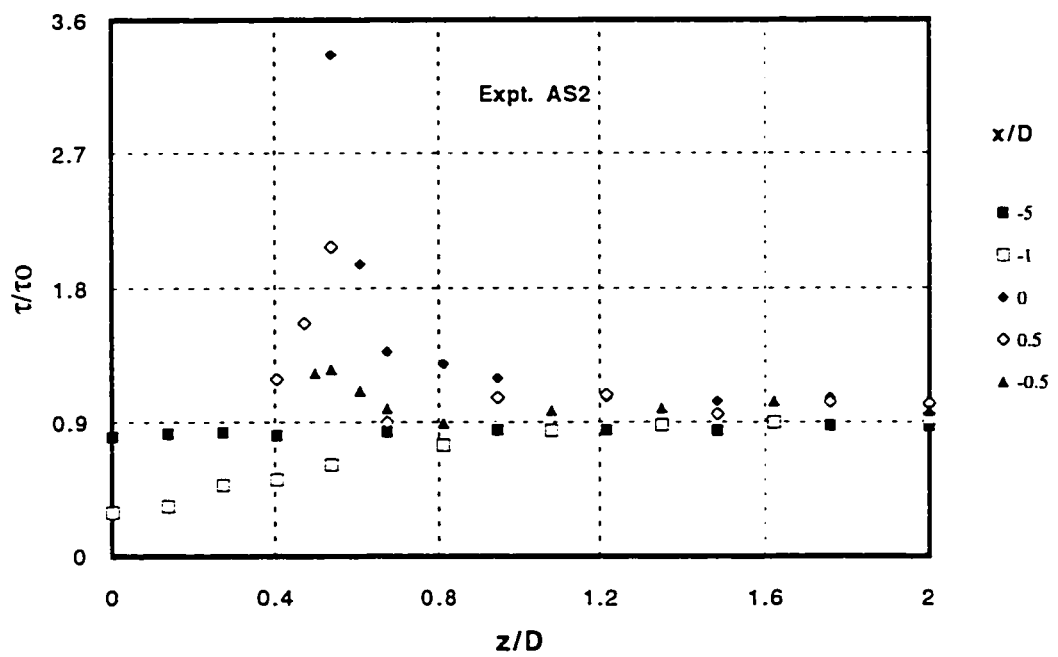Figure 5.25 (e-f) Normalized Shear Stress Profile at POS
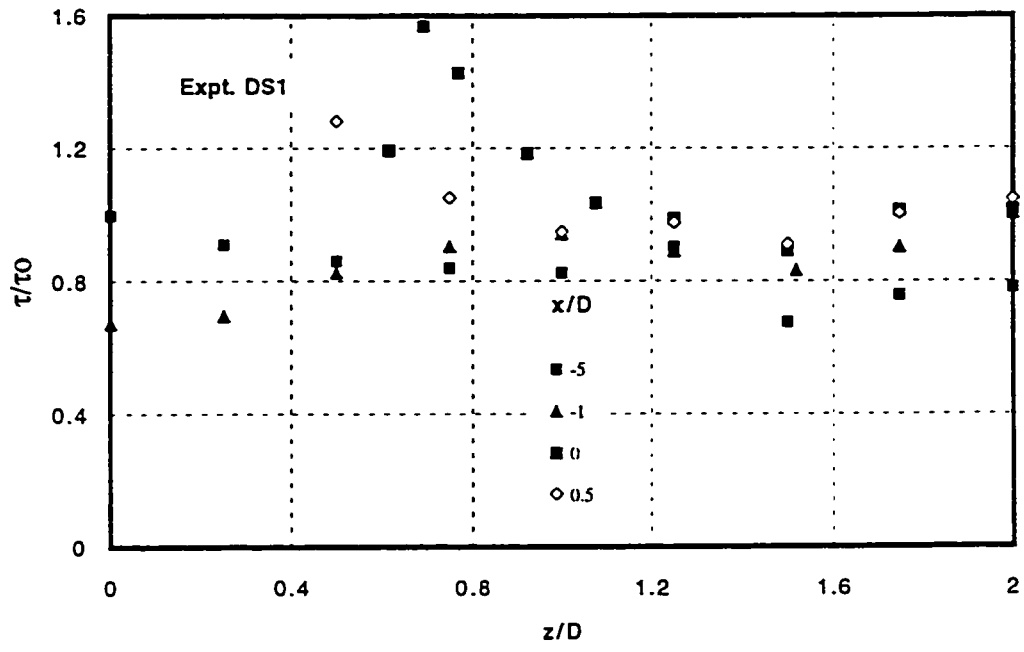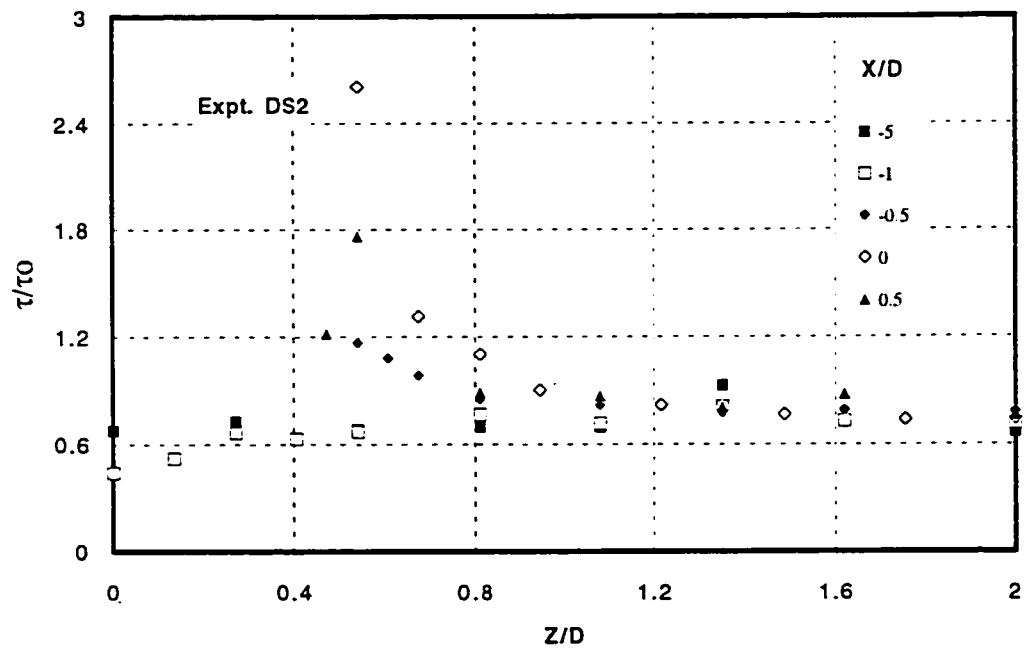
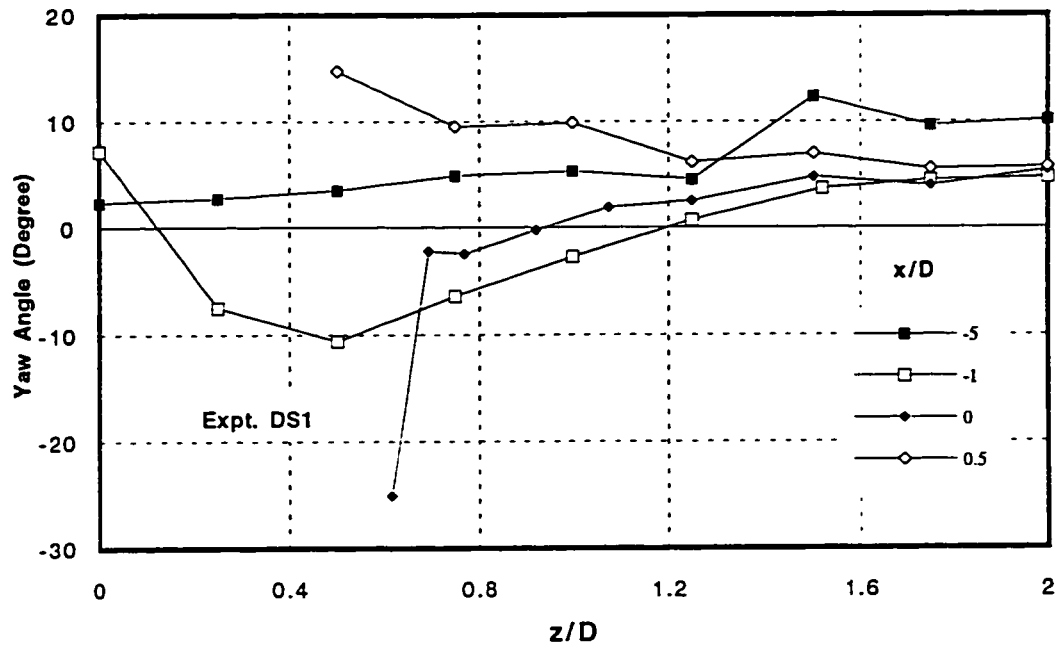Figure 5.26 (a-b) Spanwise Profiles of Normalized Bed Shear Stress

(c)
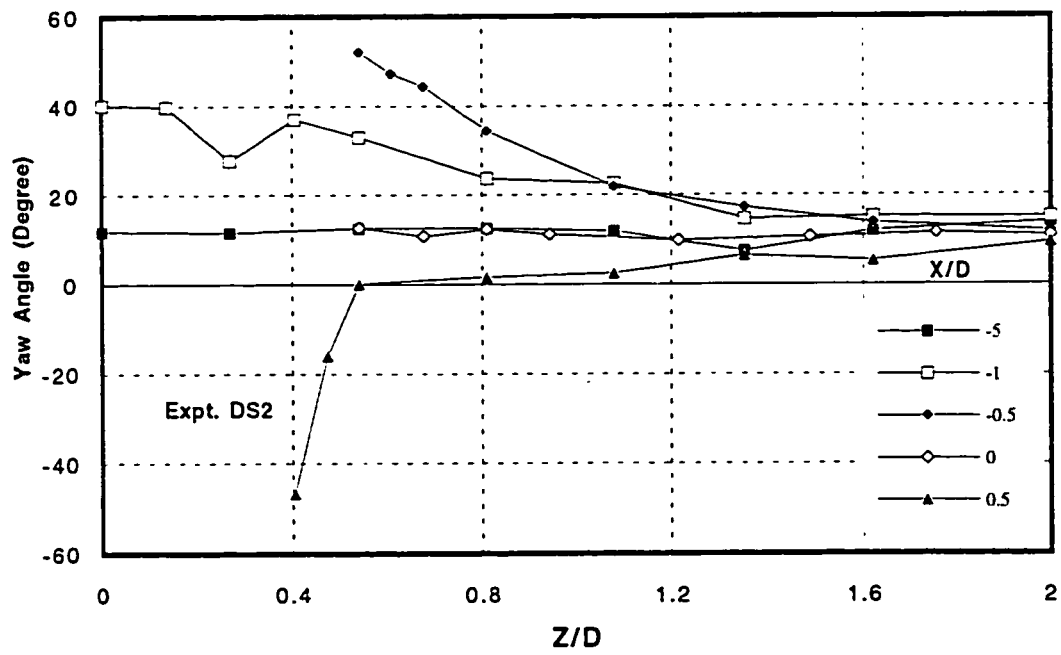

(d)

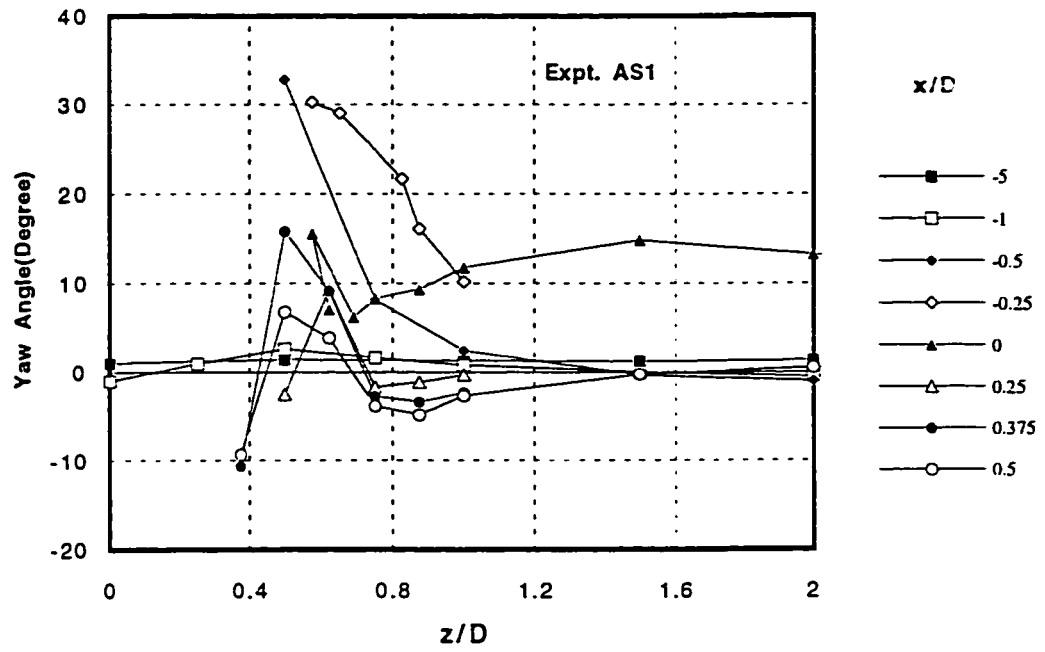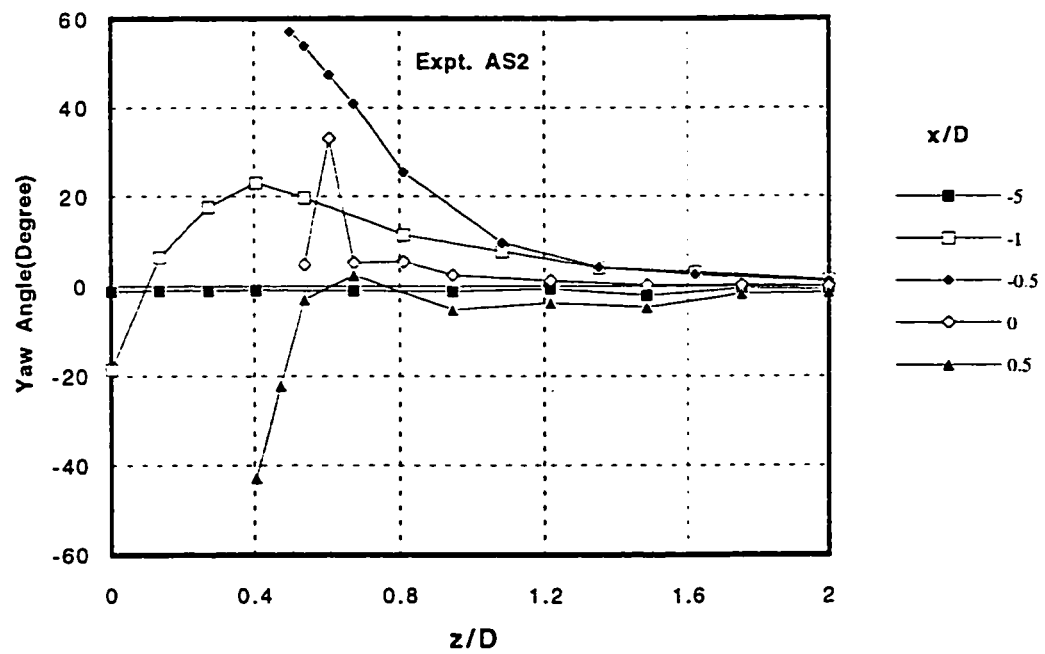Figure 5.26 (c-d) Spanwise Profiles of Normalized Bed Shear Stress

(a)

(b)

Figure 5.27 (a-b) Spanwise Profiles of Yaw Angles of Bed Shear Stress

Figure 5.27 (c-d) Spanwise Profiles of Yaw Angles of Bed Shear Stress

CHAPTER 6

EXPERIMENTAL RESULTS IN ROUGH AND MOBILE BEDS

6.1   Introduction

After investigation of the flow in the vicinity of the obstacle for the smooth bed, a series of tests was carried out on the mobile bed for similar flow conditions to study the scour around the body. Different types and sizes of obstacles and two different uniform sediment sizes were used. Bed shear stress was measured on the rigid bed and bed scour was measured at the equilibrium state and prior to that. In each case, before mounting the obstacle on the bed, several tests on the undisturbed flow were carried out to check whether the flow was fully developed and the effect of the bed roughness on the flow.

6.2   Velocity Measurements

Velocity field in presence of the loose boundary is different from that of smooth bed due to the effects of the bed roughness and the scour hole, and sediment deposition around the body. The interaction of the flow and the bed brings new variables to the already complicated problem. To prevent further complication, two sizes of uniform sediments were used with $D_{50} = 1.11$ and 2.12 mm. Two sizes of hemisphere and a cube were placed as obstacles while mounted on a cylinder of the same diameter. The cylinder was covered by the sediments. A natural rock was tested as well to verify the difference of its scour patterns.

Velocity measurements in the mobile bed were difficult to make due to the presence of the scour hole and deposition of the sediments around the body. Close to the body and inside the scour hole there was a strong 3D-flow which also limited the measurements. To overcome part of this problem, some measurements were taken on a rough bed while sediments were not allowed to move, which will be called rigid bed. By

235

gluing the sediments on the bed, the measurements could be made in the absence of any scour hole or deposition, simulating the condition at the threshold of movement of the sediments. A limited number of measurements were taken in the scour hole where possible.

6.2.1 Velocity measurements on the POS

The profiles of the normalized velocity on the POS are presented in Figures 6.1(a-d). Figures (a-c) cover the measurements on the rigid bed and Figure (d) shows the results on the mobile bed. Velocity was measured by pitch probe on the POS and the sectional average velocity Uo was used to normalize the velocity. The slowing down process is visible in the upstream profiles, similar to the profiles in the smooth bed. In Figure (a), Expt. AR11, a wall wake is present in the downstream profiles (x/D= 2, 3 and 4). Downstream profiles in Figure (b), Expt. BR11, show a developing boundary layer at the bottom, while the rest of the flow is significantly decelerated by the turbulence in the wake.

Profile of x/D= -0.85 in the mobile bed, Figure (d) Expt. AM11, indicates an acceleration region at the lower layer, which can be attributed to the flow entrance to the scour hole. The lower part of the velocity profile close to the scour hole rushes to the hole, causing more scour. Downstream of the body, the flow as part of the HS vortex departs the scour hole with a large velocity and causes a jet-like flow at the lower level. Further downstream, at x/D=4.15, high turbulence causes an almost constant velocity profile for the whole depth of flow.

Profiles of pitch angles and normalized vertical velocity on the POS are presented in Figures 6.2 (a-d) and 6.3 (a-d) respectively. The ratio of v/Uo usually becomes maximum close to the bed. It reaches its minimum of -0.1 about y/h=0.4 at the outer part of the bottom layer of wall wake, at x/D=2 in Figure 6.3 (a), dividing the profile into two sections. Based on the Figure 6.1 (a), this is the depth in which the effect

of the bed starts to change the usual bell shape of the free wake. There is a downward flow at the surface layer of the downstream profile of the v/Uo, Figure 6.3 (b). A large ratio of v/Uo=1 at x/D=1.46 in Figure (d) indicates a strong upward flow caused by out coming flow from the scour hole (in the same place that makes a jet-like flow in Figure 6.1 a).

The standard deviation of measured pitch angles are presented in Figures 6.4 (a-d). The maximum fluctuation of about 6 degrees can be seen in Figure (a) for Expt. AR11 at y/h=0.4 while the maximum in Figure (b), Expt. BR11, occurs at both surface and bottom with a value as large as 12 degrees. In regime 4, Figure (c), the maximum occurs only at the bed. This means the location of the fluctuation of the angle is changed from the middle depth of the body in regime 2 to the surface and bottom of the flow in regime 3 and stays at the bottom in regime 4. The location of the maximum in regime 2, Figure (a), occurs at the middle of the wake while it occurs at the surface in regime 2 where there is a large mixing between the tiny layer of the water moving from the top of the body and the main flow. Then in absence of this layer, regime 4 in Figure (c), the maximum stays only at the bottom. The maximum in mobile bed occurs at the middle depth downstream of the body, Figure (d).

The measured velocity profiles are compared with the law of the wall in Figures 6.5 (a-d). The velocity profile of an undisturbed flow at x/D=-7.69 is plotted in these figures. In general, the figures show the deviation of the velocity profiles due to the presence of the body, while the undisturbed profile agrees well with the log law. The upstream profiles mostly occur above the log law, indicating the small value of the shear velocity u* because of the slowing down process in front of the body. Downstream profiles deviate from the log law immediately behind the body, and by development of the flow it gets closer to the line, i.e., becomes uniform again.

6.2.2 Spanwise velocity measurements

Spanwise velocity was measured inside the scour hole with yaw probe at the side and in front of the body at x/D=0 and -0.85 respectively, Figures 6.6 (a-b). The side profiles, Figure (a), indicate a larger velocity in the vicinity of the body, which decreases towards the middle of the hole and then increases very close to the outer wall of the scour hole. Decrease of the velocity by the depth inside the scour hole shows the effect of the depth of the scour in reduction of the sediment transport. The front profiles indicate a similar trend, especially the one in y/h=0 with a lower velocity at the middle width of the scour hole.

The profiles of the yaw angles and the normalized lateral velocity, w/Uo, are presented in Figures, 6.7 and 6.8 (a-b) respectively. A strong negative lateral velocity (w/Uo = -0.55) exists at the bed level (y/h=0) on the side of the obstacle with a yaw angle of almost -60 degrees (Figure, a). The strength and the yaw angle of the lateral velocity decreases moving towards the body or the scour wall. The profile of y/h =0.46 shows a similar trend but with much less strength. Moving inside the scour hole, the maximum inward lateral velocity changes to an outward positive velocity for almost all the width of the scour hole at y/h= -0.615. A strong positive lateral velocity of w/Uo = 0.45 occurs at the scour wall in this level with a smaller value at the middle. The difference between these two level of y/h shows that there is a diverging flow at the deepest part of scour due to the action of the HS-vortex. Whereas in the upper levels, well before reaching the bed level, flow starts to converge toward the POS. High fluctuation of the yaw angle can be observed at the middle width of the scour in Figure 6.9 (a). The profiles of normalized lateral velocity and yaw angles in front of the body also indicate a similar trend, Figures 6.7 (b), 6.8 (b) and 6.9 (b).

6.3 Bed Shear Stress Measurements

Bed shear stress was measured by Prandtl tube on the POS and with the yaw probe in the transverse direction on rigid bed where the sediments were not permitted to move. The measurements were taken for regimes 2, 3, and 4 with two sizes of sediments. Bed shear stress on the POS is presented in Figures 6.10 (a-f) and its normalized profiles in Figures 6.11 (a-d). In general the τ/τ_o decreases approaching the body and increases down stream of the body where the flow develops. There is a negative shear stress at upstream profiles due to the backward flow induced by the HS vortices after the separation point.

The backward flow can be traced by negative sign of the shear stress at the downstream side of the body and inside the recirculation zone at Figure (a). In regime 3 and 4 no measurements were possible in the vortex generation zone, while there was a forward flow in most cases (due to very high fluctuations beyond the acceptable range of the probe). Decreasing the relative depth from Figure (a) to (e), the minimum measured τ/τ_o increases from -0.4 to -1.2, while the average velocity was very close. Therefore, the cause of this increase would be the relative depth. There is an increase of τ/τ_o comparing Figures (a-c-e) (smaller sediment size of $D_{50}=1.11$ mm) and Figures (b-d-f) (rougher bed, $D_{50} = 2.12$ mm).

Profiles of spanwise normalized bed shear stress are presented in Figures 6.12 (a-d) and their yaw angle profiles are presented in Figures 6.13 (a-d). The bed shear stress was measured upstream and downstream of the body with a focus at the side of the body (x=0) ,where, based on the flow visualization, there is a higher shear stress and the scour initiates. The profiles of τ/τ_o shows that its maximum value does not occur at x=0 but at a small distance upstream of this point (x/D= -0.77 to -0.192). The maximum value of τ/τ_o in regime 2, Figure (a), reaches to 6.7 while its counterpart in regime 3 and 4 reaches values as high as 19, Figures (c-e). This significant increase of the τ/τ_o occurs

239

only due to the change of the relative depth. The high shear stress stayed several times larger than the undisturbed one even downstream of the body, x/D=0.5 in Figure (a).

The width of the high shear value is less than 0.5 z/D in regime 2 while it is more than z/D=1 in regimes 3 and 4, indicating a wider possible scour, which agrees well with observations in Chapter 4. This wider range of high shear stress might be due to the larger effect of the body in a shallower flow where the flow has to divide to two sections around the obstacle with no flow from the top. Comparing the two sizes of sediments, the shear stress on the rougher bed is much more than that of the smoother bed in regime 2, Figures (a-c), but with no difference in regimes 3 and 4, Figures c-d. The width of high bed shear stress in the profile of τ/τ_0 at the rougher bed is more in regimes 3 and 4. High positive yaw angles of up to 35 degrees are present at and upstream of x=0, while downstream of this line the bed shear vector has values as high as -55 degrees, Figure 6.13 (a).

6.4 Bed Scour Profiles

The bed scour profiles were measured in consecutive times before reaching to the equilibrium state for 3 different relative depths. Results are presented in Figures 6.14 to 6.17. In each case, scour and deposition was measured by point gauge on the POS, upstream and downstream of the body, and at its side, x=0, for a period of 2-3 days. The profiles of equilibrium bed scour at the end of each period were measured at the same locations for different obstacles and sediments. Results are presented in Figures 6.17 to 6.19.

The progress of scour in time can be observed in Figures 6.14 to 6.16. The front and side scour profiles are consistently parallel with an average slope similar to the natural angle of repose of the sediments, 28°. In front profiles, Figures 6.14, two slopes exist, which confirms the results of flow visualization in Chapter 4. The scour wall has two steps. The first one at the bottom of the scour hole has a steep slope, while the other

240

one shows a mild slope. The steep slope occurs due to the presence of a strong horse shoe vortex capable of keeping sediments on a slope steeper than their natural angle of repose. The width and depth of the scour were similar for different relative depths, x/D=1.3 and y/h=1.3, suggesting that the relative depth has no effects on the front scour for the same sediment size. This fact can be explained by considering the strong effect of downflow in front of the body inside the scour hole. The downflow did not affect the scour at early stages, but it became a major parameter when the flow faced the vertical wall of the cylinder on which the hemisphere was mounted. Therefore, at the equilibrium state, the shape and depth of the scour was directly under the effect of the downflow.

The depth and width of the scour profiles at the side of the body, Figures 6.15 (a-c), are also similar for different relative depths, z/D of 1.2 and y/h of 1.1. Qadar (1981) found that the scour depth in front of the bridge pier is related to the strength of the HS-vortex which is significantly under the influence of the downflow. He found that the radius of the HS-vortex is almost 0.1 times the width of the pier and the vortex velocity decreases by width of the pier. He proposed that the sediment size is only important at the initial stages of the scouring process, and that the final scour depth depends only on the sediment transport capacity of the vortex for sediments less than 0.5 mm in diameter.

The width of the side scour is almost the same as the front scour, while its depth is less, y/h=1.1<1.3. The smaller depth at the side shows that an upward slope exists starting from the deepest point in front of the body to the deposition behind the obstacle. The profiles of the scour at the back of the body in regime 2, Figures 6.16 (a), shows the progress of the profiles over time keeping almost a constant height and parallel slopes. The height of the deposition reaches to o.6 times the height of the body with a scour of 0.4 y/h immediately downstream of the body. The profiles of (a-b) indicate a wavy pattern on the downstream slope of the profiles before reaching the original bed level.

The upstream faces of the profiles are still very similar. The height of the deposit reaches to 0.3 y/h in Figure (c) when the depth of the flow itself is y/h=0.4.

In addition to the obstacle #1, a hemisphere with diameter of 13 cm, a smaller size diameter, D=7.4 cm, was used to measure the profile of equilibrium bed scour, AM21. Similar measurements were also taken for larger sediment, AM12. In an attempt to observe the difference between scour patterns of a simple hemisphere and that of a cube or a natural rock, their scour was measured for the same flow condition. The results of these measurements in front of the body, at its side and behind the body are presented in Figures 6.17 to 6.19.

The front profile of cubic body indicates a large step between the two parts of the scour wall upstream of the body, Figures 6.17 (a-b). The smaller hemisphere caused a smaller scour hole. Comparing the profiles of different sediment sizes, the difference between their slopes can be seen in Figure (b-c). The coarser sands could hold a steeper slope resulting in a smaller width of scour and a slightly deeper scour, Figures (b-c). Considering the similar energy in the flow and strength of HS to transport the sediments, the flatter slope of smaller size sands (due to their smaller angle of repose) caused them to have a smaller scour depth compared with a larger size of sand.

The difference between the profiles of scour at the side of the hemisphere and those of the cube is significant, Figures 6.18. While the profiles of the AM11 and AM12 are similar, the depth of scour for the cubic obstacle was much less than that of the hemisphere's. The reason might be the shape of the body and the difference in the flow separation from its sides. The sharp edges of the cubic body do not allow the HS vortex to curl around the body easily like that of the hemisphere one. Therefore, the scour at the sides, which is the direct effect of the HS vortex, becomes less than its counterpart in AM11.

The back profiles for the same size obstacle but different sediments is almost the same, Figure 6.19 (a). The smaller hemisphere created smaller deposition and scour but

with similar patterns. The scour pattern of the cubic body is different from the hemisphere with a deposition immediately downstream of the body, and then a scour. In the case of the hemisphere with its round edges, the two legs of the HS vortex meet each other at the back of the body and create a scour there. But the sharp edges of the cube and its flat shape at the back keep the two legs apart and create a deposition there. The scour pattern of the natural rock is insignificant compared with that of the other obstacles because depletion of the sediments from the front of the body is very limited. The bed profiles are similar in Figures (b-c) for two types of sediments, but at the downstream slope of the profile some ripples are developed on the finer sediments, CM11 and CM12. The depth of scour on the fine sediment is less, for the same reason as previously outlined.
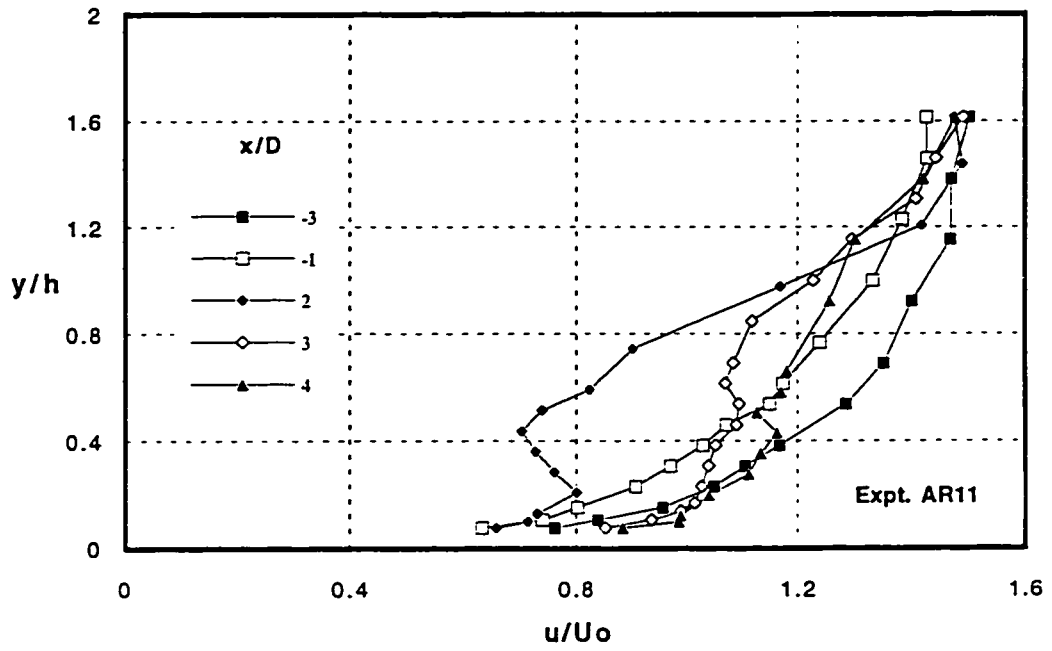
(a)
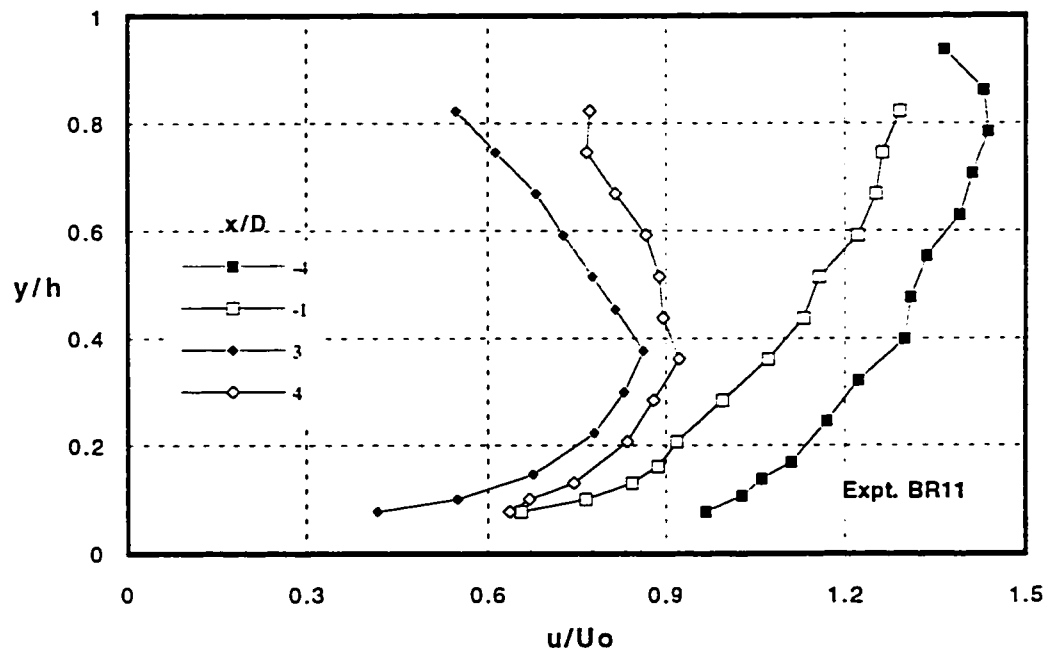
(b)

Figure 6.1 (a-b) Profiles of Normalized Velocity on the POS for Rigid Bed
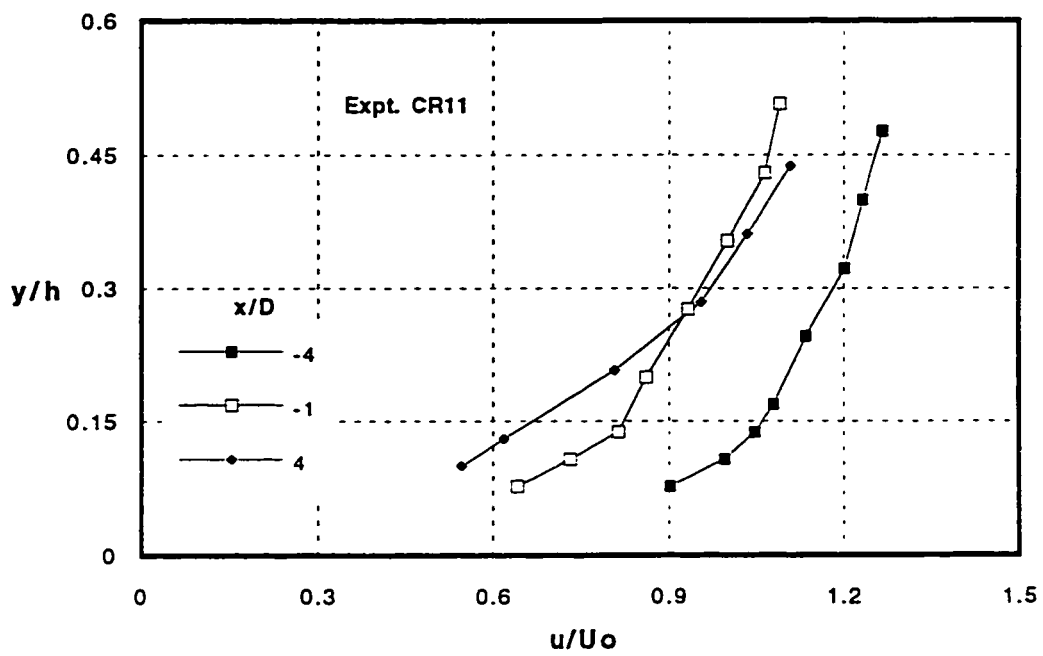
(c)
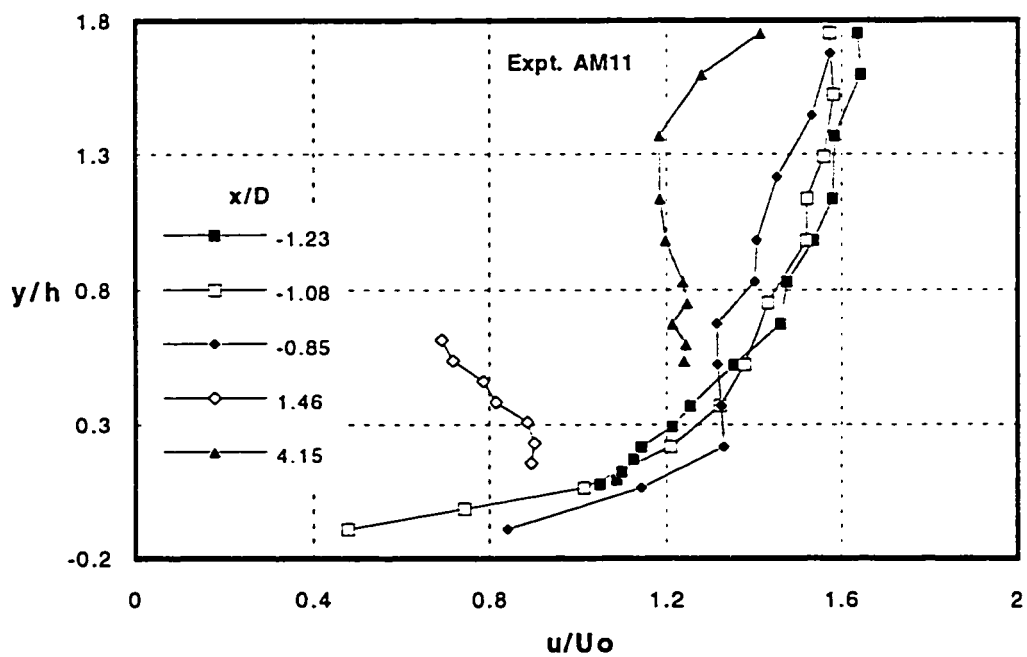
(d)

Figure 6.1 (c-d) Profiles of Normalized Velocity on the POS for Rigid Bed
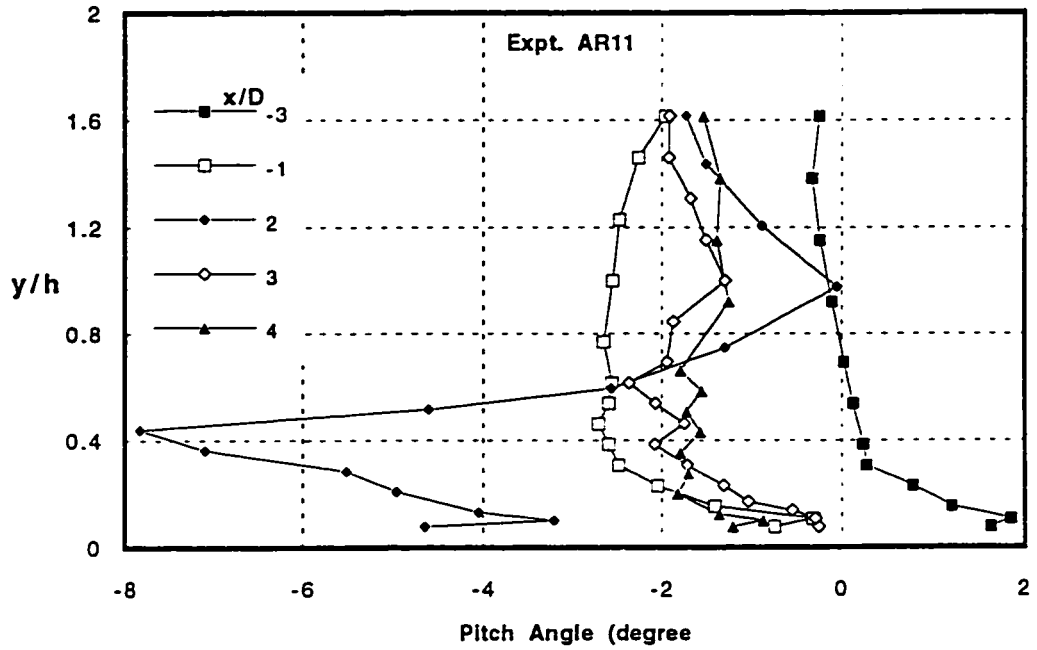
(a)
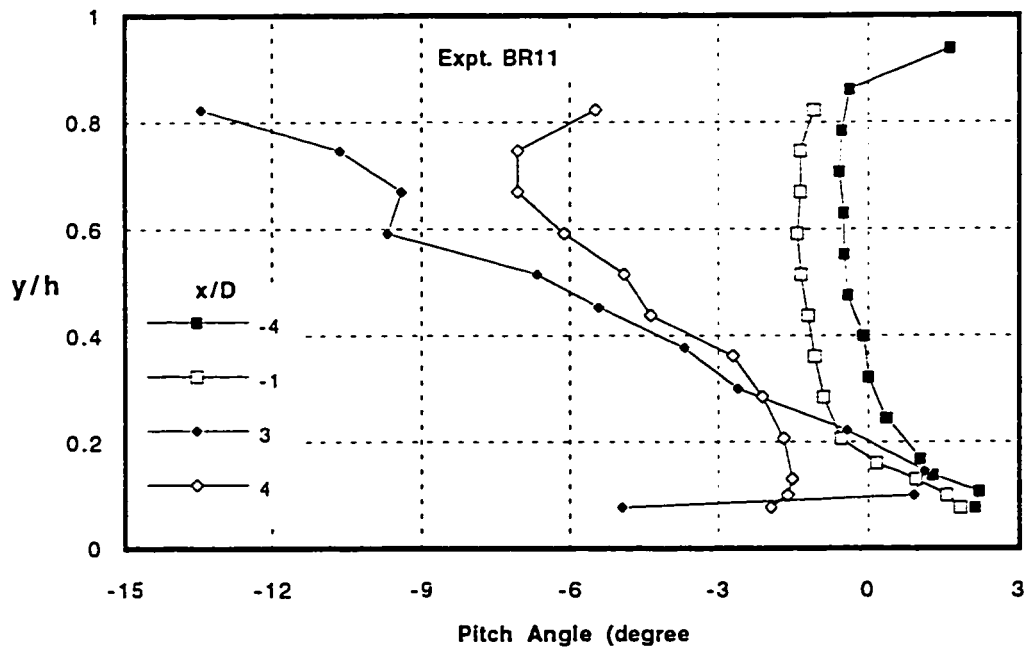
(b)

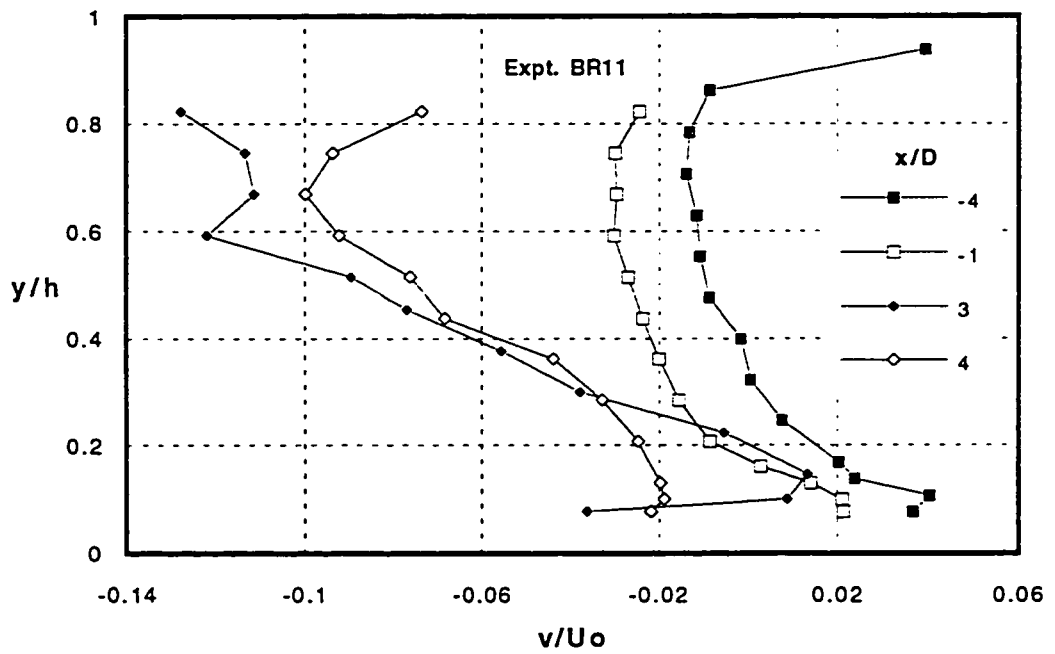Figure 6.2 (a-b) Profiles of Pitch Angle on the POS for Rigid Bed
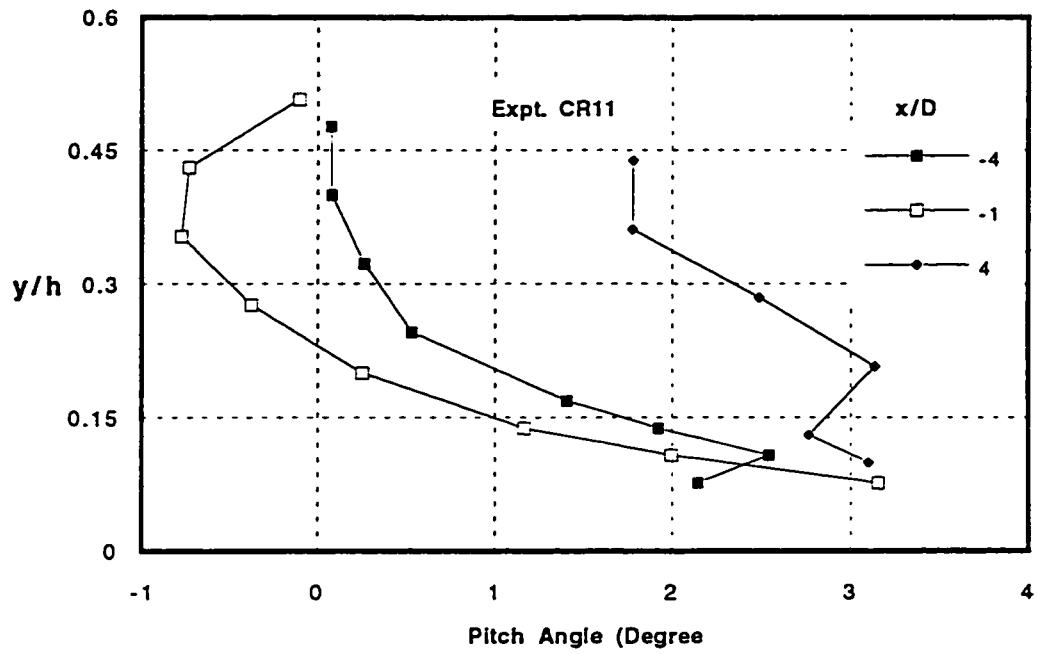
(c)
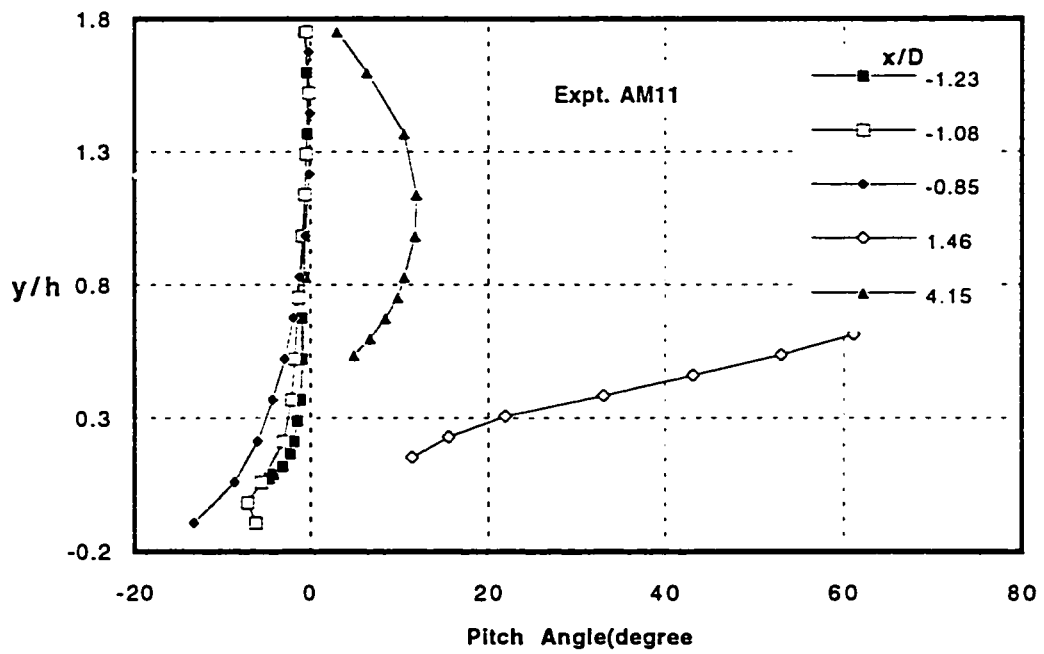
(d)

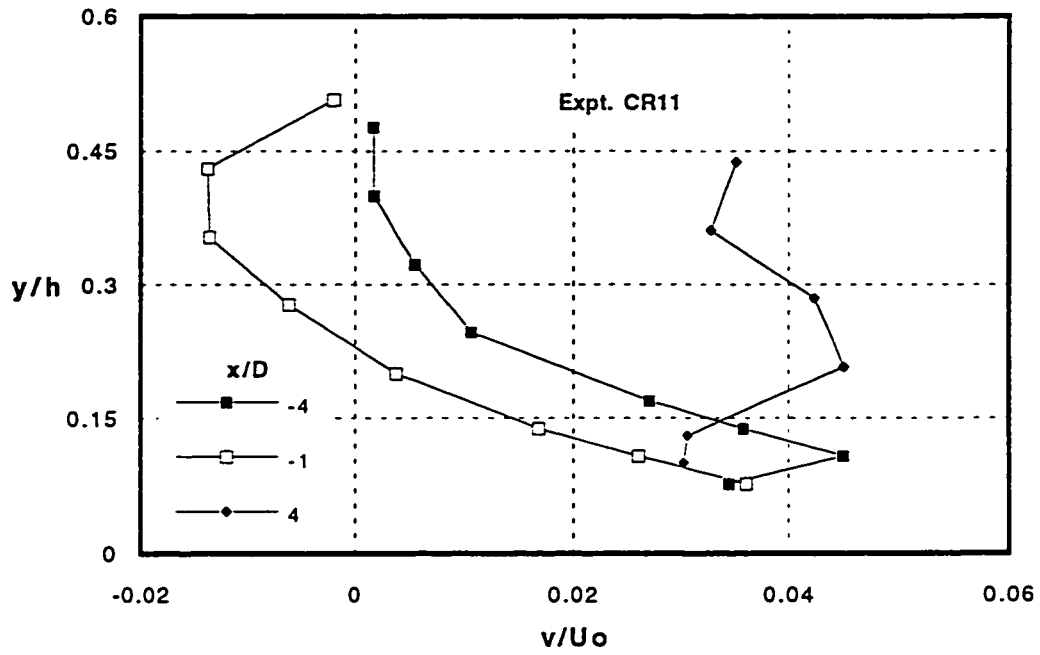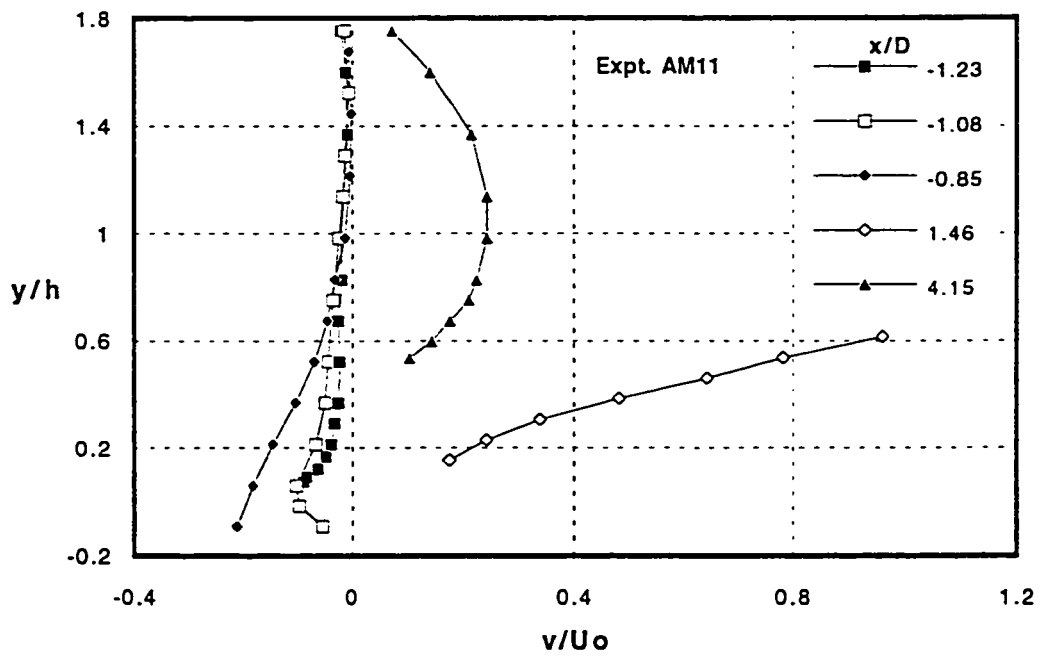Figure 6.2 (c-d) Profiles of Pitch Angle on the POS for Rigid Bed
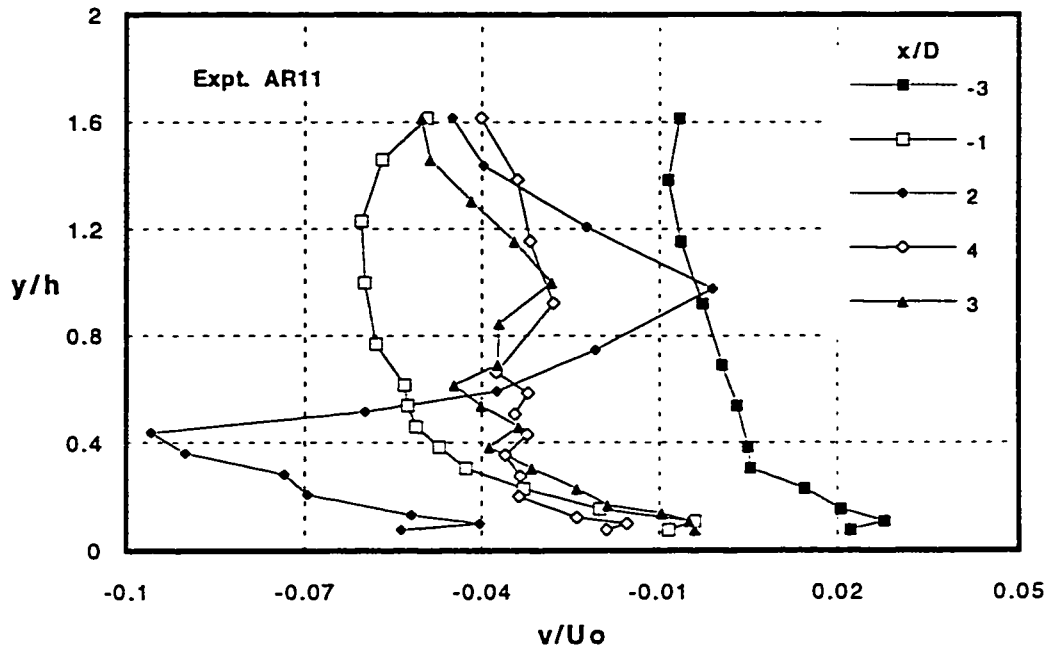
(a)

(b)

Figure 6.3 (a-b) Profiles of Normalized Vertical Velocity
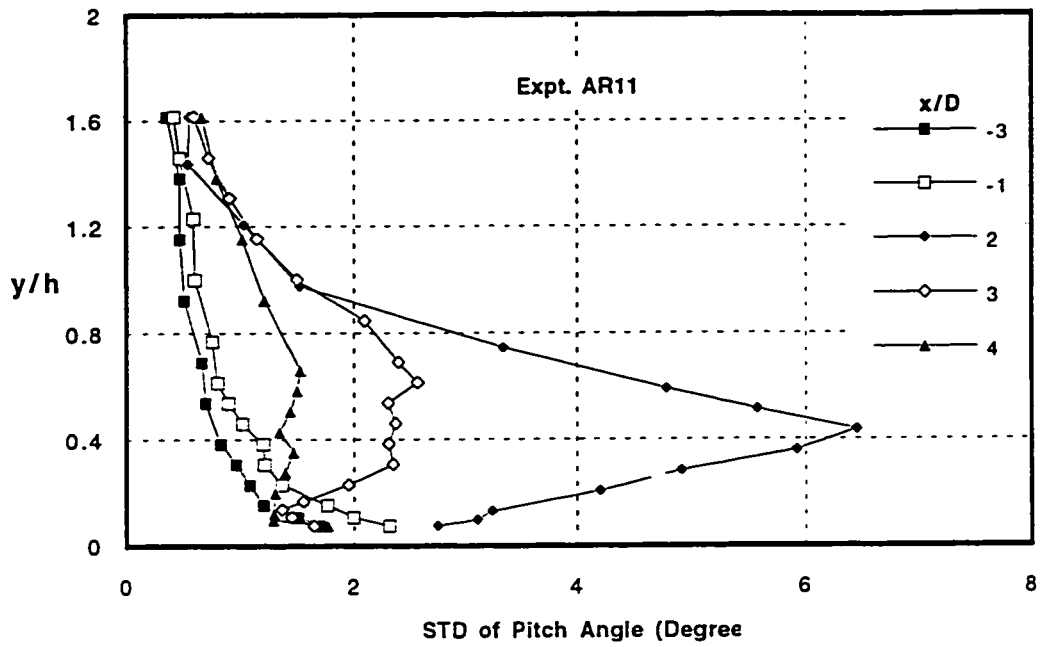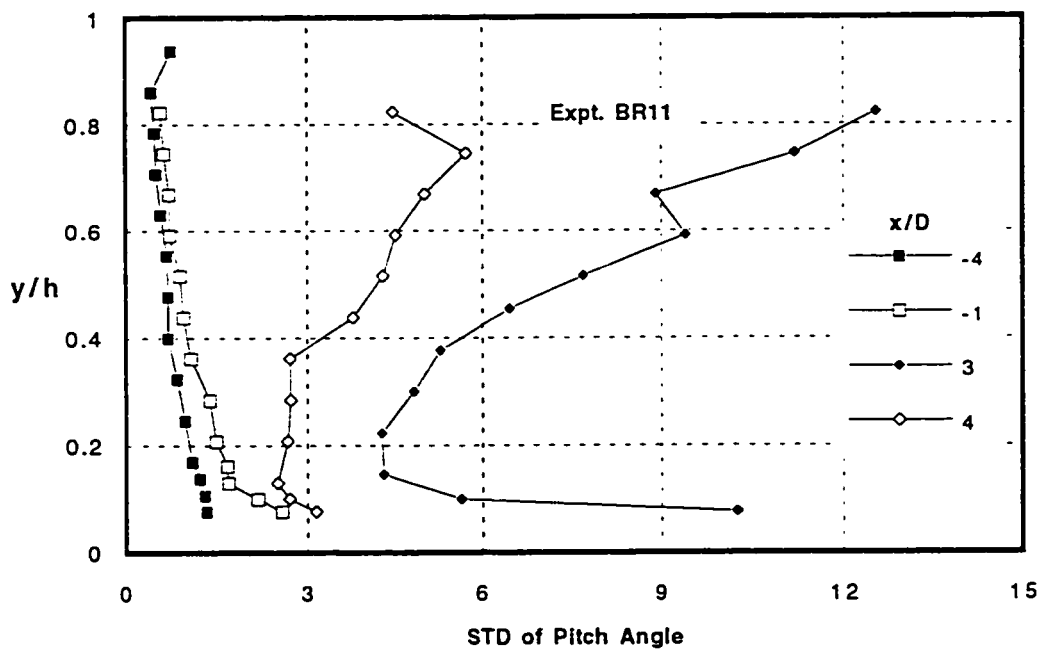on the POS for Rigid Bed

(c)

(d)

Figure 6.3 (c-d) Profiles of Normalized Vertical Velocity on the POS for Rigid Bed
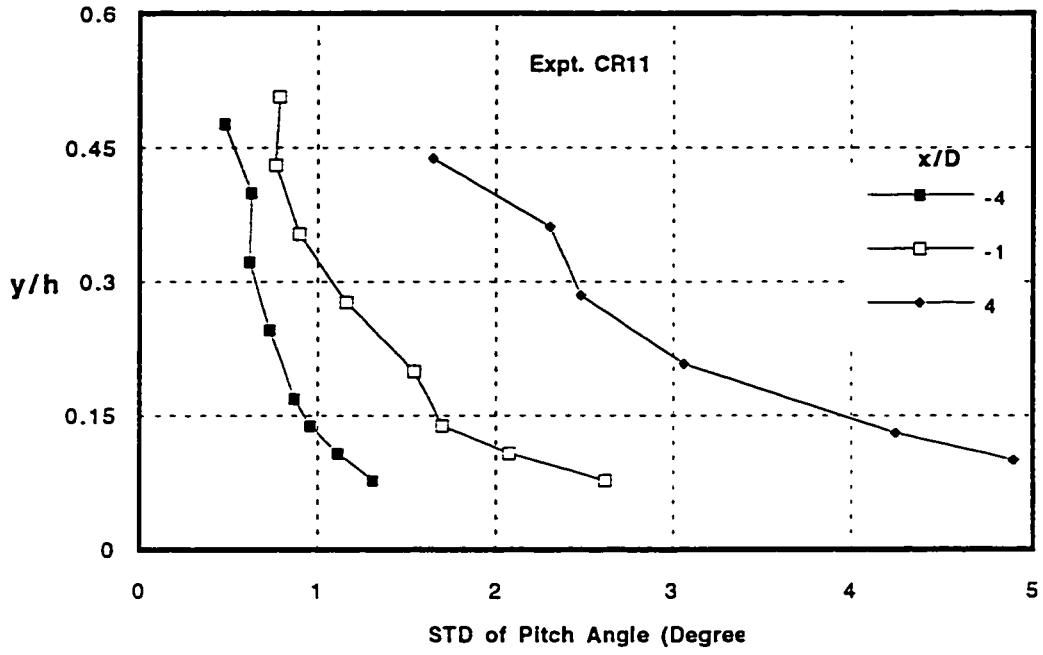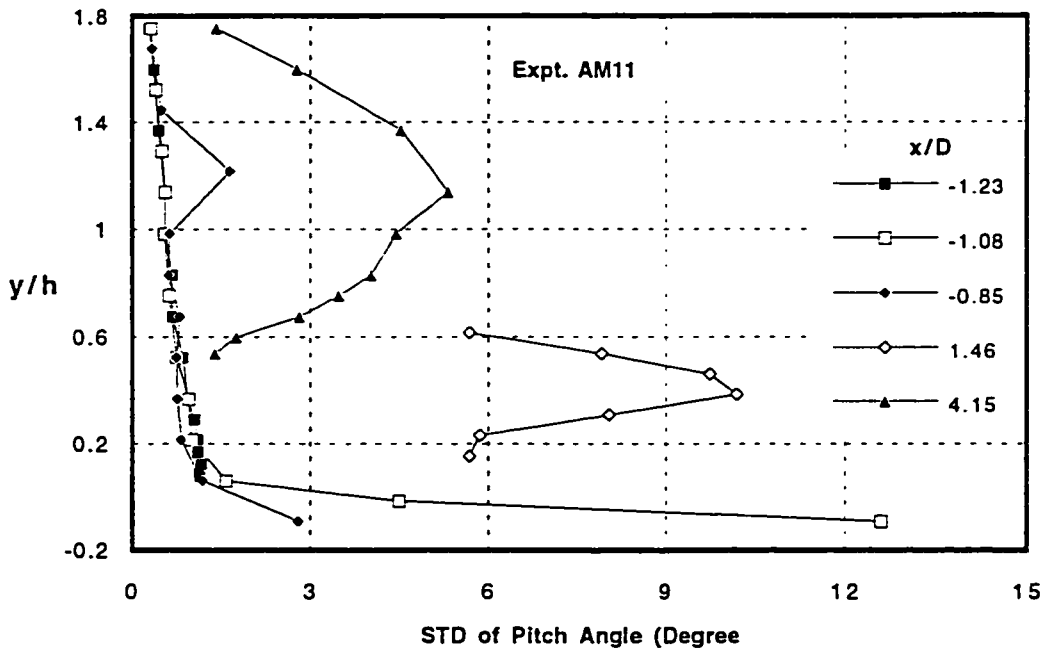
(a)

(b)

Figure 6.4 (a-b) Profiles of STD of Pitch Angle On the POS for Rigid Bed
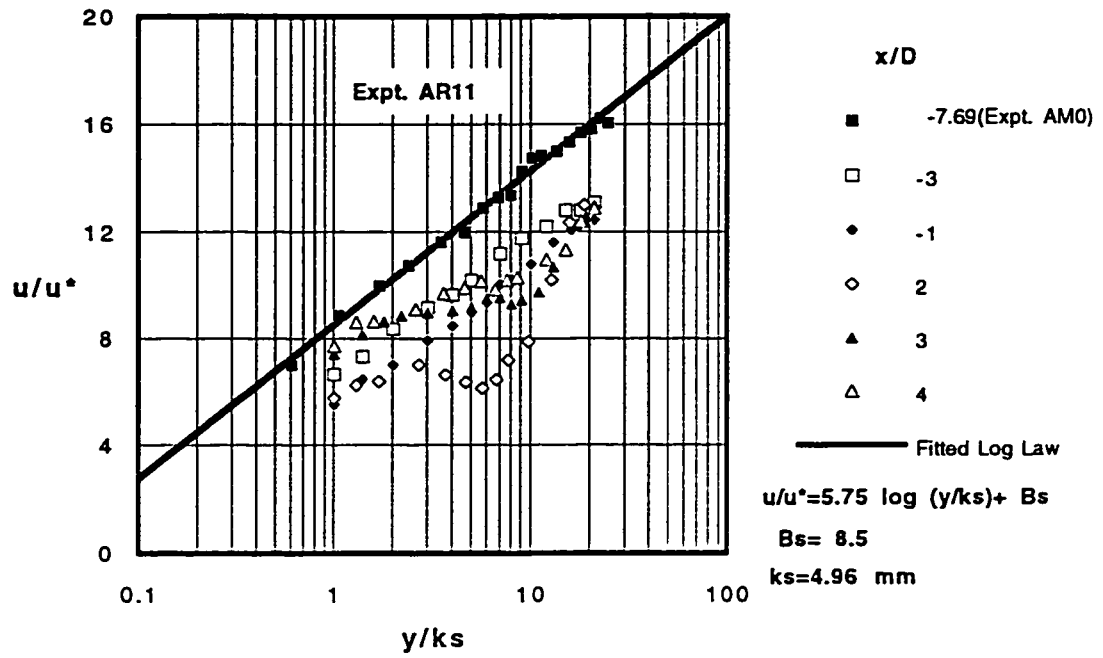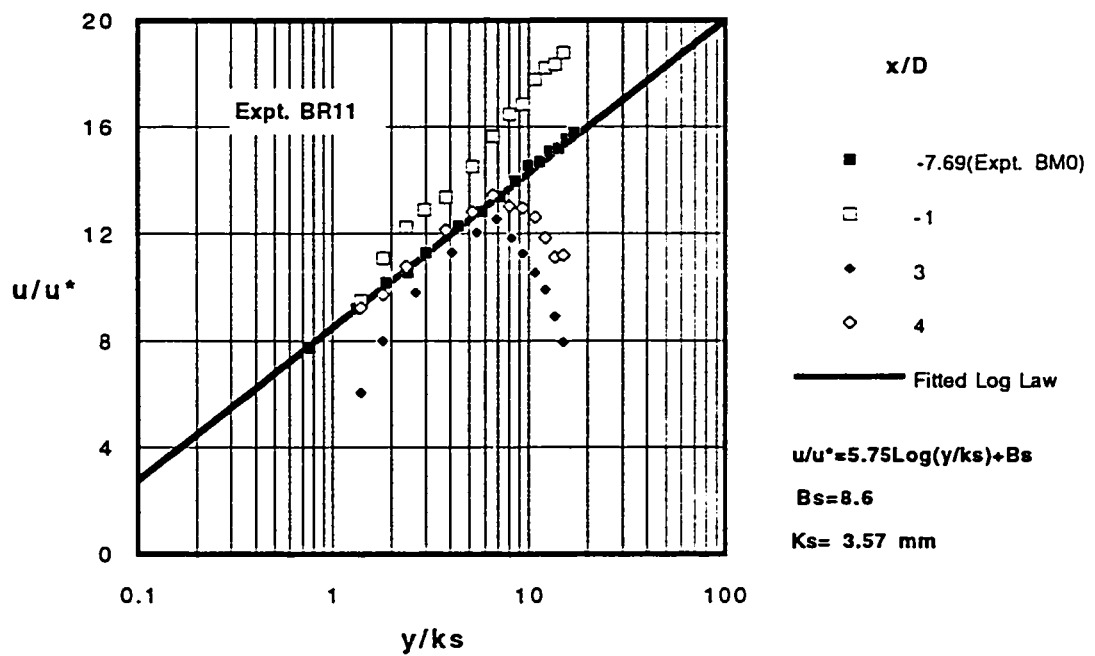
(c)

(d)

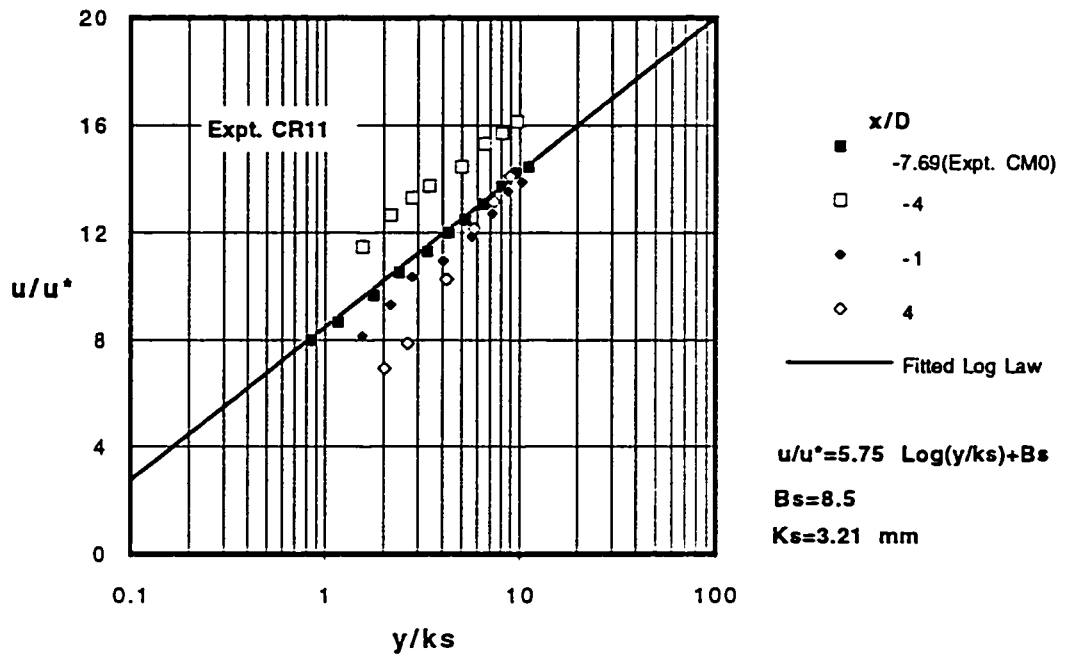Figure 6.4 (c-d) Profiles of STD of Pitch Angle on the POS for Rigid Bed
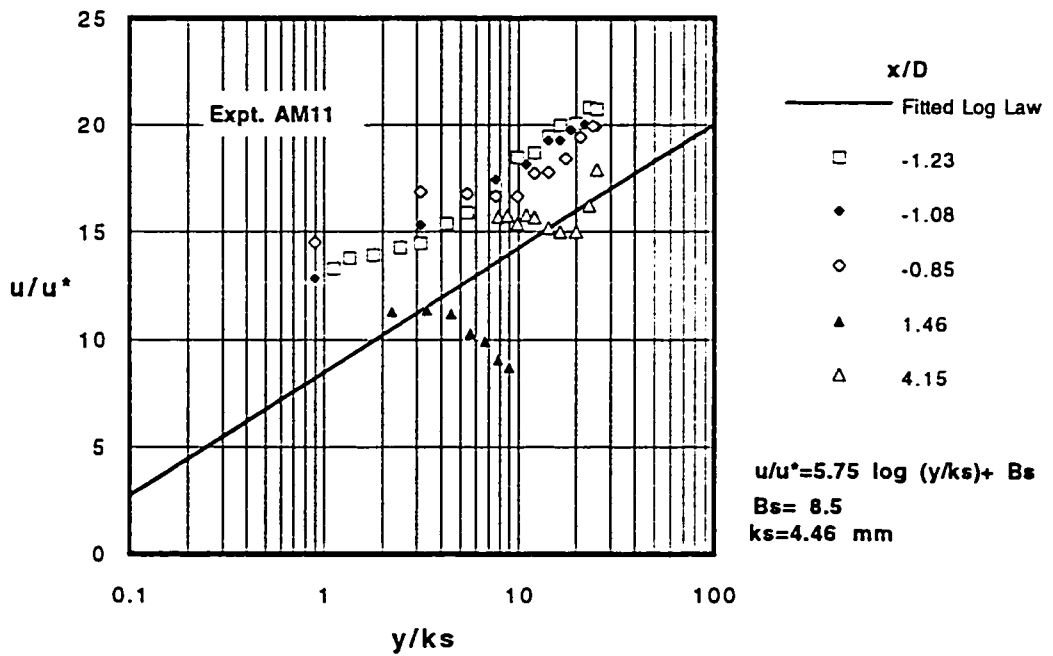
(a)

(b)

Figure 6.5 (a-b) Comparison of Velocity Profiles with the Law of the Wall

(c)

(d)

Figure 6.5 (c-d) Comparison of Velocity Profiles with Law of the Wall
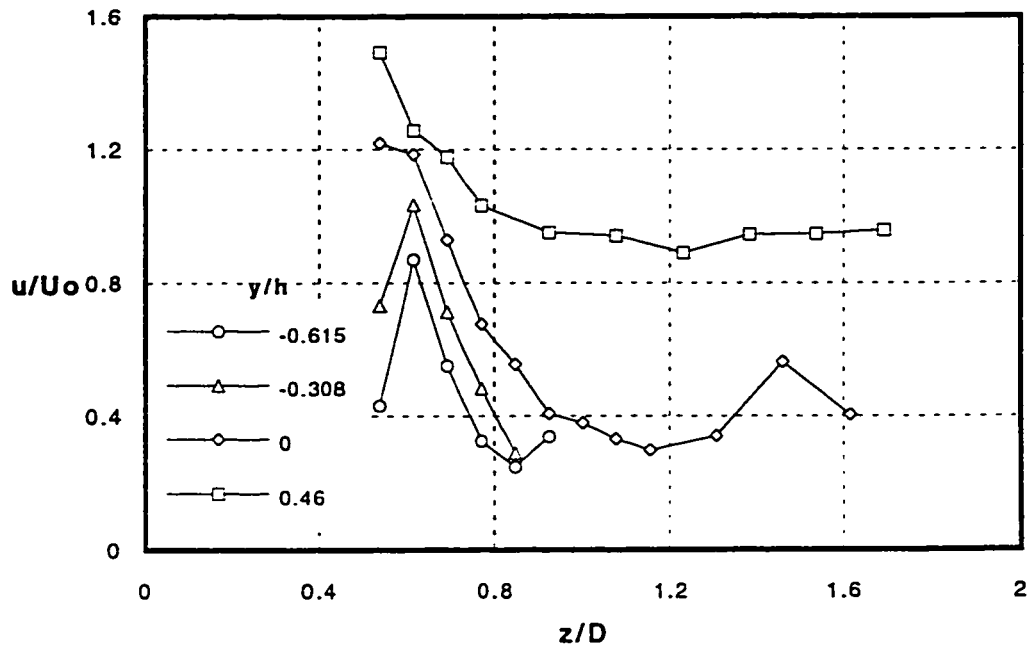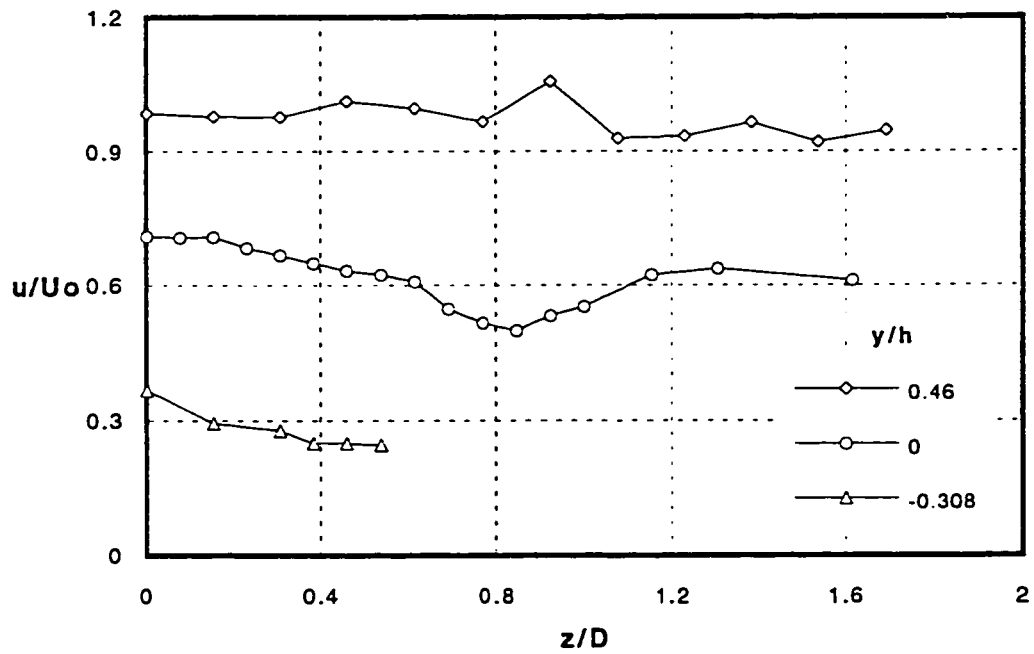
Figure 6.6 (a-b) Spanwise Profiles of Normalized Velocity at
(a) x/D=0, (b) x/D=-0.85 (Expt. AM11)
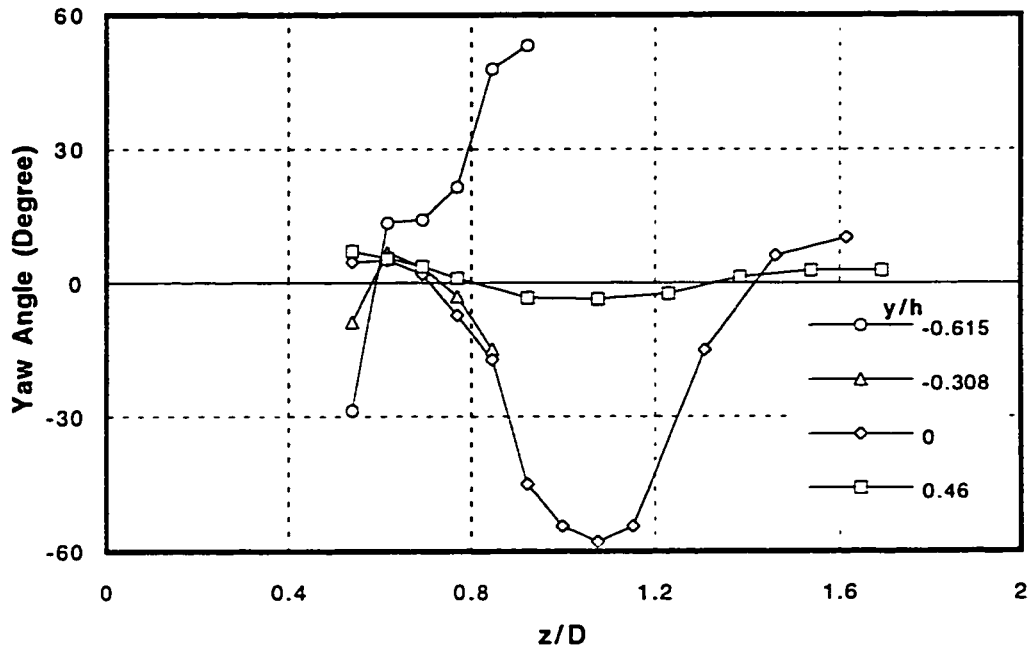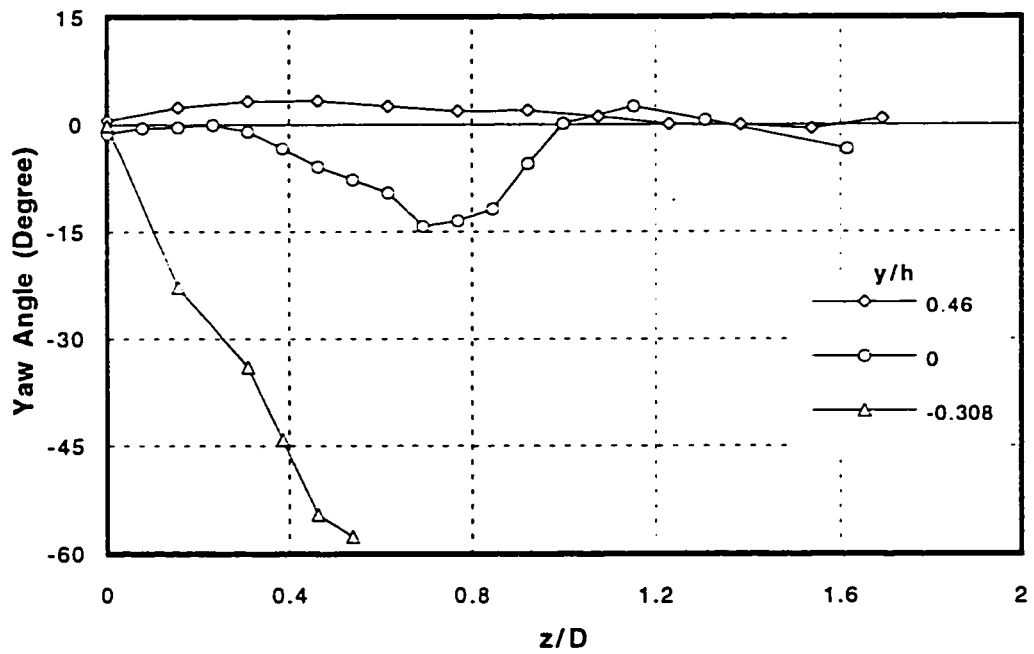
Figure 6.7 (a-b) Spanwise Profiles of Yaw Angle at (a) x/D=0, (b) x/D=-0.85 (Expt. AM11)

255
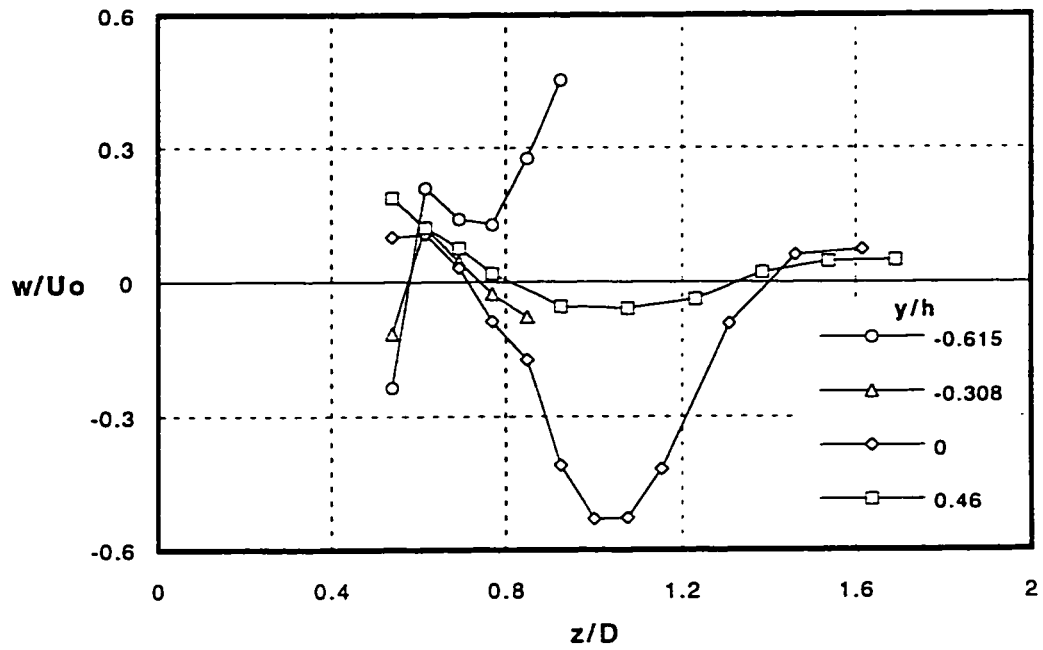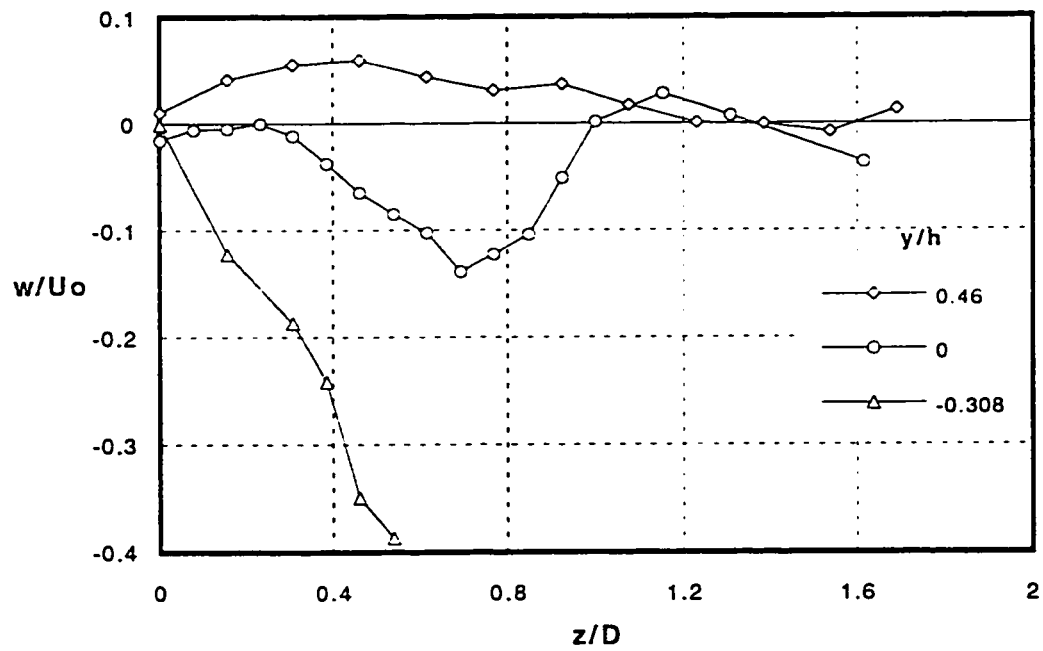
Figure 6.8 (a-b) Spanwise Profiles of Normalized Lateral Velocity at
(a) x/D=0,(b) x/D=-0.85 (Expt.AM11)
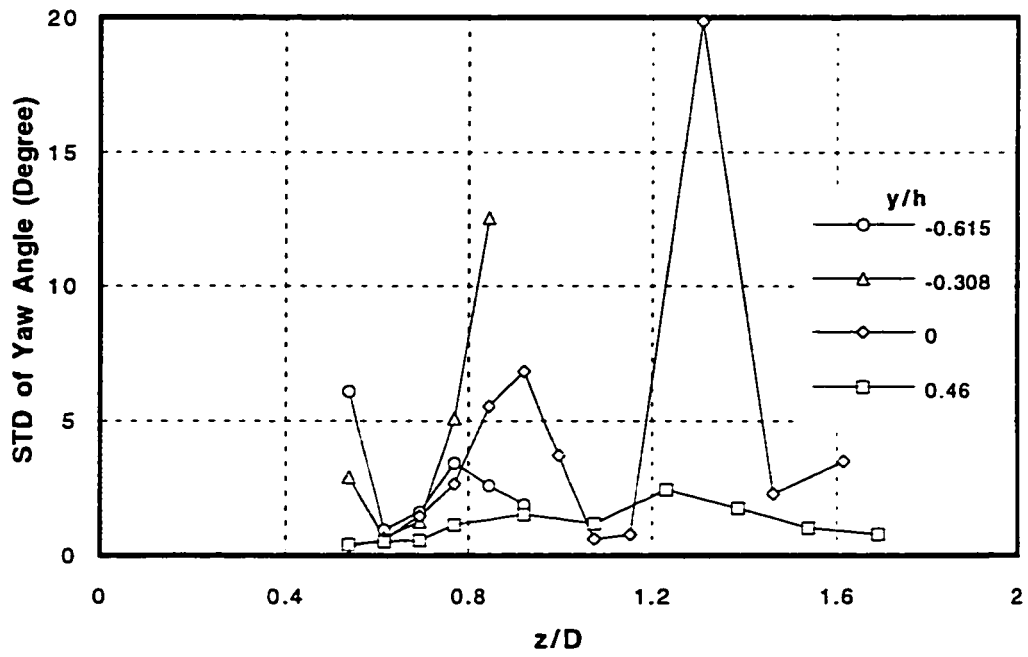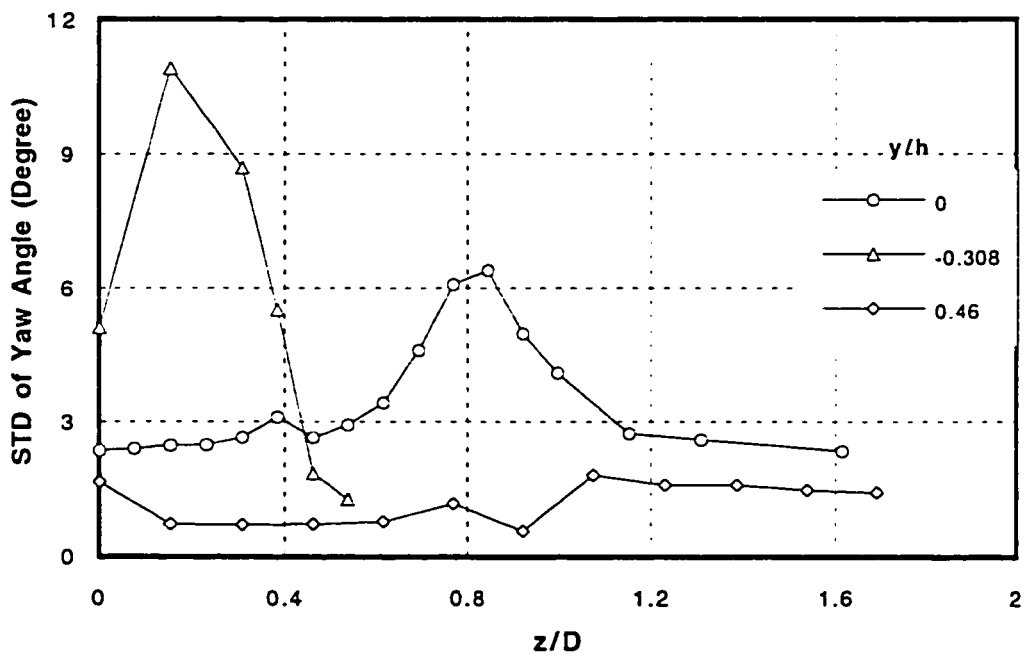
Figure 6.9 (a-b) Spanwise profiles of STD of Yaw Angle at
(a) x/D=0, (b) x/D=-0.85 (Expt. AM11)
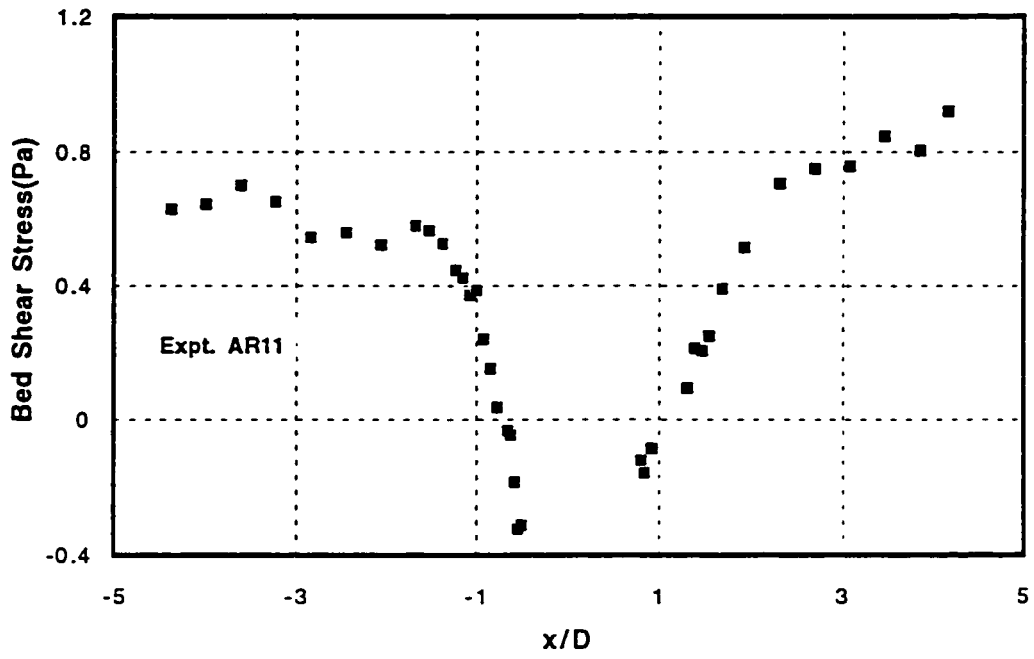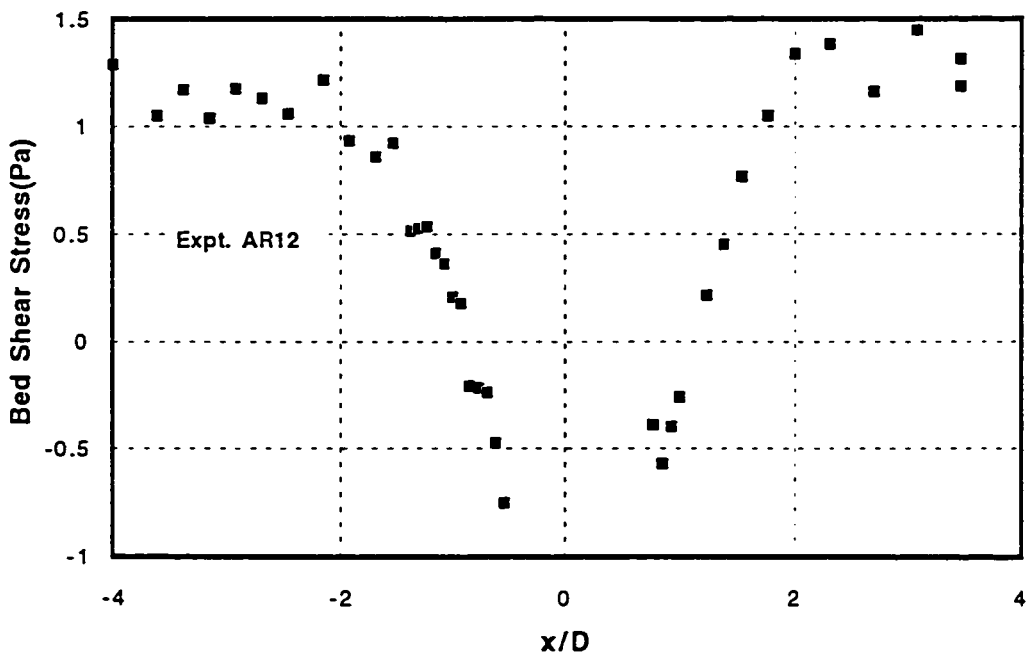
Figure 6.10 (a-b) Bed Shear Stress Profile on the POS for Rigid Bed
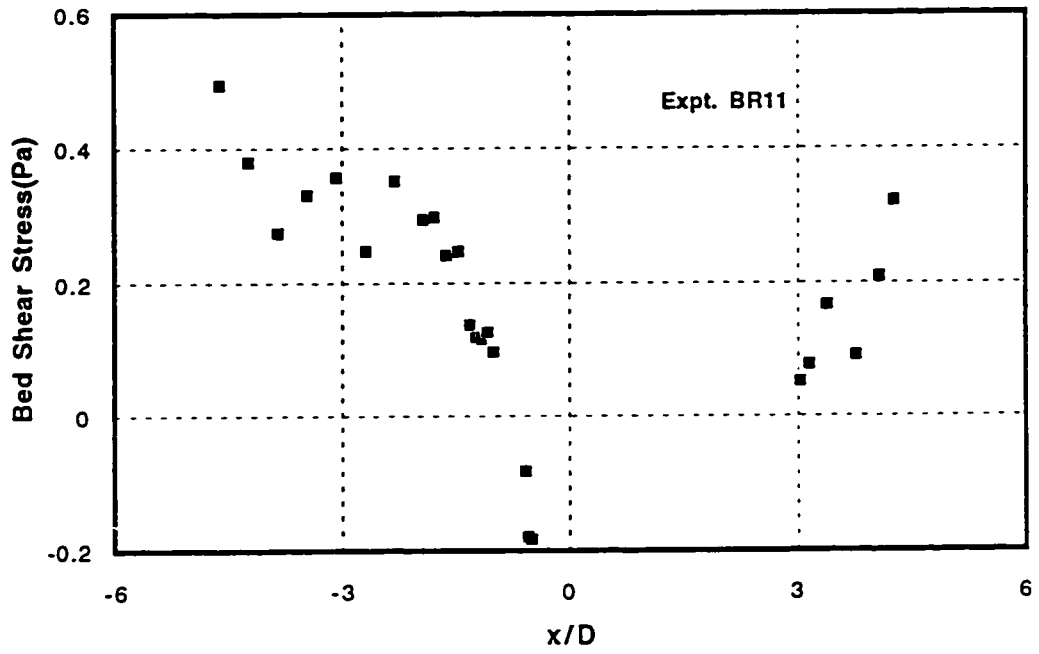
(c)
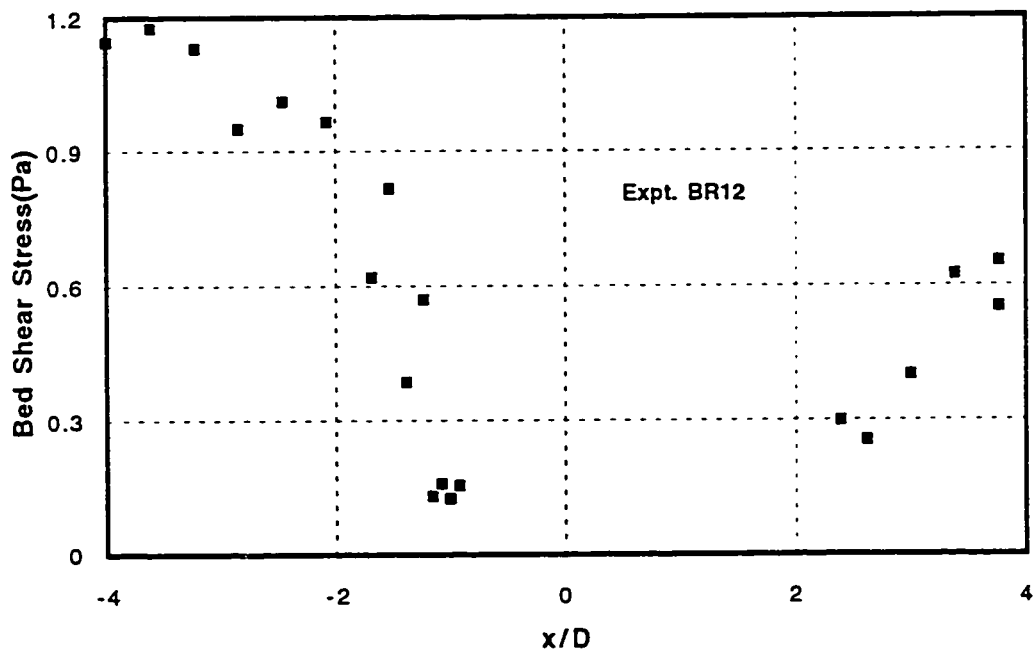
(d)

Figure 6.10 (c-d) Bed Shear Stress Profile On the POSfor Rigid Bed
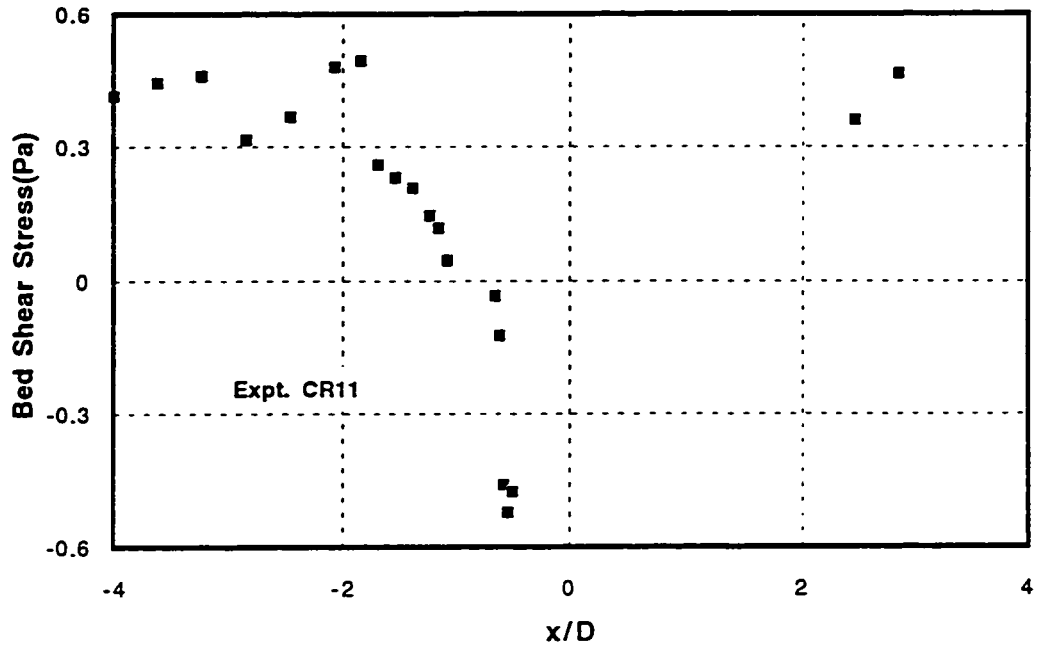
(e)
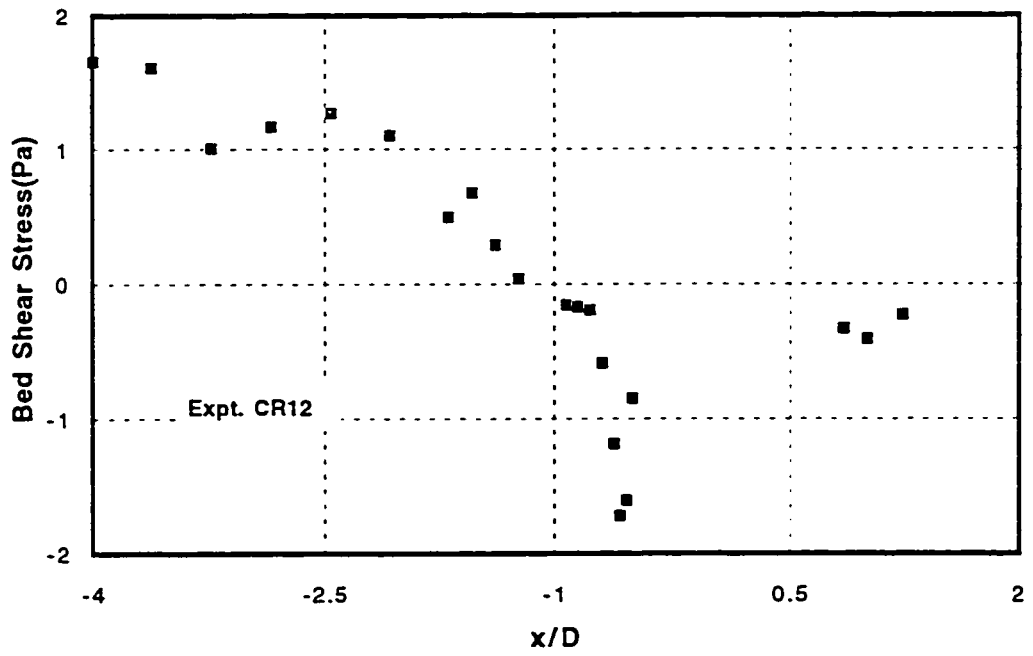
(f)

Figure 6.10 (e-f) Bed Shear Stress Profile on the POS for Rigid Bed
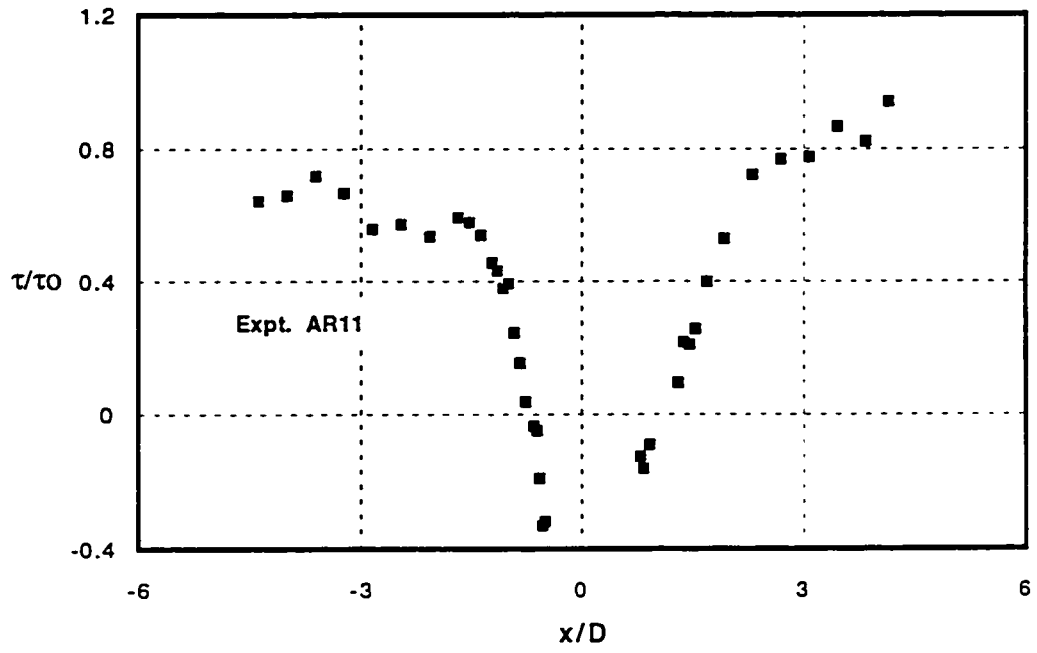
(a)
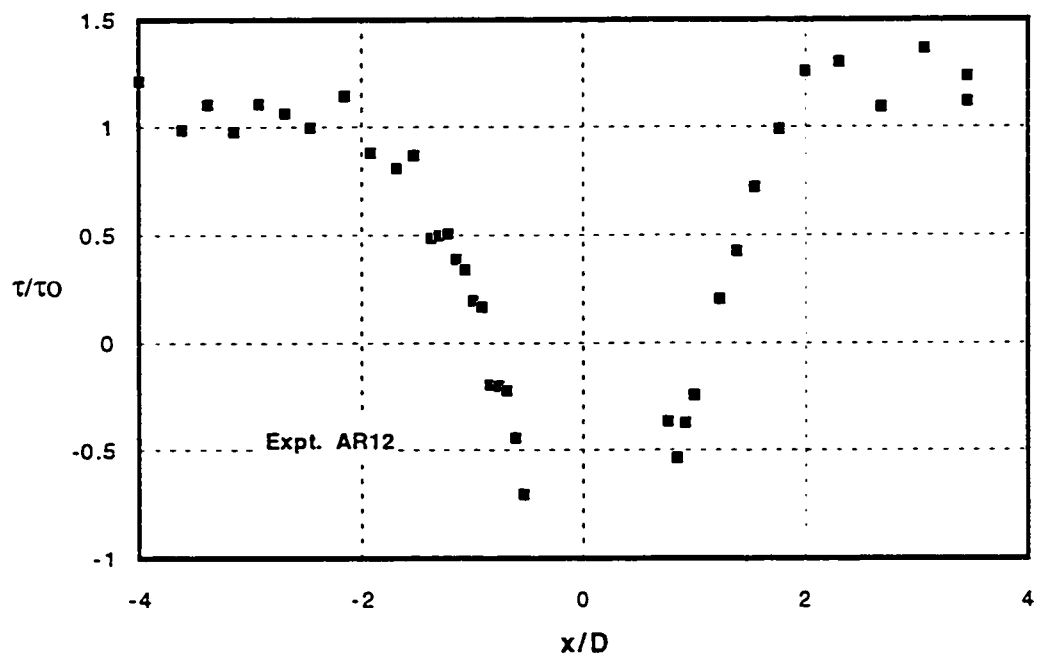
(b)

Figure 6.11 (a-b) Normalized Bed Shear Stress Profile on the POS for Rigid Bed
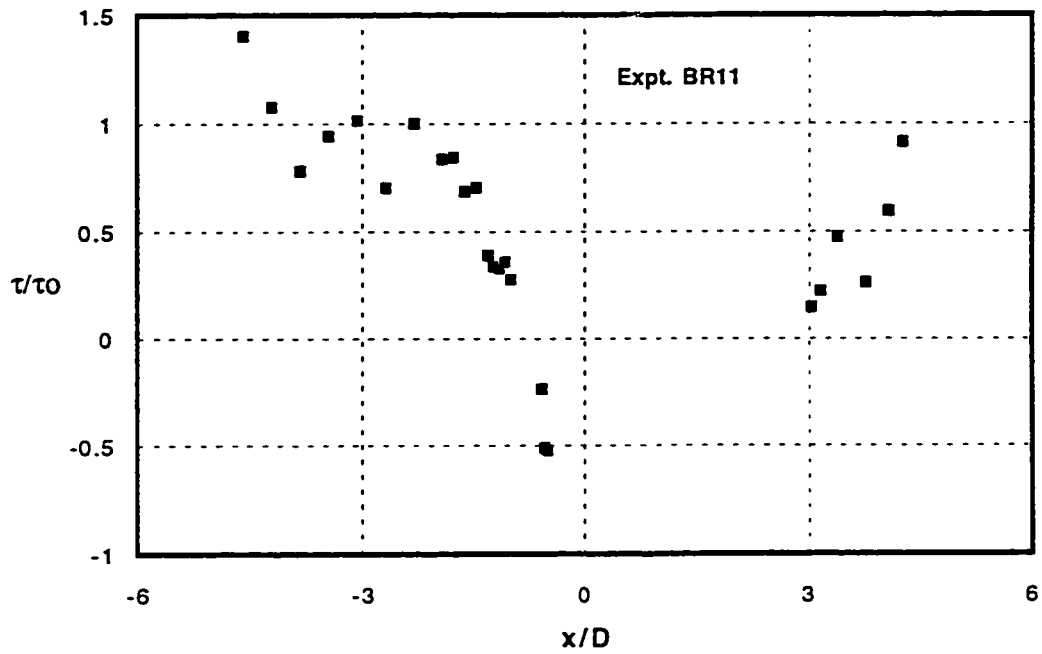
(c)
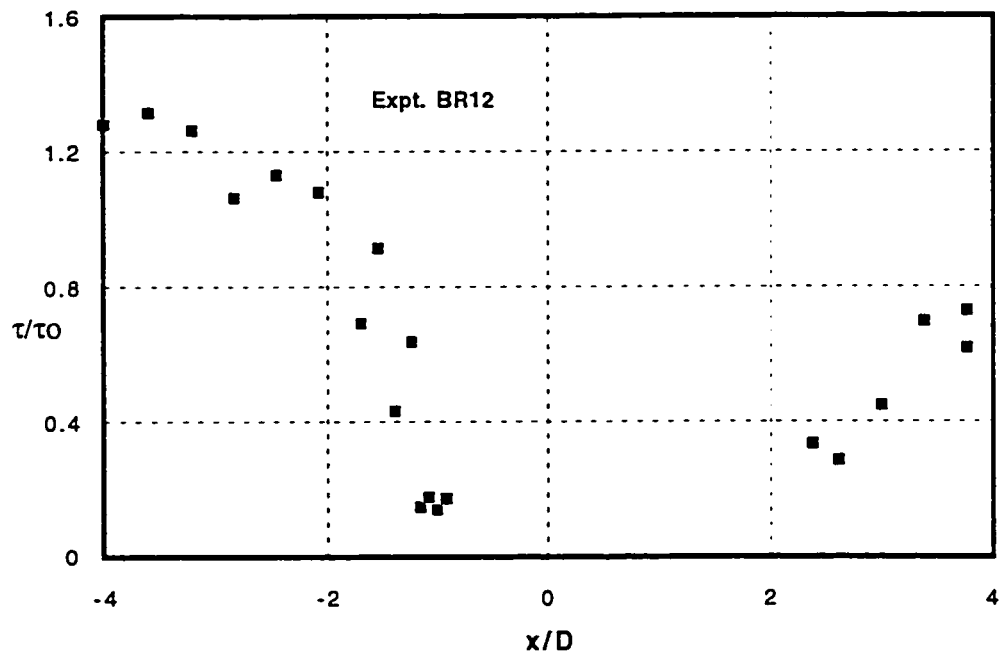
(d)

Figure 6.11 (c-d) Normalized Bed Shear Stress Profile on the POS for Rigid Bed
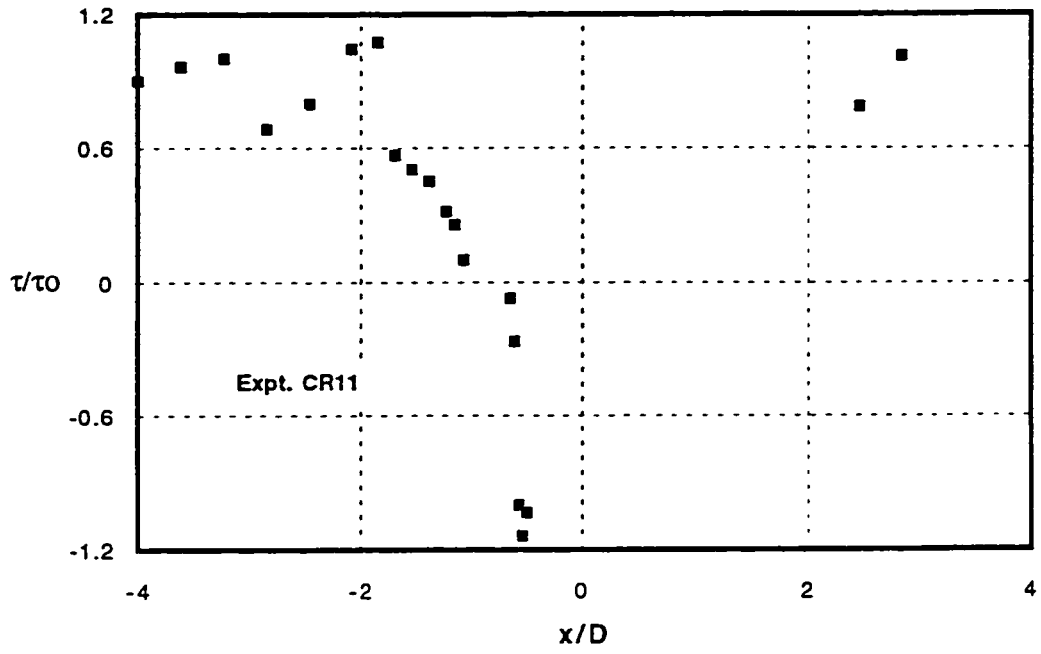
(e)
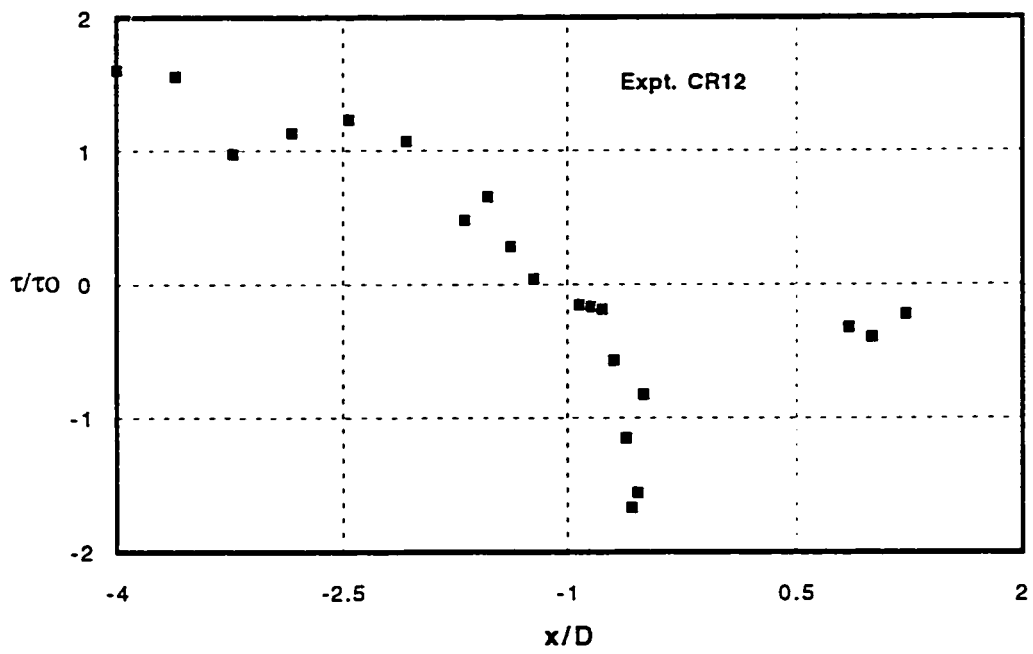
(f)

Figure 6.11 (e-f) Normalized Bed Shear Stress Profile on the POS for Rigid Bed
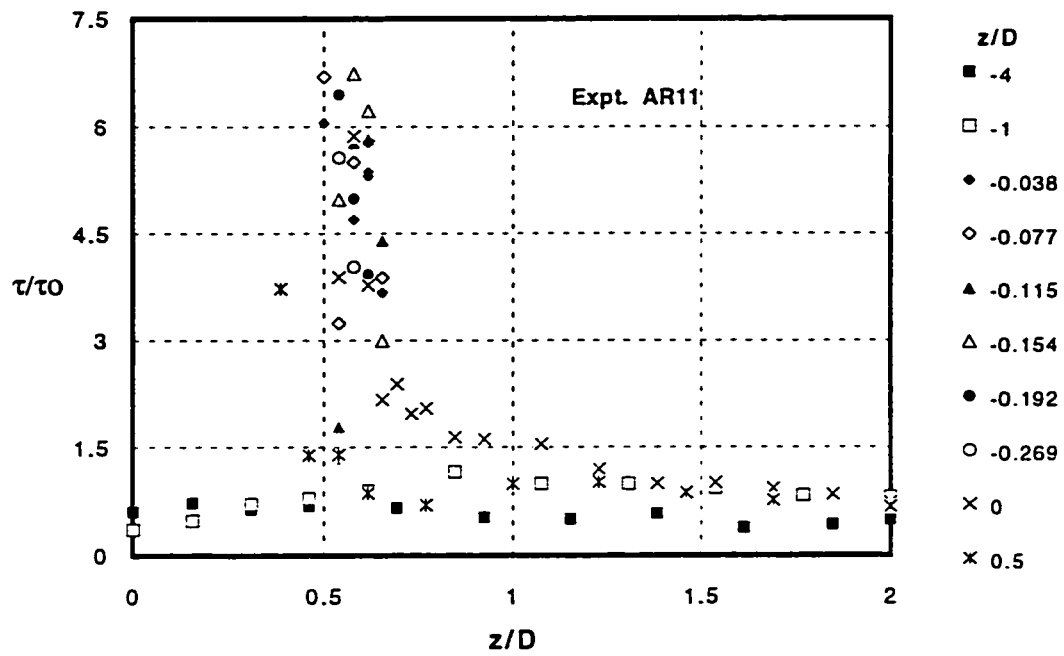
(a)
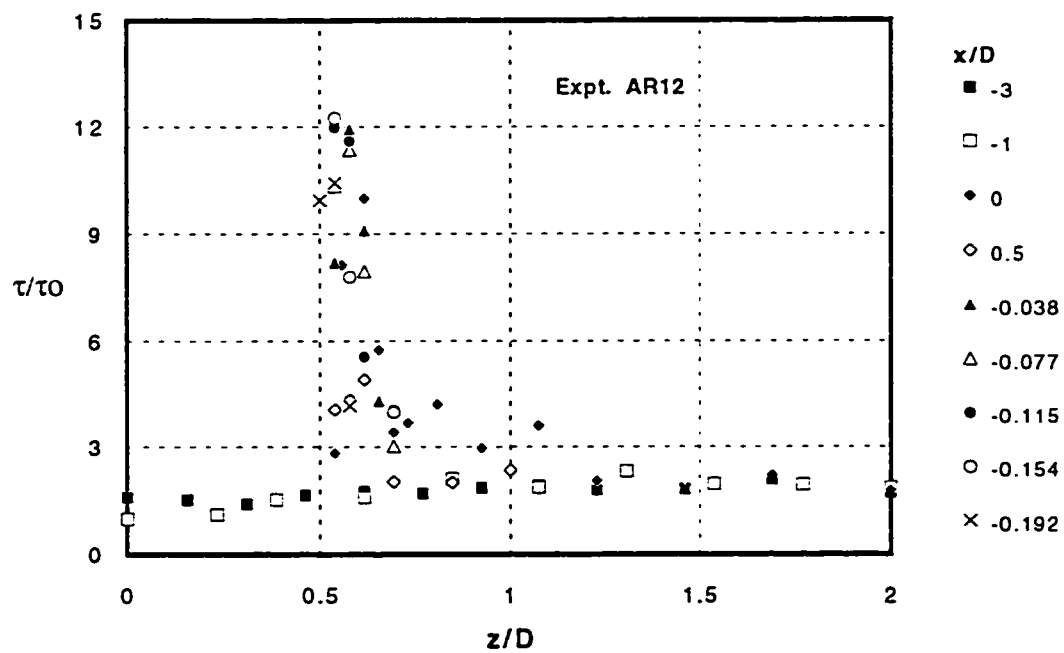
(b)

Figure 6.12 (a-b) Spanwise Profiles of Normalized Bed Shear Stress on Rigid Bed
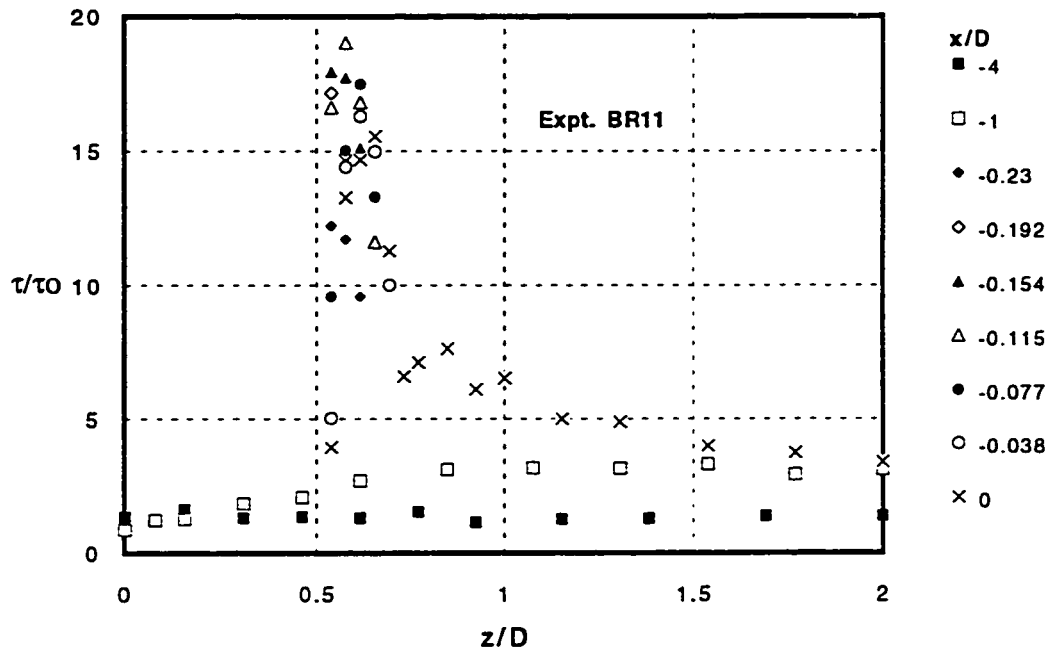
(c)
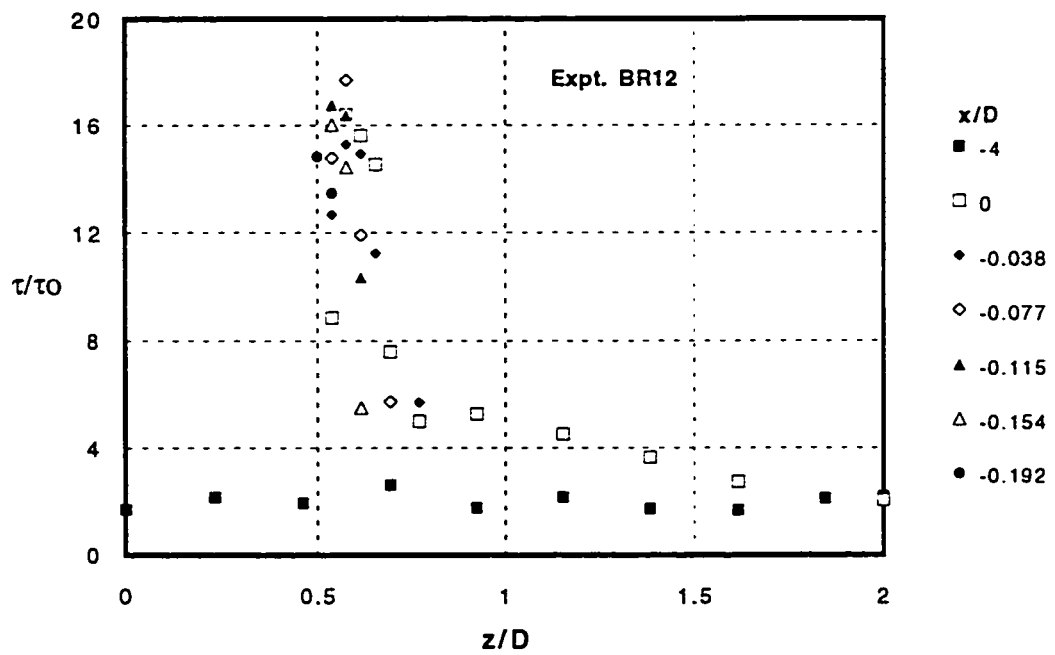
(d)

Figure 6.12 (c-d) Spanwise Profiles of Normalized Bed Shear Stress on Rigid Bed
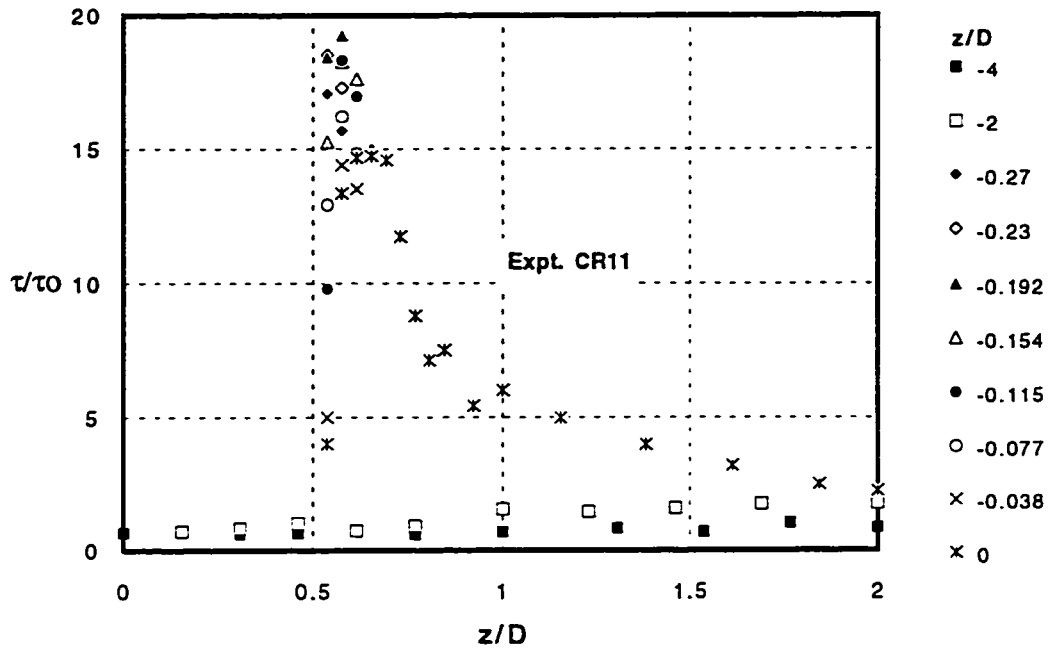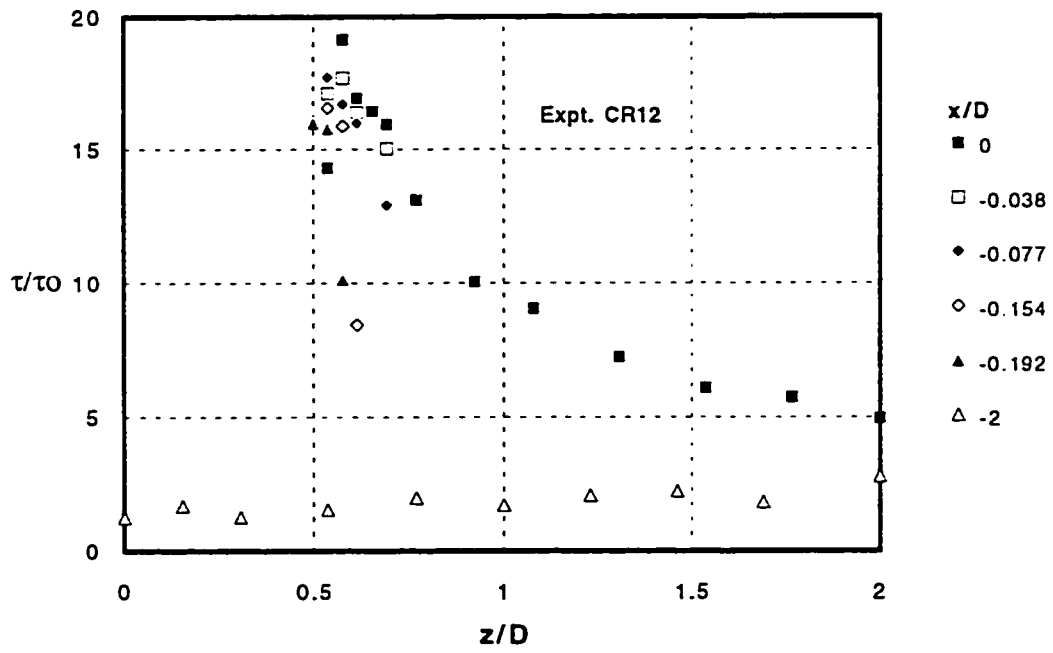
Figure 6.12 (e-f) Spanwise Profiles of Normalized Bed Shear Stress on Rigid Bed
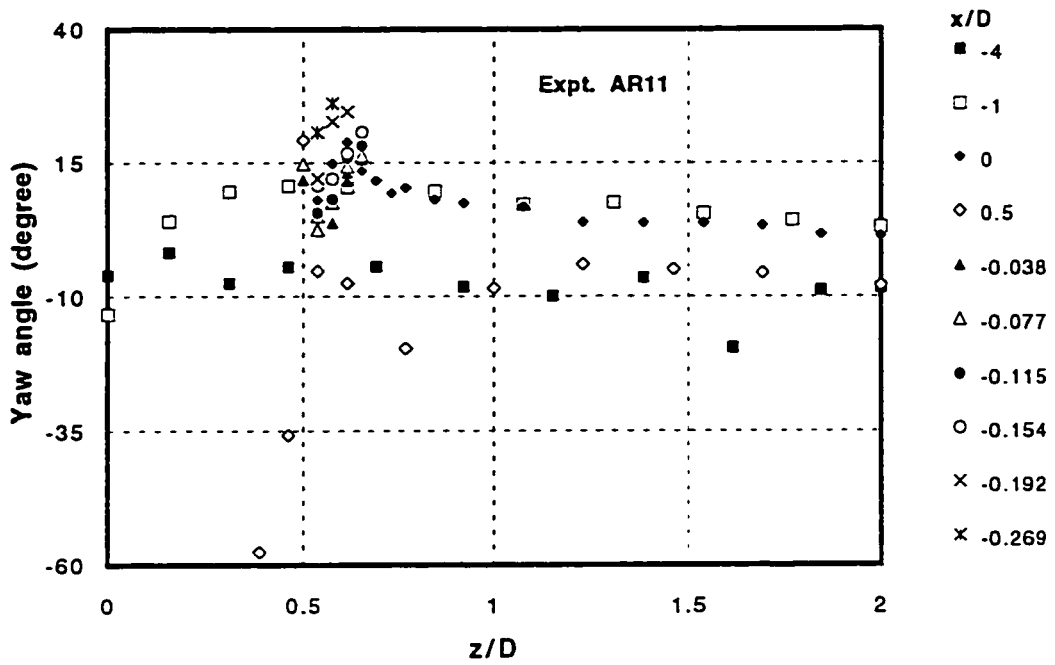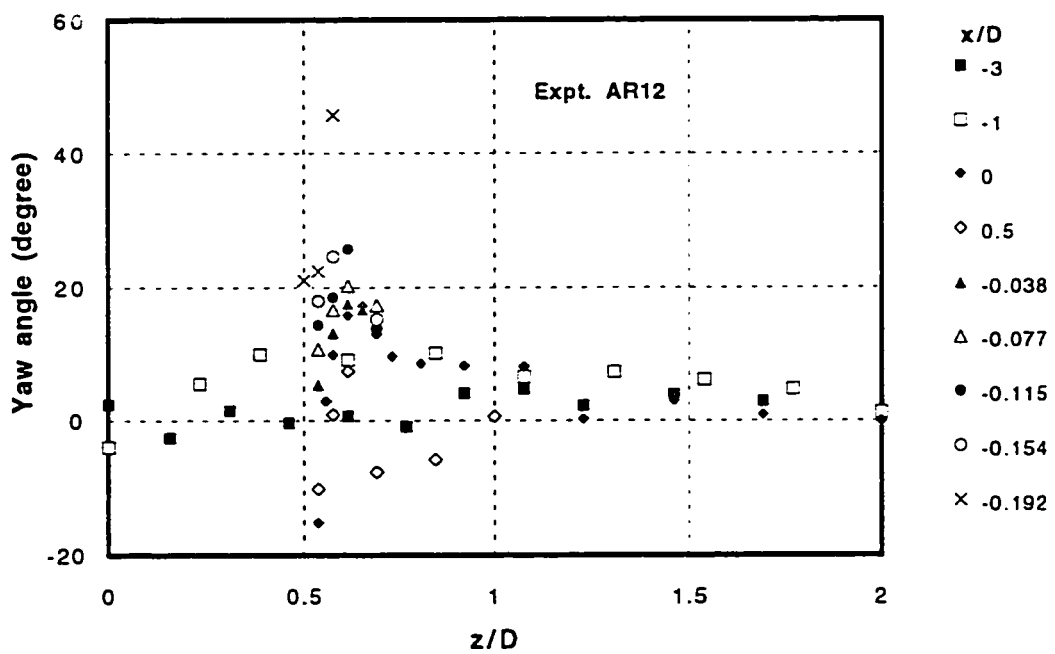
Figure 6.13 (a-b) Spanwise Profiles of Yaw Angles of Bed Shear Stress
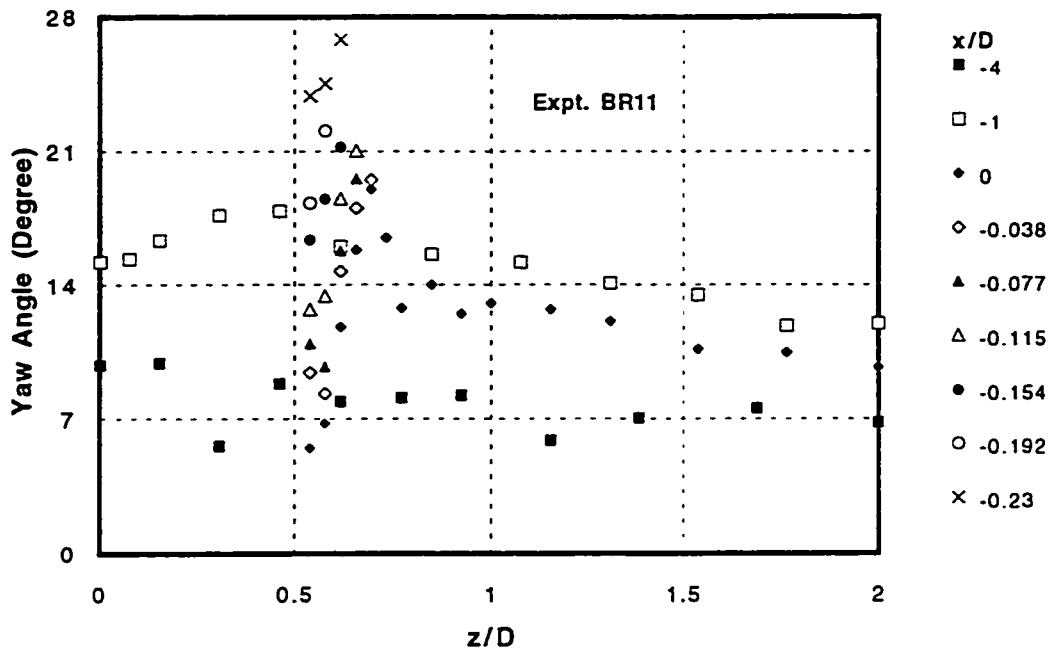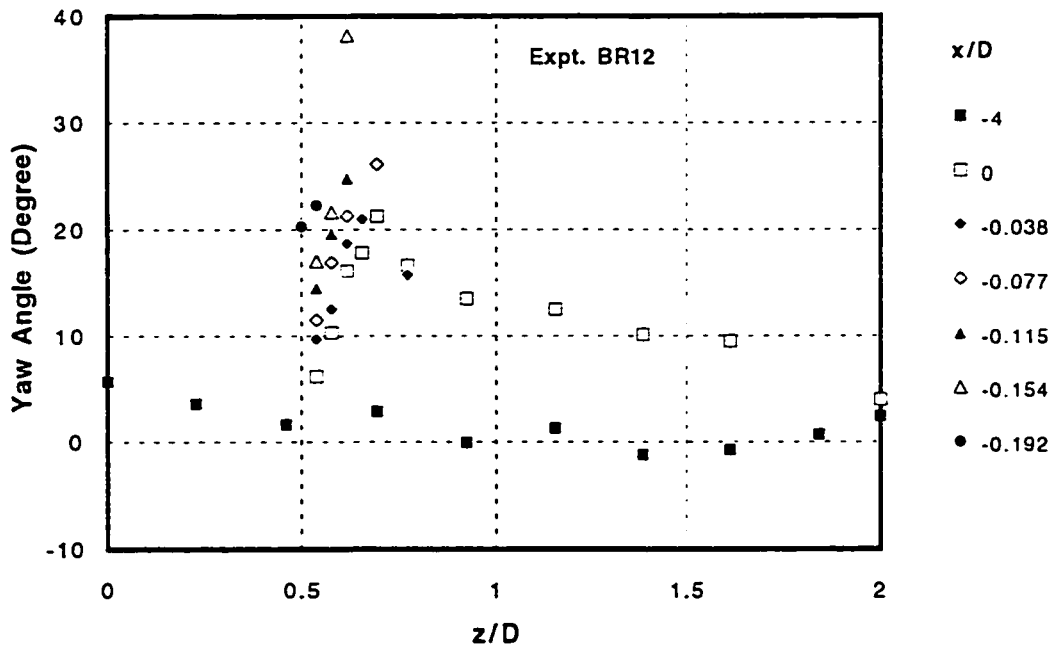
Figure 6.13 (c-d) Spanwise Profiles of Yaw Angles of Bed Shear Stress
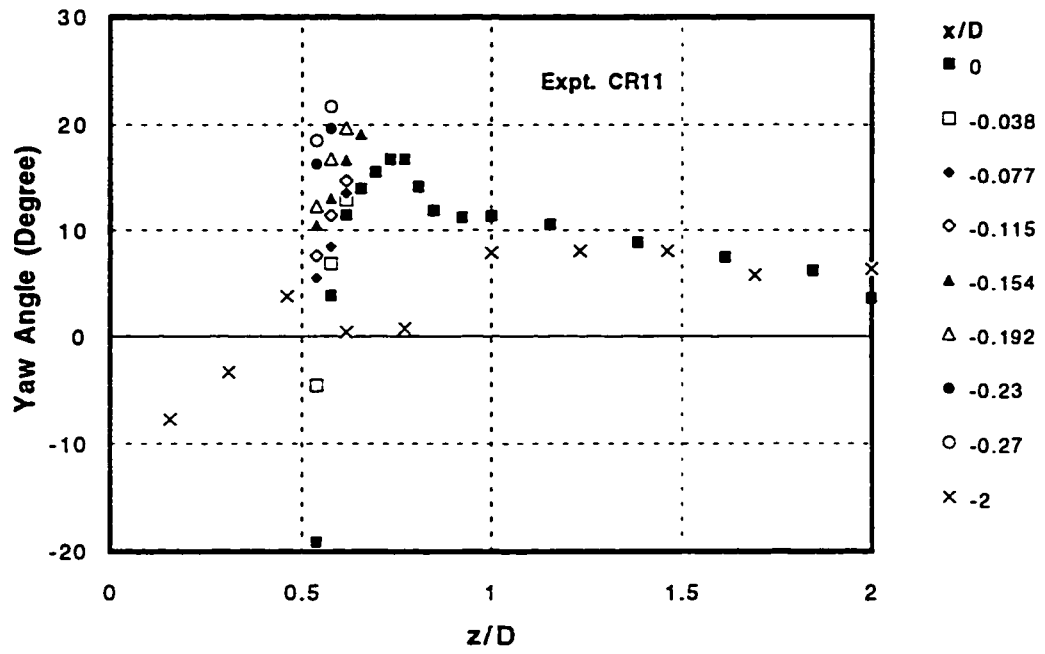
(e)
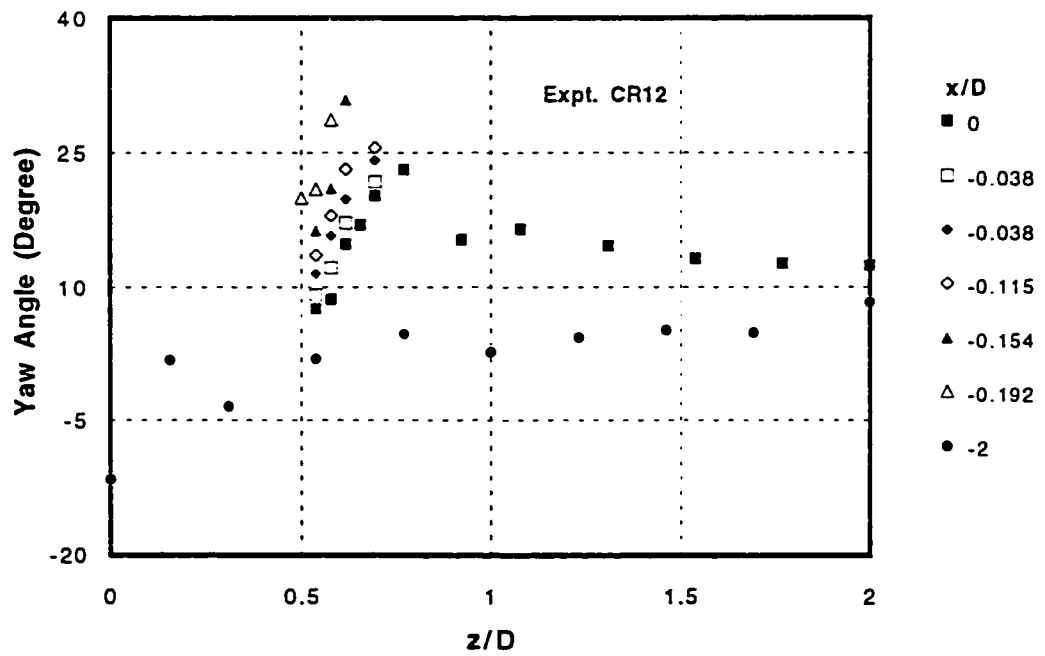
(f)

Figure 6.13 (e-f) Spanwise Profiles of Yaw Angles of Bed Shear Stress
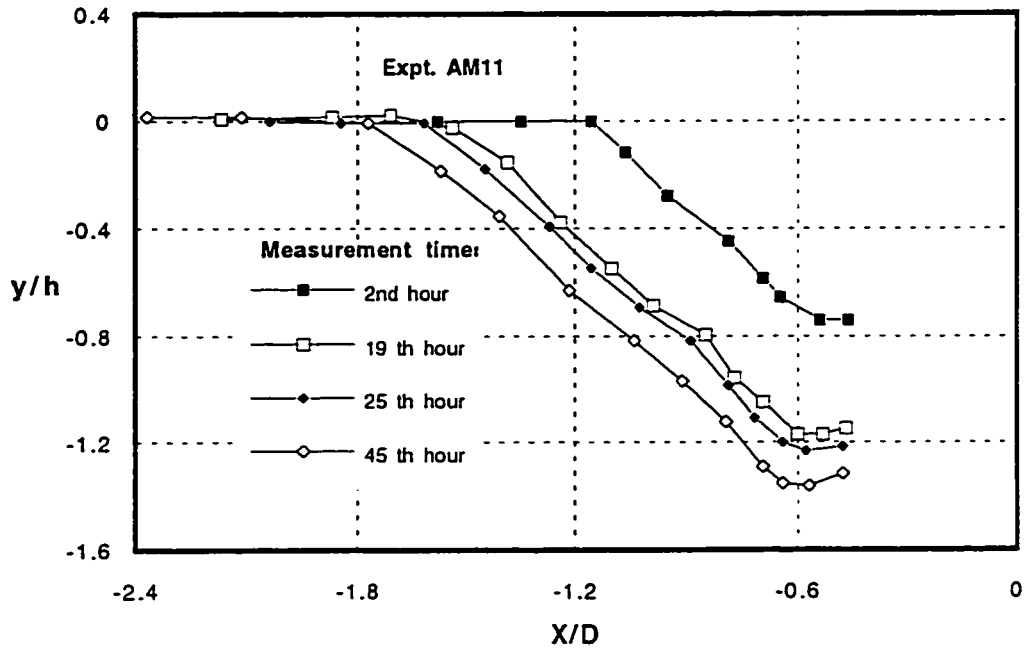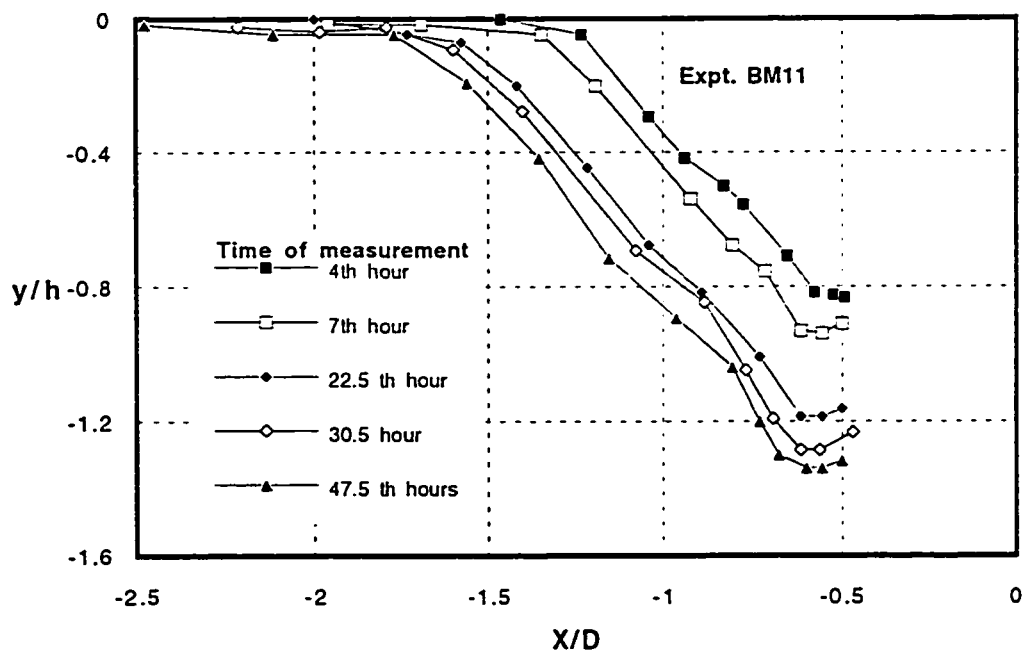
Figure 6.14 (a-b) Profiles of Scour Upstream of the Body in Consecutive Times
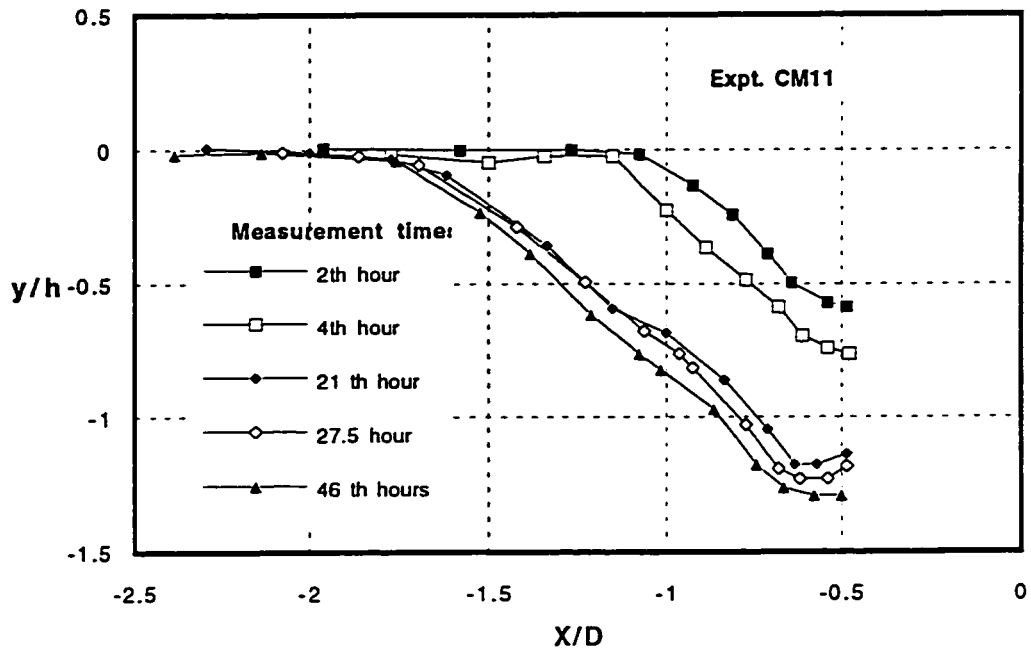
(c)

Figure 6.14 (c) Profiles of Scour at the Front of the Body in Consecutive Times
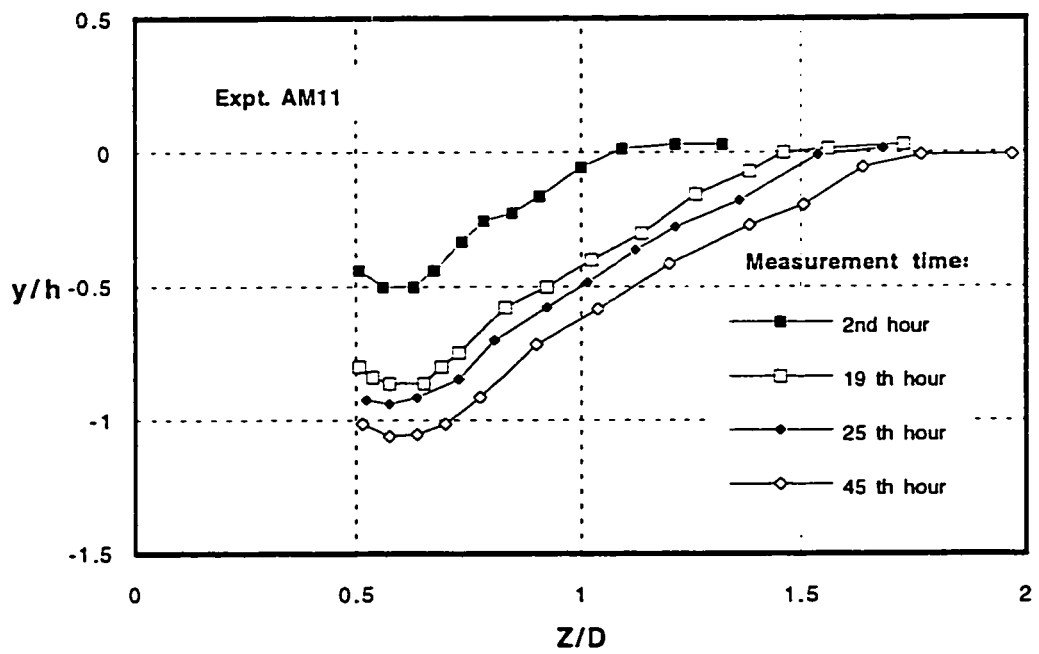
(a)

Figure 6.15 (a) Profiles of Scour at the Side of the Body in Consecutive Times

271
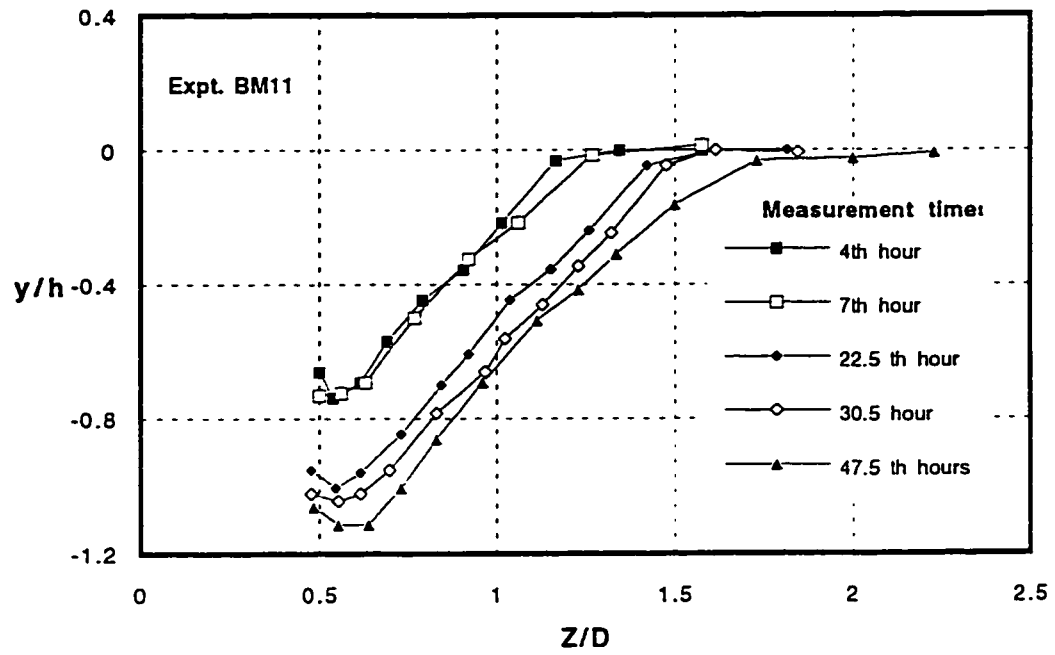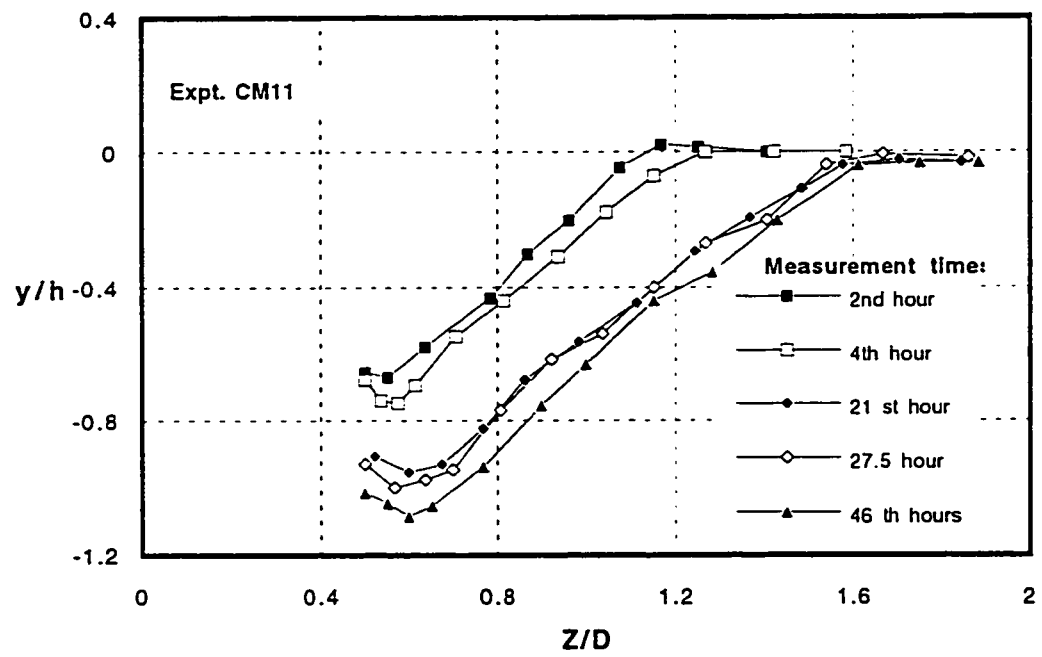
Figure 6.15 (b-c) Profiles of Scour at the Side of the Body in Consecutive Times
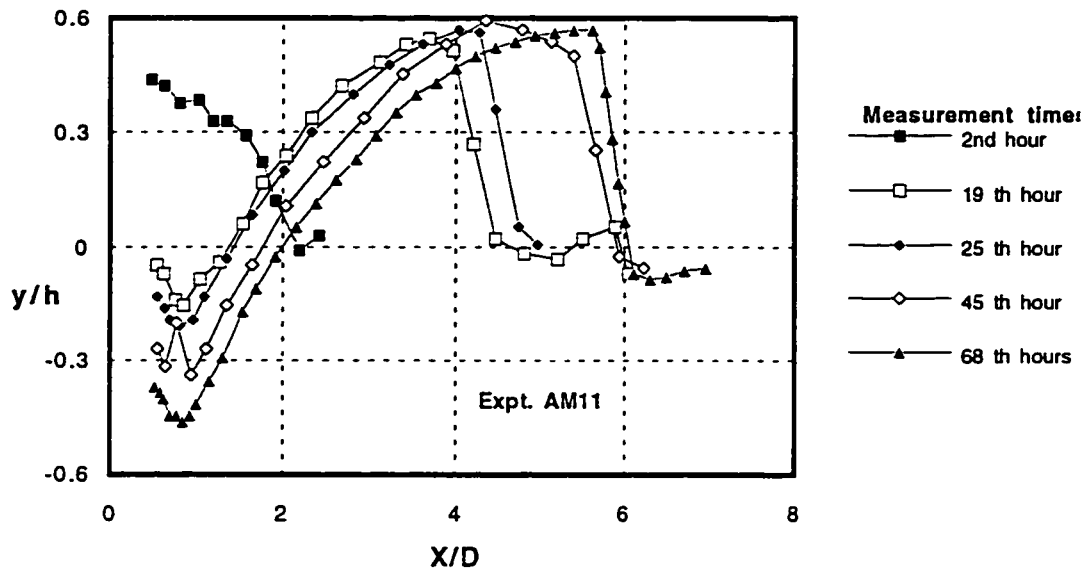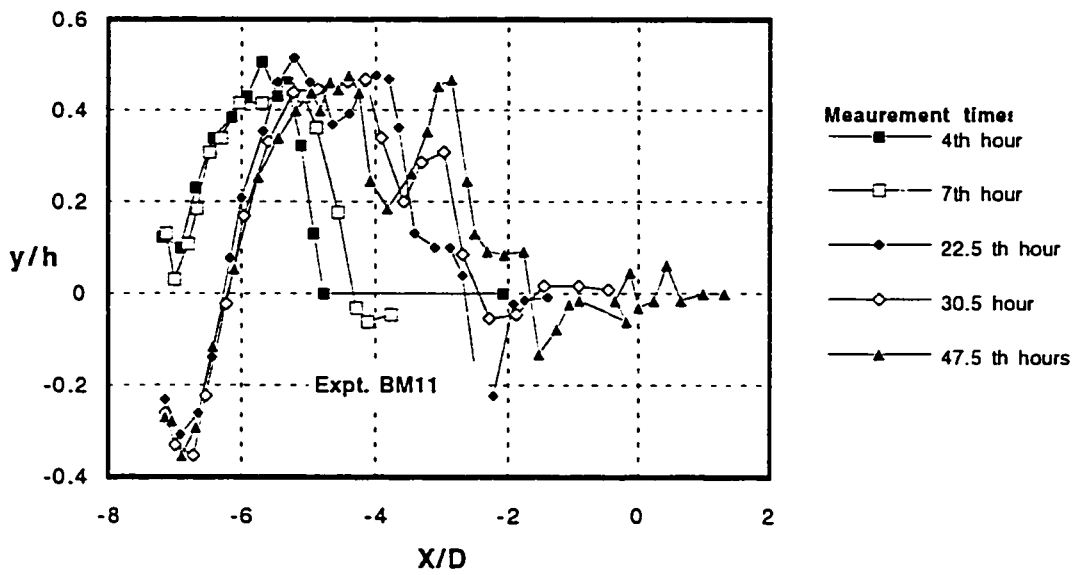
Figure 6.16 (a-b) Profiles of Scour at the Back of the Body
in Consecutive Times
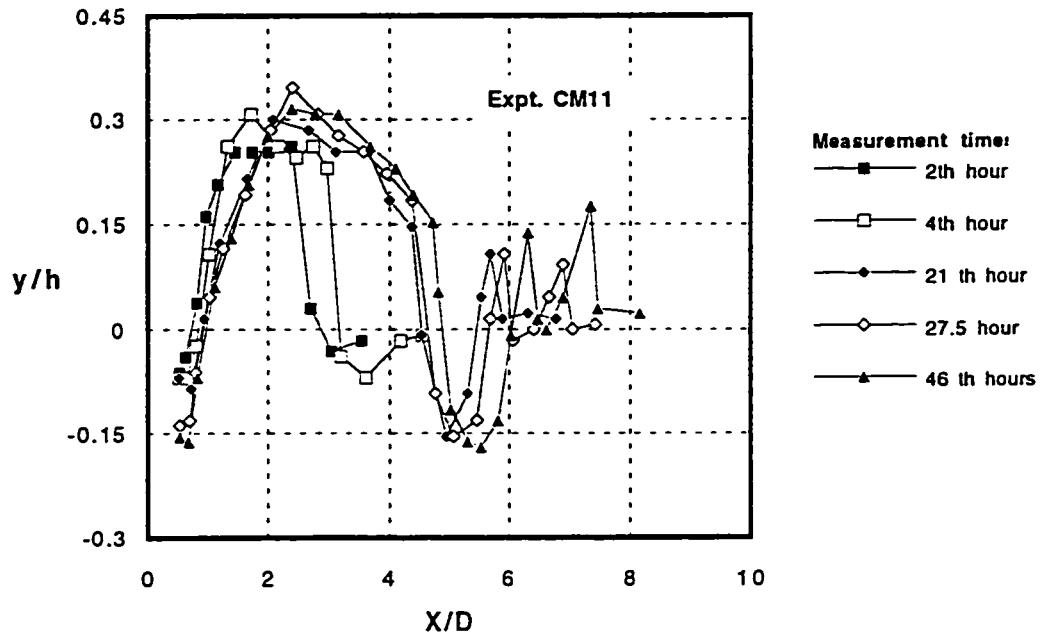
(c)

Figure 6.16 (c) Profiles of Scour at the Back of the Body in Different Times
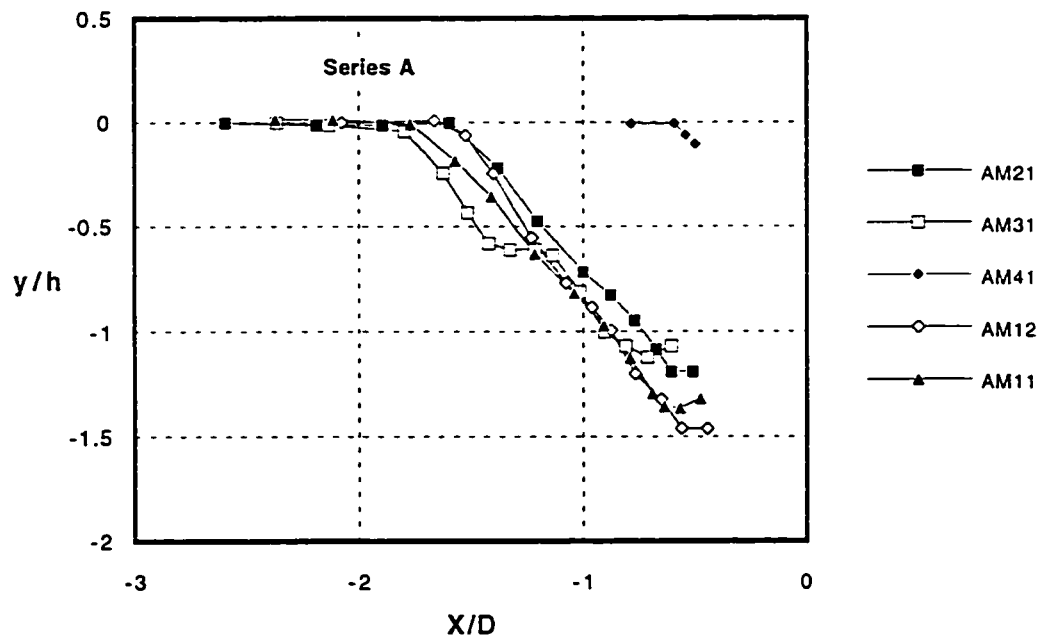
(a)

Figure 6.17 (a) Profiles of Equilibrium Bed Scour at the Front of the Body

274

(b)

(c)
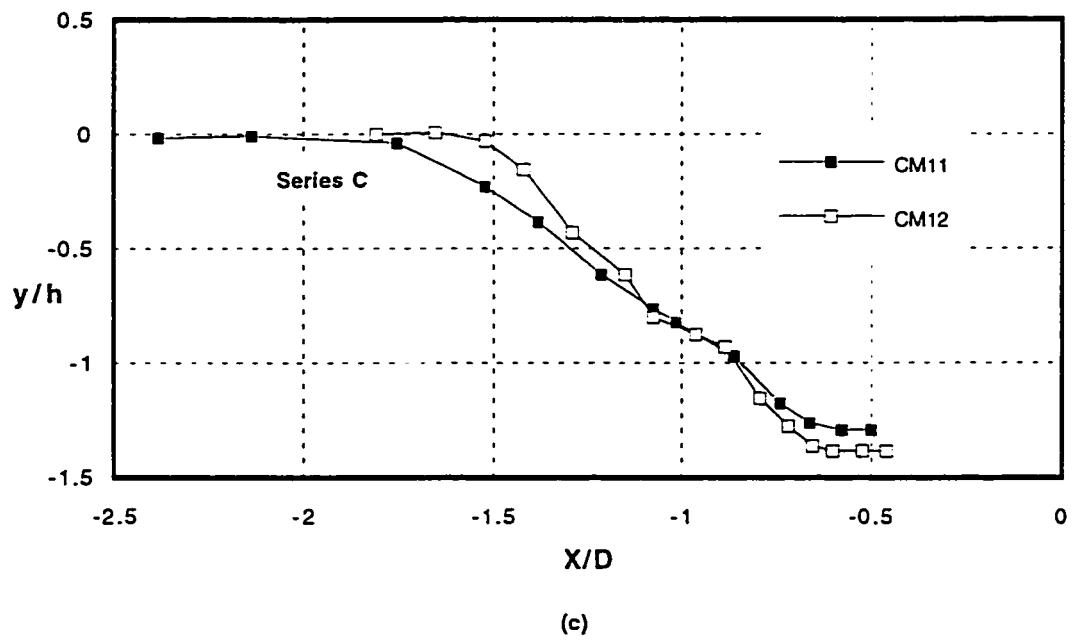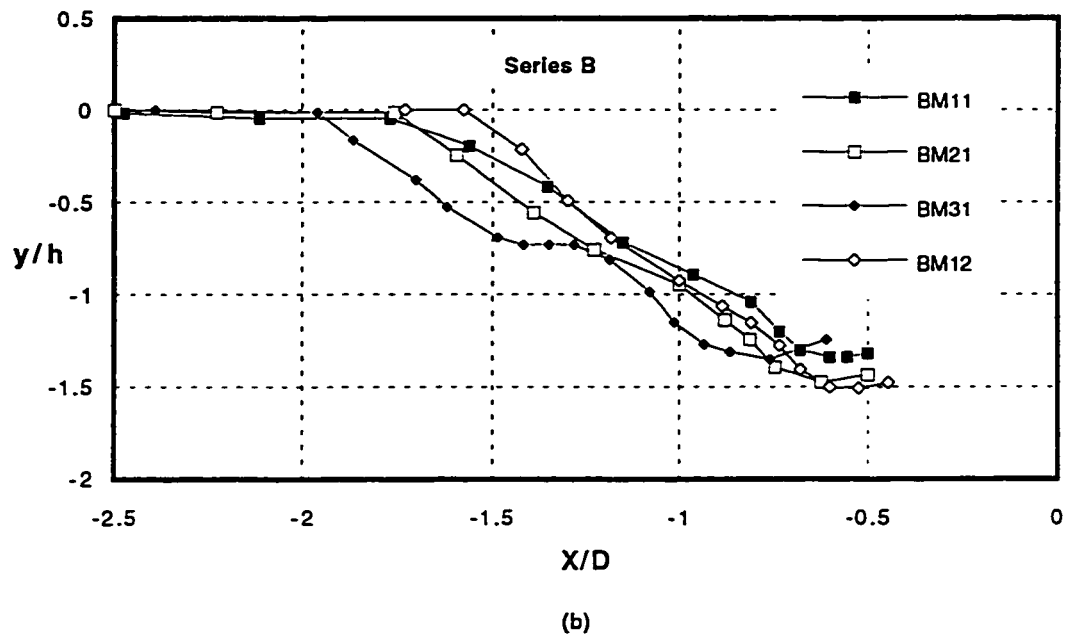
Figure 6.17 (b-c) Profiles of Equilibrium Bed Scour at
the Front of the Body
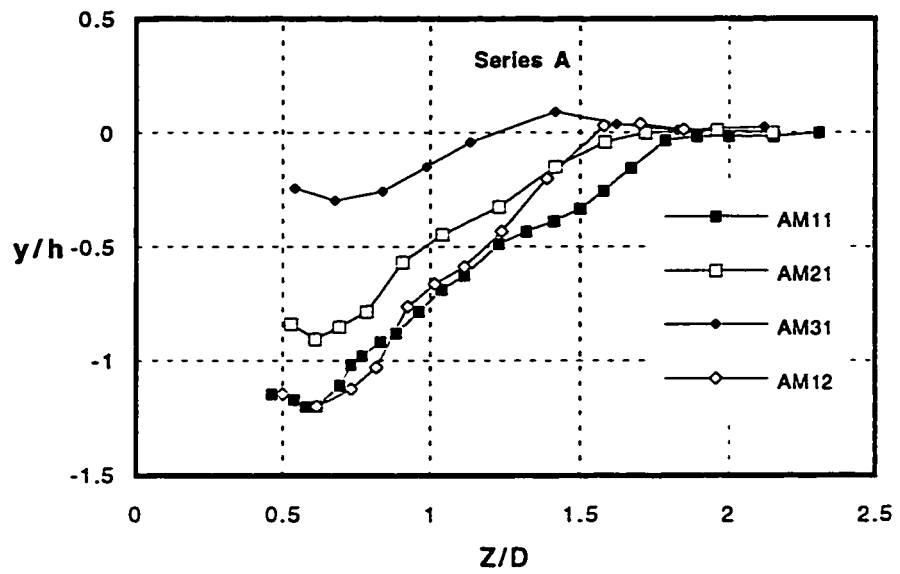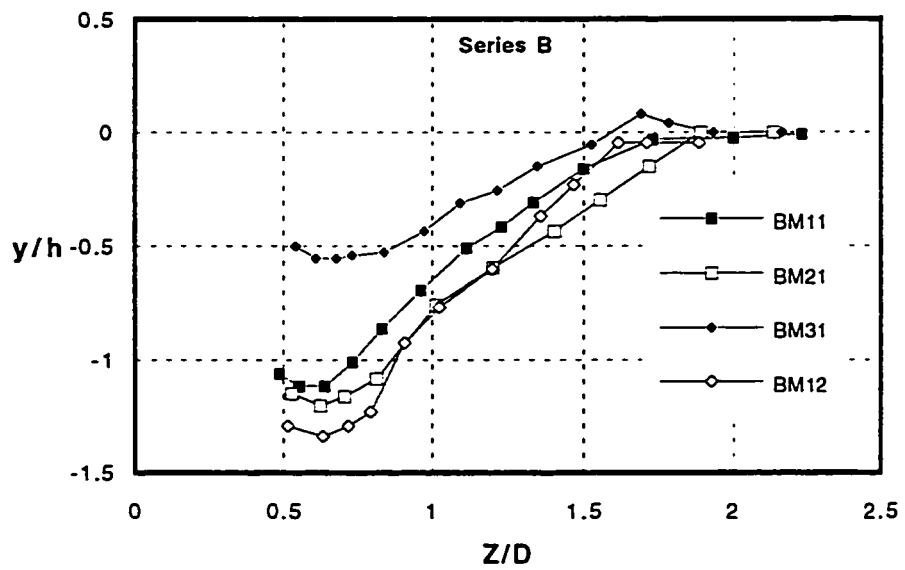
Figure 6.18 (a-b) Profiles of Equilibrium Bed Scour at the Side of the Body
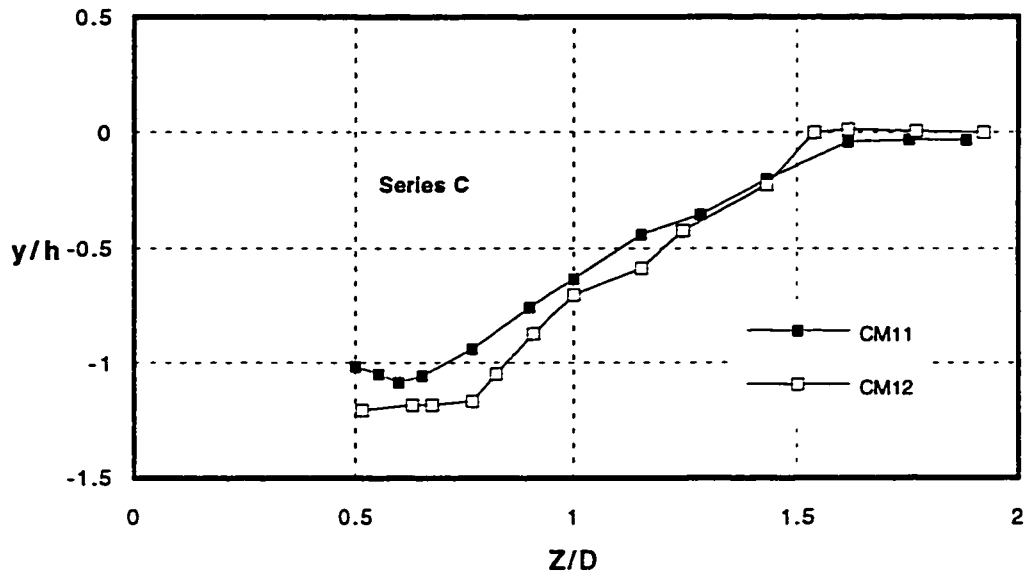
Figure 6.18 (c) Profiles of Equilibrium Bed Scour at the Side of the Body
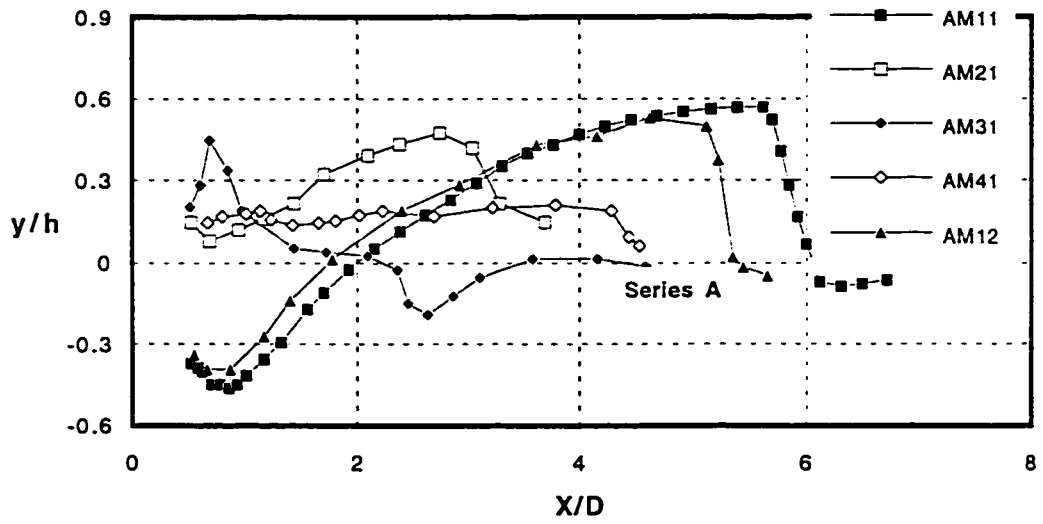
Figure 6.19 (a) Profiles of Equilibrium Bed Scour at the Back of the Body
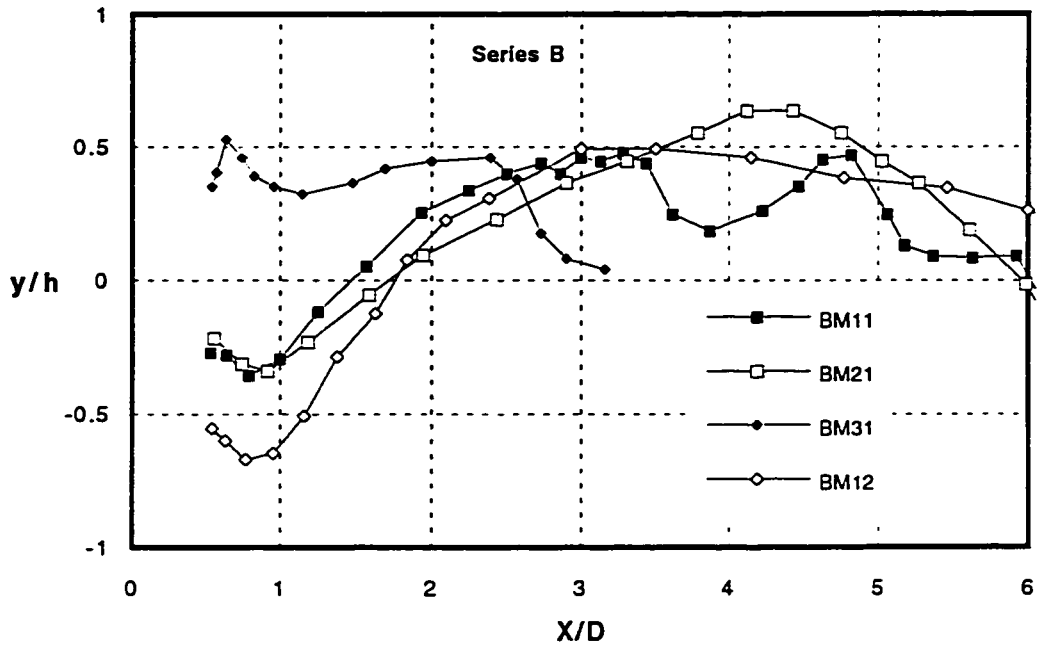
(b)
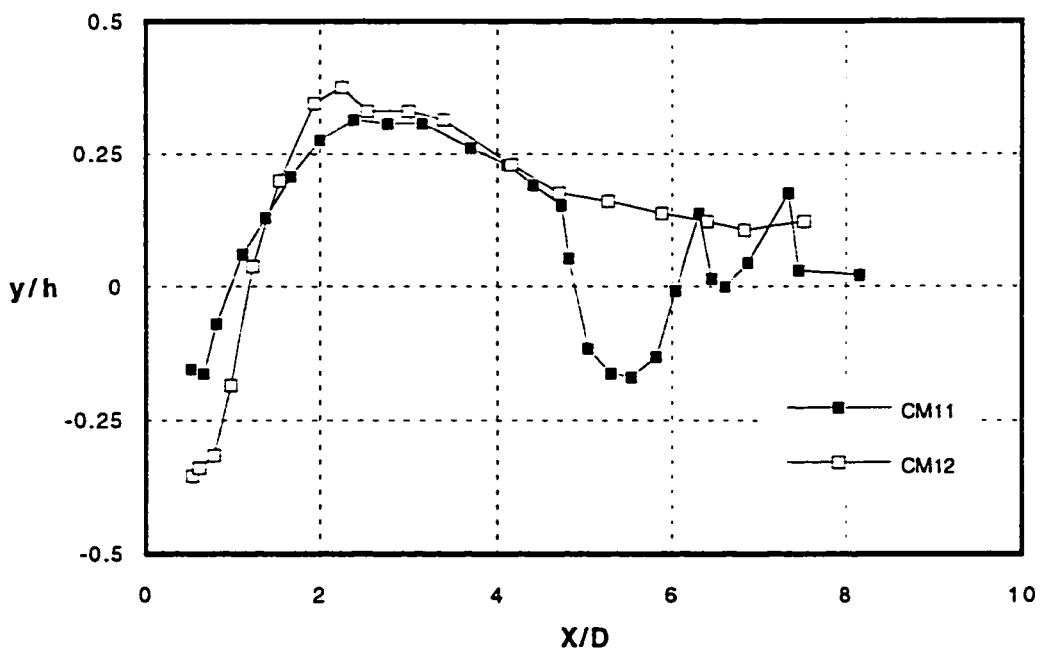
(c)

Figure 6.19 (b-c) Profiles of Equilibrium Bed Scour at the Back of the Body

CHAPTER 7

GENERAL ANALYSIS

7.1 Introduction

The experimental observations for the smooth and rough beds were presented in chapters 5 and 6. In this chapter, an analysis of those observations is presented. Analyses are presented in the same order as the measurements. Therefore, Similarity analyses in the near-wake region will be presented for: measurements in the plane of symmetry; spanwise direction, including measurements at different stations and depths; and for scour profiles. Based on dimensional considerations, related parameters on the depth of the scour are discussed. A comparison between the measured scour depth and some of the available equations for prediction of the scour in bridge piers is also presented. At the end, some of the implications for the design of habitat structures are offered.

Before moving to the analysis, let us consider Figure 7.1, which shows sketches of the velocity profiles on the POS and across the flow for smooth bed and relative depth of more than 1. The evolution of the velocity profile on the POS from fully developed region on the upstream side to the wall-wake profile on the downstream side is shown. The wall-wake will be analyzed using the plane turbulent wake equation for inner region of the velocity profiles on the POS (chapter 7.2). The effect of the downwash flow can be seen on the spanwise velocity profiles downstream of the body (Figure 7.1). In the region immediately downstream of the recirculation zone, one-peak velocity profiles are present which change to two-peak velocity profiles further downstream. These velocity profiles will be analyzed in section 7.3 as well.

279

7.2 Similarity in the Plane of Symmetry

The velocity profiles which are measured on the plane of symmetry downstream of the body on the smooth bed are analyzed in this section. The velocity profiles in regimes 1 and 2 were analyzed together when there was a significant thickness of the fluid covering the wake. In regimes 3 and 4, where the relative depth is close to 1 or less, this part of the flow is absent or the effect of the downwash is negligible. Therefore, the analysis of these two regimes will be presented together.

The velocity inside the recirculation region is turbulent and unsteady. The flow characteristics in this region can be studied by considering the vortex system and its evolution around the body. The vortex structure can lead to a rough estimate of the flow condition in this very turbulent region. Due to the highly unsteady nature of the flow, further analysis was not viable in this region only at distances further downstream of the recirculation region where . The flow starts to develop again. Even for the near-wake of the body, it has been shown that the velocity profiles of the flow can not reach the similarity and only the far-wake profiles were found to be similar (Schlichting, 1930). Due to the focus of this study and length limitations in the laboratory flumes, all the present measurements were conducted, based on the definition, in the near-wake of the body.

In turbulent flow of a fluid of small viscosity, the main structure of the flow would not be effected by the viscosity and if the flow is geometrically similar, these structures would be similar for high Reynolds number at different conditions. In a fully turbulent flow, there is a region in which the direct action of viscosity on the mean flow is negligible because the Reynolds stresses are much larger than the mean viscous stresses. Therefore, the mean motion can be determined by considering only the boundary conditions of the flow.

This fact can be explained by the nature of the transfer and dissipative action of the viscosity in the turbulent flow. Due to the non-linear form of the Navier-Stokes

equations, smooth velocity profiles change to velocity discontinuities in inviscid flow. But for a viscous flow, the diffusive nature of the viscosity would be able to smooth out these discontinuities, except very close to the original discontinuities. Therefore, change in velocity only changes the extent and the magnitude of the velocity gradient close to the original discontinuities, while between the discontinuities the flow motion would not be a function of the viscosity (Townsend, 1956-a).

As was discussed in chapter 2.3.8, there have been some attempts (Rai, 1979) to analyze the velocity profile of a plane turbulent wall-wake using a two-layer system (Figure 2.4). In the same way, the velocity profiles in the wake flow downstream of the recirculation region in regimes 1 and 2 will be analyzed using a two-layer model or two zones of influence: the outer and inner regions. The effect of the bed on the velocity profile is negligible away from the bed in the outer region, whereas close to the bed, its effect is dominant in the inner-region.

The velocity profiles of Expt. DS2 were chosen for testing against plan-wake velocity distribution in regime 1. In this experiment the ratio of width to depth of the flow B/d was 7.7 and it did not affect velocity profile. This was contrary to that of Expt. DS1 in which B/d was equal to 4.5 and affected the velocity profile significantly (chapter 5.3.3). For regime 2, profiles of Expt. AS1 and AS2 were examined. The equation for defect velocity has been derived for a plane turbulent wake, based on Prandtl's mixing length hypothesis by Schlichting (1930). Using the integral method, the derivation of the plane wake equations has been shown in chapter 2.3.8. The defect velocity distribution for the far wake region was derived as (Eq. 2.23):

$$\frac{U_0 - u}{u_{1m}} = \left(1 - 0.293.\lambda^{3/2}\right)^2$$

where u_{1m} is the maximum defect at the center of the wake and $\lambda = y/b$. This equation is used to describe the outer region of wall-wake. The longitudinal velocity increases from

zero at the bed and reaches maximum value at the free surface. Therefore, the maximum velocity selected at the outer region in the case of plan-wake theory was the free surface velocity instead of the free stream velocity .

This fact affects the performance of the proposed distribution because there was no unique free stream velocity. In fact, the free surface velocity changes at different stations downstream of the body. The free surface velocity in regimes 1 and 2 was larger than the average sectional velocity U_0 behind the recirculation region (about 10%). This increase of velocity might be due to the acceleration of the flow over the top of the body. Further downstream of the obstacle, the flow velocity decreased and reached its original undisturbed value U_0. But in regimes 3 and 4 the flow over the top of the body was not strong or present where there was a reverse flow at the surface immediately behind the hemisphere. Therefore, surface velocity increased further downstream from 0.6 and $0.8U_0$ at 4D downstream of the body in regimes 3 and 4 respectively to $0.9U_0$ at 10 D, failing to reach U_0. So the range of the change in the surface velocity relative to the average velocity was less for higher relative depths in regimes 1 and 2 compared with lower relative depths in regimes 3 and 4. Cantwell and Coles (1983) also found a sharp relaxation of the mean velocity defect along the wake centerline behind a circular cylinder, which may be classified in regime 4. They attributed this rapid acceleration to very intense mixing occurring in near wake.

The parameters U_{1m} and b (Figure 2.4) can not be determined directly from velocity profiles because there is an overlap between the profiles of the outer-region and inner-region. Therefore, assuming that the plane-wake distribution is valid in the outer-region (Eq. 2.23), and if u_1 and u_2 are the measured velocities at ordinates y_1 and y_2, the value of b can be calculated as (Rai, 1979):

$$b = \left[\frac{k_1 y_2^{3/2} - y_1^{3/2}}{3.41(k_1 - 1)} \right]^{2/3} \tag{7.1}$$

where
$$k_1 = \left[(U_m - u_1) / (U_m - u_2) \right]^{1/2}$$

Then U_{1m} can be calculated from Eq. 2.23. The plots of non-dimensional velocity distributions in the outer region of regimes 1 and 2 are shown in Figure 7.2 (a-d). No analysis was conducted for regimes 3 and 4 due to the absence of a reliable free stream or maximum velocity at the outer-region of the wake flow. Profiles of regime 1 are plotted for two sizes of the obstacle in Figures a and b for Expt. DS1 and DS2 respectively.

In Figure 7.2 (a), the number of stations were limited to three and, as well, the flow was not fully developed. Therefore, the number of measured points inside the wake were very limited, but there was still good agreement in the outer region of the flow with plane-wake distribution. The profile deviates from the wake equation at about $y/b=1$. In Figure 7.2 (b), for Expt. DS2, the flow is fully developed for the same relative depth and the number of stations increased to 6. So, the validity of the proposed distribution could be checked with more confidence. As it can be seen in Figure 7.2 (b), there is fair agreement between the velocity profiles and plane-wake distribution. The velocity profiles are more similar further downstream, such as $x/D=15$ and 20, compared with the closer profiles at $x/D=2$ and 4.

The deviation from the plane-wake profile starts at about $y/b=0.5$ close to the bed and at about $y/b=2$ for the top layer. The deviation from the plane-wake close to the bed indicates the effects of the bed and probably the end of validity of the plane-wake assumption. Therefore, in the next section, the law of the wall was used to examine the similarity of this part of the profiles. In the upper part of the profiles, contrary to the plane-wake ones, there is no constant free stream velocity, but there is increasing velocity as a sign of fully developed flow. Therefore, some deviation from the plane-wake profile was expectable. The length in which the velocity profiles could attain similarity is less

than that of their counterparts in the plane-wake, x/D= 12.5, which may be attributed to the 3-D effects and presence of the downwash flow.

Two different sizes of hemispheres were used in regime 2, Expt. AS1 and AS2 in Figures 7.2 c and d respectively. There is more deviation at the bed and close to the free surface of these profiles. The thickness of the layer on the top of the obstacle is decreased compared with that in regime 1 and the top layer interferes with the recirculation region. Therefore, the velocity distribution at the top departs from the plane-wake profile. In fact the lowering of the depth of the flow prevents the free growth of the wake profile at the outer region and limits it by the free surface. Due to the increased effect of the side flows in the presence of a weaker top layer, the disturbance in the bed area increases. Therefore, the deviation from the wake profile starts between 0.5 to 1. The effect of the wall-wake is considerable in closer stations due to the strong presence of the wake of the body. The transition of the lower part of the velocity profiles in Figures 7.2 c and d shows how further profiles are developed and the deviation due to the bed effects decreases from y/b=1 to 0.5.

There are several parameters which affect the suitability of the plane-wake distribution for the wake of a free-ended 3-D body. The analysis has been carried out only on the plane of symmetry, so it would be valid for a very narrow central band of the wake due to the presence of strong 3-D effects. The shape of the normalized velocity profile depends on the selection of u_1 and u_2 in Eq. 7.1. These values should be selected within the outer-region to represent the wake of body in absence of the bed effects. Therefore, for each station, the location of these points on the velocity profile should be checked otherwise errors would be introduced in the determination of the normalized profiles.

The effect of the free surface and generated standing waves and turbulence at the top layer changes the natural form of wake growth. Profiles closer to the body such as x/D=2 or 3 are more prone to deviation from the similarity profile because the effects of vortex generation zone are still significant. It should also be kept in mind that in this

analysis, the free surface velocity was not a constant value. The profiles of the velocity in the inner region are plotted against the universal law of the wall in Figures 7.3 (a-c). Based on these figures the inner part of the profiles is in fair agreement with the law of the wall, while the outer part of the profiles deviate from it. These figures show the development of the velocity profiles.

7.3 Similarity in the Lateral Direction

Lateral velocity measurements were carried out for different stations along the longitudinal direction and also for different depths at a single station. An analysis of these measurements is presented in the following sections. The longitudinal variation of the wake of the obstacle has been described by a single lateral velocity profile at y/h=0.5 or 0.25 for different stations in the longitudinal direction which represents the entire wake (section 7.3.1). The vertical variation of the wake is presented by the several spanwise velocity profile at a single station under different regimes in section 7.3.2.

7.3.1 Similarity profiles at different stations

All velocity profiles are normalized by U_{lm} and b. Figures 5.18 a to f indicate the presence of two categories in the profiles of velocity, downstream of the recirculation zone. There is a region in which the minimum velocity in the wake of the body is located at the POS, so the defect velocity profile has only one peak (x/D < 3 to 4). Further downstream of this region, for x/D > 4, velocity at the center of the wake increases due to the effect of the downwash of the flow rushing from the top of the body causing a high momentum flow. Therefore, the usual shape of the wake is disrupted by this jet-type of flow, creating two peaks at the side of the defect velocity profiles. These two categories are present only in regimes 1 and 2 due to the presence of the downwash, but in regimes 3 and 4 only the first category is present in the absence of the downwash. Also based on the same measurements, the HS vortex is significant in the first region and is negligible or

285

disappeared in the second region. Therefore, its presence in the first region, for x/D < 3 to 4, makes it difficult to measure the value of U_{1m} and b, producing less reliable results.

Due to the difference in the nature of these two regions, these velocity profiles can not be analyzed similarly in regimes 1 and 2. In the first region, simple plane-wake theory was checked, whereas in the second region, due to the interference of the jet with the wake, the analysis was very difficult. In general the first region is limited for a small distance downstream of the body and it seems that this is less than x/D=2, 2.5 for the regime 1 and less than x/D= 3 to 4 in regime 2. The results of the analysis are presented in Figures 7.4 (a-f) for Expt. DS1, DS2, AS1, AS2, BS1, and CS1 respectively.

In the plane-wake distribution, the value of the free stream velocity has been used as the outer limit of the wake velocity. But there is no such velocity in the laboratory flume. The velocity varies across the flow due to the presence of the side wall and it changes at different depths. Any error in the assumption of the velocity at the outer limit would cause the inclusion of an additional part of the velocity profile into the wake profile in calculating the value of b, which causes the inaccuracy. As a first trial, the average sectional velocity of the flow, U_0, was used, but proved to be unsuitable. There was a lot of scatter where z/D was increasing towards the wall of the flume due to the difference between the actual velocity and U_0. In the second attempt, the average velocity of the corresponding depth in which the measurements were carried out was used, U_y. The condition at the far end of the profile was improved but still there was a significant scatter because of the difference between the velocity at the far end of the profile and U_y. Therefore, the maximum velocity at the far end of the profile, the measured velocity at the last measured point U_{2D}, i.e., z/D=2, was used. The results were found to better match the proposed wall-wake distribution.

The range in which the plane-wake distribution might be valid in regime 1 is very limited and only two profiles at x/D= 2 and 2.5 for Expt. DS1 and one profile at x/D=2 for Expt. DS2 have been measured before the interference of the downwash. The profiles

are in rough agreement with the proposed distribution within 40% of the width of the diameter of the body or 80 % of the diameter considering the whole wake across the flow.

One factor which may introduce some error is the presence of the HS vortex in this region of the flow, $x/D<$ 3 to 4 D. The HS vortex expands the wake by causing a further decrease of the velocity where the velocity is improving, i.e. postponing the velocity development inside the wake. In this way, in calculation of corresponding defect velocity of b, U_0-u/U_{1m}, some serious errors might occur because the natural growth of the wake is interrupted by the legs of the HS vortex. Therefore, to avoid large errors, the effects of HS vortex can be neglected by assuming the natural wake or plane-wake profile. Then based on this profile, the value of the defect velocity coresponding to b can be calculated.

In regime 2, Figures 7.4 c and d, there is a fair agreement between the plane-wake profile and measured ones up to $z/b =$ 1 to 1.5 which is about 40% width of the wake. The effect of the HS vortex in disturbing the wake growth can be observed clearly afterward. Based on the profiles in Figures 7.4 (a-d), it seems that there is a transition between the two regions at about $x/D=$ 3. There is a good agreement between the plane-wake profile and the measured ones in regimes 3 and 4 (Figures 7.4 (e-f)). The number of measured profiles and the length in which measurements were conducted are reasonable for similarity analysis. As was explained in chapter 3 and 4, spanwise measurements in regimes 3 and 4 could be made only at a fair distance downstream of the hemisphere mounted on the bed. Therefore, the effect of the HS vortex disappeared and values of U_{1m} and b could be calculated more accurately. Besides, in these regimes there is no downwash of the flow from the top of the body. So, all profiles can be classified to be in the first category where there is only one peak in the defect velocity profile similar, to that of the plane-wake distribution. All these factors caused the profiles to collapse on to the plane-wake profile. The width of the agreement between profiles is about 1D, more than double that in the regimes 1 and 2.

7.3.2 Similarity profiles at different depths

The development of the wake behind the body and its longitudinal variation was described by a single lateral velocity profile at y/h=0.5 or 0.25 for different stations along the longitudinal direction as being representative of the whole wake in section 7.3.1. In this section the vertical variation of the wake characteristics at a single station is examined. Figures 7.5 (a-f) present the vertical variation of the wake characteristics and its similarity for all four flow regimes.

Figures 7.5 a and b show the results of the similarity analysis for two different Froude numbers in regime 1. All velocity profiles are normalized by U_{1m} and b. The profiles are in agreement with the plane-wake profile up to the z/b=1.5, which in these cases is about 0.35 to 0.55D for the half-wake. The presence of the HS vortex is the cause of this short and narrow agreement. Comparing Expt. DS1 and DS2, the effect of the HS vortex is more pronounced in lower Froude number flow of Expt. DS1. The effect of the HS vortex represented by the hump in the defect velocity profile decreases by increasing the depth of the flow and almost vanishes for depth of more than y/h=0.5. The width of the agreement of the profiles with y/h > 0.5 is more than that in y/h < 0.5 as a clear indication of the interruption of the natural wake profile by HS vortex. The presence of this hump in the defect profile causes the extension of the reduced-velocity region up to 1D for half-wake but with a flatter maximum, i.e., extension of the wake.

Figures 7.5 c and d show the results of the analysis for two Froude numbers in regime 2. The width of the agreement with the plane-wake distribution is similar to that in regime 1. The decrease of the effect of the HS vortex is clear by reduction of the velocity deficit from 0.5 to 0.4 for profile at y/h=0.1. Figures 7.5 e and f show the results of the analysis in regime 3 and 4 respectively. Defect profiles collapse on the plane-wake distribution in a much wider range compared with regime 1 and almost cover 1D, twice as much as before, for the half-wake. The width of the agreement in regime 4 is slightly

288

larger than that in regime 3. This fact shows that the wake of the body in regimes 3 and 4 is wider than that in regimes 1 and 2. Due to the location of the chosen station, x/D=4 and 5, the effect of the HS vortex is absent and also in these regimes, d/h < 1, there is no downwash effect.

7.4 Velocity recovery in the wake

One of the characteristics of the wake of a body is the velocity recovery or decay of the peak velocity defect along the longitudinal direction of the flow behind the body. This parameter helps us to understand the strength of the wake and its development process. Recovery of the velocity on the plane of symmetry in form of defect velocity is presented for different regimes in Figure 7.6. The developed equation of Okamoto (1979) for a hemisphere-cylinder placed on the ground floor of a wind tunnel is also presented in this figure (Eq. 2.4).

The gradient of the velocity recovery for all four regimes is smaller than their wind tunnel counterpart, indicating a higher degree of mixing for larger velocity in the wind tunnel. In regime 1 (Expt. DS1 and DS2), there are two slopes in the profile of the decay of the velocity defect. In the first region closer to the body, there is a steeper slope indicating higher mixing of the wake flow with the free stream. In the second region, further downstream, the slope is mild showing a weaker mixing process. In Higher F (Expt. DS2) the length of the first region is longer and the slope of second region is steeper than those of the lower F in Expt. DS1, indicating the effect of the F in mixing process.

In regime 2 (Expt. AS1 and AS2) the profile has a higher and more consistent slope and the difference of the slope between two regions is smaller. The slope of the profile for the smaller hemisphere in Expt. AS2 is less, probably due to the pronounced effect of the bed. General steeper slope in regime two compared with that in regime 1 might be due to the higher F. In regimes 3 and 4, the slope of the profile of the decay is

289

more than that in the other regimes where the velocity recovery for regime 4 is the fastest one. But the magnitude of the velocity in these two regimes is less than regimes 1 and two due to the probable effect of the downwash of the flow from the top of the body, which increases the velocity of the flow on the plane of the symmetry. As a general guide in estimating of the velocity on the plane of symmetry downstream of the body a curve has been fitted for all four regimes which can be expressed as :

$$\frac{U_o - u}{U_o} = 0.778\left(\frac{x}{D}\right)^{-0.792} \qquad (7.2)$$

In general it can be concluded that although the length of the recirculation region in regimes 3 and 4 is larger than that in regimes 1 and 2, the velocity recovery in these two regimes is stronger but with a smaller magnitude.

7.5 Similarity Analysis of Scour Profiles

The scour profiles of the different regimes and bodies were presented in chapter 6. Here the growth of the scour profiles over time was analyzed. The profiles of the scour for consecutive times were measured for regimes 2, 3 and 4 while the experiments were run for one size of the hemisphere (Expt. AM11, BM11 and CM11). The scour profiles were measured in the front (on the POS and $x < 0$), at the back (on POS and $x>0$) and on the lateral side (on the $x=0$ plane) of the hemisphere-cylinder. Special points and geometric scales are defined in Figure 7.7.

Due to the similarity between the down flow in front of the body and an impinging jet, the similarity equation of the latter one might be used. Ahmed (1994) found that the exponential curve of Rajaratnam and Beltaos (1977) for an impinging jet can be modified to describe the scour profile of a bridge pier. Here scour profiles are

290

normalized and were compared with this equation to check the difference between the pier profiles and the open-ended body.

In the scour profiles at the front, the deepest point is usually not located on the body itself but occurs at a small distance upstream of the obstacle (point B in Figure 7.7). Therefore, the origin of the coordinates was shifted to this point, O'. Then the coordinates were normalized by the following scales as:

$$S_{fx} = |x_{min} - x_{1/2}|$$
and
$$S_{fy} = |y_{min}|$$

where the subscripts min and 1/2 denote point B as the deepest point and the point where $y = y_{min} / 2$ respectively. The dimensionless coordinates for the front sides are defined as:

$$\bar{x} = \frac{x - x_{min}}{S_{fx}}$$
and
$$\bar{y} = \frac{y}{S_{fy}}$$

The scour profiles in front of the body are presented in Figures 7.8 (a-c). Ahmed (1994) developed following equation for bridge piers :

$$\bar{y} = -\exp\left[\ln\left(\frac{1}{2}\right)\bar{x}^2\right] + \sin(-\pi\bar{x})\left\{C_1 \exp\left[\ln\left(\frac{1}{2}\right)(2\bar{x}+1)^{20}\right]\right.$$
$$\left. + C_2 \exp\left[\ln\left(\frac{1}{2}\right)(2\bar{x}+3)^{20}\right]\right\} \qquad (7.3)$$

where the first term represents an exponential curve for impinging jets (Rajaratnam and Beltaos, 1977). The second term shows a sine curve which is confined within certain regions with two square wave-like functions. Ahmed (1994) found that the constants C_1

and C_2 are equal to 0.07 for bridge piers. In the present experiments, this equation could roughly represent the profiles, but after changing the second constant, C_2=0.01, a closer fit was made. This fitted line is presented along with the scour profiles in Figures 7.8 a to c. Based on these figures, there is good agreement between the proposed equation and scour profiles. There is a small deviation on the upstream side where the profiles show a steeper slope than that of the equation. This might be due to the nature of the sediments used in these experiments where the sediments could stand a steep slope even close to the ground level. All three regimes show the same agreement with no difference. Based on this comparison, it can be concluded that there is no difference between the scour profiles of the bridge piers and that of the hemisphere-cylinder. This fact indicates the importance of the downflow effects in the scour mechanism in front of the body, which overruns the differences between these two distinct obstacles where there is a vertical frontal face in both cases.

For the side profiles the scales are found in the same manner as :

$$S_{sz} = \left| z_{min} - z_{1/2} \right| \qquad ,$$

$$S_{sy} = \left| y_{min} \right| \qquad ,$$

$$\bar{z} = \frac{z - z_{min}}{S_{sz}} \qquad ,$$

and
$$\bar{y} = \frac{y}{S_{sy}}$$

The normalized side scour profiles are shown in Figures 7.9 (a-c). The proposed equation was changed as follows, based on the fact that in side profiles unlike x and $\bar{x}$, z and $\bar{z}$ are in the same direction (Ahmed, 1994).

$$\bar{y} = -\exp\left[\ln\left(\frac{1}{2}\right)\bar{z}^2\right] + \sin(-\pi\bar{z})\left\{C_1\left[\exp\left(\frac{1}{2}\right)(2\bar{z}-1)^{20}\right]\right.$$
$$\left. +C_2\exp\left[\ln\left(\frac{1}{2}\right)(2\bar{z}+3)^{20}\right]\right\}$$

(7.4)

The constants for this study are changed by trial and error to $C_1 = -0.05$ and $C_2 = -0.1$ to get a better fit. As shown in Figures 7.9 (a-c), the two stage scour is strongly present in the side profiles.

For the back profiles, the points of minimum and maximum elevation , C and D. were found (Figure 7.7) and the scales were defined as :

$$S_{bx} = |x_{max} - x_{min}|$$

and

$$S_{by} = |y_{max} - y_{min}|$$

The normalized coordinates were defined as:

$$\bar{x} = \frac{x - x_{min}}{S_{bx}}$$

and

$$\bar{y} = \frac{y - y_{min}}{S_{by}}$$

The normalized back profiles are presented in Figures 7.10 (a-c). Based on the shape of the growth at the rear bar following equation was proposed by Ahmed (1994):

$$\bar{y} = \frac{1}{2}\sin(\pi\bar{z} - \pi / C_3) + 0.5$$

(7.5)

where he found $C_3 = 2$. In this study, the best fit was found to occur for $C_3 = 3$. The upstream side of the rear bar in regime 2, Expt. AM11 (Figure 7.10 a), follows closely the

293

sine curve. In regime 3 and 4, Figures 7.10 b and c, there is rough agreement between the equation and the profiles. The scatter for these two regimes is more than that in regime 1.

7.6 Dimensional Considerations

There are several parameters which affect the characteristics and the final shape of the scour hole around the body. These can be classified into four groups: properties of fluid, flow, sediment, and the body itself. The most important fluid properties are density ρ, and viscosity v. Flow depth d, mean velocity U_o, bed shear stress τ_o or friction velocity u_* are some of the more effective flow properties. Sediment can be described by its size D_{50}, size distribution σ_g, density ρ_s, critical shear stress τ_c or critical shear velocity u_{*c}, angle of repose α_r, and its cohesion. The body characteristics are normally its width D, height h, and shape.

To simplify the analysis, the number of variables used can be made manageable by considering only a handful of important parameters significant in the scour process. As explained in chapter 3, the sand used in this study was uniform and cohesionless. The flow velocity was less than the critical velocity and hence the scour could be considered as clear water scour. The presence of a fully developed rough turbulent flow at the measurement site was tested and the surface of the body was smooth. So, the flow could be easily defined based on its depth, average velocity and undisturbed bed shear stress. Therefore, the equilibrium scour depth d_{se} can be written as a function of a small group of variables :

$$d_{se} = f\langle u_*, u_{*c}, d, h, D, D_{50}, U_0, g, v, \alpha_r, \rho_s, \rho \rangle \qquad (7.6)$$

The density of natural sands ρ_s and their angle of repose α_r (26-30 degree in these experiments) were almost constant and can be omitted, which reduces the number of variables. The variation of the fluid density in the controlled laboratory experiments

294

would be negligible; so by taking U_0 and D as the repeating variables, dimensional analysis leads to the following:

$$\frac{d_{se}}{D} = f\left\langle \frac{d}{h}, \frac{U_0}{\sqrt{gd}}, \frac{U_0 D}{\upsilon}, \frac{u_*}{u_{*c}}, \frac{D}{D_{50}}, \frac{h}{D}, \frac{u_*}{U_0} \right\rangle \qquad (7.7)$$

The above combination may also be rearranged in other ways based on different choices of repeating variables and their physical significance. The first term in the right hand side of the above functional form for scour depth is the relative depth of the flow. The four regime proposal was made based on this parameter. The second term shows Froude number of the flow and the third parameter is the body Reynolds number. The fourth term describes the potential of the approach flow to move the bed material, causing scour. This parameter and last one may be replaced by U_{oc}/U_o. The fifth one is the ratio of the pier diameter to the sand size and the sixth term indicates the relation of the height of the body with its width.

Based on the experimental results and the flow visualization, the first two terms at the RHS of this functional form were found to be the most effective parameters affecting the structure of the local flow around the body. These two terms affect the vortex structure and the characteristics of the wake behind the body, such as its width and length. Figure 7.11 shows the results of an attempt to classify the four regimes. Experimental results are presented in accordance with their defined regime of the flow. Based on this distribution, relative depth is very significant compared with the Froude number. The entire set of the experiments can be explained easily by their relative depth, at least for the range of Froude number used in these experiments. Perhaps more detailed studies are needed to describe the effects of the Froude number on the flow behavior around the body, especially for the low F and high d/h where the nature of the mixing of the shear layer and free stream might be different.

The body Reynolds number was found to be less important considering the significance of the Froude number and presence of the free surface. The effect of the shear stress is significant where it determines the mode of bed load transport and the bed forms. All experiments on the mobile bed in this study were carried out for clear-water and no ripple-forming conditions. The effect of the bed shear stress on the equilibrium depth of scour is well defined in pier studies. For mounted bodies on the bed, more studies are essential to investigate its significance.

Many researchers confirmed that the ratio of D/D_{50} is effective in the scour process of bridge piers (Ettema 1980; Raudkivi and Ettema 1983, 1985). Some general effects are explained in chapter 2. In this study, two sizes of sands were used and some of the results have been reported in previous chapters. The shape of the body can be described roughly by the ratio of the h/D. In this study this value was a constant, equal to 0.5 due to the use of hemispheres and further studies are needed to explore the effect of this parameter for other shapes.

7.6.1 Depth of scour

Equilibrium depth of scour d_{se} has been the main focus of research in bridge pier studies, and as mentioned in chapter 2 and appendix, many equations are available to predict this important parameter. Despite all these laboratory and field studies, there is no universal relation, based on the river characteristics, capable of predicting d_{se} with reasonable accuracy. Here, based on dimensional analysis in chapter 7.5, some of these relations will be used against the measured d_{se} of hemisphere and cube in different flows. The necessary information from mobile bed experiments are presented in Table 7.1, including the regime of the flow and the characteristics of the body and the equilibrium scour depth.

Froude number has been known to be effective in scour process and there have been several attempts to relate the depth of the scour to this parameter. Coleman (1971)

correlated the d_{se} to the Froude number (Appendix), and Shen et al. (1969), by using other data, reduced this correlation to the following form:

$$\frac{d_{se}}{D} = C_1 (F_p)^{C_2}$$ (7.8)

where pier Froude number defined as $F_p = \dfrac{U_o}{\sqrt{gD}}$ and C_1 and C_2 were 1.39 and 0.2

respectively. The distribution of the dimensionless equilibrium scour depth d_{se} for different flow depths is presented against this equation in Figure 7.12. The original Eq. overestimates the d_{se} for 50 to 60% . A better fit was found by changing C_1 to 0.9. There is a fair agreement between the measured values and the new equation except for Expt. AM21 and AM31 where the shape of the body has been changed in regime 2 from a hemisphere of diameter 130 mm to the one with a diameter of 74 mm and a cube respectively. The new equation overestimates the depth of the scour by 15 %. Change of the shape and size had no significant effects on other regimes.

Table 7.1 Characteristics of the flow, body and scour for different regimes

Regime	Expt.	D (mm)	h (mm)	d (mm)	d/h	dse/D	d/D	Uo	F
2	AM11	130	65	120	1.85	0.68	0.92	0.27	0.25
	AM21	74	37	70	1.89	0.60	0.95	0.23	0.28
	AM31	74	37	70	1.89	0.55	0.95	0.23	0.28
	AM12	130	65	120	1.85	0.73	0.92	0.44	0.41
3	BM11	130	65	70	1.08	0.67	0.54	0.23	0.28
	BM21	74	37	40	1.08	0.74	0.54	0.27	0.42
	BM31	74	37	40	1.08	0.68	0.54	0.27	0.42
	BM12	130	65	70	1.08	0.75	0.54	0.35	0.42
4	CM11	130	65	40	0.62	0.65	0.31	0.27	0.42
	CM12	130	65	45	0.69	0.69	0.35	0.36	0.55

Some studies suggest that there is a relation between the strength of the HS vortex and scour depth. Shen et al. (1966) related the circulation at the front of the pier with the DU_o, which is a function of the pier Reynolds number, $R_p=DU_o/v$. They found a correlation for d_{se} based on regression analysis of data, which later was presented in an envelope form as (Shen et al., 1969):

$$d_{se} = C_3(R_p)^{C_4} \qquad (7.9)$$

where d_{se} is in mm and C_3 and C_4 are 0.2225 and 0.619 respectively. The measured scour depths are presented against this equation in Figure 7.13. The original correlation overestimates the depth of the scour by 40 to 100%. By changing the value of C_3 to 0.125 a rough agreement was found with a maximum deviation of 15 %.

In another attempt to relate the HS vortex strength to the depth of the scour Qadar (1981) carried out a series of laboratory and field experiments. He found that the radius of the HS vortex is almost 0.1 times the width of the pier and the vortex velocity decreases with width of the pier. Considering several sets of data, he proposed that the maximum depth of scour is a function of the strength of HS-vortex :

$$d_{se}=K_s(C_o)^n \qquad (7.10)$$

where $\qquad C_o=r_o u_o$

and $\qquad r_o=0.1D \qquad$ (for D< 0.025m)

$\qquad\qquad r_o=0.1(D+0.025) \qquad$ (for D> 0.025m)

and $\qquad u_o=0.092D^{-0.5}U_o^{0.83}$

where C_o is the initial strength of the vortex, n is an exponent experimentally found to be 1.28, K_s is the coefficient of sediment size with a value of 538 for sediments of diameter

less than 0.5 mm, r_0 is the vortex radius and u_0 is the tangential velocity at a distance r_0 above the vortex center. The coefficient and exponent were different for coarser sediments. The original equation was used to estimate the scour depth and results are presented in Figure 7.14. It overestimates the scour depth by 10 to 90 %. The constant K_s was changed to 375 and a rough agreement between measured values and new version of the equation was found. The coarser sediments in Expt. AM12 of regime 2 causes a deviation of about 30%.

Neill (1964 a, b), using the data of Laursen and Toch (1956), related the scour depth to the relative depth of the water :

$$\frac{d_{se}}{D} = C_5\left(\frac{d}{D}\right)^{C_6}$$

(7.11)

where C_5 is 1.5 and C_6 0.3. The equation describes the data well for velocities of 0.3 to 0.61 m/s and flow depth of 60-275 mm with sand size of 0.44-2.25 mm mainly in live-bed, but here it is used to see the effect of relative depth (Figure 7.15). The original equation overestimates the scour depth more than the other relations, up to 120%. Using new values of 0.75 and 0.1 for C_5 and C_6 respectively causes a better agreement with measured data. Different shapes and sizes in regime 2 deviate more than the others from the developed equation (about 25% for Expt. AM21 and AM31).

In general, it was found that the depth of the scour for mounted bodies on the bed is much less than that of the bridge pier (average 50-60%). Available equations can be used to estimate the scour depth for hemisphere-cylinder body after changing some constants. More study is needed to establish a relation between scour depths of these two classes of structures.

7.7 Implications for the Design of Habitat Structures

One of the aims of this study is to improve the design of fish habitat structures. In the process of this investigation it was found that the characteristics of the wakes of free-ended bodies are not understood. Then, the focus was to study the effect of the bodies on the flow and the bed. Therefore, this study can be considered only as the first step towards a better understanding of the hydraulics of habitat structures. More detailed and descriptive methods of habitat design could be obtained by continuing this work. Some of the implications for design of habitat structures or the quality of the refuge (from a biological point of view) are presented here.

The length of the recirculation zone in regimes 1 and 2 is about 1D, less than that in regimes 3 and 4, which is about 2D. Higher Froude number usually reduces this length (from 1D in regime 2 to 0.2D). The width of the wake in regimes 3 and 4 is larger than that in regime 1 and 2, almost 2D. This fact is also confirmed by the bed shear stress measurements. The wake of the rock is restricted to a small region behind the body and attached to the bed in regimes 1 and 2, while it captures all the depth of the flow in regime 3 and 4. At the surface of the flow the wake is stronger and longer than at the bed for hemisphere type of the body in regime 3 (for example: 1D at the bed and 2D at the surface). The higher F causes a shorter backward flow at the surface.

In mobile beds, the scour pattern at the middle of the wake propagated downstream in regime 1 and 2, whereas the side patterns were stopped very shortly. In regime 3 and 4 it was the side patterns which were able to proceed downstream, not the middle one. The width of the scour pattern was also different. In former cases the width was constant whereas in latter ones it expanded forming a fan. The general form of scour causes the nose of the body to sink in its own scour hole while the back side of the body holds its original position causing the body to be inclined towards upstream, a form that can be seen in many rivers. The slope of the scour wall upstream of the body was close to

the angle of the repose of the bed material. The depth of the scour was less than its counterpart for bridge piers (average 50 to 60%).

The scour and deposition patterns downstream of the cube type of the body were parallel and could not join each other (contrary to that of the hemisphere), causing a wider wake for cubes. The depth of the scour was less than that of the hemisphere with a usual deposition immediately behind the body. Whereas for the hemisphere, there was a scour hole behind the body, and then a deposition further downstream. The frontal face of the body is very effective in the depth of the scour. The more vertical the face the deeper the scour.

The study of the velocity field of the wake can lead to a better understanding of the response of fish to this environment. Therefore, the similarity of the velocity profiles on the plane of the symmetry and on the spanwise direction downstream of the rock would be useful. The results can help biologists to have a good estimate of the velocity both in vertical and transverse direction behind the rocks.

On the plane of the symmetry, the velocity profile can be divided in two parts as outer region and inner region, which both can be estimated by plane-wake theory and law of the wall respectively. For spanwise profiles, plane-wake theory was found to be useful up to 2-2.5D in regimes 1 and 2 and 3-4D in regimes 3 and 4. The width of the agreement was 0.8D in regimes 1 and 2 and 2D in regimes 3 and 4, indicating the wider wake in the latter cases. The width of efficiency of the plane-wake theory in different depth downstream of the body was 0.7 to 1D in regime 1 and 2 and 2D in regime 3 and 4. The strength of the wake, based on its velocity recovery profile, can also be estimated by developed equation.

The lateral velocity is large close to the bed in regimes 1 to 3 and it is large close to the water surface in regime 4. It reduces with increase of the Froude number. Vertical velocity behind the body is high in regime 2 and can reach up to 30% of the average velocity. The structure of the wake in regime 1 and 2 is different from regimes 3 and 4.

The velocity at the center of the wake in the former regimes is higher than the average velocity of the flow, whereas in the latter ones it is always less than that.
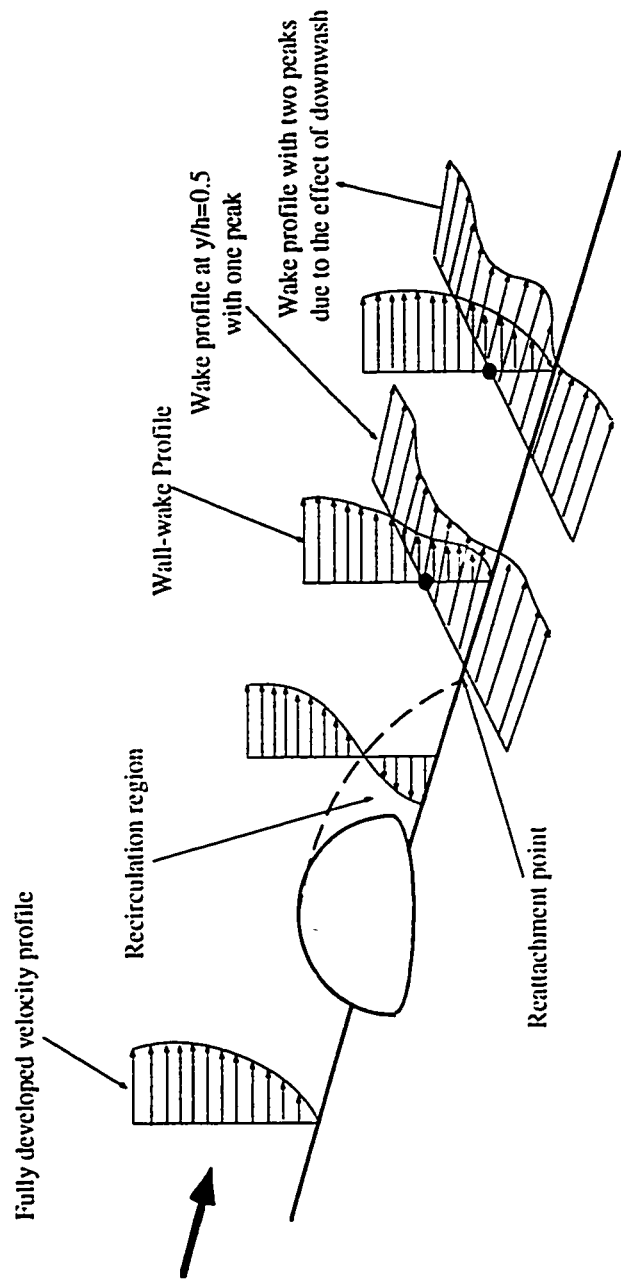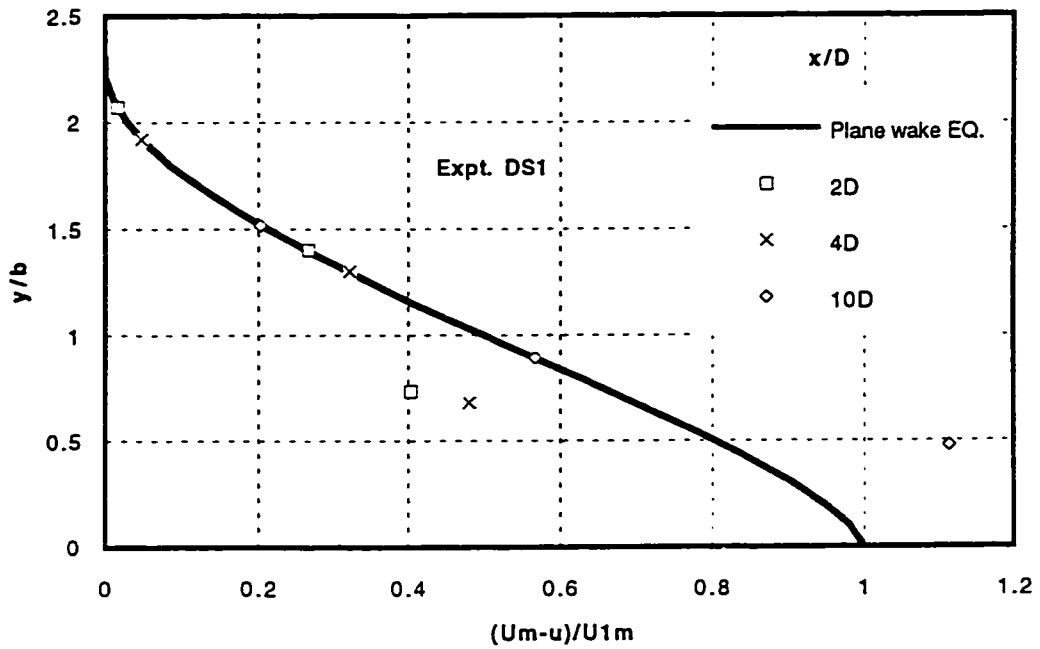
Figure 7.1 Sketch of Evolution of Velocity Profiles on the POS and Across the Flow

303
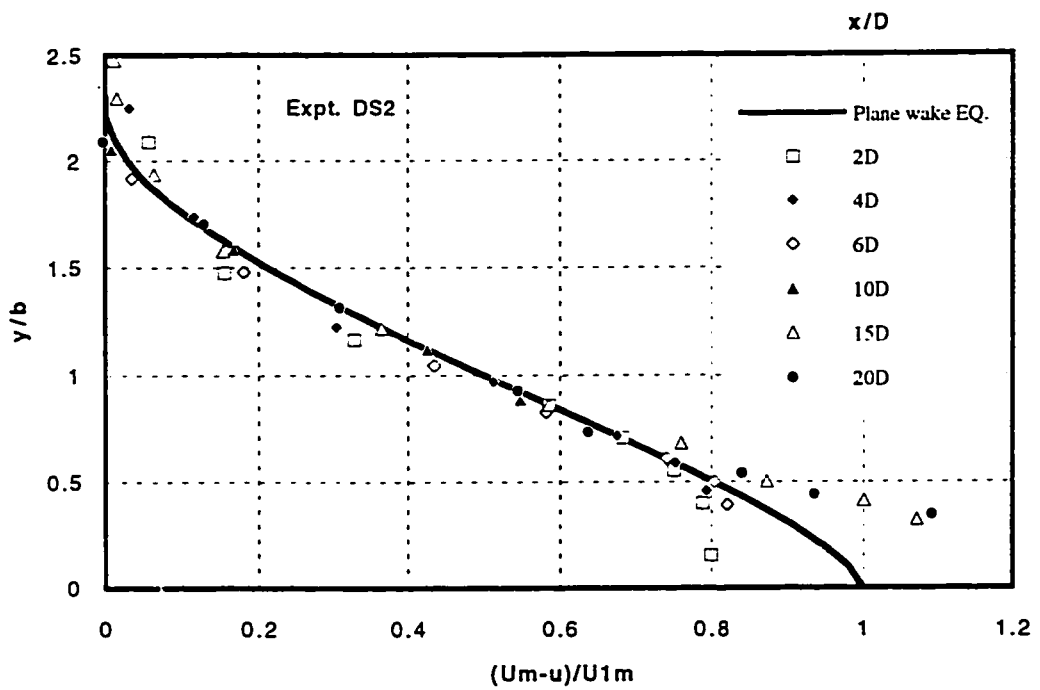
Figure 7.2 (a,b) Similarity of Velocity profiles at POS: (a) Expt. DS1, (b) Expt. DS2
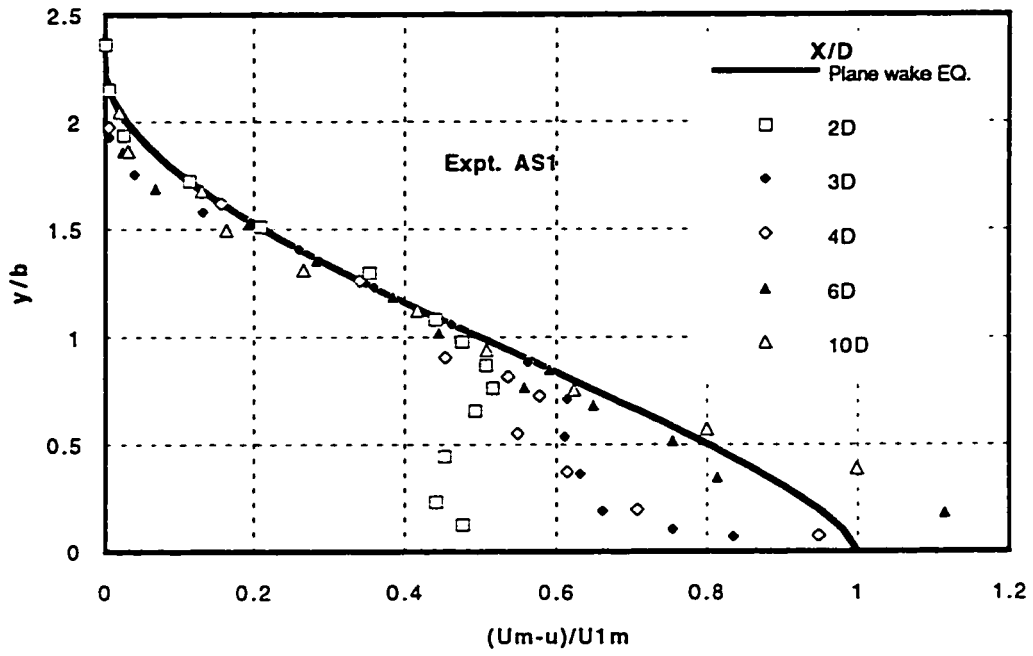
(c)
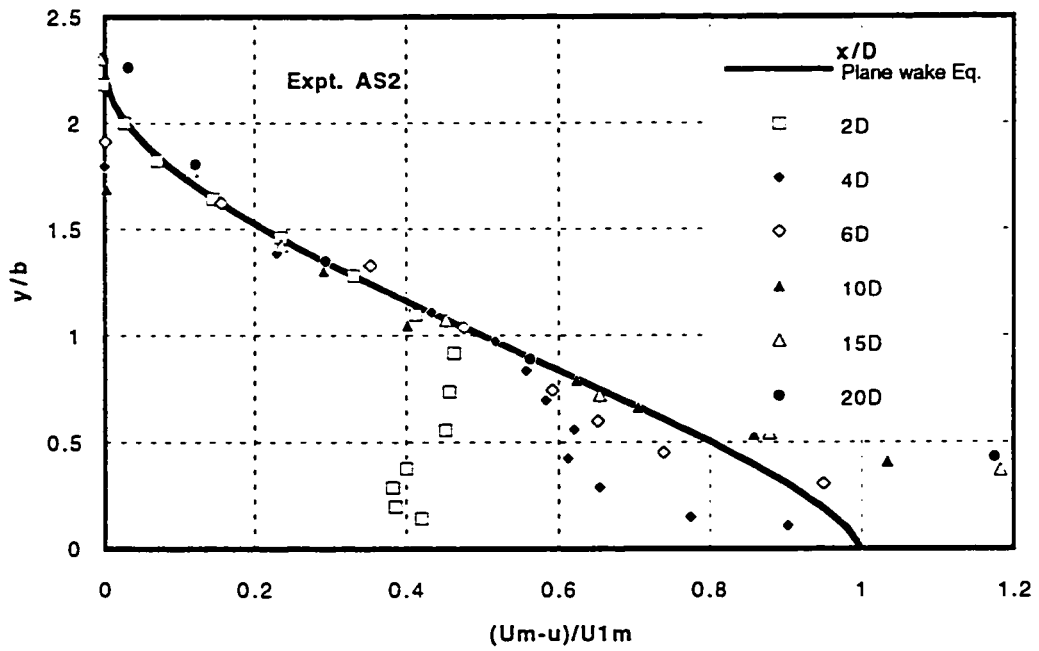
(d)

Figure 7.2 (c,d) Similarity of Velocity Profiles at POS: (c) Expt. AS1, (d) Expt. AS2
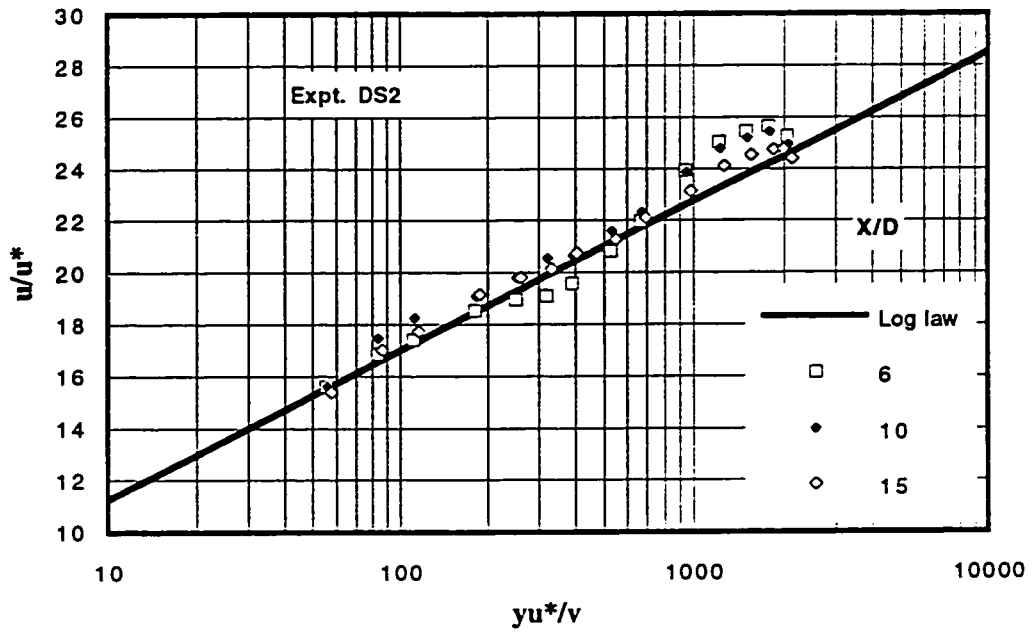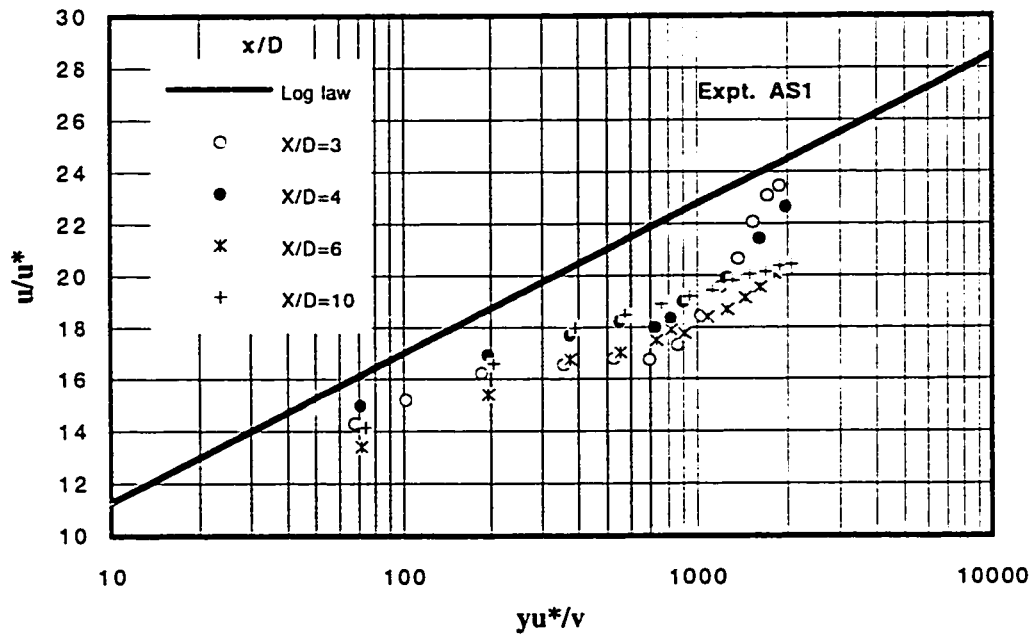
Figure 7.3 (a,b) Universal Law of Wall in the Inner-region of Wall-Wake:
(a) Expt. DS2, (b) Expt. AS1
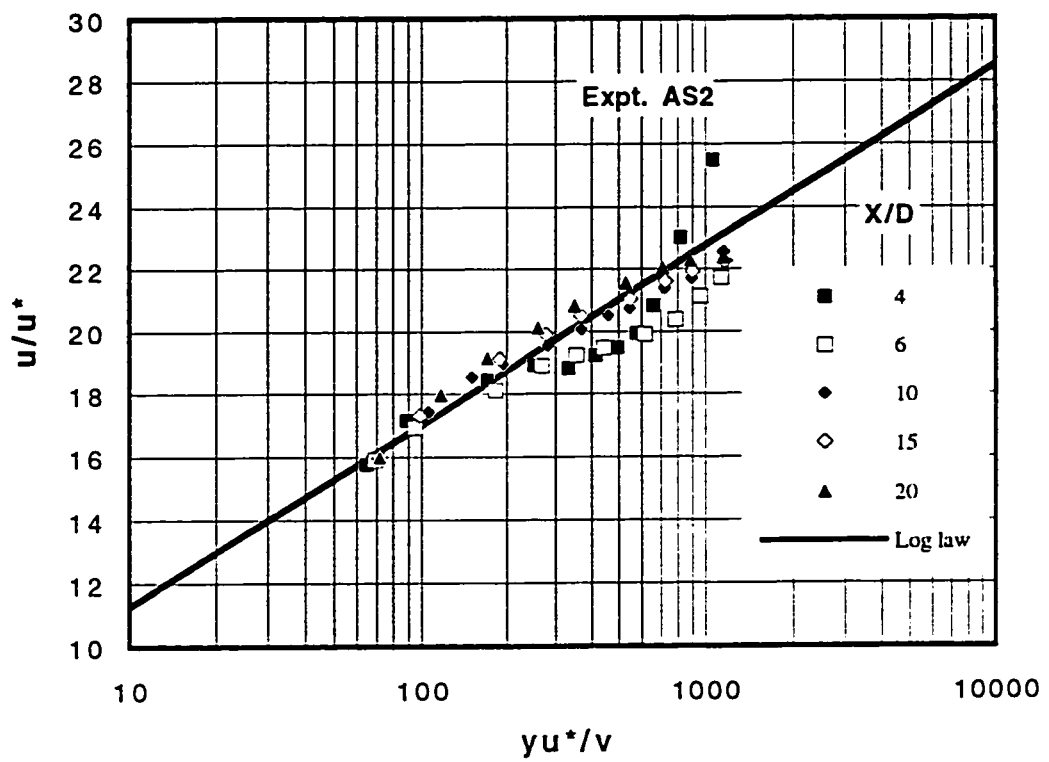
(c)

Figure 7.3 (c) Universal Law of Wall in the
Inner-Region of Wall-Wake (Expt. AS2)
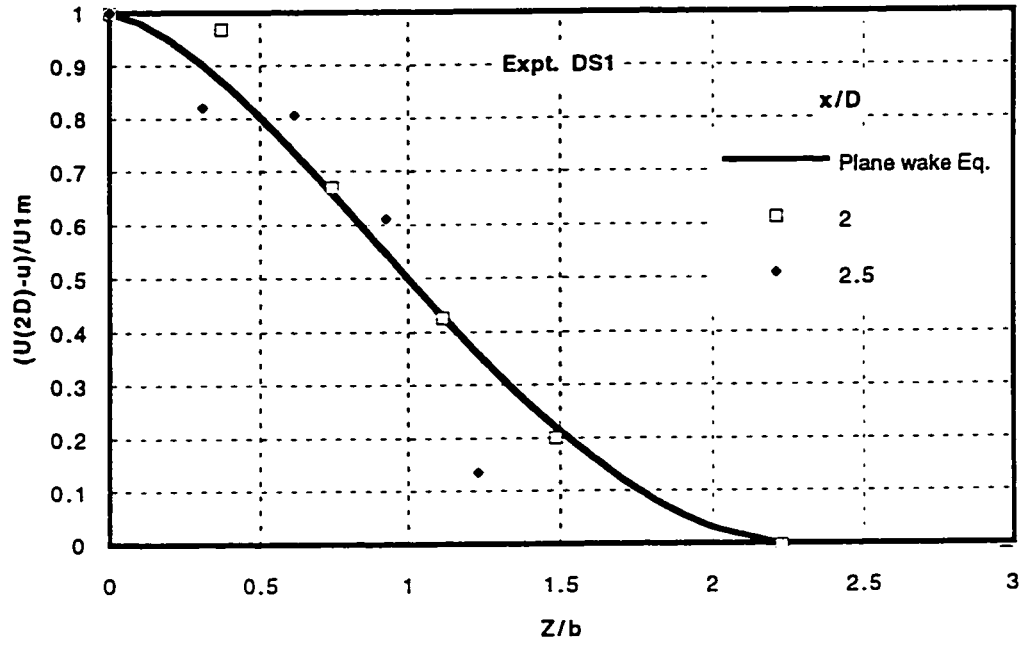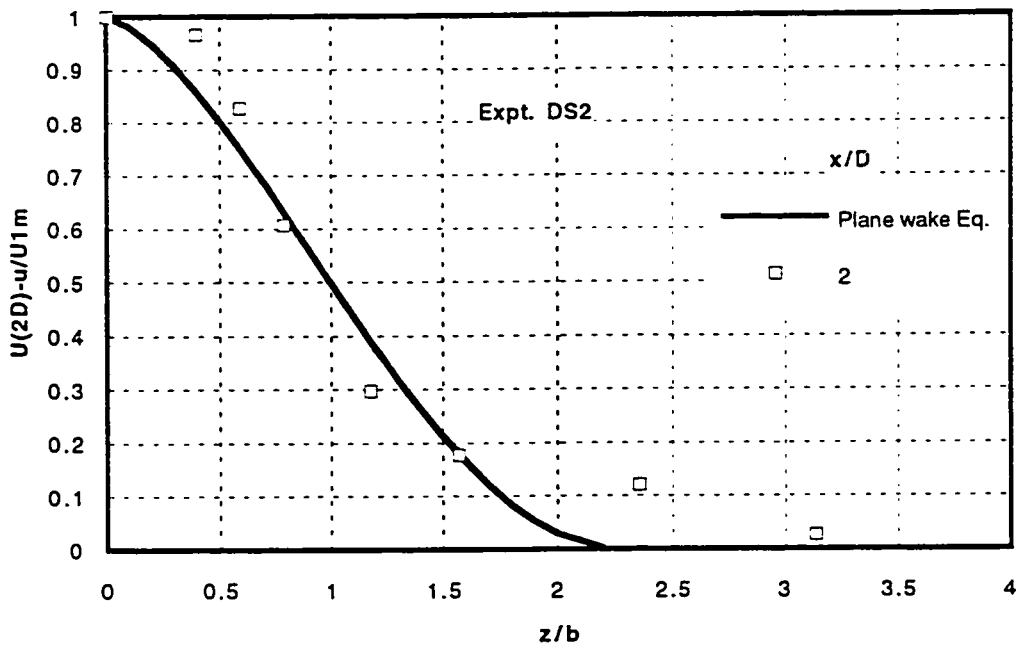
Figure 7.4 (a,b) Similarity Profiles of Velocity in Different Stations
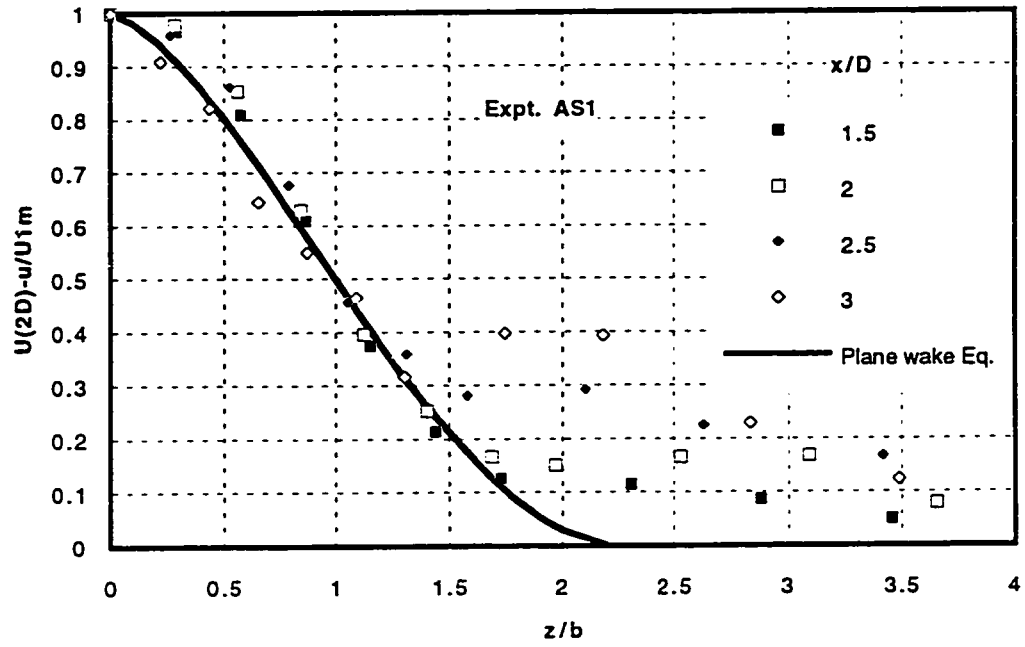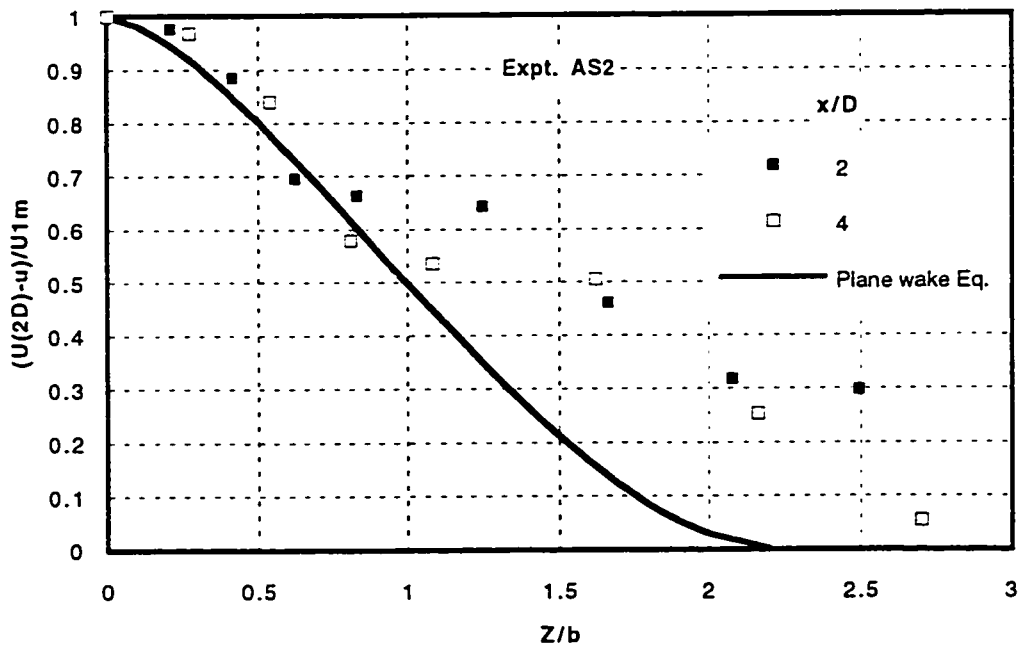
Figure 7.4 (c,d) Similarity Profiles of Velocity in Different Stations
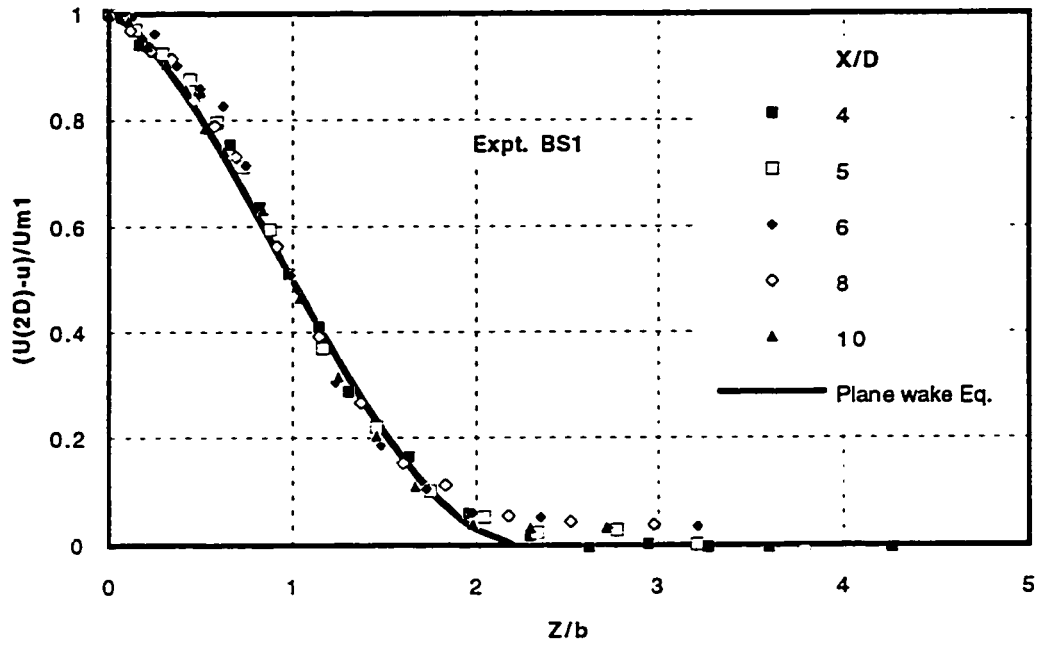
(e)
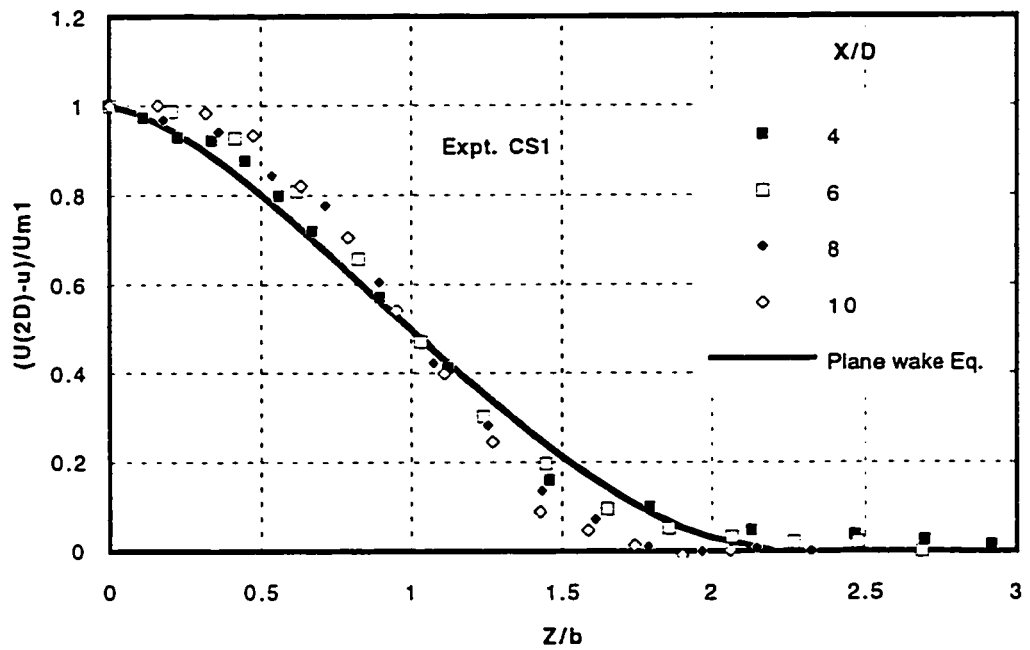
(f)

Figure 7.4 (e,f) Similarity Profiles of Velocity in Different Stations
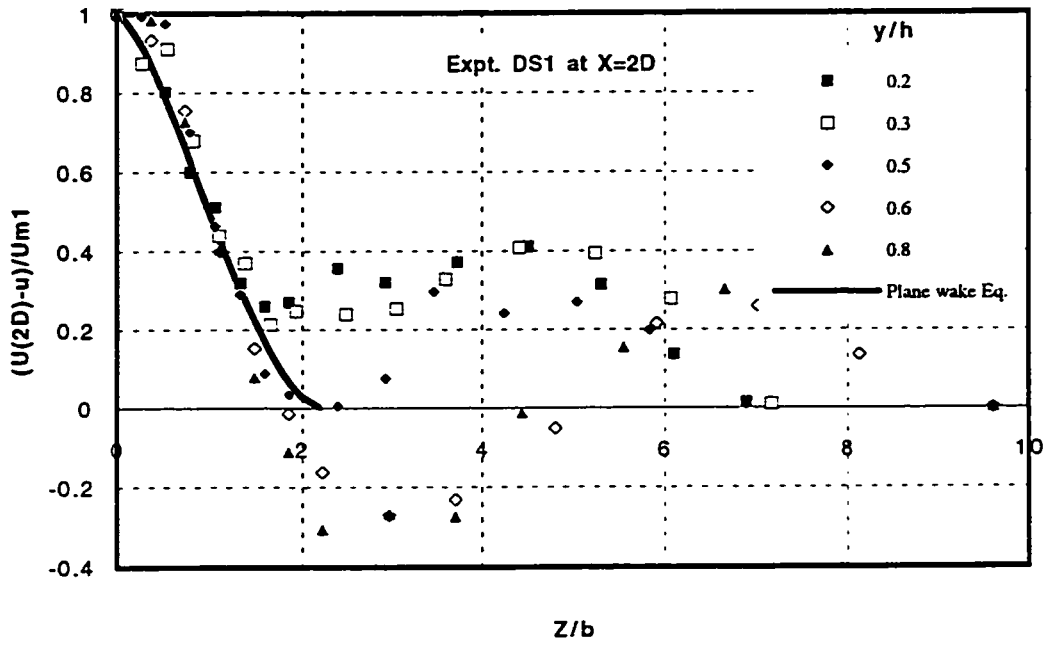
(a)
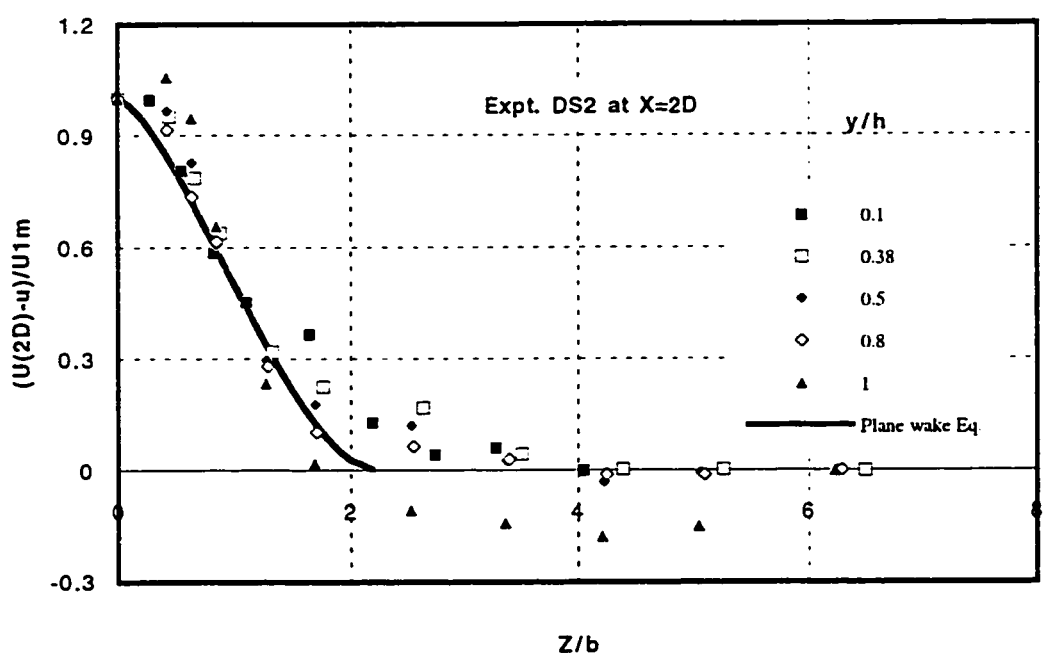
(b)

Figure 7.5 (a,b) Similarity of Velocity Profiles at Different Depths
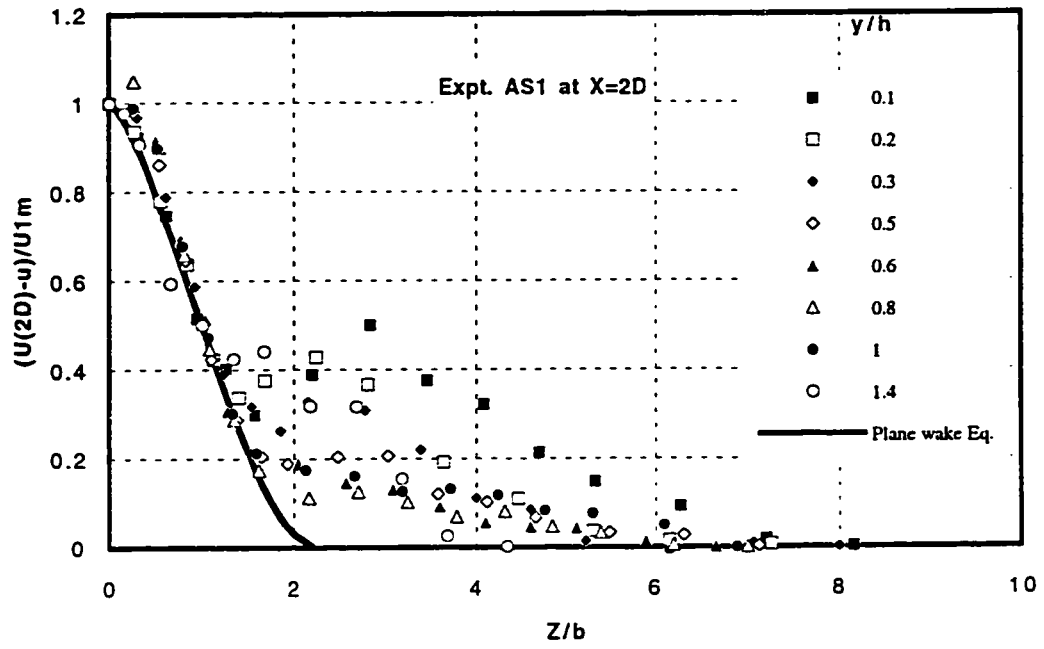
(c)
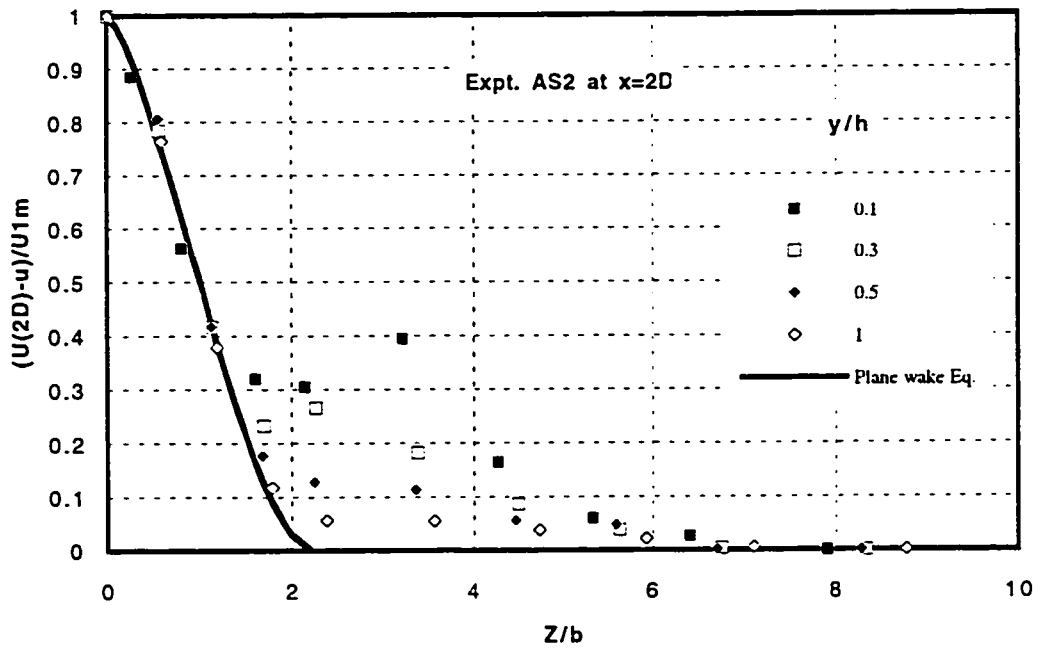
(d)

Figure 7.5 (c,d) Similarity of Velocity Profiles at Different Depths
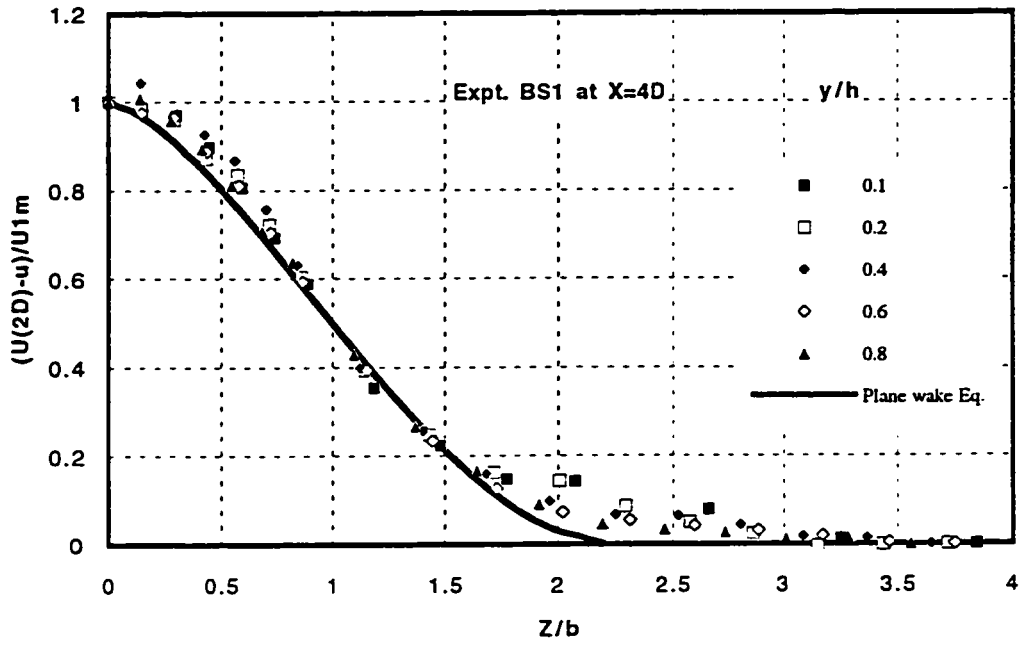
(e)
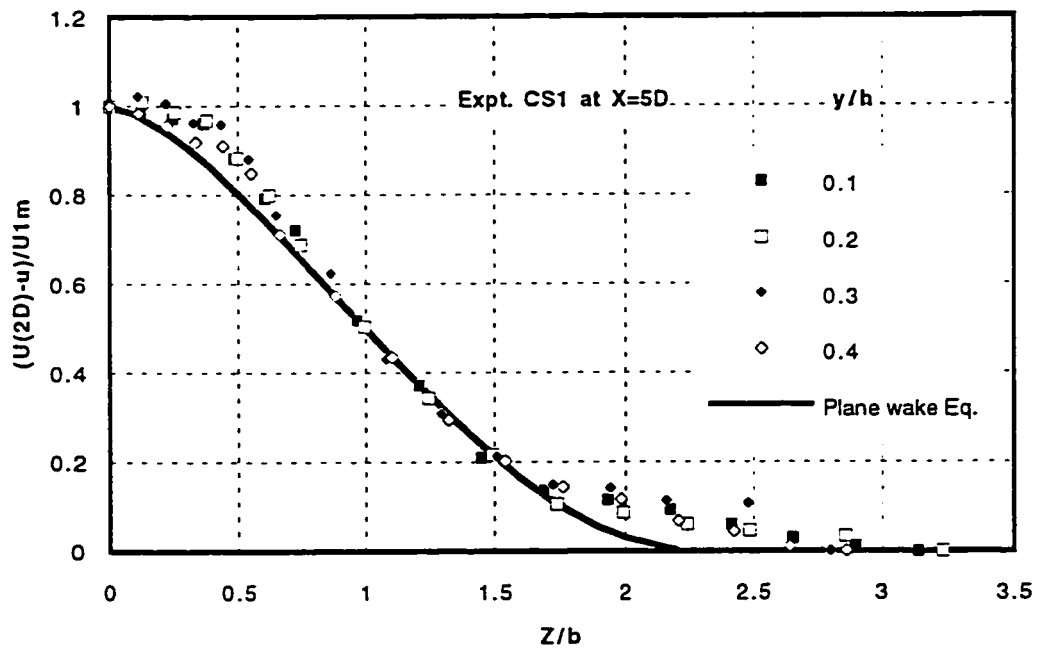
(f)

Figure 7.5 (e,f) Similarity of Velocity Profiles at Different Depths
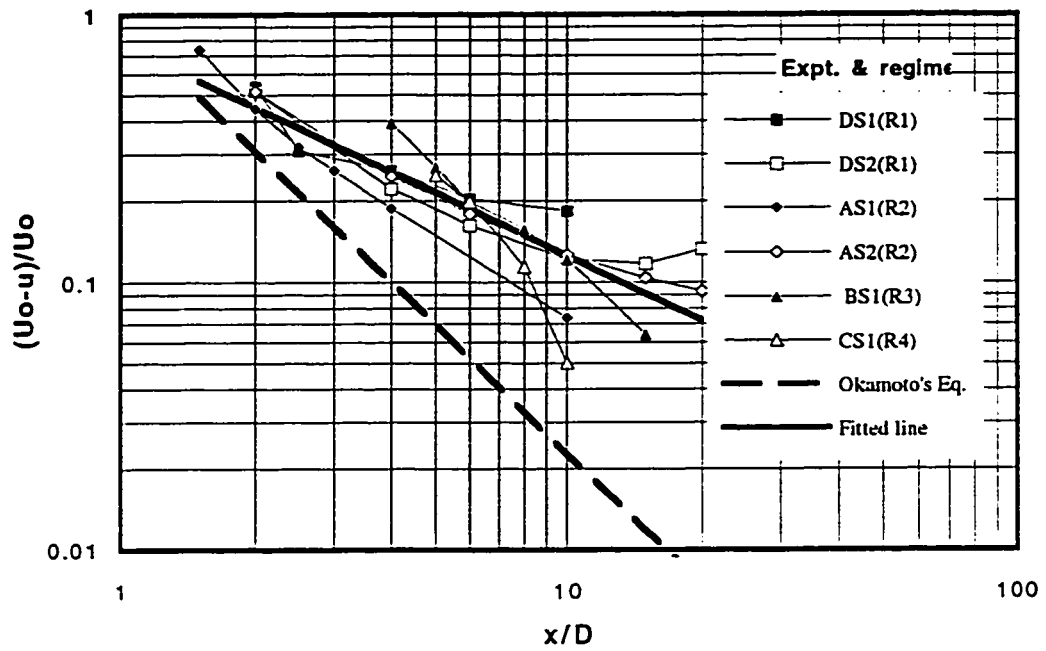
Figure 7.6. Decay of Peak Velocity Defect for Spanwise Profiles at Different Stations
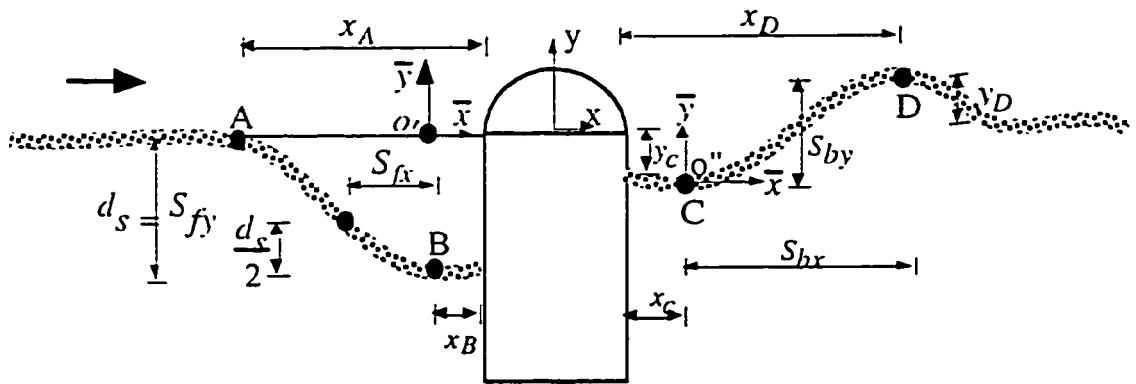
Figure 7.7 Length Scales of the Scour Profile
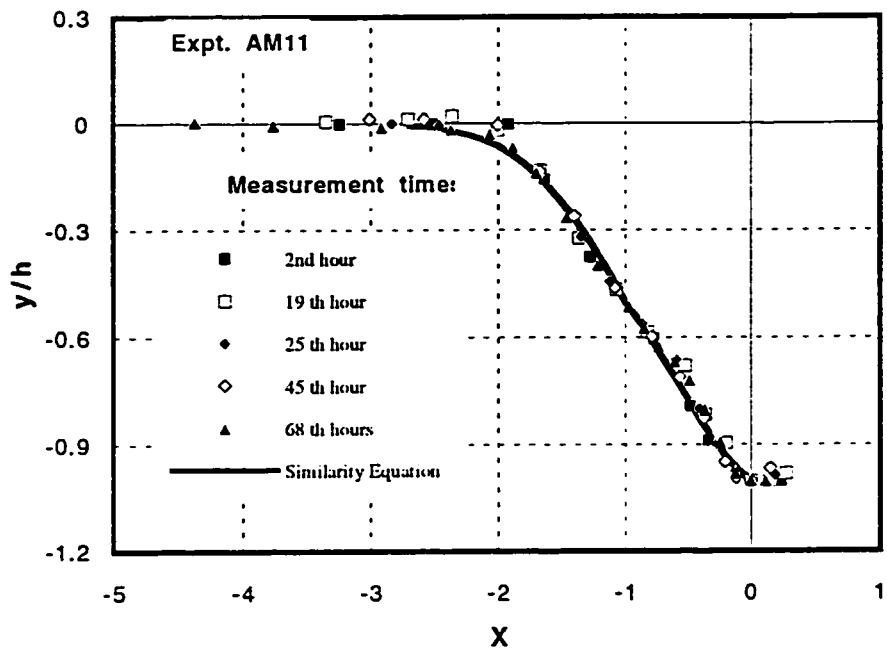
(a)
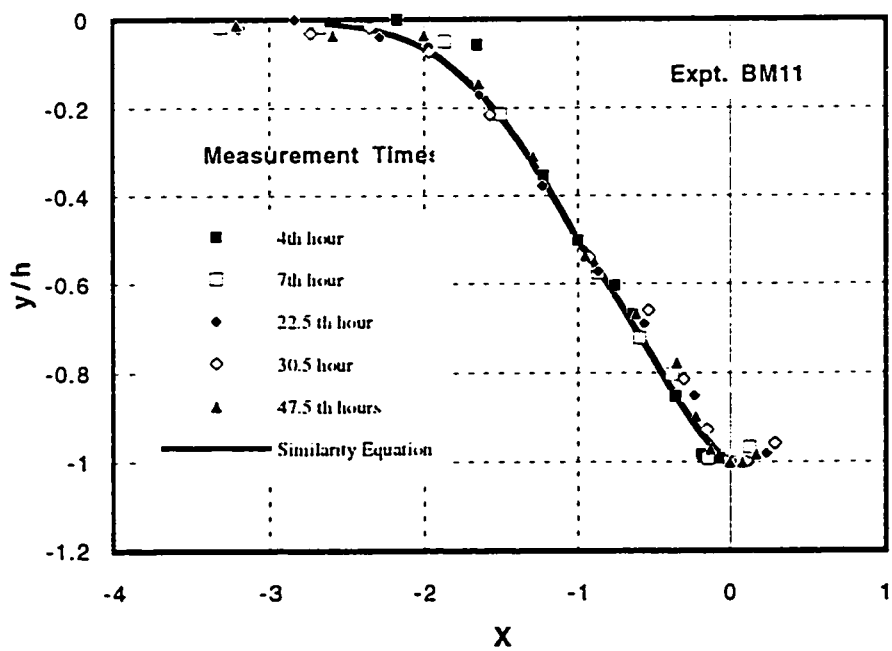
(b)

Figure 7.8 (a,b)Similarity Scour Profiles at the Front of the Body,
(a) Expt. AM11, (b) Expt. BM11

315
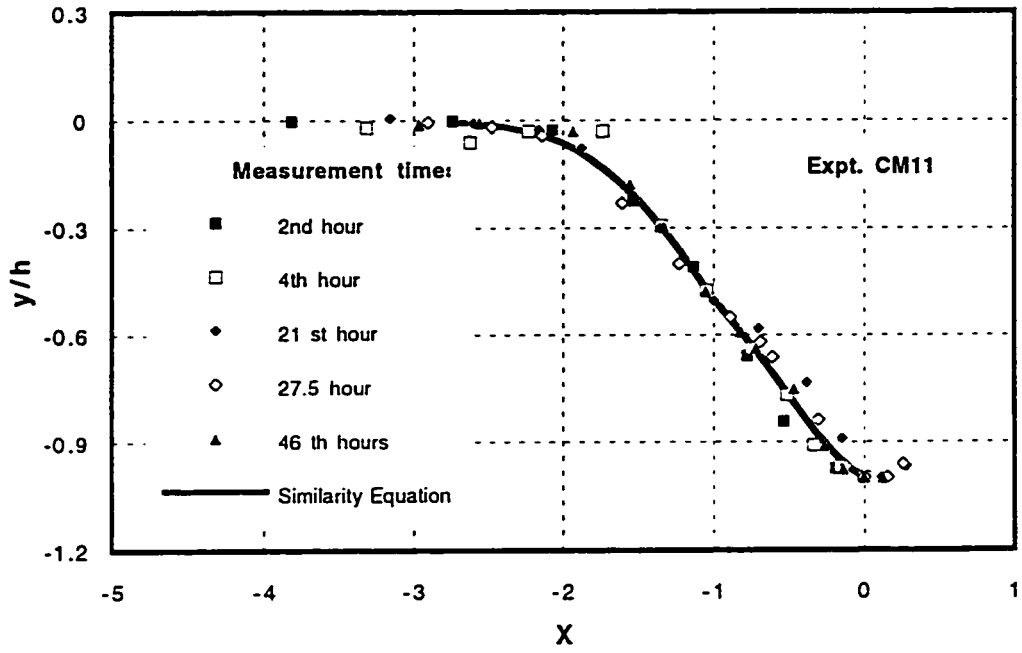
Figure 7.8 (c) Similarity Scour Profiles at the Front of the Body, (c) Expt. CM11
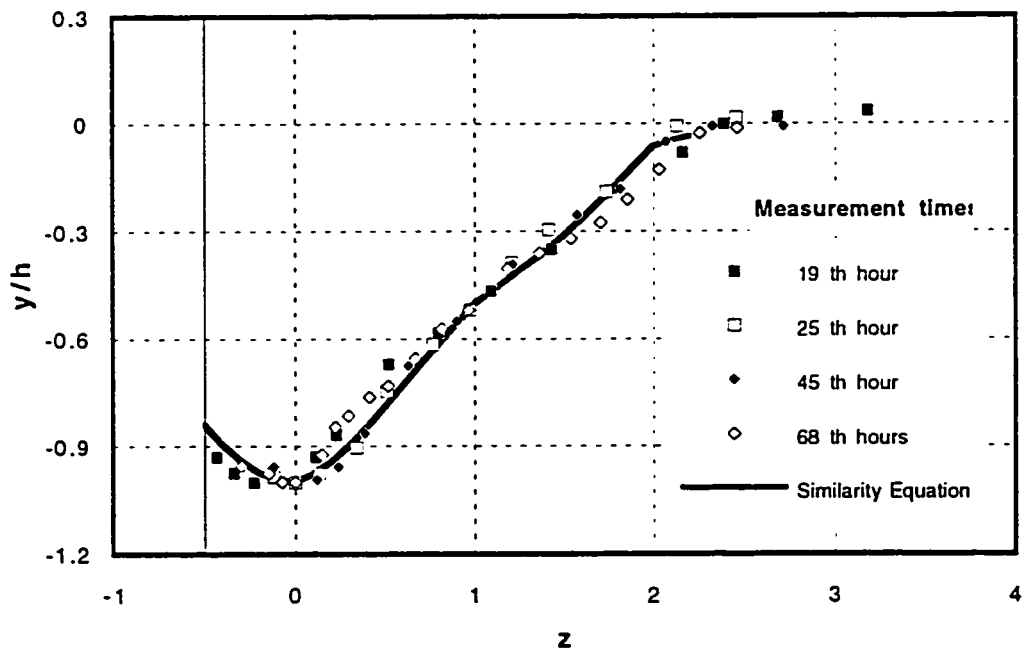
Figure 7.9 (a) Similarity Scour Profiles at the Side of the Body, (a) Expt. AM11

316
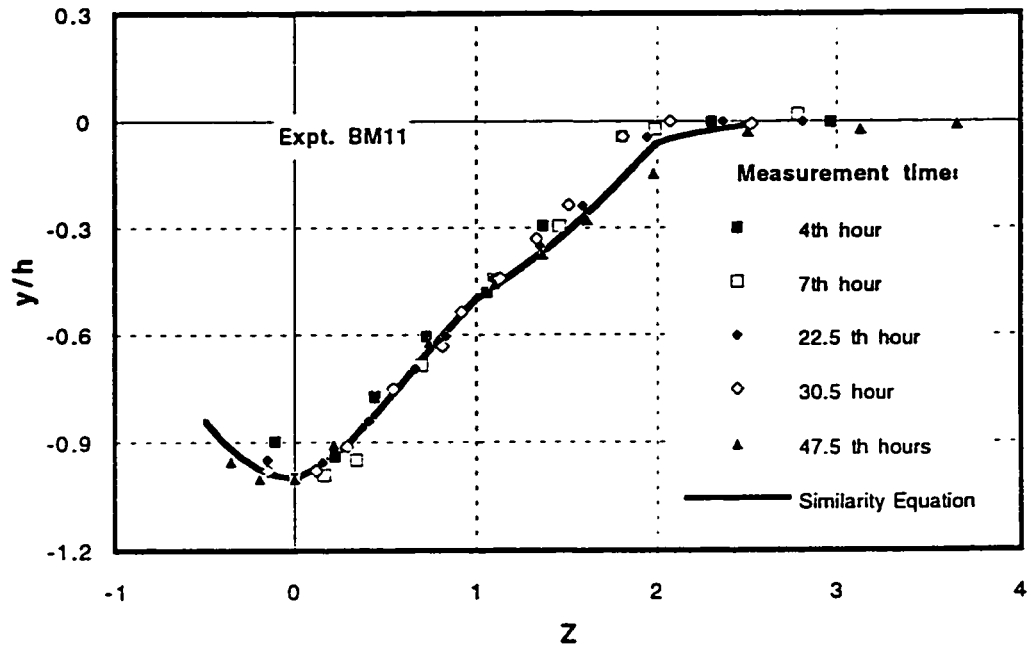
(b)
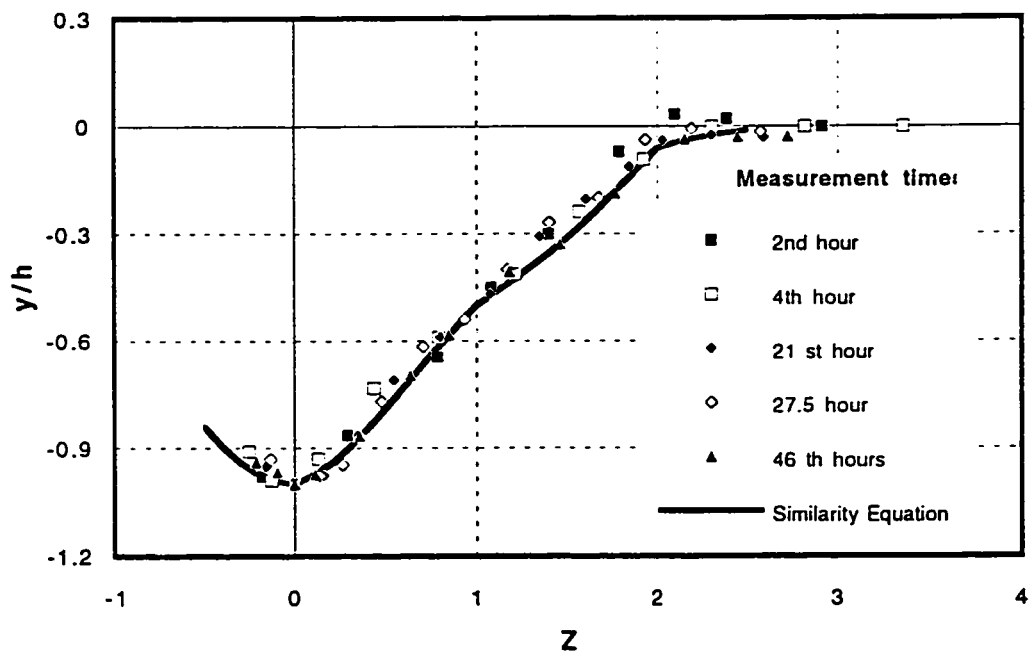
(c)

Figure 7.9 (b,c) Similarity Scour Profiles at the Side of the Body,
(b) Expt. BM11, (c) Expt. CM11

317
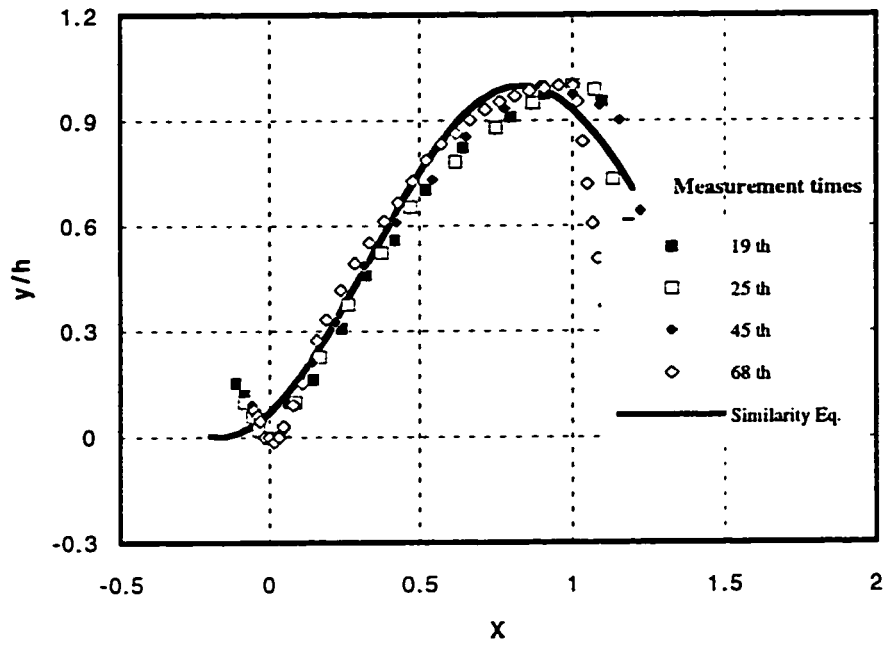
(a)
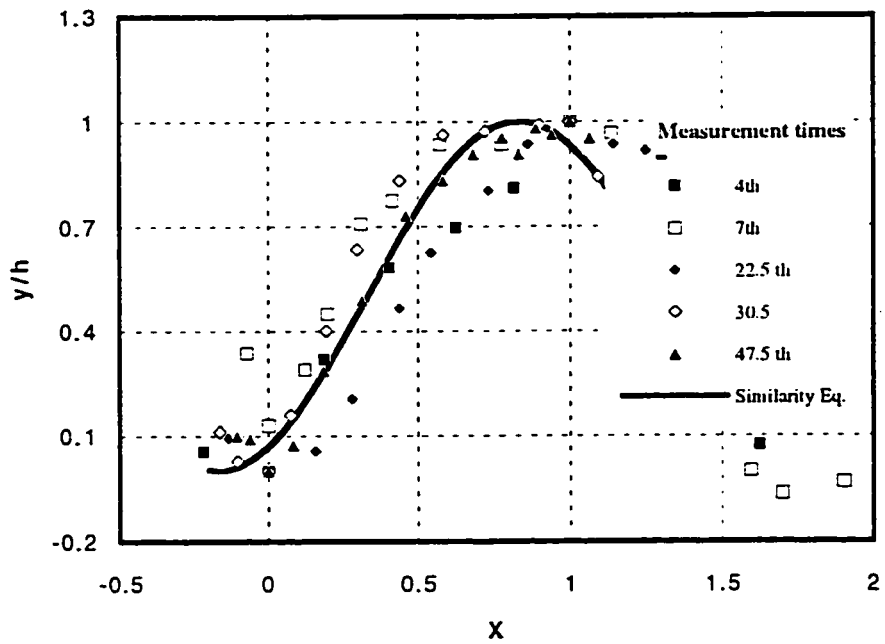
(b)

Figure 7.10 (a,b) Similarity Scour Profiles at Back of the Body,
(a) Expt. AM11, (b) Expt. BM11
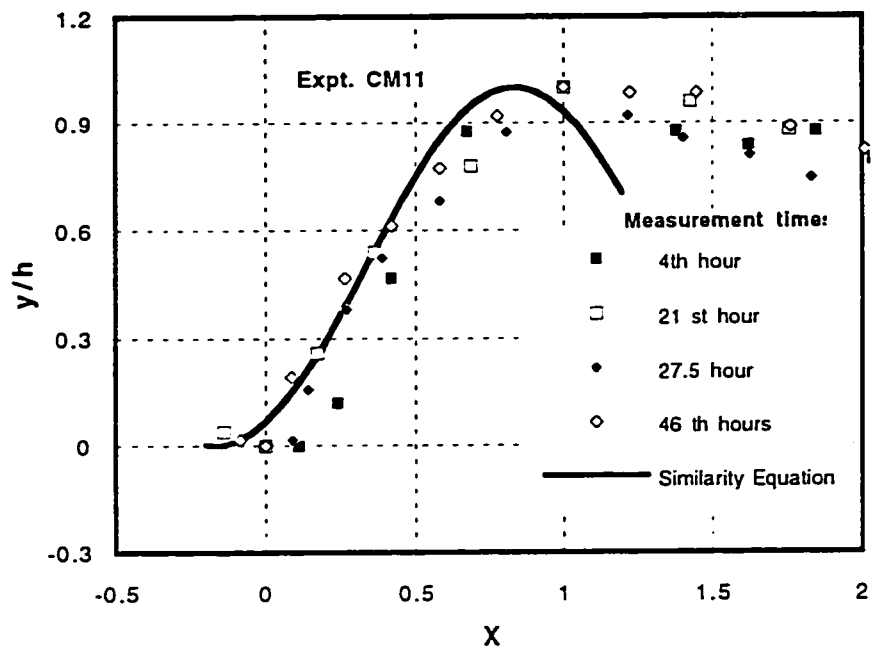
Figure 7.10 (c) Similarity Scour Profiles at the Back of the Body, (c) Expt. CM11
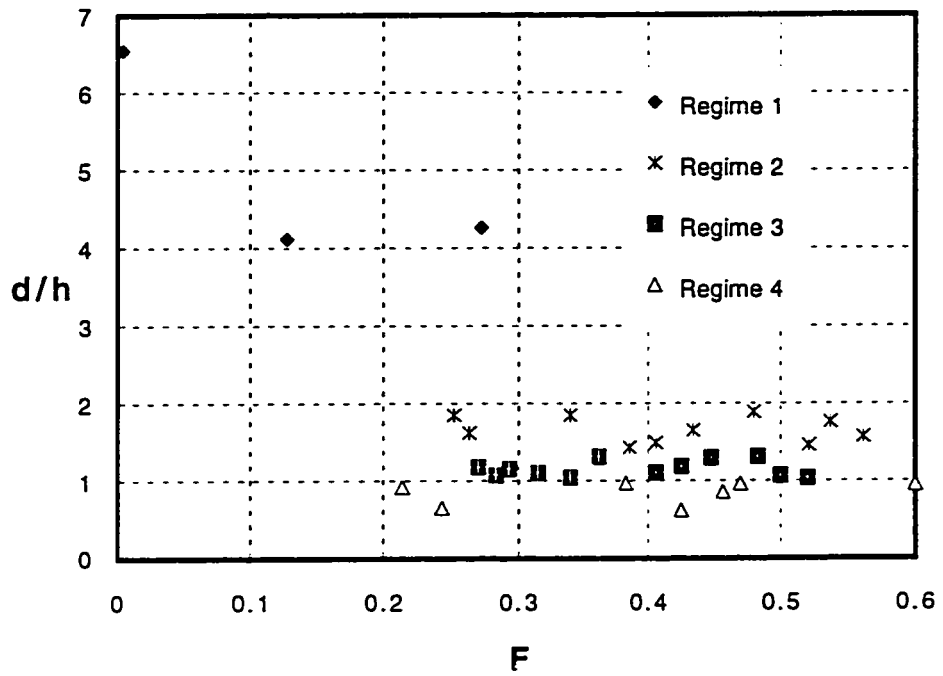
Figure 7.11. Distribution of Experiments Based on Relative depth and Froude Number
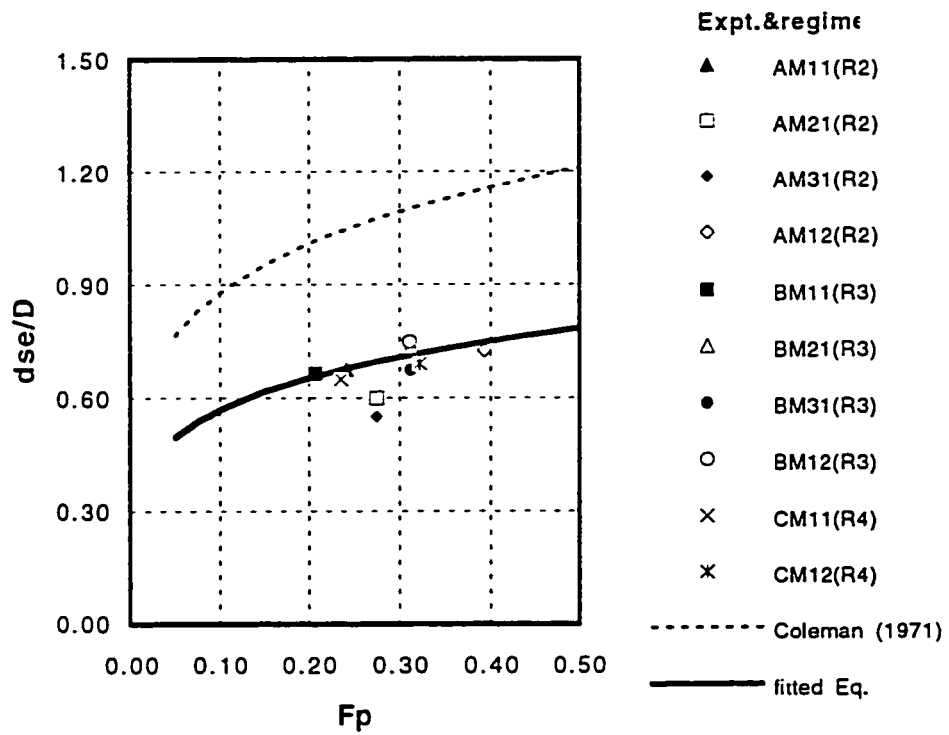
Figure 7.12. Comparison between Measured Scour Depths and Coleman's Eq.
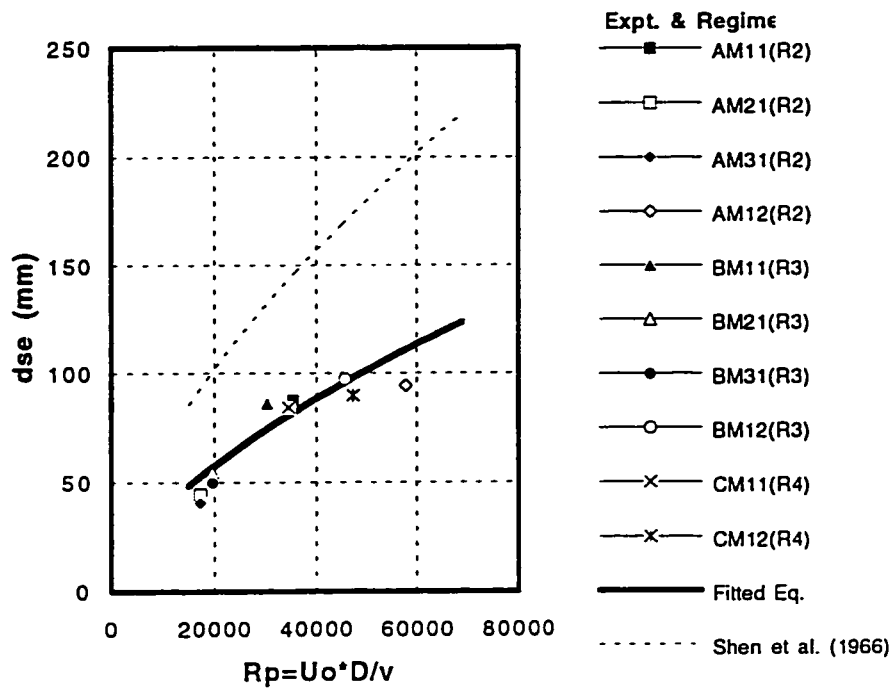
Figure 7.13. Comparison between Measured Depth of the Scour
and Shen et al.'s (1969) Eq.
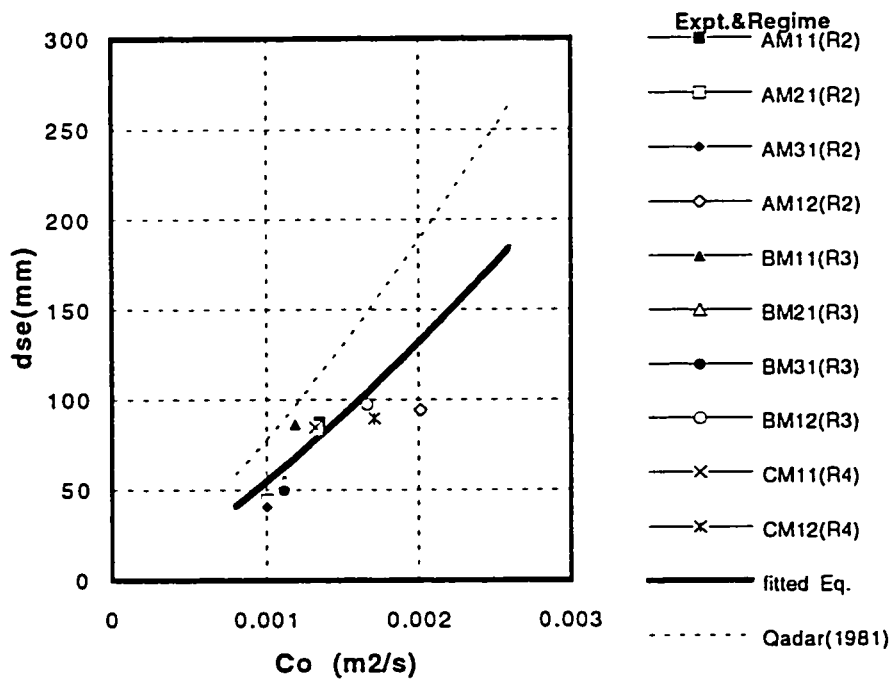
Figure 7.14. Comparison between Measured
Depth of the Scour and Qadar's (1981) Eq.
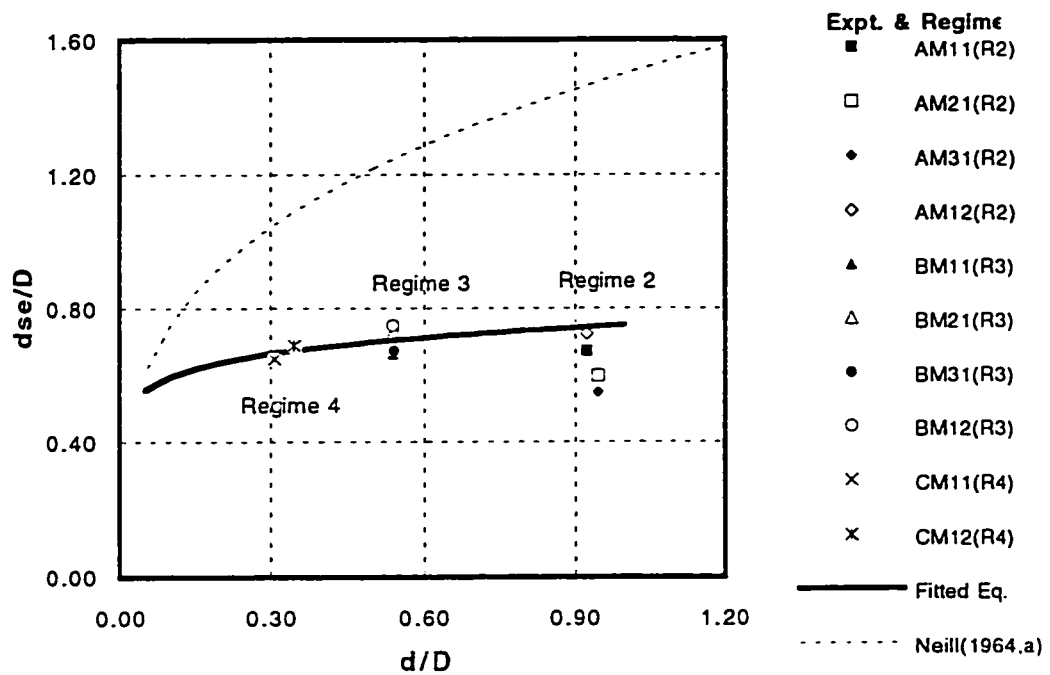
Figure 7.15. Comparison Between Measured depth of Scour and Neill's Equation

CHAPTER 8

CONCLUSIONS AND RECOMMENDATIONS

The principal focus of this study was to investigate the flow around a single obstacle, placed on both smooth and mobile beds. The scouring process in mobile beds was also studied. All measurements were analyzed and the main conclusions and recommendations are presented herein.

8.1 Smooth bed

As a result of the observations, the flow patterns around a body were divided into four regimes based on the relative depth, which is the ratio of depth of the flow d to the height of the obstacle h. Flows with relative depth greater than 4 fall into regime 1. In regime 1 the effect of the body is not felt at the surface and the top layer of the flow does not mix with the wake region. The vortex system around the body consisted of a series of horse-shoe and arch-vortices. Within the range of these experiments, there was no effect of Froude number on the flow in this regime.

For medium relative depths, $1.3 < d/h < 4$, which constitute regime 2, the upper layer would not mix with the wake region but surface waves occur. In regime 3, for $1 < d/h < 1.3$, the free shear layer causes the mixing of the whole depth of the flow. In this case, backward flow was present in the wake of the body at the surface of the flow. The backward flow region became stronger with decreasing the relative depth, causing a longer recirculation region at the surface than at the bed. While the horse-shoe vortex, HS vortex, was active, the arch-vortex was present in the upper range of relative depths and for lower relative depths its effect, if any, was restricted to a small region immediately downstream of the body. Regime 4 occurs when the relative depth is less than 1; the top of the obstacle is above the water surface and the Karman vortex street is strongly present with a strong backward flow behind the body. The arch-vortex was absent.

The effects of these regimes were found to be significant on wake geometry, the velocity field, bed shear stress and scour patterns. The width of the wake of the body in regime 3 and 4

323

was almost twice as large as that in regime 1 and 2. Higher Froude number for the same relative depth caused a stronger wake behind the body. The effect of horse-shoe vortices is present in the spanwise profiles of the velocity for depths up to half the height of the body. Due to the presence of this phenomenon, the mixing of wake flow with free stream flow was disrupted and the width of the wake became larger. The lateral velocity closer to the bed was larger in regimes 1 to 3, indicating a stronger wake at the bed, whereas in regime 4 it was larger close to the surface. This fact might be attributed to the presence of the forward flow on top of the wake in former regimes, causing weaker wake at the surface. The lateral velocity downstream of the body decreases as the Froude number increases.

The effect of HS vortices can be traced downstream of the body up to 4D in spanwise profiles of the velocity. Further downstream, they loose their identity and become part of the general turbulence in the wake. The profiles of defect velocity had two peaks in regimes 1 and 2. In regimes 3 and 4 there was only 1 peak, indicating the presence of jet-like effect of the downwash in regimes 1 and 2 or negative wake. Bed shear stress in front of the body in regime 1 and 2 was less than that in regimes 3 and 4, and the maximum shear stress occurs at the sides of the body, increasing with increase of the velocity and F, reaching values as high as 3.4 times the undisturbed shear stress. The effect of the HS vortex was more pronounced for lower Froude numbers and has almost no effects at depths more than y/h=0.5.

The wall wake downstream of the body was analyzed based on a two layer system: the outer and inner-regions. There was fair agreement between the outer region of velocity profiles and plane-wake distribution, and the law of the wall and the inner region of velocity profiles. The velocity profiles could attain similarity in the outer region at a shorter distance compared with the plane-wake due to the presence of downwash. The width of agreement between spanwise velocity profiles at different stations and depths with plane-wake theory in regime 1 and 2 was less than the diameter of the body and about 2D in regime 3 and 4. The agreement was good in regimes 3 and 4 where the effects of HS vortex and downwash were absent at further stations. Velocity recovery downstream of the body was obtained for different regimes. The velocity

recovery profiles on the plane of symmetry had two gradients in regimes 1 and 2. The gradients referred to a high mixing zone immediately downstream of the recirculation region and a mild mixing process afterward. In regimes 3 and 4, the gradient of the profiles was more indicative of a rapid recovery.

8.2 Mobile bed

In the mobile bed, there was a distinct difference between the scour patterns of regimes 1 and 2 and regimes 3 and 4. The pattern of scour and deposition in regimes 1 and 2 propagated downstream at the middle, but the side scour patterns did not. Whereas in regimes 3 and 4, in the absence of the downwash, the side scour patterns propagated while the middle one could not, creating a scour fan with two wings. For very fine sediment, even the middle pattern could proceed, creating a scour fan covered everywhere by scour holes and depositions. The width of the scour pattern in the regimes 1 and 2 was almost constant, while in the lower regimes of 3 and 4 it expanded to the sides further downstream. The scour patterns of regimes 1 and 2 were not symmetrical for larger sediment and were inclined towards one side of the flume. In regimes 3 and 4, scour patterns were symmetrical due to the probable stronger side flows, which overrides any disturbances on the bed. The wings of scour patterns were wider and deeper and expanded more in regime 4 than those in regime 3 due to the total absence of the downwash in regime 4 and its higher Froude number.

The scour patterns were found to be strongly influenced by the shape and the characteristics of the body, including the stream lining and the location of the separation of the flow. In the scour patterns of a natural rock of ellipsoid shape, the strength of the HS vortex and the separated flow was less, causing a smaller scour hole. The smaller hemisphere had a shorter downstream scour pattern due to the presence of a relatively coarser sediment and weaker effect of the body on the flow. For a cube obstacle, the difference of the two slopes in the front scour hole was pronounced, with a small flat portion in between. Due to the shape of the body, two separated flows from the sides moved parallel and were prevented by the edges from bending

towards the center, resulting in a wider scour pattern. The hemisphere on the cylinder acted similarly to a rock with a deep root in the bed and a height more than its width. Therefore, the scour at the front was similar to that for a bridge pier, due to their similarity in the downflow effects. But at the downstream of the body, the scour pattern was different due to the downwash effect. The depth of scour for cubic obstacle was much less than that of the hemisphere. The scour pattern of the cubic body was also wider and different from the hemisphere. The scour pattern of the natural rock was insignificant compared with that of the other obstacles because it was free to sink into its own scour hole.

The flow accelerated close to the bed upstream of the scour hole, rushing to the hole and departing from the scour hole in a jet-like flow close to the bed, with a high vertical velocity. Inside the scour hole, velocity was higher close to the body and the outer wall of the scour hole, and was less in larger depths, indicating less sediment transport in the deeper parts. Bed shear stress in front of the body increased with decreasing relative depth and increasing sediment size. The bed shear stress reached its maximum slightly upstream of the sides of the body at 19 times its value in undisturbed flow for regimes 3 and 4, and 6.7 times its value in regime 2. The band width of high bed shear stress in regime 3 and 4 was twice as large as that in regime 1 and 2, causing a wider scour around the body, and confirming wider observed scour patterns in these regimes. The bed shear stress for larger sediment was much more than that of the finer sediment in regime 2, but no effect of the sediment size was observed in regimes 3 and 4.

The average slope of scour profiles at the front and side of the body was equal to the natural angle of repose of the sediments. In the scour profiles at the front, there were two slopes due to the difference in the strength of HS vortices. The width and depth of the scour was almost similar for different relative depths in the front and side scour profiles, indicating the strong effect of the downflow inside the scour hole. The downflow did not affect the scour in the early stages but it became a major parameter when the flow faced the vertical wall of the cylinder on which the hemisphere was mounted. Therefore, in the equilibrium state, the shape and the depth of the scour were directly under the influence of the downflow.

The scour profiles were measured in consecutive times prior to the equilibrium. Their growth over time, especially the front and side profiles, was found to be similar. Based on these results, scour profiles of the bridge piers and the hemisphere-cylinder develop similarly, following the natural angle of repose of the bed material. The scour depths of the hemisphere-cylinders were almost half of the bridge piers' scour depth. The measured depths of the scour were compared with some of the equations developed for piers. In general it was found that these equations overestimate the scour depth for hemispheres up to 60%. After some adjustments, fair agreements could be obtained.

8.3 Recommendations

In this study, the nature of the flow and effects of the free surface on the vortex system, wake and scour of a single idealized body have been studied. Some of the parameters involved in this study, such as the effect of the shape and the ratio of h/D, roughness and Froude number, should be investigated in more detail. The four regimes proposal was based on relative depth of the flow for moderate Froude numbers. It was found that the effect of the Froude number is minor compared with that of relative depth. It would be appropriate to study more extreme Froude numbers in combination with different relative depths to verify these regimes.

Observations were made basically on very simplified bodies, such as hemispheres on smooth beds and hemisphere-cylinders on rough beds. The ratio of h/D was constant for bodies with a round and regular shape. The results of these experiments would pave the way for understanding of more complex bodies, such as natural rocks with irregular and angular bodies. In further studies, detailed observations would be necessary to investigate the effect of angular edges and irregularity of the body shape and h/D for a broader range of geometrical shapes.

In this study only two sizes of uniform sediment were used for a variety of the bed shear stress. The effect of sediment size and grading can be explained by examining a wider range of sizes and non-uniform sediments. The influence of sediment size on the depth of scour and its relation with the size of the body should be investigated. To achieve accurate predictions of

depth of scour, experiments should be carried out for several values of normalized bed shear stress $u*/u*_c$.

Some of the scour depth predictors for bridge piers were examined here for comparison purposes. More studies are needed to find a proper predictor of scour depth for different shapes and structures. This would lead us towards a simple and applicable method for design and field assessments. The sediment transport mechanism was studied in the laboratory for clear-water scour, whereas in the field, the live-bed transport is dominant for high flows and should be studied. The range of Froude numbers used in this study was such that the stability of the obstacle was not endangered. Observations in the field indicate that most of the installed rocks have been displaced during high flows. Therefore, stability of these structures needs to be studied using field data and proper laboratory equipment.

Wake of a single body provides a small refuge for fish and installation of very large rocks is expensive. For these reasons a cluster of medium sized rocks is a better choice to produce a large wake. Therefore, further investigations should be focused on different aspects of rock clusters, like their optimum spacing, size and wakes. The spacing between rocks dictates the strength and the geometry of their wakes. If the spacing is small, the wake would be stronger but smaller, and vice versa. Therefore, an optimum spacing should be determined. For rock clusters, wakes of rocks are affected by the wake of the other neighboring rocks, for a certain range of spacing. Spacing also produces a jet-like flow inside the wake downstream of the cluster. These complicating factors concerning rock clusters need further study.

REFERENCES

Achenbach, E. (1974), "Vortex Shedding from Spheres", J. Fluid Mech. 62, 209-221.

Ahmed, F. (1994), " Flow and erosion around bridge piers", Ph.D Thesis, Department of Civil Engineering, University of Alberta, Edmonton, Canada.

Baker, C. J. (1979),"The laminar horse-shoe vortex", J. Fluid Mech., Vol. 95, part 2, 347-367.

Baker, C.J. (1980), "The turbulent horse-shoe vortex", J. of Wind Engr. and Industrial Aerodynamics, 6, 9-23.

Baker, C.J. (1991), "The oscillation of horse-shoe vortex system", ASME journal of Fluids Engineering, Vol. 113, pp. 489-495.

Batchelor, G. K. (1967), *An Introduction to Fluid Dynamics*, Cambridge Univ. Press, London.

Breusers. H.N.C. and A.J. Raudkivi (1991), *Scouring*, IAHR Hydraulic structures Design Manual (2).

Breusers. H.N.C., G. Nicollet and H.W. Shen (1977), "Local scour around cylindrical piers", J. Hydr. Res. 15; 211-252.

Brown, G.L. and A. Roshko (1974), "On density effects and large structure in turbulent mixing layers", J. Fluid Mech. 64 (4), 775-816.

Cantwell, B. and D. Coles (1983), "An experimental study of entrainment and transport in the turbulent near wake of a circular cylinder", J. Fluid Mech. 136, 321-374.

Carmody, T. (1964), "Establishment of the wake behind a disk", Journal of Basic engineering, ASME, pp. 869-882

Chevray, R. (1968), "The turbulent wake of a body of revolution", Journal of Basic engineering, ASME.

Coles, D. (1956), "The law of the wake in the turbulent boundary layer", J. Fluid mech., 1: 191-226.

Cooper, R. D. and M. Lutzky (1955), "Exploratory investigation of the turbulent wakes behind bluff bodies", Department of the Navy, report 963, October.

Cullen, R.T. (1991), "Vortex mechanisms of local scour at model fish rocks", American Fisheries Society Symposium, 10:213-218.

Eckerel, W. A., and J.K. Awad (1991), "Effect of free stream velocity on the three-dimensional separated flow region in front of a cylinder", ASME Journal of Fluids Engineering, Vol. 113, 00. 37-44.

Ettema, R. (1980), "Scour at bridge piers", Univ. of Auckland, N.Z., School of Engineering, Rep. No. 216.

Fackrell, J. E., and J.E. Pearce (1981), "Parameters affecting dispersion in the near wake of buldings", CEGB Report No. RD/M/1179/N81.

Fisher, A.C., and P.C. Klingeman (1984), "Local scour at fish rocks", pp. 286-290, D.J. Schreiber, editor. "Water for resource development". Proceedings of the Conference. American Society of Civil Engineers, Hydraulics Division, Inland Empire Section, Coeur d'Alene, Idaho.

Foppl, L. (1913), "Wirbelbewegung hinter einem Kreiszylinder", Sitzber. bayer. Akad. Wiss. Munchen Mathphys. Klasse, 1-17.

Gerrard, J. H. (1966), "The mechanics of the Formation Region of Vortices behind Bluff Bodies", J. Fluid Mech. 25, 401-413.

Goldburg, A. and B.H. Florsheim (1966), "Transition and Strouhal Number for the Incompressible Wake of Various Bodies", Phys.Fluids 9, 45-50.

Hall, A. A. and G. S. Hislop (1938), "Velocity and temperature distributions in the turbulent wake behind a heated body of revolution", Proc. Cambridge Phil. Soc. 34, pp 48-67.

Houghton, E.L. and N.B. Carruthers (1976), *Wind forces on buldings and structures: an introduction* , Edvard Arnold.

Hunt, J. C. R. (1971), "The effect of single buildings and structures" Philos. Transaction Records, Soc. London A 269, 457-467.

Hunt, J.C.R., C. J. Abell, J.A. Peterka, and H.Woo (1978), "Kinematical studies of the flows around free or surface-mounted obstacles, applying topology to flow visualization", J.Fluid Mech. Vol. 86, pp.179-200.

Jarret,Robert (1984,) "Hydraulics of high gradient streams", ASCE, Journal of Hydraulics Engineering, 110(11), pp. 1519-1539.

Kelmin, A., E. B. Schaefer and J.G. Beere, (1939), "Aerodynamics of the perisphere and trylon at world's fair", Trans.Am . Soc.Civ. Eng. 2042, 1449-1472.

Keulegan, G.H. (1938), " Laws of turbulent flow in open-channels", Journal of research. national Bureau of standards, 121.

Kourta, A., H.C. Boisson, P. Chassaing and H. Ha Minh (1987), "Nonlinear interaction and the transition to tourbulence in the wake of a circular cylinder", J. Fluid Mech. 181,141-161.

Kuchemann, D. (1965), "Report on the I.U.T.A.M symposium on concentrated vortex motion in fluids", J. Fluid Mech. 21, 1-20.

Lamb, H. (1945), "Hydrodynamics", 6th ed., Dover, New York.

Larousse, A., R. Martinuzzi, and C. Tropea (1991), "Flow around surface-mounted, three-dimensional obstacles", Turbulent Shear flows (8) ; Selected Papers from the Eighth Int. Sym. on Turbulent Shear Flows, Munich, Germany, Sept. 9-11, 1991, Edited by F. Durst et al., Spring Verlag.

Logan, E., and S.H. Lin, (1982), "Wakes from arrays of buildings", NASA Cr-170666.

Magarvey, R.H. and R.L. Bishop, (1961 a), "Wakes in Liquid-Liquid Systems", Phys. Fluids 4, 800-805.

Martinuzzi, R. and C. Tropea (1993), "The flow around surface mounted, prismatic obstacles placed in a fully developed channel flow", J. of Fluids Engineering, Vol. 115, pp. 85-92.

Mohanty,Pasanta K. and Peterson, Dean F. (1959), "Flume studies of flow in steep, rough open channels", ASCE, Hydraulics Division Transactions, Fort Collins, Colorado. 34p.

Moller,W. (1938), "Experimentelle Untersuchungen zur Hydrodynamik der Kugel". Physik. Zeit.39,57-80.

Nezu, I. and H. Nakagawa (1993), Turbulence open-channel flows, IAHR monograph series, A.A Balkema publishers.

Nezu, I. and W. Rodi (1986), "Open-channel flow measurements with a lased doppler anemometer", J. hydraulic Eng., ASCE, 112: 335-355.

Okamoto, T., Yagita, M. (1973), "The experimental investigation on the flow past a circular cylinder of finite length", Bull. Jpn. Soc. Mech. Eng. 16, 805-814.

Okamoto, S. (1980), "Turbulent shear flow behind a sphere placed on a plane boundary". in: Turbulent Shear Flows 2, ed. by L.J.S. Bradbury, F. Durst, B.E. Launder, F.W. Schmidt, and J.H. Whitelaw (Springer,Berlin Heidelberg New York) 246-256.

Okamoto, S. (1979), "Turbulent shear flow behind hemisphere-cylinder placed on ground plane", in: Turbulent Shear Flows 2, ed. by L.J.S. Bradbury, F. Durst, B.E. Launder, F.W. Schmidt, and J.H. Whitelaw (Springer, Berlin Heidelberg New York) 171-185.

Okamoto, T., M. Yagita and S. Kataoka (1977), "Flow past cone placed on flat plate", Bull. Jpn. Soc. Mech. Eng. 20,329-336.

Perry, A.E., M.S. Chong and T.T. Lim (1982), "The Vortex-Shedding Process behind Two-Dimensional Bluff Bodies", J.Fluid Mech. 116, 77-90.

Peterka, J. A. and J.E. Cermak (1977), "Turbulence in building wakes ", Proc. 4th Int. Conf. on Wind Effects on Building and Structures, 447-463.

Prantl, L. (1925), " Uberdie ausgebildete turbulenz", ZAMM, 5:136.

Raudkivi, A.J. and R. Ettema (1977 a.), "Effect of sediment gradation on clear-water scour and measurement of scour depth", Proc. 17th congress IAHR, Baden-Baden 4; 521-527.

Raudkivi, A.J. and R. Ettema (1977 b.), "Effect of sediment gradation on clear-water scour", Proc. ASCE 103 (HY10); 1209-1213.

Rimon, Y. and S. I. Cheng (1969), "Numerical Solution of a Uniform Flow over a Sphere at Intermediate Reynolds Numbers", Phys.Fluids 12, 949-959.

Rosenhead, L. (1953), "Vortex Systems in Wakes", in Advances in Applied mechanics (R.von Mises and T. von Karman, eds.), Vol. III, pp. 185-195, Academic Press, New York.

Saffman, P. (1993),*Vortex Dynamics*, Cambridge University Press.

Sakamoto, H., Haniu, H. (1990), "A study on vortex shedding from spheres in a uniform flow", J. Fluids Engr. ,Vol. 112, 386-392.

Schlichting, H. (1936), "Experimentelle Untersuchungen zum Rauhigkeitsproblem", Ing. Arch. 7, 1-34.

Scofield, W.H. and E. Logan (1990,) "Turbulent shear flow over surface mounted obstacles", ASME journal of Fluids Engineering, Vol. 112,pp. 376-385.

Schwind, R. (1962), "The three-dimensional boundary layer near a strut", Gas Turbine Lab. Rep., MIT.

Townsend, A.A. (1956-a), *The structure of turbulent shear flow*, Cambridge University Press, 1956.

Tsuchiya, K. (1987), "Wake Dynamics behind a Single Gas Bubble in a liquid and Liquid-Solid Fluidized Media", Ph.D. Dissertation, Ohio State Univ., Columbus, OH.

Tsuchiya, K and L.S. Fan (1986), "Near-wake structure of a single gas bubble in a two-dimensional liquid-solid fluidized bed: Vortex shedding and wake size variation," Chem. Eng. Sci. 43, 1167-1181; Paper (10b) presented at AIChE Ann. Mtg, Miami Beach , FL, Nov.2-7(1986).

van Driest, E.R. (1956), "on turbulent flow near a wall", J. Aeron. sci., 23: 1007-1011.

von Ka'rma'n, T. (1911), "Uber den Mechanismus des Widerstandes, den ein bewegeter korper in einer Flussigkeit erfahrt", Nachr. Ges. Wiss. Gottingen, Math. Phys. Klasse, 509-517

von Ka'rma'n, T. (1912), "Uber den Mechanismus des Widerstandes, den ein bewegeter korper in einer Flussigkeit erfahrt", Nachr. Ges. Wiss. Gottingen, Math. Phys. Klasse, 547-556

Winant, C.D. and F.K. Browand (1974), "Vortex pairing: the mechanism of turbulent mixing layer growth at moderate reynolds number", J. Fluid Mech. 63, 237-255.

APPENDIX

A.1 Prediction of Scour Depth

Investigations about scour around a free-ended obstacle are limited in number and scope, but there is a great deal of information concerning scour around bridge piers. Most of the characteristics of flow around bridge piers and wall mounted obstacles are similar, which makes it reasonable to study the research on piers to understand flow in a less complex environment.

Most of the research in this area is concentrated on the predicting the maximum scour depth that can occur at a bridge site or equilibrium scour depth d_{se} for different hydraulic conditions. As is discussed earlier, scour can occur in a live-bed scour in which there is a bed load transport upstream of the bridge where sediments can be transported to the scour hole. Clear-water scour would occur when there is no bed load transport present in the approaching flow.

Ahmed (1994) reviewed available methods for prediction of the scour depth and, based on the approach and concepts behind their derivations, some of the methods are adopted here.

A.2 Different Approaches

Empirical formulas relate the scour depth to pier geometry and other flow characteristics based on laboratory and field data. Neill (1964 a,b), using Live-bed data from Laursen and Toch (1956), provided a fitted equation to relate the scour depth d_{se} and depth of approach flow y_0 using the pier width b as normalizing factor:

$$\frac{d_{se}}{b} = 1.5\left(\frac{y_0}{b}\right)^{0.3} \qquad (A.1)$$

This equation describes the data well for velocities of 0.3 to 0.61 m/s and flow depth of 60-275 mm with sand size of 0.44-2.25 mm. They used a multiplying factor for taking to account the effect of pier shape and alignment on the scour.

Coleman (1971) correlated the d_{se} to the Froude number defining a parameter as scour Euler number :

$$\frac{U_0}{\sqrt{2gd_{se}}} = 0.6\left(\frac{U_0}{\sqrt{gb}}\right)^{0.9} \qquad (A.2)$$

where pier Froude number is defined as $F_p = \frac{U_0}{\sqrt{gb}}$ and scour Euler number as $\frac{U_0}{\sqrt{2gd_{se}}}$.

Shen et al. (1969), using other data, reduced this equation to the following form, which is not suitable for large piers (0.91 m diameter tested by Shen et al., 1969):

$$\frac{d_{se}}{b} = 1.39\left(F_p\right)^{0.2} \qquad (A.3)$$

In a different approach the regime theory has been employed to predict the depth of scour in terms of regime depth which is proportional to the 2/3 power of unit discharge. This theory was originated from observations of many stable alluvial irrigation canals in India by correlating different flow characteristics. Inglis (1949) related the total scour depth D_{se}, $d_{se}=y_0$, to the unit discharge, q, and pier width, b as :

$$\frac{D_{se}}{b} = 2.32\left[\frac{q^{2/3}}{b}\right]^{0.78} \qquad (A.4)$$

The Inglis-Lacy equation, as another regime equation based on prototype data from 17 bridges in India, predicts the scour depth as twice the Lacy's regime depth:

$$D_s = 2 \times 1.55 \left[\frac{Q}{f} \right]^{1/3} \qquad \text{(A.5)}$$

where Q is the total discharge in m³/s and f is the silt factor as $f = 1.76\sqrt{D}$. Blench (1962) based on regime depth of y_r for rectangular rounded nose piers, proposed the following equation :

$$\frac{D_{se}}{y_r} = 1.8 \left[\frac{b}{y_r} \right]^{1/4} \qquad \text{(A.6)}$$

where $y_r = 1.48 \left(q^2 / F_b \right)^{1/3}$ and the bed factor, $F_b = 1.9\sqrt{D}$.

Ahmad (1962) proposed the following simple equation:

$$D_{se} = Kq^{3/2} \qquad \text{(A.7)}$$

where K is a multi-characteristics coefficient in the range of 1.7 to 2 for normal rivers, with higher values for severe flow curvature. This coefficient is a function of boundary geometry, pier shape, bed material and velocity distribution.

Arunachalam (1965) linked two classes of equations (regime theory and Laursen) where, in the first, the total depth is a function of discharge, and in the second, the scour depth is related to pier geometry and flow depth. Based on his argument the scour depth depends only on flow depth, which in turn depends only on discharge or velocity. This means that the effect of velocity on the scour depth would be through flow depth only. He proposed his modified equation for rectangular piers under live-bed conditions as:

$$\frac{d_s}{y_o} = 1.95 \left[\frac{b}{y_o} \right]^{1/6} - 1 \qquad \text{(A.8)}$$

where $y_o = 4.39\left(q^2 / f\right)^{1/3}$, and the silt factor, $f = 1.76\sqrt{D}$.

In considering a rational basis for solving this problem, numerous researchers have tried to predict the scour depth, each in a different way. Laursen (1960) considered the bridge pier as a special case of long contraction in a river with a very short contraction length, and modified the equation in this regard. He proposed the following equation for live-bed conditions at a value of m=11.5, which fits the best for data:

$$\frac{b}{y_o} = 5.5 \frac{d_s}{y_o} \left[\left(\frac{1}{m} \frac{d_s}{y_o} + 1 \right)^{1.7} - 1 \right] \qquad \text{(A.9)}$$

which later on was simplified by Melvile (1975) to :

$$\frac{d_s}{b} = \sqrt{0.107 m \left(\frac{y_o}{b} \right)} \qquad \text{(A.10)}$$

Laursen (1963) assumed that the bed shear stress is equal to the critical stress in scoured area at the equilibrium stage and proposed the following equation :

$$\frac{b}{y_o} = 5.5 \frac{d_s}{y_o} \left[\frac{\left(\frac{1}{m} \frac{d_s}{y_o} + 1 \right)^{7/6}}{\left(\frac{\tau_o}{\tau_c} \right)^{1/2}} - 1 \right] \qquad \text{(A.11)}$$

Carstens (1966) hypothesized that the sediment transport rate could be functionally related to the forces acting on a particle and the geometry of scour hole.

Then, based on similarity principles for different types of local scour and assuming that shape of the scour hole would be an inverted frustum of a cone all the times, he derived the following equation analytically for live-bed conditions :

$$\frac{d_{se}}{b} = 0.546 \left[\frac{N^2 - 1.64}{N^2 - 5.02} \right]^{5/6} \qquad (A.12)$$

where the sediment number is $N = U_0 / \sqrt{(S_s - 1)gD}$. For clear-water conditions the scouring process was not terminated based on his analysis.

Shen et al. (1966) proposed that scour depth depends on the strength of the horse shoe vortex system and, in turn, circulation. They related the circulation at the front of the pier with the bU_0 which makes it a function of the pier Reynolds number, $R_p = bU_0/v$. Based on regression analysis of data the following correlation for d_{se} was established:

$$d_{se} = 0.0588 \left[R_p \right]^{0.512} \qquad (A.13)$$

where d_{se} is in mm. For design purposes this equation is approximated as :

$$\frac{d_{se}}{y_0} = 2 \left[F^2 \left(\frac{b}{y_0} \right)^3 \right]^{0.215} \qquad (A.14)$$

Shen et al. (1969) presented this equation in an enveloping form as :

$$d_{se} = 0.2225 \left[R_p \right]^{0.619} \qquad (A.15)$$

Qadar (1981) conducted a series of laboratory and field experiments and found that the scour depth in front of the bridge pier is related to the strength of the HS-vortex,

339

which is known as basic mechanism of the scour. In his laboratory experiments he used three sizes of wooden blocks of 0.025m, 0.05m and 0.075m and three sizes of sediments: 0.17 mm, 0.7 mm, and 1.5 mm. The HS-vortex develops a scour hole in the bed and gradually sinks into the hole while expanding its size. He found that the radius of the HS-vortex is almost 0.1 times the width of the pier. By measuring the velocity of the vortex at its perimeter he also showed that the vortex velocity decreases by width of the pier. Considering several sets of data he proposed that the maximum depth of scour is a function of the strength of HS-vortex :

$$d_s = K_s (C_o)^n \qquad (A.16)$$

where d_s is the maximum scour depth below the original bed level, C_o is the initial strength of the vortex calculated as product of vortex velocity and its radius, n is an exponent experimentally found to be equal to 1.28, and K_s is the coefficient of sediment size with a value of 538 for sediments of diameter less than 0.5 mm. The coefficient and exponent were different for coarser sediments. Based on his results, he proposed that the sediment size is just as important at the initial stages of the scouring process and that for sediment less than 0.5 mm in diameter, the final scour depth depends only on the sediment transport capacity of the vortex.

Baker (1980) assumed that the circulation of the vortex core would be constant even in the scour hole. He calculated the velocity of the vortex in terms of the approach flow and related it to the forces on a particle on the scour hole sloped wall, which resulted in the following equation for clear water :

$$\frac{d_s}{b} = (a_1 N - a_2) \tanh\left(a_3 \frac{y_o}{b}\right) \qquad (A.17)$$

340

where $N = U_o / \sqrt{(S_s - 1)gD}$, $a_1 = 4/N_c$, $a_2 = 2$, $a_3 = 1$, and N_c is the value of N when general sediment motion begins.

Despite all efforts to predict the scour depth, there is still no acceptable prediction procedure, so some researchers, instead of studying the mechanism of flow and scour around the pier, have tried to solve this problem based on data correlation and regression analysis. Chitale (1962) in this way correlated the scour depth to Froude number, $F = U_o / \sqrt{gy_o}$, for $F < 0.5$ and proposed following equation:

$$\frac{d_{se}}{y_o} = -0.51 + 6.65F - 5.49F^2 \qquad (A.18)$$

For higher flow regimes, $0.5 < F < 1.5$, Jain and Fisher (1980), with a multiple linear regression analysis on their data for live bed conditions, provided the following equation:

$$\frac{d_{se}}{b} = 1.86\left(\frac{y_o}{b}\right)^{0.5} (F - F_c)^{0.25} \qquad (A.19)$$

where F_c ($= U_{oc} / \sqrt{gy_o}$) as a critical Froude number represents the critical condition of sand movement. For clear-water conditions and for a maximum scour at $F \approx F_c$ Jain(1981), by neglecting F, prescribed the following equation based on a regression analysis:

$$\frac{d_{se}}{b} = 1.41\left(\frac{y_o}{b}\right)^{0.3} (F_c)^{0.25} \qquad (A.20)$$

Kothayari et al. (1992a) assumed that for clear-water conditions, shear stress responsible for scour is proportional to the critical value of approach velocity, U_{oc}. By

regression analysis he found the following equation for the velocities higher than the critical one:

$$\frac{d_{se}}{b} = 0.66\left(\frac{b}{D_{50}}\right)^{-0.25}\left(\frac{y_o}{D_{50}}\right)^{0.16}\left(\frac{U_o^2 - U_{oc}^2}{\frac{\rho_s - \rho}{\rho}gD_{50}}\right)^{0.4} a_c^{-0.3} \quad \text{(A.21)}$$

where a_c is the contraction ratio and critical velocity as:

$$\frac{U_{oc}^2}{\frac{\rho_s - \rho}{\rho}gD_{50}} = 1.22\left(\frac{b}{D_{50}}\right)^{-0.11}\left(\frac{y_o}{D_{50}}\right)^{0.16} \quad \text{(A.22)}$$

Kothayari et al. (1992b) found the following relation for the live-bed condition :

$$\frac{d_{se}}{b} = 0.99\left(\frac{b}{D_{50}}\right)^{0.67}\left(\frac{y_o}{D_{50}}\right)^{0.4} a_c^{-0.3} \quad \text{(A.23)}$$

For measured field data at the time of high floods, Froehlich (1988) found the following equation, based on regression analysis, for live-bed conditions :

$$\frac{d_{se}}{b} = 0.32f\langle shape\rangle\left(\frac{b'}{b}\right)^{0.62}\left(\frac{y_o}{b}\right)^{0.46}F^{0.2}\left(\frac{b}{D_{50}}\right)^{0.08} \quad \text{(A.24)}$$

where $f = 1$ for round-nosed, and 1.3 for square-nosed and 0.7 for sharp-nosed piers ; b' $(= b\cos\alpha + l\sin\alpha)$ is the pier width projected normal to the approach flow.